

JEAN-LUC GENNISSON
UNIVERSITE PARIS VI – PIERRE ET MARIE CURIE
Institut Langevin – Ondes et Images
CNRS UMR 7587
ESPCI ParisTech

HABILITATION A DIRIGER DES RECHERCHES

Elastographie par ondes de cisaillement

Présentée le 10 Juin 2013 devant le jury composé de

Dr. Damien Garcia	Rapporteur
Pr. Michel Campillo	Rapporteur
Dr. Cyril Lafon	Rapporteur
Dr. Sébastien Manneville	Examineur
Pr. Olivier Lucidarme	Examineur
Dr. Mickaël Tanter	Examineur
Pr. Mathias Fink	Examineur



Institut Langevin
ONDES ET IMAGES



INDEX

I. NOTICE BIBLIOGRAPHIQUE	5
I.1. CURRICULUM VITAE.	5
I.2. PUBLICATIONS SCIENTIFIQUES	6
a. Articles internationaux avec comité de lecture	6
b. Articles de congrès internationaux	10
c. Congrès internationaux	12
I.3. VALORISATION, DIFFUSION DE LA RECHERCHE, ENSEIGNEMENT	15
a. Brevets déposés	15
b. Organisation d'écoles thématiques	16
c. Séminaires & Conférences invitées	17
d. Enseignement	17
e. Participation à des contrats de recherche	17
f. Autres activités scientifiques	18
I.4. ACTIVITES D'ENCADREMENT	19
II. MEMOIRE	21
II.1. INTRODUCTION	21
II.2. CHAPITRE 1 : ELASTOGRAPHIE	23
II.3. CHAPITRE 3 : ANISOTROPIE ELASTIQUE	44
II.4. CHAPITRE 4 : NONLINEARITE ELASTIQUE	50
II.5. CHAPITRE 5 : VISCOELASTICITE	55
III. COLLABORATIONS	60

IV. PERSPECTIVES	61
V. REFERENCES DU MEMOIRE	63
VI. PUBLICATIONS	64

I. NOTICE BIBLIOGRAPHIQUE

I.1. CURRICULUM VITAE

Etat Civil Jean-Luc Gennisson
 23 Bis, rue de Puiseux
 95000 CERGY
 Tél: 0611898100
 Nationalité Française
 Né le 27/06/1974
 Email: jl.gennisson@espci.fr
 Web: <http://www.institut-langevin.espci.fr/Jean-Luc-Gennisson>



Quelques étapes

CR1 CNRS *Institut Langevin – Ondes et Images, ESPCI, France*

Depuis Oct. 2005

- Techniques d'élastographie transitoire 1D, 2D & 3D et Supersonic Shear Imaging
- Etude de l'anisotropie en élastographie
- Acoustoélasticité et non linéarité de cisaillement
- Viscosité de cisaillement et dispersion

Post-Doctorat *Laboratoire de Biorhéologie et d'Ultrasonographie Médicale, Université de Montréal, Canada*

Oct. 2003-Oct. 2005

- « Etude de la coagulation sanguine et caractérisation de plaques vasculaires par élastographie impulsionnelle »

Thèse de doctorat *Laboratoire Ondes et Acoustique, ESPCI, France*

Sep. 2000-Sep. 2003

- « Le palpeur acoustique : un nouvel outil d'instrumentation des tissus biologiques »

Thèse de l'université de Paris VI sous la direction de Mathias Fink
Mention très honorable

DEA *Université Paris VI, Spécialité Electronique*

Sep. 1999-Sep. 2000

- Stage 8 mois : « Mise au point d'une sonde ultrasonore appliqué à la mesure d'élasticité de la peau. », Laboratoire Ondes et Acoustique, ESPCI, France.

Mention Assez Bien

Maîtrise Physique et *Université Paris VI*

Applications

Jun 1999

- Stage 4 mois: « Réparation de structure métallique par collage de matériau composite sous induction », LISIF, Université Paris VI, France.

License Physique et *Université Paris VI*

Applications

Jun 1998

DEUG MIAS *Université de Cergy-Pontoise*

Sep. 1997

- Stage 3 mois: « Elaboration d'une chambre à vide pour l'étude du rayonnement ionisant d'un plasma. », Ecole Polytechnique,

Palaiseau, France.

Publications et Brevets

Publications

- 53 Articles dans des revues internationales à comité de lecture (publiés, acceptés et soumis)
- 31 Communications à des conférences avec actes
- 5 Conférences et séminaires invités

Brevets - 5 Brevets dont 3 par le CNRS

I.2. PUBLICATIONS SCIENTIFIQUES

a. Articles internationaux avec comité de lecture

[1] "Transient elastography in anisotropic medium: Application to the measurement of slow and fast shear waves velocities in muscles." **J.L. Gennisson**, S. Catheline, S. Chaffai et M. Fink. *J. Acoust. Soc. Am.*, 114 (1), pp. 536-541, 2003.

[2] "Assessment of elastic parameters of human skin using dynamic elastography." **J.L. Gennisson**, T. Baldeweck, M. Tanter, S. Catheline, M. Fink, L. Sandrin, C. Cornillon et B. Querleux. *IEEE Trans. Ultrason., Ferroelec., Freq. Contr.*, 51 (8), pp. 980-989, 2004.

[3] "Human muscle hardness assessment during incremental isometric contraction using transient elastography." **J.L. Gennisson**, C. Cornu, S. Catheline, M. Fink et P. Portero. *J. Biomechanics*, 38 (7), pp. 1543-1550, 2005.

[4] "Sol-gel transition in agar-gelatin mixtures with transient elastography." **J.L. Gennisson** et G. Cloutier. *IEEE Trans. Ultrason., Ferroelec., Freq. Contr.*, 53 (4), pp. 716-723, 2006.

[5] "Transient elastography: a new method to assess viscoelastic properties of blood during coagulation." **J.L. Gennisson**, S. Lerouge et G. Cloutier. *Ultr. Med. & Bio.*, 32 (10), pp. 1529-1537, 2006.

[6] "Acoustoelasticity in soft solids: assessment of the nonlinear shear modulus with the acoustic radiation force." **J.L. Gennisson**, M. Rénier, S. Catheline, C. Barrière, J. Bercoff, M. Tanter et M. Fink. *J. Acoust. Soc. Am.*, 122 (6), pp.3211-3219, 2007.

[7] "Viscoelastic and anisotropic mechanical properties of in vivo muscle tissue assessed by Supersonic Shear Imaging." **J.L. Gennisson**, T. Deffieux, E. Macé, G. Montaldo, M. Fink et M. Tanter. *Ultr. Med. & Bio.*, 36 (5), pp.789-801,2010.

[8] "Supersonic Shear Wave Elastography of in vivo pig kidney: Influence of blood pressure, urinary pressure and tissue anisotropy." **J.L. Gennisson**, N. Grenier, C. Combe et M. Tanter. *Ultr. Med. & Bio.*, 38(9), pp. 1559-1567, 2012.

[9] "Quantification of elasticity changes in the myometrium during labour using Shear Wave Elastography: a pilot study." **J.L. Gennisson**, P. Gabor, M. Muller, V. Kohl, A. Benachi, R. Frydman, D. Musset, M. Tanter, O. Ami. *Soumis pour publication dans Ultr. Med. & Bio.*,2013.

- [10] "Elastographie ultrasonore : principes et procédés." **J.L. Gennisson**, T. Deffieux, M. Fink, M. Tanter. *Accepté pour publication dans* J. Radiologie, 2013.
- [11] "Ultrasound elastography: principles and techniques." **J.L. Gennisson**, T. Deffieux, M. Fink, M. Tanter. *Accepté pour publication dans* Diag. Interv. Im., 2013.
- [12] "Renal elastography." N. Grenier, **J.L. Gennisson**, F. Cornelis, Y. Le Bras, L. Couzi. *Accepté pour publication dans* J. Radiologie, 2013.
- [13] "A 3D ultrasound elastography system for breast in vivo breast cancer examination." H. Latorre-Ossa, **J.L. Gennisson**, A. Tardivon, M. Tanter et A. Athanasiou. *Soumis pour publication dans* J. Breast Cancer Res., 2013.
- [14] "On the elasticity of transverse isotropic soft tissues." D. Royer, **J.L. Gennisson**, T. Deffieux et M. Tanter. J. Acoust. Soc. Am., 129 (5) pp. 2757-2760, 2011.
- [15] "Noninvasive in vivo liver fibrosis evaluation using supersonic shear imaging : a clinical study on 113 hepatitis C virus patients." E. Bavu, **J.L. Gennisson**, M. Couade, J. Bercoff, V. Mallet, A. Badel, M. Fink, B. Nalpas, M. Tanter et S. Pol. Ultr. Med. & Bio., vol. 37 (9), pp. 1365-1373, 2011.
- [16] "Characterization of muscle belly elastic properties during passive stretching using transient elastography." A. Nordez, **J.L. Gennisson**, P. Casari, S. Catheline et C. Cornu. J. Biomech., 41, pp. 2305-2311, 2008.
- [17] "Quantitative viscoelasticity mapping of human liver using supersonic shear imaging: preliminary in vivo feasibility study." M. Muller, **J.L. Gennisson**, T. Deffieux, M. Tanter et M. Fink. Ultr. Med. & Bio., 35 (2), pp. 219-229, 2009.
- [18] "Ultrafast imaging of in vivo muscle contraction using ultrasound." T. Deffieux, **J.L. Gennisson**, A. Nordez, M. Tanter et M. Fink. Appl. Phys. Lett., 89, pp. 184107-1-3, 2006.
- [19] "Assessment of the mechanical properties of musculoskeletal system using 2D and 3D very high frame rate ultrasound." T. Deffieux, **J.L. Gennisson**, M. Tanter et M. Fink. IEEE Trans. Ultrason., Ferroelec., Freq. Contr., 55 (10), pp. 2177-2190, 2008.
- [20] "Observation of shock transverse waves in elastic media." S. Catheline, **J.L. Gennisson**, M. Tanter et M. Fink. Phys. Rev. Lett., 91 (16), pp. 43011-43014, 2003.
- [21] "Measurement of elastic nonlinearity of soft solid with transient elastography." S. Catheline, **J.L. Gennisson** et M. Fink. J. Acoust. Soc. Am., 114 (6), pp. 3087-3091, 2003.
- [22] "Measurement of viscoelastic properties of homogeneous soft solid using transient elastography : An inverse problem approach." S. Catheline, **J.L. Gennisson**, G. Delon, R. Sinkus, M. Fink, S. Abouelkaram et J. Culioli. J. Acoust. Soc. Am., 116 (6), pp. 3734-3741, 2004.
- [23] "Estimation of polyvinyl alcohol mechanical properties with 4 elastography methods and comparison with gold standard testings." J. Fromageau, **J.L. Gennisson**, C. Schmitt, R. Maurice, R. Mongrain et G. Cloutier. IEEE Trans. Ultrason., Ferroelec., Freq. Contr., 54 (3), pp. 498-509, 2007.
- [24] "Fourth-order shear elastic constant assessment in quasi-incompressible soft solids." M. Rénier, **J.L. Gennisson**, C. Barrière, D. Royer et M. Fink. Appl. Phys. Lett., 93, pp. 101912-1-3, 2008.

- [25] “Measurement of pulsatile motion with millisecond resolution by magnetic resonance imaging.” R. Souchon, **J.L. Gennisson**, M. Tanter, R. Salomir, J.-Y. Chapelon et O. Rouvière. *Magn. Res. Med.*, 67, pp. 1787-1793, 2012.
- [26] “The variance of quantitative estimates in shear wave imaging: theory and experiments.” T. Deffieux, **J.L. Gennisson**, B. Larrat, M. Fink et M. Tanter. *IEEE Trans. Ultrason., Ferroelec., Freq. Contr.*, 59 (11), pp. 2390-2410, 2012.
- [27] “Temperature dependence of shear modulus in ex vivo muscle assessed by ultrasounds.” E. Sapin, **J.-L. Gennisson**, M. Pernot, M. Fink, et M. Tanter. *Phys. Med. Biol.*, 55, pp. 1701-1718. 2010.
- [28] “On the effects of reflected waves in transient shear wave elastography.” T. Deffieux, **J.L. Gennisson**, J. Bercoff, M. Tanter. *IEEE Trans. Ultrason., Ferroelec., Freq. Contr.*, 58(10), pp. 2032-2035, 2011.
- [29] “Quantitative Imaging of Nonlinear Shear Modulus by Combining Static Elastography and Shear Wave Elastography.” H. Latorre-Ossa, **J.L. Gennisson**, E. De Brosses, M. Tanter. *IEEE Trans. Ultrason., Ferroelec., Freq. Contr.*, 59 (4), pp. 833-839, 2012.
- [30] “Application of 1D Transient Elastography for elasticity assessment of sub-wavelength layered soft tissues: comparison with Supersonic Shear Imaging technique.” J. Brum, **J.L. Gennisson**, T.M. Nguyen, N. Benech, M. Fink, M. Tanter, C. Negreira. *IEEE Trans. Ultrason., Ferroelec., Freq. Contr.*, 59 (4), pp. 703-714, 2012.
- [31] “Effects of storage temperature on the mechanical properties of porcine kidney estimated using Shear Wave Elastography” R. Ternifi, **J.L. Gennisson**, M. Tanter, P. Beilas. *Soumis pour publication dans* *J. Biomechanics.*, 2013.
- [32] “Shear wave elastography quantification of blood elasticity during clotting.” M. Bernal, **J.L. Gennisson**, P. Flaud et M. Tanter. *Ultr. Med. & Bio.*, 38 (12), pp. 2218-2228, 2012.
- [33] “Correlation between classical rheometry and Supersonic Shear Wave Imaging in blood clots.” M. Bernal, **J.L. Gennisson**, P. Flaud et M. Tanter. *Soumis pour publication dans* *Ultr. Med. & Bio.*, 2013.
- [34] “Introduction to the Focused Section on Sensing Technologies for Biomechatronics.” J. Ueda, E. Burdet, **J.L. Gennisson**, M. Kaneko et A. Mihailidis. *IEEE Trans. Mechatronics*, 16 (5), pp. 793-798, 2011.
- [35] “Application of DENSE-MR-Elastography to the human heart.” B. Robert, R. Sinkus, **J.L. Gennisson** et M. Fink. *Magn. Res. Med.*, 62 (5), pp. 1155-1163, 2009.
- [36] “Nonlinear reflexion of shock shear waves in soft elastic media.” G. Pinton, F. Coulouvrat, **J.L. Gennisson** et M. Tanter. *J. Acoust. Soc. Am.*, 127 (2), pp. 683-691, 2010.
- [37] “High resolution quantitative imaging of cornea elasticity using supersonic shear imaging.” M. Tanter, D. Touboul, **J.L. Gennisson**, J. Bercoff et M. Fink. *IEEE Trans. Med. Im.*, 28 (2), pp. 1881-1893, 2009.
- [38] “Shear elasticity probe for soft tissues with 1D transient elastography.” L. Sandrin, M. Tanter, **J.L. Gennisson**, S. Catheline et M. Fink. *IEEE Trans. Ultrason., Ferroelec., Freq. Contr.*, 49 (4), pp. 436-446, 2002.

- [39] “Nonlinear shear wave interaction in soft solids.” X. Jacob, S. Catheline, **J.L. Gennisson**, C. Barrière, D. Royer et M. Fink. *J. Acoust. Soc. Am.*, 122 (4), pp. 1917-1926, 2007.
- [40] “Real-time visualization of muscle stiffness distribution with ultrasound shear wave imaging during muscle contraction.” M. Shinohara, K. Sabra, **J.L. Gennisson**, M. Fink et M. Tanter. *Muscle & Nerve*, 42, pp. 438-441, 2010.
- [41] “Detection of intrarenal microstructural changes with Supersonic Shear Wave Elastography in rats.” M. Derieppe, Y. Delmas, **J.L. Gennisson**, C. Deminière, S. Placier, M. Tanter, C. Combe et N. Grenier. *Eur. Radiol.*, 22, pp. 243-250, 2012.
- [42] “Monitoring of cornea elastic properties changes during UV-A/Riboflavin induced corneal collagen cross-linking using Supersonic Shear Wave Imaging.” T.M. Nguyen, J.F. Aubry, D. Touboul, , **J.L. Gennisson**, J. Bercoff, M. Tanter. *IOVS*, 53 (9), pp. 5948-5954, 2012.
- [43] “Nonlinear viscoelastic properties of tissue assessed by ultrasound.” R. Sinkus, J. Bercoff, M. Tanter, **J.L. Gennisson**, C. El Khoury, V. Servois, A. Tardivon et M. Fink. *IEEE Trans. Ultrason., Ferroelec., Freq. Contr.*, 53 (11), pp. 2009-2018, 2006.
- [44] “Quantitative elastography of renal transplants using supersonic shear imaging: A pilot study.” N. Grenier, S. Poulain, S. Lepreux, **J.L. Gennisson**, R. Hubrecht, Y. Lebras, E. Bavu, A. Servais, V. Meas-Yedid, T. Bachelet, M. Tanter, P. Merville et L. Couzi. *Europ. Rad.*, 22, pp. 2138-2146, 2012.
- [45] “Quantitative assessment of breast lesions viscoelasticity using supersonic shear imaging technique: Initial clinical investigation.” M. Tanter, J. Bercoff, A. Athanasiou, T. Deffieux, **J.L. Gennisson**, G. Montaldo, A. Tardivon et M. Fink. *Ultr. Med. & Bio.*, 34 (9), pp. 1373-1386, 2008.
- [46] “Elastography using ultrasound or magnetic resonance: New imaging tools for cancer diagnosis.” M. Tanter, J. Bercoff, R. Sinkus, T. Deffieux, **J.L. Gennisson** et M. Fink. *MEDNUC Science direct*, 31, pp.132-141, 2007.
- [47] “Evaluation of no radiative clinical imaging techniques for the longitudinal assessment of tumour growth in CT26 colon carcinoma.” J. Seguin, B.T. Doan, H. Latorre-Ossa, L. Jugé, **J.L. Gennisson**, M. Tanter, D. Scherman, G. Chabot, N. Mignet. *Soumis pour publication dans Int. J. Mol. Im.*, 2013.
- [48] “In vivo breast tumor detection using transient elastography.” J. Bercoff, S. Chaffai, M. Tanter, L. Sandrin, S. Catheline, M. Fink, **J.L. Gennisson** et M. Meunier. *Ultr. Med. & Bio.*, 29 (10), pp. 1387-1396, 2003.
- [49] “Breast lesions: Quantitative elastography with supersonic shear imaging – preliminary results.” A. Athanasiou, A. Tardivon, M. Tanter, B. Sigal-Zaffrani, J. Bercoff, T. Deffieux, **J.L. Gennisson**, M. Fink et S. Neuenschwander. *Radiology*, 256 (1), pp. 297-303, 2010.
- [50] “Placental elastography in a murine intrauterine growth restriction model.” T. Quibel, B. Deloison, G. Chalouhi, F. Chamming’s, N. Siauve, M. Alison, **J.L. Gennisson**, O. Clément et L. Salomon. *Soumis pour publication dans Ultra. Obs. Gyn.*, 2013.
- [51] “Shear wave elastography of tumor growth in a human breast cancer model with pathological correlation.” F. Chamming’s, H. Latorre-Ossa, M.A. Lefrère-Belda, V. Fitoussi, T. Quibel,

F. Assayag, E. Marangoni, G. Autret, D. Balvay, L. Pidial, **J.L. Gennisson**, M. Tanter, C.A. Cuenod, O. Clément et L. Fournier. *Europ. Radiol*, DOI 10.1007/s00330-013-2828-8, 2013.

[52] “In vivo measurement of heart elasticity using DENSE MRE: A feasibility study.” B. Robert, B. Larrat, M. Fink, **J.L. Gennisson**. *Soumis pour publication dans JMRI*, 2013.

[53] “High frequency rheology of hydrogel using ultrasound transient elastography.” A. Marcelan, A. Dizeux, M. Tanter, **J.L. Gennisson**. *Soumis pour publication dans IEEE Trans. Ultrason., Ferroelec., Freq. Contr.*, 2013.

b. Articles de congrès internationaux

[1] “A 3D Elastography System based on the Concept of Ultrasound-Computed Tomography for In Vivo Breast Examination.” **J.L. Gennisson**, R. Sinkus, M. Pernot, T. Deffieux, M. Tanter et M. Fink. *Proc. IEEE Ultrasonic Symposium, Vancouver, Oct. 2006*.

[2] “Analysis of blood clot formation with transient elastography: similarity with sol-gel transition in Agar-gelatin phantoms.” **J.L. Gennisson**, F. Yu et G. Cloutier. *Proc. IEEE Ultrasonic Symposium, pp. 1134-1137, Montréal, Août 2004*.

[3] “Anisotropie en élastographie impulsionnelle.” **J.L. Gennisson**, S. Catheline, S. Chaffaï, L. Sandrin et M. Fink. *Proc. 6ème Congrès Français d'Acoustique, CFA, France, Lille Avril 2002*.

[4] “Third order elastic moduli measurements in soft solid using transient elastography.” **J.L. Gennisson**, S. Catheline et M. Fink. *Proc. European congress of Acoustics, Spain, Séville, Sep. 2002*.

[5] “Multiwave technology introducing shear wave elastography of the kidney: Pre-clinical study on a kidney fibrosis model and clinical feasibility study on 49 human renal transplants.” **J.L. Gennisson**, N. Grenier, R. Hubrecht, L. Couzy, Y. Delmas, M. Derieppe, S. Lepreux, P. Merville, A. Criton, J. Bercoff et M. Tanter. *Proc. IEEE Ultrasonic Symposium, San Diego, Oct. 2010*.

[6] “Shear wave elastography in obstetrics: quantification of cervix elasticity and uterine contraction.” **J.L. Gennisson**, M. Muller, O. Ami, V. Kohl, P. Gabor, D. Musset, M. Tanter. *Proc. IEEE Ultrasonic Symposium, Orlando, Oct. 2011*.

[7] “High frequency rheology of hybrid hydrogels using ultrasound transient elastography.” **J.L. Gennisson**, A. Marcelan, A. Dizeux, M. Tanter. *Proc. IEEE Ultrasonic Symposium, Dresde, Oct. 2012*.

[8] “Supersonic Shear Imaging Is A New Potent Morphological Non-Invasive Technique To Assess Liver Fibrosis. Part I: Technical Feasability.” E. Bavu, **J.L. Gennisson**, V. Mallet, B.F. Osmanski, M. Couade, J. Bercoff, M. Fink, P. Sogni, A. Vallet-Pichard, B. Nalpas, M. Tanter et S. Pol, *Proc. J. Hepatol, Vol. 52, pp. S166, 2010*.

[9] “Supersonic Shear Imaging Is A New Potent Morphological Non-Invasive Technique To Assess Of Liver Fibrosis. Part II: Comparison With Fibroscan.” E. Bavu, **J.L. Gennisson**, V. Mallet, B.F. Osmanski, M. Couade, J. Bercoff, M. Fink, P. Sogni, A. Vallet-Pichard, B. Nalpas, M. Tanter et S. Pol, *Proc. J. Hepatol, Vol. 52, pp. S166, 2010*.

[10] “Temperature dependence of shear modulus in ex vivo muscle assessed by ultrasounds.” E. Sapin, **J.-L. Gennisson**, M. Pernot, M. Fink et M. Tanter. *Proc. IEEE Ultrasonic Symposium, Rome, Sep. 2009*.

- [11] "Shear wave propagation in complex sub wavelength tissue geometries: Theoretical and experimental implications in the framework of cornea and skin Shear Wave Imaging." T.M. Nguyen, **J.-L. Gennisson**, M. Couade, D. Touboul, P. Humbert, J. Bercoff, M. Fink et M. Tanter. Proc. IEEE Ultrasonic Symposium, San Diego, Oct. 2010.
- [12] "Comparison between 1D Transient Elastography and Supersonic Shear Imaging Technique: Application to the Arterial Wall Elasticity Assessment." J. Brum, **J.-L. Gennisson**, N. Benech, M. Fink, M. Tanter et C. Negreira. Proc. IEEE Ultrasonic Symposium, San Diego, Oct. 2010.
- [13] "Liver fibrosis staging using SuperSonic Shear Imaging technique: a clinical study. " E. Bavu, **J.-L. Gennisson**, B.-F. Osmanski, M. Couade, J. Bercoff, M. Fink, V. Mallet, P. Sogni, A. Vallet-Pichard, B. Nalpas, M. Tanter et S. Pol. Proc. IEEE Ultrasonic Symposium, Rome, Sep. 2009.
- [14] "Nonlinear and Von Neumann reflection of elastic shock wave in soft solids." G. Pinton, **J.-L. Gennisson**, M. Tanter, M. Fink et F. Coulovrat. Proc. IEEE Ultrasonic Symposium, Rome, Sep. 2009.
- [15] "Non linear shear elastic moduli in incompressible soft solids." M. Rénier, **J.L. Gennisson**, S. Catheline, M. Tanter, C. Barrière, D.Royer et M. Fink. Proc. IEEE Ultrasonic Symposium, New York, Oct. 2007.
- [16] "Measurements of nonlinear shear elastic moduli in quasi-incompressible soft solids." M. Rénier, **J.L. Gennisson**, C. Barrière, S. Catheline, D.Royer, M. Tanter et M. Fink. Proc. ISNA, Stockholm, Juil. 2008.
- [17] "Active and passive mechanical muscle properties assessed by ultrasound techniques." T. Deffieux, **J.L. Gennisson**, M. Tanter et M. Fink. Proc. IEEE Ultrasonic Symposium, New York, Oct. 2007.
- [18] "Full 3d inversion of the viscoelasticity wave propagation problem for 3d ultrasound elastography in breast cancer diagnosis." M. Muller, **J.L. Gennisson**, T. Deffieux, R. Sinkus, P. Annic, G. Montaldo, M. Tanter et M. Fink. Proc. IEEE Ultrasonic Symposium, New York, Oct. 2007.
- [19] "Ultrafast ultrasonic imaging of in vivo muscle contraction." T. Deffieux, **J.L. Gennisson**, M. Tanter et M. Fink. Proc. IEEE Ultrasonic Symposium, Vancouver, Oct. 2006.
- [20] "A new method to assess the kinetics of rouleaux formation in human subcutaneous veins using high frequency parametric imaging: preliminary results." F. Yu, **J.L. Gennisson** et G.Cloutier. Proc. IEEE Ultrasonic Symposium, pp. 870-873, Rotterdam, Sep. 2005.
- [21] "Quantification of red blood cell aggregation using an ultrasound clinical system." A. Amararene, **J.L. Gennisson**, A. Rabhi et G.Cloutier. Proc. IEEE Ultrasonic Symposium, pp. 874-877, Rotterdam, Sep. 2005.
- [22] "Nonlinearity Studies in Soft Tissues with the Supersonic Shear Imaging System." S. Catheline, **J.L. Gennisson**, J. Bercoff, C. Barrière et M. Fink. Proc. IEEE Ultrasonic Symposium, pp. 1510-1512, Montréal, Août 2004.
- [23] "Elastic nonlinearity of soft solids with transient elastography." S. Catheline, **J.L. Gennisson**, X. Jacob, M. Tanter, C. Barrière, D. Royer et M. Fink. Proc. 7ème Congrès Français d'Acoustique, CFA, France, Strasbourg, Mars 2004.

- [24] “Study of elastic nonlinearity of soft solids with transient elastography.” X. Jacob, **J.L. Gennisson**, S. Catheline, M. Tanter, C. Barrière, D. Royer et M. Fink. Proc. IEEE Ultrasonic Symposium, pp. 660-663, Honolulu, Oct. 2003.
- [25] “Adaptative ultrasonic displacement estimation for elastic shock waves in soft solids.” G. Pinton, **J.L. Gennisson**, M. Tanter, F. Coulouvrat. Proc. IEEE Ultrasonic Symposium, Dresde, Oct. 2012.
- [26] “3D in vivo brain elasticity mapping in small animals using ultrasound.” E. Macé, I. Cohen, **J.-L. Gennisson**, G. Montaldo, R. Miles, M. Fink et M. Tanter. Proc. IEEE Ultrasonic Symposium, Rome, Sep. 2009.
- [27] “Non linear propagation of shear waves in soft solids.” S. Catheline, M. Tanter, **J.L. Gennisson** et M. Fink. Proc. Joint workshop of russian acoustical society (RAS) and french acoustical society (SFA), pp. 81-85, Moscou, Nov 2005.
- [28] “Non-invasive vascular elastography based on a new 2D strain estimator: Simulations results.” C. Schmitt, R. L. Maurice, **J.L. Gennisson** et G. Cloutier. Proc. IEEE Ultrasonic Symposium, pp. 1498-1501, Montréal, Août 2004.
- [29] “Ultrasound based non invasive shear elasticity probe soft tissues.” S. Catheline, L. Sandrin, **J.L. Gennisson**, M. Tanter et M. Fink. Proc. IEEE Ultrasonic Symposium, pp. 1799-1801, Porto Rico, Oct. 2000.
- [30] “Real time quantitative elastography using supersonic shear wave imaging.” M. Tanter, M. Pernot, G. Montaldo, **J.L. Gennisson**, E. Bavu, E. Mace, T.M. Nguyen, M. Couade et M. Fink. Proc. IEEE Symposium on Bio. Im., pp. 276-279, Rotterdam, 2010.
- [31] “Problème inverse en élastographie impulsionnelle 2D.” S. Catheline, S. Chaffai, M. Tanter, J. Bercoff, L. Sandrin, **J.L. Gennisson** et M. Fink. Proc. 6ème Congrès Français d'Acoustique, CFA, France, Lille, Avril 2002.
- [32] “Ultra high speed imaging of elasticity.” M. Fink, L. Sandrin, M. Tanter, S. Catheline, S. Chaffai, J. Bercoff et **J.L. Gennisson**. Proc. IEEE Ultrasonic Symposium, pp. 1767-1776, Munich, Oct. 2002.
- [33] “ShearWave™ Elastography: A new real time imaging mode for assessing quantitatively soft tissue viscoelasticity.” J. Bercoff, A. Criton, C. Cohen Bacrie, J. Souquet, M. Tanter, **J.L. Gennisson**, T. Deffieux, M. Fink, V. Juhan, A. Colavolpe, D. Amy et A. Athanasiou. Proc. IEEE Ultrasonic Symposium, Pékin, Nov. 2008.

c. Congrès internationaux

- [1] Full 3D elasticity reconstruction using supersonic shear imaging technique for breast cancer diagnosis. **J.L. Gennisson**, N. Felix, T. Deffieux, J. Bercoff, R. Sinkus, F. Boudet, M. Tanter et M. Fink. IEEE Ultrasonic Symposium, Pékin, Nov. 2008.
- [2] “DENSE MR-Elastography For Cardiac Application.” B. Robert, R. Sinkus, **J.L. Gennisson**, et M. Fink. ISMRM, Canada, Toronto, Mai 2008.
- [3] “Application of DENSE MR-Elastography to the human heart: first in vivo results.” B. Robert, R. Sinkus, **J.L. Gennisson**, et M. Fink. ISMRM, USA, Hawaiï, April 2009.

- [4] “Non-invasive diagnosis of liver fibrosis - comparison of MR elastography and Supersonic Imaging in an animal study.” N. Salameh, **J.L. Gennisson**, B. Larrat, T. Deffieux, M. Tanter, B.E. Van Beers, R. Sinkus et M. Fink. ISMRM, Canada, Toronto, Mai 2008.
- [5] “Transient CINE MR-Elastography of the heart – Imaging polarized pulsed shear waves induced by valves closure.” R. Sinkus, B. Robert, **J.L. Gennisson**, M. Tanter et M. Fink. ISMRM, U.S.A., New York, Juillet 2006.
- [6] “Single breath hold transient MR-Elastography of the heart – Imaging pulsed shear wave propagation induced by aortic valve closure.” R. Sinkus, B. Robert, **J.L. Gennisson**, M. Tanter et M. Fink. ISMRM, U.S.A., Seattle, Mai 2006.
- [7] “Assessment of mechanical properties of PVA-C with 4 different elastographic methods.” **J.L. Gennisson**, J. Fromageau, C. Schmitt, R.L. Maurice, R. Mongrain et G. Cloutier. 4th International Conference on the Ultrasonic Measurement and Imaging of Tissue Elasticity, U.S.A., Austin, Oct. 2005.
- [8] “Analysis of blood clot formation using transient elastography.” **J.L. Gennisson**, S. Lerouge et G. Cloutier. 3rd International Conference on the Ultrasonic Measurement and Imaging of Tissue Elasticity, U.K., Windermere, Oct. 2004.
- [9] “The supersonic shear imaging technique applied to nonlinear properties of soft tissues.” S. Catheline, **J.L. Gennisson**, J. Bercoff, C. Barrière et M. Fink. 3rd International Conference on the Ultrasonic Measurement and Imaging of Tissue Elasticity, U.K., Windermere, Oct. 2004.
- [10] “Measurement of skin elasticity using transient sonoelastography.” T. Baldeweck, **J.L. Gennisson**, C. Cornillon, M. Tanter, S. Catheline, M. Fink et B. Querleux. 8th Congress of the Intl. Society for skin imaging, Germany, Hamburg, Mai 2003.
- [11] “Viscoelastic properties of soft solids using inverse problem in transient elastography.” **J.L. Gennisson**, S. Catheline, G. Delon et M. Fink. 28th Intl. Symp. on Ultrasonic Imaging and Tissue Characterization, U.S.A., Arlington, Juin 2003.
- [12] “Monitoring thermally induced lesions with supersonic imaging.” M. Pernot, J. Bercoff, **J.L. Gennisson**, M. Tanter et M. Fink. 28th Intl. Symp. on Ultrasonic Imaging and Tissue Characterization, U.S.A., Arlington, Juin 2003.
- [13] “Nonlinear interaction of shear waves in soft solids using transient elastography.” **J.L. Gennisson**, X. Jacob, S. Catheline, M. Tanter, C. Barrière, D. Royer et M. Fink. 2nd International Conference on the Ultrasonic Measurement and Imaging of Tissue Elasticity, U.S.A., Corpus Christi Oct. 2003.
- [14] “Viscoelastic properties of soft solids using transient elastography.” S. Catheline, **J.L. Gennisson**, G. Delon et M. Fink. 2nd International Conference on the Ultrasonic Measurement and Imaging of Tissue Elasticity, U.S.A., Corpus Christi Oct. 2003.
- [15] “Elastic non linearity of soft solids using transient elastography.” S. Catheline, **J.L. Gennisson**, M. Tanter et M. Fink. 27th Intl. Symp. on Ultrasonic Imaging and Tissue Characterization, U.S.A., Arlington, Juin 2002.

- [16] "Measuring non linear elastic parameters of soft solids using transient elastography." S. Catheline, **J.L. Gennisson**, M. Tanter et M. Fink. 1st International Conference on the Ultrasonic Measurement and Imaging of Tissue Elasticity, Canada, Niagara, Oct. 2002.
- [17] "A study of muscle anisotropy with transient elastography." **J.L. Gennisson**, S. Catheline, S. Chaffai et M. Fink. 1st International Conference on the Ultrasonic Measurement and Imaging of Tissue Elasticity, Canada, Niagara, Oct. 2002.
- [18] "2D Transient elastography with an ultrafast ultrasonic scanner." M. Fink, L. Sandrin, M. Tanter, S. Catheline, S. Chaffai, J. Bercoff et **J.L. Gennisson**. 1st International Conference on the Ultrasonic Measurement and Imaging of Tissue Elasticity, Canada, Niagara, Oct. 2002.
- [19] "Study of elastic non linearity of soft solids with transient elastography: Landau coefficients and finite amplitude shear wave." S. Catheline, **J.L. Gennisson** et M. Fink. 1st Pan-American/Iberian Meeting on Acoustics, J.A.S.A., Mexico, Cancun, Dec. 2002.
- [20] "Study of muscle anisotropy with transient elastography." **J.L. Gennisson**, S. Catheline, S. Chaffai et M. Fink. 1st Pan-American/Iberian Meeting on Acoustics, J.A.S.A., Mexico, Cancun, Dec. 2002.
- [21] "Experimental evidence of anisotropy of muscle using pulsed elastography." S. Catheline, **J.L. Gennisson**, M. Tanter, L. Sandrin et M. Fink. 26th Intl. Symp. on Ultrasonic Imaging and Tissue Characterization, U.S.A., Arlington, Mai 2001.
- [22] "Elasticity imaging with time resolved pulsed elastography." L. Sandrin, S. Catheline, **J.L. Gennisson**, M. Tanter and M. Fink. 141st A.S.A. Meeting J.A.S.A., U.S.A., Chicago, Juin 2001.
- [23] "Ultrasound based shear elasticity probe." L. Sandrin, **J.L. Gennisson**, M. Tanter, S. Catheline, D. Cassereau et M. Fink. 25th Intl. Symp. on Ultrasonic Imaging and Tissue Characterization, U.S.A., Arlington, Juin 2000.
- [24] "A 3D Elastography System based on the Concept of Ultrasound-Computed Tomography for In Vivo Breast Examination.", **J.L. Gennisson**, T. Deffieux, R. Sinkus, P. Annic, M. Pernot, F. Cudeiro, G. Montaldo, J. Bercoff, M. Tanter and M. Fink. 5th International Conference on the Ultrasonic Measurement and Imaging of Tissue Elasticity, U.S.A., Salt Lake City, Oct. 2006.
- [25] "A shear wave elastography of the kidney: pre-clinical study on a kidney fibrosis model and clinical feasibility study on 70 human renal transplants.", **J.L. Gennisson**, N. Grenier, R. Hubrecht, L. Couzy, M. Dériepe, Y. Delmas, P. Merville, A. Criton, J. Bercoff et M. Tanter. 9th International Conference on the Ultrasonic Measurement and Imaging of Tissue Elasticity, U.S.A., Salt Lake City, Oct. 2010.
- [26] "Nonlinear shear modulus quantification by combining static and dynamic elastography", H. Latorre-Ossa, **J.L. Gennisson**, E. De Brosses et M. Tanter. 9th International Conference on the Ultrasonic Measurement and Imaging of Tissue Elasticity, U.S.A., Salt Lake City, Oct. 2010.
- [27] "Shear wave propagation in complex sub wavelength tissue geometries: Theoretical and experimental implications in the framework of cornea and skin Shear Wave Imaging", T.M. Nguyen, **J.L. Gennisson**, D. Touboul, P. Humbert, J. Bercoff, M. Fink et M. Tanter. 9th International Conference on the Ultrasonic Measurement and Imaging of Tissue Elasticity, U.S.A., Salt Lake City, Oct. 2010.

[28] "Shear wave elastography on in vivo pig kidney: impact of urinary and vascular pressure on viscoelastic measurements", **J.L. Gennisson**, N. Grenier et M. Tanter. 10th International Conference on the Ultrasonic Measurement and Imaging of Tissue Elasticity, U.S.A., Dallas, Oct. 2011.

[29] "Shear viscoelasticity quantification of breast cancer tumours implanted in mice before and after chemotherapy treatment", H. Latorre-Ossa, F. Chamming's, **J.L. Gennisson**, L. Fournier, O. Clément et M. Tanter. 10th International Conference on the Ultrasonic Measurement and Imaging of Tissue Elasticity, U.S.A., Dallas, Oct. 2011.

[30] "Initial clinical results of shear wave spectroscopy in chronic liver disease", T. Deffieux, **J.L. Gennisson**, M. Couade, J. Bercoff, L. Bousquet, S. Coscone, V. Mallet, S. Pol, M. Tanter. 10th International Conference on the Ultrasonic Measurement and Imaging of Tissue Elasticity, U.S.A., Dallas, Oct. 2011.

[31] "Shear wave elastography on in vivo pig kidney: impact of urinary and vascular pressure on viscoelastic measurements". **J.L. Gennisson**, N. Grenier et M. Tanter. IEEE Ultrasonic Symposium, Orlando, Oct. 2011.

[32] "Shear wave spectroscopy in liver: initial clinical results and implementation discussion". T. Deffieux, **J.L. Gennisson**, M. Couade, J. Bercoff, L. Bousquet, S. Coscone, V. Mallet, S. Pol et M. Tanter. IEEE Ultrasonic Symposium, Orlando, Oct. 2011.

[33] "High resolution elasticity imaging". **J.-L. Gennisson**, T.-M. Nguyen, H. Latorre-Ossa, C. Papadacci, J.-F. Aubry, M. Pernot, M. Fink, M. Tanter. Ultrasound Bi microscopy, Saint-Paulin, Canada, Oct. 2012.

[34] "High frequency rheology of hybrid hydrogels using ultrasound transient elastography", **J.L. Gennisson**, A. Marcelan, A. Dizeux, M. Tanter. 11th International Conference on the Ultrasonic Measurement and Imaging of Tissue Elasticity, France, Deauville, Oct. 2012.

I.3. VALORISATION, DIFFUSION DE LA RECHERCHE, ENSEIGNEMENT

a. Brevets déposés

Au cours des cinq dernières années j'ai participé fortement à la valorisation de nos activités de recherche. J'ai été amené à rédiger plusieurs dossiers de valorisation pour le CNRS, qui ont abouti au dépôt de plusieurs brevets protégeant nos activités de recherche, puis à collaborer avec le cabinet d'expert lors de la rédaction du texte du brevet.

[1] Brevet n°: FR 07 01235 / PCT/FR2007/000839 / WO 2008/139245A1: "Dispositif de mesure pour mesurer l'élasticité dans une région d'intérêt.", 2008.

[2] Brevet n°: PCT/EP2010/056130: "Method and device for measuring a physical parameter in mamal soft tissues by propagating shear waves.", 2009.

[3] Brevet en cours de dépôt soumis en Janvier 2013: "Méthode et appareil pour quantifier l'élasticité et la non linéarité élastique de tissus biologique ou d'un milieu mou.", 2013.

b. Organisation d'écoles thématiques

J'ai également participé à l'organisation de six écoles scientifiques « workshop » principalement concernant l'imagerie en milieu complexe et la thérapie par ultrasons. Les intervenants ont été sélectionnés parmi les experts mondiaux capables d'éclairer les différents aspects de l'imagerie acoustique et sismique ; ainsi que de la thérapie ultrasonore. J'ai été amené à rédiger plusieurs demandes de financement pour établir le budget de chaque école et à travailler en étroite collaboration avec les services administratifs du CNRS pour concrètement mettre en places ces dernières.

[1] Ecole internationale de Cargèse, "Therapeutic Ultrasound"

Organisateurs : J.F. Aubry, M. Tanter, **J.L. Gennisson**, M. Fink et G. ter Haar.

Institut scientifique de Cargèse, France, Avr. 2007.

[2] Ecole internationale de Cargèse, "Acoustical imaging of complex media : Application in medicine, seismology and oceanography"

Organisateurs : **J.L. Gennisson**, J.F. Aubry, M. Fink, J. Greenleaf, J.P. Montagner, W. A. Kuperman et P. Roux.

Institut scientifique de Cargèse, France, Oct. 2007.

[3] Ecole internationale des Houches, "Linear and nonlinear acoustic wave propagation in heterogeneous media "

Organisateurs : J.F. Aubry, **J.L. Gennisson**, M. Fink.

Institut scientifique des Houches, France, Mars 2008.

[4] Ecole internationale de Cargèse, "Non-conventional imaging and focusing techniques : from acoustics to optics"

Organisateurs : G. Lerosey, J. de Rosny, R. Carminatti, **J.L. Gennisson**, M. Fink.

Institut scientifique des Houches, France, Mai. 2009.

[5] Ecole internationale de Cargèse, "Therapeutic Ultrasound II"

Organisateurs : J.F. Aubry, **J.L. Gennisson**, M. Fink et G. ter Haar.

Institut scientifique de Cargèse, France, Oct. 2009.

[6] Ecole internationale des Houches, " Therapeutic Ultrasound III "

Organisateurs : G. ter Haar, V. Khoklova, J.F. Aubry, **J.L. Gennisson**, M. Fink.

Institut scientifique des Houches, France, Mars 2011.

c. Séminaires & Conférences invitées

- Premières rencontres pluridisciplinaires entre cliniciens et chercheurs: Avancée dans l'imagerie mammaire, Strasbourg, France, 22-23 Mars 2007

« Elastographie par Ultrasons et IRM : Une aide au diagnostic du cancer du sein ? »

- Laboratorio d'Acustica Ultrasonora, Montevideo, Uruguay, 15 Fév. 2010.

« Multiwave imaging : From basic physics to medical applications. »

- Medical centre university, Riyadh, Arabie Saoudite, 18 Avr. 2011.

« Multiwave imaging : From basic physics to medical applications. »

- 4th European conference on healthcare engineering, Paris, France, 30 Mai-1 Juin 2011.

« Shear wave imaging : From basic physics to medical applications. »

- 5th International Workshop on the molecular radiology of breast cancer, Valence, Espagne, 30 Octobre 2011.

« Shear wave elastography for breast cancer diagnosis: from bench to bedside. »

d. Enseignement

J'effectue dans l'année des enseignements ponctuels à l'ESPCI :

- Cours d'imagerie médicale (3 heures élastographie) : Master de bioingénierie (Responsable Emmanuel Bossy)

- Cours d'imagerie médicale (6 heures élastographie) : 3^{ième} année ESPCI. (Responsable Emmanuel Bossy)

J'ai effectué les préceptorats en acoustique sur une année (18 heures) pour les élèves de 1^{ère} année de l'ESPCI.

Je donne également un cours de 3h au Master d'ingénierie biomédicale de l'université de Paris V et 3h au Master d'ingénierie médicale de l'université de Bordeaux Jacques Segalen.

e. Participation à des contrats de recherche

- **Contrat A.F.M. (Agence française contre les Myopathies)**

Jan. 2006 – Déc. 2006

« A new tool for non invasive assessment of muscle elasticity »

- **Contrat A.N.R.S. (Agence Nationale de Recherche sur le Sida)**

Jan. 2009 – Déc. 2011

« Quantification de la fibrose hépatique par imagerie échographique d'élasticité ultrarapide »

- **A.N.R. Tecsan (MicroElasto)**

Jan. 2010 – Déc. 2012

« Elastographie Quantitative très Haute Résolution pour la Caractérisation Biomécanique des tissus en Ophtalmologie et Dermatologie »

- **A.N.R. Blanche Internationale (ULTRASWIFT)**

Jun. 2012 – Mai. 2015

« Imagerie échographique d'onde de cisaillement pour la thérapie ultrasonore du tendon. »

- **P.I.C.S. C.N.R.S. (Projet International de Coopération Scientifique) LAU Montevideo Uruguay**

Jan. 2009 - Déc. 2011

« Applications en imagerie médicale par retournement temporel et élastographie ultrasonore. »

- **Pôle de compétitivité MEDICEN (DARMUS)**

Jan. 2006 – Nov. 2010

« Diagnostic Avancé par IRM et Ultrasons combinés »

- **Pôle de compétitivité MEDICEN (PLI-K)**

Jan. 2011 – Déc. 2013

« Diagnosis & treatment of Primary Liver Cancer »

- **Contrat SAFRAN Morpho**

Oct. 2011 – Oct. 2012

« Etude d'empreinte digitale par ultrasons »

- **Contrat L'Oréal**

Jan. 2012 – Déc. 2012

« Etude du vieillissement cutané »

- **FP7 INGRESS**

Jan. 2013 – Déc. 2018

« Research and validation for fingerprint live scanners - Capability Project »

f. Autres activités scientifiques

- Formé à l'expérimentation animale **Niveau 1**.
- **Guest Editor** pour IEEE Trans. Mechatronics 2010/2011.
- Membre du conseil de laboratoire de l'Institut Langevin

- Membre de la Société Française d'Acoustique
- Membre de la Société Française de Physique
- Expertise d'articles pour *J. Acoust. Soc. Am.*, *IEEE Trans. Ultr. Ferro. Freq. Cont.*, *Ultr. Med. Bio.*, *App. Phy. Let.*, *Eur. Radiology*
- Correspondant Hygiène et Sécurité INSERM U979
- Webmaster du site de l'Institut Langevin
- Consultant scientifique pour la société Supersonic Imagine (Valorisation de brevets communs)
- Demande d'expertise pour l'ANR, COFECUB ou encore la région (Centre, Ile de France).

I.4. ACTIVITES D'ENCADREMENT

De Décembre 2005 à Décembre 2008, j'ai co-encadré le travail de recherche d'un premier étudiant en doctorat, **Thomas Deffieux**, dont le sujet faisait suite aux travaux de Jeremy Bercoff et des miens en élastographie, que j'ai également repris en tant que chercheur, et concernait la « Palpation par force de radiation ultrasonore et échographie ultrarapide : Applications à la caractérisation tissulaire in vivo. ». Thomas a depuis effectué un an de post-doc à New York, Columbia university et est revenu à l'institut Langevin réaliser un autre post-doc que j'encadre sur l'imagerie d'élasticité du foie vis le contrat ANRS.

D'autre part j'ai co-encadré la thèse d'Octobre 2005 à Décembre 2009 de **Benjamin Robert** sur une autre modalité d'imagerie, l'IRM (Imagerie par résonance magnétique). Sa thèse portait sur le développement d'une nouvelle séquence d'acquisition rapide d'IRM pour la mesure de l'élasticité du cœur : « Etude des propriétés viscoélastiques des tissus mous par élastographie IRM. Une approche multi-échelle. ».

J'ai également participé à l'encadrement de **Mathieu Rénier**, en 2007 et 2008, sur l'application de l'élastographie pour la mesure des paramètres non-linéaire des milieux mous.

De Septembre 2009 à Décembre 2012 j'ai encadré la thèse d'**Heldmuth Latorre-Ossa**, sur l'influence le suivi in vivo des changements d'élasticité de tumeur pendant leur croissance et leur traitement.

Sur la période de Novembre 2009 à Novembre 2012 j'ai co-encadré **Javier Brum** sur l'élastographie et le retournement temporel des ondes de cisaillement.

Je participe à l'encadrement de deux autres étudiants en thèse, **Clémentine Helfenstein** depuis Septembre 2010 sur l'étude de la dynamique des chocs par échographie ultrarapide et **Guillaume Dubois** depuis Septembre 2011 sur l'étude de la biomécanique du squelette musculaire humain.

Enfin, au cours des années qui ont suivi ma thèse doctorat, j'ai encadré ou co-encadré de nombreux étudiants dont je cite la liste exhaustive :

Marie Muller	(Post-doc, 2007)
Thomas Deffieux	(Post-doc, 2010-2011-2012)
Eric Bavu	(Post-doc, 2008)
Emilie De Brosse	(Post-doc, 2008)
Dora Aït-Belkaceme	(Post-doc, 2012)
Miguel Bernal	(Post-doc, 2011-2012-2013)
Javier Brum	(Post-doc, 2013)
Thu-Mai Nguyen	(ESPCI, Master Acoustique Physique, 6 mois, 2008)
Alexandre Dizeux	(Paris XI, Master Physique médicale, 6 mois, 2011)
Julien Gondrin	(Paris VII, Master Acoustique Physique, 6 mois, 2007)
Delphine Ladare	(ESPCI, 1 ^{ère} année, 6 mois, 2007)
Jean-Baptiste	(ESPCI, 3 ^{ième} année, 3 mois, 2007)
Marc Borg	(ESPCI, 3 ^{ième} année, 3 mois, 2007)
Katharina Göbel	(License, Université de Cologne, Allemagne, 6 mois, 2008)
Javier Brum	(Master Acoustique, Université de Montevideo, Uruguay, 6 mois, 2007)
Léo Robert	(Master 1 Acoustique, université Pierre et Marie Curie, 6 mois, 2012)
Léo Robert	(Master 2 Acoustique, université Pierre et Marie Curie, 6 mois, 2013)
Guillaume Dubois	(Master Biomécanique, CNAM Arts et métiers, 6 mois, 2011)

II. MEMOIRE

II.1. INTRODUCTION

Depuis la fin de mon post-doc en Octobre 2005, j'ai engagé mes recherches dans l'équipe Physique des ondes pour la médecine dirigé par **Mickaël Tanter** à l'Institut Langevin dirigé par **Mathias Fink**. Ces recherches concernent principalement l'imagerie médicale par ultrasons et plus particulièrement l'élastographie transitoire. Cette technique a entièrement été développée à l'Institut Langevin (anciennement laboratoire Ondes et Acoustique) depuis 1996, de la compréhension des phénomènes physiques liés à la propagation des ondes de cisaillement, à son intégration dans des systèmes d'imagerie échographiques, jusqu'à la mise en place de protocoles cliniques en hôpitaux. J'aimerais montrer dans ce manuscrit comment en partant de la physique fondamentale nous avons pu suivre ce parcours jusqu'aux tests cliniques et comment en travaillant avec ces outils nous avons pu mieux comprendre les problèmes quotidiens des médecins et ainsi revenir à des problèmes de physique théorique nous permettant d'envisager de nouvelles pistes de recherche. Pour ce faire j'organiserai mon mémoire en quatre chapitres orientés autour des différentes propriétés mécaniques des tissus biologiques.

Le premier chapitre de ce mémoire concerne le paramètre mécanique central de l'élastographie, l'élasticité. Je réexpliquerai les principes fondamentaux de la mesure d'élasticité à travers plusieurs techniques, l'élastographie transitoire 2D et la technique de « Supersonic Shear Imaging (SSI) ». Ces techniques se basent sur la génération d'ondes de cisaillement et le suivi de leur propagation par imagerie ultrasonore ultrarapide. Dans cette partie j'expliquerai notre démarche vers la technique SSI qui est devenue la technique centrale présentée dans ce manuscrit. Initialement développé pour le diagnostic du cancer du sein, nous verrons son évolution vers un système d'imagerie 3D, puis vers d'autres organes, comme par exemple le foie. Enfin je présenterai également son évolution vers un système haute fréquence, à la fois utile pour le petit animal et pour de petits organes tel l'œil ou la peau.

Le second chapitre ouvre la suite de ce mémoire sur les autres propriétés mécaniques du corps humain, par l'anisotropie élastique des tissus biologiques. L'anisotropie élastique, dans le sens où la rigidité des tissus est différente selon les directions de l'espace, est très fortement présente dans le corps humain. Nous illustrerons ce chapitre par deux organes majeurs en anisotropie, le muscle et le rein. Nous verrons l'importance de l'anisotropie dans leur caractérisation et comment cette dernière peut changer en fonction de l'environnement extérieur (pression, contraction).

Le troisième chapitre concerne la nonlinéarité élastique. Nous verrons comment en repartant des équations de la physique fondamentale nous pouvons redévelopper les équations de propagation des ondes en prenant en compte les phénomènes de non linéarité élastique dans les

milieux mous ou quasi-incompressible. En utilisant le formalisme de Landau nous pouvons retrouver les paramètres de cisaillement du troisième ordre A et construire des cartes de non linéarité élastique. Également nous montrerons comment en utilisant la propagation d'ondes de cisaillement choqués nous pouvons remonter à ces mêmes paramètres. Ce chapitre montre que le développement de la physique fondamentale reste important pour apporter de nouveaux paramètres de quantification au médecin pour la caractérisation des tissus biologiques.

Enfin je terminerai ce mémoire par un chapitre sur la viscoélasticité. En effet les ondes de cisaillement en se propageant s'atténuent fortement. Cette atténuation est due à plusieurs facteurs donc la viscosité. Nous verrons dans ce chapitre comment retrouver cette propriété mécanique de par la mesure de la dispersion des ondes de cisaillement mais également par d'une autre manière en estimant leur atténuation. Cette dernière méthode bien plus avantageuse permet de se passer du choix de modèle rhéologique et de retrouver les modules de conservation et de pertes, briques fondamentales des modèles rhéologiques.

II.2 CHAPITRE 1 : ELASTOGRAPHIE

Imagerie d'élasticité du corps humain par génération d'une source supersonique de cisaillement.

Entre 1998 et 2004 au laboratoire Onde et Acoustique, nouvellement Institut Langevin, nous avons aussi mis au point une nouvelle technique d'imagerie d'élasticité des tissus humains. Cette technique, appelée élastographie transitoire, est basée sur le couplage d'un prototype d'imagerie échographique ultrarapide unique au monde (capable d'atteindre des cadences échographiques supérieures à 20 000 images par seconde) et d'une vibration basse fréquence appliquée à la surface du corps. Elle permet d'imager avec une résolution millimétrique le module d'Young des tissus, paramètre particulièrement intéressant, puisqu'il caractérise la dureté des tissus. On sait en effet que ce paramètre peut être caractéristique de l'état pathologique des tissus [1]. Plusieurs études ont montré qu'un carcinome pouvait être jusqu'à trente fois plus dur que les tissus sains environnants. Les médecins cherchent à estimer ce paramètre, puisque c'est précisément ce module d'Young des tissus qu'ils essaient d'estimer lors de la palpation d'un organe. Cette technique de palpation reste toutefois subjective et difficile à appliquer pour les tumeurs de petites tailles ou situées en profondeur dans les tissus.

Le but était donc de mettre au point un système de « palpation quantitative » capable de produire des images 2D de l'élasticité des tissus. Le premier système d'imagerie consista en une barrette de transducteurs piézoélectriques classiquement utilisée en échographie montée sur un vibreur basse fréquence (Fig. 1b) [2]. Par l'intermédiaire du vibreur, la face avant de la barrette échographique donne un léger coup à la surface du corps, ce qui génère une vibration transitoire basse fréquence (de 50 à 150 Hz). Ce coup quasi-imperceptible engendre la propagation d'une onde de cisaillement basse fréquence en profondeurs dans les tissus. Cette onde se propage à quelques m.s^{-1} dans les tissus (beaucoup plus lentement que les ultrasons) et sa vitesse locale est directement reliée au module d'Young, i.e. à la dureté, des tissus. Ainsi, imager la propagation de cette onde « sismique » de cisaillement dans les tissus nous permet de mesurer localement le module d'Young des tissus, Fig. 1d. Les déplacements des tissus engendrés par la propagation de cette onde basse fréquence sont mesurés en acquérant à une cadence très rapide des images échographiques de l'organe. La comparaison deux à deux d'images échographiques successives permet par des techniques de corrélation classiques de remonter aux mouvements locaux des tissus lors du passage de la sollicitation mécanique.

Ce projet a abouti après plusieurs années de recherche à une première campagne *in vivo* de détection de tumeurs du sein à l'aide de ce nouveau système d'imagerie en collaboration avec

l'Institut Curie (Juin 2001) [2]. Les résultats obtenus ont été extrêmement encourageants. L'acquisition des données permettant de produire une image bidimensionnelle de l'élasticité des tissus est réalisée en un temps total d'une vingtaine de millisecondes. Ce temps très court rend notre système d'imagerie insensible à des mouvements du patient, problème inhérent aux techniques de mesure d'élasticité par IRM par exemple. Cependant l'utilisation d'un tel système en clinique fut un point de discussion sensible avec les médecins. En effet l'ajout d'un vibreur à la sonde échographique modifiait considérablement la manière de procéder à l'examen radiologique ce que les médecins redoutaient. C'est alors que la thèse de Jeremy Bercoff pris tout son sens par l'utilisation de la force de radiation ultrasonore comme source de vibration de cisaillement [3].

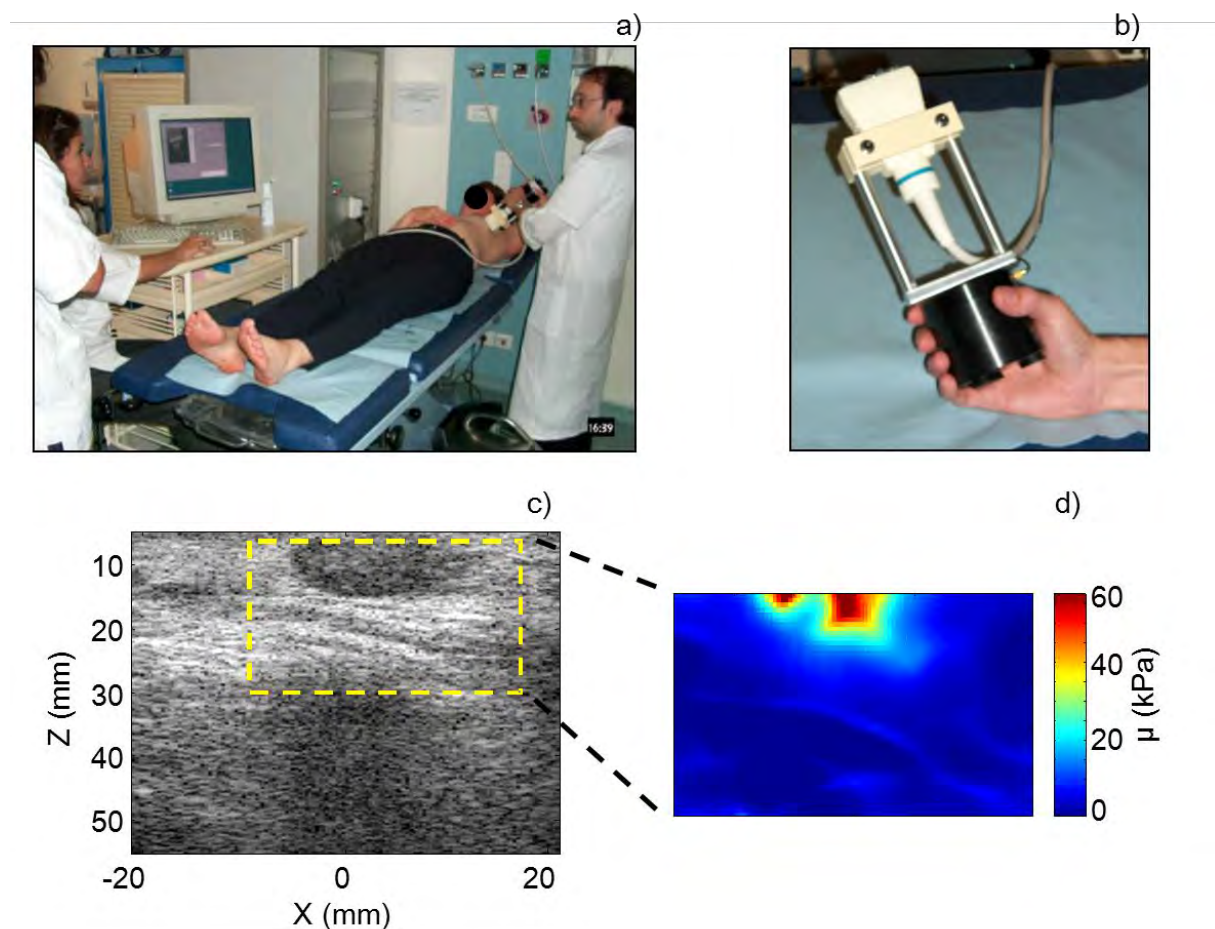


Fig. 1. Système d'imagerie par élastographie transitoire. a,b) Une barrette échographique classique est montée sur un vibreur basse fréquence. c) Image échographique obtenue sur une patiente présentant un carcinome d'environ 1 cm de diamètre visible à l'échographie. d) Image quantitative du module de cisaillement dans la zone définie en pointillés jaunes. L'échelle varie de 0 à 60 kPa.

La palpation à distance par force de radiation ultrasonore.

Comparée à la première technique d'imagerie d'élasticité 2D utilisée lors des tests cliniques à l'institut Curie en Juin 2001, nous avons apporté dans le cadre de la thèse de Jérémie Bercoff une

modification essentielle et extrêmement novatrice, qui rend le procédé à la fois plus compact, plus précis et donne accès aussi au temps de relaxation des tissus. En effet, au lieu d'utiliser des vibreurs externes en contact avec le corps du patient pour générer les ondes de cisaillement, il est possible de créer à distance, au sein des tissus, une source d'ondes de cisaillement de forme quelconque à l'aide d'un faisceau ultrasonore focalisé durant quelques centaines de microsecondes qui pousse les tissus de quelques dizaines de microns pendant l'insonification. Ce phénomène est lié à la pression de radiation ultrasonore et peut être engendré à l'aide du même réseau de transducteurs que celui d'imagerie ultrarapide. Ainsi, on peut utiliser la même barrette échographique conventionnelle à la fois pour faire vibrer à distance les tissus et imager à cadence ultrarapide les mouvements des tissus. De plus la possibilité est donnée au médecin de palper « virtuellement » les tissus exactement à l'endroit désiré en déplaçant à volonté le faisceau ultrasonore. En créant plusieurs sources de cisaillement simultanément à des endroits différents, nous avons montré qu'il était possible de créer, par exemple, une source de cisaillement se déplaçant à vitesse supersonique (Fig. 2), i.e. la source de cisaillement se déplace plus vite que l'onde de cisaillement se propageant. Cette source de cisaillement supersonique engendre deux ondes planes se propageant au sein des organes. Ainsi est recréé pour les ondes de cisaillement élastiques dans les organes, l'analogie du bang sonique créé dans l'air par un avion supersonique [4].

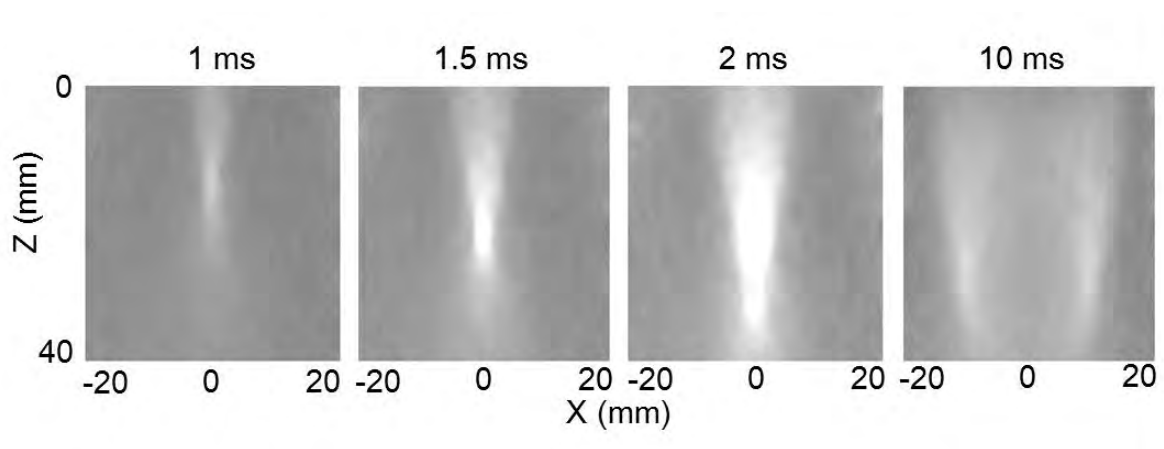


Fig. 2. Génération d'une source de cisaillement supersonique et imagerie ultrarapide de l'onde de palpation résultante par le prototype d'échographie ultrarapide. En niveau de gris, le déplacement engendré dans un fantôme homogène de tissus mous par l'application successive pendant quelques centaines de μ s d'un faisceau ultrasonore focalisé à différentes profondeurs. L'échelle de gris varie de 0 à 10 μ m.

C'est sur ces idées innovantes que les avantages économiques d'un tel système couplant imagerie échographique ultrarapide et palpation ultrasonore à distance, technique que nous avons appelée **Supersonic Shear Imaging (S.S.I.)**, sont devenus évidents :

- Tout en possédant toutes les fonctionnalités d'un échographe classique, ce système donne accès à l'imagerie de deux paramètres mécaniques extrêmement importants du corps humain : le module d'Young et le temps de relaxation de cisaillement des tissus. Cette technique se positionne comme une extension des capacités de diagnostic des échographes et n'impose aucune modification protocolaire au médecin lors de son examen clinique. Elle nécessite cependant une souplesse technologique aujourd'hui inexistante sur les échographes commerciaux et ne peut s'envisager que sur des prototypes échographiques spécialement conçus pour sa mise en œuvre.
- Le domaine d'application de cette invention est vaste. Ce système échographique ultrarapide pourrait permettre en hôpital, clinique ou cabinet de radiologie d'imager les propriétés viscoélastiques du sein, du foie, du cerveau, ... et ainsi apporter une aide lors du dépistage ou du diagnostic de certaines pathologies (Cancer, hépatites C, Cirrhoses,...). Dans le cadre du diagnostic du cancer du sein, il devrait permettre, en complémentarité avec la mammographie et l'échographie, d'affiner le diagnostic. Dans le cadre des pathologies du foie, il pourrait apporter une indication quantitative du degré de fibrose du foie.
- Ce système est basé sur la technologie des ultrasons, et donc de faible coût en comparaison avec l'imagerie d'élasticité par IRM. Sa taille correspondant à celle d'un échographe standard en fait de plus un système d'imagerie ambulatoire pouvant être utilisé tant en pré qu'en post-opératoire, voire même déplacé jusqu'à la chambre du patient.

Ainsi en Mai 2005, une start-up, Supersonic Imagine, a été créée pour valoriser cette nouvelle approche d'imagerie dans le cadre du diagnostic du cancer du sein.

Imagerie d'élasticité par la technique de « supersonic shear imaging » pour le diagnostic du cancer du sein.

Par le développement de cette start-up nous avons pu avoir accès à de nouveaux outils plus performant et plus rapide, nous permettant de valider techniquement et cliniquement cette nouvelle approche. En collaboration avec Supersonic Imagine, une campagne d'expériences *in vivo* a été mise en place avec l'Institut Curie sur 50 patientes pour le diagnostic du cancer du sein par force de radiation acoustique. Pour ce faire nous avons modifié et adapté un échographe commercial, Philips-ATL HDI1000, afin de pouvoir réaliser avec ce dernier une imagerie ultrarapide (>2000 Hz) et de créer directement dans le tissu une pression de radiation acoustique (~100 μ s). Les séquences d'imagerie standard de l'échographe ont été modifiées tout en respectant les normes FDA (normes de sécurité

des appareils d'imagerie médicale définissant les intensités et pressions maximales pouvant être appliqués au corps humain).

Cette campagne d'expérience a permis de montrer qu'une cartographie de l'élasticité du sein était possible *in vivo* en utilisant la force de radiation acoustique. Ce nouveau mode d'imagerie de l'élasticité du corps humain est indépendant de l'opérateur car cette technique utilise une sonde d'échographie classique (La campagne a été menée avec 2 radiologues intervenant sur un nombre de patientes équivalent). Le calcul post acquisition des données *in vivo* permet de retrouver une carte d'élasticité qui permet de différencier les zones grassieuses du sein et le parenchyme (Fig. 3) [5]. Les lésions malines trouvées sont significativement différentes de celles bénignes du point de vue élastique (Fig. 4). Toutes les patientes ont subi aussi pendant l'examen un prélèvement par biopsie ou une ablation des zones tumorales lorsque l'une de ces dernières était nécessaire. Dans ces cas précis, une comparaison histopathologique fut réalisée.

De plus les kystes (poches contenant essentiellement des liquides) peuvent aussi être détectés de manière très efficace car les ondes de cisaillement ne se propagent pas dans les liquides. Un algorithme de recherche astucieux dans les déplacements imagés des zones non propagatrices permet de révéler de la présence de ces lésions (Fig. 5).

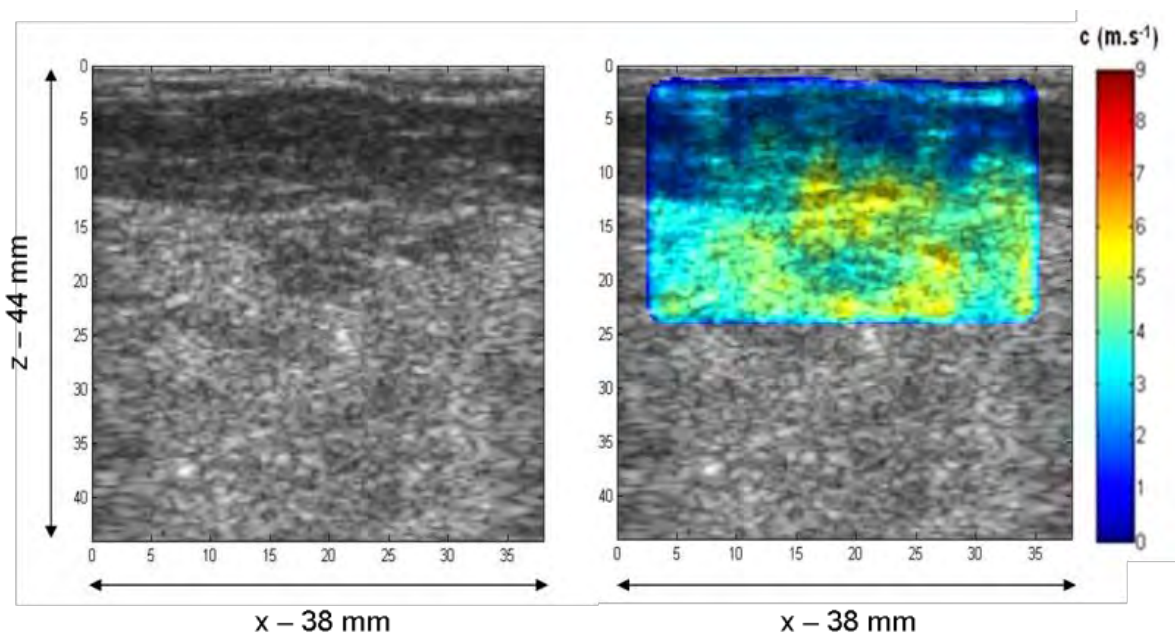


Fig. 3. Comparaison entre l'image échographique standard obtenue pendant une séquence d'imagerie ultrarapide et la carte d'élasticité (proportionnelle à la carte des vitesses de cisaillement). La carte des vitesses de cisaillement est codée en niveau de couleur entre 0 et 9 m.s^{-1} . La carte d'élasticité délimite clairement les zones de tissu mou grassieux ($E \sim 7 \text{ kPa}$) et le parenchyme ($E \sim 30 \text{ kPa}$).

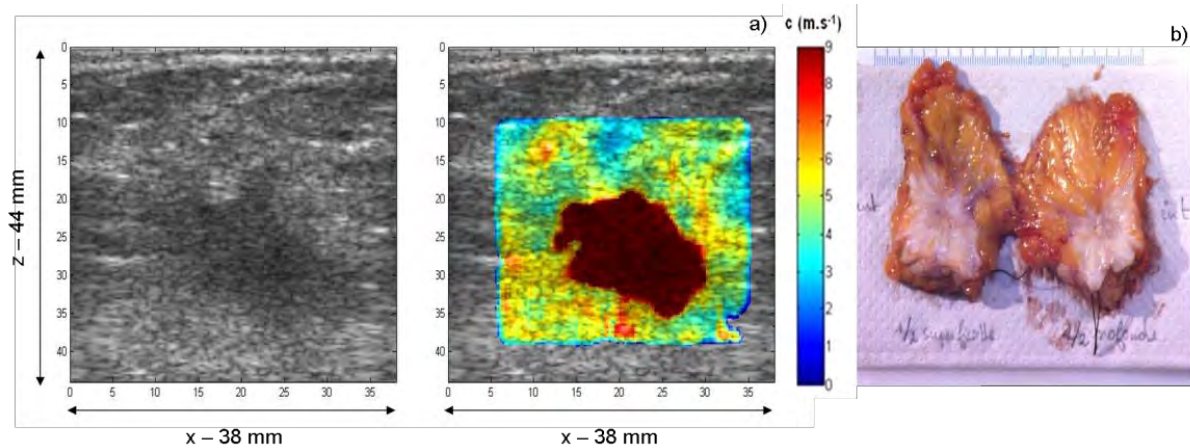


Fig. 4. a) Comparaison entre l'image échographique standard obtenue pendant une séquence d'imagerie ultrarapide et la carte d'élasticité. La carte des vitesses de cisaillement est codée en niveau de couleur entre 0 et 9 m.s^{-1} . La carte d'élasticité délimite clairement la zone de tissu dure maligne ($E \sim 220 \text{ kPa}$) et le parenchyme ($E \sim 30 \text{ kPa}$). b) Photographie de la tumeur excisée. Les formes stellaires infiltrantes de la tumeur corroborent bien celle trouvée sur la carte d'élasticité.

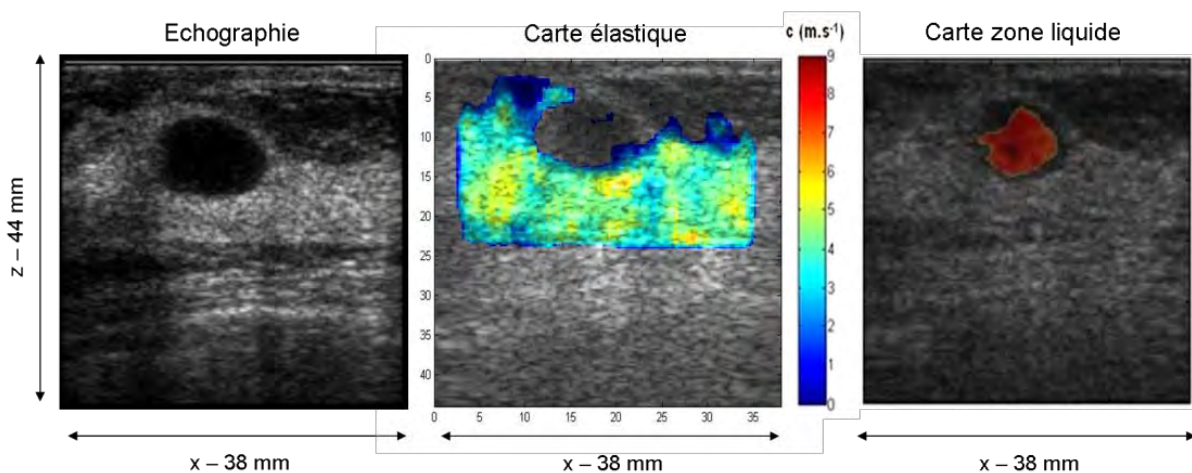


Fig. 5. Comparaison entre l'image échographique standard obtenue pendant une séquence d'imagerie ultrarapide, la carte d'élasticité et la carte des zones kystiques. La carte des vitesses de cisaillement est codée en niveau de couleur entre 0 et 9 m.s^{-1} . La carte des zones kystiques délimite clairement les zones pleines de liquides.

De part cette étude nous avons pu montrer que cette nouvelle technique pouvait devenir un complément important à l'imagerie échographique standard pour améliorer la spécificité et la sensibilité des ultrasons dans le diagnostic du cancer du sein [6]. Cette étude préliminaire a été poursuivie par la compagnie selon un nouveau protocole et en collaboration avec 18 hôpitaux internationaux (U.S.A., Europe, France). Elle a permis de montrer la grande reproductibilité de la mesure en atteignant 87.9 % sur une population de 758 patientes (Fig. 6).

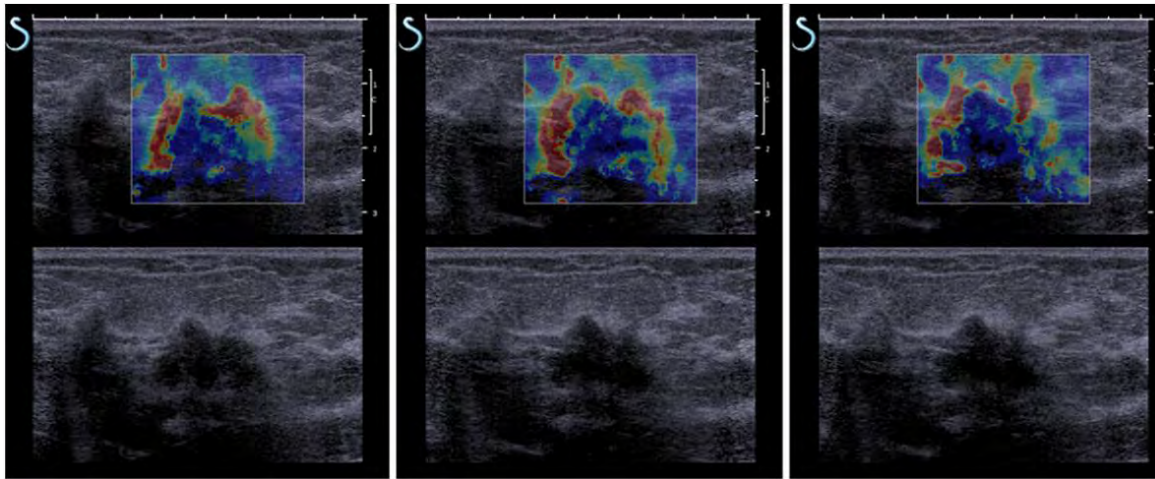


Fig. 6. Etude de la reproductibilité de la technique d'élastographie ultrasonore par ondes de cisaillement sur une patiente. Sur une cohorte de 758 patientes on atteint un taux de reproductibilité de la mesure de 87.9 % [6].

Cette étude a également pu montrer sur 939 patientes que l' spécificité de l'examen échographique grâce à l'ajout de la mesure d'élasticité augmentait de manière significative (de 61.1% à 78.5%) sans changer la sensibilité de l'échographie) [7].

Imagerie 3D pour le diagnostic du cancer du sein.

Cependant nous avons voulu aller plus loin dans l'amélioration de la technique. En effet, si par ces premières études nous avons pu montrer l'apport évident de la mesure d'élasticité dans le cadre du diagnostic, il s'avère que les enjeux du dépistage du cancer du sein sont tout autres. Dans le cadre du dépistage, il s'agit de proposer une méthode fiable, inoffensive et peu chère pour la détection d'éventuelles zones à risque. La technique standard de dépistage est aujourd'hui la mammographie. Elle reste assez chère et a des conséquences sur la santé des patientes. Elle est cependant la seule à être approuvée par les instances publiques. Le caractère inoffensif et peu cher des échographes sont autant d'arguments qui inciteraient à proposer une technique de dépistage basée sur l'échographie. Elle est cependant inenvisageable aujourd'hui pour deux raisons : premièrement, balayer à la main avec la sonde échographique l'ensemble du sein n'est pas possible lors d'un examen classique et deuxièmement l'information échographique aide à la caractérisation d'une tumeur mais n'est pas suffisamment sensible pour détecter précocement les zones à risque.

C'est pourquoi nous avons proposé de coupler une imagerie échographique volumique, capable d'acquérir des données dans l'ensemble du sein, couplée à une cartographie tridimensionnelle de l'élasticité du sein par technique d'imagerie ultrarapide par force de radiation. Avec la résolution donnée par cette technique d'imagerie d'élasticité (1 mm^3), nous pourrions

espérer détecter des lésions de manière très précoce. Ce projet a été conduit sous le nom DARMUS financé par le Cancéropôle île de France – Medicen.

Pour répondre à cette question nous avons utilisé un fantôme cylindrique, mimant le sein et calibré, sur lequel deux méthodes d'imagerie ont été réalisées : l'élastographie par IRM et l'élastographie ultrasonore. En effet actuellement, l'élastographie par IRM est la seule méthode commerciale capable d'obtenir une carte d'élasticité tridimensionnelle. Nous avons donc choisi d'utiliser cette méthode comme « Gold standard 3D ». Ces deux méthodes utilisaient des techniques complètement différentes mais toujours basées sur la propagation des ondes de cisaillement.

Dans le cas de l'IRM, le fantôme est mis en vibration monochromatique par un vibreur externe et le film de propagation des ondes de cisaillement est acquis dans le volume stroboscopiquement.

Dans le cas des ultrasons, la sonde ultrasonore de l'appareil d'échographie permettant d'acquérir une image 2D en mode SSI est apposée sur le côté du fantôme. La sonde tourne ensuite au tour du fantôme et à chaque degré d'angulation une acquisition est réalisée (Fig. 7). L'ensemble des images acquises sert ensuite à reconstruire le volume 3D.

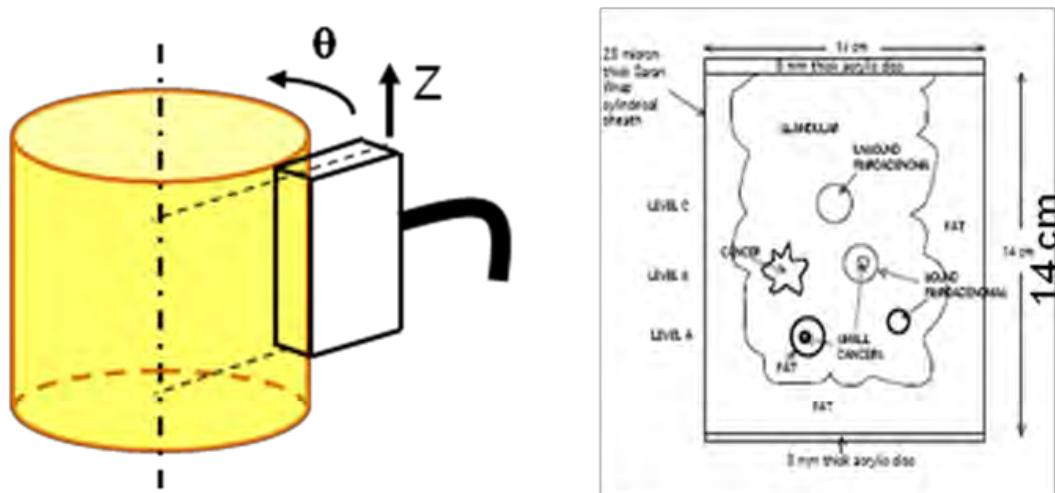


Figure 7 : Principe d'imagerie 3D ultrasonore. La barrette 2D tourne autour du fantôme cylindrique de sein calibré. Schéma des inclusions à l'intérieur du fantôme.

Nous avons pu évaluer chaque méthode en terme de contraste élastique de résolution et de rapidité d'acquisition (Fig. 8&9). Cette étude comparative a permis de montrer que l'approche ultrasonore permettait de bénéficier d'une meilleure résolution en termes de contraste et d'élasticité, et d'une rapidité d'acquisition nettement supérieure.

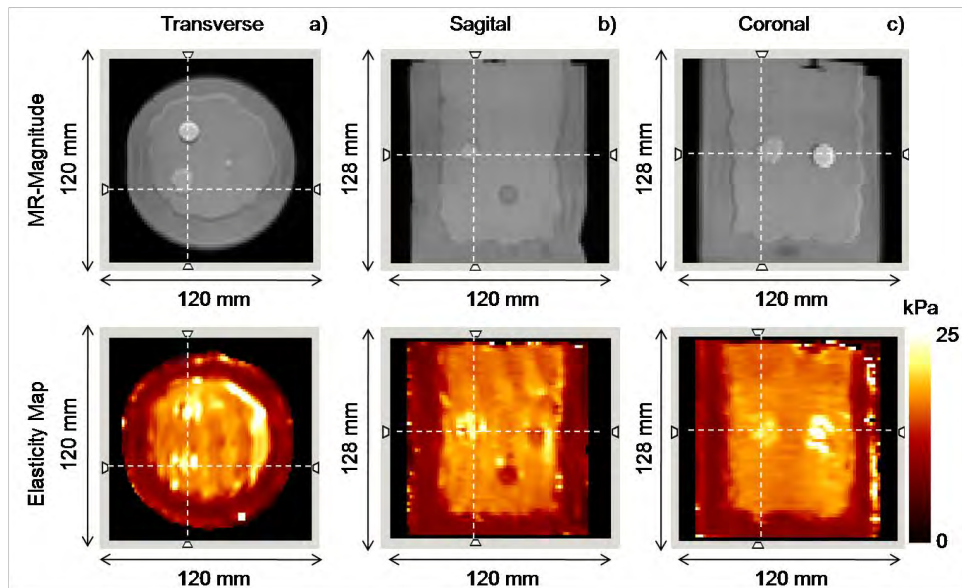


Figure 8 : Image d'amplitude par IRM du fantôme sur trois plans de coupe (noir & blanc). Reconstruction de l'élasticité du fantôme par IRM (couleur).

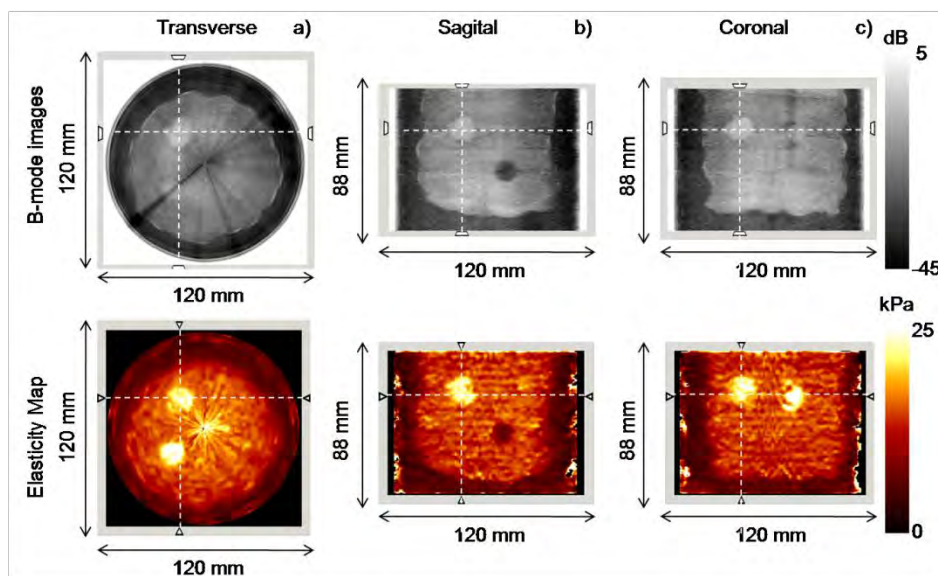


Figure 9 : Image mode-B ultrasonore du fantôme sur trois plans de coupe (noir & blanc). Reconstruction de l'élasticité du fantôme par SSI (couleur).

De cette preuve de concept [8] nous avons mis au point une sonde d'imagerie d'élasticité 3D fonctionnant selon la technique SSI. Cette sonde à balayage mécanique permet d'acquérir en un temps très court (quelques secondes) un volume d'imagerie mode-B et élastique (typiquement 40 mm³) (Fig. 10). Dans le cadre du diagnostic du cancer du sein l'acquisition du volume complet de l'organe n'est pas nécessaire. Nous avons réalisé plusieurs validations sur fantôme et nous avons soumis un protocole d'imagerie des lésions mammaires en 3D au CPP ile de France III. Une partie de ce protocole réalisé en 2011 a pu permettre de vérifier sur 25 patientes la pertinence d'une telle

sonde dans le cadre du diagnostic du cancer du sein. Nous avons pu vérifier l'accord entre la mesure de volume par IRM et la mesure de volume par ultrason. Cette étude nous a ainsi permis de vérifier que cette nouvelle sonde pouvait être un outil fiable pour la caractérisation volumique de tumeurs du sein mais également pour leur caractérisation mécanique. Ce point étant très important pour envisager utiliser ce nouvel outil pour le suivi de thérapie du sein où l'estimation du volume tumorale et le point de référence du diagnostic du médecin. Sur la figure 11 nous présentons un résultat de comparaison entre le volume mesuré par IRM et par ultrason. Actuellement nous évaluons dans une deuxième partie du protocole l'utilisation de la mesure d'élasticité en trois dimensions pour le suivi de traitement par chimiothérapie du cancer du sein (Fig. 12). Nous avons pu pour l'instant montré sur une dizaine de patiente que la mesure d'élasticité pouvait être un outil précurseur en regard de la mesure du volume tumoral pour définir la réussite du traitement, point clef pour orienter le médecin dans le choix de la procédure médicale à suivre [9]. Le protocole est toujours en cours et l'ajout de patientes nous permet d'affiner nos résultats.



Figure 10: Sonde d'imagerie ultrasonore 3D permettant d'acquérir en un temps très court (quelques secondes) un volume d'élasticité (40 mm^3)

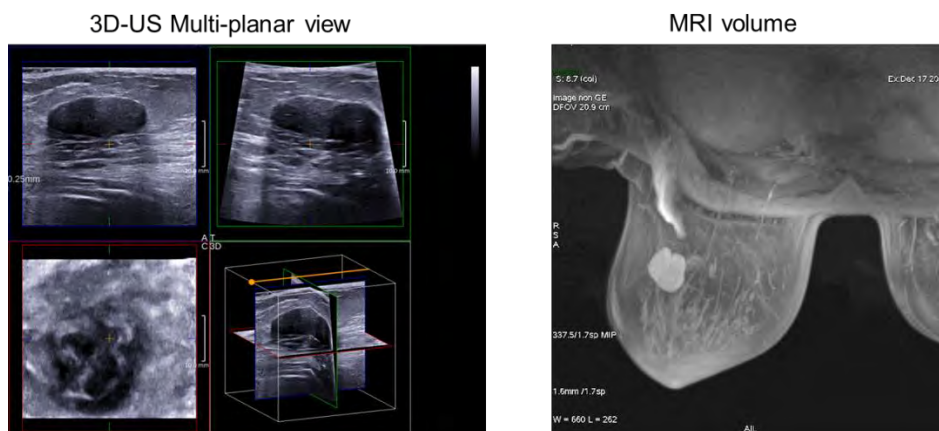


Figure 11: Imagerie 3D par ultrasons et par Imagerie par résonance magnétique d'un fibroadénome (lésion bénigne). Les ultrasons permettent de reconstruire l'image de la lésion en volume et de naviguer en temps réel selon les différent plans de l'image (coronal, sagittale, transverse).

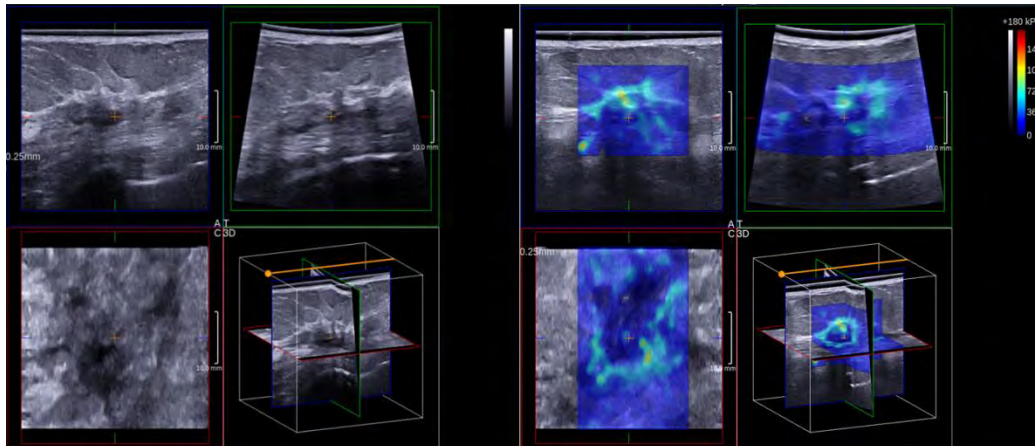


Figure 12: Imagerie 3D par ultrasons et Imagerie 3D d'élasticité d'un carcinome lobulaire infiltrant (tumeur maligne). Le caractère infiltrant et diffus de la tumeur est très clairs sur l'image échographique. La signature élastique est également très marqué et semble avoir un volume plus grand que la signature ultrasonore classique.

Imagerie d'élasticité du foie: Aide au diagnostic de la cirrhose hépatique

La technique d'imagerie ultrarapide par force de radiation a été développée au laboratoire dans le but premier d'aide au diagnostic du cancer du sein. Cependant cette technique est applicable à quasiment l'ensemble du corps humain et en particulier le foie. Récemment il a été prouvé que l'état de d'avancement de la fibrose du foie peut être obtenu de manière non invasive par une estimation moyenne de l'élasticité du foie le long d'une ligne ultrasonore. Cette estimation est fournie par un appareil du commerce, le « Fibroscan » développé par la société « Echosens » ancienne start-up du laboratoire. (Appareil issu de la thèse que j'ai suivi au laboratoire Ondes et Acoustique de 2000 à 2003, « le palpeur acoustique », sous la direction de Stefan Catheline et Mathias Fink). Cependant fournir une carte complète d'élasticité à deux dimensions pourrait être d'un grand intérêt pour la diagnostique de la fibrose hépatique, pour prévenir d'éventuelle cirrhose, mais aussi pour le diagnostic du cancer du foie.

Ainsi nous avons montré au cours de l'année de l'année 2007 que la technique d'imagerie de l'élasticité par génération d'une source supersonique de cisaillement permet d'imager *in vivo* les propriétés viscoélastiques du foie. La force de radiation ultrasonore est induite dans le foie avec une sonde échographique classique identique à celle utilisé sur le sein. La reproductibilité de la technique a été prouvée sur une vingtaine de volontaires sains *in vivo*. Sur la figure 13 est représentée une carte d'élasticité obtenue sur un volontaire sain, nous pouvons distinguer très nettement la zone des muscles intercostaux très durs de celle du foie plus mou. De plus nous avons montré que la technique est insensible aux conditions de bord et en particulier à la présence des côtes entre

lesquelles la sonde est placée. Ces dernières ne gênent pas la génération de la source supersonique de cisaillement [10].

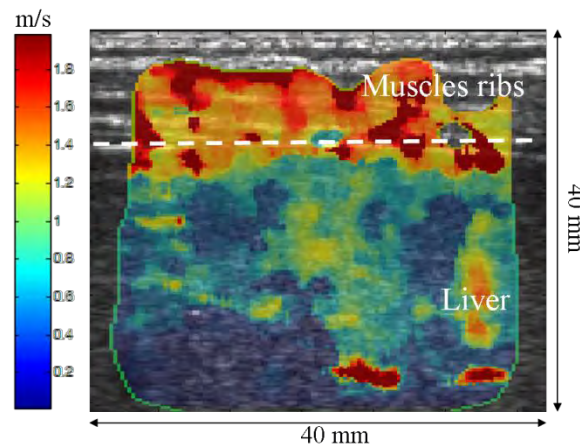


Figure 13 : Carte d'élasticité codée en niveau de couleur, obtenue par la technique de « supersonic shear imaging » et surimposée à l'image échographique classique. La différence d'élasticité entre les muscles intercostaux et le foie est notable.

A la suite de cette étude préliminaire, la technique d'élastographie a été implantée sur une sonde d'imagerie courbe afin d'améliorer l'imagerie et la génération de la source supersonique en profondeur. A l'aide de ce nouvel outil nous avons pu réaliser à l'hôpital Cochin un protocole d'évaluation non invasive de la fibrose hépatique sur 118 patients atteint d'hépatite C. Le diagnostic a été réalisé grâce à un système échographique ultrarapide permettant d'obtenir une image bidimensionnelle quantitative d'élasticité du foie (prototype d'imagerie V1, Supersonic Imagine, Aix-en-provence, France). Les mesures en temps réel d'élasticité ont été corrélées avec le degré de fibrose diagnostiqué par prélèvements sanguins et avec les mesures obtenues par élastométrie Fibroscan. Nous avons pu de cette manière vérifier l'apport significatif de cette technique pour le diagnostic du niveau de fibrose en regard du Fibroscan. L'information bidimensionnelle et multi-fréquentielle (large bande de fréquence des ondes de cisaillement $\sim 80-450$ Hz) de l'élastographie supersonique permet d'obtenir une différenciation bien plus précise de la fibrose du foie par rapport au Fibroscan. Avec la technique par pression de radiation, la mesure obtenue permet d'obtenir une mesure d'élasticité sur une large zone du foie. La moyenne de l'élasticité sur cette zone permet ici de déterminer l'élasticité moyenne du foie avec une plus grande précision que le Fibroscan. En effet, le Fibroscan évalue l'élasticité du foie sur une zone extrêmement restreinte du foie et peut ainsi mener à des erreurs d'évaluation de degré de fibrose. De plus, l'appareil d'échographie ultrarapide peut fonctionner en mode conventionnel d'échographie, permettant ainsi au praticien de coupler deux types d'images du foie pour un meilleur diagnostic. Sur la figure 14 sont présentés un ensemble de cartographie d'élasticité obtenu pour 4 patients ayant chacun un grade fibrose différent de 1 à 4

(sachant que le stade 4 est le stade final de cirrhose du foie cas le plus préoccupant pour le médecin). Nous pouvons voir nettement l'augmentation d'élasticité lié à la pathologie [11].

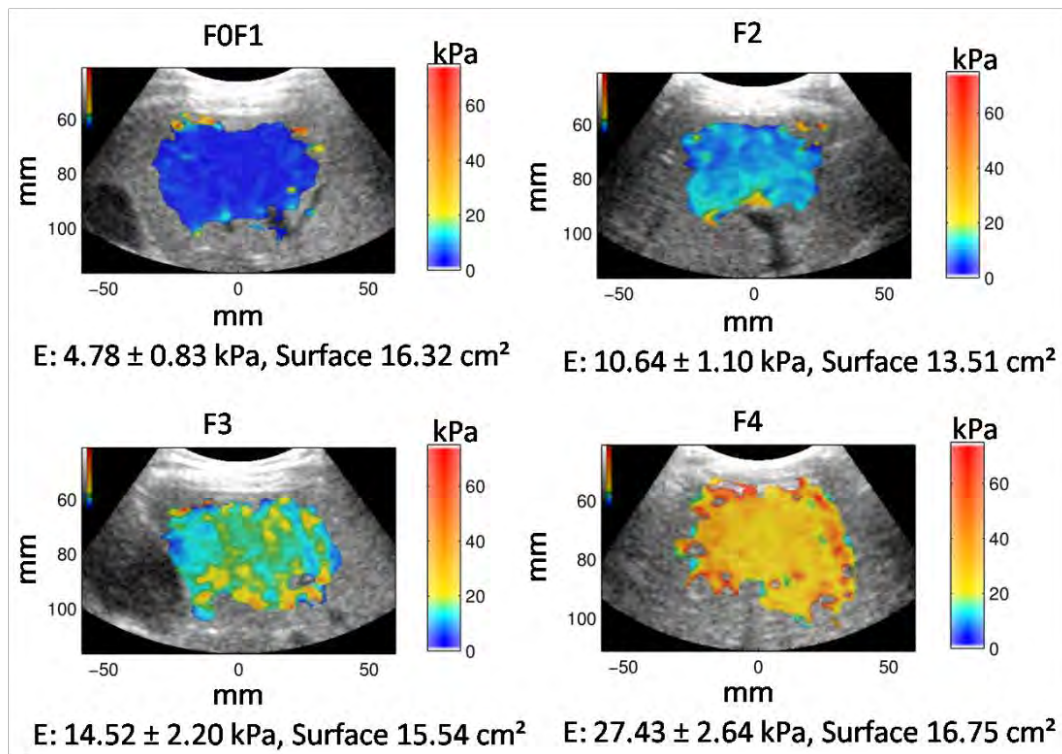


Figure 14 : Image d'élasticité du foie chez quatre patients atteint de fibrose. Le niveau de fibrose codifier de 1 à 4 est corrélé au niveau d'élasticité du foie.

Sur les figures 15 et 16 nous pouvons voir la répartition des niveaux de fibrose sur l'ensemble des patients et l'augmentation du ratio sensibilité-spécificité de la technique d'imagerie par rapport au Fibroscan pour l'ensemble des grades de fibrose.

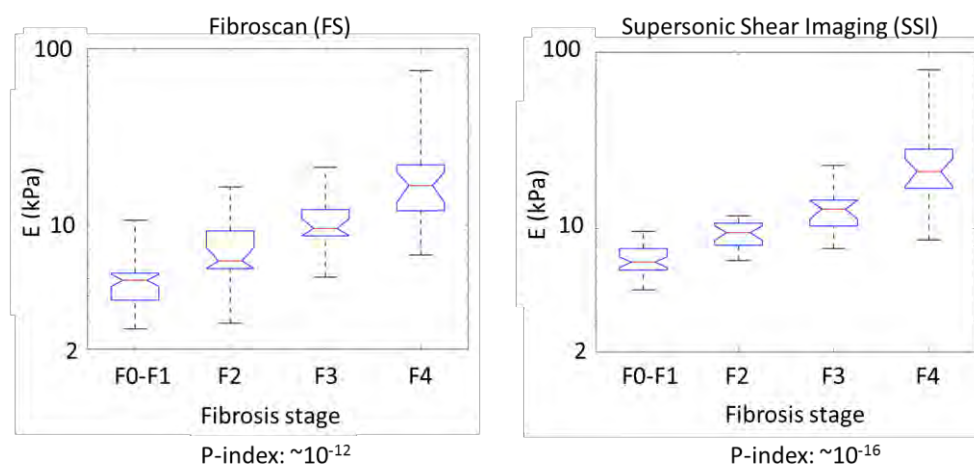


Figure 15 : Répartition des valeurs d'élasticité obtenue avec le Fibroscan et l'élastographie bidimensionnelle sous forme de boxplot. La répartition de la population est de 41% FOF1, 21% F2, 17% F3, 21% F4 sur les 118 patients intégrés à l'étude. Le niveau de fibrose est déterminé par les marqueurs sanguins.

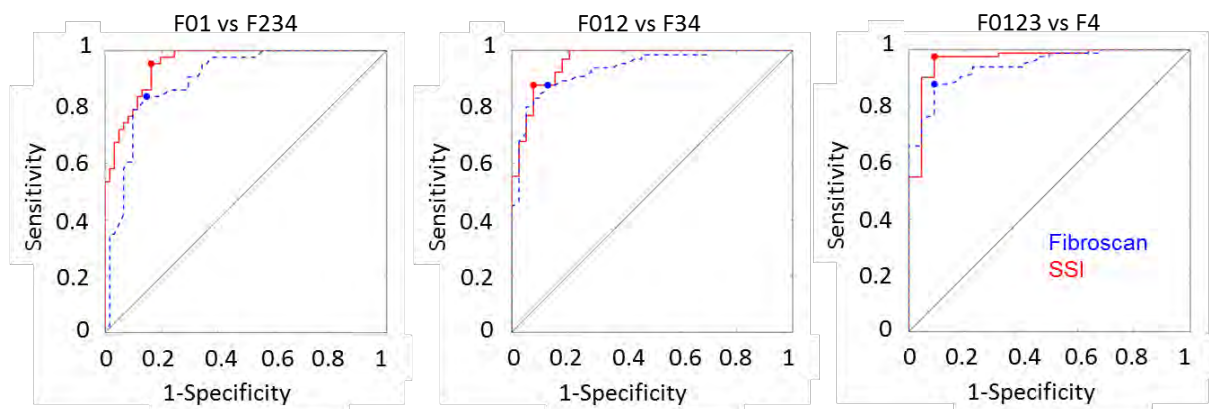


Figure 16 : Courbes dites ROC, permettant de qualifier le rapport spécificité-sensibilité d'une technique. Nous voyons nettement l'ajout de la technique Supersonic (en rouge) en termes de résultat par rapport au Fibroscan (en bleu).

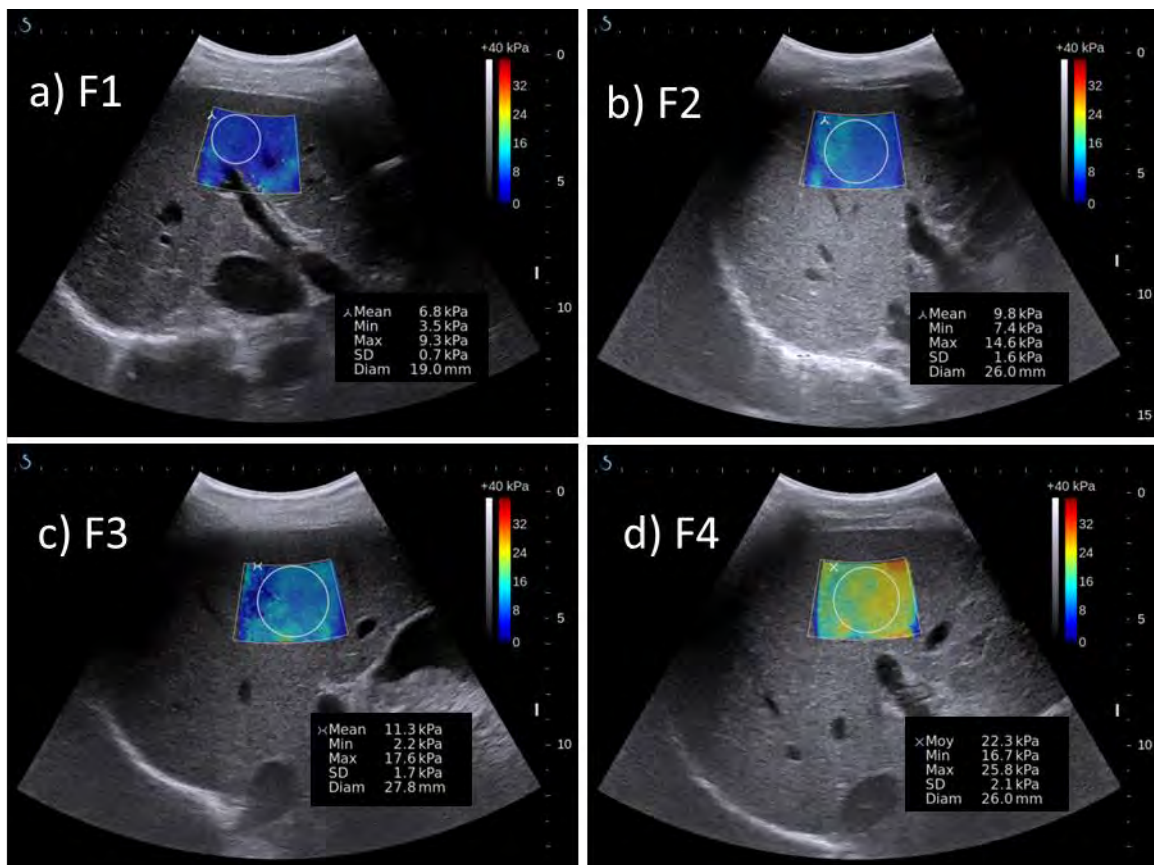


Figure 17: Quatre patients atteints d'hépatite C avec 4 niveaux de fibrose différents. Une carte d'élasticité est présentée pour chaque cas. Nous pouvons facilement distingués l'augmentation d'élasticité due à la pathologie par la carte de couleur changeante en fonction de la dureté.

Suite à cette étude encourageante, l'ensemble de la technique a été implémenté dans l'appareil clinique développé par Supersonic Imagine, l'Aixplorer muni d'une sonde courbe (SC 6-2). Avec cet

appareil nous avons pu conduire un deuxième protocole sur 115 patients, afin de corrélérer l'ensemble de nos résultats, non seulement au Fibroscan mais également à la biopsie. Cette dernière reste actuellement mondialement la référence « gold standard » pour déterminer le niveau de fibrose du foie. L'ensemble des données vient d'être recueilli fin 2012 et l'étude statistique est en cours. Sur la figure suivante nous pouvons voir 4 résultats obtenus sur 4 patients différents avec ce nouveau système. L'avantage conséquent de l'implémentation de la technique sur l'Aixplorer est d'avoir une estimation temps réel du niveau de fibrose du foie en 2 dimensions.

Vers un système haute fréquence.

Nous venons de présenter le développement de la technique Supersonic et l'utilisation de la nouvelle information d'élasticité qu'elle fournit pour le diagnostic de deux pathologies importantes et courantes du corps humain, le cancer du sein et la fibrose du foie. Cette technique a également été développée pour le diagnostic pathologique d'autres organes du corps comme par exemple la thyroïde ou la prostate. Cependant la mesure d'élasticité peut également se révéler importante pour d'autres organes plus fins, plus petits, sur lesquels l'information d'élasticité pourrait être très pertinente comme par exemple l'œil ou la peau. Mais elle peut aussi être développée pour le petit animal dans le but de caractériser l'évolution de pathologies sur quasiment n'importe quel organe avant de revenir sur l'homme.

Dans ce but nous avons développés avec la société Supersonic Imagine un échographe haute fréquence utilisant des sondes allant de 15 MHz à 20 MHz afin de réaliser non seulement des imageries ultrasonores avec une précision allant jusqu'à 70 μm , mais également des cartes d'élasticité et de nouveaux modes Doppler sensibles. Figure 18 nous présentons un ensemble de sondes que nous avons développés pour les études en ophtalmologie, en dermatologie ou sur le petit animal. Pour chaque domaine l'utilisation d'un tel système permet ou permettra d'apporter des réponses aux problèmes quotidiens des médecins ou expérimentateurs animaliers.

En ophtalmologie, l'estimation des propriétés mécaniques de la cornée ou du cristallin offrirait une information pertinente pour de multiples applications. L'aspect le plus immédiatement prometteur de la technologie Supersonic concerne une meilleure gestion des pathologies cornéennes telles que le kératocône et l'estimation de facteurs de risque d'évolutivité dus à des propriétés mécaniques anormales de la cornée atteinte. Le suivi dans le temps des kératocônes infra cliniques avant une chirurgie réfractive représenterait une aide considérable et précieuse pour éviter la dramatique ectasie cornéenne post Laser « excimer » (PLE). Même si ces cas sont relativement rares, les ectasies PLE pourraient être évitées en estimant l'élasticité de la cornée avant tout traitement. Il est important ici de rappeler que dans les cas extrêmes de PLE, l'utilisation d'anneaux

cornéens ou pire, une kératoplastie est nécessaire pour rendre une vision acceptable à ces patients généralement jeunes. Par ailleurs, cette technologie permettrait de contrôler l'efficacité de nouveaux traitements cornéens tels que la mise en place d'implants intra cornéens à présent assistées par laser femto-seconde ou l'efficacité de la photopolymérisation cornéenne thérapeutique basée sur le cross-linking du collagène obtenu par illumination UVA de la riboflavine (UVA CXL).

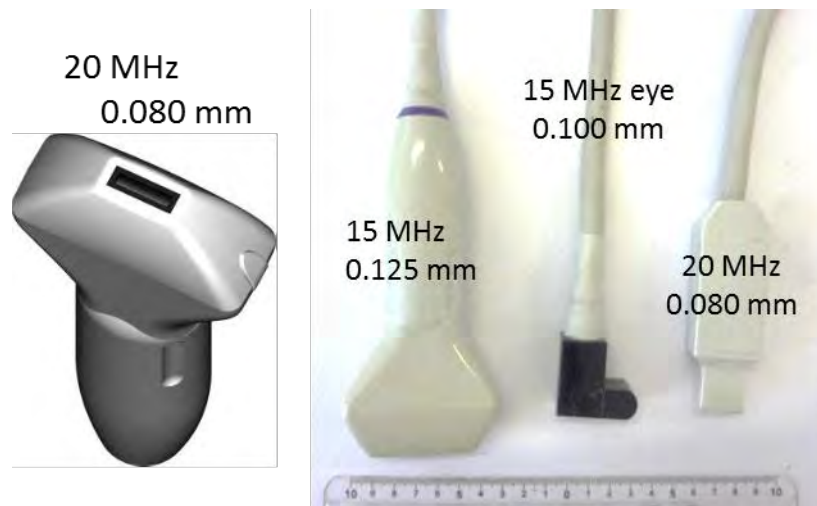


Figure 18: Sondes d'imagerie ultrasonores haute fréquence développées pour l'ophtalmologie, la dermatologie ou l'imagerie du petit animal. Pour chaque sonde la fréquence centrale ainsi que le pitch sont présentés.

Une autre application particulièrement pertinente concerne l'évaluation quantitative de la réponse biomécanique cornéenne après une chirurgie laser photoablatrice ou des procédures de remodelage par incisions relaxantes cornéennes. Il est à présent reconnu que la prédictibilité et la précision du résultat réfractif dépend en partie de la réponse biomécanique de la cornée dont la connaissance est limitée par l'absence de moyen de mesure *in vivo*. Enfin, dans un autre registre, la technologie Supersonic peut de plus aider à l'amélioration de l'estimation de la pression intra oculaire (PIO) mesurée actuellement par applanation. Une mauvaise appréhension de l'élasticité de la cornée peut entraîner une sur-correction ou une sous-correction en fonction des propriétés viscoélastiques de la cornée de chaque patient et en particulier après une chirurgie réfractive photoablatrice.

L'institut Langevin a récemment mené une étude préliminaire en collaboration avec le Dr Touboul du centre du Keratocône de Bordeaux afin d'évaluer la capacité du mode Supersonic à la fois de générer localement des vibrations de cisaillement mécaniques par forces de radiation ultrasonore dans la cornée et d'imager par échographie ultrarapide la propagation des ondes de cisaillement résultantes à l'intérieur de la cornée. La figure 19 présente plusieurs images des déplacements tissulaires dans une cornée porcine à différents instants après la poussée par force de

radiation ultrasonore (obtenu *ex vivo* sur œil d'animal énucléé entier). Après ces preuves de concept, Thu-Mai Nguyen a pu pendant sa thèse au laboratoire, comprendre quel type d'ondes élastiques se propagent dans la cornée et ainsi comprendre que les modes de propagation observés correspondaient à la propagation d'ondes de Lamb, guidées et dispersives [12]. Elle a pu également vérifier la dépendance entre la mesure d'élasticité de la cornée et la pression intraoculaire [13], ou encore suivre l'action d'un traitement chimique de la cornée « cross-linking » *in vivo* chez le porc. Ce traitement permettant de durcir la cornée chez l'homme dans le cas de pathologie comme le kératocône [14]. Les travaux de Thu-Mai dans ce domaine ont été essentiels pour mieux comprendre la propagation des ondes dans les milieux stratifiés et de petite dimension.

Suite à ces travaux nous avons développé une interface de couplage entre la sonde ultrasonore et l'œil humain pour aller vers des expériences *in vivo* sur l'homme. Ce système mécanique présenté figure 20, permet d'apposer la sonde à la surface de l'œil avec un control parfait de l'orientation et de la rotation de cette dernière. L'ensemble du montage s'adapte sur une lampe à fente, outil primordial de l'ophtalmologiste.

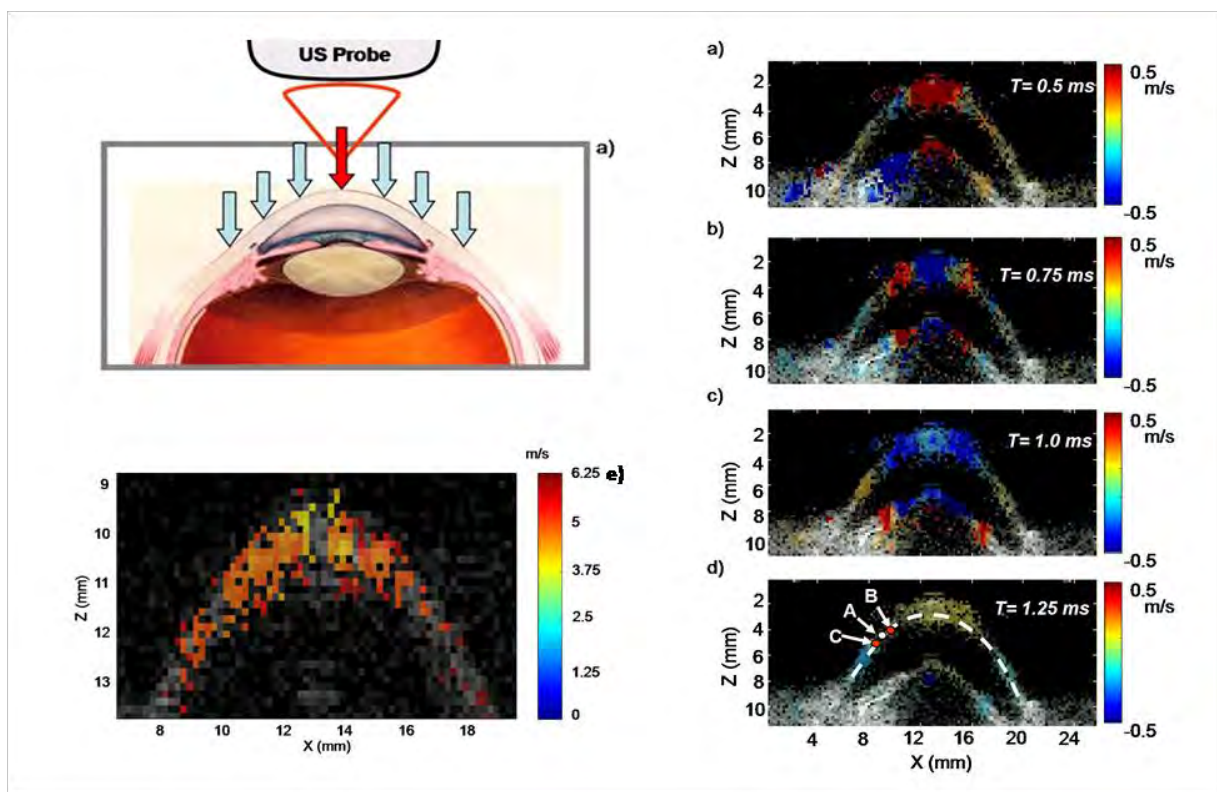


Figure 19. a) Principe du mode d'imagerie d'élastographie par Supersonic Shear Imaging (SSI). La sonde échographique génère une poussée transitoire dans la cornée (flèche rouge) qui engendre une onde de cisaillement (flèches bleues) se propageant le long de la cornée. a, b, c, d) Superposé à l'image échographique de l'œil en niveau de gris, images des déplacements micrométriques à différents instants après la poussée. e) Cartographie de la vitesse locale de l'onde de cisaillement (directement reliée au module d'Young des tissus)



Figure 20. Système d'adaptation de la sonde échographique à l'œil humain. L'ensemble se monte sur une lampe à fente pour faciliter le travail de l'ophtalmologiste.

Les travaux de Thu-Maï, nous ont également permis d'aller vers la dermatologie et l'étude de l'élasticité de la peau. En effet en dermatologie, l'exploration fonctionnelle mécanique vise à caractériser les propriétés mécaniques intrinsèques des structures tissulaires constituant la peau, dont dépendent leur fonctionnalité, et à en suivre le comportement mécanique lors d'un traitement. L'élastographie peut ainsi être mise à profit dans le suivi de pathologies telles que les scléroses cutanées (sclérodermies, radiodermites...) et dans le cadre de tests d'efficacité de produits cosmétiques, notamment à visée anti-âge. Actuellement différentes méthodes sont employées pour la caractérisation mécanique. La méthode de succion est utilisée pour des mesures avec deux appareils : le cutomètre et le Dermaflex A. La méthode de torsion est mise en œuvre pour le torquemètre. La compressibilité de la peau est mise à profit dans les techniques d'indentométrie et de balistométrie. Toutes ces techniques ne sont pas exploitables en diagnostic et dans le suivi de tumeurs cutanées. Pour ce qui est des techniques d'échographie cutanée haute résolution, elles permettent de repérer des anomalies de structure (tumeur, kyste, corps étranger) dont la composition n'est pas celle de la peau à condition que l'épaisseur minimale de la lésion soit supérieure à 100 μm .

Sur ces considérations nous avons adapté le système à l'étude des couches cutanées. Nous avons pu travailler sur deux protocoles, un clinique et un cosmétique. En clinique nous avons travaillé avec l'hôpital de Besançon où nous avons réalisé une étude de comparaison entre les lésions malignes et bénignes de la peau sur 30 patients. L'ensemble des résultats a fini d'être acquis en Décembre 2012 et une analyse statistique est en cours. Un exemple de nævus bénin est présenté sur la figure 21.

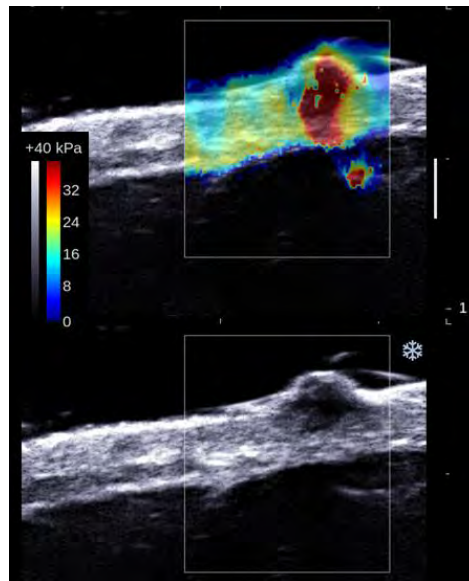


Figure 21. Imagerie d'un nævus de la peau à haute fréquence (20 MHz). En couleur nous retrouvons la carte d'élasticité du tissu montrant le caractère plus dur de la lésion bénigne.

Le deuxième protocole que nous avons mis en œuvre concerne la cosmétique et a été réalisé en collaboration avec L'Oréal. Nous avons pu étudier sur une population de 100 volontaires saines, l'effet d'un cosmétique et sur 100 autres l'évolution de l'élasticité de la peau en fonction de l'âge. Les données étant confidentielle, nous ne pouvons les publier dans ce mémoire, mais nous avons pu observer des forts changements de l'élasticité sur les deux protocoles fonction des hypothèses posées au départ.

Imagerie haute fréquence pour le petit animal

L'utilisation de la haute fréquence a permis également d'aller vers l'imagerie du petit animal. En effet avec l'utilisation de ce nouveau système nous avons pu obtenir une précision d'imagerie allant jusqu'à 70 μ m en utilisant de sondes à 20MHz. Ceci nous a permis d'étudier plusieurs pathologies sur différents organes, en utilisant des animaux traités en fonction des besoins [15]. En exemple nous avons réalisé sur le rat l'étude de la fibrose rénale, pathologie aux lourdes conséquences chez le transplanté rénal humain. En effet l'état de fibrose du rein traduit chez l'homme l'acceptation par le corps de la greffe ou non de l'organe. Ce changement d'état du rein, qui peut être révélé par la mesure de l'élasticité comme dans le cas du foie, peut être quantifié et servir de prédicteur pour le suivi de l'état rénal et de la prise en charge du patient post-transplantation. Cette étude nous a permis de vérifier et de s'assurer que l'outil élastographie pouvait être un outil clinique pertinent pour suivre la fibrose rénale et ainsi passer en clinique sur l'homme. Sur la figure 22 est présenté deux cartes d'élasticité du rein de rat selon deux plans de coupe de l'organe à un temps donné de l'étude. L'étude nous a permis de montrer l'augmentation de la valeur d'élasticité

avec la fibrose rénale. Les animaux ont suivis une diète spécifique provoquant la fibrose rénale et nous avons pu suivre l'évolution de l'élasticité du rein longitudinalement.

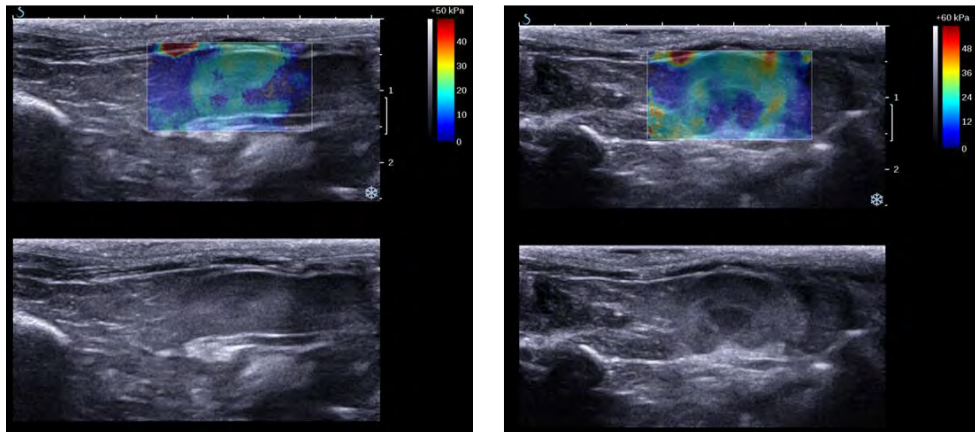


Figure 22. Carte d'élasticité et imagerie ultrasonore à un temps donné (longitudinale et transverse) d'un rein de rat pendant un traitement diététique provoquant la fibrose rénale.

Sur un autre exemple d'application nous avons pu utiliser le système pour suivre la croissance tumorale d'un cancer du sein humain greffé chez la souris. Là encore nous avons pu voir l'utilité d'un tel système qui nous a permis d'essayer de répondre à une question essentielle en cancérogénèse : à quels paramètres biologiques est due l'augmentation d'élasticité dans le cas du cancer du sein? [16]

Pour essayer de répondre à cette question nous avons suivi sur 90 jours la croissance tumorale de cancer du sein humain (BC52) greffé chez la souris (N = 30). Grâce au système nous avons pu suivre à haute fréquence (15 MHz) l'évolution de l'élasticité tumorale. Sur la figure 23 est présentée l'évolution de la croissance tumorale d'une souris à différents instants pendant les 90 jours d'expérimentation. Statistiquement nous avons pu mettre en relation le diamètre tumoral et l'élasticité des tissus cancéreux.

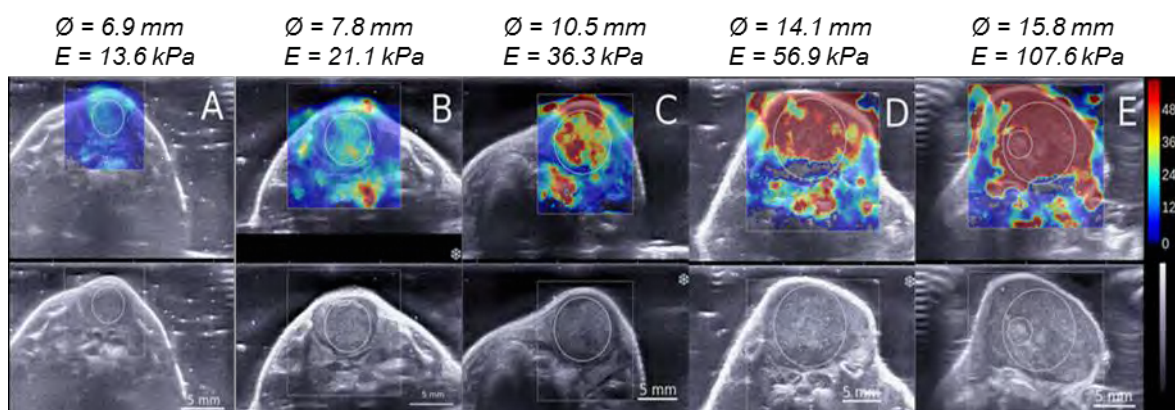


Figure 23. Evolution de l'élasticité d'une tumeur de cancer du sein (BC52) greffé chez la souris.

Au cours de ce suivi de croissance nous avons procédé à un sacrifice régulier de certains animaux pour procéder à des analyses histopathologiques afin de mettre en relation les paramètres

biologiques et la valeur d'élasticité mesurée. Ainsi nous avons pu voir que le paramètre biologique principal lié à l'élasticité était la fibrose de la tumeur (Fig. 24).

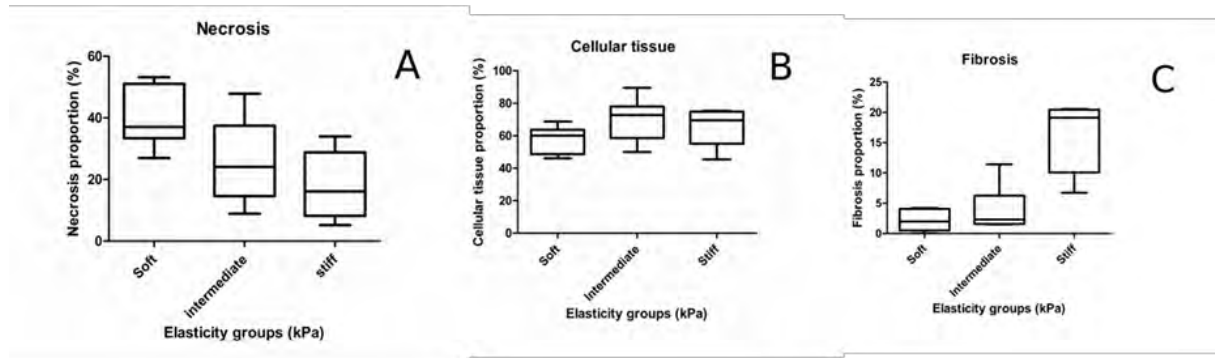


Figure 24. Paramètres histopathologiques quantifiés au cours de la croissance tumorale (Nécrose, Céllularité, Fibrose). Les mesures d'élasticité ont été rassemblées en 3 groupes (soft, intermediate, stiff). On distingue clairement la dépendance de la nécrose et de la fibrose avec l'élasticité.

Ces deux études exemples montre bien l'utilité d'un tel système d'imagerie haut fréquence pour l'imagerie du petit animal. Le champ des possibilités d'étude de différentes pathologies avant de passer à l'homme sans passer par le gros animal est plus qu'important. De plus l'utilisation du petit animal pour l'étude de nouvelle thérapie médicamenteuse, l'évolution de pathologie cancéreuse ou encore d'organisme génétiquement modifié étant très répandu un tel outil pourrai se révélé quasi-indispensable. Enfin cet outil permet l'élaboration de nouvelle technique d'imagerie, comme par exemple l'élastographie mais aussi l'imagerie Doppler sensible, techniques qui une fois vérifié sur le petit animal peuvent ensuite directement passer en utilisation clinique chez l'homme.

II.3 CHAPITRE 3 : ANISOTROPIE ELASTIQUE

L'élastographie est une technique très innovante qui permet d'étudier l'élasticité des tissus mous et en particulier du corps humain. Ce paramètre mécanique est fortement corrélé à différentes pathologies et permet d'affiner dans certain cas le diagnostic du médecin. Cependant l'élasticité n'est pas un paramètre simple, il dépend également de l'architecture des milieux étudiés et en particulier de leur anisotropie. Dans cette partie du mémoire nous présentons comment nous avons pu utiliser la technique d'élastographie supersonique pour retrouver l'anisotropie d'organes tel que le muscle ou le rein.

Imagerie d'élasticité du muscle

L'élasticité du muscle est très compliquée. Cet organe est un organe qui a la faculté de changer son élasticité en temps réel. De ce fait ce dernier est très difficile à caractériser en globalité. Dans le but d'essayer de répondre à cette question et également d'étudier les pathologies neuromusculaires, nous avons réalisé plusieurs études sur le biceps [17]. Le biceps est un organe longiligne dont les fibres parfaitement alignées facilitent l'étude de l'anisotropie. Ainsi nous avons pu caractériser avec la technique SSI le muscle au repos et en contraction, son anisotropie au repos et en contraction et son extension. Sur la figure suivante nous présentons l'architecture musculaire du biceps. Ce dernier est constitué de deux muscles, le biceps *brachii* et le *brachialis*.

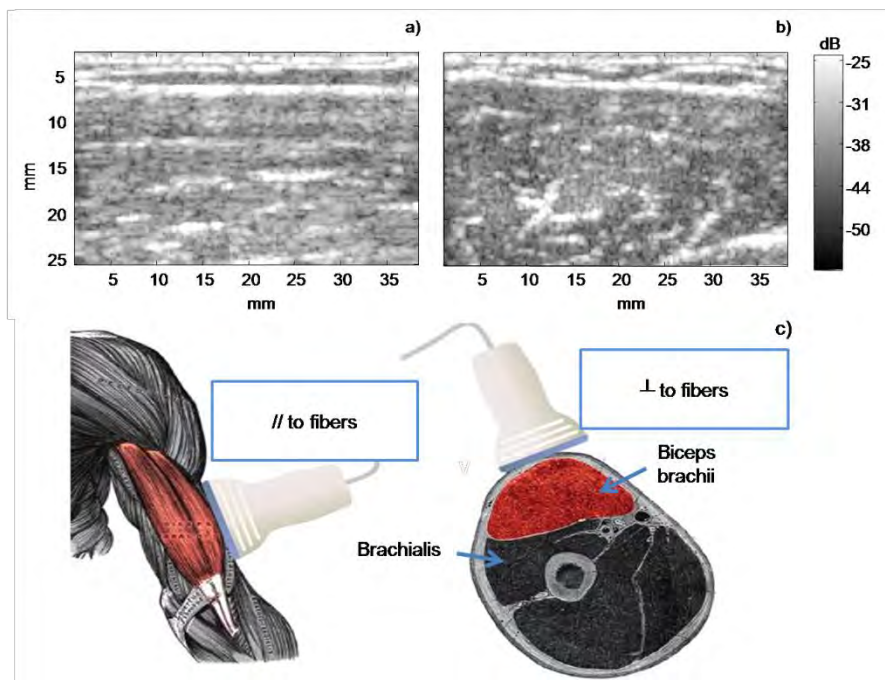


Figure 25 : Image ultrasonore du muscle en position longitudinale a) et transverse b) par rapport aux fibres musculaires.

En fonction de l'orientation de la sonde ultrasonore qui génère des ondes de cisaillement quasi-plane dans le plan de l'image, il est alors possible de retrouver l'élasticité des fibres parallèlement ou perpendiculairement aux fibres musculaires (fig. 26). Nous voyons également que la contraction musculaire influe sur le ratio d'anisotropie d'un muscle. La contraction musculaire entraîne une rigidification des muscles beaucoup plus forte le long des fibres que perpendiculairement.

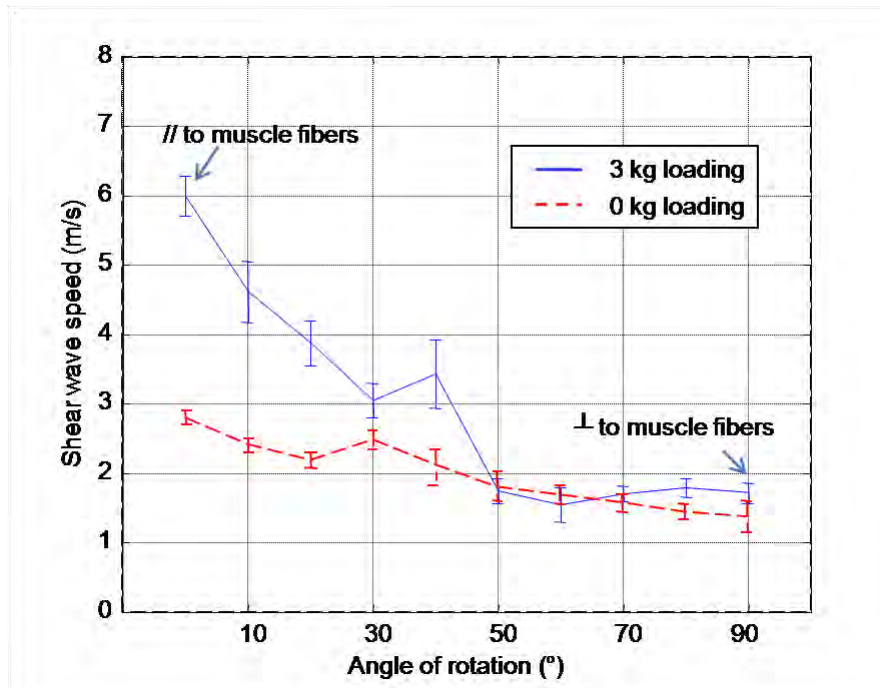


Figure 26 : Evolution de la vitesse des ondes de cisaillement dans le muscle (*biceps brachii*) par rapport à l'axe des fibres musculaires au repos et en contraction pour une charge de 3 kg.

L'utilisation de la technique supersonic pour faire des cartes, des images de l'élasticité des muscles peut permettre également de segmenter l'évolution du ratio d'anisotropie localement et de différencier le changement de ce dernier. Sur les figures suivantes (Fig. 27&28) nous pouvons voir l'évolution de l'élasticité du *biceps brachii* et du *brachialis* en fonction de l'état de contraction musculaire. Nous pouvons parfaitement distinguer perpendiculairement aux fibres les deux muscles, le *brachialis* étant plus mou, ressort codé en bleu et voir ainsi l'augmentation du ratio d'anisotropie. Il est aussi possible de retrouver l'évolution de cette même anisotropie en fonction de l'état d'étirement passif du muscle. Nous pouvons voir sur la figure 29 que l'état élastique du muscle change avec son étirement passif et que son anisotropie change également. L'ensemble de ces modifications locales de l'élasticité du muscle rend son étude à la fois très intéressante et très complexe.

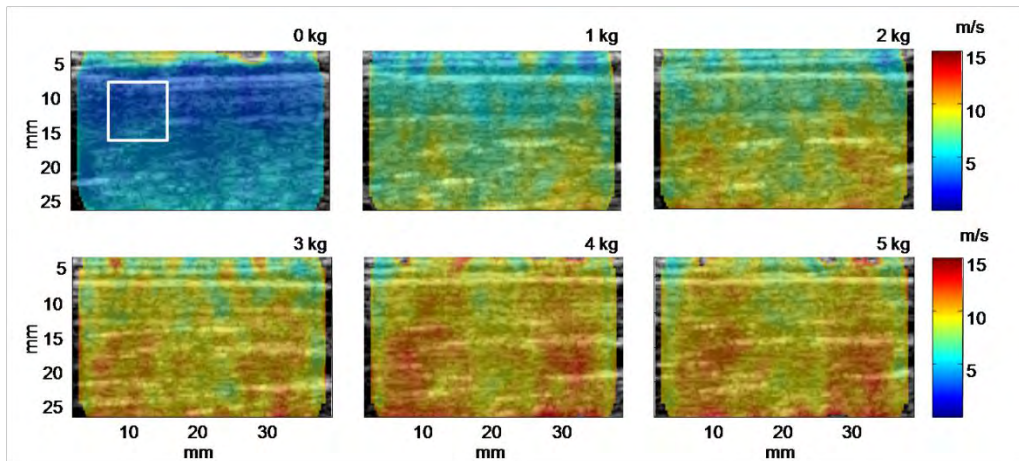


Figure 27: Carte d'élasticité du biceps brachii et du brachialis le long des fibres musculaires en fonction de la contraction correspondant à des charges de 0 à 5 kg.

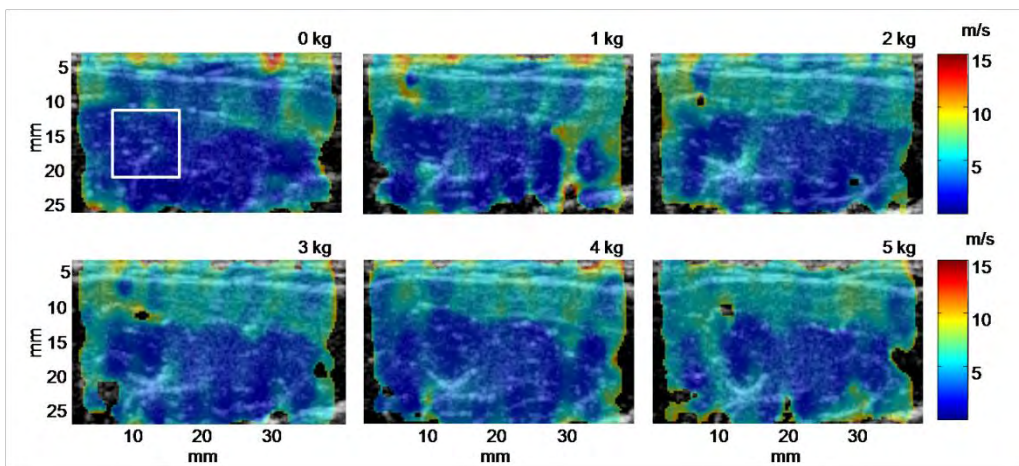


Figure 28 : Carte d'élasticité du biceps brachii et du brachialis perpendiculairement aux des fibres musculaires en fonction de la contraction correspondant à des charges de 0 à 5 kg.

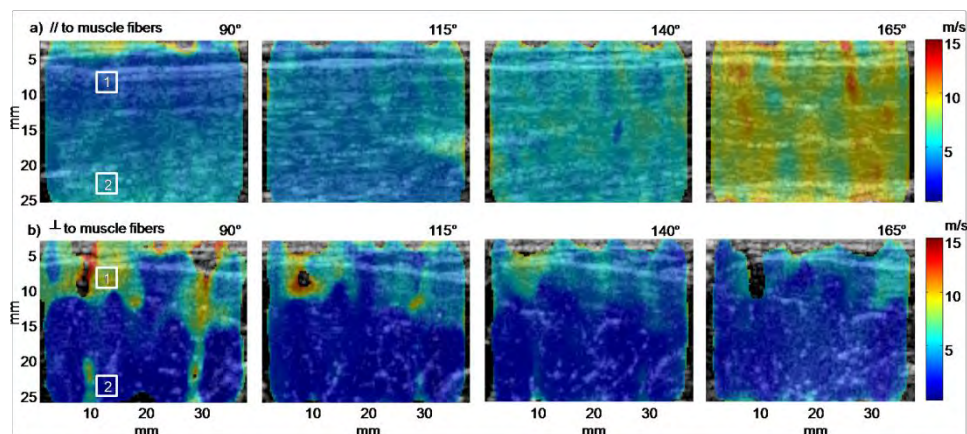


Figure 29: Carte d'élasticité du biceps brachii et du brachialis le long a) et perpendiculairement b) aux fibres musculaires en fonction de l'angulation du coude provoquant une extension des muscles.

Cette étude générale a permis de mieux comprendre le fonctionnement du muscle et d'appréhender nos futures recherches de manière plus sereine. Suite à cette étude nous avons pu en

collaboration avec Karim Sabra de Georgia Tech (USA) mettre au point un protocole de mesure de l'élasticité du muscle par ultrason prenant en compte le niveau de contraction et l'anisotropie. Cette collaboration a également permis de mettre au point des séquences d'imagerie ultrasonore du muscle donnant accès à une carte complète d'élasticité du muscle. De ce fait nous pouvons distinguer dans un muscle multicompartimenté le niveau de contraction de chaque axe musculaire (Fig. 30) [18].

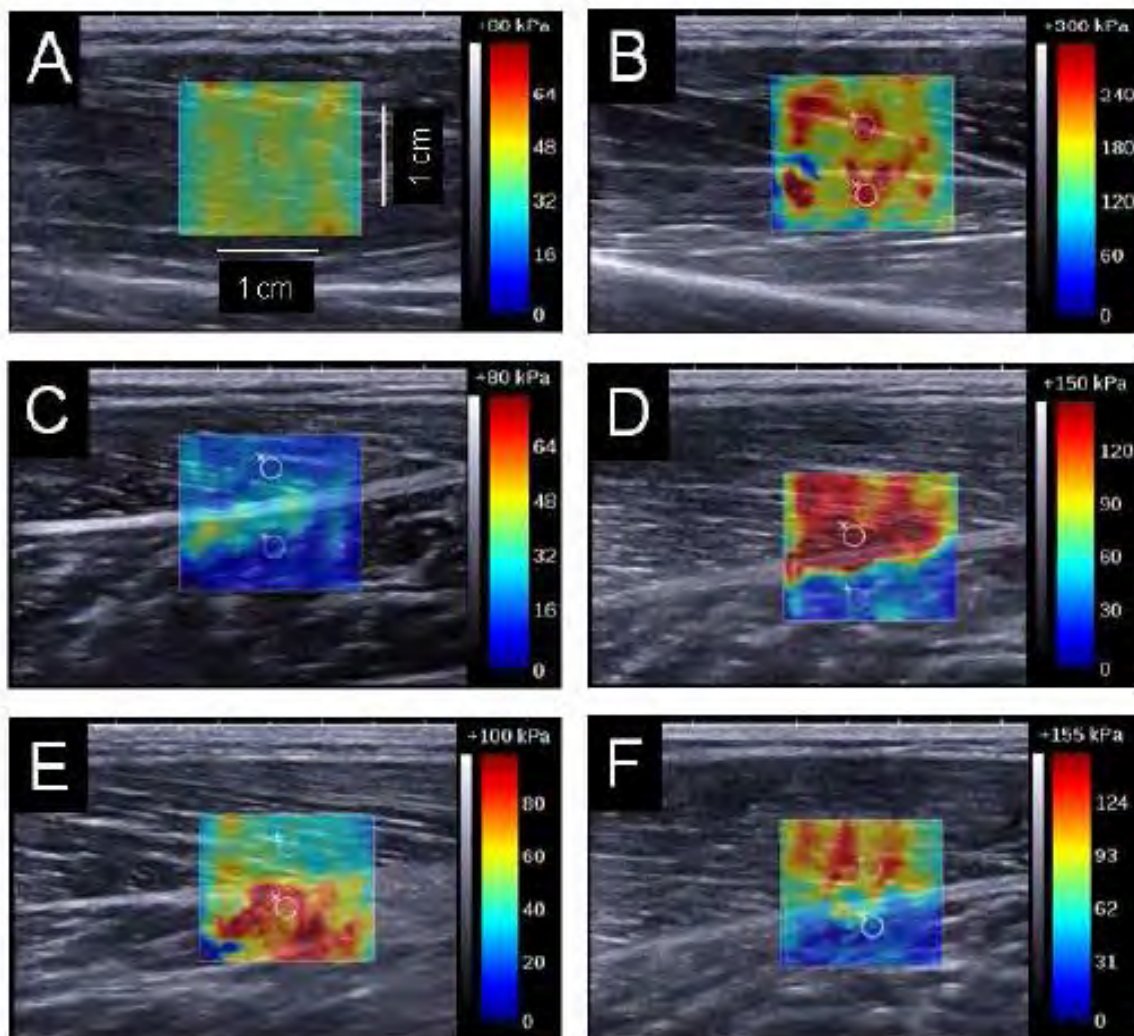


Figure 30 : Elasticité des muscles du mollet pour différentes positions de la jambe et différentes contractions. a) tibialis antérieur au repos, b) tibialis antérieur contracté, c) gastrocnemius médian et soleus au repos jambe tendue, d) gastrocnemius médian et soleus contractés jambe tendues, e) gastrocnemius médian et soleus au repos avec le genou plié, e) gastrocnemius médian et soleus contractés avec le genou plié.

Imagerie d'élasticité du rein

L'anisotropie, très forte dans le muscle, est également présente sur beaucoup d'autres organes du corps humain comme par exemple le rein. Nous avons pu montrer que la mesure du ratio d'anisotropie élastique du rein permettait de mieux comprendre son fonctionnement et ses

propriétés mécaniques [19]. Cet organe est très complexe, en effet son architecture en forme de pyramide idéalement agencée pour filtrer le sang et évacuer dans le système urinaire les déchets (Fig. 31), rend son analyse au niveau des propriétés mécaniques très complexe. En plus d'avoir une telle architecture, le rein est extrêmement pulsatile et sensible à la pression urinaire. Comme dans le muscle le ratio d'anisotropie change en fonction des conditions de pression et permet d'avoir un indicateur de ces dernières.

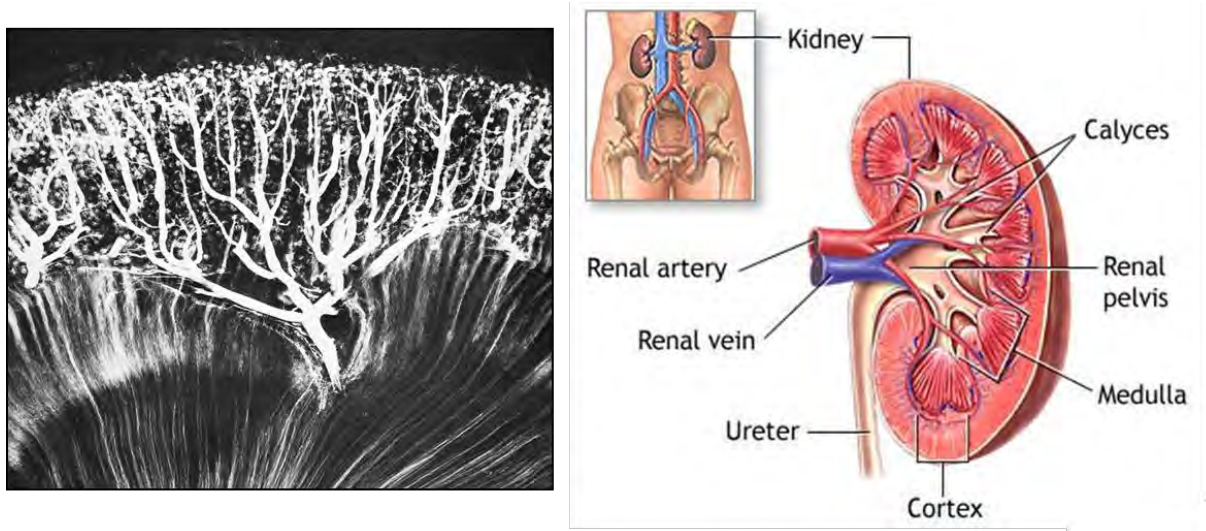


Figure 31: Coupe anatomique du rein.

Sur la figure 32, sont présentés deux images d'élasticité obtenue sur le rein de porc en peropératoire *in vivo*. A gauche la sonde est positionnée de tel manière à ce que le faisceau ultrasonore soit dans l'axe des fibres d'une des médullaires du rein. Dans cette position, nous quantifions l'élasticité perpendiculaire aux fibres de la médullaire. A droite de l'image la sonde est positionnée perpendiculairement aux fibres de la médullaire ce qui nous permet d'obtenir une quantification de l'élasticité parallèle à la médullaire. Ces deux mesures permettent de quantifier le ratio d'anisotropie des médullaires et du cortex rénal et de déterminer par exemple son évolution en fonction de la pression urinaire (Fig. 33). En ce qui concerne les changements d'élasticité dû à la variation de pression, ces derniers peuvent être expliqués par les effets de nonlinéarité élastique que nous aborderons dans le chapitre suivant.

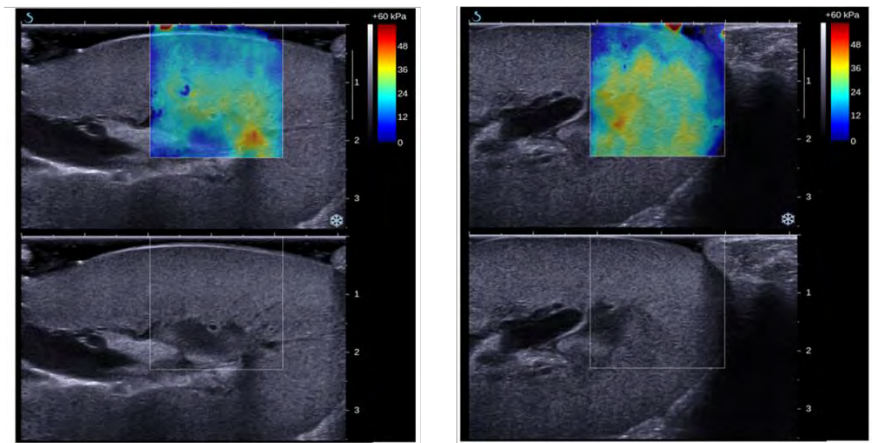


Figure 32: Carte d'élasticité d'une médullaire et du cortex rénale d'un proc acquis en peropératoire in vivo. A gauche la sonde est placée avec l'axe du faisceau ultrasonore parallèle aux fibres de la médullaire. A droite avec l'axe du faisceau ultrasonore perpendiculaire.

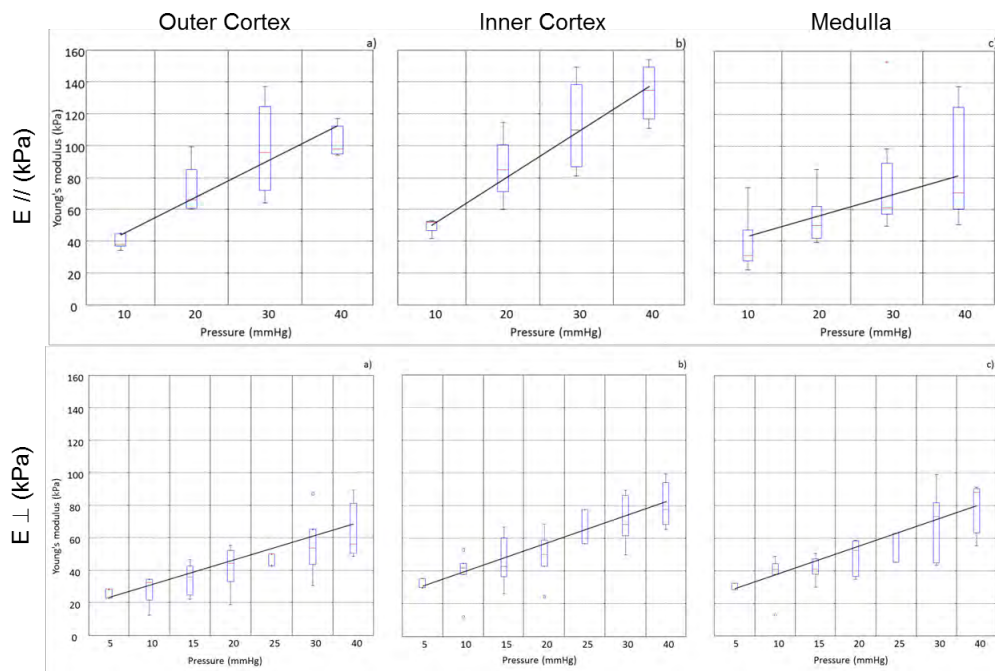


Figure 33: Evolution de l'élasticité des différents compartiments du rein en fonction de la pression urinaire parallèlement ou perpendiculairement aux fibres des pyramides du rein. Nous pouvons voir le changement du ratio d'anisotropie avec la pression.

En résumé, l'anisotropie est extrêmement présente dans le corps humain et elle peut se révéler essentiel comme paramètre mécanique. Par exemple, au laboratoire Weining Lee et Mathieu Pernot on montre que l'étude de l'anisotropie élastique pouvait permettre de parfaitement cartographier l'orientation des fibres musculaires du myocarde et ainsi de mieux qualifier certaines pathologies cardiaques [20].

II.4 CHAPITRE 4 : NONLINEARITE ELASTIQUE

Nonlinéarité de cisaillement : applications aux tissus mous.

L'élastographie transitoire développée au laboratoire fournit un moyen original et bien adapté à l'étude de la propagation nonlinéaire des ondes de cisaillement dans les solides mous, tels que les tissus biologiques. La quantification de la nonlinéarité de cisaillement peut se révéler importante en vue d'applications médicales. Par exemple elle pourrait permettre de discriminer les tumeurs malignes des tumeurs bénignes. Par ailleurs, avant les premières expériences réalisées au laboratoire aucune étude n'avait mis en évidence directement la propagation des ondes de choc transversales dans un solide isotrope [21]: les effets nonlinéaires, qui n'apparaissent alors qu'au troisième ordre, sont très faibles dans les solides classiques (cristaux, métaux...) et n'ont jamais été visualisés. Grâce aux faibles vitesses de propagation des ondes de cisaillement dans les solides mous (de l'ordre du mètre par seconde), ces dernières peuvent être engendrées avec des nombres de Mach élevés (de l'ordre de l'unité), assurant la forte nonlinéarité de leur propagation. A la suite des expériences de propagation d'ondes de choc transversales dans les solides mous, nous avons étudié l'interaction nonlinéaire de deux ondes de cisaillement planes [22]. La nonlinéarité cubique engendre alors des ondes avec des fréquences mélangeant celles des ondes initialement émises, selon des combinaisons linéaires qui lui sont propres. Les résultats ont été interprétés sur la base d'une nouvelle approche théorique de l'élasticité des solides incompressibles, récemment développée par E. A. Zabolotskaya [23]. Lorsque le faisceau émis est de forme plus complexe, comme celui engendré par un bref coup à la surface du solide mou, la diffraction modifie profondément la propagation nonlinéaire: des effets liés à la nonlinéarité quadratique surviennent.

Grâce à la technique de génération d'ondes de cisaillement planes en mode supersonique, nous avons également réalisé des expériences d'acoustoélasticité. En adaptant le cadre théorique fourni par E. A. Zabolotskaya au cas d'un solide mou soumis à une contrainte uniaxiale, nous avons mesuré l'unique module de Landau du troisième ordre (usuellement noté A) intervenant dans la propagation nonlinéaire des ondes de cisaillement. Ces résultats constituent les premières données quantitatives sur la nonlinéarité de cisaillement des solides mous [24]. Sans la configuration expérimentale imaginée pour cette étude (Fig. 34), cette mesure est particulièrement délicate car le contrôle de la contrainte uniaxiale est primordial pour l'expérience. En mesurant l'évolution de la vitesse des ondes de cisaillement en fonction de la contrainte appliquée, puis en utilisant les équations suivantes (Eq. 1&2&3) décrivant la vitesse des ondes selon les trois axes de l'espace dans un milieu quasi-incompressible ; il est alors possible de remonter à une quantification du coefficient nonlinéaire de cisaillement défini par Landau A .

$$\rho_0 V_{s12}^2 = \mu - \sigma_{22} \left(1 + \frac{A}{12\mu}\right), \quad (1)$$

$$\rho_0 V_{s21}^2 = \mu - \sigma_{22} \left(\frac{A}{12\mu}\right), \quad (2)$$

$$\rho_0 V_{s13}^2 = \mu + \sigma_{22} \left(1 + \frac{A}{6\mu}\right). \quad (3)$$

Où ρ_0 est la densité du milieu, V_s la vitesse de cisaillement, μ le module de cisaillement à contrainte nulle, σ_{22} la contrainte uniaxiale appliquée.

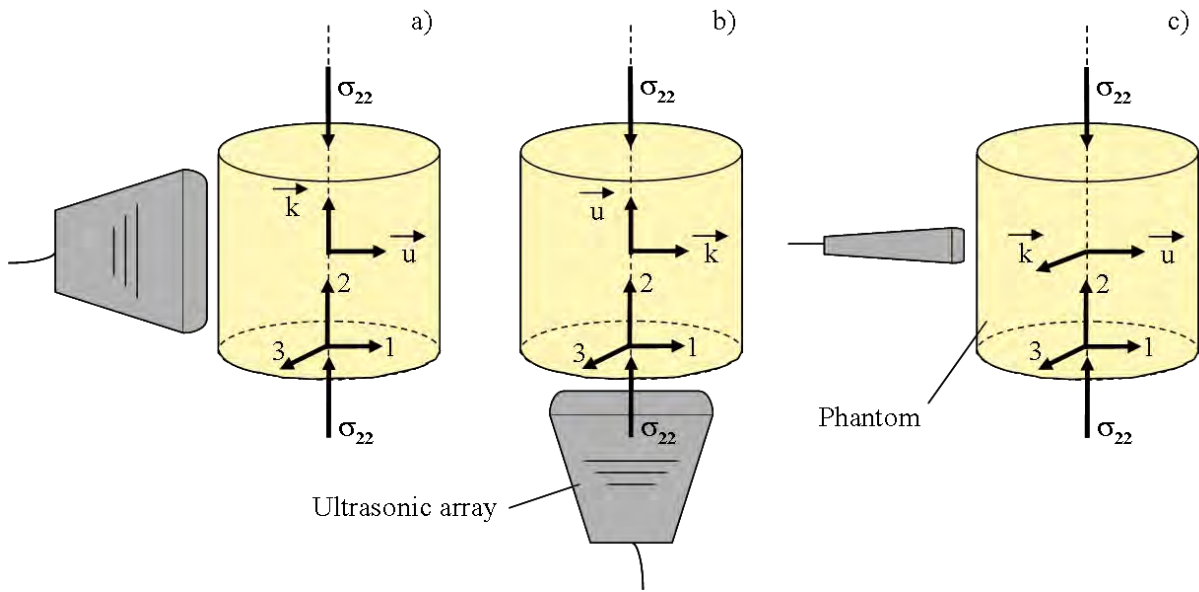


Figure 34 : Les 3 configurations expérimentales pour la technique d'acoustoélasticité. Ceci permet de générer trois ondes de cisaillement différentes désignées par [12] ou [32], [21] ou [23] et [13] ou [31] sur a), b), et c) respectivement correspondant aux trois équations Eq. 1, Eq. 2 et Eq. 3.

Suite à la compréhension de la théorie de l'acoustoélasticité en milieu quasi-incompressible nous avons combiné cette dernière avec une mesure astucieuse de la contrainte en milieux mous pour retrouver des cartes de non linéarité élastique des tissus. En utilisant la configuration expérimentale présentée en Fig. 34b, nous avons évalué par élastographie statique la déformation interne de gels d'agar-gélatine et de foies bovins *ex vivo*, en comparant deux images ultrasonore avant et après compression. De cette estimation de la déformation locale pour chaque état de compression du milieu et sachant l'évolution de l'élasticité également pour chaque état de compression du milieu nous avons pu calculer une carte locale de la contrainte à l'intérieur du matériau. En comparant alors localement l'évolution de la contrainte dans le milieu et la variation de la vitesse des ondes de cisaillement, nous avons pu ainsi reconstruire une carte de non linéarité A du matériau (Fig. 35&36).

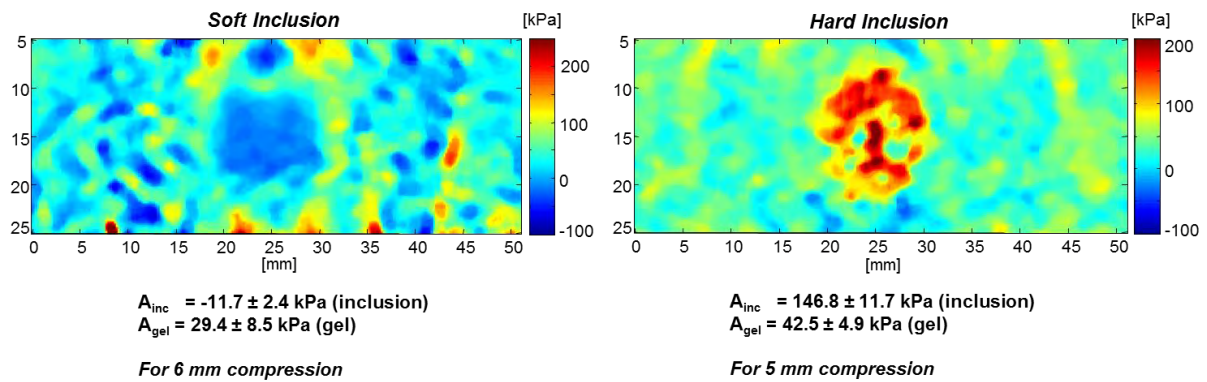


Figure 35 : Carte d'élasticité nonlinéaire (paramètre de Landau A) pour deux gels d'agar-gélatine contenant une inclusion molle et une inclusion dure pour de faible taux de compression.

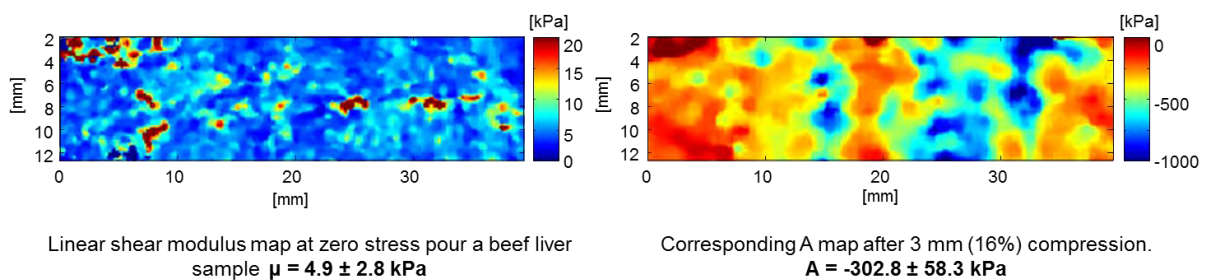


Figure 36 : Carte d'élasticité de cisaillement et carte d'élasticité nonlinéaire pour un foie de bœuf ex vivo..

De même en combinant cette expérience d'acoustoélasticité à une autre consistant à générer avec une plaque dans un solide mou des ondes de cisaillement choquées (Fig. 37), le paramètre élastique du quatrième ordre de cisaillement peut être quantifié [24]. Dans cette expérience le développement théorique nous permet d'exprimer un paramètre de nonlinéarité β_s en fonction du module de cisaillement et des paramètres élastiques du troisième et quatrième ordre (Eq. 4). L'expérience en ondes de cisaillement choquées combinée à une analyse analytique des résultats nous permet de retrouver ce paramètre. De l'expérience d'acoustoélasticité le module de cisaillement μ et le paramètre du troisième ordre A sont quantifiés, de ce fait nous retrouvons celui du quatrième ordre D (Table 1).

$$\beta_s = \frac{3}{2\mu} \left(\mu + \frac{A}{2} + D \right) \quad (4)$$

% de gélatine	μ (kPa)	A (kPa)	β_s	D (kPa)
5%	6.6 ± 0.6	-37.7 ± 9.8	4 ± 0.5	30 ± 10
7%	8.5 ± 0.8	-22.7 ± 2.5	2.5 ± 1	17 ± 10

Table 1 : Valeurs des élasticités de cisaillement du 2^{ème}, 3^{ème} et 4^{ème} pour deux gels d'agar-gélatine.

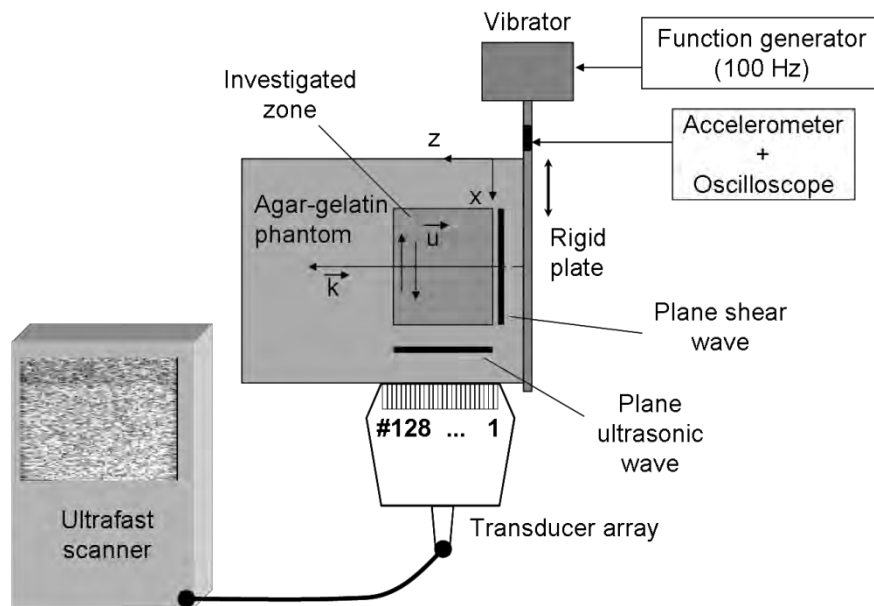


Figure 37 : Configuration expérimentale permettant de générer des ondes de cisaillement choquées.

L'ensemble de ces travaux a pour visé une application médicale de la mesure de non linéarité élastique dans le but de mieux caractériser les tissus pathologiques mais également de mieux comprendre les effets nonlinéaires des ondes de cisaillement a des buts de recherche plus fondamentaux.

Réflexion de Mach.

Fort de ces expériences nous avons pu utiliser le savoir développé sur la non linéarité de cisaillement et aborder de nouveaux thèmes de recherche relevant plus de la physique fondamentale, tels la réflexion de Mach. En collaboration avec l'Institut Jean Le Rond d'Alembert nous avons étendu la théorie de réflexion des ondes de Mach, bien établi pour les ondes longitudinales et très connu pour la problème de bang sonique, aux ondes de cisaillement. Nous avons pu alors construire un modèle numérique permettant de prédire la réflexion d'une onde de cisaillement choquée sur une interface libre.

Actuellement nous travaillons la mise en place d'un protocole expérimental permettant de valider le phénomène prédit théoriquement [25]. En fabriquant un gel mou, milieu favorisant la génération et la propagation d'ondes de cisaillement choquées, nous pouvons contrôler l'angle de la surface libre sur laquelle les ondes vont se réfléchir (Fig. 38). Là encore l'utilisation de l'échographe ultrarapide principalement dédié à l'élastographie, nous permet de suivre la propagation des ondes de cisaillement choquées générées par un vibreur fixé à une plaque. L'expérience est répétée plusieurs fois pour différente position de la barrette ultrasonore entre la plaque et le plan incliné.

L'ensemble des acquisitions spatiales nous permet ensuite de reconstruire en volume la propagation des ondes venant de la plaque se réfléchir sur l'interface libre du gel.

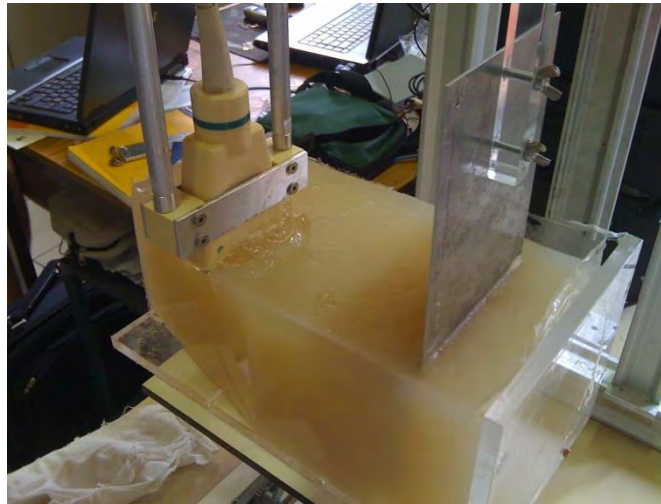


Figure 38: Configuration expérimentale permettant de générer des ondes de cisaillement choquées et d'étudier leur réflexion sur un plan incliné.

Ainsi de telles configurations expérimentales permettent de vérifier les prédictions théoriques et numériques et ainsi d'augmenter notre compréhension des phénomènes de propagation nonlinéaire des ondes de cisaillement. En parallèle, dans un premier temps nous sommes en train de travailler sur la focalisation des ondes de cisaillement choquées où le déplacement de la tache de focalisation lié à l'accumulation des phénomènes nonlinéaire a déjà été prévu numériquement. Dans un deuxième temps nous travaillons également sur la propagation des ondes de cisaillement choquées dans les milieux granulaires pour faire le lien entre l'élastographie et la sismique des couches terrestre.

II.5 CHAPITRE 5 : VISCOELASTICITE

Depuis le début de ce mémoire nous avons vu que nous étions capable de remonter aux propriétés élastiques des tissus mous, de quantifier leur anisotropie élastique et leur nonlinéarité élastique. Or ces tissus sont par définition viscoélastiques. Pour parfaitement caractériser ces derniers il faut alors prendre en compte la viscosité des matériaux. En utilisant la technique d'élastographie il est alors possible de remonter à ce paramètre par deux moyens différents : étudier la dispersion des ondes de cisaillement en les reliant à un modèle rhéologique ou étudier la propagation d'onde plane de cisaillement et particulièrement leur atténuation.

Dispersion des ondes de cisaillement

Lors de la génération de la pression de radiation dans un milieu mou, nous générons des ondes de cisaillement. Du fait du faible temps caractéristique de cette excitation nous pouvons alors considérer que la source de cisaillement est temporellement quasi-ponctuelle, ce qui entraîne dans l'espace de Fourier la génération d'un grand nombre de fréquences de cisaillement. Habituellement dans le corps humain la bande de fréquence, dépendant de l'organe étudié, se situe entre 50 Hz et 3000 Hz. En mesurant la vitesse de phase de l'onde à chaque fréquence nous pouvons alors retrouver la courbe de dispersion de l'onde de cisaillement [26].

Nous avons appliqué cette technique à l'étude du muscle pour essayer de mieux comprendre son fonctionnement [17]. Nous avons vu au chapitre 3 la complexité du muscle, de part son côté anisotrope mais également actif, son élasticité change en permanence. Par la mesure de la dispersion des ondes de cisaillement en fonction de différents états de contraction du muscle nous pouvons remonter à la viscosité du milieu. Pour ce faire nous réalisons une régression linéaire de la courbe de dispersion de l'onde de cisaillement. Le résultat obtenu nous permet alors de remonter à la viscosité du milieu en utilisant un modèle de Voigt (patin visqueux en parallèle avec un piston élastique) décrit par l'équation 5 où V_ϕ est la vitesse de phase de cisaillement, η est la viscosité, ω la fréquence de pulsation, ρ la densité et μ le module de cisaillement.

$$V_\phi(\omega) = \sqrt{\frac{2(\mu^2 + \omega^2\eta^2)}{\rho(\mu + \sqrt{\mu^2 + \omega^2\eta^2})}} \quad (5)$$

En figure 39 nous présentons les résultats obtenus pour différents états de contraction musculaire pour un sujet sain. Nous pouvons voir l'augmentation de la valeur moyenne de vitesse des ondes parallèlement aux fibres et l'augmentation de la pente de la courbe de dispersion perpendiculairement aux fibres. De l'analyse de ces courbes de dispersion nous pouvons alors

déduire l'évolution de l'élasticité et de la viscosité du milieu en fonction de la contraction (Fig. 40). Nous avons ainsi obtenue un résultat très intéressant montrant qu'un muscle se contractant augmente sa rigidité mais également sa viscosité sans doute dans le but de pouvoir absorber les chocs plus facilement. Ces résultats traduisent également le caractère anisotrope de la viscosité dans ce genre de milieu.

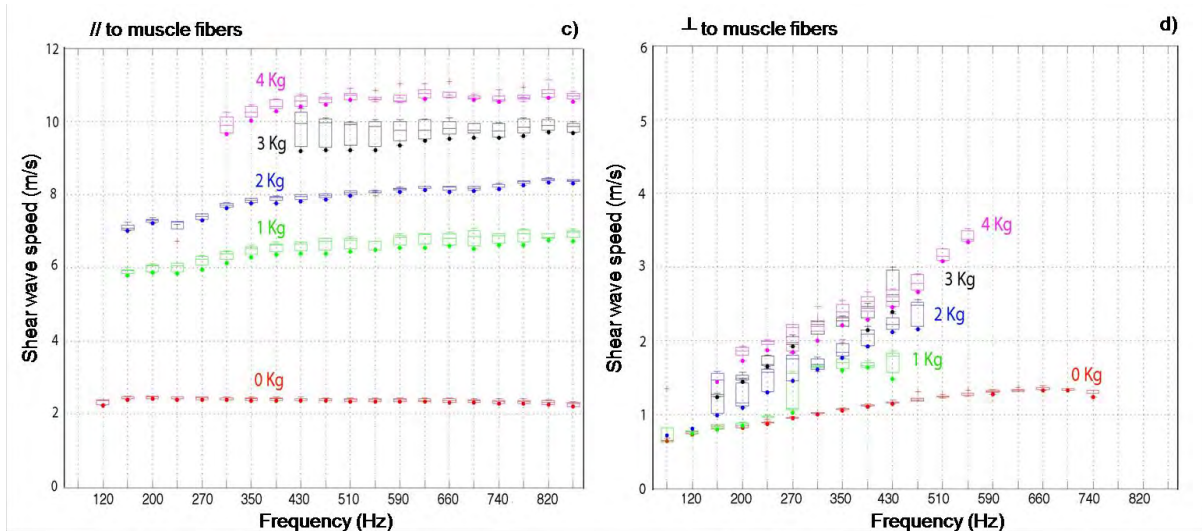


Figure 39 : Evolution des courbes de dispersion des ondes de cisaillement le long des fibres c) et perpendiculairement d) aux fibres en fonction de la charge de contraction.

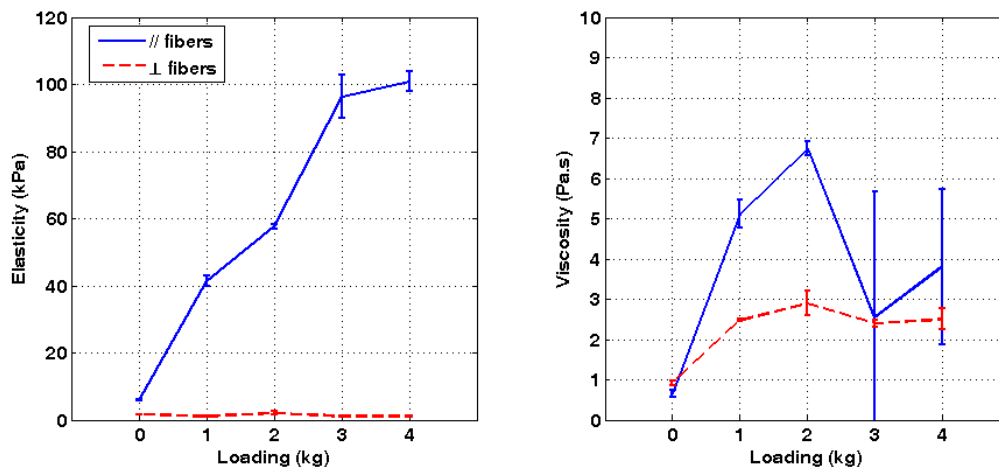


Figure 40 : Evolution de l'élasticité et de la viscosité le long des fibres et perpendiculairement aux fibres fonction de la charge de contraction en supposant un modèle rhéologique de Voigt.

Dernièrement nous avons montré en couplant la mesure de la dispersion des ondes de cisaillement à des mesures de rhéologie basse fréquence (10^{-2} Hz à 25 Hz) classique qu'il était possible de mieux comprendre quel modèle rhéologique régissait un matériaux. Nous avons réalisé cette étude dans le sang en phase de coagulation. Non seulement dans ces expériences nous avons

pu suivre l'évolution des propriétés élastiques du caillot au cours de sa formation mais nous avons pu également relier nos mesures par élastographie aux mesures de rhéologie et montrer que le modèle adéquat pour décrire ce matériau sur plusieurs décades de fréquence était le modèle de Zener [27]. Dans cette étude nous avons mesuré à basse fréquence (grâce à l'utilisation d'un rhéomètre classique) les valeurs des modules de perte (G'') et de conservation (G') du sang en phase de coagulation. De ces valeurs nous avons pu calculer la vitesse théorique $v(\omega)$ des ondes de cisaillement à basse fréquence en utilisant la relation suivante (Eq. 6) :

$$v(\omega) = \frac{\sqrt{2} \sqrt{G'^2 + G''^2}}{\rho G' \left(1 + \sqrt{1 + \left(\frac{G''}{G'} \right)^2} \right)}. \quad (6)$$

Ainsi nous pouvons retrouver le comportement de la courbe de dispersion des ondes de cisaillement sur plusieurs décades (rhéologie de 10^{-2} Hz à 25 Hz et élastographie de 50 Hz à 300 Hz). En procédant à une régression polynômiale de cette courbe de dispersion dépendant d'un modèle rhéologique, Voigt, Maxwell ou Zener, nous pouvons alors retrouver le modèle rhéologique adéquat décrivant au mieux le milieu [27] (Fig. 41).

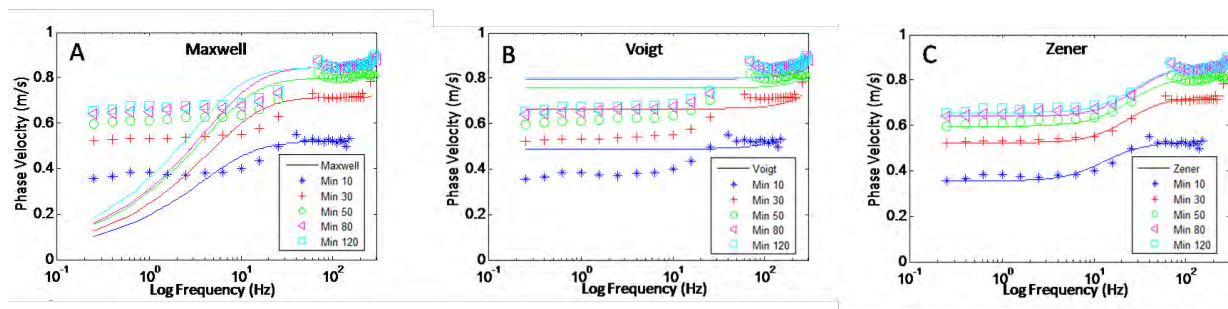


Figure 41 : Courbe de dispersion des ondes de cisaillement obtenue sur plusieurs décades en combinant deux techniques de mesures la rhéologie classique et l'élastographie. Une régression des données en utilisant différents modèle rhéologique montre que le modèle de Zener est le plus adapté.

Propagation d'onde plane de cisaillement : quantification de l'atténuation de cisaillement

L'étude de la dispersion des ondes de cisaillement seule permet, en faisant des hypothèses sur le modèle rhéologique concerné, de retrouver la viscosité du milieu. Or ces hypothèse sont toujours plus ou moins valables et peuvent être contestées. Cependant l'utilisation d'ondes planes de cisaillement peut permettre de retrouver le modèle rhéologique adéquat sans hypothèse. En effet la vitesse V_ϕ et l'atténuation α des ondes de cisaillement peuvent être en fonction des modules de conservation et perte (G' , G'') indépendants du choix du modèle rhéologique (Eq. 7&8).

$$v_{\phi}(G', G'') = \sqrt{\frac{2}{\rho G'} \frac{G'^2 + G''^2}{1 + \sqrt{1 + \left(\frac{G''}{G'}\right)^2}}} \quad (7)$$

$$\alpha(G', G'') = \omega \sqrt{\frac{\rho}{2} \frac{G'}{G'^2 + G''^2} \left(\sqrt{1 + \left(\frac{G''}{G'}\right)^2} - 1 \right)}. \quad (8)$$

Dans le cas la méthode supersonic, une onde cylindrique de cisaillement est générée. De ce fait l'atténuation de cette onde est soumise à deux conditions : la viscosité du milieu et la diffraction de l'onde hors axe du cylindre. Même si l'onde semble quasi-plane dans le plan d'imagerie elle diffracte hors axe. De ce fait il n'est pas possible sans correction adaptée de retrouver la vraie atténuation de l'onde avec cette méthode. Par contre en utilisant le mode de génération d'onde plane présenté au chapitre 4 dans le cas des ondes de cisaillement non linéaire, il est possible de quantifier l'atténuation des ondes de cisaillement très précisément à la fréquence désirée (de 50Hz à 800 Hz). En étudiant des hydrogels calibrés nous avons ainsi pu utiliser les deux techniques pour valider les mesures réalisées en élastographie que ce soit avec des ondes planes ou avec des ondes diffractantes. Figure 42 est illustré la propagation des ondes de cisaillement pour chaque méthode.

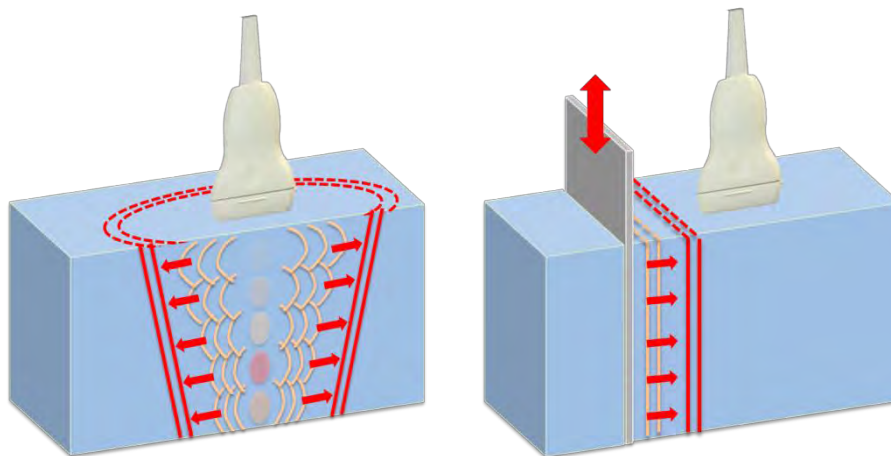


Figure 42 : Différence de propagation des ondes de cisaillement en élastographie en utilisant la pression de radiation (à droite) ou la vibration d'une plaque (à gauche).

Actuellement nous poursuivons cette recherche pour trouver un facteur de correction simple de l'atténuation de la diffraction des ondes. En effet expérimentalement et surtout en pratique clinique il est beaucoup plus simple d'utiliser la technique SSI. En utilisant les fonctions de Green en milieu élastique, connaissant la source de cisaillement il est possible simuler l'expérience et de quantifier la diffraction des ondes. En simulation, l'atténuation mesurée n'est due qu'à la diffraction. En soustrayant cette dernière des résultats expérimentaux, il est alors possible de retrouver seulement l'atténuation des ondes liées à la viscosité [29,30]. De ce fait nous pouvons en théorie en déduire une carte de l'atténuation des ondes et remonter à des cartes quantitatives des paramètres

G' et G'' . Le but final étant de retrouver un facteur correctif simple de l'atténuation prenant en compte la vitesse du milieu, la fréquence des ondes de cisaillement et la fréquence ultrasonore, applicable directement sur les mesures *in vivo* sans utiliser de simulation numérique.

III. COLLABORATIONS

J'ai collaboré au cours de mes premières années de recherche au CNRS avec différentes équipes tant médicales que scientifiques. Une liste non exhaustive de ces collaborations, en cours ou achevées, est donnée ci-dessous :

- Hôpital Cochin, Paris - Pr. Pol, Pr. V. Mallet
- Hôpital Antoine Béchère, Clamart - Dr. O. Ami.
- Institut Curie, Paris - Dr. A. Tardivon, Dr. A. Athanasiou, Dr. E. Farge.
- Hôpital Pellegrin, Bordeaux - Pr. N. Grenier, Dr. D. Touboul.
- Hôpital Européen Georges Pompidou, Paris - Pr. O. Clément, Dr. L. Fournier, Dr. F. Chamming's
- Hôpital Necker, Paris - Dr. D. Prié, Pr. A. Munnich, Pr. J.-M. Correas
- Hôpital de Besançon - Pr. P. Humbert.
- Innothera, Laplace - Dr. J.-M. Fullana.
- L'Oréal, Paris - Dr. B. Querleux.
- Supersonic Imagine, Aix en provence - Dr. J. Bercoff, Dr. A. Criton
- INRETS, Lyon - Dr. P. Beillas.
- Institut Jean Lerond d'Alembert, Paris - Dr. F. Coulouvrat.
- INSERM U556, Lyon - Dr. R. Souchon.
- Physico-Chimie des Polymères et des Milieux Dispersés, Paris - Dr. A. Marcellan
- Laboratorio de Acustica, Montevideo Uruguay - Pr. C. Negreira
- Georgia Tech, Atlanta USA – Dr. K. Sabra, Dr. M. Shinohara

IV. PERSPECTIVES

Dans un laboratoire aussi dynamique, stimulant et motivant que l'institut Langevin, les perspectives de recherches ne manquent pas. Au cours des prochaines années, je compte continuer à développer de nouvelles applications médicales basées sur la physique des ondes. Ces applications s'organisent autour de l'élastographie, technique ultrasonore ultrarapide de mesure de l'élasticité des tissus biologiques. L'échographe ultrarapide que nous avons développé au laboratoire en collaboration avec la société Supersonic Imagine nous a permis d'implanter en clinique une nouvelle technique d'imagerie ultrasonore des tissus biologiques, l'élastographie par ondes de cisaillement. Cependant cette technique, bien qu'elle ait été adaptée à plusieurs organes (rein, foie, thyroïde, prostate, ...), peut être encore améliorée pour aider à la quantification de nouveaux paramètres, comme la température ou la pression. En ce qui concerne la température nous avons montré que la variation d'élasticité était un marqueur précis de la dose thermique délivrée à un organe. En ce qui concerne la pression, nous avons pu relier les variations d'élasticité à un « monitoring » externe de la pression. Cependant essayer de déduire la pression interne d'un organe sans capteurs de pression invasif serait idéal pour le médecin. Un de mes projets de recherche pour les années à venir est d'utiliser la mesure d'élasticité pour retrouver la pression interne d'un organe. Pour se faire nous pourrions nous inspirer de la théorie de l'acoustoélasticité qui met en relation la variation d'élasticité dû à la nonlinéarité du milieu en fonction de la contrainte appliquée à l'objet. Le but de ce projet est de trouver une méthode de mesure non invasive de la pression pour améliorer le diagnostic non invasif du médecin sur différents organes, tels le rein, l'œil ou le cerveau en peropératoire. Un autre projet basé sur la propagation des ondes de cisaillement est d'utiliser et de développer l'élastographie comme une technique de rhéologie haute fréquence. En effet de l'étude de la propagation des ondes de cisaillement, il est possible de retrouver sur une large plage de fréquence (de 50 à 1000 Hz), la vitesse et l'atténuation des ondes de cisaillement. Or ces dernières sont reliées directement au modules de conservation et de perte des matériaux (G' et G'') paramètres déjà quantifié en rhéologie classique mais a plus basse fréquence (de 10^{-3} Hz à 100 Hz). L'utilisation de l'élastographie pour compléter les mesures classique peut alors se révéler comme extrêmement importante pour mieux comprendre la rhéologie des matériaux, des polymères et des tissus biologiques. Ces projets prennent suite au développement que nous avons fait depuis plusieurs années sur le thème de la mesure d'élasticité par échographie ultrarapide et propagation d'ondes de cisaillement. Or pour développer cette approche nous avons dû mettre au point un échographe ultrarapide qui nous permet d'aborder d'autres sujets de recherche fondamentaux ou appliqués. En effet l'utilisation de l'outil d'échographie ultrarapide nous permet de développer d'autres modalités d'imagerie. En utilisant des cadences d'insonification de plusieurs milliers d'Hertz, il est possible de

réaliser de nouvelles séquences d'imagerie des flux sanguins et d'augmenter d'un facteur conséquent la sensibilité des techniques Doppler. Ainsi il est possible de retrouver des cartographies extrêmement précises de la vascularisation tissulaire. Nous pouvons alors nous poser les questions suivantes dans le cas de tumeurs cancéreuses et en particulier sur le sein : Quel est l'impact d'une telle vascularisation sur les propriétés mécaniques de la lésion ? Comment les propriétés mécaniques change au cours de la croissance tumorale ? Y a-t-il un lien entre la microarchitecture lésionnelle (quelques dizaines de μm) et les mesures macroscopique (plusieurs mm) de l'élasticité ? Quel est l'impact d'un traitement anti-vasculaire, anti-angiogénique ou chimiothérapique sur les propriétés mécaniques des tissus ? Pour répondre à ces questions nous organiserons ce projet en trois phases : Une première numérique se basant sur ces cartographies pour simuler la propagation d'ondes de cisaillement dans ces milieux et l'impact de la vascularisation des tissus sur leur propagation afin de comprendre si des phénomènes de multidiffusion peuvent intervenir et modifier notre perception macroscopique des propriétés élastiques des tumeurs. La deuxième sera d'organiser un protocole d'imagerie chez le petit animal et de suivre la croissance tumorale en imagerie Doppler et élastographique afin de comparer ces résultats aux simulations numériques. La dernière partie de ce projet sera de monter un protocole d'étude clinique avec l'Institut Curie pour étudier ces paramètres de vascularisation sur une population de patientes atteintes du cancer du sein.

V. Références du mémoire

- [1] A. Sarvazyan, A. R. Skovoroda, S. Emelianov, J. B. Fowlkes, "Biophysical bases of elasticity imaging", *Acoustical Imaging*, vol. 21, Plenum Press, New-York, 1995.
- [2] J. Bercoff, S. Chaffai, M. Tanter, L. Sandrin, S. Catheline, M. Fink, J.L. Gennisson, M. Meunier, "In vivo breast tumor detection using transient elastography." *Ultr. Med. & Bio.*, 29 (10), pp. 1387-1396, 2003.
- [3] J. Bercoff. " L'imagerie échographique ultrarapide et son application à l'étude de la viscoélasticité du corps humain. " Thèse de l'Université Denis Diderot Paris VII, 2004.
- [4] J Bercoff, M Tanter, M Fink. "Supersonic shear imaging : a new technique for soft tissue elasticity mapping". *IEEE Transactions on Ultrasonics Ferroelectrics and Frequency Control*, vol. 51, no. 4, pp. 396–409, 2004.
- [5] M. Tanter, J. Bercoff, A. Athanasiou, T. Deffieux, J.L. Gennisson, G. Montaldo, A. Tardivon, M. Fink. "Quantitative assessment of breast lesions viscoelasticity using supersonic shear imaging technique: Initial clinical investigation." *Ultr. Med. & Bio.*, 34 (9), pp. 1373-1386 ,2008.
- [6] D. O. Cosgrove, W. A Berg, C. J. Doré et al. "Shear wave elastography for breast masses is highly reproducible". *Eur Radiol*, Dec 31, 2011.
- [7] W. A Berg, D. O. Cosgrove, C. J. Doré et al. "Shear-wave Elastography Improves the Specificity of Breast US: The BE1 Multinational Study of 939 Masses", *Radiology*, 262(2): 435-449. 2012.
- [8] J.L. Gennisson, N. Félix, T. Deffieux, J. Bercoff, R. Sinkus, F. Boudet, M. Tanter, M. Fink. "Full 3D elasticity reconstruction using supersonic shear imaging technique for breast cancer diagnosis." *IEEE Ultrasonic Symposium*, Pékin, Nov. 2008.
- [9] H. Latorre-Ossa. "In vivo monitoring of elastic changes during cancer development and therapeutic treatment." Thèse de l'Université Denis Diderot Paris VII, 2012.
- [10] M. Muller, J.L. Gennisson, T. Deffieux, M. Tanter et M. Fink. "Quantitative viscoelasticity mapping of human liver using supersonic shear imaging: preliminary in vivo feasibility study." *Ultr. Med. & Bio.*, 35 (2), pp. 219-229, 2009.
- [11] E. Bavu, J.L. Gennisson, M. Couade, J. Bercoff, V. Mallet, A. Badel, M. Fink, B. Nalpas, M. Tanter et S. Pol. "Noninvasive in vivo liver fibrosis evaluation using supersonic shear imaging : a clinical study on 113 hepatitis C virus patients." *Ultr. Med. & Bio.*, vol. 37 (9), pp. 1365-1373, 2011.
- [12] T.-M. Nguyen, M. Couade, J. Bercoff, M. Tanter, "Assessment of viscous and elastic properties of sub-wavelength layered soft tissues using Shear Wave Spectroscopy : theoretical framework and in vitro experimental validation" *IEEE Trans. Ultra. Fer. Freq. Contr.*, vol. 58 (11), pp. 2305-2315, 2011
- [13] T.-M. Nguyen, "Elastographie haut-résolution pour l'évaluation des propriétés élastiques de la cornée et de la peau", Thèse de l'Université Denis Diderot Paris VII, 2012.
- [14] T.M. Nguyen, J.F. Aubry, D. Touboul, , J.L. Gennisson, J. Bercoff, M. Tanter. "Monitoring of cornea elastic properties changes during UV-A/Riboflavin induced corneal collagen cross-linking using Supersonic Shear Wave Imaging." *IOVS*, 53 (9), pp. 5948-5954, 2012.
- [15] M. Derieppe, Y. Delmas, J.L. Gennisson, C. Deminière, S. Placier, M. Tanter, C. Combe et N. Grenier. "Detection of intrarenal microstructural changes with Supersonic Shear Wave Elastography in rats." *Eur. Radiol.*, 22, pp. 243-250, 2012.
- [16] F. Chamming's, H. Latorre-Ossa, M.A. Lefrère-Belda, V. Fitoussi, T. Quibel, F. Assayag, E. Marangoni, G. Autret, D. Balvay, L. Pidial, J.L. Gennisson, M. Tanter, C.A. Cuenod, O. Clément et L. Fournier. "Shear wave elastography of tumor growth in a human breast cancer model with pathological correlation." *Europ. Radiol*, DOI 10.1007/s00330-013-2828-8, 2013.
- [17] J.L. Gennisson, T. Deffieux, E. Macé, G. Montaldo, M. Fink et M. Tanter. "Viscoelastic and anisotropic mechanical properties of in vivo muscle tissue assessed by Supersonic Shear Imaging." *Ultr. Med. & Bio.*, 36 (5), pp.789-801,2010.

- [18] M. Shinohara, K. Sabra, J.L. Gennisson, M. Fink et M. Tanter. "Real-time visualization of muscle stiffness distribution with ultrasound shear wave imaging during muscle contraction." *Muscle & Nerve*, 42, pp. 438-441, 2010.
- [19] J.L. Gennisson, N. Grenier, C. Combe et M. Tanter. "Supersonic Shear Wave Elastography of in vivo pig kidney: Influence of blood pressure, urinary pressure and tissue anisotropy." *Ultr. Med. & Bio.*, 38(9), pp. 1559-1567, 2012.
- [20] W. Lee, B. Larrat, M. Pernot, M. Tanter, "Ultrasound elastic tensor imaging: comparison with MR diffusion tensor imaging in the myocardium", *Phys. Med. Bio.*, vol. 57, pp. 5075-5095, 2012.
- [21] S. Catheline, J.L. Gennisson, M. Tanter et M. Fink. "Observation of shock transverse waves in elastic media." *Phys. Rev. Lett.*, 91 (16), pp. 43011-43014, 2003.
- [22] X. Jacob, S. Catheline, J.L. Gennisson, C. Barrière, D. Royer et M. Fink. "Nonlinear shear wave interaction in soft solids." *J. Acoust. Soc. Am.*, 122 (4), pp. 1917-1926, 2007.
- [23] E. A. Zabolotskaya, M. F. Hamilton, Y. A. Ilinskii, and G. D. Meegan, "Modeling of non linear shear waves in soft solids", *J. Acoust. Soc. Am.* **116**, 2807-2813 (2004).
- [24] H. Latorre-Ossa, J.L. Gennisson, E. De Brosses, M. Tanter. "Quantitative Imaging of Nonlinear Shear Modulus by Combining Static Elastography and Shear Wave Elastography." *IEEE Trans. Ultrason., Ferroelec., Freq. Contr.*, 59 (4), pp. 833-839, 2012.
- [25] G. Pinton, F. Coulouvrat, J.L. Gennisson et M. Tanter. "Nonlinear reflexion of shock shear waves in soft elastic media." *J. Acoust. Soc. Am.*, 127 (2), pp. 683-691, 2010.
- [26] T. Deffieux, G. Montaldo, M. Tanter, M. Fink, "Shear Wave Spectroscopy for In Vivo Quantification of Human Soft Tissues Viscoelasticity", *IEEE Trans. Med. Im.* 2009;28 (3):313-322
- [27] M. Bernal, J.L. Gennisson, P. Flaud et M. Tanter. "Correlation between classical rheometry and Supersonic Shear Wave Imaging in blood clots." *Soumis pour publication dans Ultr. Med. & Bio.*, 2013.
- [28] A. Marcelan, A. Dizeux, M. Tanter, J.L. Gennisson "High frequency rheology of hydrogel using ultrasound transient elastography." *Soumis pour publication dans IEEE Trans. Ultrason., Ferroelec., Freq. Contr.*, 2013.
- [29] S. Catheline, J.L. Gennisson, G. Delon, R. Sinkus, M. Fink, S. Abouelkaram, J. Culioli. "Measurement of viscoelastic properties of homogeneous soft solid using transient elastography : An inverse problem approach." *J. Acoust. Soc. Am.*, 116 (6), pp. 3734-3741, 2004.
- [30] J.L. Gennisson, S. Lerouge, G. Cloutier. "Transient elastography: a new method to assess viscoelastic properties of blood during coagulation." *Ultr. Med. & Bio.*, 32 (10), pp. 1529-1537, 2006.

VI. Publications

Liste des publications fournies en annexes.

- [1] "Acoustoelasticity in soft solids: assessment of the nonlinear shear modulus with the acoustic radiation force." **J.L. Gennisson**, M. Rénier, S. Catheline, C. Barrière, J. Bercoff, M. Tanter et M. Fink. *J. Acoust. Soc. Am.*, 122 (6), pp.3211-3219, 2007.
- [2] "Viscoelastic and anisotropic mechanical properties of in vivo muscle tissue assessed by Supersonic Shear Imaging." **J.L. Gennisson**, T. Deffieux, E. Macé, G. Montaldo, M. Fink et M. Tanter. *Ultr. Med. & Bio.*, 36 (5), pp.789-801,2010.
- [3] "Supersonic Shear Wave Elastography of in vivo pig kidney: Influence of blood pressure, urinary pressure and tissue anisotropy." **J.L. Gennisson**, N. Grenier, C. Combe et M. Tanter. *Ultr. Med. & Bio.*, 38(9), pp. 1559-1567, 2012.

- [4] "On the elasticity of transverse isotropic soft tissues." D. Royer, **J.L. Gennisson**, T. Deffieux et M. Tanter. *J. Acoust. Soc. Am.*, 129 (5) pp. 2757-2760, 2011.
- [5] "Noninvasive in vivo liver fibrosis evaluation using supersonic shear imaging : a clinical study on 113 hepatitis C virus patients." E. Bavu, **J.L. Gennisson**, M. Couade, J. Bercoff, V. Mallet, A. Badel, M. Fink, B. Nalpas, M. Tanter et S. Pol. *Ultr. Med. & Bio.*, vol. 37 (9), pp. 1365-1373, 2011.
- [6] "Ultrafast imaging of in vivo muscle contraction using ultrasound." T. Deffieux, **J.L. Gennisson**, A. Nordez, M. Tanter et M. Fink. *Appl. Phys. Lett.*, 89, pp. 184107-1-3, 2006.
- [7] "Assessment of the mechanical properties of musculoskeletal system using 2D and 3D very high frame rate ultrasound." T. Deffieux, **J.L. Gennisson**, M. Tanter et M. Fink. *IEEE Trans. Ultrason., Ferroelec., Freq. Contr.*, 55 (10), pp. 2177-2190, 2008.
- [8] "The variance of quantitative estimates in shear wave imaging: theory and experiments." T. Deffieux, **J.L. Gennisson**, B. Larrat, M. Fink et M. Tanter. *IEEE Trans. Ultrason., Ferroelec., Freq. Contr.*, 59 (11), pp. 2390-2410, 2012.
- [9] "On the effects of reflected waves in transient shear wave elastography." T. Deffieux, **J.L. Gennisson**, J. Bercoff, M. Tanter. *IEEE Trans. Ultrason., Ferroelec., Freq. Contr.*, 58(10), pp. 2032-2035, 2011.
- [10] "High resolution quantitative imaging of cornea elasticity using supersonic shear imaging." M. Tanter, D. Touboul, **J.L. Gennisson**, J. Bercoff et M. Fink. *IEEE Trans. Med. Im.*, 28 (2), pp. 1881-1893, 2009.
- [11] "Breast lesions: Quantitative elastography with supersonic shear imaging – preliminary results." A. Athanasiou, A. Tardivon, M. Tanter, B. Sigal-Zaffrani, J. Bercoff, T. Deffieux, **J.L. Gennisson**, M. Fink et S. Neuenschwander. *Radiology*, 256 (1), pp. 297-303, 2010.

Acoustoelasticity in soft solids: Assessment of the nonlinear shear modulus with the acoustic radiation force

J.-L. Gennisson,^{a)} M. Rénier, S. Catheline, C. Barrière, J. Bercoff, M. Tanter, and M. Fink
*Laboratoire Ondes et Acoustique, ESPCI, CNRS UMR 7587, INSERM, Université Paris VII,
10 rue Vauquelin, 75231 Paris cedex 05, France*

(Received 4 July 2007; revised 28 August 2007; accepted 29 August 2007)

The assessment of viscoelastic properties of soft tissues is enjoying a growing interest in the field of medical imaging as pathologies are often correlated with a local change of stiffness. To date, advanced techniques in that field have been concentrating on the estimation of the second order elastic modulus (μ). In this paper, the nonlinear behavior of quasi-incompressible soft solids is investigated using the supersonic shear imaging technique based on the remote generation of polarized plane shear waves in tissues induced by the acoustic radiation force. Applying a theoretical approach of the strain energy in soft solid [Hamilton *et al.*, *J. Acoust. Soc. Am.* **116**, 41–44 (2004)], it is shown that the well-known acoustoelasticity experiment allowing the recovery of higher order elastic moduli can be greatly simplified. Experimentally, it requires measurements of the local speed of polarized plane shear waves in a statically and uniaxially stressed isotropic medium. These shear wave speed estimates are obtained by imaging the shear wave propagation in soft media with an ultrafast echographic scanner. In this situation, the uniaxial static stress induces anisotropy due to the nonlinear effects and results in a change of shear wave speed. Then the third order elastic modulus (A) is measured in agar-gelatin-based phantoms and polyvinyl alcohol based phantoms. © 2007 Acoustical Society of America. [DOI: 10.1121/1.2793605]

PACS number(s): 43.25.Dc, 43.25.Ed [OAS]

Pages: 3211–3219

I. INTRODUCTION

For almost two decades, the study of shear wave propagation in soft media became of a peculiar interest in the ultrasonic medical imaging community, especially in the field of dynamic elastography.^{1–3} Methods such as sonoelastography^{4,5} or transient elastography^{6,7} have shown their efficiency to determine the elastic properties of biological soft tissues. However, to date, advanced techniques in that field have been concentrated on the estimation of the second order elastic modulus (μ). In order to better understand pathologies, new refinements were developed to study other mechanical parameters such as anisotropy,⁸ viscoelasticity,^{9,10} or nonlinearity.¹¹ Transient elastography is one of the most efficient approaches, as it images in real time the transient propagation of shear waves in soft media using ultrafast echographic scanners. Based on this concept, three possible ways to quantify nonlinearity in soft solids: Propagation of shocked shear waves,¹² nonlinear interaction between shear waves¹³ and acoustoelasticity.¹¹

The acoustoelasticity theory in solids has been first established by Hugues and Kelly in 1953¹⁴ using the second order and third order elastic coefficient. These parameters come from the expansion of the strain energy density as a function of the invariants of the strain tensor in “Lagrangian” coordinates.¹⁵ The third order moduli can also be expressed as a function of the Landau coefficients (A , B , C).¹⁶ Experimentally, acoustoelasticity consists of measuring the speed of acoustic waves in stressed solids. The third order moduli are

deduced from the slope of the ultrasonic waves velocities as a function of the uniaxial stress or of the hydrostatic pressure applied to the sample. However, acoustoelastic analysis has usually been applied to compressible engineering materials. From our knowledge, regarding soft solids, biological tissues or “nearly” incompressible materials, only few works have been developed on the acoustoelasticity theory for hyperelastic media^{17,18} or on the nonlinear properties of tissue-like phantoms.¹⁹

In a recent paper, shear wave propagation theory in soft solids brought new ideas in the field of elasticity theory. Hamilton *et al.*²⁰ suggested a new expression of the elastic energy density. Applied to nonlinear shear wave experiments reported in Ref. 12, Zabolotskaya *et al.*²¹ obtained a straightforward nonlinear equation where only three elastic coefficients are involved. In this paper, this approach is applied to the field of acoustoelasticity. It results in evolution equations for shear waves in stressed incompressible media that depend on only two elastic coefficients.

In a previous paper,¹¹ we proposed the estimation of the shear wave speed in a medium submitted to an uniaxial stress, using the one dimensional (1D) transient elastography technique.⁸ In these soft solid acoustoelasticity experiments, there were two main difficulties. First, it was difficult to obtain a uniform and constant uniaxial stress, as the stress field in the samples was highly dependent on the boundary conditions. The experimental setup has been improved by using a cylindrical phantom and a mechanical guide to insure a vertical direction of the applied loads. Second, in the 1D transient elastography approach, cylindrical shear waves were generated by giving a low frequency pulse (~ 100 Hz) at the surface of the phantom with a point source

^{a)}Electronic mail: jl.gennisson@espci.fr

(the transducer itself). Thus, in the near field coupling between longitudinal waves and shear waves were nonnegligible. Moreover, model equations were established for plane waves, so experimental assessments were biased by strong diffraction effects. Consequently the experimental set-up has been enhanced by replacing the mechanical vibrator by the acoustic radiation force technique as a shear wave source.²² This technique enables the controlled generation of quasi-plane shear waves in the medium by focusing an ultrasound beam successively at several depths in the medium thus generating several in-depth sources of shear waves. The electronic steering of the ultrasonic beam permits to move the shear source at a higher speed than resulting shear waves propagation speed leading to a supersonic regime. Thus, contrary to the 1D transient elastography, shear diffraction effects were strongly minimized and interaction between longitudinal waves and shear deformations were excluded.

In this paper, the theoretical background of the acoustoelasticity technique is introduced in the first section to deduce the nonlinear shear coefficient A of soft solids. Theoretical equations derived in this section are compared with the classical approach in solids. In the next section, the experimental setup and experimental results are described. Two soft materials used as phantoms in medical imaging are tested: agar-gelatin (AG) phantoms and polyvinyl alcohol cryogel (PVA) phantoms. Finally, the experimental assessments of the nonlinear shear coefficient are discussed.

II. THEORETICAL BACKGROUND

The general principle of acoustoelasticity is based on the expressions of the speed of elastic waves in a uniaxially stressed lossless solid. Basic equations are summarized as follows. In “Lagrangian” coordinates (\mathbf{a}, t) (\mathbf{a} is the equilibrium position of the particle, t is the time), equations of motion are

$$\rho_0 \ddot{u}_i = \frac{\partial P_{ik}}{\partial a_k} \quad \text{for } 1 \leq i, \quad k \leq 3. \quad (1)$$

where ρ_0 , P_{ik} , and $\ddot{\mathbf{u}} = \partial^2 \vec{\mathbf{u}} / \partial t^2$ designate the density, the Piola–Kirchhoff stress tensor (assuming Einstein summation convention of repeated indices) and the particle acceleration (second time derivative of the displacement \mathbf{u}), respectively. The Piola–Kirchhoff stress tensor is given in Lagrangian coordinates by²³

$$P_{ik} = \frac{\partial e}{\partial \left(\frac{\partial u_i}{\partial a_k} \right)}. \quad (2)$$

where e designates the strain energy density which can be developed up to the third order:

$$e = \mu I_2 + \frac{\lambda}{2} I_1^2 + \frac{A}{3} I_3 + B I_1 I_2 + C I_1^3. \quad (3)$$

where (μ, λ) are Lamé coefficients involved in the linear behavior of the solid and (A, B, C) are third order elastic coefficients of Landau, describing the quadratic nonlinear response of the deformed solid. (I_1, I_2, I_3) are invariants of the

Lagrangian strain tensor defined by Landau and Lifshitz.²³

Now let us consider the medium as incompressible. In such a media, an alternative expansion of the strain energy that permit separation of effects due to compressibility and shear deformation was recently defined by Hamilton *et al.*²⁰ and Zabolotskaya *et al.*²¹ Rather than express the strain energy in terms of invariants I_1, I_2 and I_3 as in Eq. (3), one choose instead to express the strain energy in terms of the set of independent invariants III_c, I_2 , and I_3 , where $III_c = \rho_0^2 / \rho^2$ is the third principal invariant of the Green deformation tensor. Thus here in incompressible media, $III_c = 1$, and the strain energy is

$$e = \mu I_2 + \frac{A}{3} I_3 + D I_2^2, \quad (4)$$

where D is the fourth order elastic constant. In the following sections, only propagation of plane waves of small amplitude will be considered, so fourth order terms will be neglected. Developing the invariants using the strain tensor \bar{S} defined by

$$S_{ik} = \frac{1}{2} \left(\frac{\partial u_i}{\partial a_k} + \frac{\partial u_k}{\partial a_i} + \frac{\partial u_l}{\partial a_i} \frac{\partial u_l}{\partial a_k} \right), \quad (5)$$

and according to Eq. (1), one obtains the following expression of the equation of motion:

$$\begin{aligned} \rho_0 \frac{\partial^2 u_i}{\partial t^2} = \frac{\partial P_{ik}}{\partial a_k} = & \mu \left(\frac{\partial^2 u_i}{\partial a_k^2} + \frac{\partial^2 u_k}{\partial a_i \partial a_k} \right) + \left(\mu + \frac{A}{4} \right) \\ & \times \left(\frac{\partial^2 u_l}{\partial a_i \partial a_k} \frac{\partial u_l}{\partial a_k} + \frac{\partial u_l}{\partial a_i} \frac{\partial^2 u_l}{\partial a_k^2} + \frac{\partial^2 u_k}{\partial a_l \partial a_k} \frac{\partial u_l}{\partial a_i} \right. \\ & + \frac{\partial^2 u_l}{\partial a_k^2} \frac{\partial u_l}{\partial a_i} + 2 \frac{\partial u_k}{\partial a_l} \frac{\partial^2 u_l}{\partial a_k \partial a_i} \left. \right) + \frac{A}{4} \left(\frac{\partial^2 u_k}{\partial a_k \partial a_l} \frac{\partial u_l}{\partial a_i} \right. \\ & \left. + \frac{\partial u_k}{\partial a_l} \frac{\partial^2 u_l}{\partial a_k \partial a_i} \right). \end{aligned} \quad (6)$$

In order to simplify further analytical developments, let us consider now some important points. First, in an acoustoelasticity experiment, two main displacements are involved. The static displacement due to the uniaxial stress applied and the dynamic displacement due to the propagation of shear waves induced here by the acoustic radiation force of the ultrasonic “palpating” beam. Moreover, shear strains must be of small amplitude compared to the static deformation induced by the uniaxial stress σ , which is the case experimentally here as ultrasonic radiation force induces very small (micrometric) displacements. Thus, the displacement can be expressed as the sum of the static displacement (\vec{u}^S) induced by the uniaxial stress and of the dynamic displacement (\vec{u}^D) due to the shear wave propagation:

$$\vec{u}^{\text{TOT}} = \vec{u}^D + \vec{u}^S. \quad (7)$$

Neglecting the nonlinear propagation of the shear wave and static deformations of higher order (i.e., $i = 1, 2, 3$), the wave equation is written as

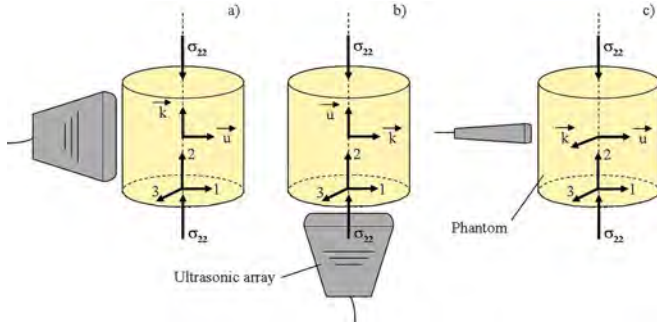


FIG. 1. (Color online) The three possible configurations generating (using the acoustic radiation pressure) and detecting (with an ultrafast scanner) the propagation of polarized shear waves in the phantom under uniaxial stress (σ_{22}). The three resulting shear waves are designated as (a) 12 or 32, (b) 21 or 23, and (c) 13 or 31.

$$\begin{aligned} \rho_0 \frac{\partial^2 u_i^D}{\partial t^2} = & \mu \left(\frac{\partial^2 u_i^D}{\partial a_k^2} + \frac{\partial^2 u_k^D}{\partial a_i \partial a_k} \right) + \left(\mu + \frac{A}{4} \right) \left(\frac{\partial^2 u_l^D}{\partial a_i \partial a_k} \frac{\partial u_l^S}{\partial a_k} \right. \\ & + \frac{\partial u_l^S}{\partial a_i} \frac{\partial^2 u_l^D}{\partial a_k^2} + \frac{\partial^2 u_k^D}{\partial a_i \partial a_k} \frac{\partial u_i^S}{\partial a_l} + \frac{\partial^2 u_l^D}{\partial a_k^2} \frac{\partial u_i^S}{\partial a_l} \\ & + 2 \frac{\partial u_k^S}{\partial a_l} \frac{\partial^2 u_i^D}{\partial a_k \partial a_l} \left. \right) + \frac{A}{4} \left(\frac{\partial^2 u_k^D}{\partial a_k \partial a_l} \frac{\partial u_l^S}{\partial a_i} \right. \\ & \left. + \frac{\partial u_k^S}{\partial a_l} \frac{\partial^2 u_l^D}{\partial a_k \partial a_i} \right). \end{aligned} \quad (8)$$

Second, for easier understanding and to simplify the calculations, one can deal with linearly polarized plane shear waves. For example, a plane wave that propagates along a_2 axis is considered, with a particle motion restricted to a_1 axis, according to those plotted on Fig. 1(a). The particle displacement in the wave is then expressed as $u_1^D(a_2, t)$. For sake of simplicity, the plane shear wave is characterized by the two indices according to the following convention 12. The first index corresponds to the direction of the shear displacement induced by radiation force (direction of polarization of the shear wave) and the second index corresponds to the axis of propagation of the shear wave. Let us chose the uniaxial stress directed along the a_2 axis. Then it comes:

$$\rho_0 \frac{\partial^2 u_1^D}{\partial t^2} = \mu \frac{\partial^2 u_1^D}{\partial a_2^2} + \left(2\mu + \frac{A}{2} \right) \left(\frac{\partial^2 u_1^D}{\partial a_2^2} \right) \left(\frac{\partial u_1^S}{\partial a_1} + \frac{\partial u_2^S}{\partial a_2} \right). \quad (9)$$

Third, because of the static uniaxial stress applied, three states and their coordinates need to be distinguished: the natural state, \mathbf{a} , the initial state, \mathbf{x} and the current state, \mathbf{y} related to shear wave propagation. It is useful to express the acoustoelastic equations in the initial coordinates, which, because of the infinitesimal nature of \mathbf{u}^D coincide with the laboratory (Eulerian) coordinates. For simplicity, one supposes that the initial stress and strain are uniform and defined by the static displacement \mathbf{u}^S : $\mathbf{x} = \mathbf{a} + \mathbf{u}^S$. The dynamic displacement \mathbf{u}^D , due to wave propagation is defined by: $\mathbf{y} = \mathbf{x} + \mathbf{u}^D$. The equation of motion for \mathbf{u}^D comes from development around the initial state of Eqs. (1) and (2). Then with the change of variable, $\mathbf{a} \rightarrow \mathbf{x}$, by neglecting again the terms of higher order and by use of the chain rule, it comes in the general case:

$$\frac{\partial^2 u_i^D}{\partial a_k^2} \cong \frac{\partial^2 u_i^D}{\partial x_k^2} \left(1 + 2 \frac{\partial u_k^S}{\partial x_k} \right), \quad \frac{\partial^2 u_k^D}{\partial a_i \partial a_k} \cong \frac{\partial^2 u_k^D}{\partial x_i \partial x_k}. \quad (10)$$

So for the plane wave $u_1^D(a_2, t)$, the wave equation in the new coordinates system becomes:

$$\begin{aligned} \rho_0 \frac{\partial^2 u_1^D}{\partial t^2} = & \frac{\partial^2 u_1^D}{\partial x_2^2} \left[\mu + 2\mu \left(\frac{\partial u_1^S}{\partial x_1} + 2 \frac{\partial u_2^S}{\partial x_2} \right) \right. \\ & \left. + \frac{A}{2} \left(\frac{\partial u_1^S}{\partial x_1} + \frac{\partial u_2^S}{\partial x_2} \right) \right]. \end{aligned} \quad (11)$$

Finally by using the Hooke's law²⁴ and assuming an incompressible medium (Poisson's ratio $\nu=0.5$), the spatial derivatives of the static displacement are:

$$\frac{\partial u_2^S}{\partial x_2} = -\frac{\sigma_{22}}{E} \approx -\frac{\sigma_{22}}{3\mu}, \quad \frac{\partial u_1^S}{\partial x_1} = \frac{\partial u_3^S}{\partial x_3} = \frac{\nu \sigma_{22}}{E} \approx \frac{\sigma_{22}}{6\mu}, \quad (12)$$

where E is Young's modulus. As one deals with compression (opposite of the dilatation), a negative stress was considered. Then, the nonlinear elastodynamic equation is rewritten as

$$\rho_0 V_{S12}^2 = \mu - \sigma_{22} \left(1 + \frac{A}{12\mu} \right), \quad (13)$$

with V_S being the shear wave velocity.

According to the axis defined by Fig. 1, the result is the same for the couple of indices 32. Regarding the other possible couples of indices, two more nonlinear elastodynamic equations are obtained.

For indices 21 or 23 the shear wave velocity is then:

$$\rho_0 V_{S21}^2 = \mu - \sigma_{22} \left(\frac{A}{12\mu} \right), \quad (14)$$

and for indices 13 or 31:

$$\rho_0 V_{S13}^2 = \mu + \sigma_{22} \left(1 + \frac{A}{6\mu} \right). \quad (15)$$

Note that Eqs. (13)–(15), if the medium is unstressed ($\sigma_{22}=0$), correspond to the classical shear wave propagation equation in an isotropic media. Thus, the medium reveals an anisotropic behavior resulting from the nonlinear effects.^{11,25} Moreover, changing the stress in Eqs. (13)–(15) is equivalent to modifying the shear modulus (μ) according to a linear dependence with a linear slope defined by the shear modulus (μ) and the third order nonlinear coefficient (A).

With this approach, theory of acoustoelasticity in incompressible media developed in this section of the present paper is fully consistent with classical acoustoelasticity theories defined in classical solids. For example, one can take as a comparison the theoretical framework developed by Hughes and Kelly.¹⁴ Hughes and Kelly establish expressions for velocities of elastic waves in stressed solids using Murnaghan's theory¹⁵ of finite deformations and third order terms in the energy. These expressions can also be expressed as a function of the Landau coefficient¹⁶ for plane shear waves under uniaxial stress. Assuming the material incompressible, one can use following statements: $\lambda \gg \mu$ and $B = -K = -(\lambda + \frac{2}{3}\mu)$,²⁶ the equations derived from Hughes and Kelly lead to Eqs.

(13)–(15). Similarly, using the theoretical approach of Thurston and Brugger²⁷ and summarized by Norris in Ref. 16, Eqs. (13)–(15) can be retrieved.

Thus, the application of both previous theories (Hugues and Kelly;¹⁴ Thurston and Brugger²⁷) to incompressible media is consistent with Hamilton *et al.*²⁰ and Zabolotskaya *et al.*²¹ papers. With this theoretical approach, in the case of soft solids, the separation of compressibility and shear deformations is possible and shear velocities depend only on the second and third order shear elastic moduli (μ, A). The influence of second and third order elastic coefficients related to longitudinal waves can be neglected. Therefore, compared to expressions in isotropic and compressible medium,¹¹ neither the third order Landau coefficients B and C [Eq. (3)] (B is defined as the nonlinear coefficient of the coupling term between shear and longitudinal waves and C is defined as the nonlinear coefficient for longitudinal waves) nor λ the second Lamé coefficient (λ is linked to the compressibility of the material) have any effect on the determination of shear velocities.

In the following section, as the supersonic shear imaging technique enables the controlled generation of quasiplane shear waves and the total discrimination in time between shear and compressional deformations during the acquisition due to the huge discrepancy between shear ($\sim 1 \text{ m s}^{-1}$) and compressional wave ($\sim 1500 \text{ m s}^{-1}$) speeds; we will take advantage of these relationships [Eqs. (13)–(15)] to estimate the linear and nonlinear elastic moduli (μ, A) in an acoustoelasticity experiment.

III. MEASUREMENT SYSTEM

The experiments were performed on two kinds of quasi-incompressible soft solids commonly used for the mimicking of soft tissues: five AG phantoms and three PVA phantoms.

The five AG phantoms were prepared with different concentrations of gelatin and agar diluted in water (initially heated at $50 \text{ }^\circ\text{C}$) following a strict procedure earlier described in Ref. 28. Two AG phantoms (GEL_1 and GEL_4) were cylinders of 12.5 cm diameter and 15 cm high, with a concentration of 3% by weight of agar (Agar, Prolabo, Fontenay/Bois, France) and 5% and 15% by weight of gelatin (Gelatin, Prolabo, Fontenay/Bois, France), respectively. The three other ones (GEL_2, GEL_3, GEL_5) were cylinders of 12 cm diameter and 15 cm high with 3% by weight of agar and 7%, 10%, and 8.5% by weight of gelatin, respectively. The agar was used as scatterers and gelatin was used as matrix.

PVA phantoms were constituted of 10% by weight of PVA (polyvinyl alcohol hydrolyzed, Sigma-Aldrich, St Louis, MO) dissolved in water. The solution container was heated in hot water to $80 \text{ }^\circ\text{C}$, and to minimize dehydration the container was covered. 3% by weight of Sigmacell (Sigmacell Cellulose type 20, Sigma-Aldrich, St Louis, MO) was added to serve as scatterers. The three PVA phantoms were cylinders of a 15 cm high and 12 cm diameter. PVA phantoms underwent two (PVA_1), three (PVA_2) and five (PVA_3) freezing–thawing cycle to polymerize them with a certain level of elasticity as described in previous papers.^{29,30}

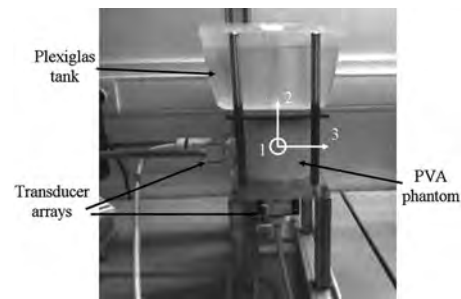


FIG. 2. Experimental set-up on a PVA phantom (PVA_2). Two transducer arrays are placed along the vertical axis of the phantom and at the bottom of the phantom, in order to measure the shear waves propagation with the 21 or 23 [Eq. (19)] and the 12 or 32 [Eq. (18)] indices respectively. During this experiment, the tank was incrementally filled with water in steps of 0.3 kg.

In experiments, a rigid Plexiglas tank was added on top of the phantoms and filled with different amounts of water [e.g., with the agar-gelatin phantom GEL_4, from 0.3 kg (weight of the Plexiglas plate and tank) to about 2.1 kg in incremental steps of 0.3 kg step] to control the uniaxial stress (Fig. 2). The loading charges were adapted depending of the phantom consistency. The Plexiglas tank and the phantom support were parallel to make the stress as uniaxial as possible. Moreover coupling gel was applied at the top and at the bottom of the phantoms to minimize friction effects between phantoms and supports.

Then, the 4.3 MHz ultrasonic array (128 elements, 0.33 mm pitch, 10 mm elevation, 60 mm elevation focus, Vermon, Tours, France) was applied at three different positions surrounding the phantoms as described on Fig. 1 to investigate the three possible shear wave propagations defined in part II. So, the ultrasonic beam was two times perpendicular [Figs. 1(a) and 1(c)] and one time parallel [Fig. 1(b)] to the uniaxial stress. The ultrasonic array was connected to an ultrafast scanner (the system was already describe in Ref. 31) and transmits ultrasound beams through a wide layer of coupling gel, which did not induce significant artifact on the applied uniaxial stress field.

To generate the radiation force, the ultrafast scanner was used to create an ultrasound-focused beam in the phantom at a chosen location (so called “supersonic push”). The typical ultrasound pulse was made of 500 oscillations at 4.3 MHz. This corresponded to a “pushing time” of $\sim 120 \mu\text{s}$. Just after the generation of the “pushing” beam, the scanner began an ultrafast imaging sequence by sending plane-wave insonifications at a high-frame rate (2000 Hz) in order to catch the shear wave created by the supersonic push.²²

In post acquisition, displacement fields were obtained by 1D cross correlation of beamformed RF signals stored with the reference echo image.³² The results were a set of images giving the displacement induced by the shear wave at each sample time (Fig. 3). In Fig. 3 one can also notice the effect of the attenuation on shear waves. Nevertheless, the attenuation is not relevant on the shear wave speed assessment because the signal to noise ratio is high enough to allow a good measurement of the displacements induced by shear waves along the imaged plane (about 25 mm, Fig. 3). The use of an inverse problem based on the Helmholtz equation, as described in previous papers,^{6,22} allowed us to map

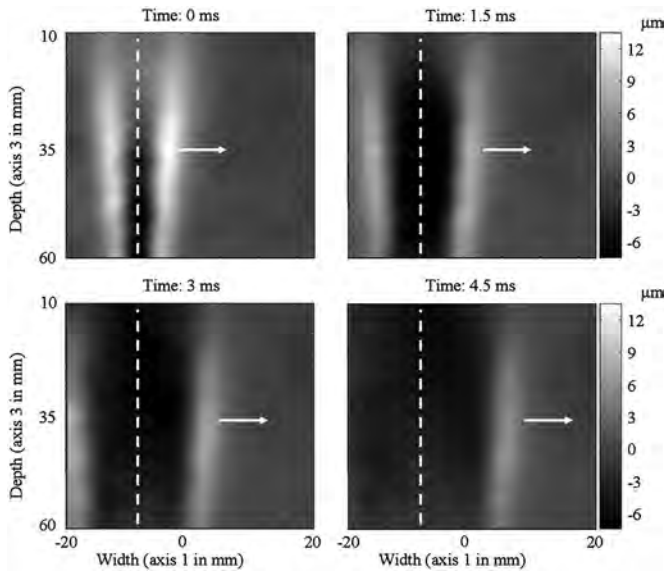


FIG. 3. Experimental displacement field in agar-gelatin phantom (GEL_1) at successive times after the “push”. The dotted line represents the axis of the polarization of the shear source (the supersonic push on axis 3) and the arrow the direction of propagation of the shear wave (axis 1).

the shear wave speed. Then knowing the density ($\rho_0 \approx 1000 \text{ kg/m}^3$), the shear modulus and its corresponding standard deviation, for each stress applied, were retrieved by taking the mean shear wave speed and its corresponding standard deviation at all depth between 0 and 20 mm in width (Fig. 4).

IV. RESULTS

The experiments on AG phantoms and on PVA phantoms were gathered in Figs. 5 and 6 respectively. Figures 5 and 6 showed an increasing speed versus applied stress for the shear wave propagating in the 13 plane and a decreasing speed in the 12 plane. The shear wave speed in the 21 plane was sometimes increasing and sometimes decreasing with respect to the applied stress, so it has an influence on both sign and value of the third order elastic coefficient (A). At the zero stress point for each data set, the shear Lamé coef-

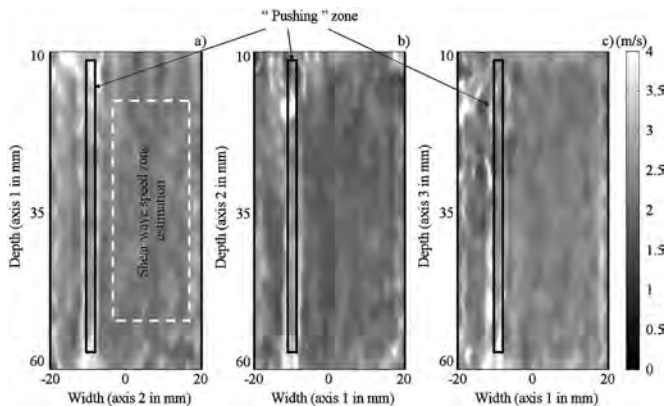


FIG. 4. Map of the shear wave speed for each position of the transducer array, (a) 12 (equivalent to 32), and (b) 21 (equivalent to 23), and (c) 31 (equivalent to 13) in AG phantom (GEL_1) at zero stress. The point line corresponds to the region of interest used for the estimation of the mean shear wave speed and its corresponding standard deviation.

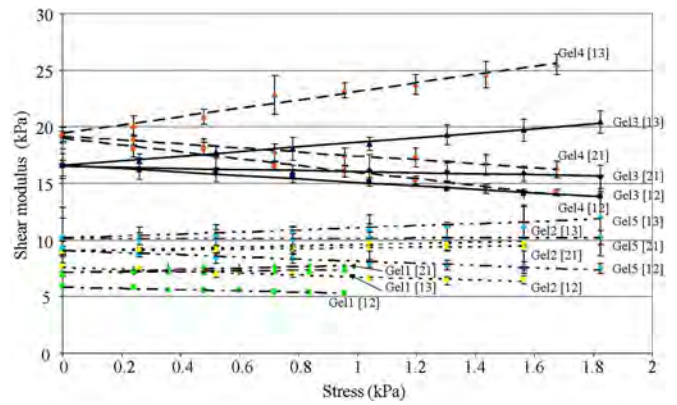


FIG. 5. (Color online) Experimental shear moduli as a function of applied uniaxial stress for each axis of propagation investigated in agar-gelatin phantoms. Four different phantoms with different gelatin concentration were investigated: Gel_1 (5% by weight of gelatin), Gel_2 (7%), Gel_3 (10%), Gel_4 (15%) and Gel_5 (8.5%). The slopes given by the dashed and solid lines were obtained from a least mean square fit.

ficient μ was computed as the mean value of the moduli measured for the three experimental configurations (Fig. 1). The values, summed up in Table I, show a good estimation of the linear shear modulus with a maximum 9% standard deviation in AG phantoms and 2% in PVA phantoms. As presented in Figs. 5 and 6, the shear modulus evolution clearly exhibits the appearance of an anisotropic behavior in all phantoms. Moreover, the shear modulus was linearly dependent with respect to the uniaxial stress in all materials as expected in the theoretical framework. From a quantitative point of view, the shear modulus affecting each quasi-plane shear wave (12, 21, 13) increased or decreased respectively with the following slopes (obtained from a least mean square fit of the data): GEL_1 (-0.56, 0.61, 0.26), GEL_2 (-0.79, 0.25, 0.59), GEL_3 (-1.55, -0.46, 2.03), GEL_4 (-3.02, -1.75, 3.71), GEL_5 (-0.94, 0.05, 0.92), PVA_1 (-0.48, 0.31, 0.55), PVA_2 (-1.11, -0.10, 1.26), and PVA_3 (-1.13, -0.23, 1.35). One can notice that when the linear shear modulus was higher, the value of slopes increased for the 13 plane and decreased for the 21 and 12 planes in both AG phantoms and PVA phantoms. Further, the slope for the

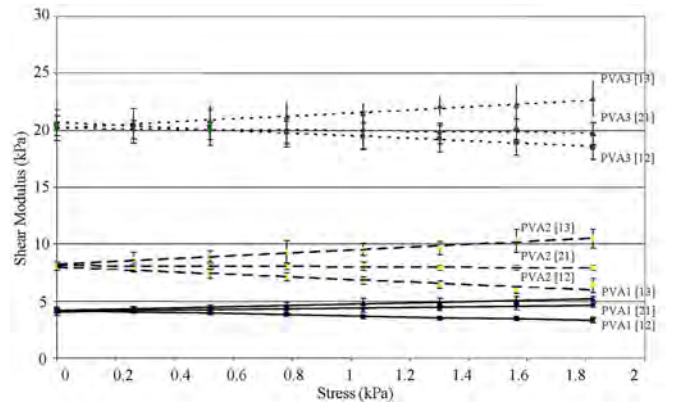


FIG. 6. (Color online) Experimental shear moduli as a function of applied uniaxial stress for each axis of propagation investigated in PVA phantoms. Three different phantoms, with different elasticity defined by the number of freezing-thawing cycles applied (2, 3, and 5 cycles), were investigated. The slopes given by the dashed and solid lines were obtained using a linear fit.

TABLE I. Elastic moduli measured in two different soft solids.

Materials	Linear shear modulus (Lamé coefficient μ (kPa) (mean value at 0 stress))	Non linear shear modulus [Landau coefficient A (kPa)]			
		Indice of propagation 12	Indice of propagation 21	Shear wave indices 13	Mean value
Agar-gelatin phantom 1	6.6±0.6	-35.0	-48.6	-29.4	-37.7±9.8
Agar-gelatin phantom 2	8.5±0.8	-21.5	-25.6	-21.0	-22.7±2.5
Agar-gelatin phantom 5	9.9±0.5	-7.1	-5.9	-4.8	-5.9±1.2
Agar-gelatin phantom 3	16.6±0.1	109.8	91.8	102.8	101.4±9.0
Agar-gelatin phantom 4	19.2±0.1	466.4	404.1	312.8	394.4±77.2
PVA phantom 1	4.1±0.1	-25.8	-15.4	-11.2	-17.5±7.5
PVA phantom 2	8.1±0.1	10.7	9.7	12.6	11.0±1.4
PVA phantom 3	20.4±0.1	31.8	56.3	42.8	43.6±12.2

[21](#) plane changed its sign with the stiffness of the material. In all experiments, correlation coefficients of estimated slopes using a linear fit were higher than 80% [except for two cases in AG phantoms (48% and 10%) and one case in PVA phantoms (51%)].

Using Eqs. [\(13\)–\(15\)](#), the experimental estimates of shear modulus versus axial stress slopes enable the calculation of the nonlinear Landau coefficient A for all soft solids. The mean value of A and its standard deviation were calculated from three independent values of A for each direction of propagation. One can notice that the standard deviation of A for all experiments in AG phantoms and PVA phantoms is less than 28% excluding for the one softer PVA phantom (43% in PVA_1).

Regarding the results presented in Table I, the nonlinear shear modulus A is plotted as a function of the shear modulus μ in Fig. 7. One can notice that A seems to evolve as an exponential as a function of μ for AG phantoms. For PVA phantoms, no specific variation can be observed.

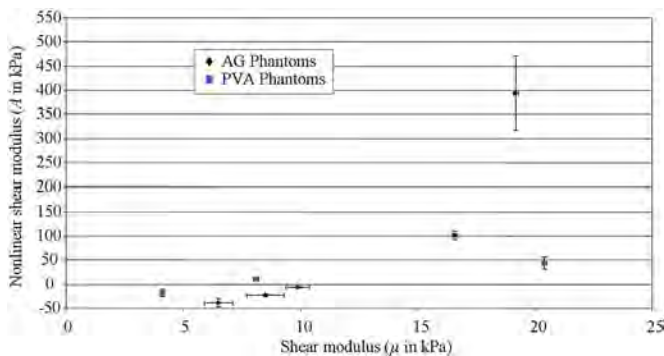


FIG. 7. (Color online) Experimental nonlinear shear moduli A as a function of experimental shear modulus μ for each phantom. In AG phantoms A seems to evolve as an exponential, but no specific variation can be noticed on PVA phantoms.

V. DISCUSSION

Results summarized in Table I confirm the fact that the experimental setup gives three independent ways to estimate the nonlinear coefficient A . Indeed, in the AG phantoms, estimates of A from the slopes obtained from shear wave velocities are in very good agreement for the four last phantoms (the standard deviation is less than 20%). AG phantom GEL_1 exhibits a 26% standard deviation for the A coefficient. In the PVA phantoms, the agreement for the different directions of propagation is also quite good: the standard deviation of the A coefficient estimates inferior to 28% for the two last phantoms. This can be explained by the difficulties to perfectly control the setup with such very soft phantoms, which cannot be submitted to large stresses in order to preserve their physical integrity, e.g., with a relatively large stress the phantoms are destroyed under the weight of the water tank. Nevertheless the same problem as in AG phantom appears for the very soft phantom PVA_1. Moreover, positioning the transducer array correctly with regards to the axis of the uniaxial stress is not trivial, since one cannot perfectly know the true spatial distribution of the uniaxial stress. However, compared to others results already reported in previous papers³³ for metals, crystals or polystyrene,³⁴ these experimental estimates of μ and A in soft solids confirm the fact that the A Landau coefficient exhibits values (kPa), consequently much lower than in classical solids.

Comparing results obtained in AG phantoms and in PVA phantoms, the shear modulus values are in the same range of elasticity for both type of phantoms. However, the behavior of the nonlinear coefficient A is quite different. For example, if one compares the AG phantom GEL_2 and the PVA phantom PVA_1, their shear moduli are practically the same (8.5±0.8 kPa and 8.15±0.1 kPa respectively). But the Landau coefficient A is negative in AG phantoms and positive in PVA phantoms. Moreover the range of elasticity of A is

TABLE II. Shear wave speed (13 direction) in an AG phantom (5% by weight of gelatin) at zero stress as a function of the height from the top of the phantom.

Shear modulus (kPa)	6.5±0.2	6.5±0.1	6.6±0.2	6.7±0.2	6.8±0.8
Height (cm)	2	4	6	8	10

larger in AG phantoms (from -37.7 to 394.4 kPa) than in PVA phantoms (from -17.5 to 43.6 kPa). Once again, comparing AG phantom GEL_4 and PVA phantom PVA_3, the shear modulus is quite identical but the A value is practically 10 times higher in AG phantom. Thus there is a big difference from the nonlinear point of view between these two kinds of material even though their linear behavior is quite similar.

The shear modulus at zero stress is determined by averaging the three measurements in each direction. On the one hand, the estimation of the shear modulus at zero stress in AG phantoms exhibits a quite small 7% standard deviation. The reason why the shear coefficient is not the same for all directions, as it should be in an ideally isotropic medium, is that the measurements were performed in the middle of the sample. For example, let us consider a horizontal plane at a given depth in the phantom with no uniaxial stress applied. Above this plane, the own weight of the phantom induces stress, which depends on the height of the column of the upper part of the material. Consequently, a uniaxial stress increasing with depth appears due to gravity effects. Thus, the speed of the shear waves measured should increase with depth. To confirm this argument, the shear wave speed was estimated at several depths within an AG phantom (GEL_1 with 5% by weight of gelatin and 3% of by weight of agar) from 2 cm top down to 10 cm with 2 cm steps. Resulting values for the 13 direction (the transducer array was horizontal) are summarized in Table II.

The shear wave speed increases as a function of the height and confirms the influence of the gravity force. Results presented on Fig. 5 show that this effect is much less pronounced as the gelatin concentration increases (and consequently shear modulus at zeros stress). On the other hand, in PVA phantoms the standard deviation also decreases to 2%. So, PVA phantoms seem to be less submitted to gravity effects. This is probably related to the internal structure of PVA phantoms³⁵ (polymer chains) more cross linked and stiffer compared to the internal structure of AG phantoms³⁶ (network of rigid gelatin rods). Nevertheless, these gravity effects do not affect drastically assessment of the third order elastic coefficient.

From Eqs. (13)–(15) one can see that starting from an isotropic solid the applied stress implies an anisotropic behavior of the material. In other words, modifying the stress is equivalent to induce an apparent anisotropy in the medium due to nonlinear effects. For a given stress one can define a specific nonlinear anisotropy corresponding to a specific set of different independent elastic constants (μ_{12} , μ_{21} , μ_{13}) depending of the nonlinear coefficient. At zero stress, velocities correspond to an isotropic solid ($\rho_0 V_{ij}^2 = \mu$; $i, j = 1, 2, 3$). It is

confirmed experimentally for PVA phantoms and the two stiffer AG phantoms, as all lines converge towards the same point at zero stress. However, for very soft solids, for example GEL_1, GEL_2, or GEL_5, an initial anisotropy was present due to gravity effects although the material was isotropic. Under their own weight net force, phantoms were naturally stressed and an apparent resulting anisotropy appears. In linear classical solids this kind of anisotropy was corresponding to a hexagonal system,²⁴ so called “transverse isotropy” because two shear waves speeds are identical in the plane defined by the polarization of the two waves; this plane can be defined as isotropic (The shear wave speeds assessed on the 21 and 13 direction were equivalent (GEL_1 (21 2.66 ± 0.06 m/s), 13 2.64 ± 0.03 m/s), GEL_2 (21 3.00 ± 0.08 m/s 13 3.00 ± 0.02 m/s), GEL_5 (21 3.20 ± 0.41 m/s, 13 3.21 ± 0.26 m/s)). Nevertheless, here the apparent anisotropy cannot be defined because anisotropy is defined with the symmetry of the second order elastic moduli. For instance the anisotropy induced by the stress effects must be distinguished from those caused by intrinsic material anisotropy.¹⁶ Now, for a higher uniaxial stress (e.g., $\sigma_{22} = 1.2$ kPa), in each material, three different velocities are observed (Figs. 5 and 6). One can notice that nonlinear effect increase the observed anisotropy and the behavior of the medium is more complicated. These experiments interestingly emphasize the fact that nonlinear effects significantly modify the anisotropic behavior of soft solids.

Moreover one can notice that when μ grows, A increases going from a negative value to a positive one for both AG phantoms and PVA phantoms. This is directly related to the slope variation of the shear wave speed along direction 21 which changes of sign, from positive to negative, as a function of the shear modulus increase. Consequently for certain shear modulus μ at zero stress, e.g., a certain concentration of agar-gelatin or a certain number of freezing–thawing cycles in PVA phantoms, the nonlinear shear modulus A is cancelled. Regarding Eqs. (13)–(15), anisotropy can be also retrieved if the nonlinear coefficient A is cancelled. In this specific configuration, the slope of the measurement for the couple of indices 21 [Eq. (14)] is null. The stress applied has no more effect on the shear wave velocity. But stress still induces anisotropy for both other couple of indices [Eqs. (13) and (15)]. Shear wave velocity in the 13 direction increases whereas shear wave velocity in 12 direction decreases with the applied stress. In fact, such an $A=0$ assumption means that the third invariant of the Lagrangian strain tensor I_3 has no effect in the development of the strain energy [Eq. (4)] (if one considers only the development of the strain energy at the third order). So, in that particular configuration, the only contribution to nonlinearity is the quadratic term from the strain tensor, also known as the geometric nonlinearity.

From Fig. 7, one can notice that the nonlinear parameter A seems to evolve as an exponential regarding to the shear modulus for the AG phantoms and it seems not to be the case for the PVA phantoms. These effects can be intuitively explained by the differences between microstructures of both materials. On the one hand, the elasticity results from the response of the polymeric filaments between cross-links,

from alterations in the network structure, or both.³⁷ On the other hand, the principles responsible for the nonlinear elasticity due to the microstructure are unknown, theories show that systems of filamentous proteins arranged in an open crosslinked mesh invariably stiffen at low strains without requiring specific architecture or multiple elements with different intrinsic stiffness.³⁸ Such behavior could be strongly interacting in such PVA phantoms known to contain crosslinked filaments. Moreover, as a comparison in classical solids such as glasses, the different constituent of the glasses used in the experiments can be related to velocity variations observed for both longitudinal and transversal waves in an acoustoelasticity experiments.^{39,40} However, the understanding of the behavior of the nonlinear shear modulus (A) as a function of the shear modulus (μ) needs further investigation.

VI. CONCLUSION

In this paper, a fast, simple, reproducible and robust method based on the supersonic shear imaging technique was used to revisit the acoustoelasticity experiment in order to characterize the nonlinear shear behavior of soft solids. This ultrasound-based technique enables both the remote generation in soft solids of quasiplane polarized shear waves and the ultrafast imaging of their resulting propagation. It enables the local assessment (or mapping) of the third order shear elastic coefficient A . Using an expression of the strain energy derived by Hamilton *et al.*²⁰ and Zabolotskaya *et al.*²¹ in quasiincompressible media, this third order coefficient can be estimated from a single ultrasonic experiment. Instead of measuring shear wave speeds for three different polarizations in order to completely determine the nonlinearity of standard solids, one single polarization experiment under a varying applied uniaxial stress is sufficient in soft solids to characterize the nonlinear shear elasticity. It means that *in vivo* assessment of this parameter could be feasible within the framework of the supersonic shear imaging approach.

ACKNOWLEDGMENTS

The authors would like to gratefully thank Patricia Daenens and Marc Yvert for technical assistance and Daniel Royer for illuminating discussion.

- ¹T. A. Krouskop, B. S. Dougherty, and F. S. Vinson, "A pulsed Doppler ultrasonic system for making noninvasive measurements of the mechanical properties of soft tissue," *J. Rehabil. Res. Dev.* **24**, 1–8 (1987).
- ²R. M. Lerner, K. J. Parker, J. Holen, R. Gramiak, and R. C. Waag, "Sonoelasticity: Medical elasticity images derives from ultrasound signals in mechanically vibrated targets," *Acoust. Imaging* **16**, 317–327 (1988).
- ³Y. Yamakoshi, J. Sato, and T. Sato, "Ultrasonic imagins of internal vibration of soft tissue under forced vibration," *IEEE Trans. Ultrason. Ferroelectr. Freq. Control* **37**, 45–53 (1990).
- ⁴K. J. Parker and R. M. Lerner, "Sonoelasticity of organs: Shearwaves ring a bell," *J. Ultrasound Med.* **11**, 387–392 (1992).
- ⁵S. F. Levinson, M. Shinagawa, and T. Sato, "Sonoelastic determination of human skeletal muscle elasticity," *J. Biomech.* **28**, 1145–1154 (1995).
- ⁶J. Bercoff, S. Chaffai, M. Tanter, L. Sandrin, S. Catheline, M. Fink, J.-L. Gennisson, and M. Meunier, "In vivo breast tumor detection using transient elastography," *Ultrasound Med. Biol.* **29**, 1387–1396 (2003).
- ⁷L. Sandrin, B. Fourquet, J.-M. Hasquenoph, S. Yon, C. Fournier, F. Mal, C. Christidis, M. Ziol, B. Poulet, F. Kazemi, M. Beauprand, and R. Palau, "Transient elastography: a new non invasive method for assessment of

- hepatic fibrosis," *Ultrasound Med. Biol.* **29**, 1705–1713 (2003).
- ⁸J.-L. Gennisson, S. Catheline, and M. Fink, "Transient elastography in anisotropic medium: application to the measurement of slow and fast shear wave speeds in muscles," *J. Acoust. Soc. Am.* **114**, 536–541 (2003).
- ⁹S. Catheline, J.-L. Gennisson, G. Delon, R. Sinkus, M. Fink, S. Abouelkaram, and J. Culioli, "Measurement of viscoelastic properties of homogeneous soft solid using transient elastography: An inverse problem approach," *J. Acoust. Soc. Am.* **116**, 3734–3741 (2004).
- ¹⁰J. Bercoff, M. Tanter, M. Muller, and M. Fink, "The role of viscosity in the impulse diffraction field of elastic waves induced by the acoustic radiation force," *IEEE Trans. Ultrason. Ferroelectr. Freq. Control* **51**, 1523–1536 (2004).
- ¹¹S. Catheline, J.-L. Gennisson, and M. Fink, "Measurement of elastic nonlinearity of soft solids with transient elastography," *J. Acoust. Soc. Am.* **114**, 3087–3091 (2003).
- ¹²S. Catheline, J.-L. Gennisson, M. Tanter, and M. Fink, "Observation of shock transverse waves in elastic media," *Phys. Rev. Lett.* **91**, 43011–43014 (2003).
- ¹³X. Jacob, J.-L. Gennisson, S. Catheline, M. Tanter, C. Barrière, D. Royer, and M. Fink, "Study of elastic nonlinearity of soft solids with transient elastography," *Proc.-IEEE Ultrason. Symp.* **1**, 660–663 (2003).
- ¹⁴D. S. Hugues and J. L. Kelly, "Second-order elastic deformation of solids," *Phys. Rev.* **92**, 1145–1149 (1953).
- ¹⁵T. D. Murnaghan, *Finite Deformation of an Elastic Solid* (Wiley, New York, 1951).
- ¹⁶A. Norris, *Non Linear Acoustics: Finite Amplitude Waves in Solids*, edited by M. Hamilton (Academic, New York, 1998).
- ¹⁷H. Kobayashi and R. Vanderby, "New strain energy function for acoustoelasticity analysis of dilatational waves in nearly incompressible hyperelastic materials," *J. Appl. Mech.* **72**, 843–851 (2005).
- ¹⁸H. Kobayashi and R. Vanderby, "Acoustoelastic analysis of reflected waves in nearly incompressible, hyper-elastic materials: Forward and inverse problem," *J. Acoust. Soc. Am.* **121**, 879–887 (2007).
- ¹⁹R. Q. Erkamp, A. R. Skovoroda, S. Y. Emelianov, and M. O'Donnell, "Measuring the nonlinear elastic properties of tissue-like phantoms," *IEEE Trans. Ultrason. Ferroelectr. Freq. Control* **51**, 410–419 (2004).
- ²⁰M. F. Hamilton, Y. A. Ilinskii, and E. A. Zabolotskaya, "Separation of compressibility and shear deformation in the elastic energy density (L)," *J. Acoust. Soc. Am.* **116**, 41–44 (2004).
- ²¹E. A. Zabolotskaya, M. F. Hamilton, Y. A. Ilinskii, and G. D. Meegan, "Modeling of non linear shear waves in soft solids," *J. Acoust. Soc. Am.* **116**, 2807–2813 (2004).
- ²²J. Bercoff, M. Tanter, and M. Fink, "Supersonic shear imaging: a new technique for soft tissues elasticity mapping," *IEEE Trans. Ultrason. Ferroelectr. Freq. Control* **51**, 374–409 (2004).
- ²³L. D. Landau and E. M. Lifshitz, *Theory of Elasticity*, 3rd ed. (Butterworth-Heinemann, Oxford, 2002).
- ²⁴D. Royer and E. Dieulesaint, *Elastic Waves in Solid* (Springer, Berlin, 1996), Vol. 1.
- ²⁵P. A. Johnson and P. Rasolofosaon, "Nonlinear elasticity and stress-induced anisotropy in rock," *J. Geophys. Res.* **101**, 3113–3124 (1995).
- ²⁶S. Kostek, B. K. Sinha, and A. N. Norris, "Third-order elastic constants for an inviscid fluid," *J. Acoust. Soc. Am.* **94**, 3014–3017 (1993).
- ²⁷R. N. Thurston and K. Brugger, "Third-order elastic constants and the velocity of small amplitude elastic waves in homogeneously stressed media," *Phys. Rev.* **133**, A1604–A1610 (1964).
- ²⁸J.-L. Gennisson and G. Cloutier, "Sol-gel transition in agar-gelatin mixtures studied with transient elastography," *IEEE Trans. Ultrason. Ferroelectr. Freq. Control* **53**, 716–723 (2006).
- ²⁹J. Fromageau, E. Brusseau, D. Vray, G. Gimenez, and P. Delachartre, "Characterization of PVA cryogel for intravascular ultrasound elasticity imaging," *IEEE Trans. Ultrason. Ferroelectr. Freq. Control* **50**, 1318–1324 (2003).
- ³⁰J. Fromageau, J.-L. Gennisson, C. Schmitt, R. Maurice, R. Mongrain, and G. Cloutier, "Estimation of polyvinyl alcohol cryogel mechanical properties with 4 ultrasound elastography methods and comparison with gold standard testings," *IEEE Trans. Ultrason. Ferroelectr. Freq. Control* **54**, 498–509 (2007).
- ³¹L. Sandrin, M. Tanter, S. Catheline, and M. Fink, "Shear modulus imaging using 2d transient elastography," *IEEE Trans. Ultrason. Ferroelectr. Freq. Control* **49**, 426–435 (2002).
- ³²J. Ophir, I. Céspedes, H. Ponnekanti, Y. Yasdi, and X. Li, "Elastography: a quantitative method for imaging the elasticity of biological soft tissues," *Ultrason. Imaging* **13**, 111–134 (1991).

- ³³M. A. Breazeale, "Comparison of the non linear behavior of fluids and solids," *Proceedings of the 13th ISNA*, World Scientific, Singapore, 1993, p. 451.
- ³⁴K. Naugolnykh and L. Ostrovsky, *Nonlinear Wave Processes in Acoustics* (Cambridge University Press, New York, 1998), Chap. 1, pp. 15–16.
- ³⁵C. M. Hassan and N. A. Peppas, "Structure and applications of polyvinyl alcohol hydrogels produced by conventional crosslinking or by freezing/thawing methods," *Adv. Polym. Sci.* **153**, 37–65 (2000).
- ³⁶C. Joly-Duhamel, D. Hellio, A. Ajdari, and M. Djabourov, "All gelatin networks: 2. The master curve for elasticity," *Langmuir* **18**, 7158–7166 (2002).
- ³⁷P. R. Onck, T. Koeman, T. van Dillen, and E. vander Giessen, "Alternative explanation of stiffening in cross-linked semiflexible networks," *Phys. Rev. Lett.* **95**, 178102 (2005).
- ³⁸C. Storm, J. J. Pastore, F. C. MacKintosh, T. C. Lubensky, and P. A. Janmey, "Nonlinear elasticity in biological gels," *Nature (London)* **435**, 191–194 (2005).
- ³⁹R. J. Wang, W. H. Wang, F. Y. Li, L. M. Wang, Y. Zhang, P. Wen, and J. F. Wang, "The Gruneisen parameter for bulk amorphous materials," *J. Phys.: Condens. Matter* **15**, 603–608 (2003).
- ⁴⁰B. Zhang, R. J. Wang, and W. H. Wang, "Response of acoustic and elastic properties to pressure and crystallization of Ce-based bulk metallic glass," *Phys. Rev. B* **72**, 104205 (2005).

● *Original Contribution*

VISCOELASTIC AND ANISOTROPIC MECHANICAL PROPERTIES OF IN VIVO MUSCLE TISSUE ASSESSED BY SUPERSONIC SHEAR IMAGING

JEAN-LUC GENNISSON, THOMAS DEFFIEUX, EMILIE MACÉ, GABRIEL MONTALDO,
MATHIAS FINK, and MICKAËL TANTER

Institut Langevin, Laboratoire Ondes et Acoustique, CNRS UMR 7587, ESPCI ParisTech, INSERM ERL U979,
Université Paris VII, Paris, France

(Received 18 August 2009; revised 23 February 2010; in final form 27 February 2010)

Abstract—The *in vivo* assessment of the biomechanical properties of the skeletal muscle is a complex issue because the muscle is an anisotropic, viscoelastic and dynamic medium. In this article, these mechanical properties are characterized for the *brachialis* muscle *in vivo* using a noninvasive ultrasound-based technique. This supersonic shear imaging technique combines an ultra-fast ultrasonic system and the remote generation of transient mechanical forces into tissue via the radiation force of focused ultrasonic beams. Such an ultrasonic radiation force is induced deep within the muscle by a conventional ultrasonic probe and the resulting shear waves are then imaged with the same probe (5 MHz) at an ultra-fast framerate (up to 5000 frames/s). Local tissue velocity maps are obtained with a conventional speckle tracking technique and provide a full movie of the shear wave propagation through the entire muscle. Shear wave group velocities are then estimated using a time of flight algorithm. This approach provides a complete set of quantitative and *in vivo* parameters describing the muscle's mechanical properties as a function of active voluntary contraction as well as passive extension of healthy volunteers. Anisotropic properties are also estimated by tilting the probe head with respects to the main muscular fibers direction. Finally, the dispersion of the shear waves is studied for these different configurations and shear modulus and shear viscosity are quantitatively assessed assuming the viscoelastic Voigt's model. (E-mail: jl.gennisson@espci.fr) © 2010 World Federation for Ultrasound in Medicine & Biology.

Key Words: Muscle tissue, Anisotropy, Viscoelastic, Supersonic shear imaging, Transient elastography.

INTRODUCTION

The biomechanical properties of the skeletal muscle are difficult to assess because this organ is a complex active and passive tissue. The skeletal muscle is composed of muscular fibers running parallel to each other called myocytes. These muscle cells, which are several centimeters long and several tens of micrometers diameter, have both the properties of excitability and contractibility. Each muscle fiber is composed of thousands of sarcomeres, which shorten when an action potential is applied to them. Consequently, the overall response of the fibers to an electrical excitation, natural or artificial, is both a mechanical response in the form of shortening, and a modification of the mechanical properties, in the form of hardening. Some techniques are specifically de-

signed and dedicated to the measurement of functional properties, such as electromyography (EMG), which records the muscle electrical activity (Aminoff 1987), surface mechanomyography (sMMG) (Orizio 1993) or acceleromyography (Viby-Mogensen et al. 2003), which respectively records pressure or acceleration on the skin surface during a contraction. These techniques describe the muscle function through its electrical activity or its mechanical response but have poor spatial resolution. Standard morphologic imaging techniques such as ultrasonography or magnetic resonance imaging (MRI) have also been applied and adapted to image muscle contraction. They follow the morphologic changes of the muscle before and after its shortening with a high spatial resolution but have poor temporal resolution. Recently, the use of ultrasonic ultra-fast imaging combined with electrical stimulation has been shown to allow both good spatial and temporal resolution for the measurement of the muscle mechanical response *in vivo* (Deffieux et al. 2008).

Address correspondence to: Jean-Luc Gennisson, Institut Langevin, Laboratoire Ondes et Acoustique, CNRS UMR 7587, ESPCI Paris Tech, INSERM ERL U979, Université Paris VII, 10 rue Vauquelin, 75231 Paris, Cedex 05, France. E-mail: jl.gennisson@espci.fr

Although the role of viscoelasticity in muscle biomechanics is well recognized, methods for measurements *in situ* are currently limited. Recently, the development of new quantitative elastography techniques has directly studied the modification of the muscle mechanical properties with the contraction. First, magnetic resonance elastography (MRE) has been applied to the measurement of the viscoelastic parameters of *in vivo* muscle. In particular, Dresner et al. (Dresner et al. 2001) have shown the first *in vivo* quantitative measurements of muscle tissue depending on the applied load. They derived a linear model for the relationship between developed strength and muscle stiffness. However, in this study, neither viscosity nor anisotropy are taken into account. In 2003, Gennisson et al. applied transient elastography to the measurements of the muscle stiffness versus developed force (Gennisson et al. 2003). A high anisotropy was observed and a hexagonal model was used for the muscle anisotropy. Using the same transient elastography approach, viscosity estimation was performed on beef muscle as a function of anisotropy (Catheline et al. 2004). These results were conducted with simultaneous recordings of the subjects EMGs (Gennisson et al. 2005). In 2005, Papazoglou et al. conducted the first MRE measurements of muscle stiffness and also demonstrated the high anisotropy of the muscle tissue (Papazoglou et al. 2005). Finally, first MRE clinical trials were conducted in 2007 (Ringleb et al. 2007) on both healthy subjects and patients and significant stiffness difference was exhibited between the two groups. However, in this study, stiffness was only measured along the main muscle direction without taking into account neither anisotropy nor viscosity. In fact, MRE techniques have the advantages of full three-dimensional (3-D) acquisition and can image deep muscles in a well defined and reproducible coordinates system. However, it also suffers limitations since the 3-D acquisition time is not applicable for clinical use (most studies use one-dimensional [1-D] or two-dimensional [2-D] estimation are used to shorten the acquisition time) and deep muscles imaging requires that shear waves generated by an external vibrator reach these deep areas. As a consequence, it limits the access of deep regions to very low frequencies (typically <100 Hz). Finally, the acquisition time and space constraints in the MRI magnet can render the measurements of muscle mechanical properties cumbersome when multiple parameters are to be investigated.

The supersonic shear imaging technique presents a reliable alternative because it measures all these parameters with a freehand and portable system. The main advantages of this approach rely on the fact that the acquisition processing time is very short (<2 s with repeatability), it has minimal contact and space constraints with the muscle through a standard ultrasonic

probe (and, thus, is not interfering with its functioning), it generates plane shear waves which nicely decouple the anisotropic problem along preferred directions and, finally, it gives access to a large spectrum of shear frequencies (100 to 800 Hz) suitable for dispersion measurements and viscoelasticity estimation in a single acquisition. The high interest of the imaging community in the quantification of muscle properties (functional through EMG, or acceleromyography, morphologic through MRI or ultrasonography or mechanical through quantitative elastography techniques) lies in the hope for helping diagnosis or monitoring of the muscle state. Neuromuscular diseases, which are genetic diseases affecting the muscular or nerve function, encompass many different and sometimes rare disorders. Most of them are incurable and can lead to life expectancy less than 25 years. Since a definitive diagnosis is mostly done by a muscle biopsy and protein identification, the pathology identification requires to have a rough idea of what to look for and any kind of information that could help to refine the screening process would greatly help physicians (usually clinical observations, blood testing and electromyography are the main tools). Quantitative elastography might help by providing a parameter that could influence the diagnosis but it could also provide a way to monitor the effectiveness of a treatment by quantifying the changes of the muscle mechanical state. Neuromuscular diseases directly affect proteins, some of them may greatly change the mechanical properties of muscle tissue as is sometimes described by clinicians (Paris and Paris 2001).

Providing a reliable and quantitative tool to estimate muscle mechanical properties could also be useful for rehabilitation and performance training. Whether all these clinical applications could benefit from these measurements is still subject to debate and would need a large amount of clinical trials to be established. We hope that the work undertaken here might pave the way toward such investigations. In this article, we try to present a wide description of the muscle's *in vivo* mechanical properties by using an ultrasound-based quantitative elastography technique known as supersonic shear imaging. We use *in vivo* shear modulus imaging and viscosity estimation to assess and quantify the muscle's mechanical complexity. Moreover, a complete *in vivo* characterization of the biomechanical properties of the biceps brachii (in terms of contraction, extension, anisotropy, elasticity and viscosity) is provided. Shear wave dispersion over a large bandwidth (100–800 Hz) providing quantitative information on shear modulus and shear viscosity are assessed as a function of the muscle contraction level (or developed force), anisotropy (direction of observation) and passive muscle extension (through the elbow's rotation) on five healthy volunteers.

MATERIALS AND METHODS

Five healthy subjects were volunteered for this study. All subjects were informed of the nature of this study and signed an informed consent form submitted to the INSERM ethic committee CQI (Institut National de la Santé et de la Recherche Médicale, Comité de Qualification Institutionnel).

The muscle studied in this study was the *brachialis*. It presents a spatially random distribution of fibers running parallel to one another. This entails the existence of a symmetry axis along the fibers. In the viscoelasticity theory, it has been shown that this kind of symmetry corresponds to a hexagonal system (transverse isotropy) (Zimmer and Cost 1970) and two main axes can thus be defined parallel and perpendicularly to the fibers. Therefore, an experimental homemade set-up was built to characterize muscle elasticity for each main axis. The volunteer upper-arm was then placed in a 90° flexion position as presented in Figure 1. The upper-arm rested on a fixed support. The palm of the subject faced the table and did not move during acquisitions. The angle between the upper-arm and the forearm was set to $\varphi = 90^\circ$. A strap attached the forearm to the dynamometer at wrist level was placed in prone position. The rotation axis of the elbow joint was visually aligned with the perpendicular axis of the dynamometer. Such set-up allows to contract the muscle in an isometric position. The ultrasonic probe was placed at the surface of the biceps brachii and fixed to a rotation axis (θ angle from 0° to 90° with 10° step) to map elasticity with different angle of insonification compared with the muscle fibers main axis. The 0° reference is taken when the probe is parallel to the distal-proximal axis of the arm. It is adjusted on each subject using the real-time ultrasound image. This 0° reference is chosen when the length of hyperechogenic lines is maximal in the B-mode image corresponding to the best alignment of fibers the imaging plane. Before the elasticity mapping, the volunteer was asked to stay at the load instruction ($T \rightarrow$ loading from 0 kg to 5 kg with 1 kg step) for 2 s. A 1-min rest interval was provided between each measurement. Moreover at rest (0 kg loading), the set-up allows the volunteer to extend the arm to characterize the muscle elasticity with the opening angle of the elbow (φ angle from 90° to 165° with 25° step).

Local elasticity measurements were obtained *in vivo* on the *brachialis* muscle using the supersonic shear imaging (SSI) technique (Bercoff *et al.* 2004) with a conventional ultrasonic probe (L7-4, ATL, Seattle, WA, USA) made of 128 elements at 5 MHz central frequency with a 0.3 mm pitch. The probe was driven by an ultrasound research system (V1; Supersonic Imagine, Aix-en-provence, France) made of 128 programmable channels (70 peak-to-peak transmit voltage, 25 kHz

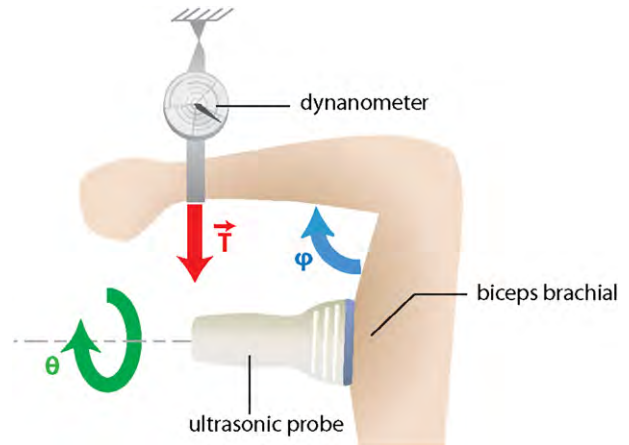


Fig. 1. Top view of the experimental set-up. The volunteer's upper-arm was placed in a 90° flexion position with the palm faced to the table. The angle between the upper-arm and the forearm was set to 90° in a parasagittal plane. A strap attached the forearm to the dynamometer lever arm at the level of the wrist that was placed in a prone position. The rotation axis of the elbow joint was visually aligned with the rotation axis of the dynamometer. Following an isometric contraction of the muscle consisting of increasing the load on the dynamometer ($T \rightarrow$ loading), maps of the biceps brachii and brachialis muscles are then acquired. Then measurements are also achieved with different angles of the elbow (φ angle) without contraction and different position of the probe (θ angle) compared to the main muscle fibers axis.

maximal pulse repetition frequency) and 64 multiplexed received channels (10 bits dynamics, 100 dB time gain amplification).

The *in vivo* SSI mode was described in details in (Tanter *et al.* 2008). It consists of a transient and remote palpation generated by the radiation force induced by a focused ultrasonic beam, the so called “pushing beam”. Each “pushing beam” generates a remote vibration that results in the propagation of a transient shear wave. After generation of this shear wave, an ultra-fast echographic imaging sequence is performed to acquire successive raw radio-frequencies (RF) data at a very high frame rate (up to 20 000 frames/s). Contrary to conventional ultrasonography where an image is achieved using line by line transmit focused beams (typically leading to 50 frames per s), ultra-fast echographic images are achieved by transmitting a single quasi-plane ultrasonic wave in tissues and achieving the beamforming process only in the receive mode. The quasi-plane terminology stands for the fact that the transmitted ultrasonic wavefront is planar in the 2-D imaging plane and slightly diffracting along the probe elevation direction beyond the elevation focal distance. Thus, for ultra-fast imaging, the frame rate is only limited by the time of flight of ultrasonic waves. In this article, the frame rate was set between 2000 and 6000 frames/s depending on the experiment.

Before entering into the SSI mode, the device is functioning as a conventional echographic device (transmit/receive beamforming at 50 frames per s) to accurately place the ultrasonic probe. The operator first asked the volunteer to reach the required load for the experiment and the elastographic sequence was then launched. Then five pushing beams were performed at different locations to explore the whole imaging area with shear waves as previously described in Tanter et al. 2008. For practical clinical configurations, this ultra-short acquisition time prevents the influence of any motion artifacts or natural motions artifacts such as arterial pulse. In this article, two kinds of sequences were used:

- (1) The supersonic shear imaging to generate a full image of the local shear wave velocity (Tanter et al. 2008); and
- (2) The shear wave spectroscopy (SWS) to probe the rheologic properties of the medium by estimating the shear wave dispersion (Defieux et al. 2009)

Supersonic shear imaging sequence

The supersonic shear imaging sequence was slightly adapted from Tanter et al. 2008 with five successive

pushing lines at transducers number 32, 48, 64, 80 and 96 (which correspond to 9.6 mm, 14.4 mm, 19.2 mm, 24 mm and 28.8 mm from the side of the array). Each pushing line consisted of four successive pushing beams at 10, 15 and 20 mm deep of duration 200 μ s. After each one of these five pushing lines, 40 images were acquired in ultra-fast mode at a framerate of 5000 images per s. A low pass filter at 800 Hz was used on the resulting velocity field to improve the signal to noise ratio and limit the effect of the wave dispersion on the measured group velocity. Thanks to a time of flight algorithm, a map of the local shear group velocity was estimated for each of the five pushing lines. The time of flight algorithm is based on cross-correlation between the time profiles of shear displacements at two points located axially at the same depth and laterally distant from four lateral beam widths. No spatial averaging or spatial kernel was introduced for the characterization. Only a 3×3 pixels median filter was done at the end of the signal processing to slightly smooth the final image, which corresponds to a 0.9 mm^2 pixel on the final image. The spatial extent of the shear wave estimate is one ultrasonic wavelength in depth (along the axial direction) and four times the array pitch in the lateral direction. There is no overlap in the axial

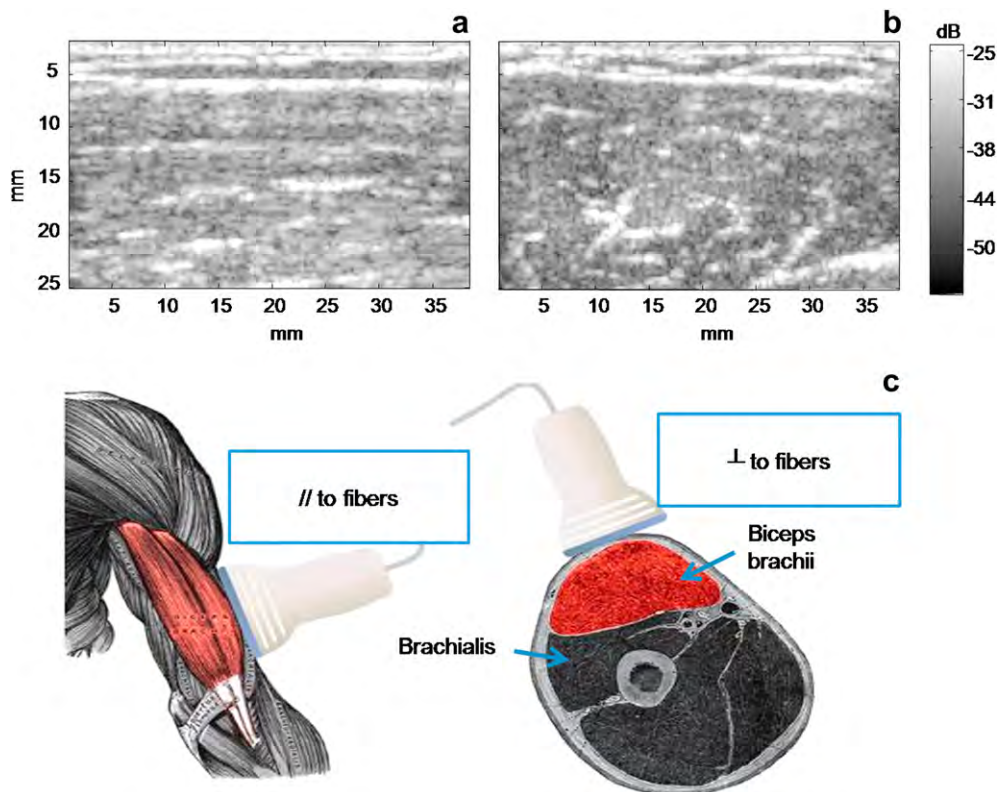


Fig. 2. B-mode image of the upper arm muscles along the fibers (a) and perpendicularly to the fibers (cross section) (b). (c) Anatomical representation the upper arm and of a transverse cross section of the upper arm. Two muscles can be seen, the biceps brachii on top and the brachialis at the bottom.

direction and a three lateral pitches overlap in order to reach the same discretization in the elasticity and ultrasonic image. The five resulting maps corresponding to the five successive excitations are concatenated using a quality factor taking into account several metrics such as ultrasonic correlation coefficient, shear correlation coefficient or signal to noise ratio. From this shear wave group velocity map, it is then possible to compute a shear elasticity map under the assumption of a purely elastic medium as the shear modulus μ can then be written,

$$\mu = \rho \cdot V_g^2, \quad (1)$$

where ρ is the density and V_g is the shear wave group velocity (Royer and Dieulesaint 1996).

The total acquisition for a complete mapping of the muscle elasticity lasted 40 ms (five times 40 frames acquired with a 5000 Hz framerate). So for practical clinical configurations, this ultra-short acquisition time will prevent the influence of any motion artifacts or natural motions artifacts. Considering the energy deposit, in the worst case scenario where we consider all pushing beams to be at the same location, the total pushing time was found to be 3 ms. This leads to an ISPTA (intensity spatial-peak temporal-average) of 400 mW/cm² for a one second pause after each acquisition, a value far below the 720 mW/cm² level recommended by the FDA. From each acquired map, a 10 × 10 mm² region-of-interest (ROI) was defined in the *brachialis* to extract the mean group velocity and compare it for different sets of parameters (anisotropy, level of contraction, elbow flexion). The standard deviation in this ROI was used as an estimate of the quality of the measure. The influences of

the contraction level on the shear wave group velocity were investigated on five healthy volunteers.

Shear wave spectroscopy sequence

The SWS sequence, dedicated to the measurement of the shear wave dispersion (phase velocity versus frequency), corresponds to the sequence proposed in Deffieux *et al.* 2009. This technique is based on the super-sonic shear imaging and it determines the shear wave phase velocity between 50 and 1800 Hz in the best cases. A Fourier transform is performed on the shear wave velocity movie to have access to the shear wave phases for each frequency of the bandwidth. Then phases are linearly fitted to get the shear wave velocity dispersion curve. In Deffieux *et al.* 2009, to improve the overall quality of the measurement, 10 successive acquisitions were averaged. Here, only one 200 μ s pushing beam per pushing line was used to limit the energy deposit strictly to the probed area. The ROI, a 10 mm long and 5 mm high box, was set in the *brachialis* muscle, approximately 20 mm deep below the skin. The position of the first pushing beam was automatically set from the position of this ROI. Considering the energy deposit, the total pushing time was found to be 2 ms leading to an ISPTA of 266 mW/cm² for a 1 s pause after each acquisition, again far below the FDA recommendation of 720 mW/cm². The SWS sequence was repeated 10 times to investigate the repeatability of the results with a 2 s pause between each acquisition. The Voigt's model, which has been used extensively to characterize the muscle viscoelastic properties (Fung 1981), describes the mechanic behavior of a medium as a parallel arrangement of a spring of elasticity (shear modulus) μ and a dashpot of viscosity η , thus,

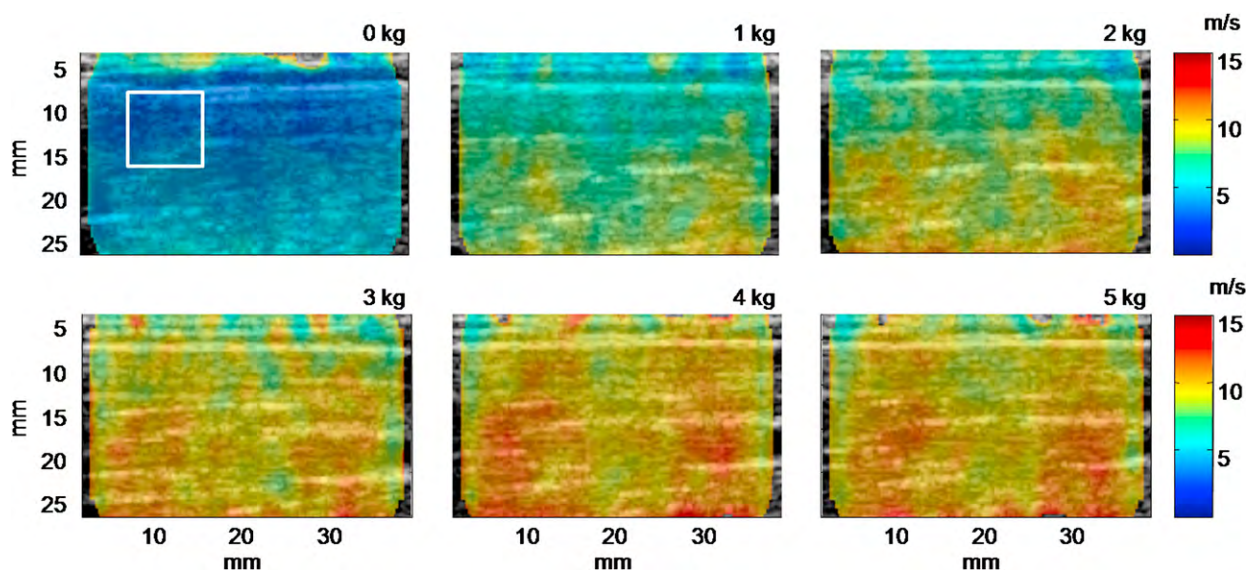


Fig. 3. Shear wave maps of the biceps brachii and brachialis muscles as a function of the load $T = 0$ to 5 kg along the fiber // (longitudinal). Volunteer no. 1 is placed in prone position with an $\varphi = 90^\circ$ angle of the elbow.

linking the applied strain σ to the resulting deformation ϵ with the well known equation:

$$\sigma = \mu\epsilon + \eta\partial\epsilon, \quad (2)$$

Under the assumption of plane shear wave propagation both perpendicular and parallel to the fibers, this governing equation leads to the derivation of two decoupled wave equations for shear waves in a transverse isotropic medium and the expression of the phase velocity for each propagation direction can be written as (Chen et al. 2004):

$$V_\phi(\omega) = \sqrt{\frac{2(\mu^2 + \omega^2\eta^2)}{\rho(\mu + \sqrt{\mu^2 + \omega^2\eta^2})}}. \quad (3)$$

The Voigt model thus allows to link the shear modulus μ and viscosity η to the dispersion law of the medium $V_\phi(\omega)$. Thanks to a non linear optimization technique, such as the classical Nelder-Mead technique (Nelder and Mead 1965), it is possible to estimate both μ and η , from the measurement of the dispersion law $V_\phi(\omega)$. Using these techniques, for each orientation of the probe compared to the main axis of the muscle fibers (in the following, along the fibers is notified by the symbol // and perpendicularly is notified by the symbol \perp) three experiments were tested: The influence of loading on the elasticity of the muscle for five different volunteers in term of global elasticity and dispersive medium; the elastic anisotropic properties of the *brachialis* muscle and the impact of the passive extension of the *brachialis* muscle on the elastic properties.

RESULTS

Typical B-mode images are presented in Figure 2 along the muscle fibers (Fig. 2a) and perpendicularly to the muscle fibers (Fig. 2b). In Figure 2c, an anatomical representation of the upper arm is presented. One can notice the presence of two main muscles, the biceps under the skin and the brachialis deep below. These two muscles are presented on the B-mode images (Fig. 2a and b). For both configurations the influence of the contraction level on the elasticity was assessed.

Mapping of shear wave group velocity during isometric contraction

The first experiment was made on volunteer no. 1 for different loads (from $T = 0$ kg to 5 kg with 1 kg step). Elasticity maps were acquired for two different axis of insonification in the muscle, along the fibers (Fig. 3) and perpendicularly to the fibers (Fig. 4). An increase of the global elasticity of both muscles is clearly visible in both configurations (from 4.0 to 36.6 kPa // and from 2.3 to 4.0 kPa \perp in shear modulus under the assumption of a purely elastic model). Moreover, the elasticity contrast between the biceps and the brachialis increases strongly with contraction when measured along the fibers (Fig. 3) but gently when measured perpendicularly to the fibers (Fig. 4). Biceps and brachialis muscles can, thus, be separated in terms of the change in elasticity with the contraction. With no contraction, the biceps brachii, softer than the brachialis when measured along the fibers, is harder than the brachialis when measured perpendicularly to the fibers.

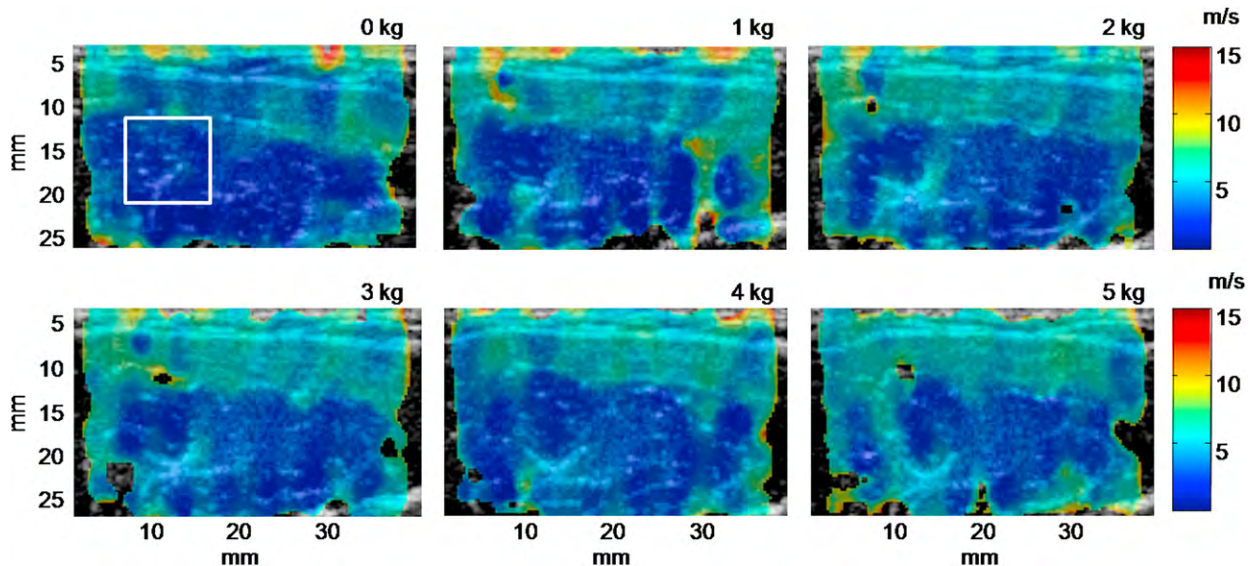


Fig. 4. Shear velocity maps of the biceps brachii and brachialis as a function of the load from $T = 0$ to 5 kg measured perpendicularly to the fibers \perp (transverse). Volunteer no. 1 is placed in prone position with a $\theta = 90^\circ$ angle of the elbow. The two muscles biceps brachii (the biceps [upper part], the brachialis [lower part]) are easily distinguishable in terms of shear wave speed.

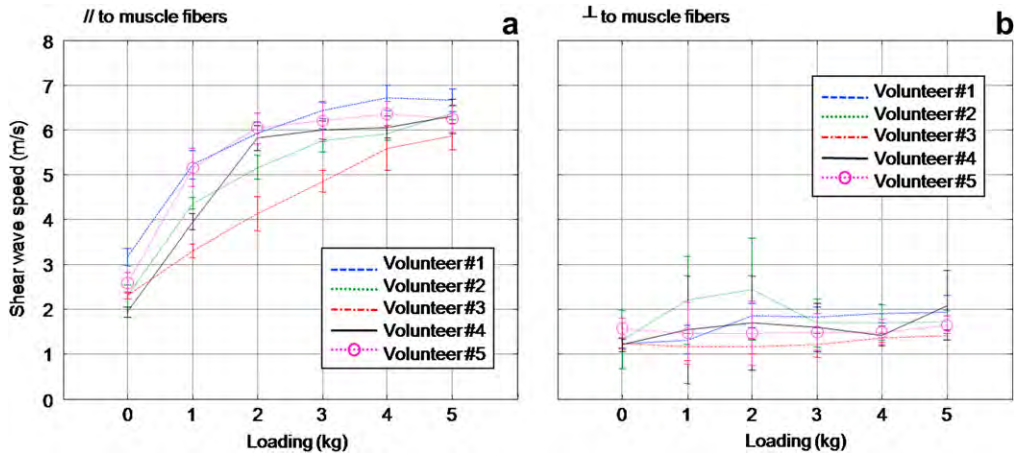


Fig. 5. Mean shear wave group velocity over the ROI brachialis along (a) and perpendicularly (b) to the muscle fibers as a function of the load from $T = 0$ to 5 kg for 5 healthy volunteers.

These contraction experiments were performed on the five healthy volunteers with the same instructions of loading from $T = 0$ kg to $T = 5$ kg for each volunteer. In Figure 5 is presented the mean shear velocity in the ROI defined in Figures 3 and 4 where error bars correspond to the standard deviation inside these ROI. Shear wave group velocity vs. load curves follow the same law for each volunteer and is presented for both positioning of the probe along (Fig. 5a) and perpendicularly (Fig. 5b) to the fibers. Along the fibers, the shear wave group velocity increases and reaches a plateau; when measured perpendicularly to the muscle fibers, the shear wave group velocity increases slowly and quasi-linearly.

Shear wave group velocity and anisotropy

Anisotropic properties measured on volunteer no. 1 are shown in Figure 6 where shear wave group velocity is plotted as a function of the angle θ between the probe and the main axis of the muscle fibers for two different loads (0 kg and 3 kg). For $\theta = 0^\circ$, corresponding to a propagation of the shear wave along the fibers, the shear wave group velocity is three times higher for a $T = 3$ kg loading than at rest. For $\theta = 90^\circ$, corresponding to a propagation of the shear wave perpendicularly to the muscle fibers, the shear wave group velocity is barely higher at rest than for a $T = 3$ kg loading. In between those two main axes ($\theta = 0^\circ$ and $\theta = 90^\circ$) the shear wave group velocity increase for both loads, result that is in good agreement with the literature (Genisson *et al.* 2003). However, one can notice that anisotropy is more visible in the contracted state that in the rest state. Each intermediate position of the probe corresponds to a mix of the elastic properties parallel and perpendicular to the fibers.

Shear wave dispersion and contraction

Shear wave phase velocity is presented in Figure 7 for different loads on volunteer no. 1 along (Fig. 7a) and perpendicularly (Fig. 7b) to the muscle fibers. Similarly to shear wave group velocity measurements, the shear wave phase velocity increases with the load for all frequencies. More precisely, the shear wave phase velocity only increases slightly with respect to frequency and for each load tested, the medium can be considered as non-dispersive when probed along the fibers. Perpendicularly to the fibers, the shear wave phase velocity increases

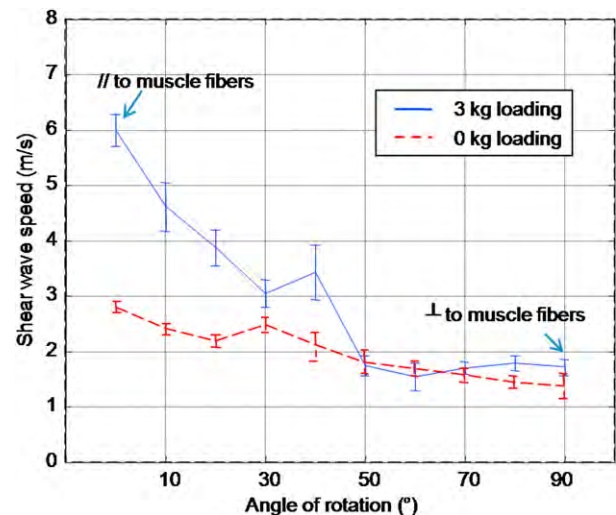


Fig. 6. Shear wave group velocity as a function of the angle of rotation θ between the ultrasonic probe and the muscle fibers. $\theta = 90^\circ$ corresponds to the probe perpendicularly to the fibers and $\theta = 0^\circ$ corresponds to the probe placed along the fibers. Two levels of contraction are presented $T = 0$ kg (blue solid curve) and $T = 3$ kg (red dashed curve). The errorbars correspond to the standard deviation over the whole elastic map for each angle of rotation.

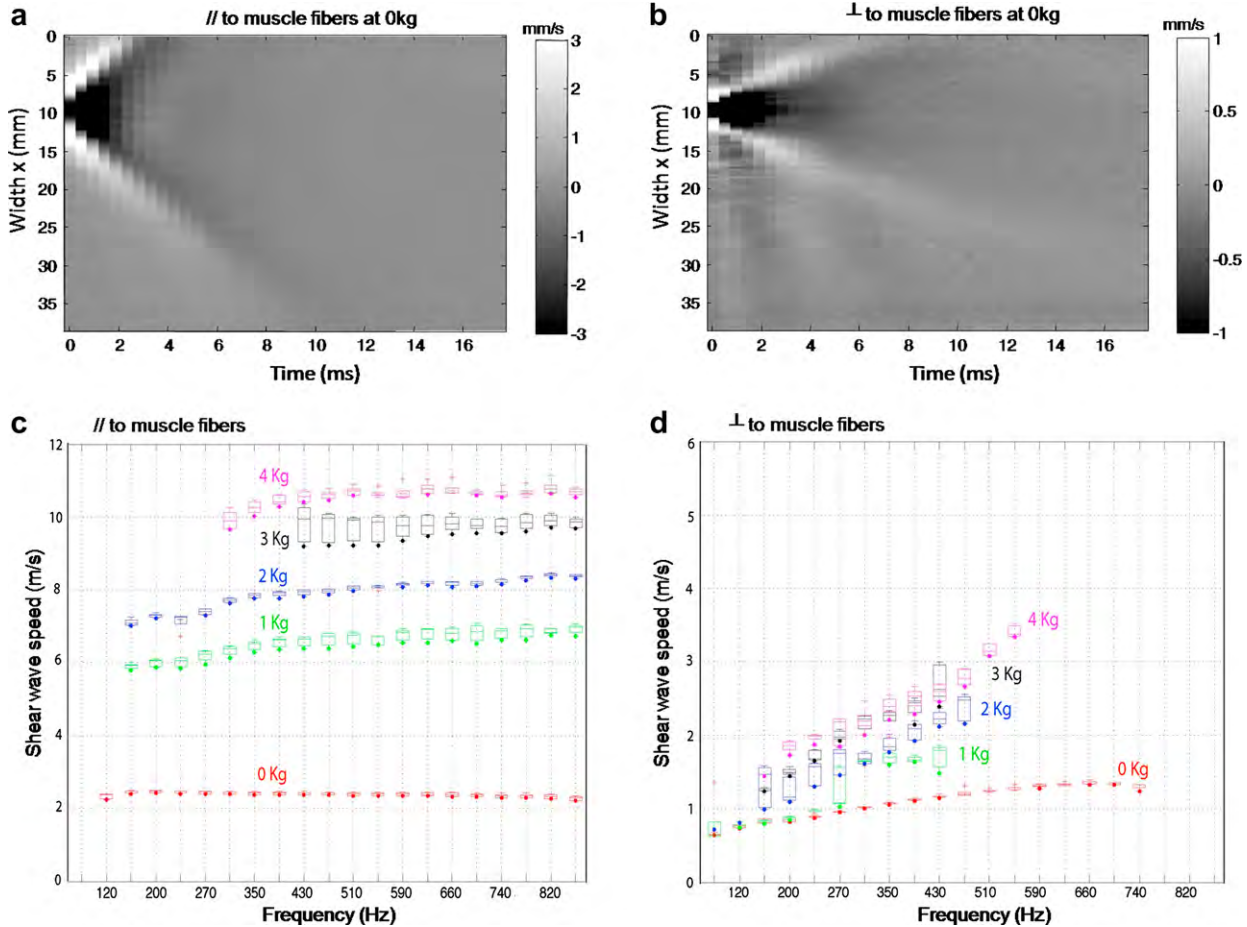


Fig. 7. Velocity field of the shear wave velocity along the fibers (a) and perpendicularly to the fibers (b) at 0 kg contraction. Shear wave phase velocity along the fibers (c) and perpendicularly to the fibers (d) for volunteer no. 1 as a function of the frequency for different loads (from 0 to 5 kg). Along the fibers the brachialis is non dispersive and *a contrario* perpendicularly the muscle is dispersive with an increasing slope from 2 to 10 mm.

strongly with respect to frequency and the slopes of the dispersion curves increase with the contraction.

Using dispersion curves and the Voigt's model, elasticity and viscosity can be deduced from eqn (3). Results are presented in Figure 8 and summarized in Table 1. Both elasticity (μ) and viscosity (η) increase with the contraction level. Nevertheless, one can notice that, for an increasing loading, elasticity grows much faster than perpendicularly to the muscle fibers. As expected, high dispersion in the shear waves velocity curves leads to higher viscosity values. Moreover, the higher the elasticity is and the larger the effect of the dispersion on the viscosity values is.

Muscle passive extension

The passive extension of the biceps was investigated in term of shear wave group velocity. Volunteer no. 1 was asked to be at rest and the elbow was passively opened from $\varphi = 90^\circ$ to 165° with 25° step. For each

positioning of the arm a shear wave group velocity map was acquired as presented in Figure 9. Along the fiber the global shear wave group velocity increases strongly (from 2.7 m/s to 5.7 m/s in the *brachialis*) and the maps remains homogeneous, whereas shear wave group velocity increases very slowly (from 1.2 to 1.8 m/s in the *brachialis*) with heterogeneous maps perpendicularly to the fibers. In fact, one can notice that the biceps and the brachialis have different shear wave group velocity when measured perpendicularly to the fibers (2.3 m/s in the biceps vs. 1.2 m/s in the brachialis for $\varphi = 90^\circ$). In this direction, the passive extension does not affect much the shear wave group velocity in both muscles (2.3 to 2.5 m/s in the biceps and 1.2 to 1.8 m/s in the brachialis).

On Table 2 and Figure 10 are presented results of the shear wave group velocity for the two ROIs defined in Figure 9 (ROI no. 1 is defined in the biceps brachii and ROI no. 2 is defined in the brachialis). Those values

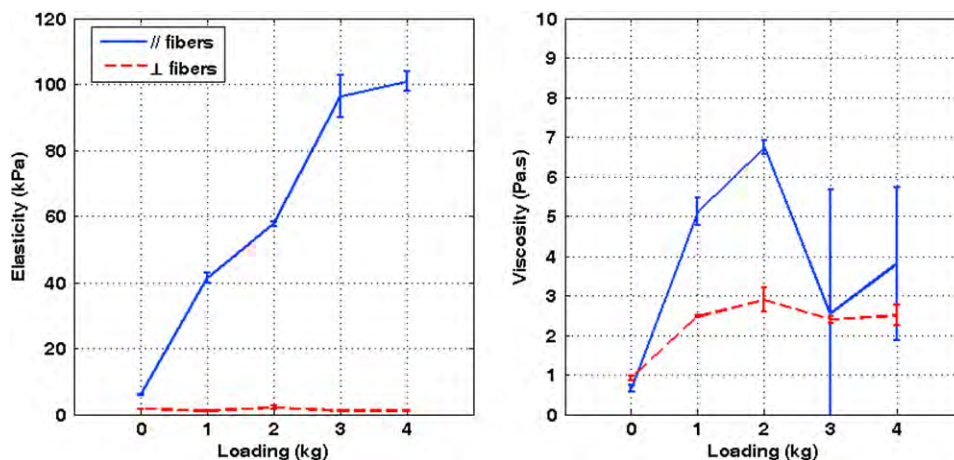


Fig. 8. Elasticity (μ) (a) and viscosity (η) (b) of the brachialis extracted from a Voigt’s model using the dispersion measurement presented in Figure 7. Values are summarized in Table 1.

correspond to the mean velocity and to the standard deviation over these 3 mm² boxes. The shear wave mean group velocities over these ROIs increase faster along the fibers than perpendicularly to the muscle fibers while extending the elbow. Regarding the two different muscles, one can notice that the stretching does not have an impact on the elasticity of the superior muscle (biceps) but significantly on the antagonist muscle (brachialis).

Figure 11 is presented the shear modulus (μ) and viscosity (η) of the brachialis as a function of the passive extension of the elbow. Values are summarized in Table 3 correspond to dispersion measurements performed only in ROI no. 2.

DISCUSSION

This study represents a complete characterization of the mechanical parameters of the brachialis muscle *in vivo*. Using two different techniques for shear wave velocity assessment, two different approaches of the mechanical properties of muscle have been evaluated. First, group velocity estimation for the mapping of the shear wave velocity. Second, phase velocity estimation for SWS measurements for elasticity and viscosity quantification using a simple viscoelastic model. The

techniques were used for different configurations: contraction, stretching and anisotropy.

One interest of the SSI approach lies in the fact that it is weakly sensitive to motion artifacts, contrary to other radiation force imaging elastography techniques. This is due to the specificity of this technology that combines ultra-fast ultrasonic imaging and radiation force. Indeed, instead of repeating experiment stroboscopically several times to get a complete movie of the shear wave propagation over a large ROI, we acquire all data in one single ultra-fast sequence. Contrary to stroboscopic approaches, this genuine ultra-fast approach does not require concatenating acquisitions acquired at different times that are sensitive to motion artifacts. Second, tissue displacements are relative and estimated from one ultrasonic image to the next one. At a 2000 Hz frame rate, typical displacements induced using the radiation force are reaching 15 μ m from one ultrasonic image to the next one. In the experimental configuration, motion artifacts can easily be kept below 5 mm/s (relative speed between the array position and muscle tissues) corresponding to a 2.5 μ m displacement from one image to the other.

Regarding the contraction, the shear wave group velocity increases more significantly for each volunteer along the fibers rather than perpendicularly to the fibers.

Table 1. Elasticity and viscosity of the whole brachialis extracted from the dispersion curves using a Voigt’s model as a function of the loading

Loading (kg)	0	1	2	3	4
Elasticity (kPa)					
//	5.86 ± 0.20	41.32 ± 1.86	57.58 ± 0.91	96.28 ± 7.13	100.80 ± 3.22
⊥	1.58 ± 0.15	1.07 ± 0.05	1.97 ± 0.52	1.12 ± 0.11	1.12 ± 0.21
Viscosity (Pa.s)					
//	0.65 ± 0.10	5.10 ± 0.38	6.72 ± 0.19	2.55 ± 3.50	3.80 ± 2.15
⊥	0.92 ± 0.06	2.47 ± 0.04	2.89 ± 0.33	2.39 ± 0.10	2.50 ± 0.29

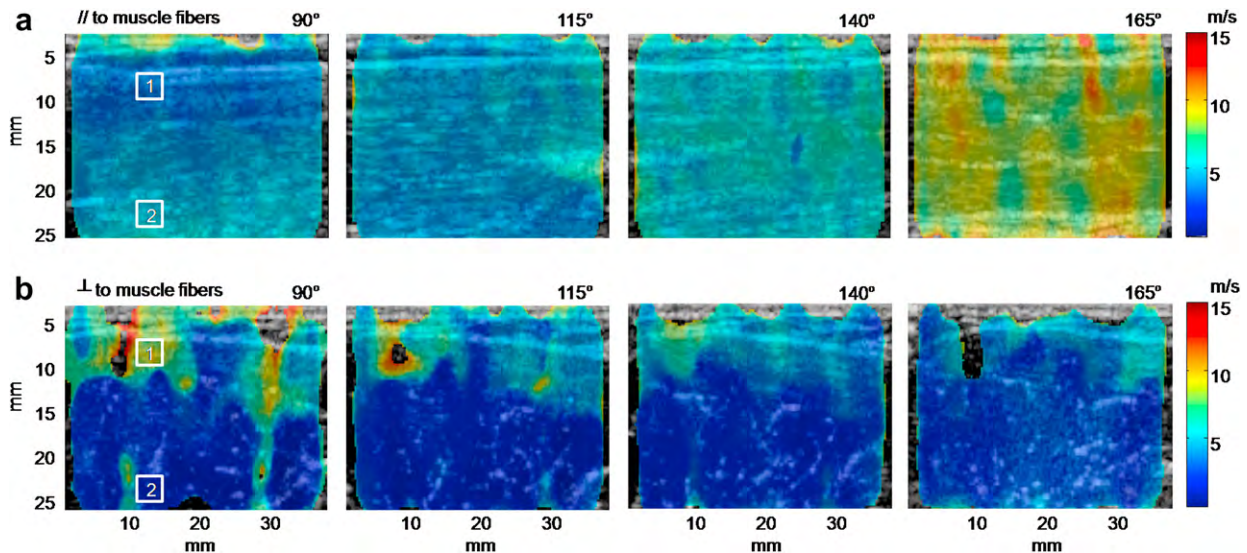


Fig. 9. Shear wave velocity maps of the biceps brachii for passive extension of the elbow with different angle (from 90° to 165° with 25° step) along the fibers (a) and perpendicularly to the fibers (b). The first ROI (3 mm^2 box) is chosen in the biceps muscle whereas the second one is in the brachialis.

In Figure 5 one can notice that the shear wave group velocity increases by about a factor 3 along the fibers and 1.5 perpendicularly to the fibers (which represents a factor of about 9 and 2.25 on shear modulus respectively). Such a difference results from the strong anisotropy of the muscle that is well known in biomechanics. Hence, the changes in transversal muscle hardness during contraction could be attributed to structural modifications. Namely, the progressive tension on myofilaments due to contractile protein longitudinal movement, leads to an increase in the transversal section and also to an increase in intra-muscular pressure as the muscle is placed in a closed volume (Fung 1981). Such a natural conception of the muscle leads to some strong anisotropic properties that are varying as a function of the contraction. In Figure 6, the shear wave group velocity in the brachialis for two different levels of loading is presented. The anisotropic ratio between rest and 3 kg loading increases strongly with the angle of propagation of shear wave with respect to the main muscular fibers axis. Compared with the acquisition performed in reference Gennisson et al. 2003, results are in the same order of magnitude.

In 2003, the acquisition was done on a slightly contracted muscle due to the experimental set-up. The position of the arm between the two experiments and the two subjects was different. In the 2003 article, the arm was vertical and the subject was contracting his muscle a little bit to facilitate the positioning of the shear elasticity probe. In this article, the arm rests horizontally without any contraction. Such set-up differences strongly affect estimates. The experimental set-up chosen in this article is much more adapted to muscle characterization as it enables to control the rest, the contraction and the positioning of the arm.

The SWS technique, which enables to measure the dispersion of shear wave *in vivo*, has been applied for diverse configurations on the same volunteer. The same behavior can be observed than for the group velocity mapping, namely the role of contraction on the shear velocity and the high anisotropy of the muscle. The SWS does not allow to produce maps but gives access in a ROI to the dispersion of the wave through the measurement of the phase velocity $v_\phi(\omega)$. The shear wave dispersion is related to the viscoelastic parameters

Table 2. Shear wave group velocity versus the elbow's angle for a passive extension, along ($//$) and perpendicularly (\perp) to the fibers in the biceps muscle and in the antagonist muscle.

Angle of the elbow φ ($^\circ$)	90°	115°	140°	165°
Shear wave group velocity ($//$) (m/s)				
ROI no. 1	2.73 ± 0.02	2.75 ± 0.03	3.93 ± 0.07	5.68 ± 0.03
ROI no. 2	3.11 ± 0.02	2.67 ± 0.02	4.09 ± 0.01	5.56 ± 0.09
Shear wave group velocity (\perp) (m/s)				
ROI no. 1	2.27 ± 0.05	2.15 ± 0.16	1.89 ± 0.05	2.48 ± 0.06
ROI no. 2	1.23 ± 0.10	1.15 ± 0.01	1.02 ± 0.02	1.78 ± 0.03

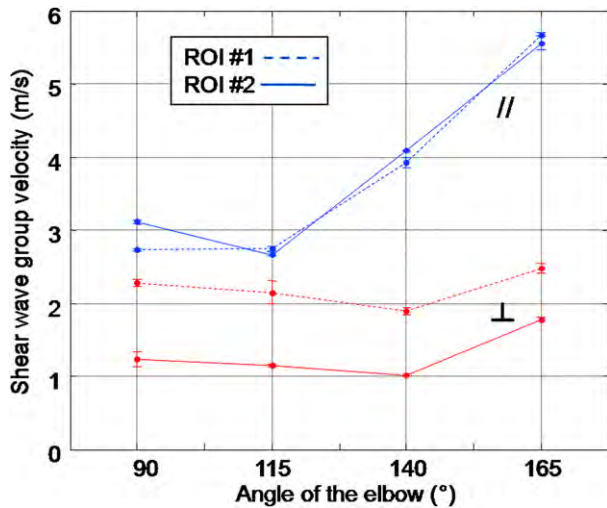


Fig. 10. Shear wave group velocity along the fibers and perpendicularly to the fibers in the two ROIs defined in Figure 11 as a function of the extension of the elbow. The two ROIs defined on the biceps brachii and on the brachialis are distinguishable only perpendicularly to the fibers.

of the medium through a rheologic model. It, thus, gives a more complete set of information on the tissue behavior than the simple mapping of the group velocity. Here, the Voigt’s model was chosen because it best describes many phantom gels and has been successfully applied to muscle tissue before (Catheline *et al.* 2004; Fung 1981). The Voigt model allows to compute both elasticity μ and viscosity η from either attenuation $\alpha(\omega)$ or phase velocity $v_\varphi(\omega)$ of a shear wave propagating in the medium. Here, the inversion of eqn (3) was done thanks to a Nelder-Mead nonlinear optimization technique that could probably be improved in future work to obtain

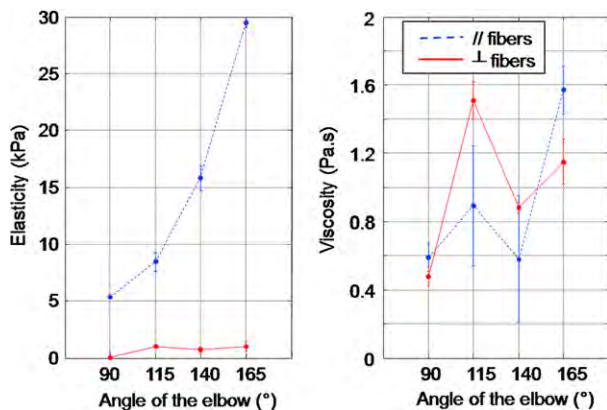


Fig. 11. Elasticity (μ) and viscosity (η) of the brachialis along (//) and perpendicularly (\perp) to the fibers as a function of the passive extension of the elbow extracted from a Voigt’s model using the dispersion measurement in ROI no. 2. For both cases, viscosity slightly increases whereas elasticity strongly increases along the fibers than perpendicularly to the fibers.

a higher stability and accuracy. As the attenuation $\alpha(\omega)$ was not measured here due to signal to noise ratio, the Voigt model was not validated on this particular dataset. It should, thus, be understood at this point as an hypothesis made on the tissue mechanical behavior. Future work would need to find a robust way to validate this model thanks to the reliable estimation of the attenuation. The analysis of the measured viscosity in terms of molecular cross bridging during the contraction process would also be of great interest.

As a function of the voluntary contraction of the muscle, both elasticity and viscosity increase along the fibers (Table 1), when perpendicularly to the fibers elasticity remains constant and viscosity increases. The elasticity increases by about a factor of 20 along the fibers and is constant perpendicularly to the fibers from 0 to 4 kg loading. Along the fibers, such elasticity increase is well known (Nordez *et al.* 2008; Genisson *et al.* 2003, 2005; Fung 1981) and the ratio of elasticity between rest and maximum contraction can be higher. In this article, the maximum contraction of each volunteer was not reached. Concerning viscosity, it increases by factor of about 10 along the fibers and 3 perpendicularly. These results are in good agreement with the literature where it is well known that viscosity increases with contraction (Desplantez *et al.* 1999; Martin *et al.* 1994). Nevertheless, the strong increase of viscosity along the fibers could also be explained by the use of Voigt’s model (Fung 1981; Kruse *et al.* 2000; Genisson *et al.* 2004), which is the simplest model usually applied for biologic tissues in which an increase of the speed of the shear wave leads to an increase of elasticity but also viscosity.

Regarding the muscle stretching without voluntary contraction, the SSI technique shows that it is able to differentiate muscles from the mapping of their elasticity changes during stretching. It clearly appears on elasticity images transversally to the fibers (Fig. 10) that brachialis and biceps are separable. Moreover, one can notice that the stretching impact principally along the fibers on elasticity (Fig. 11). Even if the slope of the viscosity with the angle of extension increases (in both cases, perpendicular and parallel to the fibers), no significant changes are noticeable. This could be explained simply by the composition of the muscle made up of hundreds of align fibers. No specific connections are present transversally between fibers (Fung 1981). Based on these results, we believe that the Supersonic Shear Imaging technique and the associated SWS technique are suitable to characterize the complexity of muscle tissue *in vivo* with little to no hassle. They might pave the way for lightweight clinical assessment of the viscoelastic parameters of muscle tissue.

The interest of assessing fully and quantitatively muscle tissue viscoelasticity lies mainly in monitoring

Table 3. Elasticity and viscosity in the brachialis as a function of the angle φ of the elbow for a passive extension along ($//$) and perpendicularly (\perp) to the fibers

Angle of the elbow φ ($^{\circ}$)	90 $^{\circ}$	115 $^{\circ}$	140 $^{\circ}$	165 $^{\circ}$
Elasticity (kPa)				
$//$	5.40 \pm 0.25	8.46 \pm 0.79	15.80 \pm 1.07	29.52 \pm 0.42
\perp	0.05 \pm 0.43	1.03 \pm 0.11	0.73 \pm 0.21	1.01 \pm 0.41
Viscosity (Pa.s)				
$//$	0.59 \pm 0.08	0.89 \pm 0.35	0.58 \pm 0.37	1.57 \pm 0.14
\perp	0.48 \pm 0.06	1.51 \pm 0.11	0.88 \pm 0.03	1.15 \pm 0.13

Values estimated using the Voigt's model.

neuromuscular diseases such as myopathies (as stated in the introduction, clinicians report a qualitative increase in hardness of muscles of myopathic people) and monitoring recovery after injury. Whereas a correlation between viscoelastic parameters can effectively be clinically proven remains an open question. We hope that this work can help set up a protocol and future clinical trials to help answer this question. It also emphasizes the need to control all parameters when measuring muscle mechanical properties and when developing muscle models. Hopefully, a better understanding of a simple skeletal muscle such as the biceps brachialis might give some insight for the most complex muscles such as the cardiac muscle where anisotropy, viscosity and passive stretching might also play an essential role but are far more difficult to assess *in vivo* independently.

CONCLUSION

A quantitative way to measure the complex viscoelastic parameters was investigated *in vivo* in healthy volunteers. It provides a first set of quantitative values for biomechanical properties of muscle perpendicularly and along the fibers. The estimation of shear modulus, shear viscosity and shear anisotropy and their respective changes during isometric contraction or passive extension was performed *in vivo* and provides a complete set of quantitative data. These data could benefit in a better understanding of muscle mechanics, provide quantitative values for biomechanical models and simulations, and finally describe quantitatively the normal characteristics of muscle in healthy volunteers for further comparisons with pathological states. Clinical validation of elastography techniques for diagnosis and monitoring of neuromuscular diseases or recovery will need to inspect the full scope of these parameters in order to produce reliable and precise results. Finally, one can hope that this stunning complexity of the muscle tissue will not simply be a drawback for elastography techniques but can also turn into a more powerful way to reveal the muscle state and a powerful screening tool.

Acknowledgements—The authors would like to thank Benoit Larrat and Gianmarco Pinton for their assistance.

REFERENCES

- Aminoff MJ. Electromyography in clinical practice. 3rd ed. New-York: Churchill Livingstone; 1987.
- Bercoff J, Tanter M, Fink M. Supersonic shear imaging: A new technique for soft tissues elasticity mapping. *IEEE Trans Ultrason Ferroelectr Freq Control* 2004;51:396–409.
- Catheline S, Gennisson JL, Delon G, Sinkus R, Fink M, Abouelkaram S, Culioli J. Measurement of viscoelastic properties of homogeneous soft solid using transient elastography: An inverse problem approach. *J Acoust Soc Am* 2004;116:3734–3741.
- Chen S, Fatemi M, Greenleaf JF. Quantifying elasticity and viscosity from measurement of shear wave speed dispersion. *J Acoust Soc Am* 2004;115:2781–2785.
- Deffieux T, Gennisson JL, Tanter M, Fink M. Assessment of the mechanical properties of musculoskeletal system using 2D and 3D very high frame rate ultrasound. *IEEE Trans Ultrason Ferroelectr Freq Control* 2008;55:2177–2190.
- Deffieux T, Montaldo G, Tanter M, Fink M. Shear wave spectroscopy for *in vivo* quantification of human soft tissues viscoelasticity. *IEEE Trans Med Imaging* 2009;28:313–322.
- Desplantez A, Cornu A, Goubel F. Viscous properties of human muscle during contraction. *J Biol* 1999;32:555–562.
- Dresner MA, Rose GH, Rossman PJ, Muthupillai R, Manduca A, Ehman RL. Magnetic resonance elastography of skeletal muscle. *J Magn Reson Imaging* 2001;13:269–276.
- Fung YC. Biomechanics: Mechanical properties of living tissues. 2nd edition. New York: Springer; 1981.
- Gennisson JL, Catheline S, Chaffai S, Fink M. Transient elastography in anisotropic medium: Application to the measurement of slow and fast shear waves velocities in muscles. *J Acoust Soc Am* 2003;114:536–541.
- Gennisson JL, Cornu C, Catheline S, Fink M, Portero P. Human muscle hardness assessment during incremental isometric contraction using transient elastography. *J Biol* 2005;38:1543–1550.
- Kruse S, Smith J, Lawrence A, Dresner M, Manduca A, Greenleaf J, Ehman R. Tissue characterization using magnetic resonance elastography: Preliminary result. *Phys Med Biol* 2000;45:1579–1590.
- Martin A, Martin L, Morlon B. Theoretical and experimental behavior of the muscle viscosity coefficient during maximal concentric actions. *Eur J Appl Physiol* 1994;69:539–544.
- Nelder J, Mead R. A simplex method for function minimization. *Computer Journal* 1965;7:308–313.
- Nordez A, Gennisson JL, Casari P, Catheline S, Cornu C. Characterization of muscle belly elastic properties during passive stretching using transient elastography. *J Biomech* 2008;41:2305–2311.
- Orizio C. Muscle sound: Bases for the introduction of a mechanomyographic signal in muscle studies. *Crit Rev Biol Eng* 1993;21:201–243.
- Papazoglou S, Braun J, Hamhaber U, Sack I. Two-dimensional wave-form analysis in MR elastography of skeletal muscles. *Phys Med Biol* 2005;50:1313–1325.

- Paris D, Paris F. Passive stiffness is increased in soleus muscle of desmin knockout mouse. *Muscle Nerve* 2001;24:1090–1092.
- Ringleb SI, Bensamoun SF, Chen Q, Manduca A, An KN, Ehman RL. Applications of magnetic resonance elastography to healthy and pathologic skeletal muscle. *J Magn Reson Imaging* 2007;25:301–309.
- Royer D, Dieulesaint E. *Elastic waves in solid*. Vol. 1. Berlin: Springer Verlag; 1996.
- Tanter M, Bercoff J, Athanasiou A, Deffieux T, Gennisson JL, Montaldo G, Tardivon A, Fink M. Quantitative assessment of breast lesions viscoelasticity using supersonic shear imaging technique: Initial clinical investigation. *Ultrasound Med Biol* 2008;34:1373–1386.
- Viby-Mogensen J, Jensen E, Werner M, Kirkegaard H. Measurement of acceleration: A new method of monitoring neuromuscular function. *J Clin Anaesth* 2003;15:145–148.
- Zimmer JE, Cost JR. Determination of the elastic constants of an unidirectional fiber composite using ultrasonic velocity measurements. *J Acoust Soc Am* 1970;47:795–803.



ELSEVIER

doi:10.1016/j.ultrasmedbio.2012.04.013

● *Original Contribution*

**SUPERSONIC SHEAR WAVE ELASTOGRAPHY OF *IN VIVO* PIG KIDNEY:
 INFLUENCE OF BLOOD PRESSURE, URINARY PRESSURE AND TISSUE
 ANISOTROPY**

JEAN-LUC GENNISSON,* NICOLAS GRENIER,†‡ CHRISTIAN COMBE,†§ and MICKAËL TANTER*

*Institut Langevin–Ondes et Images, ESPCI ParisTech, CNRS UMR7587, INSERM U979, Paris France; †Service d'Imagerie Diagnostique et Interventionnelle de l'Adulte, Groupe Hospitalier Pellegrin, Centre Hospitalier Universitaire de Bordeaux, Bordeaux, France; ‡Bioingénierie tissulaire, U1026, INSERM, Université Bordeaux Segalen, Bordeaux, France; and §Service de Néphrologie, Centre Hospitalier Universitaire de Bordeaux, F-Bordeaux, France

(Received 11 January 2012; revised 16 April 2012; in final form 18 April 2012)

Abstract—The *in vivo* influence of renal anisotropy and of urinary and vascular pressure on elasticity values using ultrasonic supersonic shear wave elastography was studied in pigs. Experiments were conducted in agreement with the European Commission guidelines and directives of the French Research Ministry. Six kidneys in three pigs were studied *in vivo*. Elasticity of renal cortex and medulla was quantified through the shear modulus (μ) by using the supersonic shear imaging technique with an 8 MHz linear ultrasound probe. All measurements were done per-operatively both in the axis and perpendicular to the main axis of pyramids, in normal condition, after progressive increase of urinary pressure, and after renal artery and renal vein ligation. In normal conditions, cortical (C) and medullary (M) elasticity values were always higher when acquisitions were realized with the ultrasound main axis perpendicular to main pyramid axis ($C_{//}$: 7.7 ± 2.3 kPa; $M_{//}$: 8.7 ± 2.5 kPa) than parallel (C_{\perp} : 6.9 ± 1.4 kPa; M_{\perp} : 6.6 ± 2.3 kPa), demonstrating an effect of renal anisotropy. In renal cortex, two bands were separated, inner cortex showing higher elasticity values (IC_{\perp} : 8.1 ± 1.9 kPa) than outer cortex (OC_{\perp} : 6.9 ± 1.4 kPa). Renal artery and renal vein ligation induced a decrease and an increase of elasticity respectively. Parenchymal elasticity increased linearly with elevation of urinary pressure. Intrarenal elasticity values vary with tissue anisotropy and, with vascular and urinary pressure levels. These parameters have to be taken into account for interpretation of tissue changes. Separation of outer and inner cortex could be attributable to perfusion differences. (E-mail: jl.gennisson@espci.fr) © 2012 World Federation for Ultrasound in Medicine & Biology.

Key Words: Renal elasticity, Intrarenal pressure, Supersonic shear wave imaging, Elastography, Anisotropy.

INTRODUCTION

Chronic kidney disease (CKD) is an increasing source of morbidity and mortality in developed countries (El Nahas 2005). The progression of CKD is linked to intrarenal fibrosis, which results in impaired kidney functions, including decreased glomerular filtration rate. Sequential measurement of renal elasticity could help in following the progression of intrarenal fibrosis. Ultrasound elastography is an attractive method for assessing elastic tissues properties. To our knowledge, very few studies have been performed on ultrasound renal elasticity assessment using

either static elastography (strain imaging) or quantitative elastography (shear modulus imaging). Using strain imaging, relative elasticity images could be obtained in fresh *ex vivo* canine kidneys embedded in gelatin phantoms showing differences between renal parenchyma and the urine collecting system (Emelianov et al. 2000). Quantitative ultrasound elastography techniques based on the measurement of the velocity of propagating shear wave, such as the Fibroscan® (Echosens, Paris, France) (Arndt et al. 2010), the acoustic radiation force impulse (ARFI) system (Siemens, Erlangen, Germany) (Seeversveen et al. 2010) and the supersonic shear wave imaging (SSI) technique (Derieppe et al. 2012), were more recently applied within kidney and showed parenchymal and cortical elasticity changes during renal dysfunction of different mechanisms. However, the relationships between these changes and the degree of fibrotic processes shown on pathology were quite controversial;

Disclosure: MT is co-founder of the company Supersonic Imagine.

Address correspondence to: Jean-Luc Gennisson, Institut Langevin–Ondes et Images, CNRS UMR7587, INSERM U979, ESPCI, ESPCI ParisTech, 10 rue Vauquelin, 75005 Paris, France. E-mail: jl.gennisson@espci.fr

some with significant correlation between renal elasticity and renal fibrosis (Arndt et al. 2010) and some without (Seeversveen et al. 2010; Derieppe et al. 2012). Magnetic resonance (MR) elastography is another way to evaluate tissue elasticity but little has been done to now on the kidney (Shah et al. 2004; Warner et al. 2011).

Whereas the kidney is a complex, highly compartmentalized and anisotropic organ, with a very high level of perfusion, no attention has been paid up till now on effects of its tissue architecture and of variations of internal pressure over tissue elasticity. Quantitative methods based on shear wave propagation are sensitive to tissue anisotropy: the shear wave velocity is higher when propagating along spatially oriented structures than perpendicular to these, responsible for an apparent higher elasticity as an example, in muscles (Gennisson et al. 2003, 2010), myocardium (Fahey et al. 2005; Lee et al. 2012) or brain (Mace et al. 2011). Anisotropy is high within the medulla, due to the predominant orientation of the tubules perpendicular to the capsule. Conversely, renal cortex anatomy is not organized in linear structures, since glomeruli are spherical and proximal and distal tubules have convoluted shape (Madsen et al. 2008). Diffusion-weighted MR imaging has shown that the fractional anisotropy was around 22% in renal cortex and around 40% in renal medulla (Ries et al. 2001). With regard to intrarenal pressure, it is well known that increases of tissue elasticity in soft tissues can also be because of external pressure (quasi-incompressible organs) (Gennisson et al. 2007). Renal diseases, such as renal graft dysfunction, can be associated with concomitant changes in blood perfusion and urinary pressure within pyelocaliceal system. Therefore, it seems essential to better understand and to be able to take into account, the effect of all these parameters on shear wave velocity for an adequate interpretation.

The purpose of this study was to evaluate *in vivo* how renal anisotropy, perfusion and urinary pressure changes could have an impact on measured elasticity values in each renal compartment. The quantitative estimation of elasticity was performed using the SSI technique.

MATERIALS AND METHODS

Animal protocol

This study involved three adult female pigs (CIR-HYO origin) with a mean body weight of 65.3 ± 7.5 kg at the time of experiments. These were conducted in agreement with the European Commission guidelines and directives of the French Research Ministry (Agreement no. 75-14-01 given to the Institut Mutualiste Montsouris Recherche, Paris, France).

The pigs were anaesthetized under isoflurane (pre-medicated with ketamine+stresnil+atropine; inducted

with pentothal; IMM Recherche, Paris, France) and intubated. Blood pressure oxymetry were monitored continuously. A bladder catheter was introduced for urinary drainage. After laparotomy, each kidney with its renal pedicle was exposed. Renal artery, renal vein and the lumbar ureter were isolated for subsequent ligation. The ureter was cannulated for retrograde filling and for intrapelvic pressure measurement.

Elastography sequence and data processing

An ultrafast ultrasound scanner (Aixplorer; SuperSonic Imagine, Aix-en-Provence, France) was used with a 8 MHz probe. Principles of SSI have been described elsewhere (Bercoff et al. 2004). Briefly, a vibration force was generated by four successive focusing ultrasound beams at different depths spaced by 5 mm. Each focused beam, so-called pushing beam, consisted of a 150 μ s burst at 8 MHz. Propagating shear waves were imaged at a very high framerate (up to 20.000 frames/s) and raw radio-frequency data were recorded. Using speckle tracking correlation technique, movies of displacements induced in tissues by the shear wave were calculated. Then the shear wave speed (c_T) was locally deduced by using a time of flight algorithm. From the shear wave speed in locally homogeneous soft tissues, the elastic modulus, so-called the Young's modulus (E), can be deduced regarding the following equation:

$$E \approx 3\mu = 3\rho c_T^2, \quad (1)$$

where μ is the shear modulus and ρ is the density.

Results were displayed on a color scale according to elasticity expressed in kPa. All results were measured by the ultrasound device in terms of Young's modulus. As in this study the medium is considered as anisotropic, the relationship $E \approx 3\mu$ is no longer valid (Royer et al. 2011). Thus, all results are presented and analyzed in terms of shear modulus μ , parallel or perpendicular the main axis of the pyramids.

To evaluate the impact of vascular pressure, renal elasticity was measured before and after total occlusion of the renal artery, then after occlusion of the renal vein. To evaluate the impact of urinary pressure, renal elasticity was measured at baseline, then during incremental retrograde filling of the pelvis with serum at pressure levels of 5, 10, 15, 20, 25, 30 and 40 mm Hg. Because of catheter and pressure control problems, occurring on four kidneys, elasticity was only acquired with 10 mm Hg steps when the probe was parallel to the main axis of the pyramids. These experiments were obtained after those acquired when the probe was perpendicular to the main axis of the pyramids. To evaluate the impact of anisotropy, at each phase of the experiment, acquisitions were performed in a renal segment with a pyramid axis parallel to US beam, then in a renal segment with a pyramid

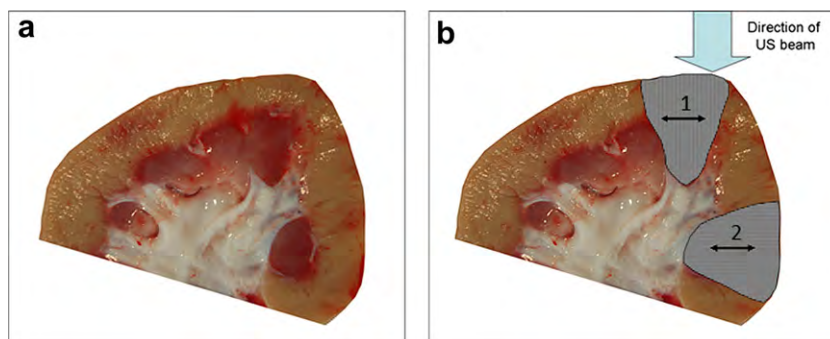


Fig. 1. Macroscopic image of a lower half of a pig kidney showing the cortico-medullary differentiation (a) and, superimposed, schematic representation of two renal segments (b): one shows a predominant vertical anisotropy in the direction of ultrasound (US) beam, the other a horizontal anisotropy perpendicular to the direction of US beam. Axis of propagation of the shear wave (black arrows) is perpendicular to the oriented renal structures in the first case and parallel in the second.

axis perpendicular to US beam (Fig. 1). In the following, the convention for qualifying measurements was based on the shear wave propagation axis. Shear waves propagate in this technique perpendicularly to the US beam. Thus, when the US beam is parallel to the main pyramid axis (axial direction), the value is referenced as perpendicular (μ_{\perp}); when the US beam is perpendicular to the main pyramid axis (transverse direction), the value is referenced as parallel (μ_{\parallel}).

For each measurement, three acquisitions were done. All acquisitions were performed by the same operator (N.G., 25 years of experience in ultrasound).

Data analysis

The color scale elasticity map had a 2 cm^2 area value and was positioned to cover an entire renal segment of interest including at least one pyramid and its surrounding cortex. Elasticity values were quantified by using two regions-of-interest (ROI) within the outer cortex and within the inner cortex and one ROI within the medulla. The resolution of the elastic map was 0.3 mm^2 . Outer and inner cortices were separated because they appeared immediately on elasticity maps and their elasticity values were always different in these compartments. The separation line between these two regions was placed in the

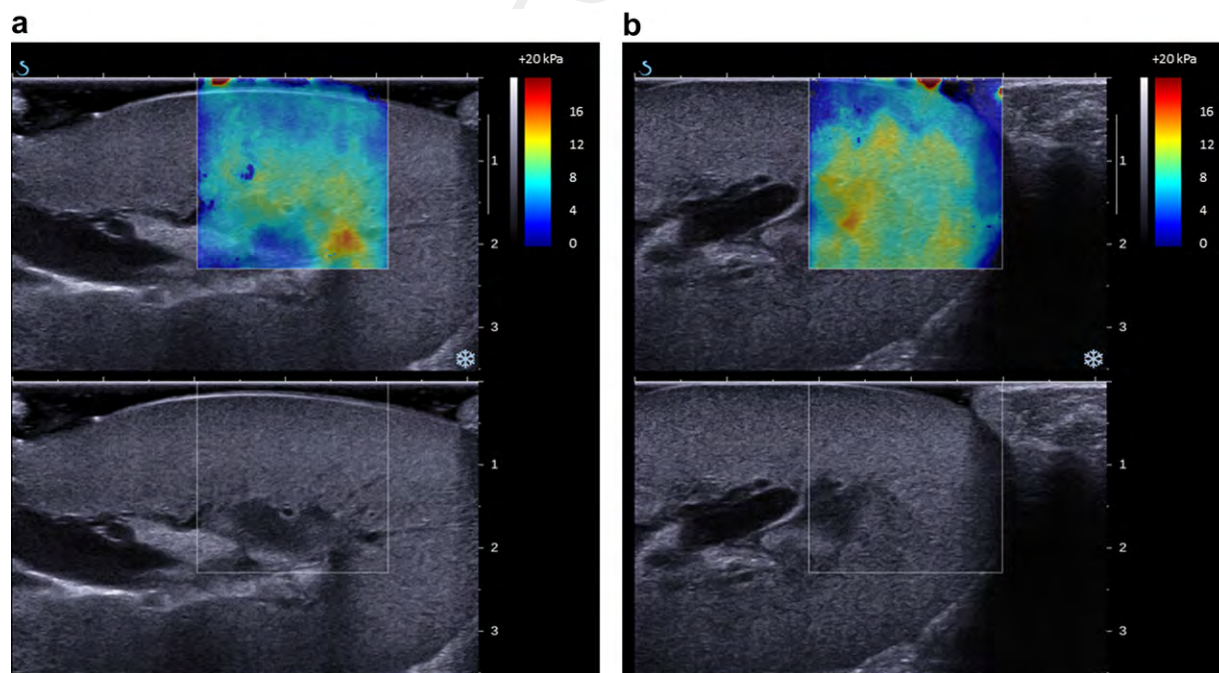


Fig. 2. Elasticity measurement of *in vivo* pig kidney (upper part shear modulus color-coded in kPa) and corresponding classical ultrasound image ($51 \times 35\text{ mm}^2$), when the US beam is placed along (μ_{\perp}) (a) or perpendicular (μ_{\parallel}) (b) to the main pyramid axis.

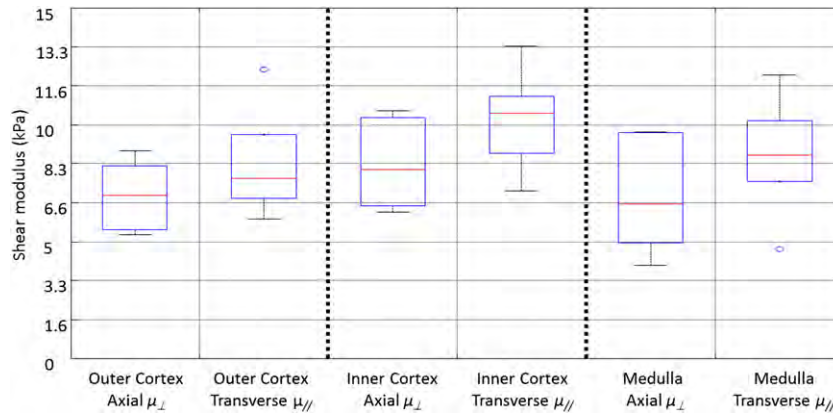


Fig. 3. Boxplot of the shear modulus assessment over the six pig kidneys in three different renal compartments: outer cortex, inner cortex and medulla. Measurements were performed with the ultrasound (US) beam along (axial, μ_{\perp}) and perpendicular (transverse, μ_{\parallel}) to the main axis of the pyramid, showing anisotropy of each compartment.

middle of the cortex (Fig. 2). Outer and inner medulla could not be separated on B-mode images or on elasticity maps. At each phase, a 5–10 mm diameter ROI was drawn, one in each of the three compartments by one of the authors (J.L.G.). At each phase, acquisition of the elasticity map and compartmental measurements were repeated three times.

Statistical analysis

Values were expressed as median \pm standard deviations. For each kidney, a median elasticity value was calculated for each compartment from the three measurements. For each compartment, elasticity values were measured parallel and perpendicular to the axis of pyramids and were compared using a paired Welch's *t*-test. A *p* value of ≤ 0.05 was considered to indicate a statistically significant difference.

RESULTS

Normal condition and effect of anisotropy

In every kidney, two layers were identified in the cortex, each around 5 mm thick, with significantly different elasticity values; the outer cortex showing lower values than the inner cortex (Fig. 2). Conversely, outer

Table 1. Median values and standard deviations of the shear modulus over all kidneys for each compartment

Axis of investigation	Outer cortex (kPa)	Inner cortex (kPa)	Medulla (kPa)
Axial (μ_{\perp})	6.9 ± 1.4	8.1 ± 1.9	6.6 ± 2.3
Transverse (μ_{\parallel})	7.7 ± 2.3	10.4 ± 2.1	8.7 ± 2.5
<i>p</i> value	6.7×10^{-4}	0.0031	0.0272

Measurements were realized with the US beam along (axial, μ_{\perp}) and perpendicular (transverse, μ_{\parallel}) to the main axis of the pyramid. A comparison paired *t*-test was performed to show the differences between axial and transverse measurements.

and inner medulla could not be separated on B-mode images or on elasticity maps. Elasticity values were lower within the medulla than within the inner cortex (Fig. 3). In normal condition, the standard deviation of variation of elasticity measurement was μ_{\parallel} : 20.5% and μ_{\perp} : 29.8% in the outer cortex, μ_{\parallel} : 23.5% and μ_{\perp} : 20.0% in the inner cortex and μ_{\parallel} : 35.8% and μ_{\perp} : 29.1% in the medulla. A paired Welch's *t*-test was used to compare perpendicular and parallel values in each compartment and showed that results were significantly different (Table 1).

Figure 4 shows the anisotropic ratio for all kidneys individually in each compartment and summarized in Table 2. This ratio was calculated by dividing the median values obtained in the considered compartment (OC, IC, M) perpendicular and parallel to the main axis of the pyramid.

Effect of perfusion

An example of the effect of perfusion on one pig kidney is presented on Figure 5. Occlusion of the renal

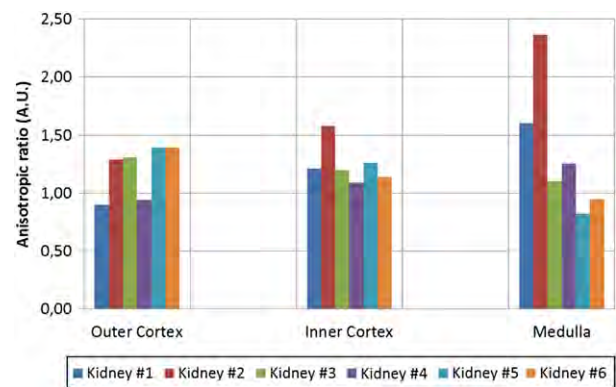


Fig. 4. Anisotropic ratio for all compartments of each kidneys individually.

Table 2. Anisotropic ratio for each kidney.

Compartment	Kidney #1	Kidney #2	Kidney #3	Kidney #4	Kidney #5	Kidney #6
Outer cortex	0.90	1.29	1.31	0.94	1.39	1.39
Inner cortex	1.21	1.58	1.20	1.09	1.26	1.14
Medulla	1.60	2.36	1.10	1.25	0.82	0.95

artery induced a significant decrease of elasticity in the three compartments (Fig. 5a). Conversely, occlusion of the vein induced a severe increase of elasticity in all compartments (Fig. 5b).

Figures 6 and 7 show boxplots of the results for all samples. Mean elasticity values for axial and transverse measurements are summarized for each compartment in Table 3. On one hand, compared with normal condition, the coefficient of variation of elasticity measurement decreased when the artery was occluded by μ_{\parallel} : 48.8% and μ_{\perp} : 44.1% in the outer cortex, μ_{\parallel} : 56.5% and μ_{\perp} : 49.0% in the inner cortex and μ_{\parallel} : 72.7% and μ_{\perp} : 64.3% in the medulla. On the other hand, compared with normal condition, the coefficient of variation of elasticity measurement increased when the vein was occluded by μ_{\parallel} : 467.9% and μ_{\perp} : 438.5% in the outer cortex, μ_{\parallel} : 540.0% and μ_{\perp} : 535.1% in the inner cortex and μ_{\parallel} : 555.0% and μ_{\perp} : 550.5% in the medulla.

Effect of urinary pressure

The effect of urinary pressure variations on elasticity could be evaluated in only five kidneys because a fornix rupture occurred in one case during the retrograde filling.

A progressive increase of renal elasticity was observed with the elevation of urinary pressure (Figs. 8 and 9 and Table 4). Compared with normal condition, percentages of increase were for outer cortex (μ_{\parallel} : 267.4% and μ_{\perp} : 423.3%), for inner cortex (μ_{\parallel} : 320.2% and μ_{\perp} : 428.3%) and for medulla (μ_{\parallel} : 445.9% and μ_{\perp} : 269.3%). Increase of elasticity is correlated to increased urinary pressure (Table 5). Effects of anisotropy were maintained during the increase of pressure principally in the cortex.

DISCUSSION

Our study shows that elasticity measurements can be influenced by the tissue architecture and intrinsic vascular and urinary pressure. A clear assessment of these factors of variation is essential to decrease the intrinsic variability of *in vivo* measurements, and to increase the reproducibility of the method, thus, avoiding false diagnosis of tissue fibrosis. The intrinsic geometry of the tissue and its degree of anisotropy, is a primary factor of variation of elasticity values. In the kidney, the intrinsic architecture of the parenchyma is highly oriented. Henle loops and vasa recta within medulla and the collecting ducts within cortex and medulla are parallel and highly oriented from the capsule to the papilla within each renal segment. Therefore, when emission of the ultrasound beam is sent parallel to these structures, the shear wave propagates perpendicular to these, creating multiple vascular and tubular interfaces, thus, decreasing its speed of propagation and resulting in lower elasticity values. Conversely, when emission of the ultrasound beam is sent perpendicular to these structures, the

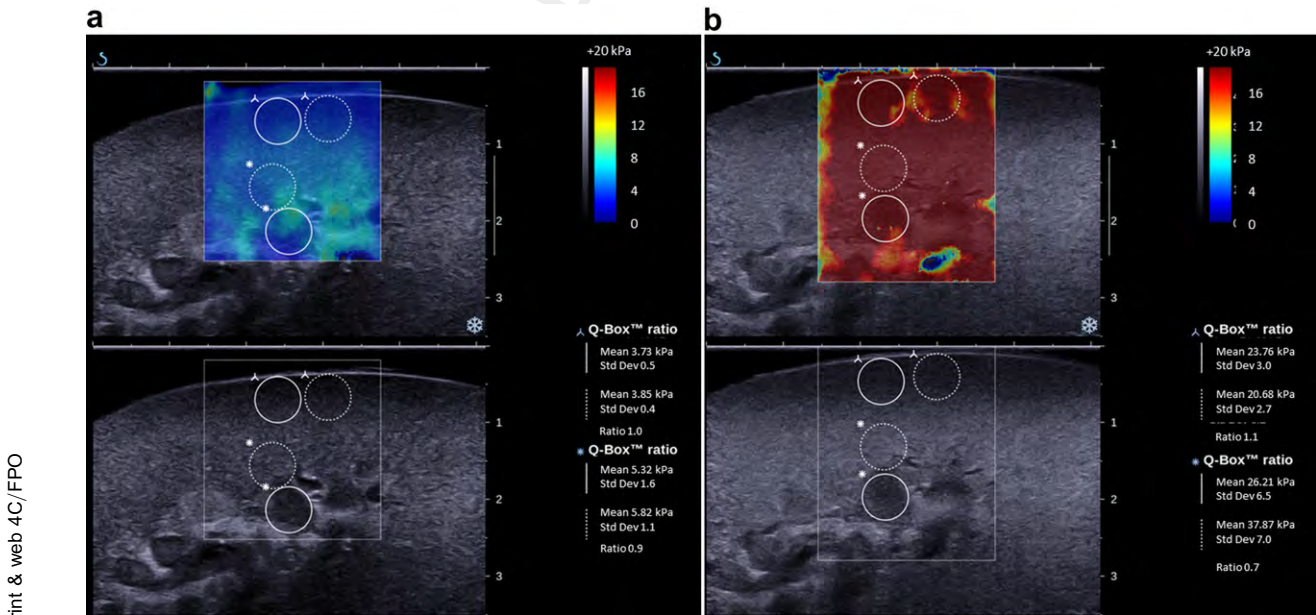


Fig. 5. Example of elasticity measurement on one pig kidney when the renal artery (a) or the renal vein is occluded (b).

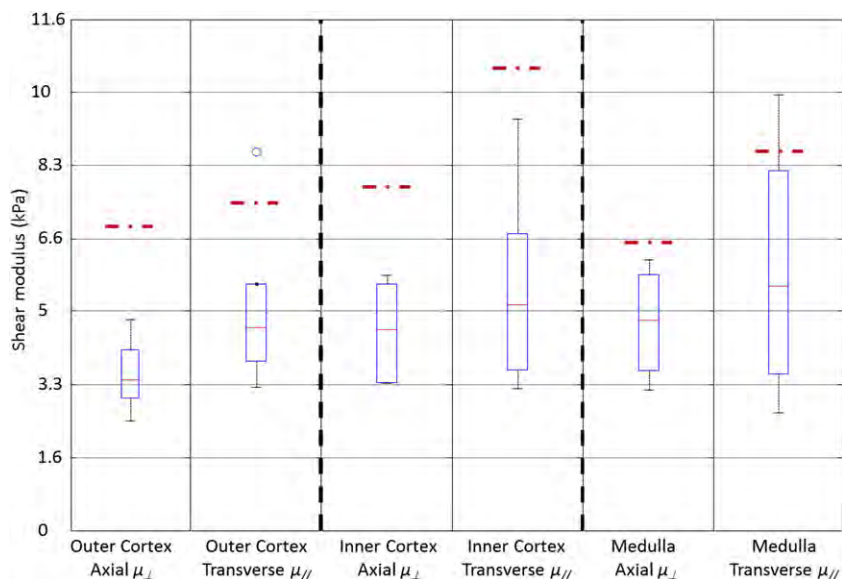


Fig. 6. Boxplots of the shear modulus during the occlusion of the renal artery for each renal compartment with the ultrasound (US) beam along (axial, μ_{\perp}) and perpendicular (transverse, μ_{\parallel}) to the main pyramid axis. Red dashed lines represent median elasticity values for each compartment in normal conditions.

shear wave propagates at a higher speed, without interfaces, resulting in higher elasticity values. The mean variation of the shear modulus due to anisotropy was 10.5% in the outer cortex, 29.7% in the inner cortex and 31.8% in the medulla in normal conditions. These results are in good accordance with those obtained with magnetic resonance imaging (MRI)-diffusion experiments (Ries et al. 2001).

When urinary pressure increased, the anisotropy increased in the cortex (for example at 20 mm Hg, OC:

61.8% and IC: 58.5% or at 40 mm Hg, OC: 57.1% and IC: 57.6%). On the contrary in the medulla, few changes were observed (at 20 mm Hg, 6.3% and at 40 mm Hg, 20.4%) and the differences between parallel and perpendicular measurements were statistically not significant. This can be explained by the fact that a median value over all the data was used to compare both measurements. Nevertheless, analyzing individually each kidney as shown in Figure 3, the anisotropic ratio had strong variations depending on the medulla observed. Moreover, the

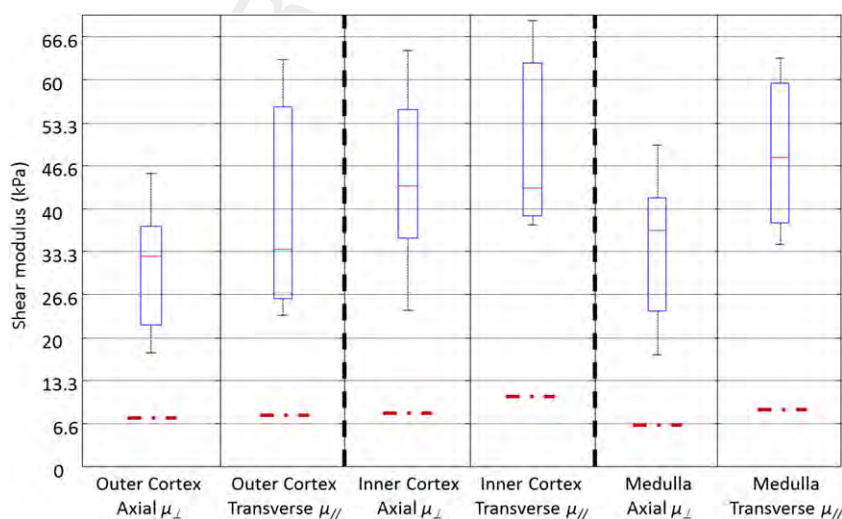


Fig. 7. Boxplots of the shear modulus during the occlusion of the renal vein for each renal compartment with the ultrasound (US) beam along (axial, μ_{\perp}) and perpendicular (transverse, μ_{\parallel}) to the main pyramid axis. Red dashed lines represent median elasticity values for each compartment in normal conditions.

Table 3. Median values and standard deviation of the shear modulus over all kidneys for each renal compartment regarding the occlusion of the renal vein or of the renal artery

Site of occlusion and axis of propagation	Outer cortex (kPa)	Inner cortex (kPa)	Medulla (kPa)
Axial vein (μ_{\perp})	32.6 ± 10.7	43.5 ± 15.1	36.6 ± 12.5
Transverse vein (μ_{\parallel})	33.7 ± 20.6	43.2 ± 16.8	47.9 ± 14.4
<i>p</i> value	0.042	0.293	0.014
Axial artery (μ_{\perp})	3.4 ± 0.8	4.6 ± 1.2	4.8 ± 1.2
Transverse artery (μ_{\parallel})	4.6 ± 2.1	5.1 ± 2.4	5.6 ± 2.9
<i>p</i> value	0.001	0.033	0.078

Measurements were acquired with the US beam along (axial, μ_{\perp}) and perpendicular (transverse, μ_{\parallel}) to the main axis of the pyramid. A comparison paired *t*-test was performed to show the differences between axial and transverse measurements.

anisotropic ratio within the cortex seemed to stay constant with the increase of pressure (Table 4).

Therefore, when performing renal ultrasound elastography, a clear identification of the renal segments will be sampled and their orientation according to the ultrasound beam and the resulting shear wave propagation is mandatory. This is of prime importance when patients are compared and for longitudinal follow-up.

On the other hand, intra-parenchymal pressure will also influence the elasticity values of a given tissue. This pressure may vary with the degree of blood perfusion, the degree of lymphatic drainage and, within the kidney, the degree of urinary drainage. This is the reason why we decided to evaluate the influence of vascular and urinary pressure changes on elasticity values, lymphatic flow changes being too difficult to induce experimentally. Our experiments showed that these values are highly influenced by the degree of urinary obstruction in a linear fashion. Consequently, urinary obstruction will have to be

ruled out beforehand to attribute an increased elasticity to tissue changes. Particular attention will have to be paid to the degree of bladder filling in kidney transplant patients. Because of the shortness of the ureter and its denervation, a filled bladder may induce a dilatation of the pyelocaliceal system (Tublin *et al.* 1995).

The degree of vascular pressure also influences elasticity values. The kidney is highly vascularized, mainly the cortex, with an eighth of the cardiac blood flow being distributed into each kidney. This is well illustrated by the huge increase of renal elasticity after ligation of the renal vein. On the contrary, we noted a significant decrease of elasticity after ligation of the renal artery; this effect predominating within the cortex. It may be postulated that central regions of the kidney are less sensitive to changes in renal perfusion pressure since blood pressure and flow are lower at baseline (Gong *et al.* 2008). Decrease of elasticity during ischemia was already observed using MR-elastography, where cortical and medulla stiffness changed by ~30% and ~20%, respectively (Warner *et al.* 2011). Conversely, an elevation of liver and spleen elasticity was demonstrated in an animal model of portal hypertension; these changes preceding the development of liver fibrosis (Nedredal *et al.* 2011). No incremental increase of portal hypertension was performed due to the model itself but positive correlations were observed between spleen and liver stiffness measurement and direct hepatic venous pressure gradient.

The statistically significant difference of elasticity between outer and inner cortex is difficult to explain. Different levels of arterial perfusion, the inner cortex of pigs being more perfused than the outer cortex, could be an explanation. However, in humans, it was shown that outer cortex was more perfused than inner cortex, inner nephrons serving as a functional reserve (Dworkin *et al.*

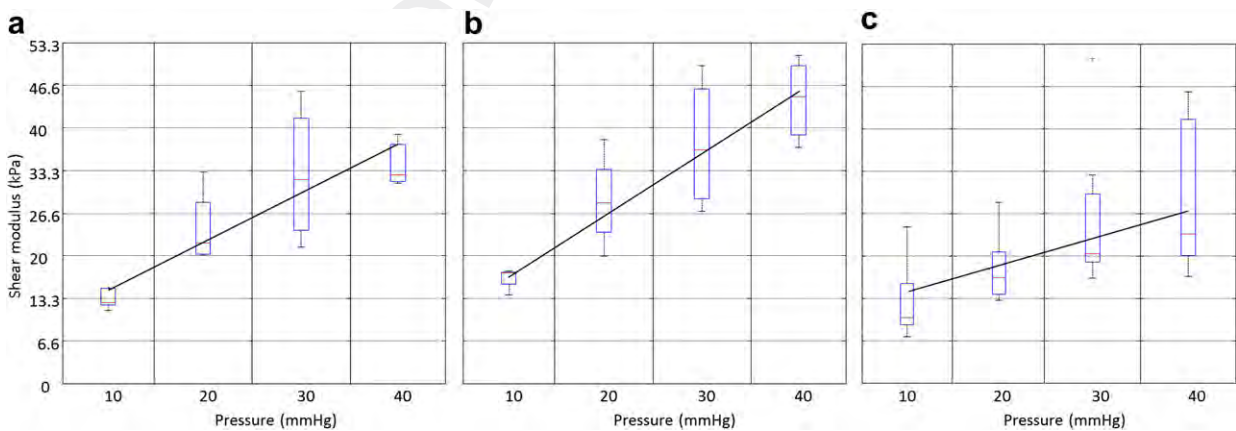


Fig. 8. Evolution of the shear modulus as a function of the urinary pressure with the ultrasound (US) beam along (μ_{\perp}) the axis of the pyramid. Stiffness increases in each compartments (a) outer cortex, (b) inner cortex and (c) medulla. Median values over all kidneys are summarized in Table 4. Black lines represent a linear fit calculated over elasticity as a function of urinary pressure (Table 5).

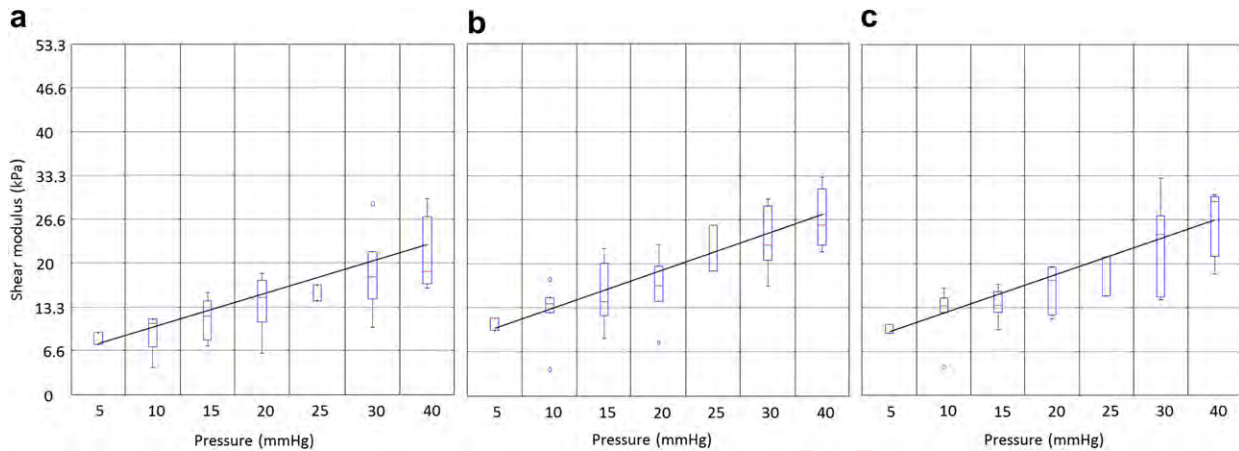


Fig. 9. Evolution of the shear modulus as a function of the urinary pressure with the ultrasound (US) beam perpendicular ($\mu_{//}$) to the axis of the pyramid. Stiffness increases in each compartments (a) outer cortex, (b) inner cortex and (c) medulla. Median values over all kidneys are summarized in Table 4. Black lines represent a linear fit calculated over elasticity as a function of urinary pressure (Table 5).

2008). No such data is available in pigs to our knowledge. Moreover, differences in anisotropy between these two cortical compartments are unexpected. These results illustrate the complexity of analyzing intrarenal elasticity because of the level of compartmentalization and to the degree of anisotropy in multipapillary kidneys.

The elastography systems without ultrasound guidance to monitor precisely the position of samplings, such as the FibroScan[®], are inappropriate for the kidney for several reasons. First, there is no B-mode control and the sample volume is fixed, 4 cm long and between 25 mm and 65 mm below the skin surface; therefore, it is extremely difficult and hazardous to position adequately the sample volume on the renal parenchyma that is located at a variable depth. A manual adjustment could be considered in transplanted kidneys because more superficially located, but it stays hazardous without real time sonographic control; moreover, such adjustment would require modifying the pressure put on the probe which would change elasticity values. Second, the

mechanical wave has to be applied on a rigid surface, such as the rib cage, to avoid compression effects by the probe, which is impossible for the kidney. However, this system was recently proposed to detect fibrosis in renal transplants (Arndt et al. 2010).

The ARFI[®] seems more promising because it is ultrasound guided. However, it is limited to 5 cm in depth and the quality control of elasticity estimation, as provided by SSI maps, is absent. Preliminary results in transplanted patients remain limited (Seeversveen et al. 2010). Finally, the one-dimensional (1-D) characteristic of these two systems is a major inconvenience knowing that the development of degenerative fibrotic processes is heterogeneous within tissues. Thus, it is very important to provide maps of the mechanical properties of the kidney. With regard to ARFI, implementation of a 2-D mode was developed, but providing only 2-D displacement maps with a strong energy deposit within the organ (Fahey et al. 2008). In that configuration SSI seems to be more appropriate and has the advantage to provide

Table 4. Median values and standard deviation of the shear modulus over all kidneys as a function of the urinary pressure for each compartments: outer cortex (OC), inner cortex (IC) and medulla (M)

Pressure (mm Hg)	5	10	15	20	25	30	40
Axial OC (μ_{\perp} kPa)	8.5 ± 1.3	10.8 ± 3.0	12.9 ± 3.5	13.6 ± 4.7	15.4 ± 1.7	17.9 ± 6.8	18.6 ± 7.2
Transverse OC ($\mu_{//}$ kPa)	–	12.6 ± 1.6	–	22.0 ± 6.1	–	31.9 ± 10.9	32.6 ± 4.1
<i>p</i> value	–	2.2 × 10 ⁻⁷	–	4.5 × 10 ⁻⁷	–	7.1 × 10 ⁻⁵	2.3 × 10 ⁻⁷
Axial IC (μ_{\perp} kPa)	10.9 ± 1.4	13.9 ± 4.7	16.4 ± 4.7	16.5 ± 4.9	22.4 ± 4.9	22.8 ± 5.3	25.8 ± 5.7
Transverse IC ($\mu_{//}$ kPa)	–	17.3 ± 1.6	–	28.2 ± 7.5	–	36.6 ± 10.5	44.8 ± 7.3
<i>p</i> value	–	4.6 × 10 ⁻⁴	–	2.5 × 10 ⁻⁶	–	4.4 × 10 ⁻⁶	4.0 × 10 ⁻⁹
Axial M (μ_{\perp} kPa)	10.1 ± 0.9	13.5 ± 4.2	14.4 ± 3.0	15.5 ± 3.6	18.1 ± 4.2	24.4 ± 7.8	29.4 ± 6.7
Transverse M ($\mu_{//}$ kPa)	–	10.3 ± 6.1	–	16.5 ± 5.7	–	20.3 ± 12.8	23.4 ± 11.9
<i>p</i> value	–	0.165	–	0.254	–	0.856	0.460

Measurements were performed with the US beam along (axial, μ_{\perp}) and perpendicular (transverse, $\mu_{//}$) to the main axis of the pyramid investigated. A comparison paired *t*-test was performed to show the differences between axial and transverse measurements.

Table 5. A linear fit over elasticity as a function of urinary pressure was calculated as well as the correlation coefficient for each compartment, both parallel and perpendicular to the main axis of the pyramid

Compartment	AOC	TOC	AIC	TIC	AM	TM
Linear fit (kPa/mm Hg)	1.30	2.25	1.55	2.84	1.48	1.28
Correlation coefficient (R^2)	0.54	0.64	0.58	0.73	0.57	0.33

dynamic 2-D quantitative elasticity maps allowing monitoring precisely the location of samplings (Derieppe *et al.* 2012).

There are two main limitations of this study. First, only six kidneys were studied in three animals. However, such experiment was quite complex to implement and limitation of the number of animals is ethically justified. Second, we did not incrementally decrease arterial perfusion and the degree of venous obstruction because no quantification tool was available for that purpose.

CONCLUSION

In conclusion, ultrasonic measurement of elasticity of the kidney requires a precise real-time positioning of samplings because of the complex compartmentalization of the parenchyma and of the high tissue anisotropy that are important factors of variation. The SSI technology seems appropriate to manage this complexity. Changes of vascular and urinary pressure may also be responsible for elasticity changes and should be identified and taken into account for interpretation of the data.

Acknowledgments—The authors are grateful to Dr. Luc Behr and its team from “Institut Mutualiste Montsouris” for their expertise in animal management. M.T. is the cofounder of the company Supersonic Imagine.

REFERENCES

Arndt R, Schmidt S, Loddenkemper C, Grünbaum M, Zidek W, Van der Giet M, Westhoff TH. Noninvasive evaluation of renal allograft fibrosis by transient elastography—A pilot study. *Transpl Int* 2010; 23:871–877.

Bercoff J, Tanter M, Fink M. Supersonic shear imaging: A new technique for soft tissue elasticity mapping. *IEEE Trans Ultrason Ferroelectr Freq Control* 2004;51:396–409.

Derieppe M, Delmas Y, Gennisson JL, Deminière C, Placier S, Tanter M, Combe C, Grenier N. Detection of intrarenal microstructural changes with supersonic shear wave elastography in rats. *Eur Radiol* 2012;22:243–250.

Dworkin LD. Normal renal function: Hemodynamics. In: Brenner BM, (ed). *Brenner & Rector's the kidney*. 8th edition. Philadelphia: WB Saunders; 2008.

El Nahas M. The global challenge of chronic kidney disease. *Kidney Int* 2005;68:2918–2929.

Emelianov S, Lubinski M, Skovodora A, Erkamp R, Leavey S, Wiggins R, O'Donnell M. Reconstructive ultrasound elasticity imaging for renal transplant diagnosis: *Kidney ex vivo* results. *Ultrasound Imaging* 2000;22:178–194.

Fahey BJ, Nightingale KR, McAleavey SA, Palmeri ML, Wolf PD, Trahey GE. Acoustic radiation force impulse imaging of myocardial radiofrequency ablation: Initial *in vivo* results. *IEEE Trans Ultrason Ferroelectr Freq Control* 2005;52:631–641.

Fahey BJ, Nelson R, Bradley D, Hsu S, Dumont D, Trahey G. *In vivo* visualization of abdominal malignancies with acoustic radiation force elastography. *Phys Med Biol* 2008;53:279–293.

Gennisson JL, Catheline S, Chaffai S, Fink M. Transient elastography in anisotropic medium: Application to the measurement of slow and fast shear wave speeds in muscles. *J Acoust Soc Am* 2003;114:536–541.

Gennisson JL, Rénier M, Catheline S, Barrière C, Bercoff J, Tanter M, Fink M. Acoustoelasticity in soft solids: Assessment of the nonlinear shear modulus with the acoustic radiation force. *J Acoust Soc Am* 2007;122:3211–3219.

Gennisson JL, Defieux T, Macé E, Montaldo G, Fink M, Tanter M. Viscoelastic and anisotropic mechanical properties of *in vivo* muscle tissue assessed by supersonic shear imaging. *Ultrasound Med Biol* 2010;36:789–801.

Gong R, Dworkin L, Brenner B, Maddox D. The renal circulations and glomerular ultrafiltration. In: Brenner B, (ed). *The kidney*. Philadelphia: Saunders Elsevier; 2008. p. 91–129.

Lee W-N, Pernot M, Couade M, Messas E, Bruneval P, Bel A, Hagege A, Fink M, Tanter M. Mapping myocardial fiber orientation using echocardiography-based shear wave imaging. *IEEE Trans Med Imaging* 2012;31:554–562.

Mace E, Cohen I, Montaldo G, Miles R, Fink M, Tanter M. *In vivo* mapping of brain elasticity in small animals using shear wave imaging. *IEEE Trans Med Imaging* 2011;30:550–558.

Madsen K, Nielsen S, Tisher C. Anatomy of the kidney. In: Brenner B, (ed). *The kidney*. Philadelphia: Saunders Elsevier; 2008. p. 25–90.

Nedredal GI, Yin M, McKenzie T, Lillegard J, Luebke-Wheeler J, Talwalkar J, Ehman R, Nyberg SL. Portal hypertension correlates with splenic stiffness as measured with MR elastography. *J Magn Reson Imaging* 2011;34:79–87.

Ries M, Jones RA, Basseau F, Moonen CT, Grenier N. Diffusion tensor MRI of the human kidney. *J Magn Reson Imaging* 2001;14:42–49.

Royer D, Gennisson JL, Defieux T, Tanter M. On the elasticity of transverse isotropic soft tissues. *J Acoust Soc Am* 2011;129:1257–1260.

Seeversveen T. Assessment of renal allograft fibrosis by acoustic radiation force impulse quantification—A pilot study. *Transpl Int* 2010;24:100–105.

Shah NS, Kruse SA, Lager DJ, Farell-Baril G, Lieske JC, King BF, Ehman RL. Evaluation of renal parenchymal disease in a rat model with magnetic resonance elastography. *Magn Reson Med* 2004;52:56–64.

Tublin ME, Dodd GD III. Sonography of renal transplantation. *Radiol Clin North Am* 1995;33:447–459.

Warner L, Yin M, Glaser K, Woollard J, Carrascal C, Korsmo M, Crane J, Ehman R, Lerman L. Noninvasive *in vivo* assessment of renal tissue elasticity during graded renal ischemia using MR-elastography. *Invest Radiol* 2011;46:509–514.

On the elasticity of transverse isotropic soft tissues (L)

Daniel Royer, Jean-Luc Gennisson,^{a)} Thomas Deffieux, and Mickaël Tanter

Institut Langevin - Ondes et Images, ESPCI ParisTech - CNRS UMR 7587 - INSERM U979 - Université Paris 7, 10, rue Vauquelin, 75231 Paris Cedex 05, France

(Received 6 December 2010; revised 31 January 2011; accepted 1 February 2011)

Quantitative elastography techniques have recently been developed to estimate the shear modulus μ of soft tissues *in vivo*. In the case of isotropic and quasi-incompressible media, the Young's modulus E is close to 3μ , which is not true in transverse anisotropic tissues such as muscles. In this letter, the transverse isotropic model established for hexagonal crystals is revisited in the case of soft solids. Relationships between elastic constants and Young's moduli are derived and validated on experimental data found in the literature. It is shown that $3\mu_{\perp} \leq E_{\perp} \leq 4\mu_{\perp}$ and that $E_{//}$ cannot only be determined from the measurements of $\mu_{//}$ and μ_{\perp} . © 2011 Acoustical Society of America.

[DOI: 10.1121/1.3559681]

PACS number(s): 43.80.Qf, 43.80.Vj, 43.80.Ev [OAS]

Pages: 2757–2760

I. INTRODUCTION

It is now well established that anisotropy plays a major role in the mechanical properties of biological media such as muscles,¹ tendons,^{2,3} or bones.⁴ Linear elastic theory, first developed for crystals,⁵ was applied for modeling the propagation of ultrasonic waves in such media. First experimental results were satisfactorily explained by assuming a transverse isotropy around a specific axis of symmetry.^{1,3} Elastic constants of the model were determined from the measurement of speed V_L of ultrasound (1–10 MHz) for longitudinal waves propagating in various directions. In these studies, shear elastic constants were neglected or assumed to be zero due to the lack of measurement systems. Some years ago, the transient elastography (TE) technique was applied to measure the speed V_S of low frequency (50–150 Hz) shear waves propagating in soft tissues.⁶ Using this technique, local elasticity of soft tissues was obtained from shear velocity measurements and a strong anisotropy was found for shear waves propagating perpendicular or parallel to the muscle fibers.⁷ Recently, the supersonic shear imaging (SSI) technique⁸ was applied to the measurement of shear wave speed in muscles and confirmed this strong anisotropy.⁹ Such experiments allow us to recover the components of the elastic tensor determining the type of anisotropy.

Nevertheless elasticity is most commonly defined in terms of Young's modulus E . In an isotropic elastic soft media (Poisson's ratio $\nu \cong 0.5$), this parameter can be deduced from the shear velocity measurements by the simple relation $E \cong 3\mu = 3\rho V_S^2$, where μ is the shear modulus. In transverse isotropic or hexagonal media, similarly to the other components of the elastic tensor, two Young's moduli are defined. However, the relationship between the Young's modulus and the shear velocity is no more so simple. In this paper, the mechanical behavior of transverse isotropic soft tissues is investigated. Relations between components of the stiffness tensor are established and used to interpret experi-

mental data found in the literature. Finally, the unusual behavior of muscles and tendons, compared with that of hexagonal crystals, is also discussed.

II. ANALYSIS

The propagation of ultrasonic waves is governed by the mechanical properties of the propagating medium.⁵ Measurements performed on muscles or tendons have shown that the isotropic model, used for many other biological tissues, is not valid. The transverse isotropic model developed for materials exhibiting at least a hexagonal or an axial symmetry is more appropriated.¹ Given the Cartesian coordinate (x_1, x_2, x_3) with the x_3 -axis parallel to the fibers, a muscle or a tendon is isotropic in the (x_1, x_2) plane. In the linear elastic theory, mechanical properties are described by the stiffness tensor c_{ijkl} or the compliance tensor s_{ijkl} ($i, j, k, l = 1-3$). Using the Voigt's notation, they are represented by 6×6 symmetric matrices $c_{\alpha\beta}$ or $s_{\alpha\beta}$ ($\alpha, \beta = 1-6$). For transverse isotropic media, the number of independent elastic constants reduces to five: c_{11} , c_{13} , c_{33} , c_{44} , and c_{66} . Other elastic constants are related to these coefficients or vanish,

$$c_{22} = c_{11}, c_{23} = c_{13}, c_{55} = c_{44}, c_{12} = c_{11} - 2c_{66}. \quad (1)$$

The same features can be established for the components of the compliance matrix $s_{\alpha\beta}$, inverse of the stiffness matrix $c_{\alpha\beta}$.

Stiffness constants c_{11} and c_{33} can be determined from the measurement of longitudinal ultrasound velocities in directions perpendicular (V_{L1}) and parallel (V_{L3}) to the fiber axis x_3 ,

$$c_{11} = \rho(V_{L1})^2, \quad c_{33} = \rho(V_{L3})^2, \quad (2)$$

where ρ is the mass density. The constant c_{13} can be deduced from the velocity of longitudinal waves propagating in a meridian plane such as (x_1, x_3) . Other constants can be obtained with TE technique (Fig. 1) from the velocity (V_{S1} or V_{S3}) of shear waves propagating in a direction perpendicular to the

^{a)}Author to whom correspondence should be addressed. Electronic mail: jl.gennisson@espci.fr

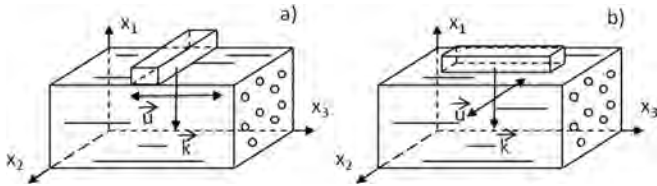


FIG. 1. Schematics of the TE technique where a rod mounted on a vibrator gives a low frequency pulse at the surface of the medium generating shear waves. (a) When the rod is perpendicular to the fibers axis, a shear wave propagates (\vec{k}) perpendicularly to the fibers axis with a polarization (\vec{u}) parallel to the fibers axis. (b) When the rod is parallel to the fibers axis, a shear wave propagates (\vec{k}) perpendicularly to the fibers axis with a polarization (\vec{u}) perpendicular to the fibers axis. Such configurations give, respectively, access to the elastic constants c_{44} and c_{66} .

fiber axis with a polarization oriented either parallel to the fibers,

$$c_{44} = \rho(V_{S3})^2, \quad (3)$$

or perpendicular to the fibers,

$$c_{66} = \rho(V_{S1})^2. \quad (4)$$

Regarding SSI technique, as presented in Fig. 2, c_{44} is deduced from the velocity of shear waves propagating along the fiber axis and polarized in any direction perpendicular to the fibers.

In the case of soft tissues, like muscle, the order of magnitude of these constants is very different. Longitudinal wave velocity measured at megahertz frequencies are in the kilometer per second range. With $\rho = 1100 \text{ kg/m}^3$, values of constants c_{11} , c_{33} , and c_{13} were on the order of 3 GPa.¹ Conversely, shear velocities were found to be in 1–10 m/s range.⁸ Then, values of constants c_{66} and c_{44} are on the order of 100 kPa, i.e., more than four orders of magnitude lower than the three other constants. These results obtained recently by TE or SSI justifies the hypothesis made by Levinson¹ that the value of the shear constant c_{44} remains equal to zero throughout the iterative process used to determine the elastic constants from the speed of ultrasound. This author approximates the velocity equation by assuming that $c_{13} \approx \sqrt{c_{11}c_{33}}$. Moreover, Levinson notes that this initial estimate meets terminal conditions of the optimization

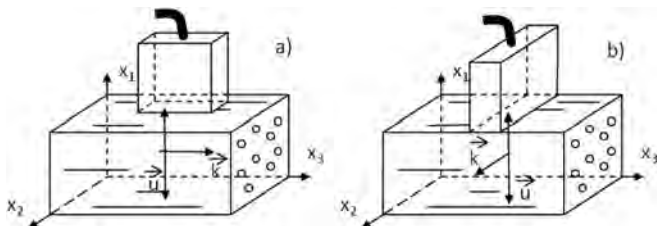


FIG. 2. Schematics of the SSI technique where a radiation force perpendicular to the fibers axis generates shear waves. (a) When the ultrasonic probe is parallel to the fibers axis, a shear wave propagates (\vec{k}) parallel to the fibers axis with a polarization (\vec{u}) perpendicular to the fibers axis. (b) When the ultrasonic probe is perpendicular to the fibers axis, a shear wave propagates (\vec{k}) perpendicularly to the fibers axis with a polarization (\vec{u}) perpendicular to the fibers axis. Such configurations give, respectively, access to the elastic constants c_{44} and c_{66} .

algorithm. In the following, this relation is demonstrated and a more general relation between elastic constants is established, which is valid in the case of tendon where the shear stiffness c_{66} cannot be neglected.³

Because the stored energy density of any material must be positive, the stiffness matrix is constrained to be definite positive.⁵ A transverse isotropic material requires the positivity of c_{44} , c_{66} , and

$$c^2 = c_{33}(c_{11} - c_{66}) - c_{13}^2. \quad (5)$$

Stability constrains imposed a limited range of variations for elastic constants.¹⁰ In Fig. 3, bounds of allowable values of c_{13}^2 are plotted in the dimensionless diagram,

$$b = \frac{2c_{13}^2}{(c_{11} + c_{12})^2} \text{ versus } a = \frac{c_{33}}{c_{11} + c_{12}}. \quad (6)$$

For transverse isotropic materials the stability condition [Eq. (5)] requires that $0 \leq b \leq a$. Symbols correspond to various crystals (Be, BeO, ZnO, CdS, Ti) of hexagonal symmetry and to soft solids like muscles and tendons. Crystal data are close to the dotted curve $b = 2(1 - a)^2$ corresponding to an isotropic material ($c_{33} = c_{11}$, $c_{13} = c_{12}$) of Poisson's ratio $\nu = 1 - a$. With $\nu = 0.5$, a fluid or a soft solid, like isotropic tissues, lies at the intersection with the line $b = a$. Representative points for muscles and tendons are far from the curve of isotropy and border the upper limit of the diagram. This representation exhibits the specific behavior of muscles and tendons as compared with that of transverse isotropic solids and soft isotropic tissues.

Since c^2 vanishes for $b = a$, this quantity plays an important role for characterizing the behavior of a soft material. It intervenes in the Young's modulus, defined as the ratio of the loading stress to the corresponding strain. For a stress parallel to the fiber axis, the Young's modulus $E_{//} = E_{33}$ is equal to,

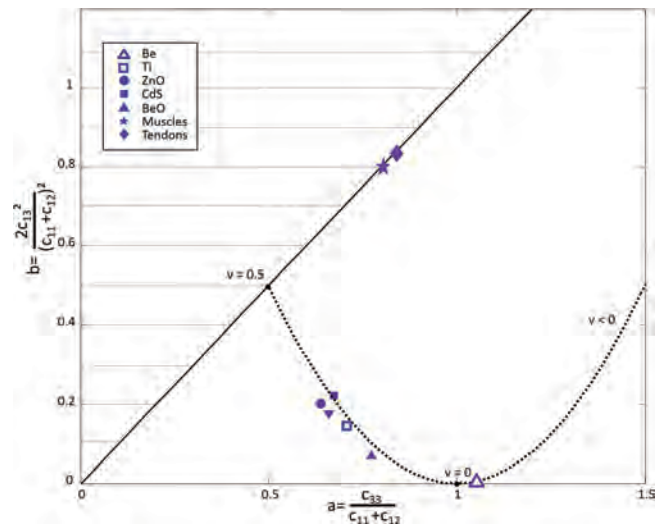


FIG. 3. (Color online) Bounds of allowable values of c_{13}^2 and data plotted for a variety of transverse isotropic crystals: Be (Δ), BeO (\blacktriangle), Ti (\square), ZnO (\bullet), CdS (\blacksquare), muscle (\ast), and tendon (\blacklozenge). a and b are defined from Eq. (6). The dotted curve is for an isotropic medium of Poisson's ratio $\nu = 1 - a$.

$$E_{//} = \frac{1}{s_{33}} = \frac{c^2}{c_{11} - c_{66}}. \quad (7)$$

For a stress perpendicular to the fiber axis, the Young's modulus $E_{\perp} = E_{11} = E_{22}$ is given by

$$E_{\perp} = \frac{1}{s_{11}} = \frac{4c_{66}c^2}{c^2 + c_{33}c_{66}}. \quad (8)$$

As pointed out by Hoffmeister, Eqs. (7) and (8) show that parallel and perpendicular Young's modulus do not depend on c_{44} , while variations in c_{66} produce changes in Young's modulus at all angles with respect to the fiber axis.²

Experimental values of $E_{//}$ are less than 100 kPa for muscle and less than 1 MPa for tendon.³ From Eq. (7), the quantity $c^2 = E_{//}(c_{11} - c_{66})$ is of the order of 10^{-3} (GPa)², i.e., three orders of magnitude lower than each term of the difference in Eq. (5). Then, the equality,

$$c_{13} \cong \sqrt{c_{33}(c_{11} - c_{66})}, \quad (9)$$

is valid with an error less than 0.1%. The determination of c_{13} requires measurements of the phase velocity of longitudinal waves propagating in any direction in a meridian plane such as (x_1, x_3) . Equation (9) allows us to calculate c_{13} with stiffness constants deduced from sound velocity measurements only in directions parallel and perpendicular to the fiber axis. We have used results found in the literature for fresh bovine Achilles tendons to check the validity of Eq. (9). The first four columns in Table I list the mean values of stiffness constants obtained by Kuo *et al.* at three strain conditions, 0%, 4.7%, and 9.5%.³ The last column shows that the values of the constant c_{13} deduced from Eq. (9) are very close to the experimental ones.

Recently, experiments performed *in vivo* with the SSI technique show that shear wave velocities perpendicular to the fiber axis of skeletal muscles are of the order of 10 m/s.⁹ Then, the corresponding elastic constants c_{66} and c_{44} are less than 100 kPa and Eq. (9) can be written in a form identical to that postulated by Levinson,

$$c_{13} \cong \sqrt{c_{11}c_{33}}. \quad (10)$$

We have used the experimental results obtained by this author to check the validity of this formula. In Table II, the first three columns list the mean values of stiffness constants obtained for the first specimen in both passive and active phase.¹ The last column shows that the values of the constant c_{13} deduced from Eq. (10) are very close to the experimental

TABLE I. Comparison between mean values of stiffness constant c_{13} measured (Ref. 3) and calculated from Eq. (9) (GPa) for bovine Achilles tendons at three strain conditions.

Strain	c_{11}	c_{33}	c_{66}	c_{13} (meas.)	c_{13} [Eq. (9)]
0%	2.93	3.90	0.61	3.00	3.01
4.7%	2.91	3.59	0.25	3.08	3.09
9.5%	2.89	3.32	0.26	2.96	2.95

TABLE II. Comparison between average values (GPa) of stiffness constant c_{13} measured (Ref. 1) and calculated from Eq. (10) for a frog sartorius muscle in the passive and active phases.

Phase	c_{11}	c_{33}	c_{13} (meas.)	c_{13} [Eq. (10)]
Active	2.60	4.17	3.29	3.29
Passive	2.60	4.46	3.40	3.41

ones. The agreement for other specimens is also very satisfactory.

The main objective of elastographic technique is to estimate the Young's modulus E of soft tissues through measurements of the shear wave velocity V_S . For an isotropic elastic media, this parameter is linked to the Lamé constants λ and μ ,

$$E = \frac{\mu(3\lambda + 2\mu)}{\lambda + \mu}. \quad (11)$$

In soft media, λ is 10^5 times larger than μ . Thus such medium are considered as quasi-incompressible and the very good approximation,

$$E \cong 3\mu = 3\rho V_S^2, \quad (12)$$

allows us to determine accurately the elasticity from shear wave velocity measurements.⁶

The elasticity of transverse isotropic media is described by the two Young's modulus $E_{//}$ and E_{\perp} according to the direction of the applied stress with respect to the fiber axis. Combining Eqs. (7) and (8) leads to

$$E_{\perp} = \frac{4c_{66}E_{//}}{E_{//} + \gamma c_{66}}, \quad (13)$$

where the coefficient,

$$\gamma = \frac{c_{33}}{c_{11} - c_{66}} = 2a, \quad (14)$$

is equal to unity for a soft isotropic medium ($c_{11} = c_{33} \gg \gamma c_{66}$). In this case, $E_{//} = E_{\perp} = E$ and Eq. (13) gives $E = 3c_{66} = 3\mu$, as expected. For transverse isotropic media such as tendons or muscles, c_{33} is larger than c_{11} . However, values of stiffness constants in Tables I and II and data in Fig. 3 show that $\gamma = 2a$ does not exceed 2. Thus, the perpendicular Young's modulus lies in between $3c_{66}$ and $4c_{66}$. The lower limit corresponds to the isotropic case. The upper limit corresponds to a transverse isotropic soft medium having a longitudinal elasticity $E_{//}$ much larger than the shear elasticity measured by the coefficient $c_{66} = \mu_{\perp}$,

$$3\mu_{\perp} \leq E_{\perp} \leq 4\mu_{\perp}. \quad (15)$$

This approximation is valid for muscles, for which $E_{//} \cong 100$ kPa and $c_{66} \leq 10$ kPa, with V_{S1} in between 1 and 3 m/s, as measured by Gennisson *et al.*⁹ Thus the measurement of the shear elastic constant c_{66} provides a good

approximation of the Young's modulus in the direction perpendicular to the fiber axis.

As pointed out by Hoffmeister, the Young's modulus $E_{//}$ cannot be estimated from the shear elastic constant c_{44} . Equation (7) shows that $E_{//}$ is proportional to c^2 . For a soft transverse isotropic media, we have shown that this quantity is the difference of two terms, $c_{33}(c_{11} - c_{66})$ and c_{13}^2 , that nearly compensate. Taking into account the accuracy of ultrasonic techniques, the relative error on the value of c^2 is very large and the estimation of the Young's modulus parallel to the fiber failed. This remark explains the discrepancy observed by Kuo *et al.* between the experimental and the estimated values of $E_{//}$. For the unstrained tendon (S_0), the measured Young's modulus is one order of magnitude larger than that estimated from elastic constants. This ratio is only twice for the sample with an initial strain state at 9.5%. At a higher strain the tendon becomes harder and the quantity c^2 increases significantly. Thus, the estimation of the Young's modulus becomes more accurate, as noted by Kuo *et al.*

III. DISCUSSION

In this paper, relationships are derived from theoretical considerations and experimental results obtained by TE or SSI techniques applied to transverse isotropic soft tissues. Relationships [Eqs. (9) and (10)] between elastic constants c_{11} , c_{13} , c_{33} , and c_{66} were verified on data reported in the literature for muscles and tendons. Moreover, it is shown that the well-known approximation $E \cong 3\mu = 3\rho V_S^2$ is no more valid in the case of transverse isotropic soft tissues. In that way, such medium in TE or SSI techniques must be preferentially defined in terms of shear velocities than in terms of Young's moduli.

A representation in the stability diagram of transverse isotropic media shows that the mechanical behavior of muscles and tendons is very different from that of hexagonal crystals and also from that of isotropic tissues. One reason of this unusual behavior of transverse isotropic tissues is the difference of anisotropy according to the type of elastic waves. Regarding the speed of ultrasound wave, the ratio of anisotropy is quite close to unity for longitudinal waves. The anisotropy of soft tissues is mainly related to the shear parameters governing the speed of slow transverse waves. This explains why the anisotropy was not very well studied in the last decades in ultrasonography. Moreover, expressions of the Young's modulus were derived from the relationship on

components of the elastic tensor. Young's modulus perpendicular to the fiber axis was found to be in between $3c_{66}$ and $4c_{66}$. Thus, this parameter can be estimated from the measurement of the speed of the shear wave perpendicular to the axis of symmetry. Conversely, Young's modulus parallel to the fiber axis cannot be expressed in terms of shear wave speed. Moreover the estimation of $E_{//}$ from stiffness constants determined by ultrasonic measurements is very uncertain. Under these conditions, the level of anisotropy defined by the ratio of the shear velocities is a quite good interpretation and Young's moduli are not pertinent parameters. For example, when a muscle is contracting, everybody feels an increase of stiffness. However, as pointed out in Refs. 9 and 11, the shear modulus parallel to the fibers axis (c_{44}) increases much stronger than the shear modulus perpendicular to the fibers axis (c_{66}) with the muscle contraction. The relationship between parallel Young's modulus and transverse stiffness (c_{66}) commonly felt by physicians during palpation remains an open question.

- ¹S. F. Levinson, "Ultrasound propagation in anisotropic soft tissues: The application of linear elastic theory," *J. Biomech.* **20**(3), 251–260 (1987).
- ²B. K. Hoffmeister, S. M. Handley, S. A. Wickline, and J. G. Miller, "Ultrasonic determination of the anisotropy of Young's modulus of fixed tendon and fixed myocardium," *J. Acoust. Soc. Am.* **100**(6), 3933–3940 (1996).
- ³P. L. Kuo, P. C. Li, and M. L. Li, "Elastic properties of tendon measured by two different approaches," *Ultrasound Med. Biol.* **27**(9), 1275–1284 (2001).
- ⁴H. S. Yoon and J. L. Katz, "Ultrasonic wave propagation in human cortical bone. I. Theoretical considerations for hexagonal symmetry," *J. Biomech.* **9**, 407–412 (1976).
- ⁵D. Royer and E. Dieulesaint, *Elastic Waves in Solids. I. Free and Guided Propagation* (Springer, Berlin, 1999), Chap. 4.
- ⁶L. Sandrin, M. Tanter, J. L. Gennisson, S. Catheline, and M. Fink, "Shear elasticity probe for soft tissue with 1D transient elastography," *IEEE Trans. Ultrason. Ferroelectr. Freq. Control* **49**(4), 436–446 (2002).
- ⁷J. L. Gennisson, S. Catheline, S. Chaffai, and M. Fink, "Transient elastography in anisotropic medium: Application to the measurement of slow and fast shear waves velocities in muscles," *J. Acoust. Soc. Am.* **114**(1), 536–541 (2003).
- ⁸J. Bercoff, M. Tanter, and M. Fink, "Supersonic shear imaging: A new technique for soft tissues elasticity mapping," *IEEE Trans. Ultrason. Ferroelectr. Freq. Control* **51**(4), 396–409 (2004).
- ⁹J. L. Gennisson, T. Defieux, E. Macé, G. Montaldo, M. Fink, and M. Tanter, "Viscoelastic and anisotropic mechanical properties of in vivo muscle tissue assessed by Supersonic Shear Imaging," *Ultrasound Med. Biol.* **36**(5), 789–801 (2010).
- ¹⁰A. Ballato, "Poisson's ratio of auxetic and other technological materials," *IEEE Trans. Ultrason. Ferroelectr. Freq. Control* **57**(1), 7–15 (2010).
- ¹¹S. Levinson, S. Catheline, and M. Fink, "Anisotropy elasticity and viscosity deduced from supersonic shear imaging in muscle," in *International Society of Biomechanics, XXth Congress, 29th Annual Meeting of the American Society of Biomechanics*, Cleveland, OH (2005), p. 101.



ELSEVIER

doi:10.1016/j.ultrasmedbio.2008.08.018

● *Original Contribution*

**QUANTITATIVE VISCOELASTICITY MAPPING OF HUMAN LIVER
 USING SUPERSONIC SHEAR IMAGING: PRELIMINARY *IN VIVO*
 FEASIBILITY STUDY**

MARIE MULLER, JEAN-LUC GENNISSON, THOMAS DEFFIEUX, MICKAËL TANTER and
 MATHIAS FINK

Laboratoire Ondes et Acoustique, ESPCI, CNRS UMR 7587, INSERM, Université Paris VII, Paris Cedex 05,
 France

(Received 16 May 2008; revised 11 August 2008; in final form 24 August 2008)

Abstract—This paper demonstrates the feasibility of *in vivo* quantitative mapping of liver viscoelasticity using the concept of supersonic shear wave imaging. This technique is based on the combination of a radiation force induced in tissues by focused ultrasonic beams and a very high frame rate ultrasound imaging sequence capable of catching in real time the transient propagation of resulting shear waves. The local shear wave velocity is recovered using a dedicated time-of-flight estimation technique and enables the 2-D quantitative mapping of shear elasticity. This imaging modality is performed using a conventional ultrasound probe during a standard intercostal ultrasonographic examination. Three supersonic shear imaging (SSI) sequences are applied successively in the left, middle and right parts of the 2-D ultrasonographic image. Resulting shear elasticity images in the three regions are concatenated to provide the final image covering the entire region-of-interest. The ability of the SSI technique to provide a quantitative and local estimation of liver shear modulus with a millimetric resolution is proven *in vivo* on 15 healthy volunteers. Liver moduli extracted from *in vivo* data from healthy volunteers are consistent with those reported in the literature (Young's modulus ranging from 4 to 7.5 kPa). Moreover, liver stiffness estimation using the SSI mode is shown to be fast (less than one second), repeatable (5.7% standard deviation) and reproducible (6.7% standard deviation). This technique, used as a complementary tool for B-mode ultrasound, could complement morphologic information both for fibrosis staging and hepatic lesions imaging (E-mail: jl.gennisson@espci.fr). © 2009 World Federation for Ultrasound in Medicine & Biology.

Key Words: Transient elastography, Ultrasound, Liver fibrosis, Shear wave imaging.

INTRODUCTION

Liver fibrosis staging is of major clinical issue because it represents key information regarding the prognosis and the surveillance of chronic liver diseases such as cirrhosis or hepatitis. It is also crucial to monitor the efficacy of antifibrotic treatments (Pinzani et al. 2005; National Institute 2002). Currently, liver biopsy and histologic testing remains the gold standard for liver fibrosis staging (Afdhal et al. 2003; Bravo et al. 2001; Ishak et al. 1995). However, this technique presents serious limitations. Its invasive characteristics can lead to patient discomfort and serious complications, especially if repeated biopsies are needed (Bravo et al. 2001; Friedman et al. 2003;

Cadranel et al. 2000; Castera et al. 1999). Furthermore, this liver investigation method shows serious deficiencies, mainly related to the fact that fibrosis affects the liver tissue in a heterogeneous manner, leading to sampling errors during puncture (Regev et al. 2002; Maharaj et al. 1986) and inter-observer variability during the histopathological measurements (The French METAVIR 1994; Bedossa et al. 1988). To circumvent these limitations, noninvasive biochemical and hematologic tests (Wai et al. 2003), as well as tests measuring the presence of surrogate serum fibrosis markers, have been developed (Suzuki et al. 2005; Patel et al. 2003). Blood tests such as Fibrotest (Imbert-Bismut et al. 2001) and platelet count (Ono et al. 1999) measure a combination of various blood parameters considered as indirect markers of fibrosis staging. The sensitivity and specificity of these tests, measuring items having no direct link with fibrosis, are still debated (Bataller et al. 2005). The accuracy of

Address correspondence to: Jean-Luc Gennisson, LOA – ESPCI, 10 rue Vauquelin, 75231 Paris Cedex 05 France. E-mail: jl.gennisson@espci.fr

their results could indeed be impaired by extra hepatic diseases such as systemic inflammatory phenomena (Stauber et al. 2007; Beaugrand et al. 2006). As far as imaging methods are concerned, magnetic resonance imaging (MRI) has been reported to show satisfying sensitivity and specificity (Aguirre et al. 2006), thus being a useful tool for biopsy guidance (Konig et al. 2004), but MRI, as well as computed tomography and ultrasonic imaging, seem to be unable to determine early stages of fibrosis (Klatt et al. 2006).

Elasticity imaging is now commonly accepted as a relevant tool for soft tissue characterization (Sarvazyan et al. 1998; Ophir et al. 1991) in general, and for the liver in particular (Yeh et al. 2002). The feasibility of MR-elastography for liver fibrosis staging has been recently demonstrated (Klatt et al. 2006; Huwart et al. 2006), but the costs at stake are too large to allow screening or monitoring applications. Another technique, based on 1-D transient elastography (Fibroscan[®]) has been proposed for the noninvasive staging of liver fibrosis. With this technique, the assessment of fibrosis degree is based on the estimation of a global shear elasticity along an ultrasonic A-line (Sandrin et al. 2003). Various studies have shown a correlation between the liver shear modulus measured using Fibroscan[®] and the degree of fibrosis obtained through liver biopsy, particularly when the elasticity measurement is combined with a blood marker of fibrosis (Beaugrand et al. 2006; Castera et al. 2005; Saito et al. 2004). However, the Fibroscan[®] technique estimates a mean elasticity of the liver (over a centimetric volume), and the heterogeneities of shear elasticity at higher fibrosis degree are assumed to introduce biases in this global estimation. Thus, the clinical interest of 2-D real-time elasticity imaging modality would be twofold. First, the estimation of the global liver stiffness over a larger area should result in more accurate scores of fibrosis level. Second, beyond fibrosis staging, the quantitative mapping of local stiffness heterogeneities should allow the localization of the presence of hepatic lesions both for diagnosis and biopsy guidance. Some techniques have been developed that measured the deformation of the liver tissue before and under static compression (Friedrich-Rust et al. 2007). Unfortunately, such static elastography techniques do not allow a quantitative evaluation of the liver elasticity. Another technique based on the use of a local acoustic radiation force impulse (ARFI) technique has been proposed recently for the visualization of abdominal lesions on the liver and the kidney (Fahey et al. 2008; Palmeri et al. 2008). In this approach, 2-D elastography images are obtained by combining successive sequences of ultrasonic radiation forces, each radiation force sequence enabling the estimation of elasticity along one line of the final image. However, this technique requires an important number of insonifica-

tions to build a complete elasticity image of the medium and is consequently sensitive to respiratory motion artefacts (Fahey et al. 2006, 2007).

In the study presented here, a 2-D real-time and freehand elastography method is proposed for liver investigation as a multiparametric technique. This approach, called supersonic shear imaging, tries to merge the advantages of the previous techniques by combining the remote palpation of the acoustic radiation force imaging technique (Palmeri et al. 2008) and the ultrafast echographic imaging approach of transient elastography into a single ultrasonic sequence (lasting less than several tens of milliseconds). This combination is expected to provide a quantitative elasticity imaging mode, with a significant reduction of operator dependence compared with static elastography. First, the global estimation of the liver elasticity is performed over a large area to reduce sampling errors and enable the recovery of a global mean elasticity of liver that benefits from very small variance. Second, the local estimation of the liver elasticity is conducted, allowing the mapping of local stiffness heterogeneities. Third, in addition to elasticity, other parameters are assessed such as the dispersive behavior of the liver, by exploiting the frequency diversity of the shear waves propagating in the liver.

In the following, the SSI technique used in this study is presented and the methods for global and local elasticity estimation are presented, as well as the method used for the shear wave dispersion measurements. Finally, *in vivo* reproducibility and repeatability results are presented, as well as measurement on a group of 15 healthy volunteers.

MATERIALS AND METHODS

All subjects were informed of the nature and aims of this study. They signed an informed consent form and the study was approved by the national agency for health (AFSSAPS); authorization # 2008-A00006-49.

Supersonic shear imaging technique

The SSI technique is a tissue elasticity imaging technique based on the velocity estimation of a shear wave generated by radiation force. This technique has been described in previous papers (Bercoff et al. 2004a, 2004b, 2004c; Tanter et al. 2008) and is currently being tested clinically on breast lesion imaging with promising results. A remote radiation force or "pushing beam" is generated by focusing ultrasound using a conventional ultrasonic probe. This radiation force results in a few micrometers displacement of tissue that propagates as a transient shear wave in the medium. By successively focusing multiple beams at increasing depths, a quasi-plane shear wave can be generated. After the generation

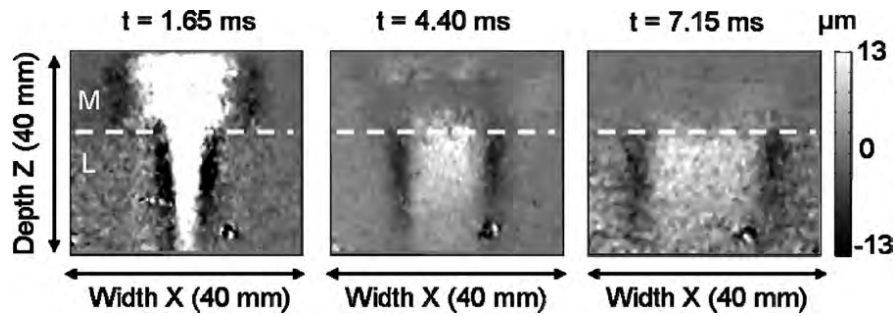


Fig. 1. Shear displacement field in the liver at different time steps. A quasi-plane shear wave is visible, travelling faster in the intercostal muscle region (M) than in the liver region (L). Gray scale levels are expressed in μm , corresponding to local tissue displacement between two successive images (at a 3750-Hz frame rate).

of the shear wave, the echographic device switches to the ultrafast imaging mode by acquiring raw radiofrequency (RF) data at a very high frame rate (up to 5000 frames/s) using the same ultrasonic probe. Each ultrafast echographic image is achieved by transmitting a single ultrasonic plane wave and beamforming only in the receive mode in postprocessing. Then by using a 1-D cross-correlation algorithm, consecutive ultrasonic images were compared to determine the axial displacement field U (along the Z axis) induced by the propagation of the shear wave inside the tissues (Fig. 1).

In these *in vivo* investigations, the SSI technique was implemented on a modified commercial ultrasonic scanner HDI 1000 (ATL, Seattle, WA, USA) with a 5-MHz linear probe (L7.4, ATL, 5 MHz central frequency, 128 elements). The shear wave was generated by successively focusing four 5-MHz ultrasonic beams 20, 25, 30 and 35 mm deep. Each pushing beam lasted 150 μs , with a f/day number of 1.5. The following ultrafast echographic mode was performed at 3750 Hz frame rate, with 128 successive ultrafast echographic images. As the HDI 1000 scanner is only relying on 32 receive channels (and 64 transmit channels), the ultrafast echographic frame is achieved by transmitting four successive plane waves with 32 elements of the probe. The duration of each transmit/receive event (about 50 μs) is only limited by the ultrasonic travel path and, consequently, the maximal imaging depth fixed between 0 and 37 mm. A complete ultrasound image, comprising 128 lines spaced at 0.3 mm (space between each elements of the probe), is thus achieved in the minimum duration of 200 μs with this scanner. The whole SSI acquisition itself corresponds to a total duration of about 25 ms with 128 images recorded; however, a 200-ms pause automatically follows each acquisition.

Regarding the FDA requirements, the acoustic pressure levels and intensities were measured using a calibrated MHB 500B (NTR systems, 0.5 mm resolution, frequency bandwidth ranging from 1 to 16 MHz). The peak pressure measured at 2 cm depth in the water was

4 MPa; this pressure must be corrected inside the tissue by an attenuation of 0.3 dB/cm/MHz, leading to a peak pressure of $p_0 = 2$ MPa inside the tissue (at $f_0 = 5$ MHz). The $Ispta$ is defined as:

$$Ispta = \frac{p_0^2}{2\rho_0 c} \cdot \frac{\Delta t_{push}}{\Delta t_{experiment}}. \quad (1)$$

Considering the “worst cases” where all four pushing beams are focused at the same location, $\Delta t_{push} = 4 \cdot 150 = 600 \mu\text{s}$ in $\Delta t_{experiment} = 225$ ms, the $Ispta$ would be 591, 447, 306 and 239 mW/cm^2 , respectively, at focal depths $z = 20$ mm, $z = 25$ mm, $z = 30$ mm and $z = 35$ mm. Note that all these “worst cases” values corresponding to insonifications, which were never used *in vivo*, are below the $720 \text{mW}/\text{cm}^2$ 510(k) recommendation imposed by the FDA. The $Ispta$ value corresponding to the case used for *in vivo* investigations (four successive “pushes” each lasting 150 μs and focused at $z = 20, 25, 30$ and 35 mm) is equal to $395 \text{mW}/\text{cm}^2$. The mechanical index for the pushing sequence was found to be, respectively, 1.42, 1.3, 1.15 and 0.95 for $z = 20, 25, 30$ and 35 mm depth and 0.67 for the ultrafast imaging sequence, also below the 1.9 limit imposed by the FDA.

In vivo shear waves displacements are represented in Fig. 1 at different time steps after the radiation force generation. One can clearly notice the quasi-planar shear wave front propagating faster in the upper region of the image corresponding to the intercostal muscle. The intercostal muscle (M), usually stiffer than the liver (L), exhibits a higher shear velocity. In Figs. 1 and 2, one can also notice large vessels (circular shapes in the bottom of the images) where the displacement field uncorrelated because of the presence of fluid and, consequently, a lack of echogenicity.

Moreover, to investigate a larger region of the liver and to increase the shear velocity estimation zone by zone, three quasi-plane shear waves were successively generated in three different locations of the image. This

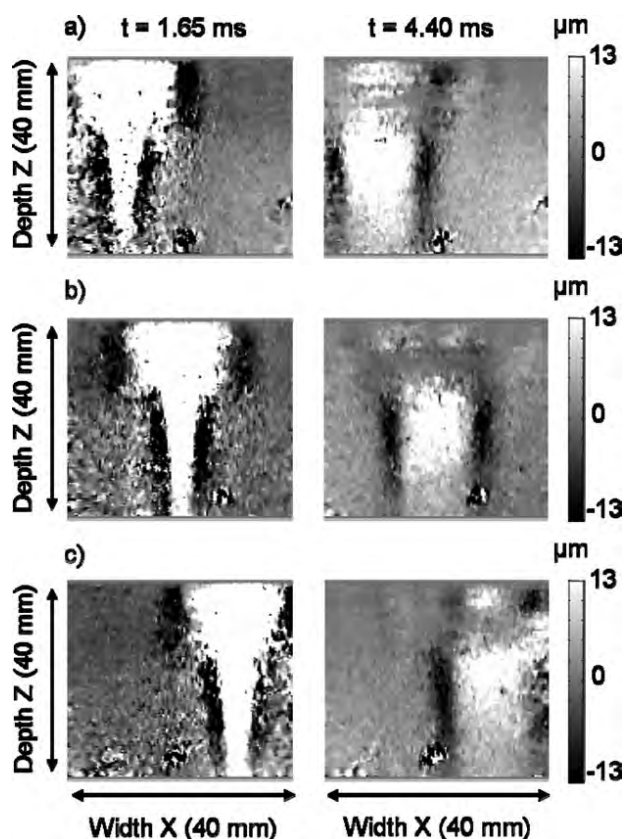


Fig. 2. Displacement field at two times ($t = 1.65$ ms and $t = 4.40$ ms) for three different locations: right (a), center (b) and left (c) of the echographic image. The shear wave then propagates both ways from the push location. For each location of the pushing beam, a movie of the displacement is recorded to investigate the full imaged area of the liver. Grayscale levels are expressed in μm , corresponding to local tissue displacement between two successive images (at a 3750-Hz frame rate).

results in a set of three different movies of the same liver region presented on Fig. 2, from which shear velocity can be estimated.

From these quasi-plane shear wave propagation movies, three different kinds of information can be extracted.

An elasticity map

The local estimation of the shear wave group velocity enables the creation of an elasticity map of the liver *via* the classical relation $E = 3\rho c^2$, where ρ is the local tissue density (assumed to be constant and equal to $1000 \text{ kg}\cdot\text{m}^{-3}$), c is the shear wave group velocity and E is the Young's modulus (Royer and Dieulesaint 2000). For each pixel (z, x), the local shear group velocity c is estimated *via* a time-of-flight algorithm, which computes the delay dt between two points separated from a distance dx through cross correlation.

$$U\left(x - \frac{dx}{2}, z, t\right) = s(t) \quad (2)$$

and

$$U\left(x + \frac{dx}{2}, z, t\right) = s(t + dt), \quad (3)$$

where U is the displacement field, dx the distance between the two points used, s is the signal waveform and dt is the time delay between the two points. Multiple distances dx can be used to provide multiple estimations of the shear velocity ($c = dx/dt$) at the same pixel and improve the overall quality of the measurement through averaging. The maximum distance dx chosen for the shear wave group velocity estimation sets the resolution of the map.

A global elasticity score

From a large region-of-interest (ROI) chosen in the image (typically $30 \times 40 \text{ mm}^2$), a single estimation of the elasticity can be estimated. This global estimation relies on the use of multiple separation distances dx (dx values chosen not to exceed the ROI) for the shear wave group velocity estimation, as well as averaging inside the ROI. This ROI is chosen from the B-mode image to avoid the intercostal muscle or fat present in the upper region, as well as to avoid the pushing area itself (Fig. 3a); a histogram of the estimated shear velocity is also represented (Fig. 3b). This enables the assessment of a global elasticity value with a smaller variance adapted for liver staging. Similar to 1-D transient elastography provided by Fibrosan[®], this 2-D global elasticity value can be seen as a score for fibrosis staging.

A complete rheological analysis using shear wave spectroscopy

A more detailed analysis of the semilocal shear mechanical behavior of the liver can be performed using

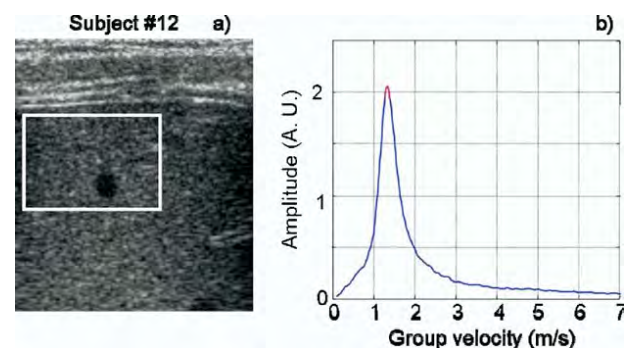


Fig. 3. (a) Standard B-mode image of the liver of a healthy volunteer. In the upper part, the intercostal muscle is clearly visible. (b) Group velocity estimation estimated from the ROI (white rectangle). The maximal value of the histogram corresponds to a shear wave group velocity equal to 1.37 m/s.

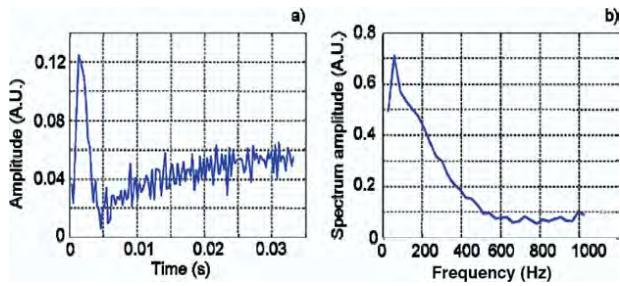


Fig. 4. (a) Amplitude in arbitrary unit (A.U.) of the shear displacement as a function of time. The tissue velocity wave field is visible after 5 ms. (b) Spectrum of the shear wave displacement field in arbitrary unit (A.U.). The signal is clearly broadband and the signal-to-noise ratio is well defined between 50 Hz and 400 Hz.

the shear wave spectroscopy technique as described by Deffieux *et al.* (2008). This last approach corresponds to the determination of shear wave phase velocity dispersion over a large frequency range (typically 50 to 500 Hz). The large bandwidth of the shear wave generated through the ultrasonic radiation force allows this measurement in one shot.

Figure 4 shows a typical waveform of the shear velocity profile as a function of time at one given depth (Fig. 4a) and its corresponding frequency spectrum (Fig. 4b) in the liver. It appears that a large bandwidth can be exploited, from 50 to ~400 Hz.

The signal is first averaged over the depth of the ROI (15 mm depth in liver) to increase the signal ratio. Its Fourier transform is then computed and, for each frequency, the phase is extracted and unwrapped along the x axis. The last step consists in fitting the phase along the distance to retrieve the wave number k for each frequency. In Fig. 5a, only four phases (90 Hz, 120 Hz, 150 Hz and 180 Hz) as a function of depth are plotted to clarify the figure. In Fig. 5b, the frequency dispersion of

the shear wave speed is illustrated by the phase information extracted from the spectrum of the local tissue displacement field as a function of the propagation distance. The slope of this phase function is changing with respect to the frequency component. Such a method could allow study of the full rheological behavior of the liver, through the assessment of the frequency dispersion of the shear wave speed. Using this approach, it was possible to perform a spectroscopic analysis in 10 of the 15 volunteers.

Experimental protocol

The objective of this study was (i) to demonstrate the feasibility of mapping elasticity of the liver through intercostal measurements *in vivo*, (ii) to assess the reproducibility of the shear velocity through intercostal measurements *in vivo*, (iii) to assess the repeatability of the shear velocity through intercostal measurements *in vivo*, (iv) to assess the interindividual variability of the shear velocity among a group of healthy volunteers and (v) to evaluate the benefit of shear wave spectroscopy in liver.

For each point of the objectives, the volunteers were asked to hold their breath during acquisition, and the ultrasonic device parameters were always the same. The mean body mass index was equal to 23.3 and values ranged from 19.2–29.3.

Reproducibility measurements were conducted by repeating 50 intercostal shear velocity measurements on one single volunteer, repositioning the probe between each measurement.

Repeatability measurements were conducted by repeating the same intercostal shear velocity measurement 50 times, without repositioning the probe, to increase the colocation of all measurements.

Reproducibility and repeatability measurements were performed using a single pushing line generated on the left of the B-mode image. A 15×25 -mm ROI was

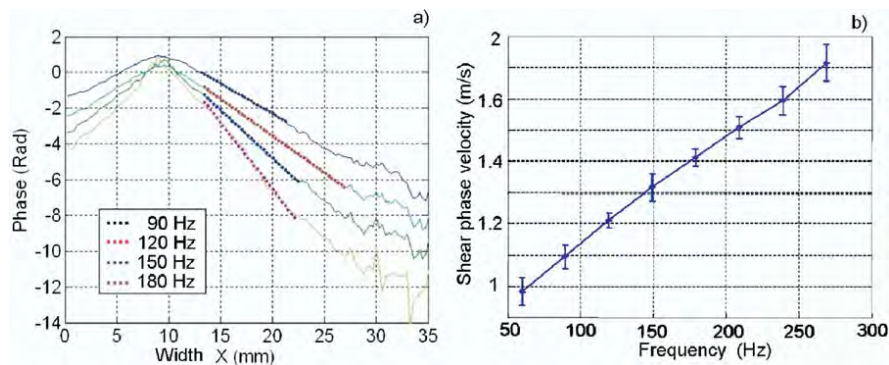


Fig. 5. (a) Four phases of the shear displacement for different frequencies (90 Hz, 120 Hz, 150 Hz and 180 Hz) as a function of distance (the width is the size of the transducer array). (b) Frequency dispersion of the shear wave speed calculated from the phases extracted between 60 Hz and 270 Hz.

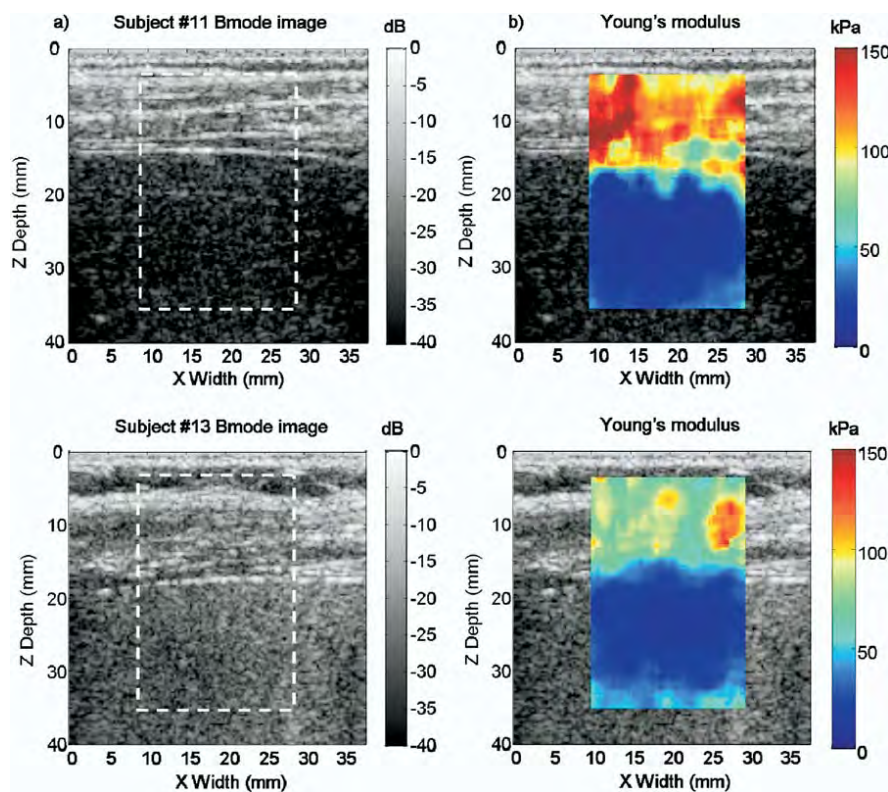


Fig. 6. Local shear velocity imaging in two healthy volunteers. (a) B-mode images of the liver for two healthy volunteers. (b) Mapping of the Young's modulus. The liver appears roughly four times softer than the intercostal muscle. One can also notice that both regions are homogeneous in terms of shear velocity.

used to evaluate the shear wave velocity in the middle of the B-mode image. So the sequence for these dispersion measurements was slightly different from the sequence used for elasticity imaging on the 15 volunteers. The same ROI was chosen for all measurements for the estimation of the global shear velocity.

In addition, intercostal liver shear velocity measurements were performed on 15 healthy volunteers using the supersonic shear imaging technique described above. Each imaging sequence was repeated five times. The ultrasonic probe was repositioned between each of the five reproducibility measurements. For each imaging sequence, three plane waves were generated on the left, center and right of the ROI to reduce the variance by averaging the velocity estimates and to provide a quantitative elasticity map over a large $40 \times 40 \text{ mm}^2$ rectangular area.

For the repeatability/reproducibility experiment, the same protocol was used in terms of positioning the probe and controlling breathing (a 2-s breath-hold was asked of the volunteer for each acquisition). Regarding the sequences, the same parameters were used for mapping or assessing the repeatability/reproducibility measurement. The only difference between these two types of acquisitions was the number of pushing line (a pushing line

corresponded to a set of 4 pushing beams at depth 20, 25, 30 and 35 mm) used. To map the entire region of the liver comprised in the B-mode image, three pushing lines were used: at the left, center and right of the image. For the repeatability/reproducibility experiment, only the left pushing line was used. Except this number of pushing lines, all other parameters were the same.

RESULTS

Imaging of local shear velocity on healthy volunteers

Shear velocity mapping results are presented for two healthy volunteers in Fig. 6, along with the corresponding B-mode images. Fat and muscle regions are well differentiated both in ultrasonographic and elasticity images. From the selected zone defined by the white rectangle on the B-mode image (Fig. 6a), the corresponding Young's modulus mapping is derived in Fig. 6b. Young's modulus appears almost homogeneous for a healthy volunteer in both liver and muscle regions. Mean shear velocity in the muscle region was found equal to 6.3 m/s, with a standard deviation of 1.2 m/s, whereas mean shear velocity in the liver region was found equal to 1.6 m/s, with a standard deviation of 0.15 m/s for subject 11. The higher standard deviation obtained in the

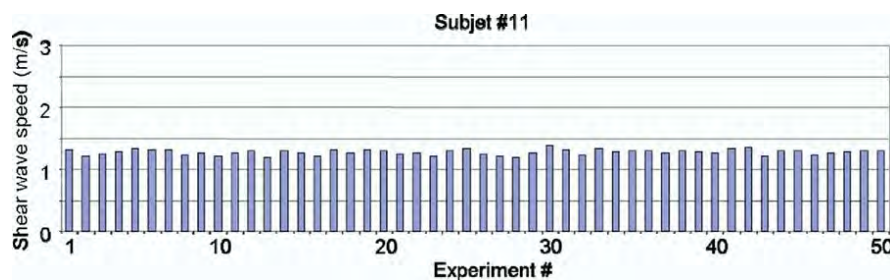


Fig. 7. Reproducibility measurement on a single healthy volunteer. The probe was removed and replaced on the abdomen of the subject and the subject held his breath between each acquisition. Standard deviation corresponds to 3.9 % of the mean value.

fat/muscle region is related to the higher heterogeneity of the region compared with the liver tissue.

Global group velocity estimation: reproducibility, repeatability and interindividual variability measurements on healthy volunteers

Figure 7 presents the shear group velocity distribution obtained from the reproducibility measurements (50 consecutive measurements with repositioning of the probe between each measurement) on a single healthy volunteer (subject 11). The volunteer was holding breath for 5 s to minimize any motion artifacts. The 50 measurements resulted in a mean group velocity value of 1.27 m/s (corresponding to a Young's modulus of 4.89 kPa), with a standard deviation of 0.05 m/s (corresponding to a 0.33 kPa standard deviation).

Results on repeatability are presented in Fig. 8. The repeatability measurements were performed by repeating 50 times the global shear wave speed on the same healthy volunteer (subject 11). The probe was maintained in the exact same position, and the subject held his breath during acquisition. The global velocity estimation obtained with this method resulted in a distribution with a mean value of 1.46 m/s (corresponding to a Young's modulus of 6.38 kPa) and a standard deviation of 0.04 m/s (corresponding to 0.37 kPa).

Furthermore global shear velocity was also assessed *in vivo* for a group of 15 healthy volunteers. Five mea-

surements were conducted on each volunteer. Each measurement combined three plane waves: on the left, center and right of the ROI. The three velocity estimates were averaged to reduce the variability. The shear wave velocity distributions for all volunteers are presented in Fig. 9, along with the standard deviation of the measurements provided by the distribution of the five consecutive velocity measurements. The mean velocity value for the whole group of volunteers is 1.48 m/s (corresponding to a Young's modulus of 6.61 kPa), with a standard deviation of 0.16 m/s (respectively, 1.41 kPa).

Shear velocity dispersion estimation

In addition to the global shear velocity estimation, a much more refined study of the mechanical behavior of liver tissue can be conducted by estimating the frequency dependence (dispersion) of the shear phase velocity.

These dispersion curves were calculated for all 10 healthy volunteers in a large-frequency bandwidth. Interestingly, similar slopes were found for all volunteers for the phase velocity dispersion. Among all cases, the mean slope for the shear phase velocity dispersion was found to be 3.60 ± 0.82 mm (Fig. 10b). On Fig. 10, the three solid lines represent the F2, F3 and F4 scores defined by physicians at low frequency (Ziol *et al.* 2005) to characterize the liver fibrosis. The dashed lines represent the supposed evolution of these score at higher frequencies. Moreover, error measurements for these

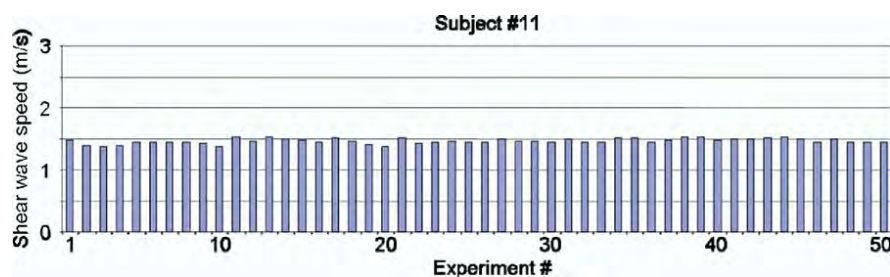


Fig. 8. Repeatability measurement on a single healthy volunteer. The probe was not moving and the subject held his breath during each acquisition. The standard deviation corresponds to 2.7% of the mean value.

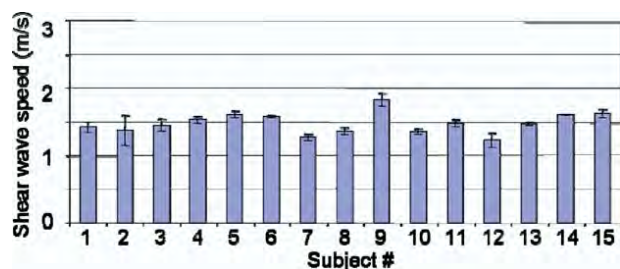


Fig. 9. Global shear group velocity estimation for 15 healthy volunteers. The error bars are the standard deviation calculated over 15 acquisitions. The probe was removed and replaced on the abdomen of the subject between all acquisitions.

shear velocity dispersion profiles were estimated by conducting reproducibility measurements of the shear velocity dispersion on a single volunteer (Fig. 10a). It resulted in a 0.38-mm error on the slope, smaller than the 0.82 mm standard deviation obtained for the studied population.

For volunteer 3, the median elasticity at 50 Hz is found to be $E = 3\rho c^2 = 4.42 \pm 0.64$ kPa. The median elasticity at 50 Hz (corresponding to the excitation frequency of Fibroscan[®]) is $E = 3\rho c^2 = 4.18 \pm 1.37$ kPa and is consistent with the results reported in the literature for a healthy group.

DISCUSSION

In this study, the feasibility of scanning viscoelastic properties of liver was investigated using the SSI technique on 15 healthy volunteers. Various liver characteristics have been estimated using different processes. Depending on the kind of required information (respectively, fibrosis staging or liver tumor imaging), it is possible to characterize global or local elastic properties of the liver.

Regarding global shear wave group velocity estimation, the SSI technique proved to be highly reproducible and repeatable (standard deviations equal, respectively, to 0.05 m/s [0.33 kPa] and 0.04 m/s [0.37 kPa] for 50 consecutive measurements). These low standard deviations foretell a very low measurement error (typically 6% of the mean Young's modulus), and therefore a particularly strong accuracy of the measurement. Using the SSI mode, the standard deviation on the estimated Young's modulus is smaller (at least three times smaller) than the ones obtained by the ARFI approach reported in Palmeri et al. (2008). Regarding the mean velocity values of the reproducibility and repeatability measurements, a difference of 0.19 m/s is noticeable on the same subject. This could be explained by three points. First, the assessments were not done the same days. Second, the position of the probe for the repeatability and the reproducibility mea-

surements was probably not the same. The probe was placed between the same two ribs as close as possible at the same distance from the abdominal part, so it was not precisely the same part of the liver investigated, which could have some weak heterogeneity. Finally, the positioning of the probe between the ribs is crucial and could generate some biases. The intercostal space can lead to ultrasonic beam aberrations. Such aberrations and absorption effects on the ultrasonic beam could also have a slight impact on the bandwidth of the generated shear wave (which is linked to the ultrasonic beam shape). As liver tissue is dispersive, a change in the shear wave bandwidth could also lead to slight changes in the shear wave group velocity.

Nevertheless, good accuracy should be a *sine qua non* condition to discriminate pathologic states *via* elas-

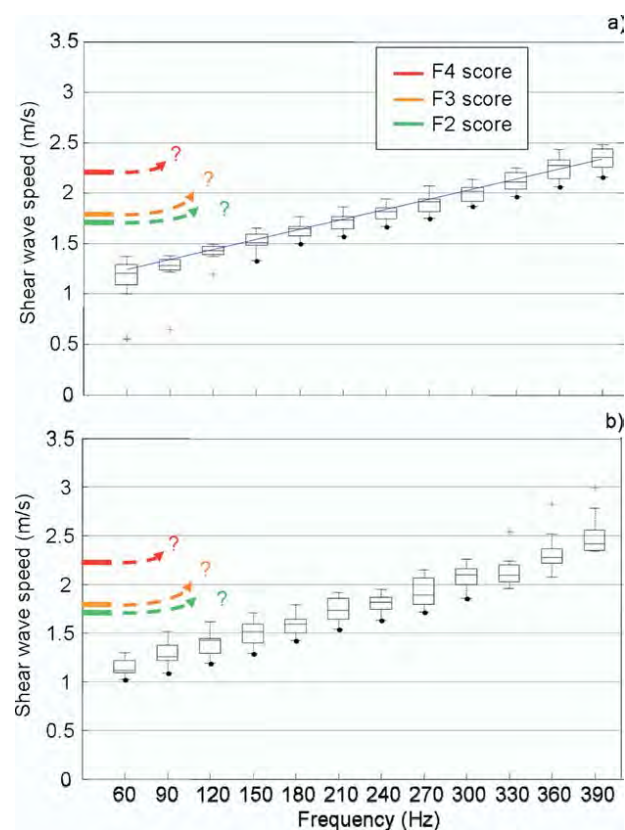


Fig. 10. (a) Repeatability of the dispersion curves for volunteer 3. The box and whiskers diagram was computed over 10 repeated measurements and are minimum in the 60–390 Hz range. The slope is 3.30 ± 0.38 mm and the extrapolated values at 50 Hz are 1.21 ± 0.09 m/s, indicating an F0 score. (b) Shear phase velocity dispersion for 10 healthy volunteers. Interestingly, the slope is in the same range for all volunteers and around 3.60 ± 0.82 mm, and the extrapolated values at 50 Hz are 1.18 ± 0.18 m/s, also indicating an F0 score for the group. Thresholds on the right correspond to the fibrosis scores estimated using Fibroscan[®] and so provided at 50 Hz only (Ziol et al. 2005). It does not mean that these thresholds are the same at higher frequencies, as suggested by the arrows.

ticity measurements that are very close at early stages of liver fibrosis as shown by [Huwart et al. \(2006\)](#). In particular, for a 50-Hz mechanical excitation, F0–F2 stages, characterizing the transition from normal to the first pathologic stage, are confined in a short range of Young's moduli (from 3.35 to 7.60 kPa), corresponding to close shear velocities (from 1.06 to 1.59 m/s) ([Sandrin et al. 2003](#)). Because MR-elastography benefits from much more accurate estimations than Fibroscan[®] at the same excitation frequency (50 Hz), it permits to distinguish F0–F2 and F3 stages ([Salameh et al. 2008](#)).

Interestingly, the shear group velocities assessed in 15 healthy volunteers using our SSI approach were found to be larger (mean value 1.48 ± 0.16 m/s) than the average value usually measured with clinical tools such as Fibroscan[®]. Indeed, at the F0 and F1 stages of fibrosis, the Fibroscan[®] measurement provides an elasticity of roughly 3.35 kPa and 5.10 kPa ([Sandrin et al. 2003](#)) (corresponding to shear velocity of 1.06 m/s and 1.30 m/s), whereas a mean value of 6.57 kPa was found using the SSI modality. This elasticity gap is a result of the broadband characteristic of the mechanical excitation generated using the ultrasonic radiation force of the SSI mode. As presented in [Fig. 4](#), the shear wave velocity is estimated over a much larger frequency bandwidth, and *in vivo* liver tissues are demonstrated to be very dispersive in that 50–350 Hz frequency range. Thus, high-frequency components of the shear wave propagate much faster than lower ones. The shear phase velocity dispersion relation obtained demonstrates that the shear velocity increases with frequency ([Fig. 5b](#)). Thus, liver elasticity is probed in a higher frequency range than Fibroscan[®] (50 Hz) or MR-elastography (51 Hz) ([Klutt et al. 2006](#)). An increased global elasticity was, therefore, expected using such a higher spectral content and this point was confirmed experimentally. These results are of particular interest because they emphasize the ability of this new SSI modality to provide additional information compared with Fibroscan[®] or MR-elastography: the full mechanical response of liver tissues over a large bandwidth of mechanical excitation. To provide a comparison with the state-of-the-art values provided by MR-elastography and Fibroscan[®], a linear fit of the shear wave velocity dispersion curve was performed for each healthy volunteer, from which the shear wave velocity at 50 Hz was extracted. The shear wave velocity estimated at 50 Hz was found to be 1.18 ± 0.18 m/s for the volunteer group (corresponding to Young's modulus equal to 4.18 ± 1.37 kPa). In addition to a very small variance of these estimates, these values are in agreement with the data provided in the literature. Thus, the broadband feature of the SSI modality permits to estimate elasticity values at a low excitation frequency corresponding to the other clinical approaches, but addition-

ally provides new information in a wider and higher frequency range.

An interesting result concerns the good reproducibility of the shear velocity dispersion for each single healthy volunteer. The assessment of the frequency slope of shear wave velocity for a volunteer resulted in a 16% variability (mean shear velocity dispersion value: 3.30 mm, standard deviation: 0.38 mm). More interestingly, for all healthy volunteers, similar shear dispersion behavior was observed. Frequency slopes of the shear wave dispersion were estimated for each volunteer, and a 20% variation was obtained for the whole population (mean shear velocity dispersion value: 3.60 mm, standard deviation: 0.82 mm) ([Fig. 10b](#)). Further work will be required to determine if the assessment of these dispersion parameters (linked to shear viscosity) will represent an added value for the diagnostics of pathologic liver diseases. However, it is possible that this type of parameter could provide interesting information on tissue organization at the microscopic level. Ongoing work is investigating this assumption. It has been demonstrated in this study that the rheological behavior of the liver can be estimated locally over a large bandwidth of mechanical excitation. Dispersion curves estimated for all healthy volunteers give elasticity values at 50 Hz that are in total agreement with narrowband approaches (MR-elastography and Fibroscan[®]). At this particular frequency, all healthy volunteers were in the F0–F1 region as defined by state of the art ([Ziol et al. 2005](#); [Pinzani et al. 2005](#)). It would be extremely interesting to study the frequency dependence of these fibrosis scores boundary values. In particular, the elasticity values provided for the F2/F3 differentiation using MR-elastography and Fibroscan[®] are extremely close at 50 Hz. A clinical evaluation of shear wave spectroscopy for fibrosis staging should be conducted to estimate the evolution of these boundary elasticity values at higher frequencies, because it is anticipated that differentiation could be better at higher frequencies. Finally, different regions with a typical size of some millimeters can be estimated independently. The influence of the size of the selected region for the spectroscopic analysis is carefully studied in the paper by [Defieux et al. \(2008\)](#). This is therefore a very promising step toward the full mapping of the rheological properties of the liver.

Additionally, to such local shear wave spectroscopy a simplified approach can be used by estimating the local elasticity through a straightforward time-of-flight algorithm, leading to the determination of elasticity maps with a millimeter resolution. For such an imaging approach, the Young's modulus estimation is not as refined as in the previous spectroscopy case because the time-of-flight algorithm provides a shear group velocity corresponding to an averaged value in the case of a disper-

sive medium. The Young's modulus estimate corresponds to the value of the shear modulus at the central frequency of our broadband radiation force excitation. Results presented in Fig. 6, obtained on healthy volunteers, show that it is possible to discriminate higher elasticity regions such as the muscle regions. Such quantitative elasticity mapping could provide very useful information on the pathologic state of the liver *via* stiffness heterogeneity, as well as provide information on the presence of tumors.

Some technical limitations encountered during this feasibility study could be overcome to improve the results. One of the limitations of this study relies on the fact that *in vivo* experiments were conducted using a linear transducer array, implying that the full organ could not be scanned. Subcostal measurements were hard to perform using such a linear array because of the limited imaging depth. To improve this discrepancy, a curved array working at a lower ultrasonic frequency (~ 3 MHz) should be considered. This implies additional work because it requires the implementation of the ultrafast echographic modality for a curved array. Such easy technical improvements should considerably help for subcostal liver imaging to cover the full size of the liver.

Finally, one of the particularly interesting aspects of the SSI technique relies in its ultrafast imaging characteristics. The ability to reach frame rates up to 5000 frames/s removes the influence of the low-frequency displacements artefacts, such as respiratory motion or cardiac vibrations, which tend to degrade other approaches (Fahey et al. 2006, 2007). No significant influence of motion artefacts were seen during ultrafast acquisitions.

CONCLUSION

Quantitative mapping of liver tissue viscoelasticity is feasible *in vivo* using the SSI approach. By combining the use of ultrafast echographic imaging and the generation of remote and in-depth palpations using the acoustic radiation force induced by the echographic probe, it enables the overcoming of many limitations of elastographic techniques for liver applications. On the one hand, it is insensitive to respiratory motion artefacts. On the other hand, the generation of shear waves can be achieved in depth and consequently are not influenced by liquid barriers. Using the intercostal window, the SSI mode is able to generate shear wave fronts propagating through several centimeters of liver tissue and to monitor these shear waves *via* an ultrafast acquisition capability. Quantitative shear elasticity images were obtained *in vivo* on 15 healthy volunteers and a clear delineation between the Young's modulus value derived from shear group velocity for intercostal muscle ($E \approx 100$ kPa) and

normal liver ($E < 10$ kPa) is obtained. Elasticity images obtained in healthy volunteers are found to be quite homogeneous as expected and corresponding values are consistent with the literature. Moreover, a global mean elasticity of liver for fibrosis staging can be provided by averaging elasticity maps over very large areas (> 10 cm²). This estimation of this mean elasticity value is shown to be very repeatable and reproducible in healthy volunteers. Finally, the assessment of the mechanical behavior of liver tissues over quite a large bandwidth (typically 50 to 400 Hz) *via* the shear wave dispersion can be achieved *in vivo*, paving the way to a shear wave spectroscopy of liver tissues. This feasibility study clearly emphasizes the potential of the SSI approach for liver viscoelasticity imaging and the interest of a future clinical investigation.

REFERENCES

- Afdhal NH. Diagnosis fibrosis in hepatitis C: Is the pendulum swinging from biopsy to blood tests? *Hepatology* 2003;37:972–974.
- Aguirre DA, Behling CA, Alpert E, Hassanein TI, Sirlin CB. Liver fibrosis: Noninvasive diagnosis with double contrast material-enhanced MR imaging. *Radiology* 2006;239:425–437.
- Bataller R, Brenner DA. Liver fibrosis. *J Clin Invest* 2005;115:209–218.
- Beaugrand M. How to assess liver fibrosis and for what purpose? *J Hepatol* 2006;44:444–445.
- Bedossa P, Poinard T, Naveau S, Martin ED, Agostini H, Chaput JC. Observer variation in assessment of liver biopsies of alcoholic patients. *Alcohol Clin Exp Res* 1988;12:173–178.
- Bercoff J, Tanter M, Muller M, Fink M. The role of viscosity in the impulse diffraction field of elastic waves induced by the acoustic radiation force. *IEEE Trans Ultrason Ferroelectr Freq Control* 2004a;51:1523–1536.
- Bercoff J, Tanter M, Fink M. Sonic boom in soft materials: The elastic Cerenkov effect. *Appl Phys Lett* 2004b;84(12):2202–2204.
- Bercoff J, Tanter M, Fink M. Supersonic shear imaging: A new technique for soft tissues elasticity mapping. *IEEE Trans Ultrason Ferroelectr Freq Control* 2004c;51(4):396–409.
- Bravo AA, Sheth SG, Chopra S. Liver biopsy. *N Engl J Med* 2001;344:495–500.
- Cadranel JF, Rufat P, Degos F. Practices of liver biopsies in France: Results of a prospective nationwide survey. For the Group of Epidemiology of the French Association for the Study of the Liver. *Hepatology* 2000;37:477–481.
- Castera L, Negre I, Samii K, Buffet C. Pain experienced during percutaneous liver biopsy. *Hepatology* 1999;30:1529–1530.
- Castera L, Vergniol J, Foucher J, Brigitte Le Bail B, Chanteloup E, Haaser M, Darriet M, Couzigou P, de Lédinghen V. Prospective comparison of transient elastography, Fibrotest, APRI, and liver biopsy for the assessment of fibrosis in chronic hepatitis C. *Gastroenterology* 2005;128:343–350.
- Deffieux T, Montaldo G, Tanter M, Fink M. Shear wave spectroscopy for *in vivo* quantification of human soft tissues viscoelasticity. *IEEE Trans Med Imaging* 2008; in press.
- Fahey BJ, Nelson RC, Bradway DP, Hsu SJ, Dumont DM, Trahey GE. *In vivo* visualization of abdominal malignancy with acoustic radiation force elastography. *Phys Med Biol* 2008;53:279–293.
- Fahey BJ, Palmeri ML, Trahey GE. The impact of physiological motion on tissue tracking during radiation force imaging. *Ultrasound Med Biol* 2007;33:1149–1166.
- Fahey BJ, Palmeri ML, Trahey GE. Frame rate considerations for real-time abdominal acoustic radiation force impulse imaging. *Ultrasound Imaging* 2006;28:193–210.

- Friedman SL. Liver biopsies, from bench to bedside. *J Hepatol* 2003; 38(suppl1):S38–S53.
- Friedrich-Rust M, Ong MF, Herrman E, Dries V, Samaras P, Zeuzem S, Sarrazin C. Real-time elastography for noninvasive assessment of liver fibrosis in chronic viral hepatitis. *AJR Am J Roentgenol* 2007;188:758–764.
- Huwart L, Peeters F, Sinkus R, Annet L, Salameh N, ter Beek LC, Horsmans Y, Van Beers BE. Liver fibrosis: non-invasive assessment with MR-elastography. *NMR Biomed* 2006;19:173–179.
- Imbert-Bismut F, Ratziu V, Pieroni L, Charlotte F, Benhamou Y, Poinard T. Biochemical markers of liver fibrosis in patients with hepatitis C virus infection: A prospective study. *Lancet* 2001;357: 1069–1075.
- Ishak K, Baptista A, Bianchi L, Callea F, De Groote J, Gudat F, Denk H, Desmet V, Korb G, MacSween RN, Phillips MJ, Portmann BG, Poulsen H, Scheuer PJ, Schmid M, Thaler. Histological grading and staging of chronic hepatitis. *J Hepatol* 1995;22:696–699.
- Klatt D, Asbach P, Rump J, Papazoglou S, Somasunaram R, Modrow J, Braun J, Sack I. In vivo determination of hepatic stiffness using steady state free precession magnetic resonance elastography. *Invest Radiol* 2006;42:841–848.
- Konig CW, Trubenbach J, Fritz J. Contrast enhanced MR-guided biopsy of hepatocellular carcinoma. *Abdom Imaging* 2004;29:71–76.
- Maharaj B, Maharaj RJ, Leary WP, Cooppan RM, Naran AD, Pirie D, Pudifin DJ. Sampling variability and its influence on the diagnostic yield of percutaneous needle biopsy of the liver. *Lancet* 1986;1: 523–525.
- National Institute of Health Consensus Development Conference Statement. Management of Hepatitis C: June 2002. *Hepatology* 2002; 36[5 suppl 1]:S3–S20.
- Ono E, Shiratori Y, Okudaira T, Imamura M, Teratani T, Kanai F, Kato N, Yoshida H, Shiina S, Omata M. Platelet count reflects stage of chronic hepatitis C. *Hepatology* 1999;15:192–200.
- Ophir J, Cespedes I, Ponnekanti H, Yazdi Y, Li X. Elastography: A quantitative method for imaging the elasticity of biological tissues *Ultrason Imaging* 1991;13(2):111–134.
- Palmeri ML, Wang MH, Dahl JJ, Frinkley KD, Nightingale KR. Quantifying hepatic shear modulus in vivo using acoustic radiation force. *Ultrasound Med Biol* 2008;34:546–558.
- Patel K, Lajoie A, Heaton S, Pianko S, Behling C, Bylund D, Pockros P, Blatt L, Conrad A, Mchutchison J. Clinical use of hyaluronic acid as a predictor of fibrosis change in hepatitis C. *J Gastroenterol Hepatol* 2003;18:253–257.
- Pinzani M, Rombouts K, Colagrande S. Fibrosis in chronic liver diseases: Diagnosis and management. *J Hepatol* 2005;42:S22–S36.
- Regev A, Berho M, Jeffers LJ, Milikowski C, Molina EG, Pyrsopoulos NT, Feng ZZ, Reddy KR, Schiff ER. Sampling error and intraobserver variation in liver biopsy in patients with chronic HCV infection. *Am J Gastroenterol* 2002;97:2614–2618.
- Royer D, Dieulesaint E. Elastic waves in solids, vol. 1. Springer-Verlag, 2000.
- Saito H, Tada S, Nakamoto N, Kitamura K, Horikawa H, Kurita S, Saito Y, Iwai H, Ishii H. Efficacy of non-invasive elastometry on staging of hepatic fibrosis. *Hepatology* 2004;29:97–103.
- Sandrin L, Fourquet B, Hasquenoph JM, Yon S, Fournier C, Mal F, Christidis C, Ziol M, Poulet B, Kazemi F, Beaugrand M, Palau R. Transient elastography: A new non-invasive method for assessment of hepatic fibrosis. *Ultrasound Med Biol* 2003;29:1705–1713.
- Sarvazyan AP, Rudenko OV, Swanson SD, Fowlkes JB, Emelianov SY. Shear wave elasticity imaging: A new ultrasonic technology of medical diagnostics. *Ultrasound Med Biol* 1998;24(9):1419–1435.
- Stauber RE, Lackner C. Noninvasive diagnosis of hepatic fibrosis in chronic hepatitis C. *World J Gastroenterol* 2007;13(32):4287–4294.
- Suzuki A, Angulo P, Lymp J, Li D, Satomura S, Lindor K. Hyaluronic acid, an accurate serum marker for severe hepatic fibrosis in patients with non-alcoholic fatty liver disease. *Liver Int* 2005;25:779–786.
- Tanter M, Bercoff J, Athanasiou A, Deffieux T, Gennisson J-L, Montaldo G, Muller M, Tardivon A, Fink M. Quantitative assessment of breast lesion viscoelasticity: Initial clinical results using supersonic shear imaging. *Ultrasound Med. Biol* 2008;34.
- The French METAVIR Cooperative Study Group. Intraobserver and interobserver variations in liver biopsy interpretations in patients with chronic hepatitis C. *Hepatology* 1994;20:15–20.
- Wai, CT, Greenson JK, Fontana RJ, Kalbfleisch JD, Marrero JA, Conjeevaram HS, Lok AS. A simple noninvasive index can predict both significant fibrosis and cirrhosis in patients with chronic hepatitis C. *Hepatology* 2003;38:518–526.
- Yeh WC, Li PC, Jeng YM, Hsu HC, Kuo PL, Li ML, Yang PM, Lee PH. Elastic modulus measurements of human liver and correlation with pathology. *Ultrasound Med Biol* 2002;28(4):467–474.
- Ziol M, Handra-Luca A, Kettaneh A, Christidis C, Mal F, Kazemi F, de Lédinghen V, Marcellin P, Dhumeaux D, Trinchet JC, Beaugrand M. Noninvasive assessment of liver fibrosis by measurement of stiffness in patients with chronic hepatitis C. *Hepatology* 2005;41: 48–54.

Ultrafast imaging of *in vivo* muscle contraction using ultrasound

Thomas Deffieux,^{a)} Jean-Luc Gennisson, Mickaël Tanter, and Mathias Fink
Laboratoire Ondes et Acoustique, ESPCI, Université Paris VII, CNRS UMR 7587, 10 Rue Vauquelin 75005 Paris, France

Antoine Nordez
Laboratoire "Motricité, Interactions, Performance," JE 2438, UFR STAPS, Université de Nantes, Nantes Atlantique Universités, 25 bis Bd. Guy Mollet BP 72206, Nantes F-44000, France

(Received 7 July 2006; accepted 21 September 2006; published online 3 November 2006)

In this letter, an innovative way of imaging transient and local shear vibrations of an *in vivo* contracting muscle is proposed. The principle is to use an ultrafast ultrasound scanner (up to 5000 frames s^{-1}) able to follow with a submillimeter resolution the motion of the muscle tissue in a two dimensional plane. This ultrafast echographic imaging technique leads to both local and transient *in vivo* studies of the contraction of a muscle as reported by these first experiments done on the biceps brachii. © 2006 American Institute of Physics. [DOI: 10.1063/1.2378616]

Numerous monitoring techniques are commonly used to study muscular or neuromuscular function. Electromyography (EMG) is used to record the electrical activity of the muscle. It can be reported as the sum of action potentials propagating in a muscle's fibers.¹ Mechanomyography is the recording of the muscular vibrations produced by the active muscle. It can be used as a monitor of muscle stiffness and could be related to the muscle force production.² Unfortunately, all of these methods have a poor accuracy to assess local measurements and are thus not suitable for fully understanding the underlying structure and mechanical behavior of the muscle. In order to create maps of the local response of the muscle, a few techniques have been applied to reconstruct the local velocity distributions of the muscle in three or two dimensions (3D or 2D): phase-contrast magnetic-resonance imaging can reconstruct full 3D images of the muscle motion in a stroboscopic way. From these images local strains are calculated.³ Doppler tissue imaging gives the tissues' velocity distribution in a 2D plane and allows axial strain assessments.⁴ Recently, ultrasound image correlations at low frame rates have also been used to track the muscle motion.⁵ While very promising, these techniques can only image the muscle up to a few tens of frames per second. These low frame rates cannot be considered high enough to fully visualize the transient phenomena occurring during muscle activation.

Recently, ultrafast ultrasound scanners were designed by our group. Our last generation of echographic devices gives access to 2D radio frequency (rf) images at a few thousand hertz using a modified imaging sequence, i.e., a hundred times faster than any conventional ultrasound scanner. From these rf images, *B*-mode images are constructed. The cross correlation between two successive images permits us to assess the local axial particle velocity, and a complete movie of the axial velocity maps can be finally deduced. Such an approach allows us to provide both very high spatial (submillimetric) and temporal accuracy (less than a millisecond sampling), overcoming all the respective drawbacks of the previously cited techniques. This scanner⁶ is a 128 multi-channel fully programmable system driving any kind of con-

ventional ultrasonic probe. The sequence consists in emitting a single plane wave pulse. Ultrasonic echoes backscattered by tissue heterogeneities are then stored in memories. These ultrasonic raw data are processed in a posttreatment to create images with submillimetric resolution by applying a conventional beam formation (time delay and sum operations) in the receive mode. Finally, consecutive echographic images are compared using one dimensional cross correlation along the ultrasound beam axis in order to compute their axial relative displacements⁷ (note that "axial" terminology refers to the ultrasonic beam *z* direction and not to the fibers' main axis, see Fig. 1). This method enables us to measure relative displacements as low as 1 μm between two consecutive frames and thus gives an estimation of tissue local velocity.

To trigger the muscle contraction with the imaging system, surface neuromuscular electrostimulation was achieved. A homemade electrostimulation device composed of a function generator (Agilent, model 33220A, Palo Alto, CA, USA), a power amplifier (Brüel & Kjær, type 2718, Nærum, Denmark), and two noninvasive surface electrodes (Compex, Ecublens, Switzerland) were used. The cathode was placed on the motor point, localized by qualitatively looking for the maximum muscle excitation, and the anode was placed on the distal portion of the biceps. A 30 V amplitude, 400 μs

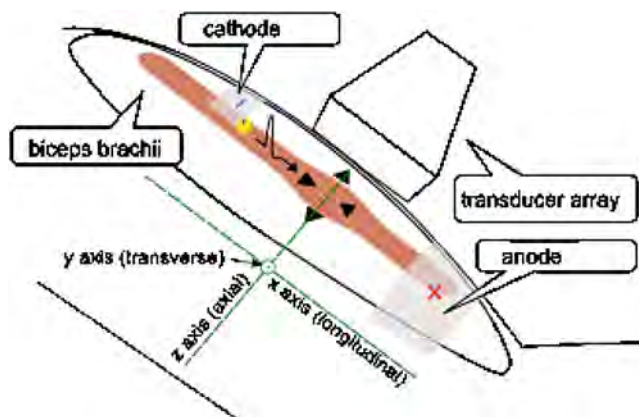


FIG. 1. (Color online) Measurement protocol. Muscle fibers were excited with neuromuscular electrostimulation on the motor point, and the axial displacements were acquired with the 2D ultrasound ultrafast scanner. Both the arm and the transducer array were strongly fixed to avoid movements.

^{a)}Electronic mail: thomas.deffieux@espci.fr

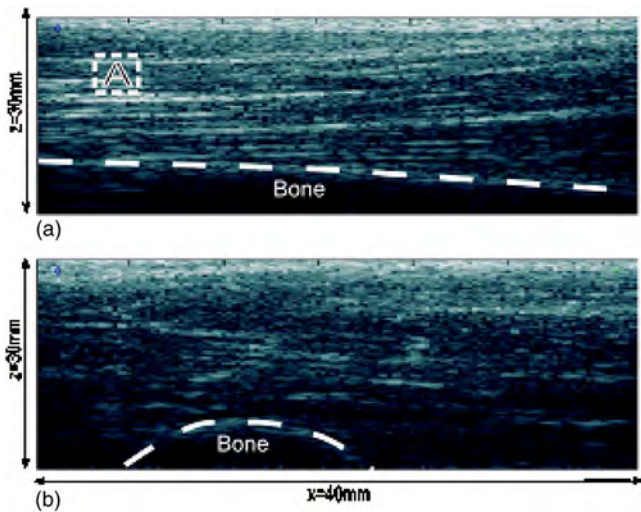


FIG. 2. (Color online) B-mode images of the muscle. Probe was either parallel (a) or perpendicular (b) to the fibers. The aligned fibers of the biceps brachii are clearly visible.

wide rectangular pulse was used to fire an action potential in the fibers just below the motor point (Fig. 1).

In our first experiments, a conventional 8 MHz transducer array was placed either parallel (longitudinal position) or perpendicular (transverse position) to the fibers' main direction in order to follow the contraction in different planes (Fig. 1). This means that the displacements seen were never those corresponding to the shortening of the fibers but rather those corresponding to their lateral widening.

After the acquisition of a conventional gray-scale echographic image (Fig. 2), the scanner took 500 images at 1500 Hz, and a movie of the axial velocity (Fig. 3) was computed. This movie was used to retrieve contraction and relaxation times and create maps of the maximum axial displacement. The average tissue velocity (cm/s) in the *in situ* region of interest A (Fig. 2) is plotted as a function of time (Fig. 4). Contraction time is taken as the positive part of the axial velocity (fiber bundles contracting and thus moving toward the probe), while relaxation time is the negative part (fiber bundles moving back to its original position). Contraction time is thus found to be around 58 ms and relaxation time around 120 ms, values that are consistent with the literature.⁸ The axial (*z* direction) displacements can be computed from the integration of the axial tissue velocity. De-

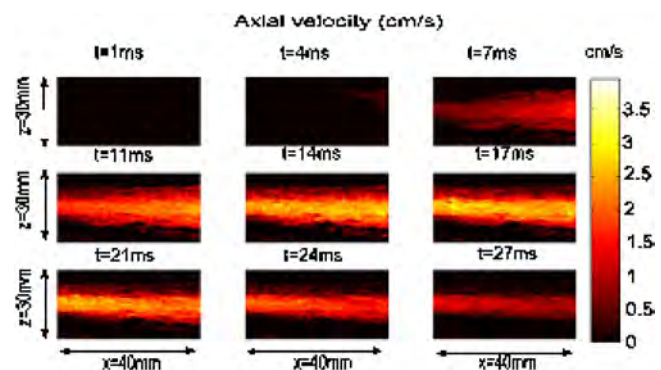


FIG. 3. (Color online) Movie of the axial velocity (cm/s). A 30 V amplitude, 400 μ s wide square pulse excitation on the motor point triggers the contraction. The contracting area can easily be visualized. The ultrasonic probe is placed parallel to the fibers; the imaging frame rate is set to 1500 Hz.

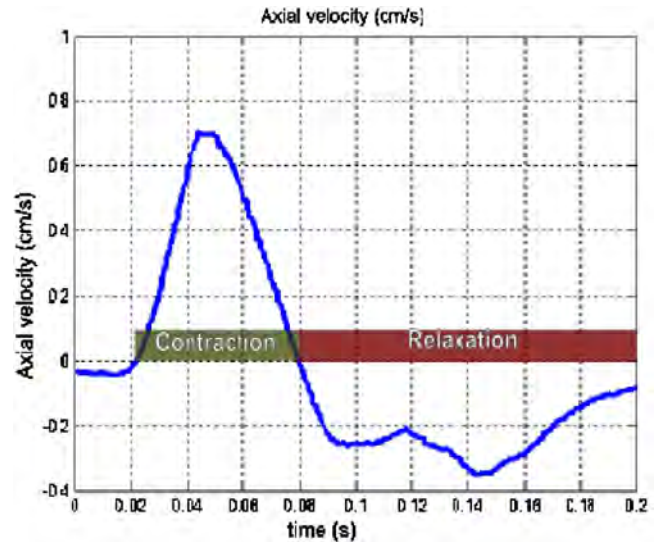


FIG. 4. (Color online) Axial velocity profile (cm/s) vs time (s) in region of interest A (Fig. 2).

tecting the maximum local displacements over time enables us to create maps of the contracting fiber bundles (Fig. 5).

To illustrate the temporal accuracy of the scanner, periodic excitations with different pulse repetition rates (from 5 to 20 Hz with 5 Hz steps) have been used and displacements computed inside a region of interest A (Fig. 2). Depending on the frequency of the excitation and as expected from surface EMG measurements but now for each point inside the muscle, temporal summation and tetany can be observed (Fig. 6). As the frequency of excitation rises, muscle fibers do not have the time to come back to their initial position and temporal summation occurs, leading to a stronger contraction.¹ When the sum of the contraction and relaxation times is less than the period of stimulation pulse, no temporal summation occurs (5 Hz). When the contraction time is less but the sum of the contraction and relaxation times is greater, oscillations can be seen (10 and 15 Hz). Finally, when the contraction time is greater than the period of excitation, the displacement is an increasing curve, reaching a maximum (20 Hz).

The ultrafast echographic imaging approach enables the assessment of the transient mechanical behavior of entire muscles with a millimetric resolution. From the acquisition of local axial tissue velocities of tissues over the entire organ, one can compute not only axial displacements but also axial strains by simply deriving the displacement field along

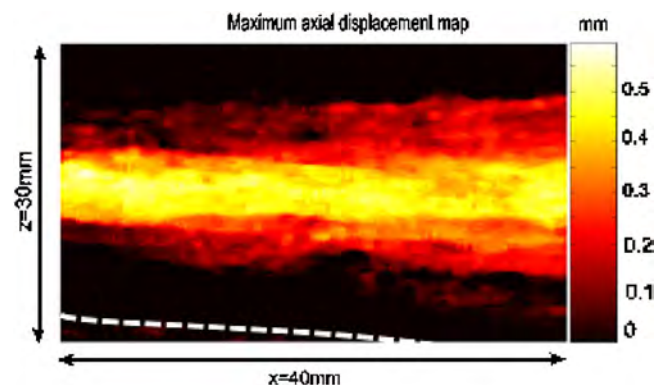


FIG. 5. (Color online) Maximum axial displacement map (mm).

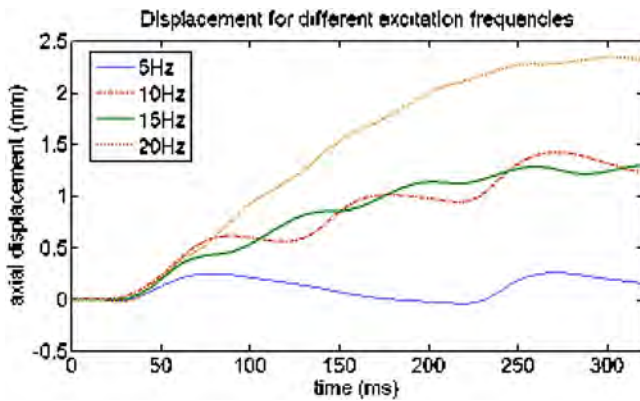


FIG. 6. (Color online) Displacement (mm) vs time (ms) in a region of interest for different excitation frequencies.

the z direction in a posttreatment step. It allows us to get rid of the global translational movements of the muscle. However, this operation is always sensitive to noise and do not discriminate active and passive movements.

Much beyond the visualization of strains, the spatial and temporal accuracies of the system will allow us to retrieve the exact localization of the contracting bundles. This requires us to recover the active displacement sources by solving the inverse source problem of the elastic wave propagation. Assuming the medium to be linear, homogeneous, isotropic, incompressible, and piecewise homogeneous, and considering only the null divergence terms (shear components), the elastodynamics equation⁹ describing the elastic wave propagation can be described as follows:

$$\rho \frac{\partial^2 \mathbf{u}}{\partial t^2}(\mathbf{r}, t) = \mu \Delta \mathbf{u}(\mathbf{r}, t) + \mathbf{s}(\mathbf{r}, t), \quad (1)$$

where ρ , μ , $\mathbf{u}(\mathbf{r}, t)$, and $\mathbf{s}(\mathbf{r}, t)$ represent density, Young's modulus, displacement fields, and the volumetric force source terms, respectively. Equation (1) requires the knowledge of Young's modulus (stiffness) as well as the longitudinal (x axis, along the fibers) and transverse (y axis, perpendicular to the imaging plane) displacements. Shear modulus has already been measured in the biceps brachii^{10,11} and also

shown to be transverse isotropic along fibers.¹⁰ Transverse displacements can thus be assumed to have the same order of magnitude as the measured axial (z axis) displacements. Moreover, longitudinal displacements along fibers could be computed using a synthetic aperture technique¹² already implemented on ultrafast echographic devices. Using this complementary information, the only remaining unknown is $\mathbf{s}(\mathbf{r}, t)$. The inverse source problem can be solved, permitting us to retrieve the localization of the transient sources of contraction inducing the global contraction of the muscle.

Using this ultrafast device, a high space and time resolution imaging of a transient *in vivo* muscle contraction was achieved. We were able to follow the contraction of the muscle and to extract both local and transient properties such as the contraction time, the relaxation time, or maps of the contracting areas. The ultrafast echographic scanner, coupled with an EMG device, will provide a powerful tool to understand the link between electrical and mechanical activities of the muscle and to study the spatial recruitment of fibers and its associated disorders such as fatigue and neuromuscular diseases.

¹J. V. Basmajian and C. De Luca, *Muscles Alive* (Williams and Wilkins, Baltimore, 1983), Vol. 1.

²T. W. Beck, T. J. Housh, J. T. Cramer, J. P. Weir, G. O. Johnson, J. W. Coburn, M. H. Malek, and M. Mielke, *Biomed. Eng. Online* **4**, 67 (2005).

³J. E. Drace and N. J. Pelc, *Radiology* **193**, 423 (1994).

⁴N. R. Grubb, A. Fleming, G. R. Sutherland, and K. A. Fox, *Radiology* **194**, 837 (1995).

⁵I. D. Loram, C. N. Maganaris, and M. Lakie, *J. Appl. Physiol.* **100**, 1311 (2006).

⁶L. Sandrin, M. Tanter, S. Catheline, and M. Fink, *IEEE Trans. Ultrason. Ferroelectr. Freq. Control* **49**, 426 (2002).

⁷J. Ophir, I. Céspedes, H. Ponnekanti, Y. Yasdi, and X. Li, *Ultrason. Imaging* **13**, 111 (1991).

⁸F. Buchtal and H. Schmalbruch, *Acta Physiol. Scand.* **79**, 435 (1970).

⁹L. M. Brekhovskikh and V. Goncharov, *Mechanics of Continua and Wave Dynamics* (Springer, Berlin, 1993), Vol. 1.

¹⁰J. L. Gennisson, S. Catheline, S. Chaffai, and M. Fink, *J. Acoust. Soc. Am.* **114**, 536 (2003).

¹¹J. Bercoff, M. Tanter, and M. Fink, *IEEE Trans. Ultrason. Ferroelectr. Freq. Control* **51**, 396 (2004).

¹²M. Tanter, J. Bercoff, L. Sandrin, and M. Fink, *IEEE Trans. Ultrason. Ferroelectr. Freq. Control* **49**, 1363 (2002).

Assessment of the Mechanical Properties of the Musculoskeletal System Using 2-D and 3-D Very High Frame Rate Ultrasound

Thomas Deffieux, Jean-Luc Gennisson, Mickaël Tanter, and Mathias Fink

Abstract—One of the great challenges for understanding muscular diseases is to assess noninvasively the active and passive mechanical properties of the musculoskeletal system. In this paper we report the use of ultrafast ultrasound imaging to explore with a submillimeter resolution the behavior of the contracting tissues *in vivo* (biceps brachii). To image the contraction, which is a very brief phenomenon (<100 ms), a recently designed ultrasound scanner prototype able to take up to 6000 frames/s was used. A very high frame rate from 1000 to 2500 frames/s was used to image the cross section plane of the muscle (transverse to fibers) enabling us to catch in real time the muscle contraction during a transient electrostimulation. Tissue velocities were obtained from radio frequency-based speckle tracking techniques and their profiles are discussed with respect to electrostimulation intensities and pulse repetition frequencies for different volunteers. Three-dimensional (3-D) very high frame rate movies were also acquired by repeating the experiment for different acquisition planes while triggering the imaging system with the electrostimulation device. The reconstructed 3-D velocity field allows the full localization of the contracting fibers bundle. This ultrasound technique, referred to as echo mechanomyography, offers new perspectives for *in vivo* and *in situ* noninvasive muscle diagnosis of an active contractile tissue.

I. INTRODUCTION

MEASUREMENT methods of muscle properties are of great clinical interest for physical therapists seeking to diagnose muscle diseases and plan accurate treatments. They are also very helpful to narrow the search for genetic disorders by improving the diagnosis [1].

Among these methods, some are specifically designed and are fully dedicated to the measurement of muscle functional properties, such as electromyography (EMG), which records the muscle electrical activity [2], and surface mechanomyography [3] (sMMG) or acceleromyography [4], which records pressure or acceleration on the skin surface during a contraction. Electromyography is a powerful tool to discriminate between neuromuscular and physiological disorders by recording the compound action potential with a needle electrode or by using surface electrodes. Presence at rest as well as size and shape of the action potentials are all key factors in the diagnosis of

a neuromuscular disease [2], especially neuropathies and myopathies.

Standard imaging techniques have also been applied and adapted to the muscle. They provide full anatomic as well as functional images of the muscle. Among them are mainly T1 and T2 weighted magnetic resonance (MR) imaging [5], MR spectroscopy [6], cine phase contrast MR imaging [7], MR elastography [8], Doppler imaging [9], and ultrasonography [10]. Although they provide valuable information on different functional parameters of the muscle, many of them, too expensive, are not yet used clinically and are still in an early research phase.

Based on the tissue velocity field estimation during contraction, cine phase contrast MR [7] or ultrasound Doppler [9] present new functional imaging techniques of the mechanical activity of a muscle and are thus complementary to electromyography which measures its electrical activity and a natural extension to mechanomyography which records the mechanical activity at the surface. Unfortunately, those techniques lack a good time resolution and can only image slow mechanical response of the muscle; therefore they are blind to transient phenomena occurring during a muscle contraction such as those recorded by EMG [11] or sMMG [12].

High frame rate ultrasound techniques (>100 Hz) are able to track small displacements noninvasively with both good spatial and good temporal resolutions. In 2004, Witte *et al.* conducted an experiment with a single ultrasound element on an electrostimulated *ex vivo* rat muscle, demonstrating the use of radio frequency (RF)-based speckle tracking techniques to record an *in situ* contraction with a high sampling rate [13]. In 2006, another experiment was devoted to the role of fatigue with the imaging of an *in vivo* contraction of the flexor digitorum superficialis muscle with an iU22 scanner able to reach 320 images per second [14]. Also in 2006, Deffieux *et al.* published a proof of concept paper demonstrating the feasibility of using ultrafast ultrasound imaging to track the *in vivo* contraction of the biceps brachii [15]. Beyond tetanization or fatigue study, this approach results in both localization of the contracting fiber bundle and extraction of the temporal profile of the tissue velocity field inside the contracting fiber bundle. This technique was named echo mechanomyography (eMMG) in reference to surface mechanomyography (sMMG).

In the present paper, we aim to consolidate these findings and investigate the repeatability of eMMG with a

Manuscript received August 13, 2007; accepted February 29, 2008.

The authors are with the Laboratoire Ondes et Acoustique, ESPCI, CNRS UMR 7587, INSERM, Université Paris VII, 75231 Paris Cedex 05, France (e-mail: thomas.deffieux@espci.fr).

Digital Object Identifier 10.1109/TUFFC.917

new ultrafast ultrasound scanner. Based on research on transient elastography [16], our new ultrafast ultrasound scanner prototype can store up to 1000 ultrafast echographic frames with a framerate ranging from 500 up to 20,000 frames/s. The acquisition is synchronized with an electrostimulation device. The contraction can thus be fully imaged and its associated tissue velocity field recorded in a region of interest (ROI) of the image. The maxima of the tissue velocity field perpendicular to the fiber muscle are found to be a quadratic function of the stimulation amplitude.

An experimental setup is also proposed enabling a three-dimensional (3-D) acquisition of the velocity field, providing a much better spatial localization of the contracting fiber bundle. The feasibility of this imaging technique is demonstrated *in vivo* and discussed, as well as the results and the difficulties of these preliminary sets of experiments. Finally, *in vivo* assessment of the propagation speed of mechanical tissue displacements induced by transient electrostimulations was measured in healthy volunteers ($v \approx 4 \text{ m.s}^{-1}$) and compared with the propagation speed of shear waves induced in the same area using a remote ultrasonic radiation force (v ranging from 2.5 m.s^{-1} at rest to 5 m.s^{-1} for a 4 kg loading).

By adding information on the mechanical response of the muscle, we hope that the technique can turn into a powerful tool complimentary to electromyography and can extend surface mechanomyography, resulting in a measuring technique taking into account the whole command-response chain of the muscle system *in situ*.

II. MATERIALS AND METHODS

A. Muscle

Experiments were focused on the biceps brachii, a muscle of the arm controlling elbow flexion as well as wrist

supination. The biceps lies just under the skin and is innervated by the musculocutaneous nerve. Its motor point, the nerve entry into the muscle, is usually located midway of the muscle, between the shoulder and the elbow (Fig. 1).

Muscle contraction is a complex electromechanical phenomenon, which is controlled by the nervous system. An action potential propagating along a motoneuron of the nerve is chemically transmitted to a muscle fiber at the neuromuscular junction. Each motoneuron can control several muscle fibers constituting a single motor unit. The transmitted action potential then propagates along the muscle fiber membrane, the sarcolemma, and initiates an entry of calcium ions into the muscle fiber cytoplasm [17]. The calcium then binds to the troponin-tropomyosin molecules allowing myosin molecules to freely interact with actin, an interaction that develops force (Fig. 2). Calcium is then pumped out of the cell, and adenosine triphosphate (ATP) is used to reset the actin-myosin complex to its initial state [18]. Contraction propagates along a muscle fiber with the action potential at a few meters per second, as measured by the muscle fiber conduction velocity (MFCV) technique [11], a special mode of electromyography.

The whole contraction process lasts less than one hundred milliseconds depending on the fiber type [19]; it is thus very difficult to image as a single mechanical event by traditional imaging techniques, although it can easily be electrically recorded by an electromyography system (single motor unit action potential recording) or surface mechanomyography.

B. Imaging Device

The technique is based on the use of an ultrafast scanner coupled with an electrostimulation device. The elec-

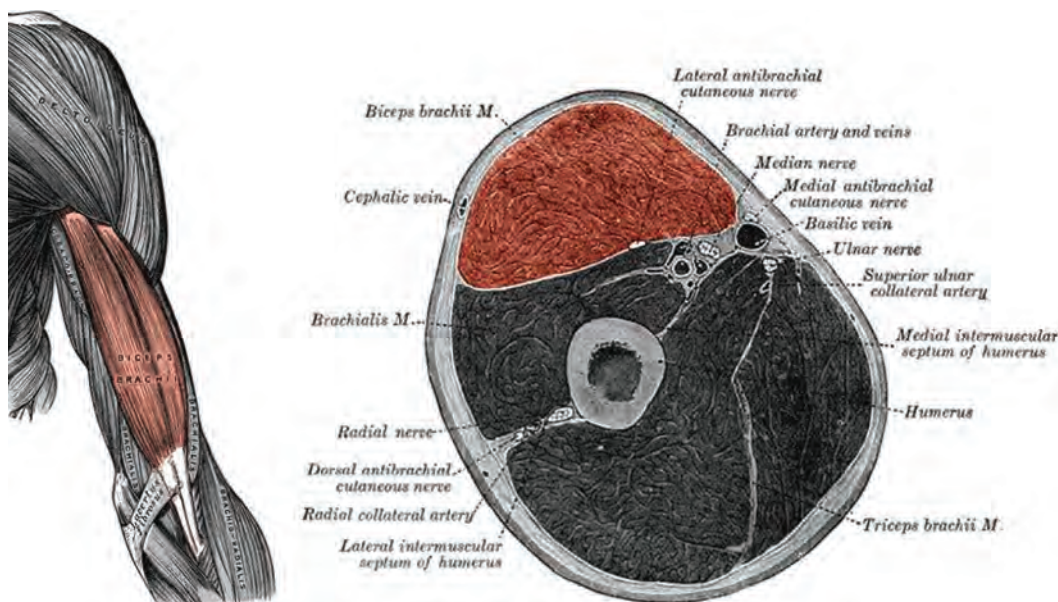


Fig. 1. Anatomy of the arm. In the online version, the biceps brachii is highlighted in red. The image was taken from the 1918 edition of *Gray's Anatomy*.

trostimulation device is used to allow a perfect synchronization of the contraction with the acquisition. Moreover, the electrostimulation device allows a repeat of the acquisition under the same conditions, enabling a stroboscopic 3-D scan as well as evaluation of the repeatability.

The ultrasonic scanner used for these measurements is a prototype designed by SuperSonic Imagine Company (Aix en Provence, France) for clinical trials of the supersonic shear imaging technique (an imaging technique capable of indicating the shear modulus of *in vivo* tissue and based on the coupling between ultrafast echographic sequences and remote palpation induced by the ultrasonic radiation force [20]). This scanner offers a medical grade image quality, ultrafast imaging as well as a Matlab api (The MathWorks, Inc., Natick, MA) and has been approved for clinical trials. This scanner was coupled with a 5 Mhz linear transducer array (4 to 7 MHz bandwidth; L7-4, ATL, Seattle, WA).

Applying ultrasound imaging to the acquisition of the muscular contraction requires mainly 3 conditions:

- A submillimetric resolution to obtain good image quality and good localization of structures inside the muscle; this is generally achieved by all conventional ultrasound scanners.
- A high frame rate to track the modification of the muscle in a very short period of time during the contraction (lasting less than 100 ms). This translates into frame rates higher than 200 Hz (for 20 samples). Very high frame rates (>500 Hz) improve the sampling time, enabling more accurate measurements of contraction and half relaxation times. This is also required in order to measure the velocity of the propagation of the contraction, which is expected to follow the muscle fiber conduction velocity close to 4 m/s [11]. A propagation distance of about 2 cm results in a time delay of 5 ms from end to end and as such requires at least 2000 Hz for a delay of 10 samples.
- A micrometer sensitivity to displacement between consecutive ultrasound images. For high frame rates, displacements appear smaller requiring higher accuracy in their measurements. It is also possible to correlate nonconsecutive ultrasound images to reach a lower frame rate to increase the apparent amplitude of the displacements; however, this operation is similar to that of a low pass filter [21]. In practice, we use consecutive images keeping the full bandwidth of the acquired signal.

The physical principle behind ultrafast imaging is to reach very high frame rates by using plane wave insonifications of the medium instead of the conventional line per line focusing techniques. Single plane wave insonifications are known to decrease the B-mode image quality but allow much higher frame rates because only one transmit step is needed to build a full image.

Backscattered signals are then directly stored in the device's memories, and images are reconstructed in a post-

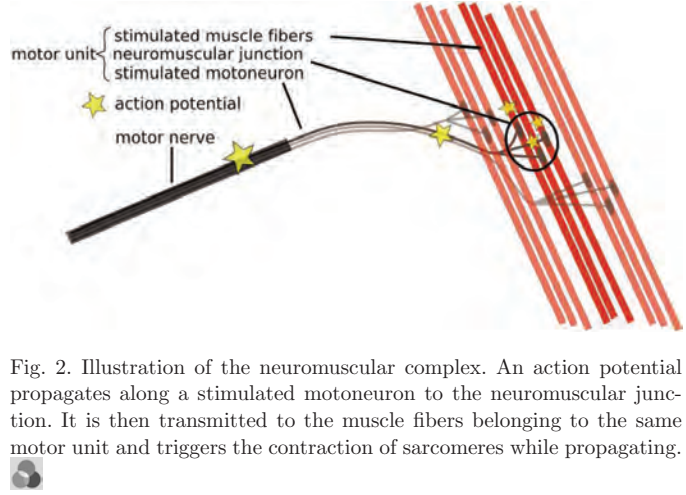


Fig. 2. Illustration of the neuromuscular complex. An action potential propagates along a stimulated motoneuron to the neuromuscular junction. It is then transmitted to the muscle fibers belonging to the same motor unit and triggers the contraction of sarcomeres while propagating.

processing step using a conventional beamforming technique, that is to say, applying a time delay operation to compensate for the travel times differences.

The velocity field is then estimated from 2, usually consecutive, frames by applying one-dimensional cross-correlations of windows of the RF signal along the beam axis (RF signals are sampled at a much higher sampling rate and thus feature a much higher precision than the envelope signal), a technique known as RF-based speckle tracking [22]. The scanner performs an automatic In phase (I) and Quadrature (Q) demodulation of the acquired signals at the central frequency:

$$S_i(x, t) = I_i(x, t) \times \cos(\omega_{ust}) + Q_i(x, t) \times \sin(\omega_{ust}), \quad (1)$$

where S_i is the conventional beamformed ultrasound signal (t being along the beam axis and x along the transducers), and I_i and Q_i represent the In phase and Quadrature demodulated and beamformed signals as stored by the scanner for the i^{th} image. At the same time, the RF-based speckle tracking step is directly implemented as a phase shift $d\phi$ estimation along the beam axis between 2 ultrasound images:

$$d\phi_{i \rightarrow i+k}(x, t) = \frac{1}{\omega_{us}} \tan^{-1} \left(\frac{\mathbf{Q}_i(x, t)\mathbf{I}_{i+k}(x, t) - \mathbf{I}_i(x, t)\mathbf{Q}_{i+k}(x, t)}{\mathbf{I}_i(x, t)\mathbf{I}_{i+k}(x, t) + \mathbf{Q}_i(x, t)\mathbf{Q}_{i+k}(x, t)} \right), \quad (2)$$

where the phase shift $d\phi$ can be computed from the In phase and Quadrature signals for the i^{th} and the $i+k^{\text{th}}$ images. When higher accuracy is required and time sampling is not critical, the lag k between the ultrasound images can be increased; the result is then equivalent to a high sampled signal but filtered with a low-pass sliding window. In practice, we used consecutive images ($k = 1$), keeping the original bandwidth of the signal. One can then estimate the z component of the tissue velocity field V_z from the phase shift $d\phi$ between successive images:

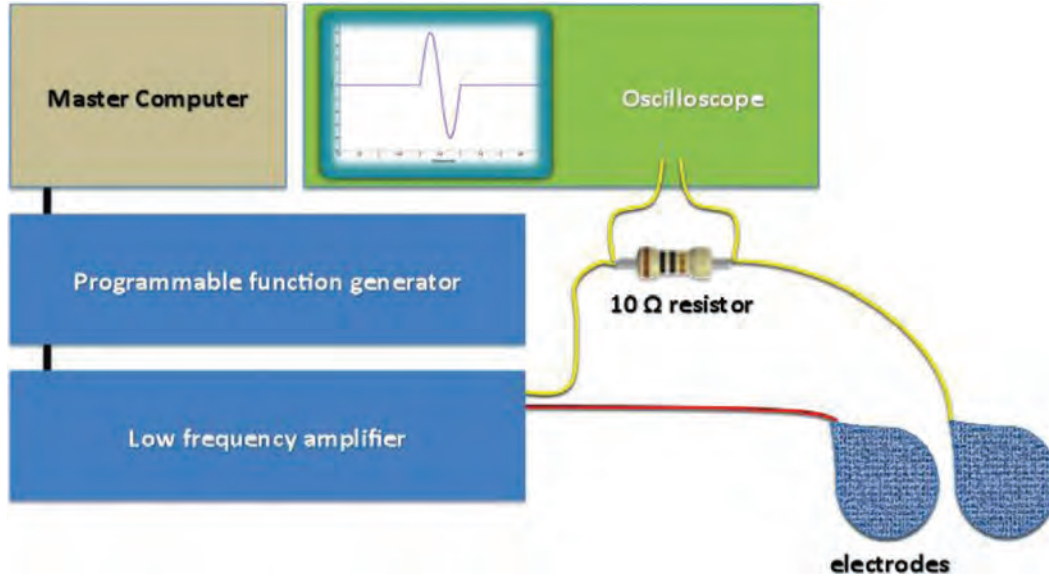



Fig. 3. Schema of the electrostimulation setup. The programmable function generator's output is connected to a low frequency amplifier, which is directly connected to the electrodes. The monitoring of the tension of a 10 Ω resistor in series allows a check of the intensity used. Electrodes are positioned on the biceps brachii, one over the motor point and one near the elbow. 

$$V_z(x, z, i) = \frac{1}{2} \times \frac{d\varphi_{i \rightarrow i+k}(x, t)}{2\pi} \times \lambda_{us} \times \frac{F_{im}}{k}, \quad (3)$$

where λ_{us} is the ultrasound wavelength, $z = c_{us} \cdot t$ is the depth, F_{im} is the imaging frame rate, and k is the lag between compared images.

One can notice that the measured tissue velocity field V_z is only the component parallel to the beam axis z of the true tissue velocity vector V and that a displacement superior to half the wavelength ($d\phi > 2\pi$) requires unwrapping. The high frame rate enables us to track smaller movements but also to record higher frequency signals more accurately, thanks to an increased sampling rate.

C. Electrostimulation Device

An electrostimulation device was used to trigger the contraction in order to enhance repeatability, synchronization, and better overall control over a voluntary contraction (Fig. 3). The electrostimulation was set up to be triggered by the imaging device through a standard TTL entry, thus avoiding any additional delay in the experimental setup. The electrostimulation device was composed of a programmable function generator (Model 33220A; Agilent Technologies, Inc., Palo Alto, CA) controlled by a computer through a GPIB interface, a low frequency amplifier (Type 2718; Brüel & Kjær, Nærum, Denmark), an oscilloscope (Tectronix, Inc., Dyersburg, TN), and a pair of noninvasive surface electrodes. Electrical pulse duration was set to 1 ms. A 10 Ω resistor was put in series with the electrodes and its tension was visualized on the oscilloscope to measure the corresponding intensity.

Electrodes had to be carefully placed to excite the nerve on the motor point of the biceps brachii, a well-innervated

region of the muscle where contraction is maximal for a given excitation. Applying an electric stimulation on the motor point leads to the depolarization of some motor axons of the nerve. An action potential is then generated in each excited axon and propagates to the end motor plates of the axon where it is transmitted to associated muscle fibers. Each axon is connected to several adjacent muscle fibers forming a single coherent motor unit. The transmitted action potential propagates on the surface of each excited muscle fiber and makes it twitch, resulting in a short and small contraction of the fiber (Fig. 2). Depending on the number of recruited motor units and their firing rate, different contraction strengths can be generated. That being said, electrostimulation is always heavily dependent on the position of the electrodes and the muscle state regarding its efficiency and localization [23].

To fine-tune the electrostimulation, the voltage was gradually incremented and the local tissue velocity analyzed as a function of time and current values; all of these measurements have been fully automatized through the use of the GPIB interface. Voltages used were typically around a few volts (corresponding to a few mA), a trade-off between signal-to-noise ratio in the velocity field and the locality (to avoid excitation of many motor units resulting in a large contraction). In these experiments, we tried to have a small excitation corresponding to the activation of a few motor units while keeping a reasonable signal-to-noise ratio.

Since the muscle is also a viscoelastic medium [8], [24], a dilatation of one area compresses the surrounding tissue according to the boundary conditions (bone, skin, tendon, or other soft tissues) resulting in a complex tissue velocity field. Smaller contractions enable us to avoid most of the hard boundary conditions and remain local. However, all hard boundary effects could not be avoided and a twist of

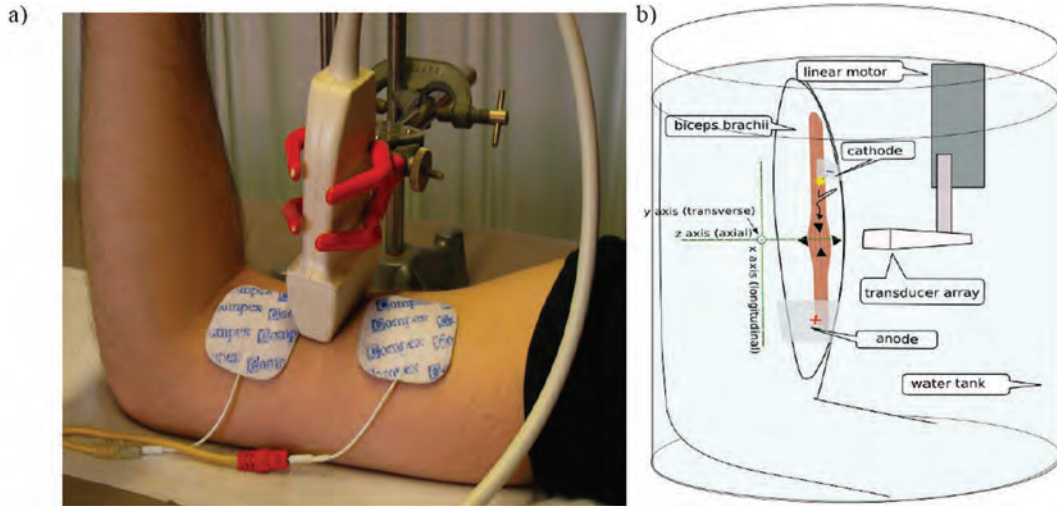


Fig. 4. Experimental setup for a 2D single acquisition (a) or a full 3-D scan (b). The imaging probe is positioned perpendicular to the muscle fibers in both cases and can be translated in the 3-D case. A few-millimeter layer of gel was inserted between the probe and the muscle to avoid contact during contraction.

the excited muscle fiber is visible in most experiments and will be discussed later.

D. Experimental Setups

A master computer controls both the imaging device and the electrostimulation device. Running the ultrafast imaging sequence automatically launches the electrostimulation device through a hardware trigger. The probe was always positioned perpendicularly to the bone, meaning the imaging plane was a transverse cross section in regard to the fiber's main axis [Fig. 4(a)].

As noted previously, the measured tissue velocity corresponds only to the component parallel to the ultrasound beam axis of the true tissue velocity vector. This means that the measured tissue velocity was always perpendicular to the bone and thus perpendicular to the muscle fibers. However, a contracting fiber is naturally shortening in its longitudinal direction, thus mainly creating a displacement of the tissue in the longitudinal direction, a displacement that cannot be imaged precisely by our system. Fortunately, while contracting, the fiber also happens to grow in diameter explaining why a muscle increases in diameter when contracting. The empiric law linking the lateral stretch to the longitudinal stretch can be written [25]:

$$\lambda_{\text{lateral}} = \frac{1}{\sqrt{\lambda_{\text{longitudinal}}}}. \quad (4)$$

The first set of experiments was dedicated to a single twitch while slowly increasing the stimulation amplitude. The experiment was then repeated on 3 healthy volunteers and the repeatability discussed. As a true imaging technique, geometrical and spatial extension can be fully visualized. Contraction and relaxation times were also extracted for each volunteer and their physiological meaning

discussed. The imaging sequence was set to 1000 frames per second for 300 images.

In a second experiment, the electrostimulation pulse repetition was increased to induce a tetany of the muscle. The velocity profiles were then extracted for each frequency. For this experiment, 1000 images were acquired at 1000 frames per second.

Finally, a 3-D setup was also developed and tested to allow the imaging of the whole contracting bundle and follow any propagation that could occur along the fiber axis (Fig. 4). To perform such a scan of the biceps brachii, we used a linear motor (Micos; SMC Pollux, Freiburg, Germany) moved along the bone axis and took an ultrafast acquisition in the transverse plane at each position [Fig. 4(b)]. Ultrafast acquisitions were performed at 2000 or 2500 frames/s and was set up to trigger the electrostimulation device. The electrical stimulation was thus repeated for each position and a 3-D movie of the contraction was computed.

III. RESULTS

A. Electrostimulation Amplitude and Recruitment

1. *Measurement of Tissue Velocity Profile:* We tried to keep the excitation as small as possible to have only a small region of the biceps contracting and to keep a local response, thus avoiding boundary conditions and complex movements of the muscle. Transverse images show a good localization of the maximum of the contracting fiber bundle that will lay the grounds for the 3-D tracking of the contracting fiber bundle. The velocity profile was extracted from the mean inside a $3 \times 3 \text{ mm}^2$ square positioned as close as possible to the maximum [Fig. 5(a)]. The measured intensity through the resistor also happens to follow the voltage meaning that the skin impedance

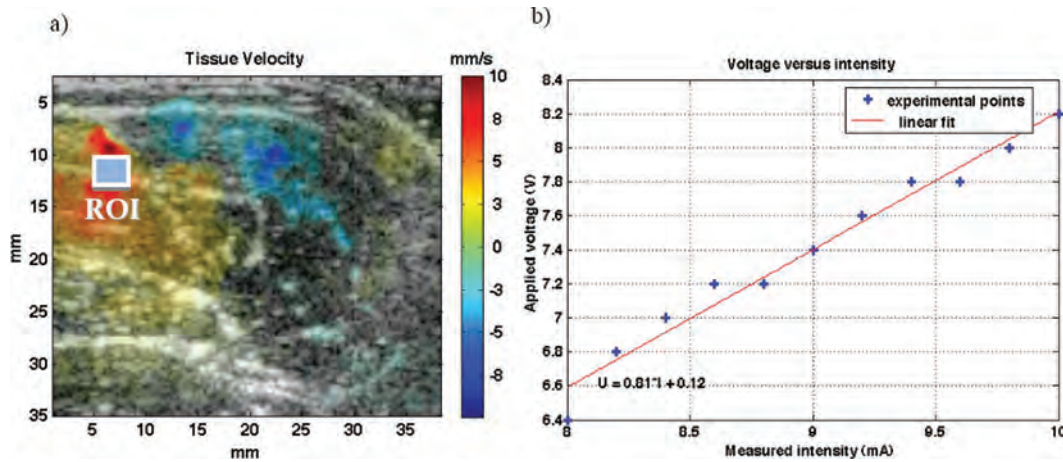


Fig. 5. (a) Tissue velocity field in a transverse image of the biceps brachii 14 ms after an 9 V (11 mA) electrostimulation. An approximately 3×3 mm² region of interest (ROI) is defined around the maximum. (b) Measured intensity versus applied voltage shows a quasi-constant impedance of approximately 810 Ω .

did not change much for a given position of the electrodes [Fig. 5(b)].

2. Repeatability of Tissue Velocity Profile: To estimate the repeatability of a single electrostimulation experiment, 30 acquisitions were done with fixed amplitude (9 V) without changing the electrodes or imaging probe positions (Fig. 6).

The maximum is found to be $2.9 \text{ mm/s} \pm 0.2 \text{ mm/s}$ (relative error of 6%) and the minimum at $-0.9 \text{ mm/s} \pm 0.1 \text{ mm/s}$ (relative error of 11%). This standard deviation is relatively low considering the *in vivo* nature of the measurements, amplified by the highly nonlinear behavior of the muscle as well as the electrostimulation strength variation. It is also not clear if the subject's ability to contract its own muscle can interfere, consciously or not. Although

repeatability seems rather good, we expect reproducibility to be much lower particularly due to the position of the arm and the placement of the electrodes.

3. Influence of Stimulation Amplitude: Slowly incrementing the voltage of the electrostimulation device, the velocity field induced by the contraction was recorded. Results show that the velocity, as expected, gradually increases with the voltage, thus showing that more and more motor units are recruited [26] (Fig. 7). The *in situ* tissue velocity curves also illustrate the threshold effect of the excitation found to be around 10 mA for each volunteer.

Interestingly, maximum tissue velocity seems to depend on the square of the stimulation amplitude (Fig. 8); however, more data are needed to confirm this hypothesis. The stimulus threshold appears at 7.7 V corresponding

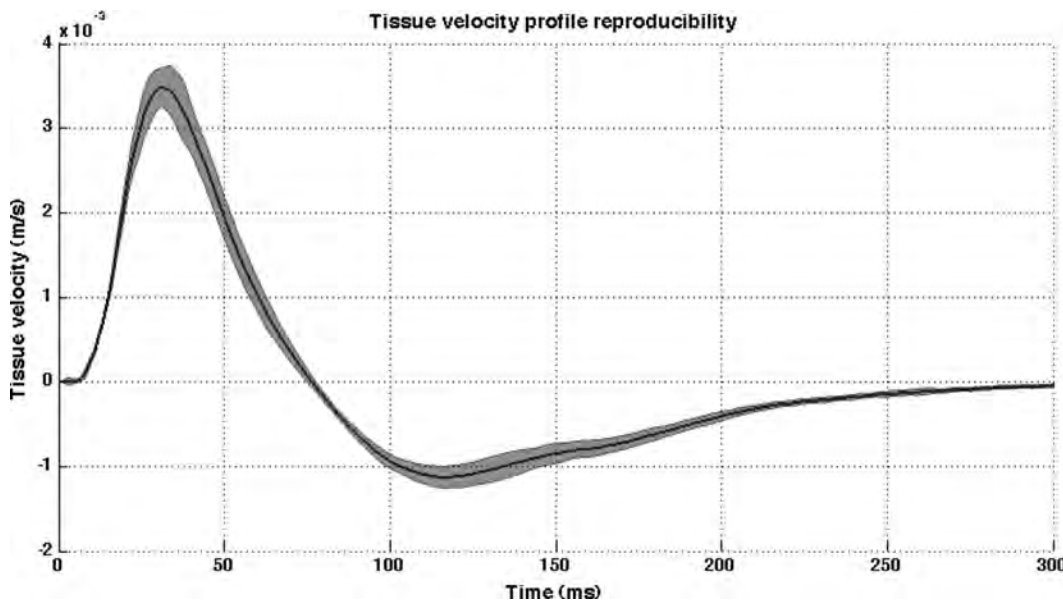


Fig. 6. Tissue velocity profile: mean of the 30 acquisitions with its standard deviation envelope. The relative error is approximately 10% at peak velocities. Total duration of these 30 acquisitions was approximately 5 min (Volunteer #2).

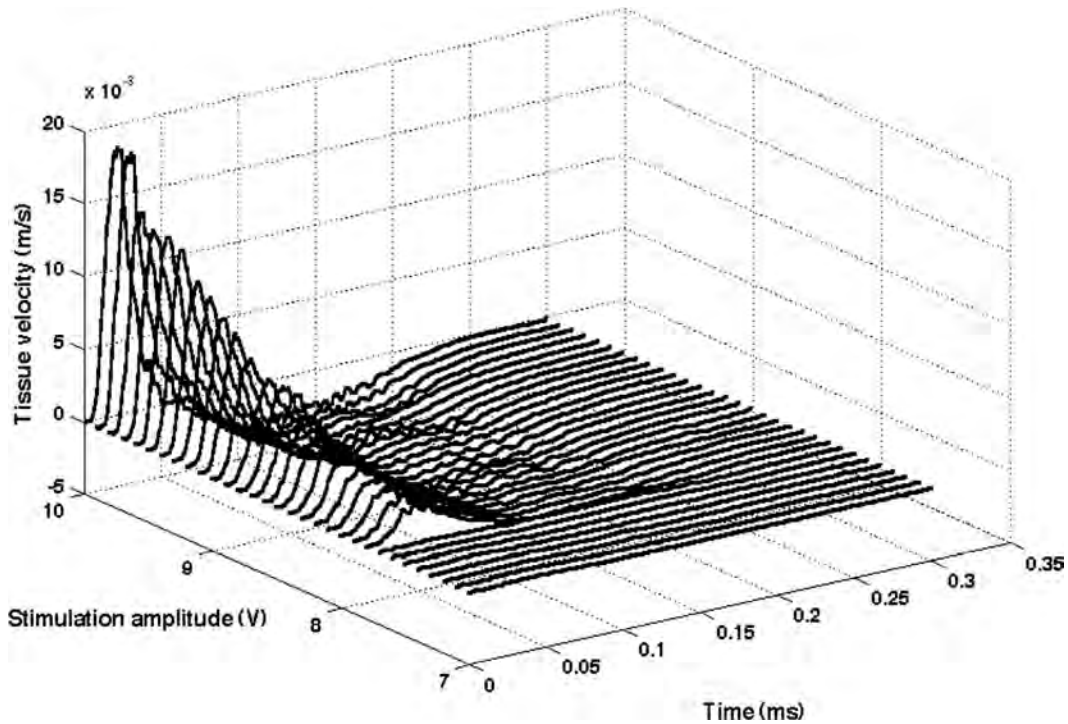


Fig. 7. Tissue velocity field versus time and stimulation amplitude. Amplitude is progressively increased from 7 to 10 V by a 0.1 V step (corresponding roughly to 8.5 mA to 12.5 mA with a 0.1 mA step). The threshold of contraction is visible for a 8 V stimulation (approximately 10 mA).

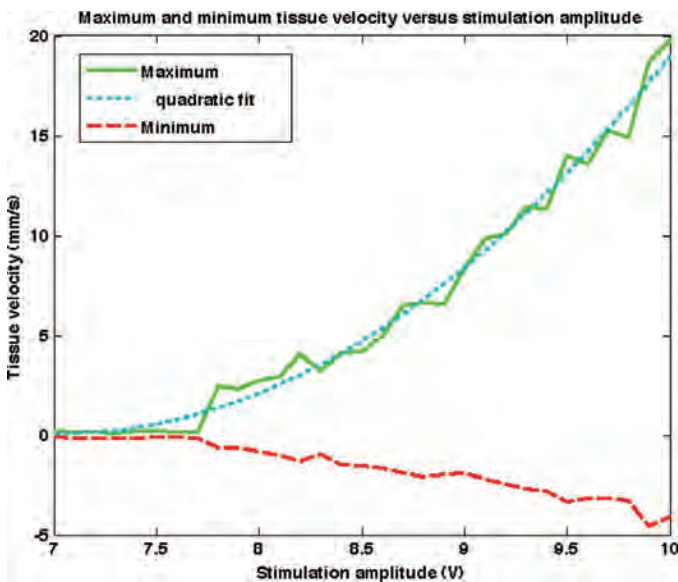


Fig. 8. Maximum and minimum of the tissue velocity field versus stimulation amplitude. A quadratic fit has been added (Volunteer #2).

here to 10 mA. The extracted tissue velocity profiles are very close to those obtained for typical surface mechanomyograms [12].

4. *Inter-Subject Comparison:* Measurements on 3 healthy volunteers show that the behavior is similar among all subjects, and tissue velocity field is roughly in the same range (Fig. 9). However, there seem to be differences in maximum tissue velocity field as well as on the threshold value. We speculate that these differences

have, again, more to do with electrostimulation parameters [23] (mainly position) than physiological differences of the muscles.

B. Contraction and Relaxation Times

1. *Definition of Characteristic Times:* By extracting the velocity field in a region of interest (ROI) corresponding to the tracked fiber bundle, it is possible to display the temporal profile of the velocity field along the muscle fiber bundle (Fig. 10). This representation illustrates the contraction and its amplitude. Temporal features can also easily be extracted, such as the contraction time (when velocity is positive) and relaxation time (when velocity is negative). To do that we define characteristic points on the velocity profile.

Extraction of these characteristic points has been done through a simple procedure: first maximum and minimum of the velocity profile is computed. The start point is found thanks to a threshold on the curve and the last point is defined as half relaxation time.

2. *Repeatability of Characteristic Times Measurement:* Repeatability is first investigated on 30 successive acquisitions with the same stimulation amplitude; characteristic times are extracted and their standard deviations computed (Table I).

Using ultrafast imaging allows an increase in the time resolution and an improvement in the overall quality of these measurements. One can also define the contraction and half relaxation times as the part when the tissue velocity is positive and negative, respectively ($T_{\text{contraction}} =$

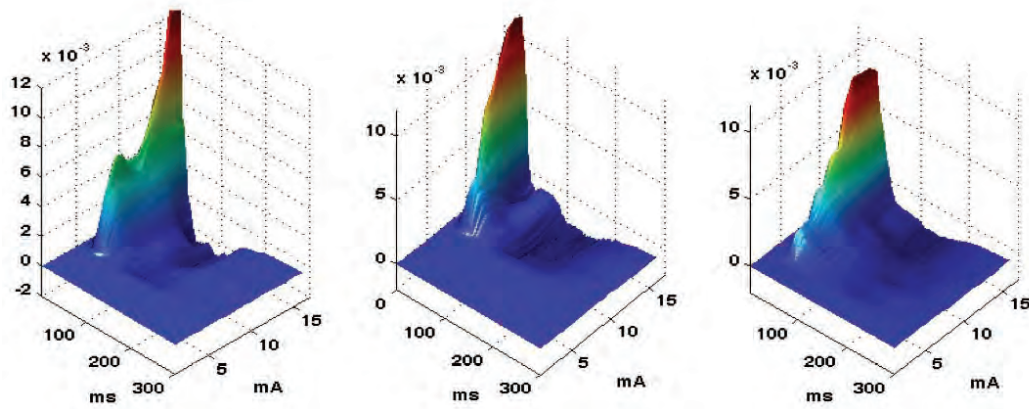



Fig. 9. Inter-subject comparison (3 volunteers) of the tissue velocity field versus time and electrostimulation intensity. 

$T_{\text{zero crossing}} - T_{\text{start}}$, $T_{\text{relaxation}} = T_{\text{half min}} - T_{\text{zero crossing}}$). The contraction and half relaxation times found in the current study match results from the literature [10] for *in vitro* surface mechanomyograms [12] or results from *in vivo* surface mechanomyograms [19].

3. Influence of Stimulation Amplitude on Characteristic Times: The influence of the stimulation amplitude on the characteristic times was investigated (Fig. 11).

The characteristic times do not depend much on the stimulation amplitude, which should thus make their measurements more robust to the electrodes positions. On the measurable part of the graph (where tissue velocity is high enough), their values are respectively 6.2 ± 1.3 ms, 27.2 ± 4.1 ms, 69.1 ± 8.8 ms, 110.7 ± 4.7 ms and 192.5 ± 12.6 ms.

4. Inter-Subject Comparison: Ten acquisitions were done on the biceps brachii of 3 healthy volunteers using the same setup. Contraction and half relaxation times were then extracted as well as their standard deviation (Table II).

No significant differences can be noted among the 3 healthy volunteers' contraction and half relaxation times (differences are within the standard deviation range). However, comparing results of the 2 different sets of measurements on volunteer #2 (Tables I and II) together with the independence of electrostimulation amplitude and characteristic times suggest that reproducibility should be reasonable. Those measurements demonstrate *in vivo* and *in situ* measurements of the mechanical contraction and half relaxation times in a human biceps brachii. Contraction and half relaxation times correlate well with sur-

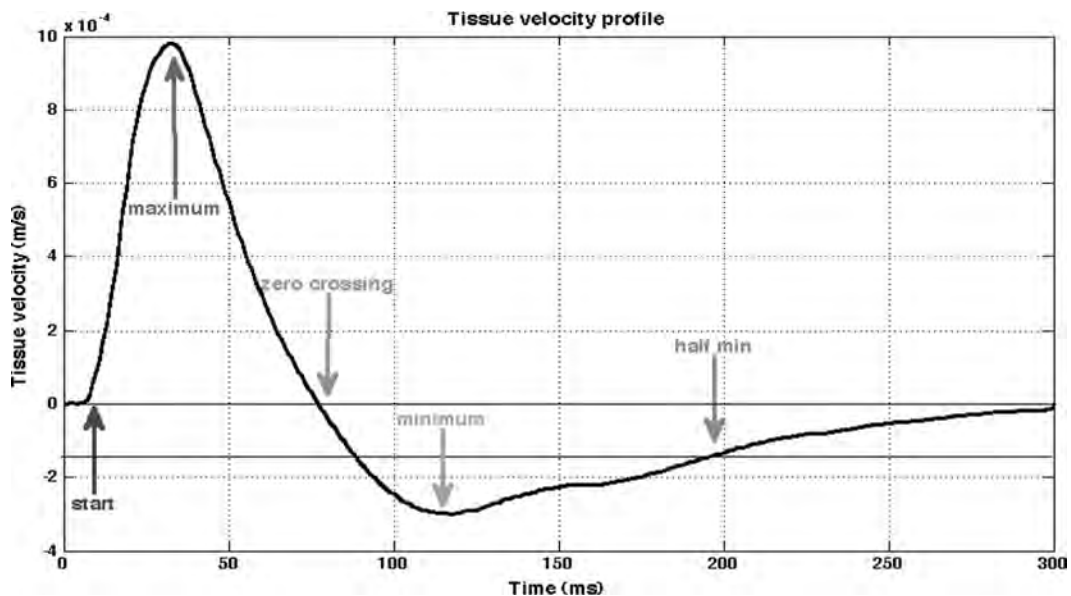


Fig. 10. Example of tissue velocity profile and definition of the extracted points (Volunteer #2).

TABLE I. REPEATABILITY OF MEASUREMENTS OF CHARACTERISTIC TIMES AND STANDARD DEVIATION (VOLUNTEER #2).

	Start	Maximum	Zero crossing	Minimum	Half min	Contraction	Half relaxation
Mean (ms)	7.1	30.4	77.2	115.4	182.3	70.1	105.2
Standard deviation (ms)	1.2	3.2	1.6	7.8	11.3	2	11

TABLE II. MEASUREMENTS OF CONTRACTION AND HALF RELAXATION TIMES AND STANDARD DEVIATION ON THREE HEALTHY VOLUNTEERS.

	Volunteer #1	Volunteer #2	Volunteer #3
Contraction (ms)	66.3 ± 5.7	70 ± 2.3	73.4 ± 8.6
Half relaxation (ms)	102.9 ± 11	104 ± 12.5	114.5 ± 24

face mechanomyography. Contraction and half relaxation times are important to measure since they are specific to the contracting fiber types, e.g., slow or fast fibers [19].

C. Tetany

These velocity profiles can also be used concurrently with a periodical electrical stimulation leading to a periodical mechanical response or a tetany of the muscle depending on the frequency used for the stimulation (Fig. 12). These profiles show the tetany threshold in the stationary state of the muscle when tetany occurs.

The 1 ms electrostimulation pulse was repeated with different pulse repetition rates (from 1 to 20 Hz with a 0.5 Hz step). The velocity profiles in a $3 \times 3 \text{ mm}^2$ ROI were acquired at 500 Hz during one second. The data are represented as a pulse repetition rate versus time matrix [Fig. 12(a)]. Maximum amplitude of the velocity profiles have been extracted for each frequency [Fig. 12(b)].

Below the tetany threshold, the tissue velocity follows the excitation; above it, a summation of the response takes place and the contraction increases. In the stationary case, the muscle is fully contracted and incoherently vibrates

around this position: the velocity profiles show lower amplitudes and a rich spectral content.

D. Spatial Measurements

Until now all measurements were focused on the time profile of the contraction by looking at the velocity field inside an approximately $3 \times 3 \text{ mm}^2$ ROI. We will now demonstrate how using a true imaging technique such as eMMG enables visualization of the spatial extension of the contracting fiber bundle and its behavior. It has an advantage over surface mechanomyography, which has to deal with the summation of responses from large areas. With eMMG, it is possible to measure the tissue velocity field inside the contracting sources.

1. *Spatial Extension and Maps:* Using a threshold on the tissue velocity field enables the drawing of curves that illustrate the spatial extension of the contracting area (Fig. 13). This moving area consists of the true contracting bundle and the passive surrounding elastic tissue.

2. *Twist of the Tissue:* Many acquisitions clearly show a twist of the contracting fiber bundle (Fig. 14); the measured component of the tissue velocity is positive and negative side by side in the image, following the contraction dynamics, and the phenomenon is then reversed during the relaxation. Whether the twist is due to the contractile tissue itself or to hard boundary conditions at the end of the fiber bundles is unknown.

Geometrical features that cannot be visualized by surface mechanomyograms are available.

E. 3-D Fiber Bundle Tracking and Visualization

By performing a 3-D stroboscopic scan along the biceps, a whole volume of the tissue velocity field can be acquired. We chose to scan 22 positions with a 2-mm step for a total scanned volume of $44 \times 38 \times 50 \text{ mm}^3$ (Fig. 15); a 1500 Hz frame rate was used. Results show that the tissue velocity distribution mainly follows a curve that matches visible echogenic structures and is thought to be

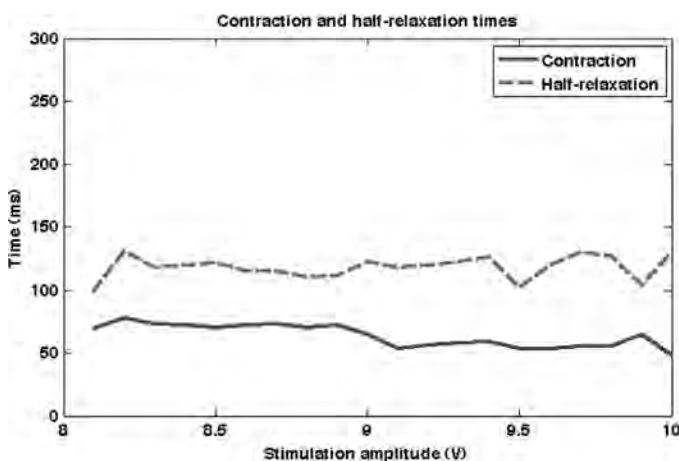


Fig. 11. Influence of the stimulation amplitude on the characteristic times (Volunteer #2).

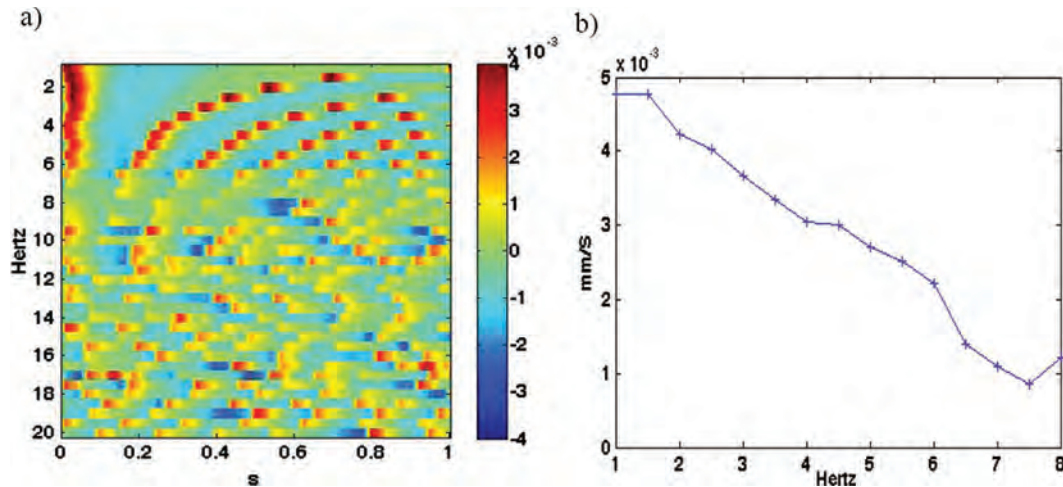


Fig. 12. (a) Response of the muscle to different excitation frequencies. Its behavior becomes erratic at greater than 7.5 Hz. (b) Tissue velocity maximum amplitude versus excitation frequency.

a fiber bundle. The coordinates of this curve are automatically extracted and the equation of encompassing planes computed. These coordinates are useful for 3-D visualization of the data as well as for the reconstruction of the tissue velocity profile along the fiber bundle [Fig. 15(b)]. We can then reconstruct the contracting fiber bundle using an isosurface.

These results show the feasibility of the *in vivo* tracking of a contracting fiber bundle with a low electrically induced stimulation. The localization of the contracting fiber bundle is retrieved in a 3-D volume and matches echogenic structures of the muscle (Fig. 16). This represents the first attempt of tracking contracting muscle fibers *in vivo*. Diffusion tensor imaging, an MR imaging-based technique has been applied to the anatomical tracking of skeletal muscle fibers [27], but can give only ana-

tomical information and no functional information on the mechanical response of a muscle to a given stimulation.

However, this experiment is difficult in practice. Choosing the right position for the arm, the probe, and the electrodes and good electrostimulation parameters inside the water tank is tricky and uncomfortable, whereas moving the probe directly on the skin leads to changes in the electrostimulation strength and a drop in repeatability, thus preventing a stroboscopic acquisition.

IV. DISCUSSION

From a similar experiment acquired every millimeter with a 2000 Hz frame rate, we have been able to extract characteristic times inside the contracting area, such as the maximum, the zero crossing, and the minimum times,

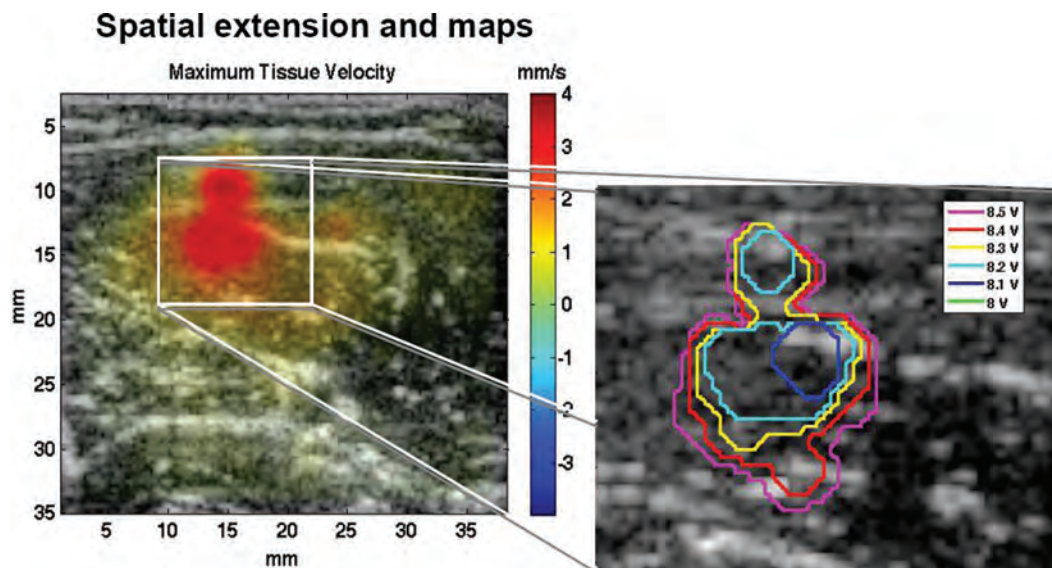


Fig. 13. Map (left) of the maximum of the tissue velocity field (8.3 V stimulation) and spatial extension (right) of the contraction as visualized by an isocontour on the velocity tissue field. A threshold of 2 mm/s was used.

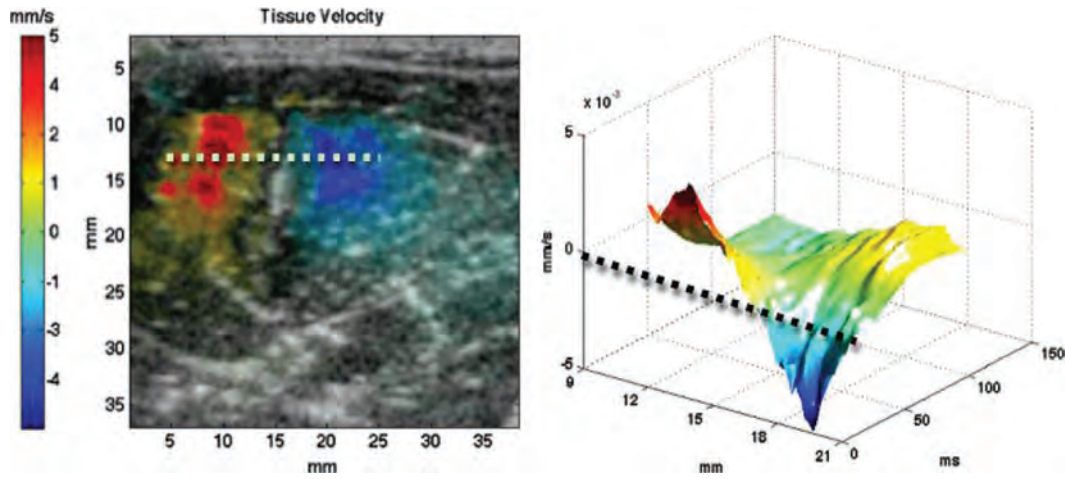


Fig. 14. Illustration (left) of the twist of a contracting fiber bundle. Red means going up whereas blue means going down. The projected components (right) of a clockwise rotation are visible, and the associated time profiles along a sample line (dashed line) illustrate the anticlockwise rotation during relaxation.

every millimeter along 2 cm of the biceps brachii (Fig. 17).

These velocity profile maxima, zeros, and minima can be fitted to straight lines (Fig. 17, right); the slope of each series of points gives respectively propagation velocities of 4.2, 3.3 and 3.8 m/s. The accuracy of this measurement is highly limited by the width of the signal, and the range of velocity requires a high frame rate.

It is striking to compare such measured velocities to other characteristic propagation velocities of the biceps brachii muscle, muscle fiber conduction velocity, and shear wave velocity.

An application of electromyography well known by muscle physiologists and named muscle fiber conduction velocity (MFCV) enables the measurement of the velocity of action potentials traveling along the muscle fibers. The electromyography signals recorded by an array of electrodes on the muscle surface are correlated; from the time shift between 2 positions, a velocity of the underlying electrical wave can be computed. This “wave” called M-wave is found to have a velocity ranging from 3.5 to

5.5 m/s [11] in the biceps brachii. The striking similitude between the electric and mechanic propagation is not that surprising since the mechanical response is thought to be triggered by the M-wave.

Another characteristic velocity can play a role in the observed phenomenon, mechanical shear waves. Shear waves or transversal waves propagate in soft tissues between 1 and 10 m/s a thousand times slower than longitudinal waves (1500 m/s); moreover, their velocities are directly linked to the stiffness of the material. To measure the shear velocity of an *in vivo* biceps brachii (Volunteer #3) along the fibers, the same echograph was simply put in the supersonic shear imaging mode [20] and all electrostimulation devices were shut down. For illustrative purposes, the subject was asked either to stay relaxed or to carry a 4 kg load. Details measurements on the biceps brachii are beyond the scope of this paper and will be provided in a following paper. A quick analysis of the shear wave profiles show a propagation velocity of 2 m/s with no load and 4 m/s with the 4 kg load, illustrating that the muscle is getting stiffer with the contraction strength (Fig. 18). These

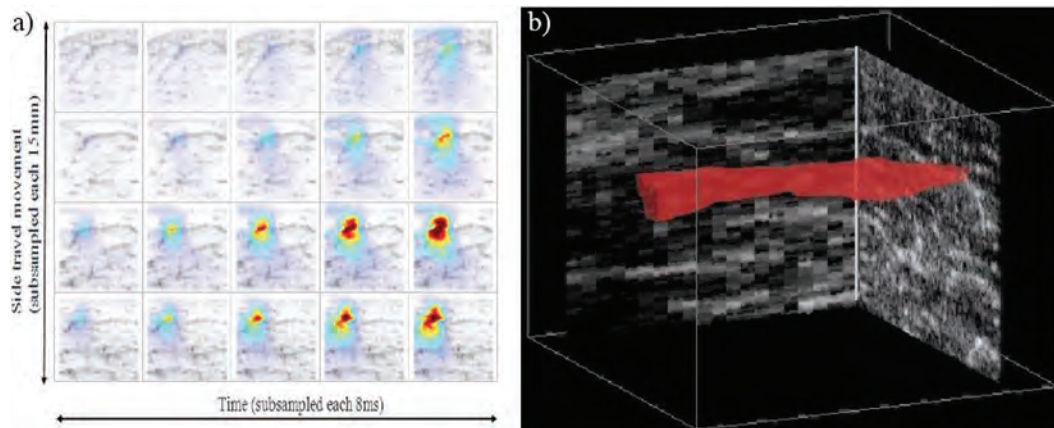


Fig. 15. (a) Raw data acquired in the transverse plane (38 × 50 mm). (b) Fiber bundle’s envelope extraction after thresholding at 80% of the maximum of each renormalized transverse acquisition.

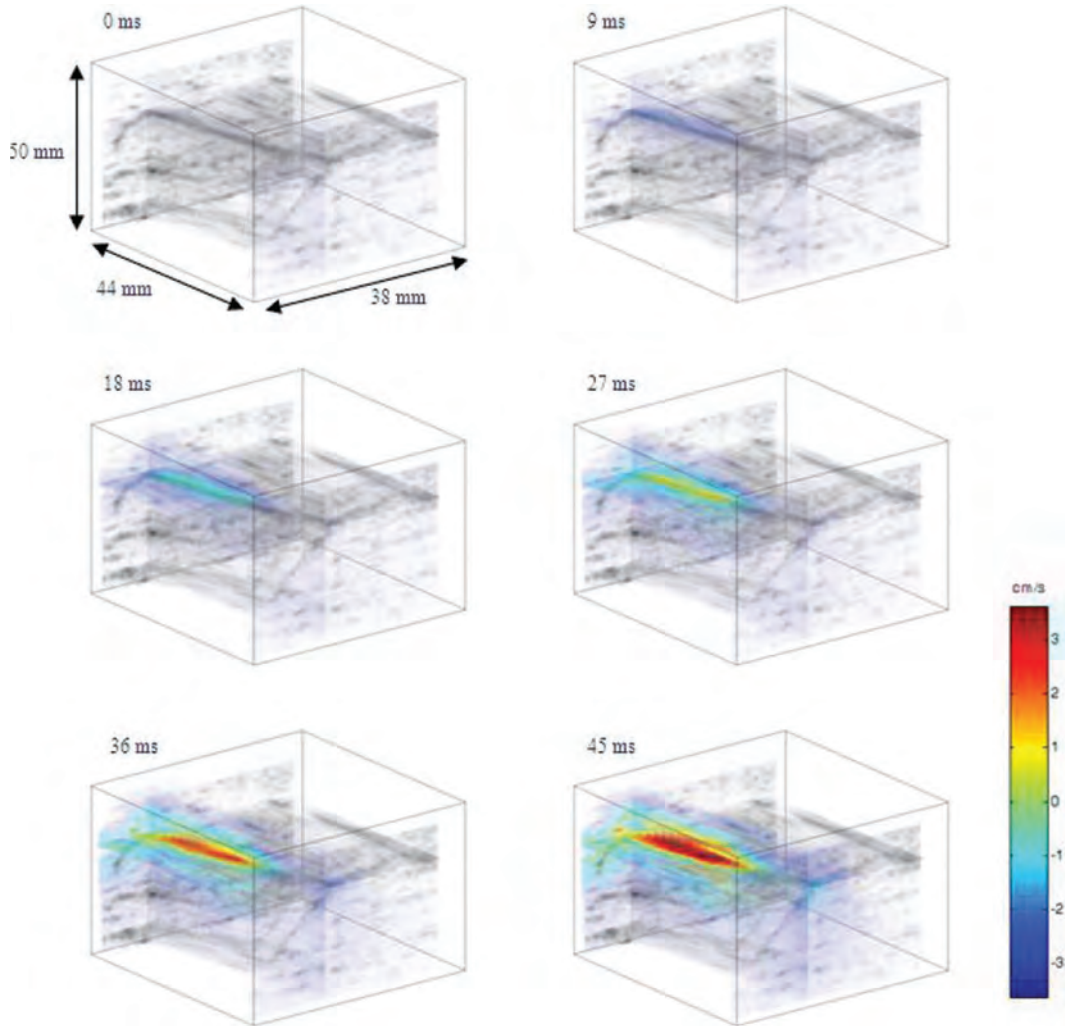


Fig. 16. A 3-D visualization of the tissue velocity field at various times after electrostimulation. The contraction of a fiber bundle is clearly visible and matches echogenic structures.

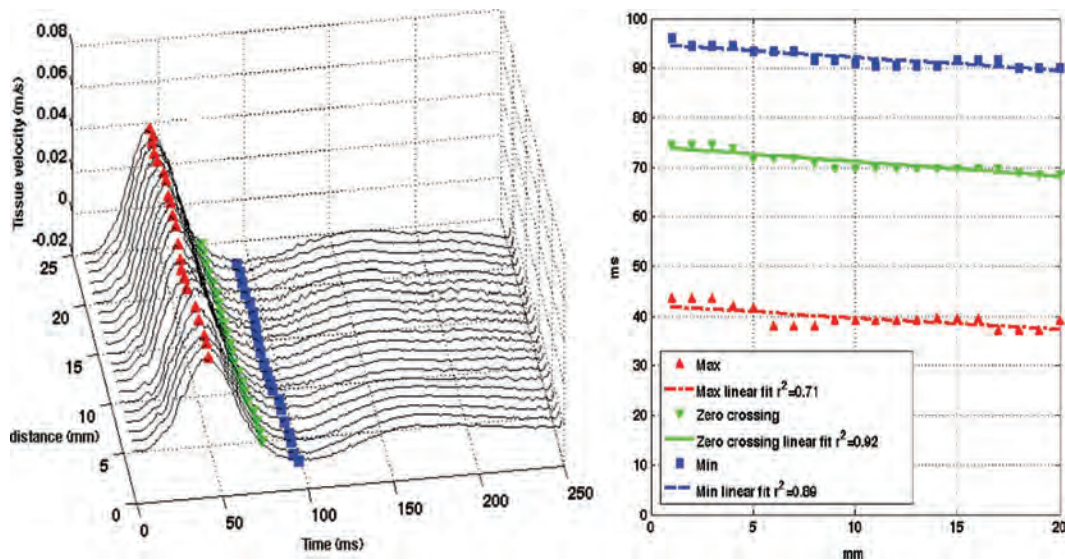


Fig. 17. Electrostimulation. Left: visualization of the velocity profile for different positions along the biceps brachii (Volunteer #3). Right: a linear fit of the characteristic points of the curve at a propagation velocity of approximately 4 m/s.

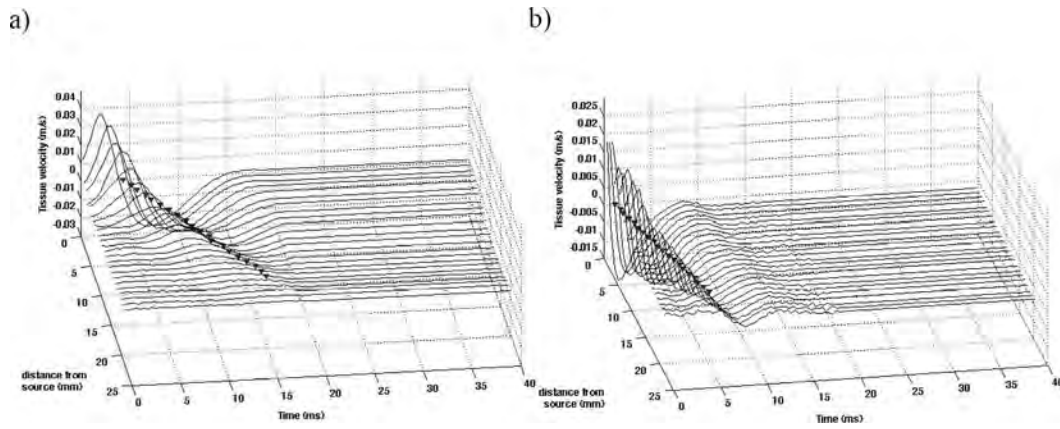


Fig. 18. No electrostimulation. The supersonic shear imaging technique is applied on an *in vivo* biceps brachii parallel to the fibers (Volunteer #3) to initiate and follow a shear wave. (a) Velocity profile when muscle is in rest state; shear velocity is 2 m/s. (b) A 4 kg load is applied; shear velocity increases to 4 m/s.

velocities, especially when the muscle is contracting, are very close to the velocity measured and to the much more known M-wave velocity.

By combining the measurements of electrostimulated muscle contraction with local elasticity estimation of passive muscular tissue [20] on the same probe, it should be possible to understand if the mechanical pattern recorded during this electrostimulation experiment is due either to the single propagation of the action potential, to the propagation of mechanical shear waves due to the contraction, or, more interestingly, to a natural and clever coupling of both waves. In particular, this resulting mechanical wave could be an elegant way to increase excitability along the skeletal muscle fiber by mechanically triggering stretch-activated ion channels [28], a mechanism known as the myogenic response for cardiac [29] and smooth [30] muscles.

V. CONCLUSION

The clinical emergence of ultrafast scanners could soon propose echo mechanomyography as a unique and original way of imaging the transient mechanical response of a muscle to an electrical stimulation. Using very high frame rate ultrasound, the contractile properties of a fiber bundle can be fully measured *in situ*, imaged, and tracked in 2D or 3-D, upgrading surface mechanomyography to *in depth* imaging with optimal time and spatial resolutions for *in vivo* applications. It permits both the *in situ* estimation of muscle fiber conduction speed and the localization of muscle fibers recruitment. The technique now needs to be tested with standard electrostimulation procedures used by surface mechanomyography studies to compare and improve results. It could then lead to a new *in situ* tool for muscle physiologists. Coupled with electromyography, clinicians would have both the electrical command and the *in situ* mechanical response of a muscle, information that could improve diagnosis and monitoring of neuromuscular diseases.

REFERENCES

- [1] R. L. Segal, "Use of imaging to assess normal and adaptive muscle function," *Phys. Ther.*, vol. 87, no. 6, pp. 704–718, June 2007.
- [2] M. J. Aminoff, *Electromyography in Clinical Practice*, 2nd ed. New York: Churchill Livingstone, 1987.
- [3] C. Orizio, "Muscle sound: Bases for the introduction of a mechanomyographic signal in muscle studies," *Crit. Rev. Biomed. Eng.*, vol. 21, no. 3, pp. 201–243, 1993.
- [4] J. Viby-Mogensen, E. Jensen, M. Werner, and H. K. Nielsen, "Measurement of acceleration: A new method of monitoring neuromuscular function," *Acta Anesthesiol. Scand.*, vol. 32, no. 1, pp. 45–48, Jan. 1988.
- [5] C. Patten, R. A. Meyer, and J. L. Fleckenstein, "T2 mapping of muscle," *Semin. Musculoskelet. Radiol.*, vol. 7, no. 4, pp. 297–305, Dec. 2003.
- [6] R. Taylor, T. B. Price, D. L. Rothman, R. G. Shulman, and G. I. Shulman, "Validation of ^{13}C NMR measurement of human skeletal muscle glycogen by direct biochemical assay of needle biopsy samples," *Magn. Reson. Med.*, vol. 27, no. 1, pp. 13–20, Sep. 1992.
- [7] G. P. Pappas, D. S. Asakawa, S. L. Delp, F. E. Zajac, and J. E. Drace, "Nonuniform shortening in the biceps brachii during elbow flexion," *J. Appl. Physiol.*, vol. 92, no. 6, pp. 2381–2386, June 2002.
- [8] M. A. Dresner, G. H. Rose, P. J. Rossman, R. Muthupillai, A. Manduca, and R. L. Ehman, "Magnetic resonance elastography of skeletal muscle," *J. Magn. Reson. Imaging*, vol. 13, no. 2, pp. 269–276, Feb. 2001.
- [9] N. R. Grubb, A. Fleming, G. R. Sutherland, and K. A. Fox, "Skeletal muscle contraction in healthy volunteers: Assessment with Doppler tissue imaging," *Radiology*, vol. 194, no. 3, pp. 837–842, Mar. 1995.
- [10] S. Pillen, M. van Keimpema, R. A. J. Nivelstein, A. Verrips, W. van Kruijsbergen-Raijman, and M. J. Zwarts, "Skeletal muscle ultrasonography: Visual versus quantitative evaluation," *Ultrasound Med. Biol.*, vol. 32, no. 9, pp. 1315–1321, Sep. 2006.
- [11] D. Farina, W. Muhammad, E. Fortunato, O. Meste, R. Merletti, and H. Rix, "Estimation of single motor unit conduction velocity from surface electromyogram signals detected with linear electrode arrays," *Med. Biol. Eng. Comput.*, vol. 39, no. 2, pp. 225–236, Mar. 2001.
- [12] Y. Yoshitake, M. Shinohara, H. Ue, and T. Moritani, "Characteristics of surface mechanomyogram are dependent on development of fusion of motor units in humans," *J. Appl. Physiol.*, vol. 93, no. 5, pp. 1744–1752, Nov. 2002.
- [13] R. S. Witte, D. E. Dow, R. Olafsson, Y. Shi, and M. O'Donnell, "High resolution ultrasound imaging of skeletal muscle dynamics and effects of fatigue," in *Proc. IEEE Ultrason. Symp.*, vol. 1, Aug. 2004, pp. 764–767.
- [14] R. S. Witte, K. Kim, B. J. Martin, and M. O'Donnell, "Effect of fatigue on muscle elasticity in the human forearm using ultrasound

- strain imaging," in *Proc. IEEE Int. Conf. Eng. Med. Biol. Soc.*, vol. 1, Aug. 2006, pp. 4490–4493.
- [15] T. Deffieux, J.-L. Gennisson, M. Tanter, and M. Fink, "Ultrafast imaging of *in vivo* muscle contraction using ultrasound," *Appl. Phys. Lett.*, vol. 89, no. 18, art. no. 184107, Nov. 2006.
- [16] L. Sandrin, M. Tanter, S. Catheline, and M. Fink, "Shear modulus imaging with 2-D transient elastography," *IEEE Trans. Ultrason., Ferroelect., Freq. Contr.*, vol. 49, no. 4, pp. 426–435, Apr. 2002.
- [17] A. Sandow, "Electromechanical transforms and the mechanism of excitation-contraction coupling," *J. Mechanochem. Cell Motil.*, vol. 2, no. 3, pp. 193–207, Nov. 1973.
- [18] J. V. Basmajian and C. J. De Luca, *Muscles Alive: Their Functions Revealed by Electromyography*, 2nd ed. Baltimore: Williams & Wilkins, 1985.
- [19] A. Eberstein and J. Goodgold, "Slow and fast twitch fibers in human skeletal muscle," *Am. J. Physiol.*, vol. 215, no. 3, pp. 535–541, Sep. 1968.
- [20] J. Bercoff, M. Tanter, and M. Fink, "Supersonic shear imaging: A new technique for soft tissue elasticity mapping," *IEEE Trans. Ultrason., Ferroelect., Freq. Contr.*, vol. 51, no. 4, pp. 396–409, Apr. 2004.
- [21] M. Tanter, J. Bercoff, L. Sandrin, and M. Fink, "Ultrafast compound imaging for 2D motion vector estimation: Application to transient elastography," *IEEE Trans. Ultrason., Ferroelect., Freq. Contr.*, vol. 49, no. 10, pp. 1363–1374, 2002.
- [22] J. Ophir, I. Cespedes, H. Ponnekanti, Y. Yazdi, and X. Li, "Elastography: A quantitative method for imaging the elasticity of biological tissues," *Ultrason. Imag.*, vol. 13, pp. 111–134, Apr. 1991.
- [23] B. J. Forrester and J. S. Petrofsky, "Effect of electrode size, shape, and placement during electrical stimulation," *J. Appl. Res.*, vol. 4, no. 2, pp. 346–354, 2004.
- [24] J. L. Gennisson, C. Cornu, S. Catheline, and M. Fink, "Human muscle hardness assessment during incremental isometric contraction using transient elastography," *J. Biomech.*, vol. 38, no. 7, pp. 1543–1550, July. 2005.
- [25] Y. C. Fung, *Biomechanics: Mechanical Properties of Living Tissues*, 2nd ed. New York: Springer, 1993.
- [26] S. J. Dorgan and M. J. O'Malley, "A mathematical model for skeletal muscle activated by N-let pulse trains," *IEEE Trans. Rehabil. Eng.*, vol. 6, no. 3, pp. 286–299, Sep. 1998.
- [27] C. C. Van Donkelaar, L. J. G. Kretzers, and P. H. M. Bovendeerd, "Diffusion tensor imaging in biomechanical studies of skeletal muscle function," *J. Anat.*, vol. 194, no. 1, pp. 79–88, Jan. 1999.
- [28] N. Mallouk and B. Allard, "Stretch-induced activation of Ca²⁺-activated K⁺ channels in mouse skeletal muscle fibers," *Am. J. Physiol. Cell Physiol.*, vol. 278, no. 3, pp. C473–C479, Mar. 2000.
- [29] H. Hu and F. Sachs, "Stretch-activated ion channels in the heart," *J. Mol. Cell. Cardiol.*, vol. 29, no. 6, pp. 1511–1523, June. 1997.
- [30] M. J. Davis, J. A. Donovitz, and J. D. Hood, "Stretch-activated single-channel and whole cell currents in vascular smooth muscle cells," *Am. J. Physiol. Cell Physiol.*, vol. 262, no. 4, pp. C1083–C1088, Mar. 1992.



Thomas Deffieux was born in 1982 in Paris, France. He received his MsC. degree in physics and image processing in 2005 from the University Louis Pasteur of Strasbourg. Since 2005, he has been a Ph.D. student, directed by Mickaël Tanter, at the Laboratoire Ondes et Acoustique (ESPCI) in Paris, France. His current research fields include ultrafast ultrasonic imaging and quantitative elastography of soft tissues by shear wave propagation (supersonic shear imaging) applied to *in vivo* breast, liver, and muscle tissues.



include medical ultrasonic imaging, shear wave propagation in soft tissues for cancer detection, and nonlinear shear waves.



Mickaël Tanter was born in December 1970 in Paimpol, France. He received the engineering degree in electronics from Ecole Supérieure d'Electricité (SUPELEC) in 1994. In 1999, he received the Ph.D. degree in physics (acoustics) from the University of Paris VII for his work on the application of time reversal to ultrasonic brain therapy and the "Habilitation de Recherche" in 2004. From 2000 to 2005, he was an associate research professor at the French Center for Scientific Research (CNRS) at ESPCI (Ecole Supérieure de Physique et de Chimie Industrielle), Paris, France. In 2005, he became a research professor at the French Institute for Medical Research (INSERM). He is currently the head of the research team "Wave Physics for Medicine" at the Laboratoire Ondes et Acoustique (ESPCI) laboratory, directed by Mathias Fink. His current research interests include ultrasonic imaging and therapy (adaptive focusing techniques in heterogeneous media, medical ultrasonic imaging, ultrasonic brain imaging, shear wave propagation in soft tissues for cancer detection, ultrasonic therapy, nonlinear acoustics, and active noise control). He holds 7 patents in the field of ultrasound and he has published more than 50 articles. He is a co-founder of the start-up company SuperSonic Imagine in the field of medical ultrasound.



Mathias A. Fink received the diplôme de Doctorat de 3^{ème} cycle in solid state physics in 1970 and the Doctorat ès-Sciences degree in acoustics in 1978 from Paris University, France. From 1981 to 1984, he was a professor of acoustics at Strasbourg University, France. Since 1984, he has been a professor of physics at Paris University (Denis Diderot), France. In 1990 he founded the Laboratoire Ondes et Acoustique at the Ecole Supérieure de Physique et de Chimie Industrielles de la Ville de Paris (ESPCI). In 1994, he was elected to the Institut Universitaire de France. His current research interests include medical ultrasonic imaging, ultrasonic therapy, nondestructive testing, underwater acoustics, active control of sound and vibration, analogies between optics and acoustics, wave coherence in multiple scattering media, and time reversal in physics. He has developed different techniques in speckle reduction, in wave focusing in inhomogeneous media, and in ultrasonic laser generation. He holds 20 patents, and he has published more than 220 articles. In 2003, he was elected to the French Academy of Science.

The Variance of Quantitative Estimates in Shear Wave Imaging: Theory and Experiments

Thomas Deffieux, Jean-Luc Gennisson, Benoit Larrat, Mathias Fink, and Mickael Tanter

Abstract—In this paper, we investigate the relationship between the estimated shear modulus produced in shear wave imaging and the acquisition parameters. Using the framework of estimation theory and the Cramer–Rao lower bound applied both to the estimation of the velocity field variance and to the estimation of the shear wave travel time, we can derive the analytical formulation of the shear modulus variance σ_μ^2 using relevant physical parameters such as the shear wave frequency, bandwidth, and ultrasonic parameters. This variance corresponds to the reproducibility of shear modulus reconstruction for a deterministic, quasi-homogeneous, and purely elastic medium. We thus consider the shear wave propagation as a deterministic process which is then corrupted during its observation by electronic noise and speckle decorrelation caused by shearing. A good correlation was found between analytical, numerical, and experimental results, which indicates that this formulation is well suited to understand the parameters’ influence in those cases. The analytical formula stresses the importance of high-frequency and wideband shear waves for good estimation. Stiffer media are more difficult to assess reliably with identical acquisition signal-to-noise ratios, and a tradeoff between the reconstruction resolution of the shear modulus maps and the shear modulus variance is demonstrated. We then propose to use this formulation as a physical ground for a pixel-based quality measure that could be helpful for improving the reconstruction of real-time shear modulus maps for clinical applications.

I. INTRODUCTION

THE recent development of quantitative elastography methods is regarded as a highly promising step toward improved diagnosis. Since its introduction, many studies have been published by several groups demonstrating several clinical applications such as breast cancer detection [1]–[4], liver fibrosis staging [5]–[9], kidney monitoring [10], thyroid gland [11] and prostate cancer detection [12], and musculoskeletal monitoring [13]–[15], ophthalmologic [16], cardiac [17], or vascular applications [18]. Some clinical applications, such as liver fibrosis staging [19], require a very accurate and quantitative estimation of the shear modulus to make a diagnosis because the estimated value is directly compared with a pre-established quantitative scale. A quantitative approach is also mandatory for the

longitudinal monitoring of drug treatment efficacy (such as chemotherapy, antiangiogenic, or antivasculature treatments).

To allow a quantitative estimation of the shear modulus of tissue, dynamic elastography techniques—or in other words, shear-wave-based imaging techniques—use mechanical shear waves whose propagation velocity is directly linked to the shear modulus of the medium, i.e., its stiffness. After generation of shear waves in the medium, their propagation is recorded either in real time or using a stroboscopic acquisition. By solving the wave equation, it is then possible to retrieve a quantitative value of the shear modulus. There are generally two groups of dynamic elastography techniques depending on the regime of the shear waves used. In steady-state elastography, such as in magnetic resonance (MR) elastography, a monochromatic shear wave is generated and imaged with a stroboscopic acquisition, but in 3-D, using an MR imaging system. These techniques were first developed by Muthupillai and Manduca [20], [21] and are used today for clinical research. Although they allow the full 3-D reconstruction of the shear wave field, the overall complex patterns of the steady-state shear waves require the complete solving of the shear wave equation, which leads to difficulties with regard to robustness and bias because the estimation of second-order derivatives is required [22], [23]. Sonoelasticity [24] is another example of a steady-state elastography technique, in which shear waves are acquired with an ultrasound system.

Conversely, in transient elastography, such as in 1-D transient elastography (TE) [25], shear wave elasticity imaging (SWEI) [26], acoustic radiation force imaging with shear wave speed estimation (ARFI SWS) [27], supersonic shear imaging (SSI) [28], shear wave dispersion ultrasound vibrometry (SDUV) [29], spatially modulated ultrasound radiation force (SMURF) [30], dynamic micro elastography (DME) [31] or transient MR elastography [32] (t-MRE), a transient—and consequently wideband—shear wave is generated and tracked during its propagation either in real time or using a gated acquisition. The key difference is that the shear wave is imaged before it can reach the boundaries and is generally considered as a transient wave front. Under this assumption, the shear modulus can then be estimated by solving the eikonal equation for the wave front instead of the full wave equation with much simpler algorithms, such as a time-of-flight algorithm [2] which locally estimates the shear group velocity along the propagation direction. This approach is more robust to

Manuscript received November 18, 2011; accepted July 6, 2012. This work was partly supported by the French national agency for research on AIDS and Viral Hepatitis (ANRS).

The authors are with the Institut Langevin, Ondes et Images, Ecole Supérieure de Physique et de Chimie Industrielles (ESPCI, ParisTech), Centre National de la Recherche Scientifique (CNRS) UMR 7587, INSERM U979, France (e-mail: tdeffieux@gmail.com).

DOI <http://dx.doi.org/10.1109/TUFFC.2012.2472>

noise than solving the full wave equation because it relies on cross-correlations of wave profiles instead of the estimation of the ratios of temporal and spatial second-order derivatives, which can be very unstable.

In SSI, the acoustic radiation force is used to generate a transient shear wave directly inside the tissue. The shear wave is then acquired in real time during its propagation using ultrafast imaging, and the local shear wave propagation group velocity is estimated to create a shear modulus map. SSI has been applied to several organs and pathologies for which tissue elasticity maps could provide valuable insight for a diagnosis. Because the shear velocity is estimated by measuring a time delay between waveforms at different locations, the quality of the estimation will be dependent on several factors, such as the shear wave amplitude, the ultrasound image quality, the system noise, and other physical parameters (shear wave frequency, shear wave bandwidth, tissue stiffness range, frame rate, etc.).

It is our goal in this paper to derive a simple approximation for the shear modulus variance and bias that can take into account those different factors. This analytical formula and associated discussion will give us insight into which parameters are most critical and into the inevitable tradeoffs between them.

The theory behind the SSI physics will first be presented, together with the model of the shear wave propagation and the ultrafast acquisition. The analytical derivation of the shear modulus variance and expected value, based on the Cramer–Rao lower bound, will then follow. After the presentation of the material and methods—namely, the SSI experiments and the numerical simulation framework—the theoretical results will be compared with the experimental and numerical results. Finally, we will discuss the possible use of this formula as a basis for the real-time implementation of quality maps for clinical applications and its use for possible improvements in the ultrasound sequences.

II. THEORY

In this part, we will first describe the physics behind an SSI acquisition and propose a simple model for the shear wave propagation in purely elastic weakly heterogeneous media and the ultrafast imaging acquisition. The random variables corresponding to the received ultrasound data, the estimated tissue velocity field, and the estimated shear modulus map will be presented, as well as the formulas used to estimate one from another. The approximation of their variances and expected values will be presented and discussed.

A. SSI

1) *Generating a Quasi-Plane Shear Wave With Acoustic Radiation Force:* By focusing ultrasound (from 3 to 15 MHz, depending on the application) for a few hundred

microseconds, the acoustic radiation force, or “push,” generates a small localized and detectable shear displacement ($<10\ \mu\text{m}$) that propagates as a transient shear wave. By successively pushing the tissue along a line at different depths (typically between 10 to 30 mm for breast imaging [2] and between 30 to 80 mm for liver imaging [33]), it is possible to generate an approximately cylindrical shear wave that is observed as a plane wave in the 2-D ultrasound imaging plane. This shear wave is polarized along the ultrasound beam axis (axis of the radiation force) and propagates transversally to this axis, parallel to the probe face (see Fig. 1).

2) *Ultrafast Acquisition of the Propagating Shear Wave:* Ultrafast ultrasound imaging uses plane-wave ultrasound emissions to reach very high frame rates of up to 20 000 frames per second, depending primarily on the imaging depth. Backscattered echoes are digitally stored in memory for each acquisition channel and then beamformed to generate a standard B-mode image. Because the transmit beam is not focused (a plane wave is used), the point spread function (PSF) of the imaging system is larger than in conventional B-mode imaging where focused transmit beams are used, and the contrast and resolution of the final image is decreased. The lower quality is the price paid for higher frame rates.

By introducing coherent compounding of images resulting from plane wave emissions with different incident angles, it is possible to improve the imaging contrast and resolution [34]. The number of independent angles used in the compounding provides a continuous and elegant tradeoff between the imaging framerate and the image quality as described by Montaldo *et al.* [34]. In the presented experiments, a typical coherent compounding sequence was used with 7 angles between -6° and 6° .

To decrease the transfer bandwidth required for real-time applications, the backscattered echoes signals (RF signals) are demodulated and sampled as in-phase and quadrature signals (IQ signals), decreasing the signal bandwidth but also the total number of samples (typically 4 samples per wavelength).

Similarly to cross-correlation techniques used on RF signals for speckle tracking, the autocorrelator technique (first described by Kasai *et al.* [35]) is applied to the beamformed IQ signals to estimate, pixel by pixel, the frame-to-frame phase shift. From the phase shift, the tissue displacement between successive frames (typically $<5\ \mu\text{m}$ in soft tissue) and finally the tissue velocity (typically $<2\ \text{mm/s}$) can be estimated. This technique is very similar to color tissue Doppler imaging (TDI) using plane waves to achieve high frame rate (usually 5000 frames per second, depending on imaging depth) and full-frame imaging (128 parallel channels at once). It suffers the same limitation and can only give access to the displacement polarized along the ultrasound beam axis.

By combining the push sequence with the ultrafast sequence, a shear wave can be generated and acquired in real time during its propagation ($<20\ \text{ms}$). The shear

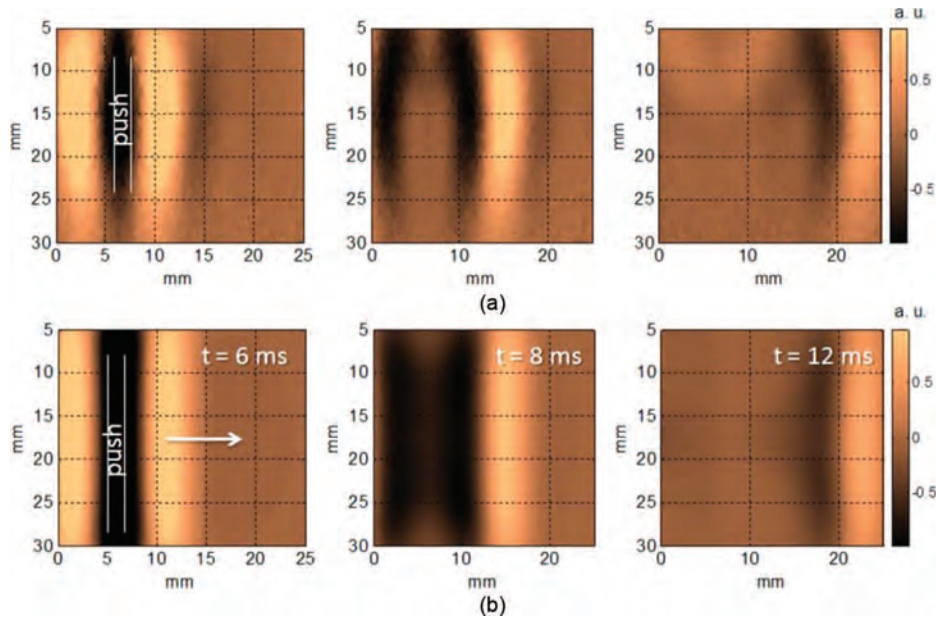



Fig. 1. Shear waves generated by a supersonic shear imaging (SSI) sequence: (a) experiment in phantom and (b) simulation. All parameters were similar except for the shear wave source length. The 400-Hz shear wave is polarized along the z -axis and propagates from the push area in the x -direction (along the white arrow) in a 5-kPa medium and is acquired with a 2500 Hz framerate. 

wave propagation data can then be used to estimate the local shear modulus of the tissue by locally estimating the shear wave group velocity (see Fig. 2).

3) *Elasticity Map Reconstruction From Shear Wave Propagation Data*: In a homogenous, linearly elastic, isotropic, and quasi-incompressible medium, the shear wave generated by an infinite “push” line excitation along the beam axis z can be approximated by

$$V_z(z, x, y, t) = \int S(\omega) \frac{i}{4} H_0^{(1)}(k\sqrt{x^2 + y^2}) e^{-i\omega t} d\omega, \quad (1)$$

where ω is the angular frequency, $S(\omega)$ is the elastic source spectrum, $H_0^{(1)}$ is the first kind of Hankel function of order 0, and k is the shear wave number.

This cylindrical shear wave is the model we use to describe the generated shear wave in 3-D. In the imaging plane ($y = 0$), after expansion of the Hankel function and far from the source ($k \cdot x > 1$, a condition we impose), the effect of the curvature of the cylindrical wave front can be neglected and the wave can be approximated as a plane

wave with a modified amplitude but a linear phase as described in Deffieux *et al.* [36]:

$$\begin{aligned} V_z(z, x, t) &\approx \int S(\omega) \frac{i}{4} \sqrt{\frac{2}{\pi k x}} e^{-i(kx - \omega t + (\pi/4))} d\omega \\ &\approx \int A(\omega, x) e^{-i(kx - \omega t + \phi_0)} d\omega, \end{aligned} \quad (2)$$

where $A(\omega, x)$ is the shear wave amplitude at the location x , and ϕ_0 is the origin phase.

In a purely elastic media, the wave number k is real and the shear wave velocity c is independent of frequency and depends only on the shear modulus μ and acoustic density of the medium ρ :

$$k = \frac{\omega}{c} \quad \text{where } c = \sqrt{\frac{\mu}{\rho}}. \quad (3)$$

Based on (3), the shear modulus can thus be estimated directly from the group velocity of the wave. From (2), the group velocity can itself simply be determined by the time delay between two waveforms taken along the propagation

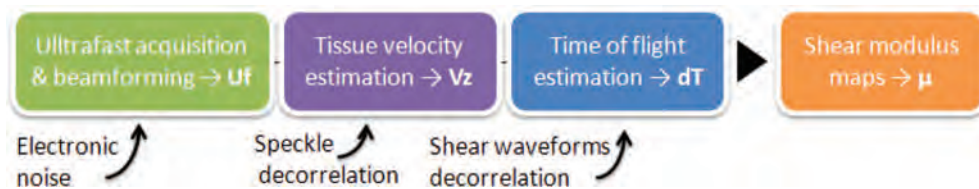



Fig. 2. Reconstruction of the shear modulus maps from acquired data. The propagating shear wave is acquired with an ultrafast imaging sequence (green box) in the form of in-phase and quadrature data (IQ) corrupted by the electronic noise before the analog to digital conversion. From the frame-to-frame phase shift, the tissue velocity field is estimated along the axial direction z (purple box). The shear modulus map is then estimated from the local shear wave velocity using a time-of-flight algorithm along the propagation axis (white arrow in Fig. 1). 

direction and separated by a known distance (denoted dr in the remainder of the paper). In the purely elastic and homogeneous case, the cylindrical shear wave at a location $xb = xa + dr$ is thus a scaled translation of the shear wave at a point xa :

$$\begin{aligned} V_z(z, xb, t) &= \int A(\omega, xb) e^{-i(kxb - \omega t + \phi_0)} d\omega \\ &= \int \sqrt{\frac{xa}{xb}} A(\omega, xa) e^{-i(kxa - \omega t + \phi_0)} e^{-ik(xb - xa)} d\omega \quad (4) \\ &= \sqrt{\frac{xa}{xb}} V_z\left(z, xa, t - \frac{xb - xa}{c}\right). \end{aligned}$$

The time-of-flight algorithm we developed uses cross-correlation and parabolic interpolation [37] to estimate a time delay dT between the waveforms and thus the local average group velocity $c = (xb - xa)/dT$ between two points along the propagation direction (here, along the x -axis).

The same approach can be extended to the heterogeneous case by considering the eikonal equation which describes the wave front propagation (amplitude, direction, and velocity) under the weak inhomogeneity approximation [38]:

$$\frac{\nabla^2 A}{A\omega^2} + \left[\frac{1}{c(x)^2} - (\nabla\phi(x))^2 \right] = 0, \quad (5)$$

where A is the wave amplitude, ω is the angular frequency, c is the shear velocity in the medium, and ϕ is the phase of the wavefront.

When the wavelength is short with regard to the lengths of the objects in the medium, the eikonal equation can be further simplified [38] and can be solved locally by measuring only the phase gradient of the wave front using a time-of-flight approach under the purely elastic assumption:

$$\left[\frac{1}{c(x)^2} - (\nabla\phi(x))^2 \right] = \left[\frac{1}{c(x)^2} - \left(\frac{dT_x^2}{dr^2} + \frac{dT_z^2}{dr^2} \right) \right] = 0, \quad (6)$$

where dTx and dTz are the time delays of the wave front along the x and z axis for a fixed distance dr and are simply related to the phase gradient of the wave front in a purely elastic medium.

More complex cases, such as a very stiff object yielding reflections on its boundaries or small objects, may require the use of a directional filter [39] to keep only the forward propagating wave front or may require (5) to be solved directly.

In the rest of this paper, however, we will concentrate on the simplest case of weak heterogeneity, where the shear wave front is assumed to propagate only along the x -axis (4). This is sufficient to describe most applications for weakly heterogeneous tissues, such as liver fibrosis staging, which is an important motivation for this work. The results of the paper can be further extended to work

with any propagation direction by modifying (16)–(18) to take into account two separate time delays, one along the x -axis and one along the z -axis, as described in (6).

Note also that (4) and (6) are only valid for nonviscous media because viscosity will necessarily induce dispersion in the phase velocity $c(\omega)$ which will change with frequency. In that case, the shear wave dispersion curve must be estimated using a different method, such as shear wave spectroscopy [36], and a rheological model must be assumed to infer mechanical parameters such as shear modulus and viscosity. In practice, viscosity will lead to a correlation loss because of dispersion and deformation of the waveforms and to an amplitude loss; both will lead to a decrease of the overall SNR. Moreover, the estimated group velocity will depend on the dispersion curve and frequency content of the shear wave, which will lead to a bias in the shear modulus estimation if not properly taken into account.

The shear wave amplitude which affects the acquisition quality is dependent on important parameters such as the shear modulus or center frequency that will not be modeled explicitly in the equations here. Instead, the shear wave amplitude is directly assessed numerically or experimentally because it is difficult to model and relatively easy to measure.

B. Noise Propagation Model

There are several sources of noise or correlation loss that can arise in an experiment. Here we list the main sources as they arise during a real-time acquisition (see Fig. 2):

- 1) The shear wave forms' correlation loss resulting from dispersion or diffraction effects. This is not linked to a random process of its own because we suppose the medium is not changing through time.
- 2) The mechanical noise resulting from natural motion such as breathing or pulsatility. This leads to displacement bias and increased variance and even false correlation peak in the time-of-flight for large amplitudes.
- 3) The displacement bias resulting from spatial averaging in the PSF when the moving area is smaller than the tracking PSF.
- 4) The speckle correlation loss resulting from speckle displacement by the shear wave, which leads to increased variance in the estimated displacement.
- 5) The electronic noise.

In the following, some of those sources were neglected or partially implemented:

- The displacement amplitude bias caused by the PSF size (source 3). This multiplicative bias, well described by McAleavey *et al.* [40] in the case of a Gaussian displacement volume, is due to the smoothing of the

shear wave field by the imaging PSF. The bias is proportional to the ratio of the PSF size over the shear wavelength. The expression of this bias in the case of shear wave propagation is developed in Appendix B and was studied extensively with numerical simulations in Palmeri *et al.* [41]. Because the amplitude of the shear wave was not explicitly modeled but measured experimentally, this amplitude bias is implicitly taken into account in experiments and its exact impact on shear modulus was left for future work. As a modification of the observed wave amplitude and not its phase, it is not believed to play a major role aside from the decrease in the observed wave energy and associated SNR. The simulations did not model this effect either because only the elastic shear wave propagation step was simulated, not the motion estimation by ultrafast imaging.

- The speckle correlation loss resulting from speckle shearing (source 4) was taken into account by introducing a correlation coefficient r in the theory. The correlation loss in the speckle signal is implicitly taken into account when the tissue velocity field SNR is directly measured experimentally. It is, however, not taken into account in the numerical simulations, which only model the elastic shear wave propagation and not the motion estimation step. A rough estimation of the speckle correlation coefficient r based on the shear wavelength and displacement amplitude is given in Appendix B.
- The natural vibrations (source 2) were not taken into account. The justification is the low frequency of these vibrations (<100 Hz) that can be filtered out, but also the duration of a typical SSI experiment which is very short (20 ms) compared with a natural cardiac or breathing period. Those vibrations could, however, create artifacts in some cases, as well as speckle decorrelation, and should also be investigated to better understand *in vivo* conditions.
- The shear wave correlation loss resulting from shear wave dispersion or diffraction (source 1) is not taken into account. Unlike the speckle signal, the shear wave form is not a stochastic process because we don't consider any change to the medium or to the shear wave source here.

Finally, in this simple model, the random variable is the beamformed ultrasonic frame corrupted by electronic noise and decorrelated by the shearing resulting from the shear wave propagation. The theory is presented in the reversed order of the acquisition steps, which corresponds to the different processing steps.

1) *Ultrasonic Frame Acquisition and Beamforming:* As mentioned previously, the backscattered echoes (RF signals) are sampled as IQ signals, as described in Kasai *et al.* [35]. This spatiotemporal variable that depends only on the imaging characteristics and tissue scatterers is denoted $\text{IQ}_0(t, n)$ and the electronic noise, assumed to be

an additive white Gaussian noise (AWGN) is denoted $N_{\text{IQ}}(t, n)$, where t is the time and n is the channel number. The corresponding SNR can be defined for each channel i and fast-time sample t_n as: $\text{SNR}_{\text{IQ}}(t_n, i) = E[\text{IQ}_0(t_n, i)]^2 / E[N_{\text{IQ}}]^2$.

Despite the beamforming operation, which may introduce slight correlation between adjacent pixels, the noise in the beamformed image is also assumed to be an AWGN. The beamformed variable is denoted $\text{Bf}_0(z, x)$ and its zero-mean associated noise $N_{\text{Bf}}(z, x)$, yielding a SNR for the beamformed image of $\text{SNR}_{\text{Bf}}(z, x) = E[\text{Bf}_0(z, x)]^2 / E[N_{\text{Bf}}(z, x)]^2$. On a side note, the energy spatial distribution of the noise N_{Bf} is not uniform, but is mostly dependent on the beamforming operation, i.e., the aperture and the apodization coefficients used. It is competing with the signal energy which decreases rapidly with the depth because of attenuation.

The coherent compounding technique coherently adds beamformed frames with different emission angles for the ultrasonic plane waves. The new random variable corresponding to this coherent summation can be denoted as $\text{Uf}_0(z, x)$ with a noise $N_{\text{Uf}}(z, x)$ that is again assumed to be an AWGN with zero mean, yielding an SNR for the compounded image of $\text{SNR}_{\text{Uf}}(z, x) = E[\text{Uf}_0(z, x)]^2 / E[N_{\text{Uf}}(z, x)]^2$. To illustrate the AWGN hypothesis, the energy and noise spatial distribution of this variable, as well as the averaged inter-correlation between beamformed noise samples along time, along depth, and along the x -axis are presented later in Section VII.

In practice and subsequently in the paper, the acquisition SNR of the ultrasonic frames refers directly to the SNR of the beamformed and compounded ultrasonic frames and is thus defined as: $\text{SNR}_{\text{Uf}}(z, x) = E[\text{Uf}_0(z, x)]^2 / E[N_{\text{Uf}}(z, x)]^2$. The ultrasonic frames SNR can be estimated by different means:

- by directly estimating the energy and variance of a time series of beamformed and compounded ultrasonic frames without any displacement in the medium (ultrafast sequence, described in Section VI).
- by estimating the signal energy $E[\text{Uf}_0(z, x)]^2$ from a single beamformed and compounded frame and then the noise energy $E[N_{\text{Uf}}(z, x)]^2$ from the variance of a time series of empty frames without any ultrasound emissions (null sequence, described in Section VI).

2) *Tissue Velocity Field Estimation From Ultrasonic Frames:* The velocity field can be estimated from the reconstructed images using a classical approach such as speckle tracking or phase shift estimation. In the case of raw waveform data (RF signals), speckle tracking can be used to estimate the time delay, and thus the displacement, between the two consecutive frames and the tissue velocity [42]. For IQ data, the phase shift between consecutive frames can be estimated using one of the classic zero-lag phase estimator techniques [35], [43]. In our case, we used the Kasai 1-D autocorrelator, which is known to

be statistically suboptimal but computationally efficient [44]. The estimator for the tissue velocity can be written as [43]

$$V_z = \frac{c}{2} \frac{\text{FPS}}{2\pi F_{\text{us}}} \tan^{-1} \left\{ \frac{Q_{\text{int}}(0)I_{\text{int}}(1) - Q_{\text{int}}(1)I_{\text{int}}(0)}{Q_{\text{int}}(0)Q_{\text{int}}(1) + I_{\text{int}}(0)I_{\text{int}}(1)} \right\}, \quad (7)$$

where FPS is the ultrafast frame rate, F_{us} is the ultrasound frequency, c is the ultrasound velocity, $I_{\text{int}}(0)$, $Q_{\text{int}}(0)$ are the axially integrated IQ signals of the first frame, and $I_{\text{int}}(1)$, $Q_{\text{int}}(1)$ are those of the second frame. IQ signals correspond to the demodulated, beamformed, and compounded ultrasonic frames: $\text{IQ} = \text{IQ}_{\text{Uf}} = I_{\text{Uf}} + j \cdot Q_{\text{Uf}}$.

The derivation of the variance of the Kasai estimator can be derived from Loupas *et al.* [43] and is given in Appendix A. The variance of the tissue velocity along the z -axis, $\sigma_{V_z}^2$, can then be approximated by

$$\sigma_{V_z}^2 \approx \frac{c^2 \text{FPS}^2}{64 F_{\text{us}}^2} \frac{1}{\pi^2 r^2} \left(1 - r^2 + \frac{2}{\text{SNR}_{\text{Uf}}} \right), \quad (8)$$

where r is the correlation coefficient between successive frames in a noiseless environment resulting from the stochastic nature of ultrasonic speckle as defined in Appendix B.

This can also be rewritten as in Cespedes *et al.* [45] by introducing a decorrelation SNR such as $\text{SNR}_r = r/(1-r)$:

$$\sigma_{V_z}^2 \approx \frac{c^2 \text{FPS}^2}{32 \pi^2 F_{\text{us}}^2} \left(\frac{1}{\text{SNR}_r} + \frac{1}{\text{SNR}_{\text{Uf}}} \right) \quad \text{where } \text{SNR}_r = \frac{r}{1-r}. \quad (9)$$

This equation gives the relation between a given acquisition SNR (SNR_{Uf}) which depends on the acquired ultrasonic frame intensity ($E[\text{Uf}_0(z, x)^2]$), the speckle correlation coefficient r , and the electronic noise ($\sigma_{\text{Uf}}^2 = E[N_{\text{Uf}}^2]$) and the variance of the resulting estimated velocity field $\sigma_{V_z}^2$. One can observe that, for a given acquisition SNR, a higher ultrasound frequency gives higher accuracy in the estimation of the velocity field, which is intuitive because the phase shift between two frames is larger for higher frequencies and thus easier to estimate in constant noise level. In reality, because of higher attenuation of ultrasound at high frequencies, the higher the frequency is, the lower the will be acquisition SNR_{Uf} . Lower framerates yield larger displacement amplitude between consecutive frames which are easier to measure in the noise, but also yield lower correlation values (cf. Appendix B). To fine-tune an ultrafast sequence, all of these effects must be carefully chosen to minimize the noise variance $\sigma_{V_z}^2$ on the axial velocity estimation V_z .

For the rest of the paper, it is assumed that the estimated tissue velocity field V_z can be modeled as a normal distribution of variance $\sigma_{V_z}^2$ given by (9) and a mean V_{z0} , corresponding to the true unbiased tissue velocity.

3) *Shear Wave SNR and Effects of Filters:* In this part, we define the shear wave SNR as the ratio of the shear

wave energy and the tissue velocity variance $\sigma_{V_z}^2$ given by (9). The shear wave energy corresponds to the energy of the tissue velocity field during the propagation of the shear wave, which can easily be estimated experimentally.

In practice, the estimated tissue velocity field along the z -axis $V_z(z, x, t)$ is filtered to match the shear wave frequency content and reduce unnecessary noise. Under the white noise hypothesis, the SNR of the filtered field can be written as a band-limited version of the unfiltered field SNR by considering that the signal energy remains unchanged and that the noise energy is decreased by the ratio between the original acquisition bandwidth $\text{FPS}/2$ and the remaining bandwidth:

$$\text{SNR}_{\text{V[BW]}}(z, x) = \frac{\text{FPS}}{2\text{BW}} \text{SNR}_{\text{V}}(z, x) = \frac{\text{FPS}}{2\text{BW}} \frac{\int_T V_z(z, x, t)^2 dt}{\sigma_{V_z}^2}, \quad (10)$$

where FPS is the acquisition frame rate, T is the acquisition duration, and BW is the shear wave bandwidth.

Additionally, if a directional filter is used as we proposed in previous work [46], the SNR must be changed accordingly. The directional filter works by decomposing the 1-D plane wave propagation in the Fourier domain $[k, \omega]$ and by suppressing two quadrants out of four— $k > 0, \omega < 0$ and $k < 0, \omega > 0$ —which correspond to negative shear wave velocities. For shear waves with low reflected energy, such as in a weakly heterogeneous medium, the SNR of the directionally filtered tissue velocity field is simply twice the SNR of the unfiltered field because the two suppressed quadrants contain no signal energy but half of the total noise energy. The directional filter is required for imaging high-contrast objects or stiff inclusions without artifacts but is not absolutely necessary for weakly inhomogeneous media such as liver tissue, and it was not applied here.

$$\text{SNR}_{\text{V}_{z+}}(z, x) = 2\text{SNR}_{\text{V}_z}(z, x), \quad (11)$$

where SNR_{V_z} is the SNR of the field before the directional filter and $\text{SNR}_{\text{V}_{z+}}$ is the SNR of the field after the directional filter; this formula can be used with the band-limited SNR definition in (10).

III. TIME-OF-FLIGHT ESTIMATION

A time-of-flight algorithm can be used to locally estimate the shear wave group velocity. The shear waveforms of two points separated by a fixed distance dr are cross-correlated and the maximum of the cross-correlation function is obtained using a quadratic fit to determine the time delay with a sub-frame resolution. Even though the time-of-flight algorithm is a sliding window estimator, the axial resolution of the final image will thus depend on the kernel size of the algorithm which, in this case, is equal to the fixed distance dr between the correlated points.

The expected variance of the shear modulus as computed by the time-of-flight algorithm can be estimated

from the Cramer–Rao lower bound. The Cramer–Rao lower bound gives the minimum variance of a time-delay-based estimator from the SNR of a signal and its properties. The Cramer–Rao lower bound can be either written directly from the magnitude squared coherence function of the cross-correlated signals or estimated from higher level parameters such as the signal center frequency, bandwidth, and window length [47], [48]. In the latter case, the derivation can be simplified by considering a band-limited flat spectrum approximation for both the signal and noise with an equal bandwidth BW. This approximation can be used provided the tissue velocity field is filtered to equate noise and signal bandwidths, and provided the expression of the tissue velocity field SNR is corrected as stated in (10). In this work, we chose the second approach, which allows the use of physical parameters to describe the shear wave and to derive the variance and bias expressions.

Assuming a normal distribution for the noise of the tissue velocity field V_z with a variance $\sigma_{V_z}^2$ estimated from (9), the probability density function of the velocity field V_z can be written as

$$f_{V_z}(V_z) = \frac{1}{\sqrt{2\pi}\sigma_{V_z}} e^{-(1/2)((V_z - V_{z0})^2/\sigma_{V_z}^2)} \quad (12)$$

where V_{z0} is the true velocity field.

The variance of the time delay σ_{dT}^2 measured between two corrupted shear waveforms at two points A and B lying, respectively, at the positions xa and xb and at the same depth z can be written as a function of the tissue velocity band-limited SNR, the shear wave center frequency F_{sw} , shear bandwidth BW, and acquisition duration T . Under the assumptions of high tissue velocity field SNRs and no decorrelation of the shear waveforms as a result of other processes, such as diffraction or dispersion, the expression for the time delay minimum variance can be derived from the literature [47], [48] as

$$\sigma_{dT}^2(z, x) \geq \frac{3}{2\pi^2 \cdot F_{sw}^3 T (B^3 + 12B)} \times \left(\left(1 + \frac{1}{\text{SNR}_{V_z}(z, xa)} \right) \left(1 + \frac{1}{\text{SNR}_{V_z}(z, xb)} \right) - 1 \right), \quad (13)$$

where $B = \text{BW}/F_{sw}$ is the fractional bandwidth and is close to 1 in the case of a single sinusoidal cycle. The variance can thus be bounded by

$$\sigma_{dT}^2(z, x) \geq \frac{1}{8\pi^2 \cdot F_{sw}^2 T \text{BW}} \times \left(\left(1 + \frac{1}{\text{SNR}_{V_z}(z, xa)} \right) \left(1 + \frac{1}{\text{SNR}_{V_z}(z, xb)} \right) - 1 \right). \quad (14)$$

Here, the tissue velocity SNR is defined as the band-limited SNR as in (10); note that it is not the ratio of rms amplitude as in Walker and Trahey [48].

When the two points A and B are chosen at a fixed distance dr from each other, the time delay variance σ_{dT}^2 can be expressed for each pair of points of the field, provided they lie at the same depth:

$$\sigma_{dT}^2(z, x) \geq \frac{1}{8\pi^2 \cdot F_{sw}^2 \text{BW} T} \times \left(\left(1 + \frac{1}{\text{SNR}_{V_z}(z, x - \frac{dr}{2})} \right) \times \left(1 + \frac{1}{\text{SNR}_{V_z}(z, x + \frac{dr}{2})} \right) - 1 \right). \quad (15)$$

The shear wave bandwidth BW and center frequency F_{sw} can be estimated from the mean values in a 1 cm² region of interest to reduce the noise (see Section VI).

IV. SHEAR MODULUS ESTIMATION

For each point, the estimated time delay follows a normal distribution of variance $\sigma_{dT}^2(z, x)$ and mean $dT_0(z, x)$ which is the true time delay and can be rewritten as a function of the true and unknown shear modulus $\mu_0(z, x)$, the acoustic density ρ , and the distance dr between the two points used for the delay estimation in (15):

$$dT_0(z, x) = dr \sqrt{\frac{\rho}{\mu_0(z, x)}}. \quad (16)$$

The probability function of dT can thus be written as

$$f_{dT}(dT) = \frac{1}{\sqrt{2\pi}\sigma_{dT}} e^{-(1/2)((dT - dT_0)^2/\sigma_{dT}^2)}. \quad (17)$$

Using the same relationship between dT and μ for a change of variable in the probability density function of the time delay, one can compute the probability density function f_μ of the shear modulus μ :

$$f_\mu(\mu) = \frac{\sqrt{\rho} dr}{\mu^{3/2}} \frac{1}{2\sqrt{2\pi}\sigma_{dT}} e^{-(1/2)((dr/\sqrt{\mu/\rho}) - (dr/\sqrt{\mu_0/\rho}))^2/\sigma_{dT}^2}. \quad (18)$$

Unfortunately, it is not possible to give a closed-form expression either of the expected value $E[f_\mu]$ or of the variance σ_μ^2 of this probability density function in the general case. Nevertheless, it is possible to derive the Taylor expansion of the function near $\mu = \mu_0$, i.e., when the estimated time delay dT is close to the true time delay dT_0 , which corresponds to an approximation for high-tissue-velocity SNRs. In that case, the expected value $E[f_\mu]$, denoted simply μ after that and the variance σ_μ^2 can be approximated by (see Appendix C)

$$E[f_\mu] \approx \mu_0 + \frac{3\mu_0^2 \sigma_{dT}^2}{dr^2 \rho} \quad (19)$$

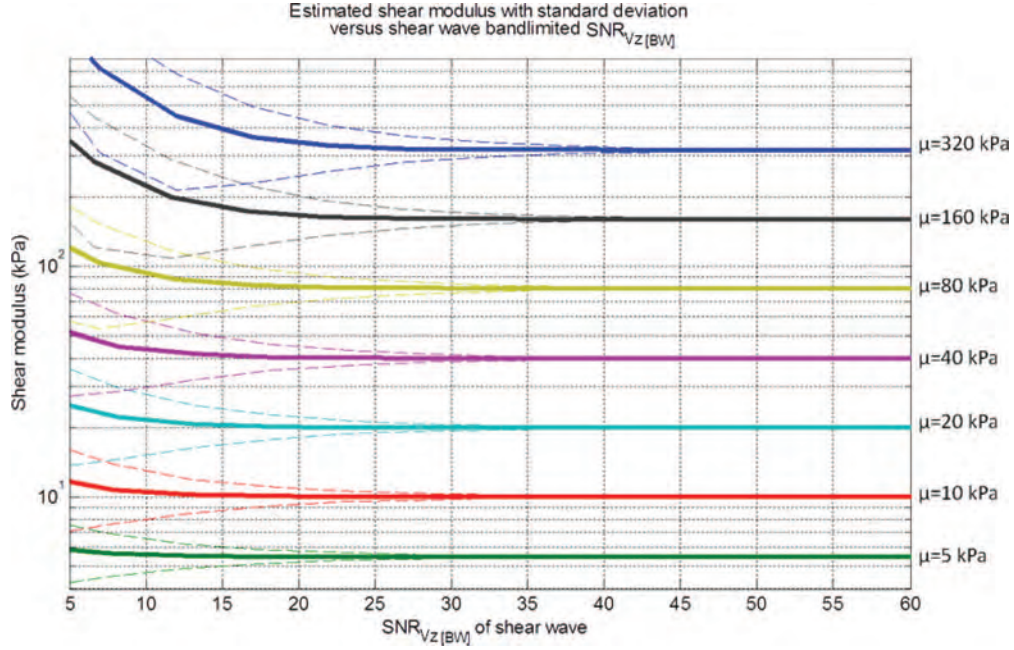


Fig. 3. The shear modulus expected value (plain lines) and standard deviation (dashed lines as error bars) for different background stiffness values ($\mu = 5, 10, 20, 40, 80, 160, 320$ kPa) and band-limited velocity field SNR. Curves are given for a shear wave bandwidth $BW = 400$ Hz, center frequency $F_{sw} = 400$ Hz, inter-correlation distance $dr = 1$ mm, and acoustic density $\rho = 1000$ kg·m⁻³.

$$\sigma_{\mu}^2 \approx \frac{4\mu_0^3 \sigma_{dT}^2}{dr^2 \rho}. \quad (20)$$

Those expressions, only valid for high-tissue-velocity SNRs, form the basis of this analysis. Here, σ_{dT}^2 is a function of space as well as μ_0 , which is the true shear modulus map. This last expression can be rewritten in terms of the shear wave parameters using (15):

$$\sigma_{\mu}^2 \approx \frac{\mu_0^3}{dr^2} \frac{1}{2\pi^2 \cdot F^2 BW T} \cdot \left(\left(1 + \frac{1}{\text{SNR}_{Vz}(x - \frac{dr}{2}, y)} \right) \times \left(1 + \frac{1}{\text{SNR}_{Vz}(x + \frac{dr}{2}, y)} \right) - 1 \right). \quad (21)$$

In this final expression, it is noticeable that:

- High-frequency (F_{sw}) and wideband (BW) shear waves are more accurate for the shear modulus estimation for a given SNR in the shear wave band.
- The stiffer the medium (μ_0) is, the less accurate is the estimation. Stiffer media, and thus faster shear wave speeds, yield smaller time delays for an identical jitter which ultimately leads to higher relative error in the time delay and shear modulus estimations. This relative error grows as the square root of μ_0 (cf. Fig. 3).
- The larger the distance dr between the correlated points is, the better is the shear modulus estimation. A larger distance dr will, however, decrease the final shear modulus map resolution.
- The variance itself requires the knowledge of the true shear modulus μ_0 , which is unknown experimentally.

As a first-order approximation, it is possible to use the estimate of the shear modulus maps $\mu(z, x)$ as our true shear modulus μ_0 for the estimation of the shear modulus variance σ_{μ}^2 .

In Fig. 3, the expected value of the shear modulus and its standard deviation were plotted against the tissue velocity field SNR based on (19) and (20). Different stiffness values are considered and a log representation was used to help visualize the large range of shear modulus values. As expected, for low SNRs and very stiff media, it can be difficult to obtain a good estimation. The estimated shear modulus is much more robust and accurate for soft media such as liver tissue (μ_0 from 2 to 10 kPa, 5 to 30 kPa in Young's modulus) or healthy breast tissue ($\mu_0 \sim 15$ kPa) and is still quite good for malignant breast tissue ($\mu_0 \sim 50$ kPa) depending on the acquisition SNR.

V. MATERIAL AND METHODS

We now propose to validate the expression using experimental measurements in gelatin phantoms with SSI, and by using 3-D numerical simulations.

A. SSI Experiments

SSI experiments were conducted on the different media using an ultrafast scanner prototype designed as a collaboration between the Langevin Institute (Paris, France) and Supersonic Imagine (Aix en Provence, France) [49]. All experimental data were acquired with an 8-MHz linear probe. The scanner was directly controlled using Matlab (The MathWorks Inc., Natick, MA).

Acquisitions consisted of three sequences : one imaging sequence made of 10 frames with null transmissions (0 V emission) to estimate the electronic noise, one true ultrafast sequence made of 80 frames at a fixed frame rate (standard emission) [50] to estimate tissue velocity variance, and one standard SSI sequence [2], [28] i.e., generation of a shear wave mach cone using successive radiation force pushes (150 μ s ultrasound focalization for each push) and the ultrafast 2-D imaging of the generated plane shear wave (60 frames at the same framerate); see Fig. 3. Frame rate ranged from 2000 to 4000 Hz after plane wave compounding. Seven compounded angles from -6° to 6° (2° step) were used for each image.

The scanner used IQ demodulation of the ultrasonic signals to limit the size of the data because all subsequent operations are software-based and real time, and we have therefore chosen to base this study on the same processing technique. Successive ultrafast images $V_z(z, x, t)$ of tissue velocities were reconstructed directly using phase shift estimation from the IQ data using the autocorrelator technique [35]. Therefore, only the axial component of the velocity field V_z could be retrieved, the component which corresponds to the main polarization of the generated plane shear wave which mainly propagates along the x -axis (see Fig. 1).

Reconstruction of the shear modulus maps from the shear wave propagation movies was then performed using the time of flight algorithm as described earlier, using a kernel size dr of 1 mm.

To estimate the shear modulus variance, the experiments were repeated successively 50 times without moving the probe or displacing the phantom. Shear modulus variance measurements were conducted on several homogeneous phantoms and in *in vitro* beef muscle and liver.

Parameters such as the bandwidth BW, the center frequency F , and the true shear modulus μ_0 of the medium were estimated from their averaged values in a large region of interest and over the 50 acquisitions. The bandwidth is estimated from the -3 -db limit of the spectrum and the center frequency F is estimated from the peak of the shear wave spectrum. Because the true shear modulus is assessed experimentally and unknown, it was impossible to assess any measured bias experimentally. Experiments are therefore only compared with the theory for the shear modulus variance expression.

B. Numerical Simulations

Numerical simulations were conducted using a 3-D finite-difference time-domain (FDTD) simulation software (ACEL) developed at the Langevin Institute [51]. The core FDTD implementation is based on a Viriue scheme [52] able to model the propagation of both longitudinal and transverse waves in viscous and heterogeneous solid media. The simulations were conducted using a 0.2 mm grid size and a time step automatically set to fulfill the Courant stability criterion [53]. They were performed in 3-D ($128 \times 234 \times 20$ mesh size) with absorbing boundar-

ies to simulate an infinite medium. Boundary absorbing conditions were implemented using a numerical method based on perfectly matched layers (PML) [54]. The source generating the shear wave was modeled as a line polarized and aligned along the z -axis (depth). The emission waveform consisted of a single period of a sinus function set at the center frequency $F_{sw} = 400$ Hz with a bandwidth approximately equal to the center frequency (100% bandwidth).

Seven different homogeneous and purely elastic media were simulated with shear moduli ranging from 5.5 to 320 kPa and doubling between each simulation to investigate a large range of stiffnesses. The tissue velocity field V_z along the z -axis was simulated for 20 ms of propagation with a 2500 Hz frame rate and 0.2 mm spatial grid (see Fig. 1).

To simulate acquisition noise, different spatially uniform and AWGN fields were directly added to the simulated fields with different levels and the resulting fields were band-pass filtered. The time-of-flight algorithm was then directly run on the simulated and successively corrupted tissue velocity fields to estimate the shear modulus maps. For each tissue velocity SNR value, 50 different realizations of noise were used to estimate the statistics of the shear modulus reconstruction. Parameters such as the shear wave bandwidth, center frequency, energy (SNR_{V_z}), and duration were estimated using a 1 cm^2 region of interest from the average of the simulated field to reduce the noise influence on those estimations.

A limitation of this numerical study is that the motion estimation step or autocorrelator technique was not simulated and could not be used to investigate the effects of speckle decorrelation numerically. We refer the reader to Appendix B and Palmeri's numerical study [41] for more information on this effect.

VI. RESULTS

This section illustrates the formulas found previously for both the estimation of tissue velocity variances and for the estimation of final shear modulus variances. Theoretical curves are compared with experimental and/or simulated ones. Quantitative shear modulus SNR maps predicted by the theory are compared with experimentally acquired SNR maps and a quality map for the shear modulus estimation is proposed.

A. Tissue Velocity Variance: Comparison Between Theory and Experiments

Fig. 5 presents the spatial distribution of the energy of the beamformed ultrasonic signal [Fig. 5(a)] on an *in vivo* biceps brachii as well as the beamformed noise energy [Fig. 5(b)] assessed from the null sequence (without any ultrasound emission, blue sequence in Fig. 4; all references to color refer to the online version of this paper). The normalized histogram of the noise energy samples in a small

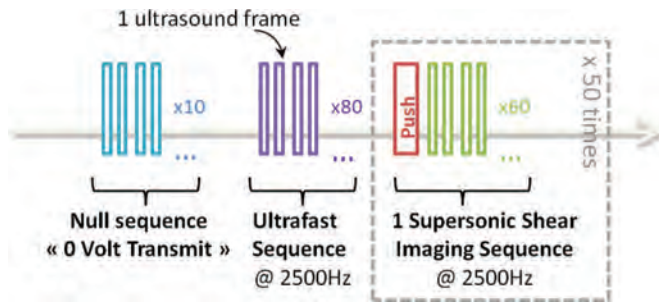


Fig. 4. The sequences used for electronic noise estimation (blue sequence), tissue velocity variance (purple sequence) and the supersonic shear imaging (SSI) sequence (one push and 60 ultrafast frames) to evaluate the shear modulus of tissue. The SSI sequence is repeated 50 times to estimate the experimental shear modulus variance.

region of interest over the 80 frames shows a zero-mean Gaussian profile. The intercorrelation between beamformed noise samples along the z -axis (depth axis), and along time show an almost uncorrelated noise. A slight correlation along the x -axis (between acquisition channels)

can be observed which is hypothesized to be due to the beamforming.

Using (8), one can estimate the tissue velocity field variance from the ultrasonic frames' energy and variance for each pixel. This can be compared with the experimentally assessed variance of the tissue velocity field which was estimated from the autocorrelation of ultrasonic frames acquired with the ultrafast sequence (see Fig. 4, purple sequence) corresponding to a sequence of 80 ultrasound frames. No shear wave is thus involved in this part.

Data were acquired on an *in vivo* biceps brachii of a healthy volunteer and are presented in Fig. 6. We can observe a very good correlation between the experimental variance map and the estimated map. The fibers of the biceps brachii are clearly visible; their strong echogenicity yields a more robust estimation of the tissue velocity as seen in the variance maps. To visualize the behavior of tissue velocity variance with respect to ultrasonic frame SNR, we plotted each pixel of the maps as a single dot. The predicted curve and the experimental points correlate very well, as seen on Fig. 6(b). The predicted variance

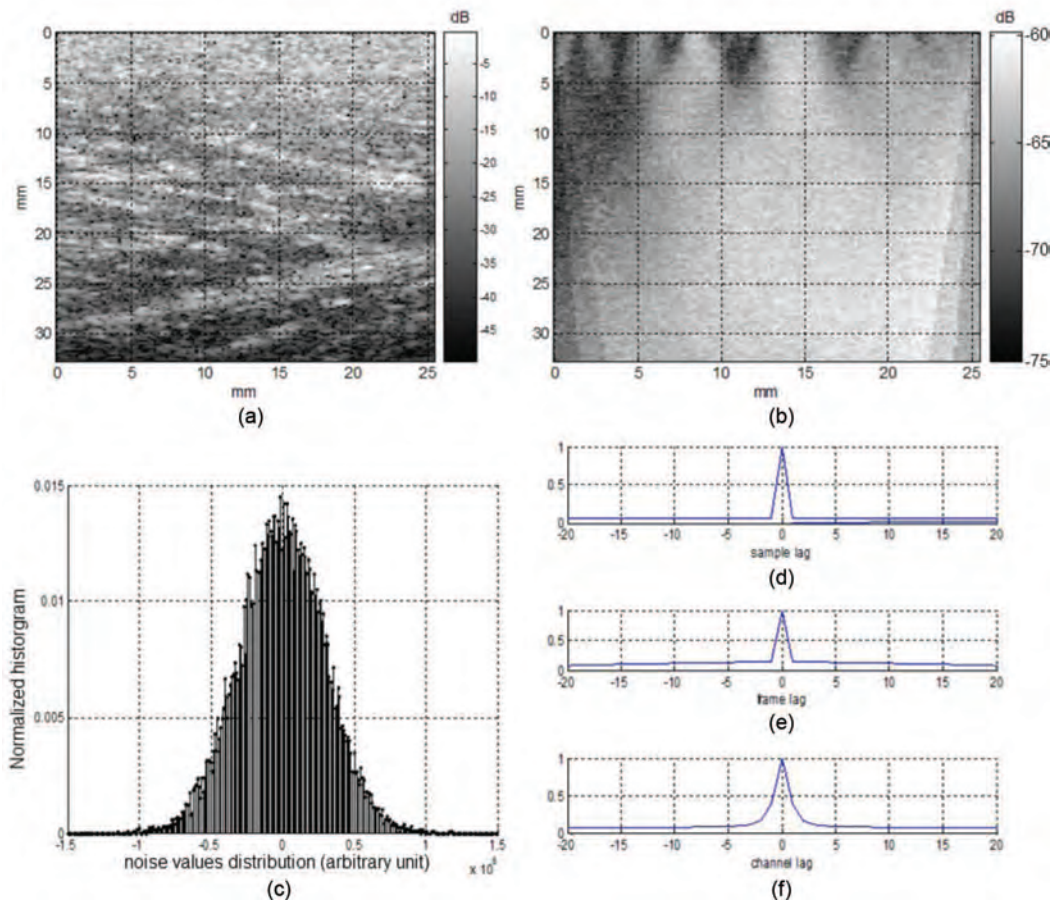


Fig. 5. (a) Spatial distribution of the beamformed ultrasonic signal energy (log compressed). (b) Spatial distribution of the beamformed electronic noise energy (log compressed) estimated directly from the ultrasonic frame acquired with the null sequence, i.e., without emission (blue sequence in Fig. 4). (c) Histogram of the beamformed noise distribution from the frames acquired with the null sequence. The additive noise follows a zero mean normal distribution. (d) Averaged inter-correlation function between beamformed noise samples along the z -axis, the beamformed noise is uncorrelated along the z -axis. (e) Averaged inter-correlation function between successively acquired and beamformed noise samples, the noise is uncorrelated along time. (f) Averaged inter-correlation function between beamformed noise samples along the x -axis, the noise is slightly correlated along the x -axis due to the beamforming.

(dashed red curve) is slightly below the experimental one (plain green curve) as expected from the formulation of the variance as lower bound. Please note that the derivation is not purely theoretical because the different parameters and the ultrasonic frame SNR used in the theory are experimentally assessed, as shown in Fig. 5.

B. Shear Modulus Variance: Comparison Between Theory, Experiments, and Simulation

In this second part, we propose to validate the expression of (21) that links the shear wave parameters and the ultrasonic acquisition SNR to the final shear modulus variance. In the experimental validation, we will also merge this expression with the theoretical expression of the acquisition SNR from the ultrasonic frame energy and electronic noise (8) to provide the validation of the full framework.

The theoretical formulation of the shear modulus variance was first compared with the numerical simulations with various background stiffness and artificial noise levels as presented in Section VI (see Fig. 7). The predicted curves are very close to the ones found numerically and slightly below, which is expected from the lower bound formulation of the shear modulus variance.

Similarly, the theory was compared with experiments in phantoms and *in vitro* beef liver and muscle tissue (see Fig. 8). For each sample, the SSI acquisition was thus repeated 50 times to allow the estimation of the shear modulus variance (see Fig. 4).

In this case, instead of just estimating the measured tissue velocity SNR (SNR_{V_z}) directly from the ultrafast sequence (purple sequence in Fig. 4), we opted to directly estimate the tissue velocity SNR from the electronic noise estimation of the machine (blue sequence in Fig. 4) as we

just did in Section VII-A. The shear wave SNR was thus estimated directly from the ratio of the experimentally assessed shear wave energy over the tissue velocity variance obtained from (8) and corrected for the bandwidth with (10). The speckle decorrelation was not taken into account here ($r = 1$). Parameters such as the shear wave bandwidth BW, center frequency F , and shear modulus μ_0 were estimated directly from the acquired velocity field in a fixed region of interest (1 cm^2) over all 50 experiments, as described in Section VI.

In Fig. 8, we can observe a good match between predicted curves and experimental ones for the phantom and the *in vitro* samples. Experimentally assessed standard deviations appeared to be close to this limit in phantom and muscle experiments and slightly larger in the liver sample. Discrepancies such as those in the case of the liver sample could either be caused by speckle decorrelation resulting from shearing, by shear wave dispersion caused by viscosity, by inhomogeneities in the sample, or by an incorrect estimation of the correct shear modulus μ_0 .

C. Toward Real-Time and Quantitative Quality Maps of the Shear Modulus

Using the previously described formulation, it is also possible to derive an all-in-one pixel-based approximation of the expected shear modulus variance using only one SSI sequence, one B-mode image to determine the ultrasonic frame energy, and a few preliminary null emissions to determine the electronic noise of the machine in real time.

Because, from (8) and (21), the dynamic of the shear modulus SNR is proportional to the dynamic of the ultrasonic frame SNR, we propose to use the shear modulus SNR expressed in decibels as a ground for a quality map: $\text{SNR}_\mu = 10 \cdot \log(\mu^2 \sigma_\mu^2)$. These quality maps can give a

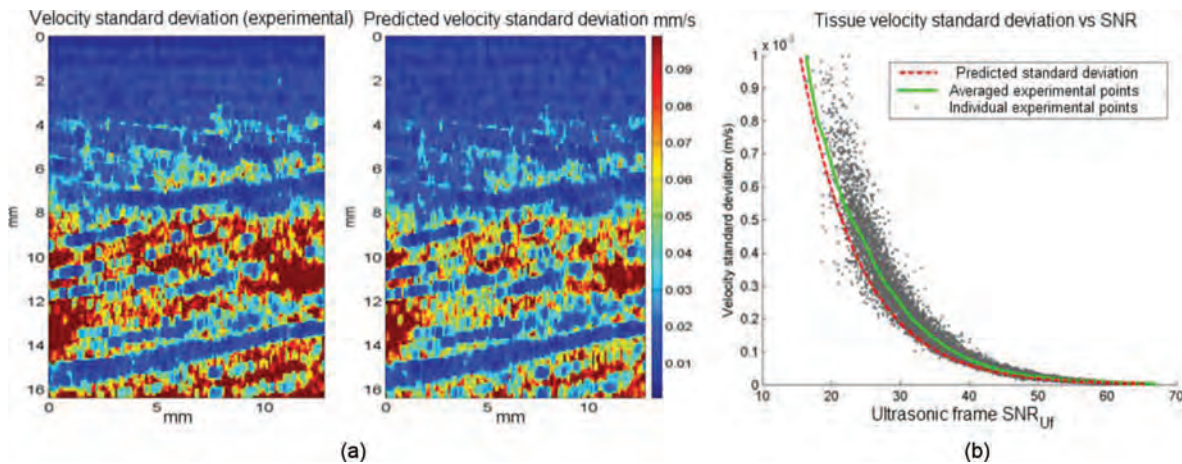


Fig. 6. Quantitative tissue velocity field standard deviation. (a) Experimental and predicted maps of the standard deviation of the tissue velocity field. Here the natural echogenicity of the biceps brachii fibers leads to higher ultrasonic frame SNR and, thus, to lower tissue velocity standard deviation (blue stripes). (b) Tissue velocity standard deviation versus the ultrasonic frame SNR, comparison between theoretical curve (red dashed) and experimental points (gray dots) whose coordinates correspond to each point of the tissue velocity field experimental standard deviation map (a) associated to the corresponding points of the ultrasonic frame SNR map. The plain green curve corresponds to the average of the experimental points over a 5-dB sliding window. There is no actual displacement in this part and thus no speckle decorrelation is taken into account ($r = 1$), only electronic noise yielding noise in the tissue velocity field estimation.

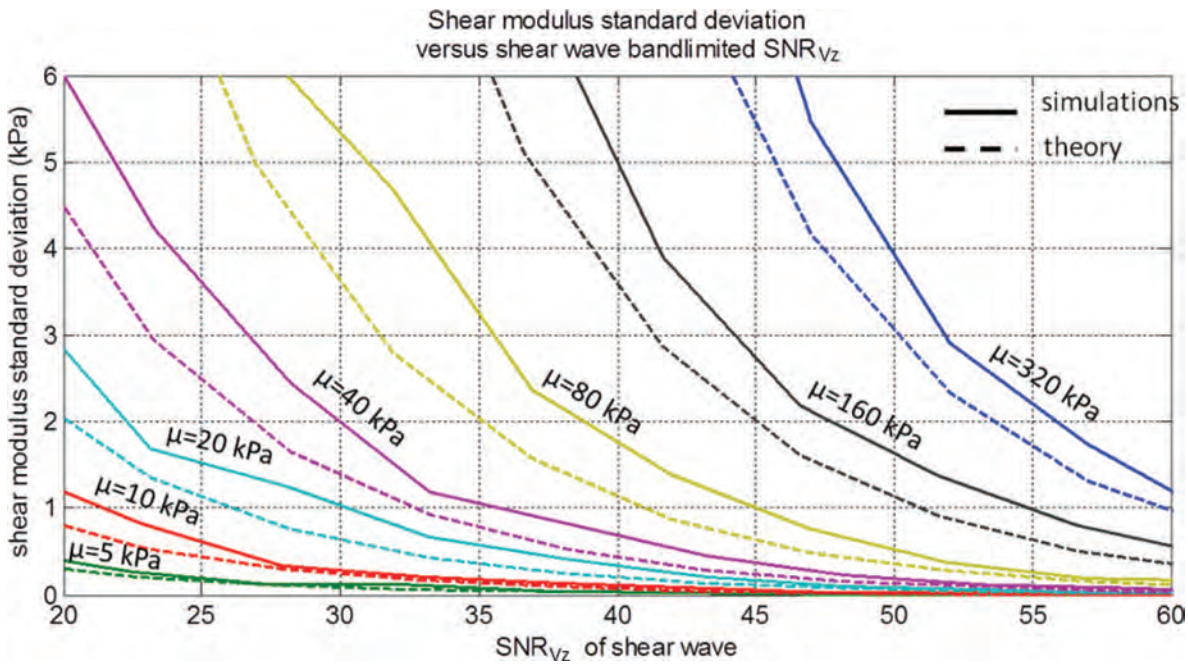


Fig. 7. Comparison between (solid lines) predicted and (dashed lines) simulated standard deviation for different levels of background stiffness ($\mu = 5, 10, 20, 40, 80, 160, 320$ kPa) and band-limited velocity field $\text{SNR}_{U_{[BW]}}$. A good correlation is obtained between the predicted and simulated curves with the same behavior as illustrated in Fig. 5. The motion estimation part is not simulated here.

good estimation of the expected shear modulus SNR, provided the different parameters of the shear wave are reliably estimated (frequency, bandwidth, energy, and the shear velocity) and the time-of-flight hypotheses are fulfilled (locally plane shear wave with low viscosity).

In Fig. 9, the predicted quality maps are very accurate in phantoms. Slightly less accurate results are obtained for

in vitro experiments, which we believe can be explained by a lower acquisition SNR and a less accurate initial shear modulus estimate [required in (21) as μ_0]. It is very interesting to see that the method can take into account natural hypoechogenic structures such as veins (hypoechogenicity yields low ultrasonic signal energy, high tissue velocity variance, and thus poor shear modulus SNR).

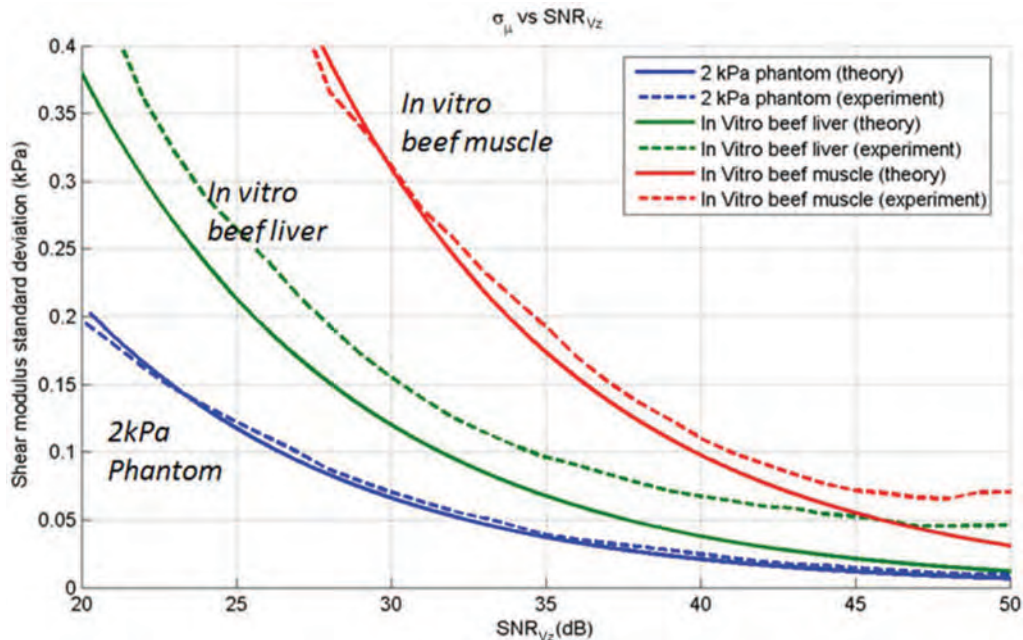


Fig. 8. (solid lines) Theoretical and (dashed lines) experimental shear modulus standard deviation in a 2-kPa phantom, in an *in vitro* beef liver, and in an *in vitro* beef muscle. Shear modulus standard deviation values are averaged over a sliding window of 5 dB to generate the curves from the scattered dots [as depicted in Fig. 6(b)].

Those quality maps (cf. Fig. 9) could provide a physical ground to determine the quality of an experiment without having to repeat it multiple times. This is of particular interest for real-time applications where repeating multiple experiments is not always possible. Given the number of hypotheses made, it is probably safe to assume that the shear modulus variance won't be as quantitative for *in vivo* cases although the thresholded value may remain valuable information to build a quality mask and help remove the unreliable areas of the image.

Thresholded quality masks (see Fig. 10) may help to choose which pixels must be kept from each acquisition when averaging shear modulus maps constructed from different push lines or from successive acquisitions (temporal averaging) to improve real-time image quality.

VII. DISCUSSION

In this paper, we derived an approximation of the variance for the tissue axial velocity estimation (8) and for the shear modulus estimation (21) in the context of shear wave elasticity imaging for high SNRs. Those formulas can be combined to provide a single path from the ultrasonic acquisition SNR to the final shear modulus SNR using a single shear wave movie and a single ultrasonic frame image.

Eq. (8) describes the relationship between ultrasonic frame SNR (beamformed and compounded IQ data in our case) and the tissue velocity estimation; this equation is derived from considerable work by Cespedes *et al.* [55], Walker and Trahey [48], and others, and was here applied to beamformed IQ signals and IQ phase shift based on the formulation of Loupas *et al.* [43] of the 1-D autocorrelator technique [35]. The resulting formula gives a good approximation of the minimum variance *in vitro* or *in vivo* for the small displacements that arise in an SSI experiment. The electronic noise measured in the beamformed IQ data appears to retain its spatial independence and is almost homogeneous (cf. Fig. 5) despite the beamforming and plane wave coherent compounding [34]. The initial ultrasonic frame SNR is thus mostly proportional to the ultrasonic frame energy, i.e., to the B-mode image. We have shown that the acquisition of a few frames without any ultrasound emission (null sequence) and a single ultrasonic image can be used to accurately estimate the variance of the displacement.

Regarding the formulation of the tissue velocity variance (8), one can note that the higher the ultrasound frequency is, the more accurate is the axial velocity estimation. The higher the acquisition frame rate is, the higher is the velocity variance. This is because the displacement between consecutive correlated frames appears smaller and smaller for higher frame rates, whereas the noise level is kept constant between two independent frames. This does not take into account the fact that oversampling with a high frame rate allows use of a low-pass filter on the data

and, thus, increasing the SNR. One must also take into account the speckle decorrelation if the frame rate is too low (cf. Appendix B). The decorrelation resulting from shear wave displacement of the speckle was introduced as a correlation factor and roughly estimated in Appendix B based on the theoretical work of McAvealey *et al.* [40], however it was tested neither experimentally nor numerically here. Readers may also refer to the numerical study of Palmeri *et al.* [41] for more information on this decorrelation effect. A better way to estimate both decorrelation and electronic noise might be to measure directly the autocovariance of the beamformed IQ signals experimentally; this will be investigated in future work.

We have then derived an analytical approximation of the minimum variance of the shear modulus estimator from the Cramer–Rao lower bound applied to the time delay estimator [47], [48]. By looking at the expression of the time delay estimator variance (15), one can notice that the higher the shear frequency and shear bandwidth are, the better is the estimation; it is thus preferable to use wideband and high-frequency shear waves to improve the estimation. Under a high ultrasonic frame SNR assumption, it is possible to derive approximations of the shear modulus expected value and variance using a Taylor series [(46), Appendix C]. The approximation of the shear modulus variance is given by (21). Two new parameters are introduced: the distance dr between correlated points and the true average shear modulus between those points μ_0 . The expression of the shear modulus expected value $E[\mu]$ shows that there is a bias that increases with noise and with the square of the true shear modulus, μ_0^2 . This bias is minimal for high SNR and soft medium but can increase significantly for very stiff tissue; additionally, the shear wave amplitude would also be smaller in those media. Note that this bias was not present in the estimation of the time delay dT and was introduced when taking the inverse and the square of the time delay to express the shear modulus: $\mu = \rho * (dr/dT)^2$. This stresses an important point: when estimating the average shear modulus in a region of interest, it is more robust, regarding measurement bias, to first estimate an average time delay $\langle dT \rangle$ over the region of interest and then estimate the average shear modulus $\langle \mu \rangle = \rho \cdot (dr/\langle dT \rangle)^2$ from this value: the bias of the values' average is smaller than the average of the biased values.

The variance of the shear modulus σ_μ^2 has the same behavior and increases with the background stiffness to the power 3, μ_0^3 [cf. (19)]. The other main factors are, of course, the acquisition SNR (mainly proportional to the B-mode contrast), the shear wave energy (dependent on the medium properties, attenuation, and stiffness) and its frequency content (frequency and bandwidth, which are also dependent on the medium, but also on the ultrasound frequency and pushing beam geometry).

Transient shear waves with large bandwidth will yield smaller variance than shear waves of the same energy with more limited bandwidth. For the same energy, a larger

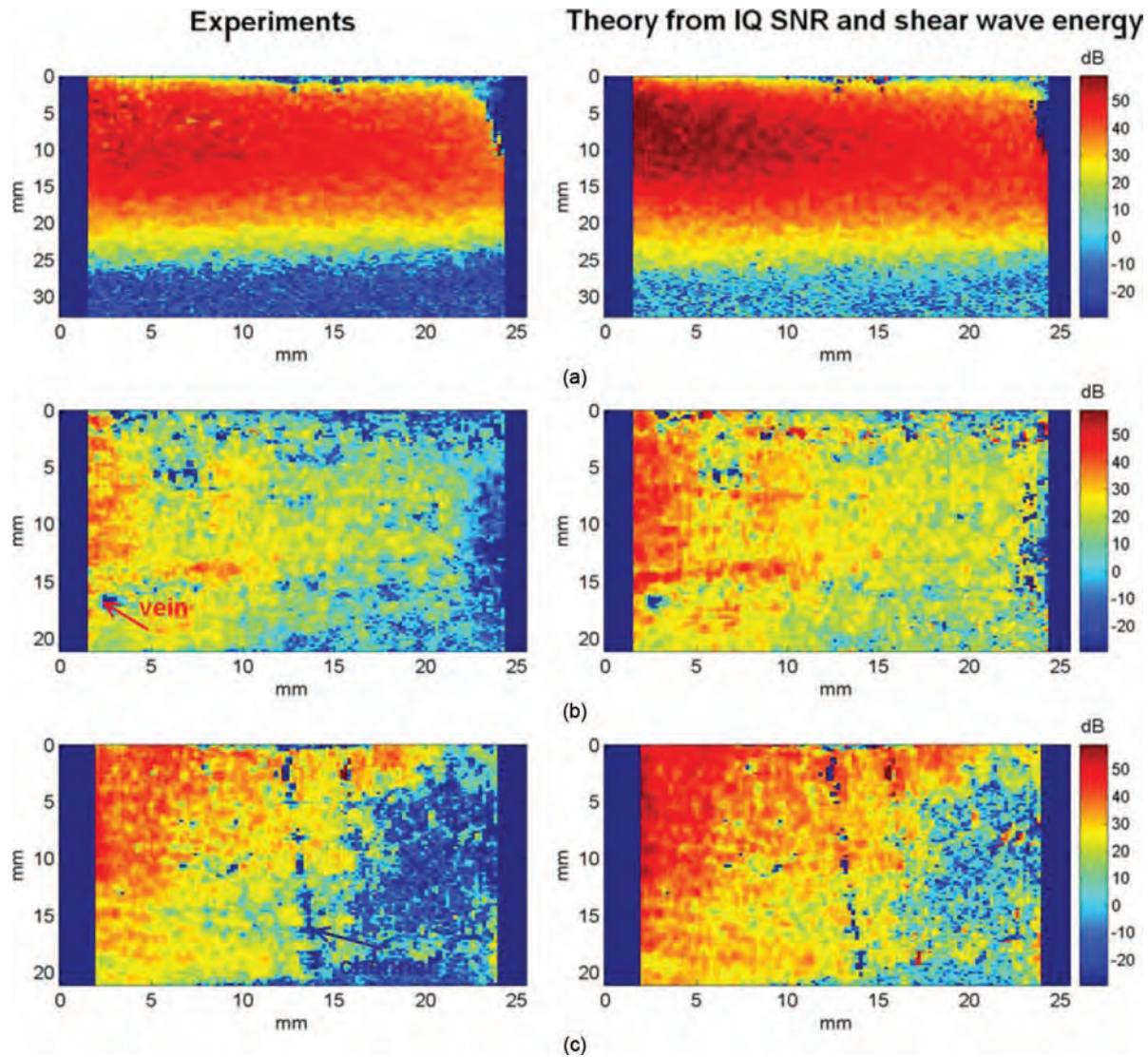



Fig. 9. Quality maps of several supersonic shear imaging (SSI) experiments in (a) a 2-kPa phantom, (b) an *in vitro* beef liver, and (c) an *in vitro* beef muscle. The maps are expressed as shear modulus SNR: $\text{SNR}_\mu = 10 * \log(\mu_0^2/\sigma_\mu^2)$ in decibels, where μ_0 is the estimated average shear modulus. The predicted shear modulus SNR values (right column) are always higher than the experimental ones (left column) because the predicted shear modulus variance is always smaller than the real variance. The push sequence is generated on the left of the image and the shear wave is attenuated as it propagates toward the right edge of the image. In clinical application, multiple push lines are generated to obtain a homogeneous quality. In (b), a small vein is visible on both maps, showing that it is correctly taken into account by the method. 

bandwidth requires a shorter radiation force push with a higher intensity which will ultimately be bounded by the Food and Drug Administration (FDA) limitations (intensity spatial peak time averaged, $I_{\text{sp}}^{\text{pta}}$, limited to 720 mW/cm^2). Moreover, there is also a tradeoff between increasing the shear wave bandwidth and center frequency and the shear wave SNR because of the higher attenuation of the shear waves at higher frequency.

The distance between the correlated points d_r is also a very interesting parameter because it influences both the shear modulus bias and variance. Larger d_r values lead to better estimates of the shear modulus. This can be simply explained by the fact that the longer the distance between the two correlated points is, the larger is the propagation delay dT between them and the smaller is the relative

error in the time-delay estimation because the absolute error of the time-delay is itself independent of the distance d_r . Unfortunately, it is not possible to increase this distance d_r too much, because it is related to the kernel size of the time-of-flight algorithm: increasing this distance would decrease the actual resolution of the elasticity image: this is the expression of the noise/resolution tradeoff of the time-of-flight algorithm. Conversely, the resolution cannot be increased infinitely, because at some point the noise level in the estimated shear modulus value might be larger than the true shear modulus contrast of the image, making it impossible to distinguish inclusions. A resolution limit could thus be defined, for each noise level, to ensure that small inclusions are still distinguishable from the background value. A spatially variant resolution based

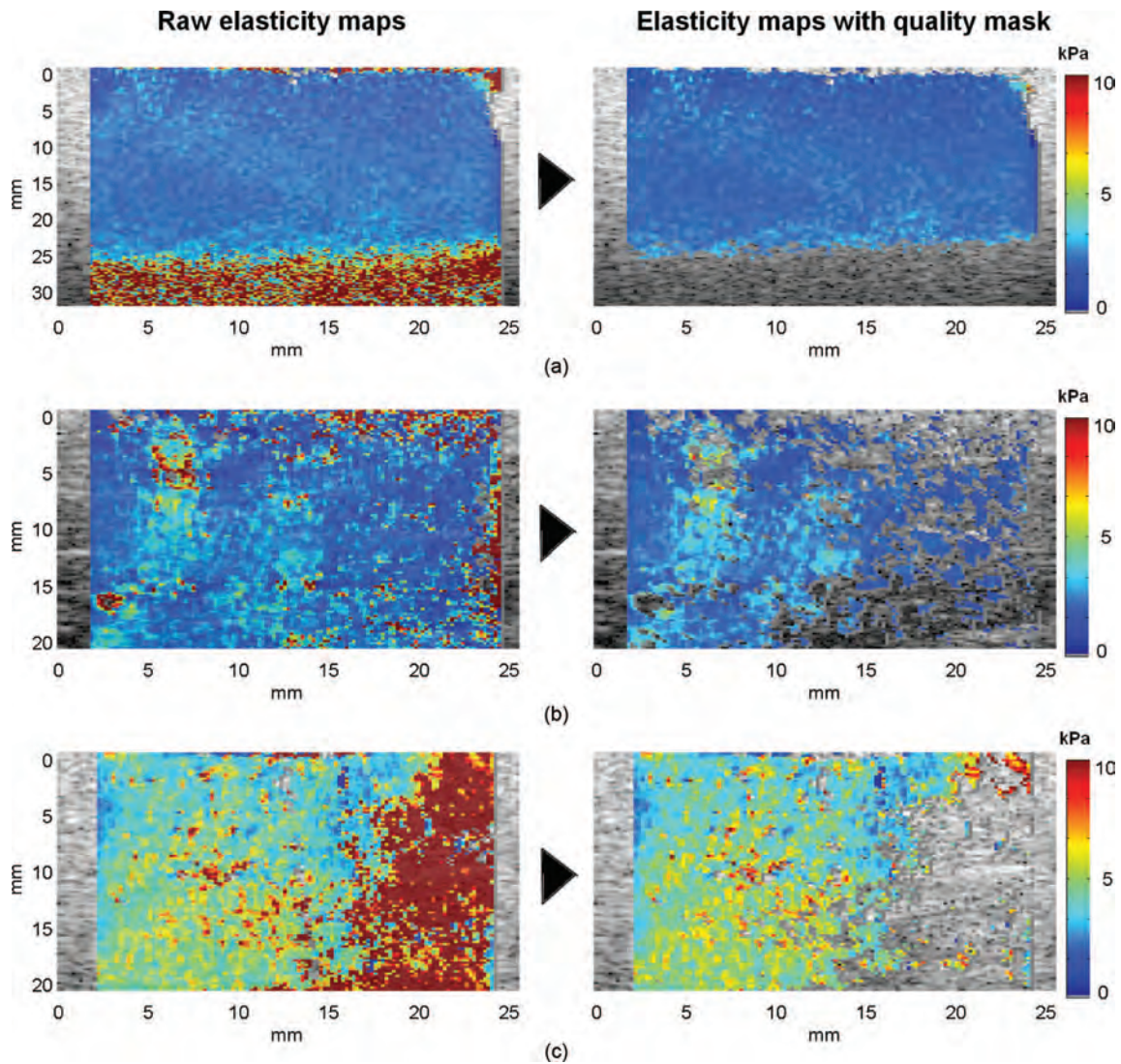


Fig. 10. Shear modulus maps of several supersonic shear imaging (SSI) experiments in (a) a 2-kPa phantom, (b) an *in vitro* beef liver, and (c) an *in vitro* beef muscle; without (left column) and with (right column) a mask based on the thresholding of quality maps of Fig. 9. The values are expressed in kilopascals. A threshold of 20 dB (relative error of 10%) was used in the quality maps of Fig. 9 to display only pixels with a higher expected SNR value. The mask allows removal of most areas, down to the pixel level, that clearly appear to be corrupted by noise. Those areas would not otherwise be easily distinguished from high-stiffness regions. Note that the plane shear wave is generated on the left of the image, which explains the higher SNR in this area for all figures of this paper. To build a complete image, multiple acoustic radiation force pushing lines are required.

on the locally estimated variance could also be developed to improve estimation in noisy areas by locally degrading the resolution.

This model is equivalent, for transient shear waves, to the model of Urban *et al.* [56] which estimates the shear modulus and viscosity variance of monochromatic shear waves using the SDUV technique [29], which relies on the estimation of the phase velocity for different shear wave frequencies. We can observe that both the transient and monochromatic approaches yield similar conclusions with regard to the different parameters of the model such as the kernel size, the shear wave frequency (or center frequency in the transient case), and shear modulus of the medium.

A few other approaches have been developed in the literature for the improvement of shear wave data based on quality estimation of data or inherently more robust

estimators. For example, Wang *et al.* proposed use of the RANSAC algorithm on time-to-peak estimates [57]; this can be quite efficient to remove outliers but does not estimate nor improve normally distributed noise. Urban and Greenleaf proposed a quality estimator for dispersion curves estimation based on the Kramers–Kronig relationship [58] between the estimated phase velocity and attenuation in the framework of shear wave dispersion ultrasound vibrometry [29]; this approach has a strong physical basis and could be very helpful, provided attenuation can be reliably measured. Here, we proposed use of the shear modulus variance maps and shear modulus SNR maps [$\text{SNR}_\mu = 10 \times \log(\mu_0^2/\sigma_\mu^2)$] constructed from the minimum shear modulus variance expression σ_μ^2 (21). Those maps enable quantitatively rating of regions that can be trusted in an SSI experiment. The maps are shown to correlate

well with the maps estimated experimentally from the shear modulus variance from successive SSI measurements (see Fig. 9). It is difficult to state that the resulting maps will remain as quantitative *in vivo*, because of speckle decorrelation processes or background motion, although, thresholded, they could be used as quality masks to help remove noisy areas from the displayed shear modulus maps (see Fig. 10). Used as a weight in a weighted average scheme, the shear modulus maps could possibly be greatly improved using the spatial compounding of several pushes or the temporal averaging of successive frames.

Finally, the model of the shear waves used here was rather simple, because a locally plane shear wave is considered in weakly heterogeneous media. These results are useful to understand the role of different imaging parameters in simple cases and could already be applied to specific applications such as liver fibrosis imaging where reflections and heterogeneities are small and estimation quality is of great interest. Future work will be focused on the quantification of the shear modulus estimator in the case of more complex media such as heterogeneous or viscous media by updating the rather simple equation (16) with (6) and considering the dispersion of shear waves.

VIII. CONCLUSION

In this paper, we developed approximations of the tissue velocity variance and the shear modulus variance based on the Cramer–Rao lower bound and on the physical parameters of the medium, the generated shear wave, and the ultrasound scanner. This formulation gives a good agreement with the numerical simulations and *in vitro* experiments and allows the creation of quality maps based on a solid physical ground. The formula stresses the importance of high-frequency, wideband shear waves to improve the estimated shear modulus quality and highlights the risk of shear modulus biases for low-SNR or very stiff media. It can be useful to help understand and build better sequences for shear wave elastography techniques relying on a time-of-flight approach for the shear velocity estimation. Future work will be focused on shear modulus quantification in more complex media such as heterogeneous or viscous media where the locally plane shear wave assumption might break.

APPENDIX A

This appendix describes the derivation of the formula for the tissue velocity variance when using 1-D autocorrelator technique of Kasai *et al.* [35]. It is derived from Loupas *et al.* [43].

The beamformed and compounded IQ signal (IQ*c*) for a given channel *i* can be represented as

$$\text{IQ}c_i(m, n) = I(m, n) + j \cdot Q(m, n), \quad (22)$$

where *m* represents the samples along the depth line and *n* the frame number.

The signal IQ*c_i* can be integrated over *M* axial samples to increase SNR such that

$$\text{IQ}c_{\text{int}}(n) = \sum_{m=m'}^{M-1} I(m, n) + j \cdot Q(m, n) = I_{\text{int}}(n) + j \cdot Q_{\text{int}}(n), \quad (23)$$

where the channel index *i* and axial sample index *m'* are removed to simplify the expression.

The autocorrelation of this signal over *N* frames can be written as

$$\gamma_{\text{int}}(n') = \sum_{n=0}^{N-n'-1} \text{IQ}c_{\text{int}}(n) \cdot \text{IQ}c_{\text{int}}^*(n+n'), \quad (24)$$

and the tissue velocity *V_z* is estimated by

$$V_z = \frac{c}{2} \frac{\text{FPS}}{2\pi F_{\text{us}}} \tan^{-1} \left\{ \frac{\Im(\gamma_{\text{int}}(1))}{\Re(\gamma_{\text{int}}(1))} \right\}, \quad (25)$$

where *c* is the sound velocity, *F_{us}* is the ultrasound frequency, and FPS is the ultrafast framerate.

In our case where *N* = 2 (two frames used per estimation), the formula can be rewritten as

$$V_z = \frac{c}{2} \frac{\text{FPS}}{2\pi F_{\text{us}}} \tan^{-1} \left\{ \frac{Q_{\text{int}}(0)I_{\text{int}}(1) - Q_{\text{int}}(1)I_{\text{int}}(0)}{Q_{\text{int}}(0)Q_{\text{int}}(1) + I_{\text{int}}(0)I_{\text{int}}(1)} \right\}. \quad (26)$$

By rewriting the signal IQ*c* as the sum of the true signal IQ*c₁* and an AWGN IQ*c₂*, the IQ*c* autocorrelation for a lag *n'* can be written as

$$\gamma(n') = \gamma_1(n') + \gamma_2(n'), \quad (27)$$

where $\gamma_1(0)$ is the true signal IQ*c₁* energy, $r = \gamma_1(1)/\gamma_1(0)$ is the correlation of two successive IQ*c₁* frames, $\gamma_2(0)$ is the noise energy, and $\gamma_2(1) = 0$ for a white noise.

This allows the axially integrated IQ*c* SNR to be defined as

$$\text{SNR}_{\text{Uf}} = \text{SNR}_{\text{IQ}} = \frac{|\gamma_{\text{int}1}(0)|}{|\gamma_{\text{int}2}(0)|} = \frac{E[|\text{IQ}c_{\text{int}1}|^2]}{E[|\text{IQ}c_{\text{int}2}|^2]}. \quad (28)$$

The variance of the tissue velocity estimator is given by

$$\sigma_{V_z}^2 = \frac{c^2 \text{FPS}^2 \left(1 + \frac{1}{\text{SNR}_{\text{Uf}}} \right)^2 - \left| \frac{\gamma_{\text{int}1}(1)}{\gamma_{\text{int}1}(0)} \right|^2}{4F_{\text{us}}^2 \cdot 8N\pi^2 \left| \frac{\gamma_{\text{int}1}(1)}{\gamma_{\text{int}1}(0)} \right|^2}, \quad (29)$$

which can be rewritten as (for *N* = 2 frames)

$$\sigma_{V_z}^2 = \frac{c^2 \text{FPS}^2}{64\pi^2 F_{\text{us}}^2} \left(\frac{1}{r^2} \left(1 + \frac{1}{\text{SNR}_{\text{Uf}}} \right)^2 - 1 \right). \quad (30)$$

For a high SNR and correlation value, and introducing a decorrelation SNR_r as originally proposed in Cespedes *et al.* [45], this expression can be approximated by

$$\sigma_{V_z}^2 \approx \frac{c^2 \text{FPS}^2}{32\pi^2 F_{\text{us}}^2} \left(\frac{1}{\text{SNR}_r} + \frac{1}{\text{SNR}_{\text{uf}}} \right) \quad \text{where } \text{SNR}_r = \frac{r}{1-r}. \quad (31)$$

A rough estimation of the correlation coefficient r between successive ultrasonic frames is presented in Appendix B, as well as the corresponding estimation of the decorrelation SNR.

APPENDIX B

This part describes a rough estimation of the IQ correlation loss resulting from speckle shearing caused by the shear wave displacement. It is based on McAvealey *et al.* [40], which compares the size of the imaging PSF and the size of the displacement volume to estimate the correlation factor of the speckle before and after the displacement. The original paper is focused on the displacement at the radiation force focus and is adapted here to be used with the displacement generated by a propagating shear wave.

Because the generated shear wave is close to a cylindrical wave, it is much longer in the axial direction than the PSF and this dimension can be neglected, as was proposed in the original paper for similar reasons. We will therefore concentrate the analysis on comparing the shear wave dimensions in the lateral and elevation directions with the corresponding PSF dimensions.

By targeting a common full-width at half-maximum (FWHM) between a cosine function (representing the shear wave in the propagation direction) and a Gaussian function (used as the displacement model in [40]), we can obtain a relationship between the shear wavelength and the lateral Gaussian variance P_x^2 used in the original paper, which is valid around the shear wave peak:

$$P_x \approx \frac{1}{12} \frac{\lambda\sqrt{2}}{\sqrt{\ln(2)}}. \quad (32)$$

We can then derive the ratio W_x between the lateral dimension of the displaced area (P_x) and the lateral dimension of the tracking PSF (T_x):

$$W_x = \frac{P_x}{T_x} \approx \frac{1}{12} \frac{\sqrt{2}}{\sqrt{\ln(2)}} \frac{\lambda_{\text{sw}}}{\lambda_{\text{us}} \text{fd}}, \quad (33)$$

where λ_{sw} and λ_{us} are, respectively, the shear and ultrasound wavelength and fd is the imaging f-number.

The shear wave is also much larger than the PSF in the elevation direction because the shear wave is approximately cylindrical.

We now must estimate the ratio between the PSF elevation size and the shear wave elevation size, defined as its FWHM in this direction in [40]. In the relevant elevation-lateral plane $[x, y]$, which is perpendicular to the imaging plane, the shear wave appears circular with a radius given by the distance of propagation from the source and

a width related to its wavelength. The larger the propagation distance from the source is, the larger is the radius and the larger is the FWHM of the wave in the elevation direction (see Fig. 11).

By solving for the coordinates of the point P (Fig. 11) using the Pythagorean theorem and considering a propagation distance x_0 from the source, one can estimate that the shear wave elevation FWHM, denoted FWHM_y , is

$$\text{FWHM}_y = 2\sqrt{\frac{\lambda_{\text{sw}}}{6} \cdot \left(2 \cdot x_0 + \frac{\lambda_{\text{sw}}}{6} \right)}. \quad (34)$$

By targeting again a common FWHM from a Gaussian profile, we can find the variance P_y^2 of the equivalent Gaussian profile such that

$$P_y = \frac{\sqrt{2}}{12\sqrt{\ln(2)}} \sqrt{\lambda_{\text{sw}}(12x_0 + \lambda_{\text{sw}})}. \quad (35)$$

We can then derive the ratio W_y between the width of the displaced area (P_y) and the width of the tracking PSF (T_y):

$$W_y = \frac{\sqrt{2}}{12\sqrt{\ln(2)}} \frac{\sqrt{\lambda_{\text{sw}}(12x_0 + \lambda_{\text{sw}})}}{\lambda_{\text{us}} \text{fd}_y}, \quad (36)$$

where fd_y is the f-number in the elevation direction, which depends mainly on the depth and array element heights. Minimum distance between the first reconstructed points and the center of the shear wave source is usually not less than one-half of the shear wavelength ($x_0 > \lambda_{\text{sw}}/2$).

The fitting of the shear wave profiles on Gaussian profiles by (32) and (35) is illustrated in Fig. 11.

From McAvealey *et al.* [40, Eq. (11) and (12)], we can rewrite the expression of the biased tissue velocity V_z and the associated correlation coefficient r as

$$V_z = \frac{2W_x W_y}{\sqrt{(2W_x^2 + 1)(2W_y^2 + 1)}} \text{FPS} d_{z0} \quad (37)$$

$$r = 1 - 64\pi^2 W_x W_y \left(\frac{1}{\sqrt{(2W_x^2 + 2)(2W_y^2 + 2)}} - \frac{2W_x W_y}{(2W_x^2 + 1)(2W_y^2 + 1)} \right) \left(\frac{d_{z0}}{\lambda_{\text{us}}} \right)^2, \quad (38)$$

where d_{z0} is the true displacement between two consecutive frames. The true displacement d_{z0} can be inferred from the absolute peak displacement A_{z0} (absolute = from its original position), its center frequency F_{sw} , and the imaging frame rate FPS:

$$d_{z0}(k) = A_{z0} \left[\sin \left(2\pi F_{\text{sw}} \frac{k+1}{\text{FPS}} + \phi_0 \right) - \sin \left(2\pi F_{\text{sw}} \frac{k}{\text{FPS}} + \phi_0 \right) \right], \quad (39)$$

where the tissue relative displacement $d_{z0}(k)$ is estimated between the k th and $k+1$ th frames.

By rewriting this expression as an intergral, we can write the inequality

$$\begin{aligned} d_{z0}(k) &= 2\pi \frac{F_{sw}}{FPS} A_{z0} \int_0^1 \cos\left(2\pi F_{sw} \frac{k}{FPS}\right) dk \\ &\leq 2\pi A_{z0} \frac{F_{sw}}{FPS} \quad \text{since } \forall \theta, \cos(\theta) \leq 1. \end{aligned} \quad (40)$$

The correlation coefficient between the tissue velocity profiles will thus depend on the true peak displacement A_{z0} , the shear wave center frequency F_{sw} , and also on the imaging frame rate FPS and ultrasound wavelength λ_{us} , so that

$$\begin{aligned} r \geq 1 - 64\pi^2 W_x W_y &\left(\frac{1}{\sqrt{(2W_x^2 + 2)(2W_y^2 + 2)}} \right. \\ &\left. - \frac{2W_x W_y}{(2W_x^2 + 1)(2W_y^2 + 1)} \right) \left(\frac{2\pi A_{z0} F_{sw}}{FPS \lambda_{us}} \right)^2. \end{aligned} \quad (41)$$

Because the unbiased true displacement d_{z0} or true peak displacement A_{z0} might be difficult to assess experimentally, it might more useful to express the correlation coefficient directly from the biased quantities such as the maximal experimentally assessed and biased tissue displacement d_{zmax} or tissue velocity V_{zmax} which can be introduced by substituting (36) into (37):

$$r \geq 1 - 2 \left(\frac{2\pi}{\lambda_{us}} \right)^2 \left(\frac{(2W_x^2 + 1)(2W_y^2 + 1)}{2W_x W_y \sqrt{(2W_x^2 + 2)(2W_y^2 + 2)}} - 1 \right) \frac{V_{zmax}^2}{FPS^2}. \quad (42)$$

Using the typical values from the experimental part of this paper, i.e., an 8-Mhz transducer and a 200-Hz shear wave, we can estimate the correlation coefficient and multiplicative bias due to speckle shearing. The 8-Mhz transducer yields a PSF FWHM comparable to that of the focused transmit mode, thanks to the coherent plane wave compounding sequence that reconstructs a PSF from 7 plane waves with different transmit angles [34]. As a high hy-

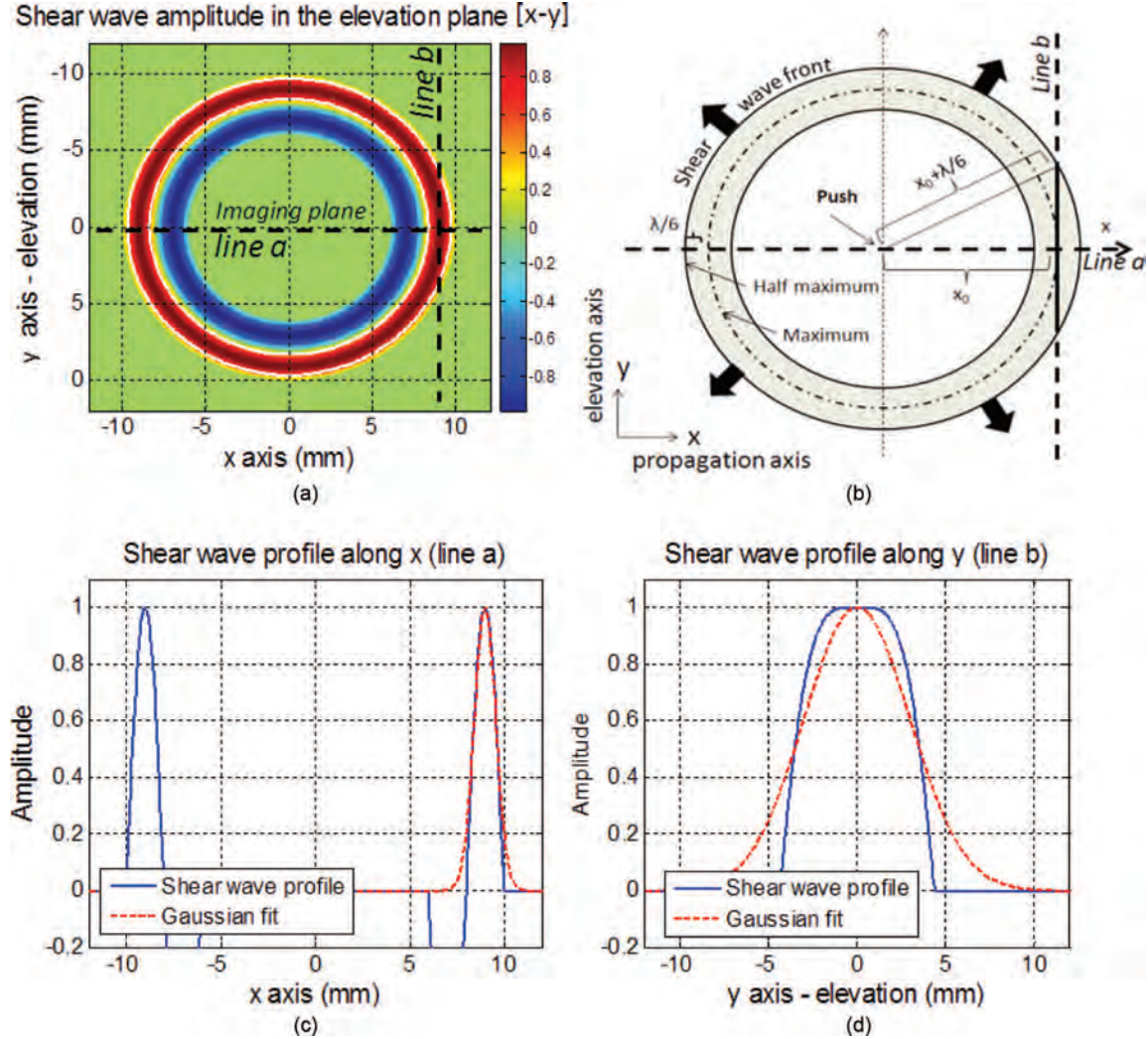


Fig. 11. (a) Representation of the normalized shear wave amplitude in the elevation plane $[x, y]$. (b) The elevation full-width at half-maximum of the shear wave can be estimated geometrically based on the wavelength λ_{sw} and propagation distance x_0 using the Pythagorean theorem. (c) Profile of the normalized shear wave amplitude along the line **a** in the lateral direction (x -axis) and the corresponding Gaussian profile fit from (32). (d) Profile of the normalized shear wave amplitude along the line **b** in the elevation direction (y -axis) and the corresponding Gaussian profile fit from (35).

TABLE I. ESTIMATION OF THE SHEAR WAVE PARAMETERS AND DECORRELATION SNR FOR THE DIFFERENT EXPERIMENTS.

	Estimated experimentally					Estimated from (41)	
	V_z max (mm/s)	FPS (Hz)	$\langle F_{sw} \rangle$ (Hz)	$\langle \mu_0 \rangle$ (kPa)	$\langle \text{SNR}_{IQ} \rangle$ (dB)	Bias	SNR_r (dB)
2-kPa phantom	2.2	3000	190	2	48	0.95	54
Beef liver	1.1	2000	170	2.4	48	0.96	59
Beef muscle	1.8	4000	200	5	50	0.98	64

pothesis, a larger f-number of $fd = 1.5$ was used for the imaging plane with an average f-number of $fd_z = 5$ in the elevation direction considering the height of the elements (4 mm) and the elevation focus (20 mm) of the probe. Table I gives some estimation of the correlation coefficient and associated decorrelation SNR [cf. (31)] based on the medium and experimental parameters.

Shear wave tracking is a domain where electronic noise can easily be predominant ($\text{SNR}_{Uf} < \text{SNR}_r$) because of the relatively low amplitude of shear waves and high frame rate, which yields a low displacement over wavelength ratio compared with other strain-like approaches. Nevertheless, it should be clear by looking at the numbers in Table I that correlation loss will happen due to shearing and mechanically increase the observed tissue velocity variance as stated by (8). A direct estimator of the autocorrelation of IQ signals with a shear wave propagating from (22) might be a better way to estimate both electronic noise and decorrelation and will be investigated in future work.

It is interesting that increasing shear wave amplitude will yield a competition between the decrease of the tissue velocity variance resulting from larger IQ phase shifts and its increase resulting from increased decorrelation between IQ samples. In some cases, such as for high shear wave amplitude, very soft medium, or low achievable frame rate, it might be necessary to use a better estimator for the tissue velocity as proposed by Loupas *et al.* [43] to reduce the influence of IQ signal decorrelation and avoid this tradeoff.

APPENDIX C

The multivariate Taylor expansion of a function of a random variable around its expected value can be written as [59]

$$f(X) \approx f(E[X]) + f'(E[X])(X - E[X]) + \frac{1}{2} f''(E[X])(X - E[X])^2. \quad (43)$$

The expected value of this function is

$$\begin{aligned} E[f(X)] &\approx f(E[X]) + E[f'(E[X])(X - E[X])] \\ &\quad + E\left[\frac{1}{2} f''(E[X])(X - E[X])^2\right] \\ &\approx f(E[X]) + f'(E[X])(E[X] - E[X]) \\ &\quad + \frac{1}{2} f''(E[X])E[(X - E[X])^2] \\ &\approx f(E[X]) + \frac{1}{2} f''(E[X])\text{Var}[X], \end{aligned} \quad (44)$$

and its variance can be simplified to

$$\begin{aligned} \text{Var}[f(X)] &\approx \text{Var}[f(E[X])] + \text{Var}[f'(E[X])(X - E[X])] \\ &\quad + \text{Var}\left[\frac{1}{2} f''(E[X])(X - E[X])^2\right] \\ &\approx f'(E[X])^2 \text{Var}[X]. \end{aligned} \quad (45)$$

Considering the function $f(x) = 1/x^2$ and posing $M = f(E[x]) = 1/E[x]^2$, we can write

$$\begin{aligned} E\left[\frac{1}{X^2}\right] &\approx \frac{1}{E[X]^2} + \frac{3}{E[X]^4} \text{Var}[X] \\ &\approx M + 3M^2 \text{Var}[X] \end{aligned} \quad (46)$$

and

$$\begin{aligned} \text{Var}\left[\frac{1}{X^2}\right] &\approx \frac{4}{E[X]^5} \text{Var}[X] \\ &\approx 4M^3 \text{Var}[X]. \end{aligned} \quad (47)$$

ACKNOWLEDGMENTS

We are grateful for the comments and help from T. Loupas, as well as to the anonymous reviewers for their constructive and strongly relevant comments on the issue of speckle decorrelation and improvements of the manuscript quality.

REFERENCES

- [1] A. Athanasiou, A. Tardivon, M. Tanter, B. Sigal-Zafrani, J. Bercoff, T. Defieux, J. L. Gennisson, M. Fink, and S. Neunenschwander, "Breast lesions: Quantitative elastography with supersonic shear imaging—preliminary results," *Radiology*, vol. 256, no. 1, pp. 297–303, Jul. 2010.
- [2] M. Tanter, J. Bercoff, A. Athanasiou, T. Defieux, J. L. Gennisson, G. Montaldo, M. Muller, A. Tardivon, and M. Fink, "Quantitative assessment of breast lesion viscoelasticity: Initial clinical results using supersonic shear imaging," *Ultrasound Med. Biol.*, vol. 34, no. 9, pp. 1373–1386, Sep. 2008.
- [3] R. Sinkus, M. Tanter, T. Xydeas, and S. Catheline, "Viscoelastic shear properties of in vivo breast lesions measured by MR elastography," *Magn. Reson. Imaging*, vol. 23, no. 2, pp. 159–165, 2005.
- [4] A. Tardivon, C. E. Khoury, F. Thibault, A. Wyler, B. Barreau, and S. Neunenschwander, "Elastography of the breast: A prospective study of 122 lesions," *J. Radiol.*, vol. 88, no. 5, pt. 1, pp. 657–662, 2007.
- [5] L. Sandrin, B. Fourquet, J. M. Hasquenoph, S. Yon, C. Fournier, F. Mal, C. Christidis, M. Ziol, B. Poulet, F. Kazemi, M. Beaugrand, and R. Palau, "Transient elastography: A new noninvasive method

- for assessment of hepatic fibrosis," *Ultrasound Med. Biol.*, vol. 29, no. 12, pp. 1705–1713, 2003.
- [6] L. Castera, J. Vergniol, J. Foucher, and B. L. Bail, "Prospective comparison of transient elastography, Fibrotest, APRI, and liver biopsy for the assessment of fibrosis in chronic hepatitis C," *Gastroenterology*, vol. 128, no. 2, pp. 343–350, 2005.
- [7] D. Klatt, P. Asbach, J. Rump, S. Papazoglou, R. Somasundaram, J. Modrow, J. Braun, and I. Sack, "In vivo determination of hepatic stiffness using steady-state free precession magnetic resonance elastography," *Invest. Radiol.*, vol. 41, no. 12, pp. 841–848, Dec. 2006.
- [8] L. Huwart, F. Peeters, R. Sinkus, L. Annet, N. Salameh, L. C. ter Beek, Y. Horsmans, and B. E. Van Beers, "Liver fibrosis: Non-invasive assessment with MR elastography," *NMR Biomed.*, vol. 19, no. 2, pp. 173–179, Apr. 2006.
- [9] M. Muller, J.-L. Gennisson, T. Defieux, M. Tanter, and M. Fink, "Quantitative viscoelasticity mapping of human liver using supersonic shear imaging: Preliminary in vivo feasibility study," *Ultrasound Med. Biol.*, vol. 35, no. 2, pp. 219–229, Feb. 2009.
- [10] J.-L. Gennisson, N. Grenier, R. Hubrecht, L. Couzy, Y. Delmas, M. Derieppe, S. Lepreux, P. Merville, A. Criton, J. Bercoff, and M. Tanter, "Multiwave technology introducing shear wave elastography of the kidney: Pre-clinical study on a kidney fibrosis model and clinical feasibility study on 49 human renal transplants," in *Proc. IEEE Ultrasonic Symp.*, San Diego, CA, 2010, pp. 1356–1359.
- [11] F. Sebag, J. Vaillant-Lombard, J. Berbis, V. Griscti, J. F. Henry, P. Petit, and C. Oliver, "Shear wave elastography: A new ultrasound imaging mode for the differential diagnosis of benign and malignant thyroid nodules," *J. Clin. Endocrinol. Metab.*, vol. 95, no. 12, pp. 5281–5288, Sep. 2010.
- [12] R. Chopra, A. Arani, Y. Huang, M. Musquera, J. Wachsmuth, M. Bronskill, and D. Plewes, "In vivo MR elastography of the prostate gland using a transurethral actuator," *Magn. Reson. Med.*, vol. 62, no. 3, pp. 665–671, Sep. 2009.
- [13] S. I. Ringleb, S. F. Bensamoun, Q. Chen, A. Manduca, K. N. An, and R. L. Ehman, "Applications of magnetic resonance elastography to healthy and pathologic skeletal muscle," *J. Magn. Reson. Imaging*, vol. 25, no. 2, pp. 301–309, 2007.
- [14] J. Basford, T. Jenkyn, K. An, R. Ehman, G. Heers, and K. Kaufman, "Evaluation of healthy and diseased muscle with magnetic resonance elastography," *Arch. Phys. Med. Rehabil.*, vol. 83, no. 11, pp. 1530–1536, Nov. 2002.
- [15] M. A. Dresner, G. Rose, P. J. Rossman, and R. Muthupillai, "Magnetic resonance elastography of skeletal muscle," *J. Magn. Reson. Imaging*, vol. 13, no. 2, pp. 269–276, Jan. 2001.
- [16] T.-M. Nguyen, M. Couade, J. Bercoff, and M. Tanter, "Assessment of viscous and elastic properties of sub-wavelength layered soft tissues using shear wave spectroscopy: Theoretical framework and in vitro experimental validation," *IEEE Trans. Ultrason. Ferroelectr. Freq. Control*, vol. 58, no. 11, pp. 2305–2315, Nov. 2011.
- [17] M. Couade, M. Pernot, E. Messas, A. Bel, M. Ba, A. Hagege, M. Fink, and M. Tanter, "In vivo quantitative mapping of myocardial stiffening and transmural anisotropy during the cardiac cycle," *IEEE Trans. Med. Imaging*, vol. 30, no. 2, pp. 295–305, Sep. 2010.
- [18] M. Couade, M. Pernot, C. Prada, E. Messas, J. Emmerich, P. Bruneval, A. Criton, M. Fink, and M. Tanter, "Quantitative assessment of arterial wall biomechanical properties using shear wave imaging," *Ultrasound Med. Biol.*, vol. 36, no. 10, pp. 1662–1676, Oct. 2010.
- [19] L. Castera, X. Forns, and A. Alberti, "Non-invasive evaluation of liver fibrosis using transient elastography," *J. Hepatol.*, vol. 48, no. 5, pp. 835–847, May 2008.
- [20] R. Muthupillai and R. Ehman, "Magnetic resonance elastography," *Nat. Med.*, vol. 2, no. 5, pp. 601–603, May 1996.
- [21] A. Manduca, "Magnetic resonance elastography: Non-invasive mapping of tissue elasticity," *Med. Image Anal.*, vol. 5, no. 4, pp. 237–254, 2001.
- [22] T. E. Oliphant, A. Manduca, R. Ehman, and J. F. Greenleaf, "Complex-valued stiffness reconstruction for magnetic resonance elastography by algebraic inversion of the differential equation," *Magn. Reson. Med.*, vol. 45, no. 2, pp. 299–310, Mar. 2001.
- [23] K. Lin and J. McLaughlin, "An error estimate on the direct inversion model in shear stiffness imaging," *Inverse Probl.*, vol. 25, no. 7, art. no. 075003, Jul. 2009.
- [24] K. Parker and R. M. Lerner, "Sonoelasticity of organs: Shear waves ring a bell," *J. Ultrasound Med.*, vol. 11, no. 8, pp. 387–392, 1992.
- [25] L. Sandrin, M. Tanter, J.-L. Gennisson, S. Catheline, and M. Fink, "Shear elasticity probe for soft tissues with 1-D transient elastography," *IEEE Trans. Ultrason. Ferroelectr. Freq. Control*, vol. 49, no. 4, pp. 436–446, 2002.
- [26] A. P. Sarvazyan, O. V. Rudenko, S. D. Swanson, J. B. Fowlkes, and S. Y. Emelianov, "Shear wave elasticity imaging: A new ultrasonic technology for medical diagnostics," *Ultrasound Med. Biol.*, vol. 24, no. 9, pp. 1419–1435, Nov. 1998.
- [27] M. L. Palmeri, M. H. Wang, J. J. Dahl, K. D. Frinkley, and K. R. Nightingale, "Quantifying hepatic shear modulus in vivo using acoustic radiation force," *Ultrasound Med. Biol.*, vol. 34, no. 4, pp. 546–558, Apr. 2008.
- [28] J. Bercoff, M. Tanter, and M. Fink, "Supersonic shear imaging: A new technique for soft tissue elasticity mapping," *IEEE Trans. Ultrason. Ferroelectr. Freq. Control*, vol. 51, no. 4, pp. 396–409, Apr. 2004.
- [29] S. Chen, M. Fatemi, and J. F. Greenleaf, "Quantifying elasticity and viscosity from measurement of shear wave speed dispersion," *J. Acoust. Soc. Am.*, vol. 115, no. 6, pp. 2781–2785, Jun. 2004.
- [30] S. A. McAleavey and E. Collins, "Comparison of unconfined compression and spatially modulated ultrasound radiation force estimates of shear modulus," *J. Acoust. Soc. Am.*, vol. 125, no. 4, p. 2552, 2009.
- [31] C. Schmitt, A. H. Henni, and G. Cloutier, "Ultrasound dynamic micro-elastography applied to the viscoelastic characterization of soft tissues and arterial walls," *Ultrasound Med. Biol.*, vol. 36, no. 9, pp. 1492–1503, 2010.
- [32] R. Souchon, R. Salomir, O. Beuf, L. Milot, D. Grenier, D. Lyonnet, J. Y. Chapelon, and O. Rouvière, "Transient MR elastography (t-MRE) using ultrasound radiation force: Theory, safety, and initial experiments in vitro," *Magn. Reson. Med.*, vol. 60, no. 4, pp. 871–881, Oct. 2008.
- [33] E. Bavu, J. L. Gennisson, M. Couade, J. Bercoff, V. Mallet, M. Fink, A. Badel, A. Vallet-Pichard, B. Nalpas, M. Tanter, and S. Pol, "Noninvasive in vivo liver fibrosis evaluation using supersonic shear imaging: A clinical study on 113 hepatitis C virus patients," *Ultrasound Med. Biol.*, vol. 37, no. 9, pp. 1361–1373, 2011.
- [34] G. Montaldo, M. Tanter, J. Bercoff, N. Benceh, and M. Fink, "Coherent plane-wave compounding for very high frame rate ultrasonography and transient elastography," *IEEE Trans. Ultrason. Ferroelectr. Freq. Control*, vol. 56, no. 3, pp. 489–506, Mar. 2009.
- [35] C. Kasai, K. Namekawa, A. Koyano, and R. Omoto, "Real-time two-dimensional blood flow imaging using an autocorrelation technique," *IEEE Trans. Sonics Ultrason.*, vol. 32, no. 3, pp. 458–464, 1985.
- [36] T. Defieux, G. Montaldo, M. M. Tanter, and M. Fink, "Shear wave spectroscopy for in vivo quantification of human soft tissues viscoelasticity," *IEEE Trans. Med. Imaging*, vol. 28, no. 3, pp. 313–322, Mar. 2009.
- [37] I. Céspedes, Y. Huang, J. Ophir, and S. Spratt, "Methods for estimation of subsample time delays of digitized echo signals," *Ultrason. Imaging*, vol. 17, no. 2, pp. 142–171, 1995.
- [38] M. A. Slawinski, Ed., *Waves and Rays in Elastic Continua*, 2nd ed., Hackensack, NJ: World Scientific, 2010.
- [39] T. Defieux and J. Gennisson, "On the effects of reflected waves in transient shear wave elastography," *IEEE Trans. Ultrason. Ferroelectr. Freq. Control*, vol. 58, no. 10, pp. 2032–2035, 2011.
- [40] S. A. McAleavey, K. R. Nightingale, and G. Trahey, "Estimates of echo correlation and measurement bias in acoustic radiation force impulse imaging," *IEEE Trans. Ultrason. Ferroelectr. Freq. Control*, vol. 50, no. 6, pp. 631–641, Jun. 2003.
- [41] M. L. Palmeri, S. A. McAleavey, G. E. Trahey, and K. R. Nightingale, "Ultrasonic tracking of acoustic radiation force-induced displacements in homogeneous media," *IEEE Trans. Ultrason. Ferroelectr. Freq. Control*, vol. 53, no. 7, pp. 1300–1313, Jul. 2006.
- [42] M. O'Donnell, A. R. Skovoroda, B. M. Shapo, and S. Y. Emelianov, "Internal displacement and strain imaging using ultrasonic speckle tracking," *IEEE Trans. Ultrason. Ferroelectr. Freq. Control*, vol. 41, no. 3, pp. 314–325, 1994.
- [43] T. Loupas, J. T. Powers, and R. W. Gill, "An axial velocity estimator for ultrasound blood flow imaging, based on a full evaluation of the two-dimensional autocorrelation approach," *IEEE Trans. Ultrason. Ferroelectr. Freq. Control*, vol. 42, no. 4, pp. 672–688, 1995.
- [44] G. F. Pinton, J. J. Dahl, and G. E. Trahey, "Rapid tracking of small displacements with ultrasound," *IEEE Trans. Ultrason. Ferroelectr. Freq. Control*, vol. 53, no. 6, pp. 1103–1117, Jun. 2006.
- [45] I. Céspedes, J. Ophir, and S. K. Alam, "The combined effect of signal decorrelation and random noise on the variance of time delay estimation," *IEEE Trans. Ultrason. Ferroelectr. Freq. Control*, vol. 44, no. 1, pp. 220–225, 1997.

- [46] T. Deffieux, J.-L. Gennisson, J. Bercoff, and M. Tanter, "On the effects of reflected waves in transient shear wave elastography," *IEEE Trans. Ultrason. Ferroelectr. Freq. Control*, vol. 58, no. 10, pp. 2032–2035, Oct. 2011.
- [47] A. Quazi, "An overview on the time delay estimate in active and passive systems for target localization," *IEEE Trans. Acoust. Speech Signal Process.*, vol. 29, no. 3, pp. 527–533, Jun. 1981.
- [48] W. F. Walker and G. Trahey, "A fundamental limit on delay estimation using partially correlated speckle signals," *IEEE Trans. Ultrason. Ferroelectr. Freq. Control*, vol. 42, no. 2, pp. 301–308, Mar. 1995.
- [49] J.-L. Gennisson, T. Deffieux, E. Macé, G. Montaldo, M. Fink, and M. Tanter, "Viscoelastic and anisotropic mechanical properties of in vivo muscle tissue assessed by supersonic shear imaging," *Ultrasound Med. Biol.*, vol. 36, no. 5, pp. 789–801, May 2010.
- [50] T. Deffieux, J.-L. Gennisson, M. Tanter, and M. Fink, "Assessment of the mechanical properties of the musculoskeletal system using 2-D and 3-D very high frame rate ultrasound," *IEEE Trans. Ultrason. Ferroelectr. Freq. Control*, vol. 55, no. 10, pp. 2177–2190, 2008.
- [51] J. Bercoff, M. Tanter, M. Muller, and M. Fink, "The role of viscosity in the impulse diffraction field of elastic waves induced by the acoustic radiation force," *IEEE Trans. Ultrason. Ferroelectr. Freq. Control*, vol. 51, no. 11, pp. 1523–1536, Nov. 2004.
- [52] J. Virieux, "P-SV wave propagation in heterogeneous media: Velocity-stress finite-difference method," *Geophysics*, vol. 51, no. 4, pp. 889–901, 1986.
- [53] K. S. Kunz and R. J. Luebbers, *The Finite Difference Time Domain Method for Electromagnetics*. Boca Raton, FL: CRC Press, 1993.
- [54] J. Berenger, "A perfectly matched layer for the absorption of electromagnetic waves," *J. Comput. Phys.*, vol. 114, no. 2, pp. 185–200, 1994.
- [55] E. I. Cespedes, M. F. Insana, and J. Ophir, "Theoretical bounds on strain estimation in elastography," *IEEE Trans. Ultrason. Ferroelectr. Freq. Control*, vol. 42, no. 5, pp. 969–972, Sep. 1995.
- [56] M. W. Urban, S. Chen, and J. F. Greenleaf, "Error in estimates of tissue material properties from shear wave dispersion ultrasound vibrometry," *IEEE Trans. Ultrason. Ferroelectr. Freq. Control*, vol. 56, no. 4, pp. 748–758, Apr. 2009.
- [57] M. H. Wang, M. L. Palmeri, V. M. Rotemberg, N. C. Rouze, and K. R. Nightingale, "Improving the robustness of time-of-flight based shear wave speed reconstruction methods using RANSAC in human liver in vivo," *Ultrasound Med. Biol.*, vol. 36, no. 5, pp. 802–813, May 2010.
- [58] M. W. Urban and J. F. Greenleaf, "A Kramers–Kronig-based quality factor for shear wave propagation in soft tissue," *Phys. Med. Biol.*, vol. 54, no. 19, pp. 5919–5933, 2009.
- [59] G. Casella and R. L. Berger, *Statistical inference*, 2nd ed. Duxbury Press, 2001, p. 660.

Authors' photographs and biographies were unavailable at time of publication.

Letters

On the Effects of Reflected Waves in Transient Shear Wave Elastography

Thomas Deffieux, Jean-Luc Gennisson, Jeremy Bercoff, and Mickael Tanter

Abstract—In recent years, novel quantitative techniques have been developed to provide noninvasive and quantitative stiffness images based on shear wave propagation. Using radiation force and ultrafast ultrasound imaging, the supersonic shear imaging technique allows one to remotely generate and follow a transient plane shear wave propagating *in vivo* in real time. The tissue shear modulus, i.e., its stiffness, can then be estimated from the shear wave local velocity. However, because the local shear wave velocity is estimated using a time-of-flight approach, reflected shear waves can cause artifacts in the estimated shear velocity because the incident and reflected waves propagate in opposite directions. Such effects have been reported in the literature as a potential drawback of elastography techniques based on shear wave speed, particularly in the case of high stiffness contrasts, such as in atherosclerotic plaque or stiff lesions. In this letter, we present our implementation of a simple directional filter, previously used for magnetic resonance elastography, which separates the forward- and backward-propagating waves to solve this problem. Such a directional filter could be applied to many elastography techniques based on the local estimation of shear wave speed propagation, such as acoustic radiation force imaging (ARFI), shearwave dispersion ultrasound vibrometry (SDUV), needle-based elastography, harmonic motion imaging, or crawling waves when the local propagation direction is known and high-resolution spatial and temporal data are acquired.

BASED on the propagation of mechanical shear waves in tissue, quantitative elastography techniques [1]–[6] are able to noninvasively and quantitatively estimate the shear modulus of tissues, i.e., their stiffness. Because palpation is so important as a diagnosis tool, which is emphasized by its dominant role in breast cancer screening, these methods are regarded as highly promising. They are already being clinically tested at different stages for breast cancer detection [7], [8], liver fibrosis staging [2], [9]–[11], kidney monitoring [12], thyroid gland [13] and prostate cancer detection [3], [14], musculoskeletal monitoring [15], [16], and ophthalmologic [17] or vascular applications [18], [19].

In supersonic shear imaging, a transient plane shear wave is generated remotely *in situ* using acoustic radiation force [1]. The shear wave is then acquired, while propagat-

ing and in real time, using ultrafast ultrasound imaging (up to 20 kHz) [20]. Based on the shear wave propagation movie, it is then possible to estimate, pixel by pixel, the local shear group velocity, v_g , of the transient plane wave using a time-of-flight approach [21]. Using time-domain cross correlation, the time-of-flight approach allows estimation of the time delay of the shear wave between adjacent points to estimate the local shear wave group velocity, v_g . By estimating this velocity, it is possible to estimate the shear modulus μ either using the well-known equation $\mu = \rho \cdot v_g^2$ for quasi homogeneous media, where ρ is the density and v_g the estimated shear wave velocity group, or the full dispersion relation in guided media such as thin layers or tubes (for example, for the cornea [17] or arteries [18]).

Unfortunately, estimating the local shear wave velocity with this time-of-flight approach can yield artifacts if incident and reflected shear waves are present simultaneously, which can be the case when there is a high elastic contrast in the image [22], [23]. Those artifacts can be complex to understand when multiple elastic reconstructions are combined to form a single elasticity image.

Based on the spatio-temporal directional filter proposed by Manduca *et al.* [24], which was applied to magnetic resonance elastography, we present here an implementation of a directional filter for ultrasound-based shear wave elastography and its associated results. This filter, which was introduced several years ago in our reconstruction algorithms, yields strong improvements on the reconstruction quality by separating the incident and reflected propagating shear waves. Because the wave is assumed to be locally planar, it can be written, for a low dispersive and locally homogeneous medium, as the sum of one-dimensional forward- and backward-propagating waves (respectively, U_i and U_r) traveling with a velocity c :

$$\begin{aligned} U(x, t) &= \iint (U_i(\omega) e^{j(\omega t - kx)} + U_r(\omega) e^{j(\omega t + kx)}) d\omega dk \\ &= \int U_i(\omega) e^{j(\omega t - (\omega x)/c)} + U_r(\omega) e^{j(\omega t + (\omega x)/c)} d\omega. \end{aligned} \quad (1)$$

By looking at the k -space representation $[k, \omega]$ of a propagating plane wave (1), the domain can easily be separated in four quadrants, $k > 0$ and $\omega > 0$, $k < 0$ and $\omega < 0$, $k < 0$ and $\omega > 0$, and finally $k > 0$ and $\omega < 0$. Depending on the sign of the phase velocity $c = \omega/k$, one can separate the forward ($c > 0$) and backward ($c < 0$) components of a wave by simply multiplying the k -space data by a mask. By smoothly apodizing the borders of this mask to avoid brutal cuts in the spectrum and subsequent Gibbs oscillations in the $[x, t]$ domain, it is possible to design a very simple, yet efficient, directional filter that can entirely remove the reflected components of a propagating wave without any artifacts. This filter operates on each

Manuscript received April 15, 2011; accepted June 28, 2011. This work was partly supported by the French National Agency for Research on AIDS and Viral Hepatitis (ANRS).

T. Deffieux, J.-L. Gennisson, and M. Tanter are with the Institut Langevin, Ondes et Images, École Supérieure de Physique et de Chimie Industrielles de la Ville de Paris ParisTech, Centre National de la Recherche Scientifique UMR 7587, Institut National de la Santé et de la Recherche Médicale U979, Paris, France (e-mail: tdeffieux@gmail.com).

J. Bercoff is with Supersonic Imagine, Aix en Provence, France.

Digital Object Identifier 10.1109/TUFFC.2011.2052

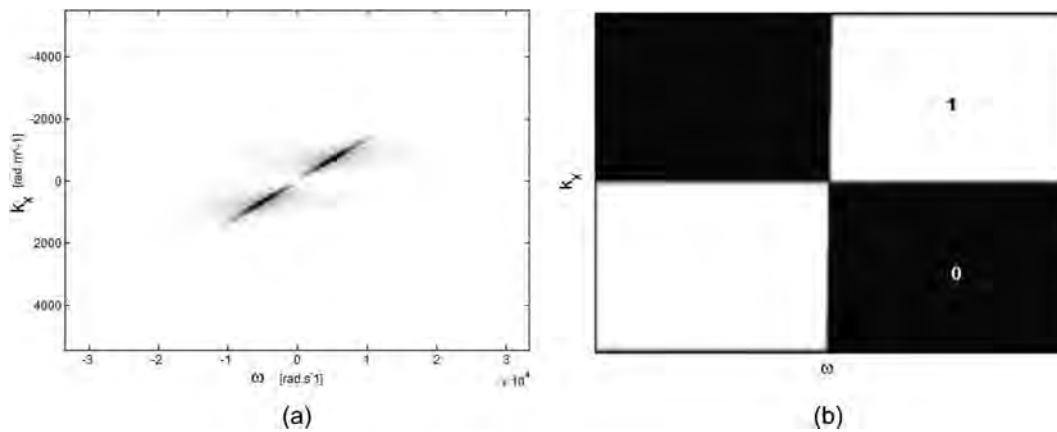


Fig. 1. (a) K-space representation of a propagating plane and transient shear wave (2-D Fourier transform for a given depth). Simulated data of wideband plane shear wave. (b) Coefficients of the filter in the Fourier plane $[k_x, \omega]$. The filter is apodized on the edges to prevent oscillations; its center corresponds to the zero frequencies. The filter is applied using the 2-D fast Fourier transform (FFT) on each depth line of the shear wave propagation movies.

depth line and its design is shown in Fig. 1; the results on experimental and simulated data sets (10-mm spherical inclusion of stiffness 10 kPa in a 5-kPa background) are presented in Fig. 2.

Using elastic finite-difference time-domain numerical simulations [25] of the shear wave propagation (visible in Fig. 2) and *in vitro* elastic phantom experiments, we can illustrate the effects of the directional filter on the shear modulus images (results presented in Figs. 3 and 4).

Reconstruction of shear modulus maps from simulated shear wave propagation movies (finite-difference time-domain elastic solver) are presented in Fig. 3 with and without the directional filter. Different elastic inclusion diameters (8 and 12 mm) and stiffness (10, 15, and 20 kPa) are used to illustrate the efficiency of the filter in different situations.

Fig. 4 presents results obtained in breast elastic phantoms for 3 different inclusions. As shown with simulated data, the effect of the directional filter is quite important. White arrows indicate the artifact positions without the directional filter.

Such a filter, which is easy to implement and fast, can drastically improve the reconstructed shear modulus in stiff inclusions, as seen in Figs. 3 and 4. It can be applied in real time and has always been activated by default for all supersonic shear wave propagation data and associated results. A movie of the shear wave propagation with high spatial and temporal resolution (such as that provided by ultrafast imaging [1]) is required to compute the 2-D Fourier transform accurately and apply this filter.

The proposed filter can also be used to improve the signal-to-noise ratio of the acquired data. By removing nearly half of the k -space domain in which nearly no useful signal is present but where half of the white noise energy is distributed, the filter can significantly improve the signal-to-noise ratio of an acquisition by up to 2-fold.

In conclusion, although reflected shear waves might be rapidly attenuated with larger viscosity, especially *in vivo*, a directional filter is often required in transient shear wave

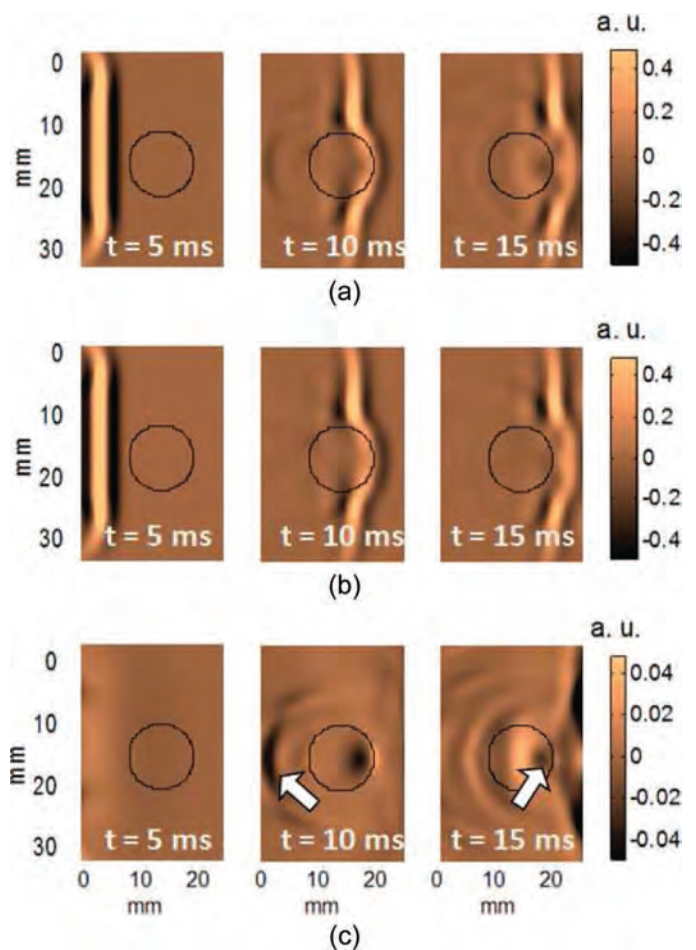


Fig. 2. Simulated shear waves propagating through a 3-D spherical inclusion in arbitrary units (a.u.): (a) unfiltered waves, (b) incident shear wave as separated by the directional filter, (c) reflected shear wave as separated by the directional filter (scale $\times 10$). Here, the reflected wave amplitude is one-tenth of the incident wave but still has an impact on the reconstructed shear modulus value (cf. Fig. 3). The black circle denotes the position of the spherical inclusion.

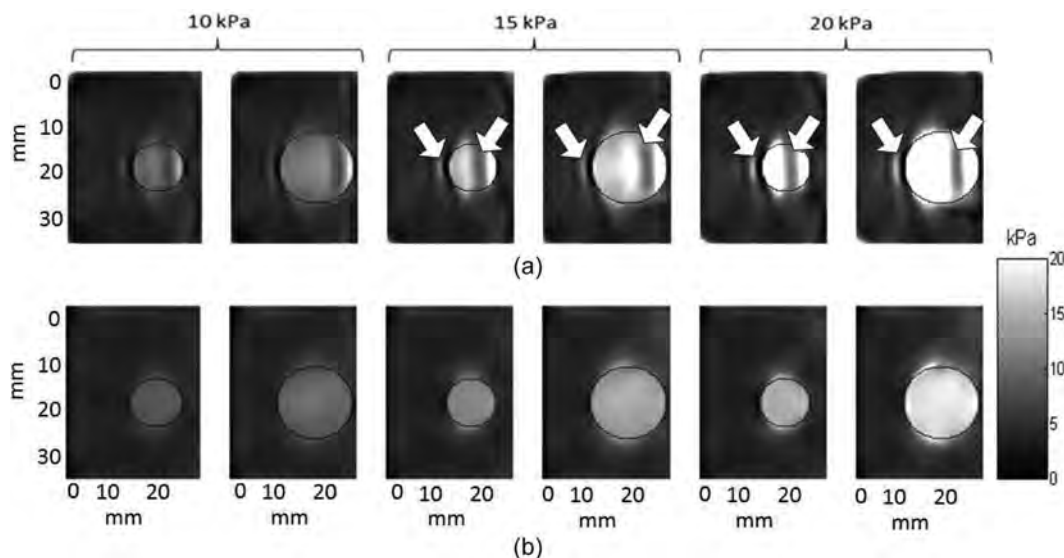


Fig. 3. Shear modulus maps from simulated shear wave propagation data in elastic inclusions of various diameters (8 and 12 mm) and stiffnesses (10, 15, and 20 kPa). (a) Without the directional filter, artifacts are visible in the inclusions with a characteristic overestimation on the edges and an underestimation in the center of the inclusions, as can be observed in experiments (Fig. 4). This pattern is due to interferences between the incident and reflected shear waves. (b) With the directional filter, the artifacts are completely removed.

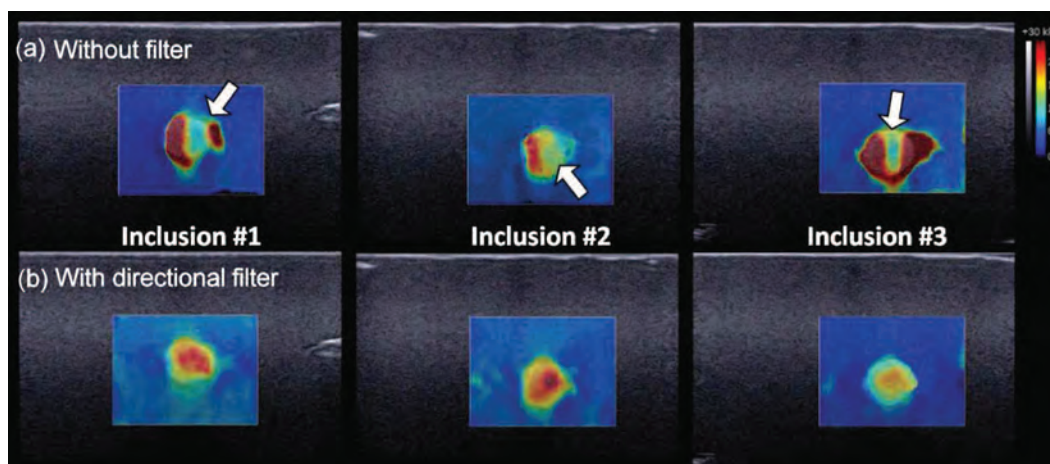


Fig. 4. Shear modulus maps from experimental data acquired on a breast phantom on 3 different inclusions. (a) Without the directional filter, artifacts caused by the reflected shear waves are visible inside the inclusions (white arrows). (b) With the directional filter, those artifacts are greatly reduced. Background shear modulus is 5 kPa and inclusions' stiffnesses are between 15 and 20 kPa.

elastography to prevent bias from appearing in the local shear velocity estimation. By separating the forward and backward components, it is possible to almost entirely remove the reflected wave and reduce those artifacts in the shear modulus maps of a stiff inclusion. In practice, and for all clinical applications, such a simple filter is always used by default to improve image quality. It is highly recommended in transient shear wave applications [2]–[6], [26] to avoid reflection artifacts.

REFERENCES

- [1] J. Bercoff, M. Tanter, and M. Fink, "Supersonic shear imaging: A new technique for soft tissue elasticity mapping," *IEEE Trans. Ultrason. Ferroelectr. Freq. Control*, vol. 51, pp. 396–409, 2004.
- [2] M. L. Palmeri, M. H. Wang, J. J. Dahl, K. D. Frinkley, and K. R. Nightingale, "Quantifying hepatic shear modulus in vivo using acoustic radiation force," *Ultrasound Med. Biol.*, vol. 34, pp. 546–558, 2008.
- [3] F. G. Mitri, M. W. Urban, M. Fatemi, and J. F. Greenleaf, "Shear wave dispersion ultrasonic vibrometry for measuring prostate shear stiffness and viscosity: An in vitro pilot study," *IEEE Trans. Biomed. Eng.*, vol. 58, no. 2, pp. 235–242, Feb. 2011.
- [4] M. Orescanin, M. A. Qayyum, K. S. Tooley, and M. F. Insana, "Dispersion and shear modulus measurements of porcine liver," *Ultrason. Imaging*, vol. 32, no. 4, pp. 255–266, Oct. 2010.
- [5] J. Vappou, C. Maleke, and E. E. Konofagou, "Quantitative viscoelastic parameters measured by harmonic motion imaging," *Phys. Med. Biol.*, vol. 54, no. 11, pp. 3579–3594, Jun. 2009.
- [6] Z. Hah, C. Hazard, Y. T. Cho, D. Rubens, and K. Parker, "Crawling waves from radiation force excitation," *Ultrason. Imaging*, vol. 32, no. 3, pp. 177–189, Jul. 2010.
- [7] A. Athanasiou, A. Tardivon, M. Tanter, B. Sigal-Zafrani, J. Bercoff, T. Defieux, J.-L. Gennisson, M. Fink, and S. Neuenschwander, "Breast lesions: Quantitative elastography with supersonic shear im-

- aging—Preliminary results,” *Radiology*, vol. 256, no. 1, pp. 297–303, Jul. 2010.
- [8] R. Sinkus, M. Tanter, T. Xydeas, and S. Catheline, “Viscoelastic shear properties of in vivo breast lesions measured by MR elastography,” *Magn. Reson. Imaging*, vol. 23, no. 2, pp. 159–165, 2005.
- [9] L. Castéra, J. Vergniol, J. Foucher, and B. L. Bail, “Prospective comparison of transient elastography, FibrotTest, APRI, and liver biopsy for the assessment of fibrosis in chronic hepatitis C,” *Gastroenterology*, vol. 128, no. 2, pp. 343–350, 2005.
- [10] L. Huwart, C. Sempoux, E. Vicaut, N. Salameh, L. Annet, E. Danse, F. Peeters, L. ter Beek, J. Rahier, and R. Sinkus, “Magnetic resonance elastography for the noninvasive staging of liver fibrosis,” *Gastroenterology*, vol. 135, no. 1, pp. 32–40, 2008.
- [11] M. Muller, J.-L. Gennisson, T. Deffieux, M. Tanter, and M. Fink, “Quantitative viscoelasticity mapping of human liver using supersonic shear imaging: Preliminary in vivo feasibility study,” *Ultrasound Med. Biol.*, vol. 35, no. 2, pp. 219–229, Feb. 2009.
- [12] J. L. Gennisson, N. Grenier, R. Hubrecht, L. Couzy, Y. Delmas, M. Derieppe, S. Lepreux, P. Merville, A. Criton, J. Bercoff, and M. Tanter, “Multiwave technology introducing shear wave elastography of the kidney: Pre-clinical study on a kidney fibrosis model and clinical feasibility study on 49 human renal transplants,” in *Proc. IEEE Ultrasonic Symp.*, San Diego, CA, 2010.
- [13] F. Sebag, J. Vaillant-Lombard, J. Berbis, V. Griset, J. F. Henry, P. Petit, and C. Oliver, “Shear wave elastography: A new ultrasound imaging mode for the differential diagnosis of benign and malignant thyroid nodules,” *J. Clin. Endocrinol. Metab.*, vol. 95, no. 12, pp. 5281–5288, Sep. 2010.
- [14] R. Chopra, A. Arani, Y. Huang, M. Musquera, J. Wachsmuth, M. Bronskill, and D. Plewes, “In vivo MR elastography of the prostate gland using a transurethral actuator,” *Magn. Reson. Med.*, vol. 62, no. 3, pp. 665–671, Sep. 2009.
- [15] J. Basford, T. Jenkyn, K. An, R. Ehman, G. Heers, and K. Kaufman, “Evaluation of healthy and diseased muscle with magnetic resonance elastography,” *Arch. Phys. Med. Rehabil.*, vol. 83, no. 11, pp. 1530–1536, Nov. 2002.
- [16] J.-L. Gennisson, T. Deffieux, E. Macé, G. Montaldo, M. Fink, and M. Tanter, “Viscoelastic and anisotropic mechanical properties of in vivo muscle tissue assessed by supersonic shear imaging,” *Ultrasound Med. Biol.*, vol. 36, no. 5, pp. 789–801, May 2010.
- [17] M. Tanter, D. Touboul, J. L. Gennisson, J. Bercoff, and M. Fink, “High-resolution quantitative imaging of cornea elasticity using supersonic shear imaging,” *IEEE Trans. Med. Imaging*, vol. 28, no. 12, pp. 1881–1893, 2009.
- [18] M. Couade, M. Pernot, C. Prada, E. Messas, J. Emmerich, P. Brunel, A. Criton, M. Fink, and M. Tanter, “Quantitative assessment of arterial wall biomechanical properties using shear wave imaging,” *Ultrasound Med. Biol.*, vol. 36, no. 10, pp. 1662–1676, Oct. 2010.
- [19] M. Couade, M. Pernot, E. Messas, A. Bel, M. Ba, H. Albert, M. Fink, and M. Tanter, “In vivo quantitative mapping of myocardial stiffening and transmural anisotropy during the cardiac cycle,” *IEEE Trans. Med. Imaging*, vol. 30, no. 2, pp. 295–305, Feb. 2011.
- [20] L. Sandrin, M. Tanter, S. Catheline, and M. Fink, “Shear modulus imaging with 2-D transient elastography,” *IEEE Trans. Ultrason. Ferroelectr. Freq. Control*, vol. 49, no. 4, pp. 426–435, 2002.
- [21] M. Tanter, J. Bercoff, A. Athanasiou, T. Deffieux, J.-L. Gennisson, G. Montaldo, M. Muller, A. Tardivon, and M. Fink, “Quantitative assessment of breast lesion viscoelasticity: Initial clinical results using supersonic shear imaging,” *Ultrasound Med. Biol.*, vol. 34, no. 9, pp. 1373–1386, Sep. 2008.
- [22] R. H. Behler, T. C. Nichols, E. P. Merricks, and C. M. Gallippi, “Reflected shear wave imaging of atherosclerosis,” in *2009 IEEE International Ultrasonics Symposium*, pp. 2445–2448.
- [23] M. Palmeri, N. Rouze, M. Wang, X. Ding, and K. Nightingale, “Quantifying the impact of kernel size on the accuracy and precision of shear wave estimation,” in *Proc. 2010 IEEE Ultrasonics Symp.*, 2010, pp. 13–16.
- [24] A. Manduca, D. S. Lake, S. A. Kruse, and R. L. Ehman, “Spatio-temporal directional filtering for improved inversion of MR elastography images,” *Med. Image Anal.*, vol. 7, no. 4, pp. 465–473, Dec. 2003.
- [25] J. Bercoff, M. Tanter, M. Muller, and M. Fink, “The role of viscosity in the impulse diffraction field of elastic waves induced by the acoustic radiation force,” *IEEE Trans. Ultrason. Ferroelectr. Freq. Control*, vol. 51, no. 11, pp. 1523–1536, 2004.
- [26] N. C. Rouze, M. H. Wang, M. L. Palmeri, and K. R. Nightingale, “Robust estimation of time-of-flight shear wave speed using a Radon sum transformation,” *IEEE Trans. Ultrason. Ferroelectr. Freq. Control*, vol. 57, no. 12, pp. 2662–2670, Dec. 2010.

High-Resolution Quantitative Imaging of Cornea Elasticity Using Supersonic Shear Imaging

M. Tanter*, D. Touboul, Jean-Luc Gennisson, Jeremy Bercoff, and Mathias Fink

Abstract—The noninvasive estimation of *in vivo* mechanical properties of cornea is envisioned to find several applications in ophthalmology. Such high-resolution measurements of local cornea stiffness could lead to a better anticipation and understanding of corneal pathologies such as Keratoconus. It could also provide a quantitative evaluation of corneal biomechanical response after corneal refractive surgeries and a tool for evaluating the efficacy of new cornea treatments such as cornea transplant using femtosecond laser or therapy based on Riboflavin/UltraViolet-A Corneal Cross Linking (UVA CXL). In the very important issue of glaucoma diagnosis and management, the fine tuning corneal elasticity measurement could also succeed to strongly correlate the applanation tonometry with the “true” intra-ocular pressure (IOP). This initial investigation evaluates the ability of ultrafast and high-resolution ultrasonic systems to provide a real-time and quantitative mapping of corneal viscoelasticity. Quantitative elasticity maps were acquired *ex vivo* on porcine cornea using the supersonic shear imaging (SSI) technique. A conventional 15 MHz linear probe was used to perform conventional ultrasonic imaging of the cornea. A dedicated ultrasonic sequence combines the generation of a remote palpation in the cornea and ultrafast (20 000 frames/s) ultrasonic imaging of the resulting corneal displacements that evolve into a shear wave propagation whose local speed was directly linked to local elasticity. A quantitative high-resolution map (150 μm resolution) of local corneal elasticity can be provided by this dedicated sequence of ultrasonic insonifications. Quantitative maps of corneal elasticity were obtained on *ex vivo* freshly enucleated porcine corneas. In the cornea, a quite homogenous stiffness map was found with a 190 kPa \pm 32 kPa mean elasticity. The influence of photodynamic Riboflavin/UVA induced CXL was measured. A significant Young’s modulus increase was obtained with a mean 890 kPa \pm 250 kPa posttreatment Young’s modulus (460% increase), located in the anterior part of the cornea. Simulations based on 3-D time domain finite differences simulation were also performed and found to be in good agreement with *ex vivo* experiments. The SSI technique can perform real-time, noninvasive, high-resolution, and quantitative maps of the whole corneal elasticity. This technique could be real time and straightforward adapted for a very wide field of *in vivo* investigations.

Index Terms—Biomechanics, cornea, elastography, stiffness, ultrasound.

Manuscript received January 25, 2009; revised April 06, 2009. Asterisk indicates corresponding author.

*M. Tanter is with the Langevin Institute (CNRS UMR 7587), ESPCI, Inserm, Paris 75005, France (e-mail: mickael.tanter@espci.fr).

J.-L. Gennisson and M. Fink are with the Langevin Institute (CNRS UMR 7587), ESPCI, Inserm, Paris 75005, France.

D. Touboul is with the Ophthalmology Department, Centre Hospitalo-Universitaire, Bordeaux 33000, France.

J. Bercoff is with the Supersonic Imagine Company, 13857 Aix en Provence, France.

Color versions of one or more of the figures in this paper are available online at <http://ieeexplore.ieee.org>.

I. INTRODUCTION

IN THE PAST DECADE, ultrasound-based elastography became a major research topic in the medical ultrasound community. Researchers postulated that information about tissue mechanical properties would represent an interesting added value either to conventional B-mode ultrasound imaging or magnetic resonance imaging (MRI) imaging. Ultrasound-based methods assessing viscoelastic properties of tissue are studied for many diagnostic applications such as breast cancer diagnosis [1], [2], liver fibrosis staging [3]–[5], arterial wall [6], [7], and cardiac muscle elasticity imaging [8], [9]. These techniques are also envisioned for the monitoring of thermal ablation using high intensity focused ultrasound [10]. Whereas most proposed ultrasound-based approaches are limited to a qualitative assessment of tissue stiffness, a method based on the use of ultrafast echographic scanners able to reach very high frame rates (higher than a thousand images per second) enables the assessment of the local and quantitative value of tissue Young’s modulus E [11]–[14]. The very high frame rate enables the transient and real time imaging of shear mechanical vibrations induced deep inside organs using the radiation force of an ultrasonic beam [15]. In homogeneous media, the local propagation speed c_s of the resulting shear waves is directly linked with stiffness defined as Young’s modulus E via the theoretical relation $E = 3\rho c_s^2$ where ρ is the tissue density (assumed to be constant in soft tissue, typically 1000 kg/m³). This method, called Supersonic Shear Imaging, was recently applied for breast cancer diagnosis [2] with promising results. Its *in vivo* applicability for the quantitative imaging of liver stiffness [16] and musculoskeletal system [17] was also recently validated.

In ophthalmology, the assessment of viscoelastic properties of cornea could also provide very valuable information for various applications [18]. Indeed, it could provide a powerful tool for evaluating the efficacy of new cornea treatments such as cornea transplant using femtosecond laser [19], [20] or therapy based on Riboflavin/UltraViolet-A corneal cross linking (UVA CXL) [21]. Another potential application could be the quantitative evaluation of the corneal biomechanical response after photo-ablative laser surgeries or cutting relaxant corneal procedures. It could be envisioned for an early clinical detection of corneal ectatic disease [22], [23] or improved accuracy of intraocular pressure (IOP) measurement [24], [25]. Perhaps even more promising, it could also lead to a better management of corneal pathologies such as Keratoconus [26] and to the estimation of risk factors due to abnormal mechanical properties of

Digital Object Identifier 10.1109/TMI.2009.2021471

cornea before refractive surgery (screening of the infra clinical Keratoconus form fruste). Refractive surgery techniques such as Laser-Assisted *in situ* Keratomileusis (LASIK) are currently encountering huge success with considerable growth in terms of annual procedures. A misunderstanding of the corneal biomechanics properties can lead to over-corrections or under-corrections of corneal refractive photo ablative procedures. More important, even if this complication is very rare, the dramatic case of postlaser excimer ectasia (PLE) should be prevented [27]. It is important to mention that in the case of extreme PLE, the use of intracorneal rings or, in worst case, a keratoplasty would be necessary to restore useful vision in these usually young patients.

The precise and quantitative assessment of corneal elasticity (Young's Modulus) is crucial to ensure the safety of LASIK refractive surgery, as the corneal final shape results from the relaxation of the cornea tissue up to a new equilibrium curvature state after cutting a flap of anterior corneal tissue. This new equilibrium state is strongly affected by corneal tissue elasticity. Thus, any technological approach that could provide a reliable and quantitative 3-D mapping of corneal structure Young's modulus would offer new insights in refractive surgery procedures. To date, the assessment of cornea Young's modulus was mainly performed *ex vivo*. *In vivo* applications are usually limited to the estimation of technique-dedicated parameters linked to stiffness but not to stiffness itself [28]. Recently, Hollman *et al.* proposed an ultrasound-based system for strain imaging of corneal tissue [18]. This Ultrasound Elasticity Microscope provided very promising images of strain induced by a compression plate on the corneal surface of *ex vivo* porcine eye. This device corresponds to the application of Static Elastography proposed 20 years ago by Ophir *et al.* [29] to the domain of high-frequency ultrasound. However, the deduction of quantitative estimates of local Young's modulus from the knowledge of the strain field provided in static elastography is a very complex task which is not properly solved to date at least for practical clinical applicability. Surface wave elastometry was also recently proposed in order to assess cornea mechanical properties [30].

A system based on the generation of noncontact transient air-pulse and an dynamic electrooptical system used to record two applanation pressure measurements at the surface of the cornea [31] was recently proposed and named Ocular Response Analyzer (ORA, Reichert). It is still today the only technology available for the *in vivo* corneal biomechanical evaluation. However, despite a very ingenious system, the ORA was not yet proven to characterize with a good predictability the biomechanical normality of the cornea. The estimated parameter called corneal hysteresis (CH) corresponds to the difference of pressure levels at which the applanation of corneal surface is reached during inward and outward corneal displacement. It is linked to the time needed for the corneal displacement at air pulse location to reach a given value during inward and backward motion. Although presented as an estimation of corneal viscous damping, this parameter is linked in a complex way to several geometrical (corneal thickness) and viscoelastic properties (Young's modulus E and shear viscosity η) of cornea and this could explain the limited predictability of the system. Indeed, the generation of an air pulse at the surface of the cornea induces

the generation of a shear mechanical wave that travels in a few milliseconds along the entire corneal wall. Estimating the underlying viscoelastic properties of the propagation medium from these displacements requires a refined imaging and analysis of the shear wave propagation. By estimating only two applanation pressures at a single location on the cornea, the ORA cannot fully resolve the inverse problem of this shear wave propagation and recover direct estimates of physical biomechanical parameters such corneal elasticity or viscosity. Finally, the attainment of applanation requires high cornea displacements (higher than 1 mm), resulting undoubtedly into nonlinear behavior of cornea response to a mechanical stress.

On the contrary, the SSI modality induces only micrometric displacements (much lower than cornea thickness), thus insuring a linear behavior of the cornea tissue. Moreover, instead of estimating only the slope of inward and backward displacement at the transient pushing location, the SSI technique images a complete two-dimensional movie of the displacement field in the corneal layer at an ultrafast frame rate. This set of data is much more complete and contains the required information that enables recovering precisely the local shear wave speed in the cornea.

For corneal stiffness estimation, the relation between Young's modulus and shear wave speed is more complex than the well-known $E = 3\rho c_s^2$ formula. Indeed, contrary to large organs such as breast or liver, where boundary conditions do not affect significantly shear wave propagation, the cornea plate is thin (typically 1 mm) compared to the shear wavelength. Moreover, there is a strong contrast between shear velocities in the Cornea and the surrounding media. Cornea (typical Young's modulus of several hundreds of kPa) is surrounded on one side by the aqueous humor (viscous liquid with nearly 0 kPa Young's modulus) and on the other side by a coupling liquid during the experimental investigation (Young's modulus = 0 kPa). As a consequence, when shear waves propagate along cornea, strong reflections and mode conversions at these interfaces generate partially guided wave propagation. The propagation of elastic waves in infinite and thin elastic plates, known as Lamb waves [41], has been extensively investigated and extended to the case of cylindrical shells [42]. Lamb waves propagate with specific modes that have highly dispersive behaviors but in the very low frequency range, only one symmetric (S0) and one anti-symmetric (A0) modes are found. For thin elastic plates in vacuum, a low-frequency analytical approximation has been established for the phase velocity $c(\omega)$ of the mode A0 [43]

$$c(\omega) = \sqrt{\frac{\omega h c_s}{\sqrt{3}}} \quad (1)$$

where ω is the angular frequency, h the plate thickness, c_s the shear wave speed given by the Young's modulus E and the volumic mass ρ of the plate, via the relation $c_s = \sqrt{E/3\rho}$.

However, when the plate is surrounded by liquids or soft solids instead of vacuum, it becomes more difficult to derive an analytical formula of type (1), due to the fact that the small contrast in longitudinal velocities of the different materials (around 1500 m/s \pm 5%) generates a total leakage of the longitudinal wave at the wall interfaces ("leaky" Lamb wave),

where as the shear part is totally reflected at both interfaces and remains trapped inside cornea. Recently, Pernot *et al.* [44] proposed an empirical analytical formula that approximates with a good accuracy the phase velocity of a leaky Lamb wave propagating in the arterial wall (i.e., in the case of soft tissues surrounded by liquid media). This formula is similar to the classical Lamb wave (1) but corrected by a factor $1/\sqrt{2}$

$$c(\omega) = \sqrt{\frac{\omega h c_s}{2\sqrt{3}}}. \quad (2)$$

Thus, it is possible to deduce the Young's modulus from the knowledge of the shear dispersion curve $c(\omega)$ and local thickness h of the cornea. This frequency dependency of the shear wave speed can be estimated using the SSI modality [34].

To date, to our knowledge, this manuscript proposes a first clinically applicable technique for the *in vivo* imaging of the quantitative Young's modulus of the cornea with a very high resolution. This quantitative elasticity imaging mode is performed using conventional high-frequency ultrasonic probes and can thus be implemented on ultrafast scanners providing both stiffness and ultrasonic images.

II. MATERIAL AND METHODS

A. Experimental Setup

The Supersonic Shear Imaging technique is based on the use of conventional ultrasonic probes. For applying this modality in ophthalmology, a 15 MHz linear array (Vermon, Tours, France) is used. The array is made of 128 elements with a 0.201 mm spatial pitch and a 12 mm elevation focus. Fresh excised postmortem porcine eyes obtained from the slaughterhouse are placed in a positioning cap immersed into a small water tank. In all experiments, the intra-ocular pressure of the *ex vivo* eyes was at atmospheric pressure. The linear array is immersed in water and positioned 5 mm above the cornea surface as described in Fig. 1.

The probe is driven by an ultrasound research prototype (V1 System developed by Supersonic Imagine, Aix en Provence, France) made of 128 programmable transmit channels (70 peak-to-peak transmit voltage, 25 kHz maximal pulse repetition frequency) and 64 multiplexed received channels (10 bits dynamics, 100 dB time gain amplification).

B. Imaging Methods

The *in vivo* SSI mode was described in details in [2]. It consists of a remote palpation induced by the radiation force of a focused ultrasonic beam (typically 100 μ s long burst), the so called "pushing beam" (Fig. 2(a), red arrow). Each "pushing beam" generates a remote vibration that results in the propagation of a transient shear wave (Fig. 2(a), blue arrows) [32]. After generation of this shear wave, an ultrafast echographic imaging sequence is performed in order to acquire successive raw radio-frequencies (RF) data at a very high frame rate. Contrary to conventional ultrasonography where an image is achieved using line by line transmit focused beams (typically 50 frames/s), ultrafast echographic images are achieved by transmitting a single quasi-plane ultrasonic wave in tissues and achieving the beamforming process only in the receive

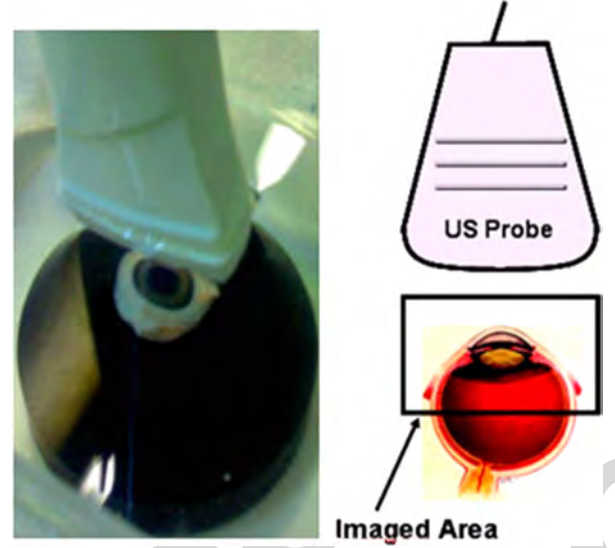


Fig. 1. Experimental setup. A 1-D linear array (128 elements, 15 MHz) is imaging the *ex vivo* freshly enucleated porcine eye. The echographic probe, eye porcine eye, and the eye holder are immersed into pure water.

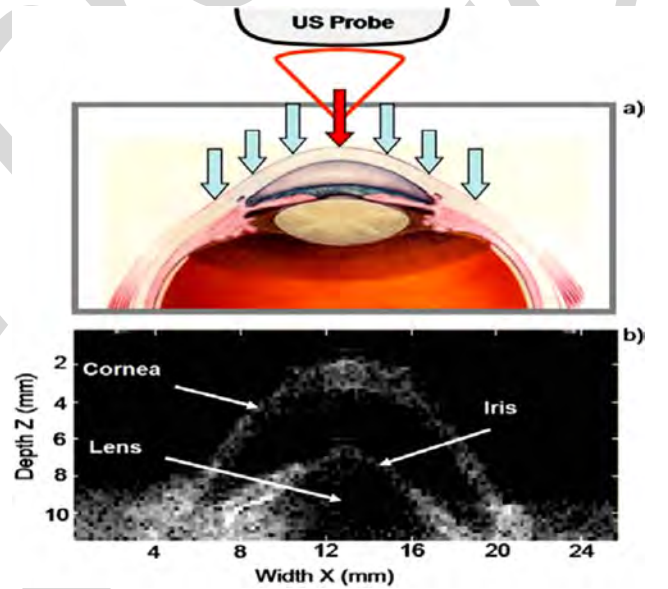


Fig. 2. (a) Echographic probe emits an ultrasonic focused beam that generates a localized radiation force (red arrow) at the surface of the cornea. Resulting shear waves (blue arrows) propagate in the cornea on both side of the pushing location. (b) Conventional B-mode echographic image of an *ex vivo* porcine eye acquired before the generation of the ultrasonic radiation force.

mode. The quasi-plane terminology stands for the fact that the transmitted ultrasonic wavefront is planar in the 2-D imaging plane and slightly diffracting along the probe elevation direction beyond the elevation focal distance. Thus, for ultrafast imaging, the frame rate is only limited by the time of flight of ultrasonic waves. For ophthalmologic applications, the imaging depth does not exceed 20 mm. It corresponds to a typical 27 μ s time of flight that defines a maximal frame rate of 37 000/s. In our experiments, the frame rate was set to 20 000 frames/s.

Before entering into the SSI mode, the device is functioning as a conventional echographic device (transmit/receive beamforming at 50 frames/s). A typical echographic image of *ex*

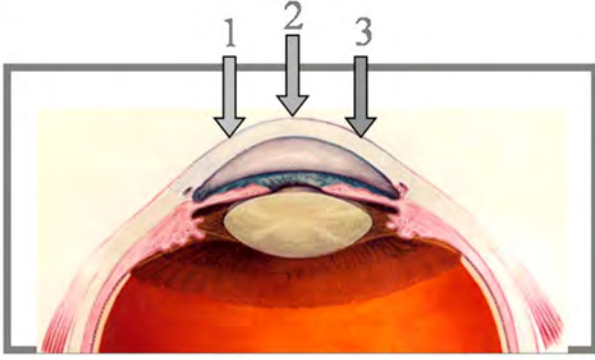


Fig. 3. SSI imaging mode. Three successive pushing beams are transmitted and focused on the left, center and right part of the cornea surface (locations no. 1, 2, 3). After each “push,” the ultrasonic scanner images the resulting transient displacement by entering into an ultrafast frame rate during 3 ms. The total acquisition time for imaging the three generated shear waves is no longer than 12 ms.

in vivo porcine eye is presented in Fig. 2(b). The cornea is clearly visible in the echographic image. The operator is first asked to position the desired locations of three pushing beams using a cursor on the real time echographic images. These pushing beams have to be positioned at the left, center and right parts of the cornea (Fig. 3). Then, a first SSI sequence is performed using the left “pushing” beam and an ultrafast ultrasonic sequence is performed in order to catch the resulting corneal displacements. The total experiment lasts 3 ms (60 frames acquired at a 20 000 Hz frame rate). This first sequence (pushing beam no. 1, Fig. 3) allows elasticity imaging on the right side of the pushing line location. Just at the end of this first sequence, a second SSI sequence (pushing beam no. 2, Fig. 3) is performed with the central “pushing” beam. Finally, a third sequence is performed with a right “pushing” beam (pushing beam no. 3, Fig. 3). The pushing modes no. 1 and 3 enable elasticity imaging in the middle of the imaging plane whereas the pushing mode no. 2 enable elasticity imaging on the edges of the imaged area. The total acquisition time for a complete mapping of cornea elasticity lasts 12 ms (3×4 ms). For practical clinical configurations, this ultra-short acquisition time will prevent the influence of any motion artifacts or natural motion such as arterial pulsatility.

C. Safety Considerations

In order to meet the FDA (Food and Drug Administration) requirements for ophthalmologic applications, the acoustic intensities have been strongly decreased in comparison with other organs such as breast [2], liver [16] or muscle [17]. The acoustic intensity induced during the SSI sequence remained lower than the recommendations provided by the FDA for ultrasonic imaging devices (510 k recommendations). The methodology used for the measurements is described in the paragraph 4.6.1 “acoustic output reporting” of these recommendations [33].

For these *ex vivo* investigations, each “pushing” beam is typically focused between 6 and 12 mm depth. Each focused insonification lasts $30 \mu\text{s}$ for the generation of the “pushing” radiation force. Typically, it corresponds to 1000 sinusoids at 15 MHz. This results in a total of $90 \mu\text{s}$ insonification for the *in vivo* generation of a complete data set for stiffness imaging. The acoustic

TABLE I
ACOUSTIC PARAMETERS USED IN THE SSI MODALITY COMPARISON WITH THE 510 (K) FDA RECOMMENDATIONS FOR ULTRASOUND DIAGNOSTIC IMAGING SYSTEMS

Sequences	Mechanical Index		I_{SPTA} (mW/cm^2)	
	Worst case measurement	510k FDA Limits	Worst case measurement	510k FDA Limits
Shear wave generation	0.21 ¹	0.23	2.2	17
Ultrafast imaging	0.08	0.23	0.13	17
Global SSI sequence	-	-	2.33	17

pressure levels and intensities were measured using a calibrated AH-2020 hydrophone (OndaCorp., Sunnyvale, CA, 0.1 mm resolution, frequency bandwidth ranging from 1 to 25 MHz). Measurements were made in water. For these measurements, the acoustic parameters were estimated at the “worst” focal distance (corresponding to the elevation focus $z = 12$ mm). These parameters correspond respectively to the mechanical index (MI) and the spatial peak time averaged intensity (I_{SPTA}), as defined in the FDA recommendations [33]. All values were not derated in order to take into account the worst case corresponding to a pushing and elevation focus simultaneously located exactly at the external surface of the cornea. The results corresponding to the acquisition of one elasticity image per second (i.e., 3 pushes each lasting $30 \mu\text{s}$ and 3×60 ultrafast images) for this worst pushing case are summarized in Table I.

It can be seen in Table I that the ultrafast imaging mode is characterized by a very low I_{SPTA} value as it does not imply any focusing in the transmit mode. Finally, even in the worst configuration chosen for the acoustic parameter measurements, the SSI mode fulfils the requirements of the 510 (k) FDA recommendations. The total $2.33 \text{ mW}/\text{cm}^2$ I_{SPTA} value for a single elasticity image acquisition per second is much lower than the $17 \text{ mW}/\text{cm}^2$ FDA limit. A maximal frame rate of 7 elasticity frames/s could even be performed while respecting the FDA guidelines.

D. Postprocessing of Raw Data for Quantitative Imaging of the Shear Wave Group Velocity

Raw RF data are transferred via a PCI Xpress bus on a PC board. Signal processing is then divided into the following steps.

- 1) Receive beamforming of the raw RF data acquired in order to produce flat transmit echographic images.
- 2) One dimensional (1-D) speckle tracking using conventional 1-D cross-correlation of successive echographic images for the building of 128 images of tissue relative displacements (along the z -axis, Fig. 1). Relative displacement means tissue displacement between two successive ultrafast echographic images. Consequently, it corresponds to a local tissue particle velocity (in m/s). Out-of-line motion are negligible as tissue displacements along the ultrasonic beam path are typically ten times higher than the ones in transverse directions.

3) Local assessment of the mechanical shear wave speed c_s by means of a time of flight estimation between two points during the shear wave propagation. This time of flight estimation is based on the cross-correlation of local displacement time profiles recorded at two different locations along the s -axis (Fig. 4 dashed white line) corresponding to a curvilinear line that follows the cornea curvature. Lateral distance between the two measurement points along this line corresponds typically to 8 times the inter-element spacing of the linear probe (i.e., $8 \times 0.2 \text{ mm} = 1.6 \text{ mm}$). By estimating a time of flight between two wideband shear displacement signals, this algorithm performs an averaged estimate of the shear wave group velocity over the whole shear wave bandwidth. In a locally homogeneous medium, the Young's modulus E is then directly linked to shear wave speed c_s via the relation $E = 3\rho c_s^2$, where ρ is the density. In the case of cornea, this relationship does not hold anymore as the mechanical wave is constrained and guided in a plate (i.e., the cornea) thinner than the shear wavelength. However, a slightly more complex relationship relating shear wave speed and the Young's modulus can be derived by considering the leaky Lamb wave theory.

Recombination of the shear wave speed image obtained with the pushing mode no. 1, 2, and 3 (Fig. 3). The local wave speed can be converted into the local Young's modulus value as described in the next subsections.

E. Analysis of Shear Wave Dispersion for Quantitative Recovery of Young's Modulus

A more detailed analysis of the local mechanical behavior of the cornea can be performed using a shear wave spectroscopy algorithm as previously described by Deffieux *et al.* [34]. This approach corresponds to the determination of shear wave phase velocity dispersion over a large frequency range. The large bandwidth of the shear wave generated through the ultrasonic radiation force allows this kind of measurement in one single acquisition sequence. Whereas the shear wave spectroscopy analysis can be performed in a typical 100–500 Hz in deep organs like breast or abdominal organs), the bandwidth of the shear wave generated by the ultrasonic beam radiation force is much larger in the cornea application. Fig. 4(a) shows typical waveforms of the shear velocity profile obtained in *ex vivo* porcine eyes at one given depth in the cornea as a function of time [Fig. 4(a)] for an increasing distance from the “pushing location.” Fig. 4(b) shows the corresponding frequency spectrum. It appears that the use of a 15 MHz linear array (generating a remote palpation on an approximate 0.2-mm-diameter sharp beam) enables exploiting a very large 500–3000 Hz bandwidth contrary to deeper organs like breast or liver where the upper limit of the bandwidth is limited to 500 Hz [34], [16]. Such very high shear wave frequencies can only be reached due to the sharpness of the ultrasonic beams generated by very high frequency ultrasonic probes.

The Fourier transform of these signals is then computed. At each frequency, the dependence of the phase versus propagation distance is extracted. The last step consists applying a linear fitting to this phase function in order to retrieve the wave number

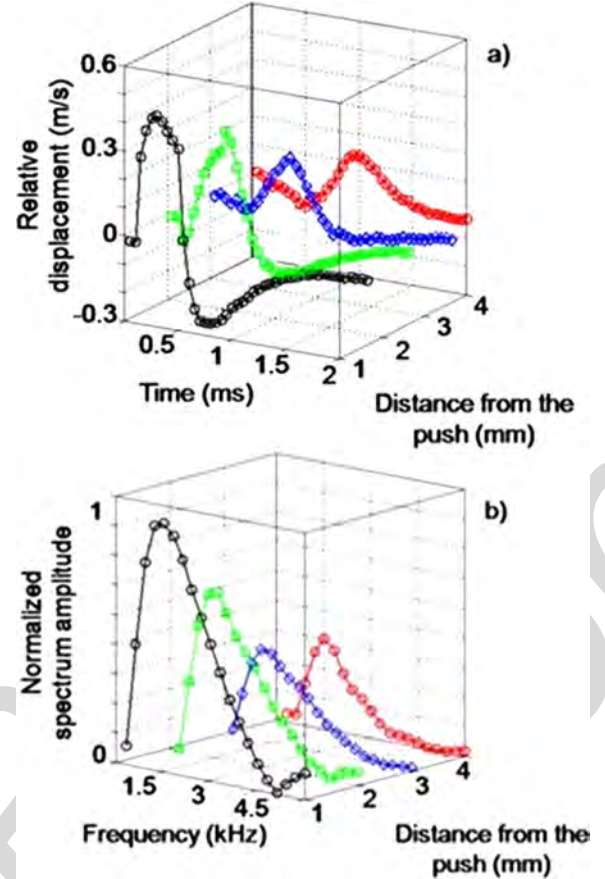


Fig. 4. (a) Typical experimental waveforms of the shear relative displacement profile (displacement from frame to frame at a PRF 20 000 Hz) obtained in *ex vivo* porcine eyes (displacement for different locations at one given depth in the cornea as a function of time for an increasing distance from the “pushing location.”) (b) Corresponding spectra for each shear waves displacement profile presented in Fig. 4(a).

k for each frequency and consequently the phase speed of the shear wave at each frequency. One has thus access to the shear wave dispersion curve.

F. Estimation of Young's Modulus From Leaky Lamb Wave Guided Propagation in the Cornea

Due to the dispersion induced by the guided propagation into the cornea, the conversion of shear wave speed into a quantitative Young's modulus mapping can be deduced by reformulating (2) into the form

$$E = 36 \frac{\rho c(\omega)^4}{h^2 \omega^2}. \quad (3)$$

By using cornea thickness and the central frequency of the mechanical wave spectrum as entry parameter, (3) provides the Young's modulus value from the estimated mechanical wave speed. As an example or a typical $c = 5.1 \text{ m/s}$ propagation and a 1500 Hz central frequency excitation in a 1.2 mm thick cornea, one retrieves $c_s = 7.96 \text{ m/s}$ corresponding to $E = 190 \text{ kPa}$ Young's modulus of the cornea.

G. Simulations

In order to corroborate experimental results, the 3-D displacement field induced by the ultrasonic radiation force in the

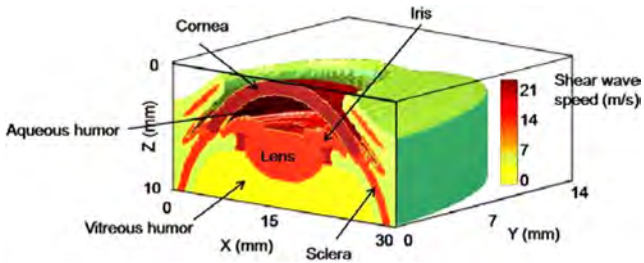


Fig. 5. Three-dimensional spatial distribution of the shear wave speed c_s (corresponding to the local Young's modulus E via $E = 3\rho c_s^2$) used in the time domain finite differences simulations of the cornea mechanical response using Acel, a package of 3-D wave simulation libraries developed at Laboratoire Ondes et Acoustique, Paris, France.

cornea was also fully modeled using a 3-D discretization of the elastodynamic continuity equations. The model is based on a first-order finite-difference time-domain (FDTD) algorithm for elastodynamic equations. The implemented scheme is based on a staggered grid technique initially introduced by Virieux for applications in seismology [35]. Perfectly matched layers [36] were also implemented at the boundaries of the 3-D mesh volume in order to avoid unwanted reflections of the propagating waves. The medium is considered to be elastic, isotropic, and nondissipative. It is discretized into a rectangular volume made of $550 \times 300 \times 550$ points. Each grid voxel is defined by its local density, shear wave speed and bulk wave speed (linked directly to mechanical shear and bulk moduli).

Table II summarizes the physical parameters chosen for the FDTD simulations. The Bulk wave speed was 1500 m/s in all tissues. Aqueous humor was considered as a liquid. Although few and sometimes contradictory values were available in the literature, the chosen parameters were found both to corroborate several reported values and to agree with the typically obtained experimental results [37], [38]. Fig. 5 shows a 3-D view of the shear wave speed values in the 3-D volume. The eye was considered to be immersed in water. Transparent areas of the 3-D volume correspond to a zero-valued Young's modulus (i.e., fluid areas).

H. Photodynamic Riboflavin/UVA Induced Corneal Collagen Cross-Linking (CXL)

Keratoconus is an idiopathic corneal dystrophy characterized by progressive thinning and ectasia which results in a decrease of vision and also the quality of life. As the disease begins in young adults, it affects the most productive years of life. A recent modality of treatment, CXL with the help of UVA, 370 nm, and the photosensitizer Riboflavin phosphate 0.1%, has been described which changes the intrinsic biomechanical properties of the cornea. Resulting in the stiffening of the stroma layer of the cornea, this treatment has shown to slow down or prevent the progression of Keratoconus in numerous studies all over the world [39], [40].

In our study, fresh postmortem porcine eyes were treated using the following procedure: In order to allow the spreading of the Riboflavin into the cornea, the epithelium (first external layer of the cornea) was gently removed with a smooth spatula. Then, corneas were immersed into 0.1% Riboflavin

TABLE II
MECHANICAL PARAMETERS FOR 3-D SIMULATIONS

	Density ($\text{kg}\cdot\text{m}^{-3}$)	Shear Wave Speed ($\text{m}\cdot\text{s}^{-1}$)	Stiffness E (MPa)
Cornea			
Simulation N°1	1000	10	0.3
Simulation N°2	1000	20	1.2
Simulation N°3	1000	25	1.8
Iris	1000	20	1.2
Lens	1000	20	1.2
Sclera	1000	17	0.6
Aqueous humor	1000	0	0
Vitreous humor	1000	0.2	10^{-4}

(Ricola-Sooft-Italy) solution for 15 min (with an handmade system of corneal lens recipe). Finally, UVA irradiation was performed for 30 min by using a UVA diode laser (370 nm, IROC-Germany) with a focusing spot diameter of 8 mm and constant irradiance of $3 \text{ mW}/\text{cm}^2$. One eye drops of isotonic saline solution (BSS) followed by one eye drop of Riboflavin 0.1% was applied on the cornea every five minutes for respectively hydration and renew of the photosensibilizer. Young's modulus imaging sequences were performed just before the CXL and at the end of the CXL with the SSI system and corneal elasticity mapping was performed.

III. RESULTS

A. Simulations

The radiation force induced by the ultrasonic beam focused on the cornea surface was introduced as a transient source term in the elastodynamic equations. In order to mimic the typical experimental configuration, the 3-D spatial distribution of this transient source term corresponds to a $0.2 \times 0.4 \times 2 \text{ mm}^3$ cigar shape volume in which each pixel generates a force along the z -axis. The 0.2 mm dimension corresponds to the lateral resolution of the 1-D linear probe. The 0.4 mm resolution corresponds to the beam width in the probe elevation direction (y -axis). As the ultrasonic "pushing" beam along z -axis is roughly equal to 2 mm, it generates an uniaxial force over the entire depth of the cornea. The black ellipse in Fig. 6(a) corresponds to the trace of this cigar shape on the cornea surface.

The color maps correspond to the spatial distribution of tissue displacements along the z -axis at the cornea surface for different time steps after the force generation. One can notice that the slight asymmetry of the pushing beam does not result in any asymmetry of the shear wave propagation that propagates with a spherical shape. This is easily explained by the fact that the average wavelength of the generated shear wave is much larger than the source dimensions. Moreover, as local microscopic displacements are four orders of magnitudes smaller than

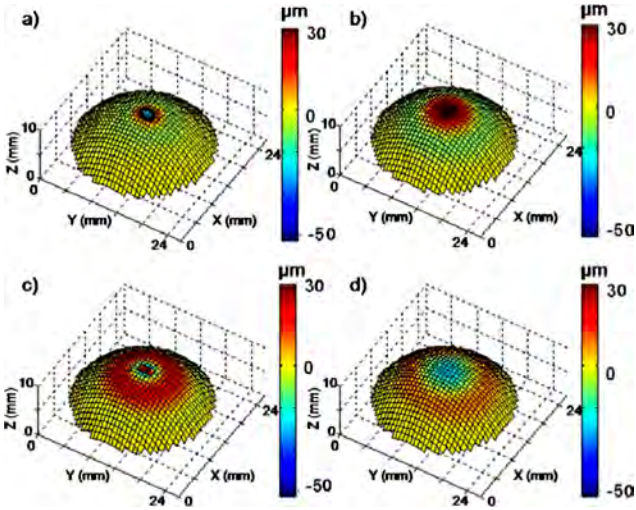


Fig. 6. Spatial distribution of cornea tissue displacements along the z -axis at the cornea surface for different time steps after the force generation: (a) $t = 0.25$ ms, (b) $t = 0.5$ ms, (c) $t = 0.75$ ms, and (d) $t = 1$ ms. The color scale ranges between $-50 \mu\text{m}$ and $+30 \mu\text{m}$. As local displacements are four orders of magnitudes smaller than the global eye dimensions, the eye curvature can be considered as in a steady state.

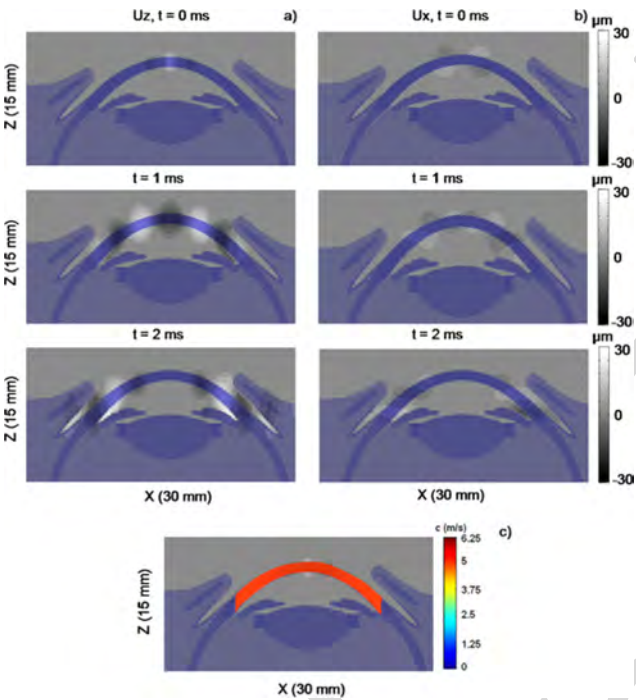


Fig. 7. Spatial distribution of tissue displacements, respectively, (a) along z -axis and (b) along x -axis in a vertical X-Z slice for different time steps after the mechanical force generation. Displacements are ranging from $-30 \mu\text{m}$ to $30 \mu\text{m}$ in both figures. (c) Shear wave speed map estimated by the time of flight algorithm using z -displacements from Fig. 7(a).

the global eye dimensions, the eye curvature can be considered as stationary. Interestingly, Fig. 7(a) and (b) represent for the same simulation the mapping of displacements respectively along z and x axis in a vertical X-Z slice for different time steps after the mechanical force generation. Two points can be noted: first, the displacements along the x -axis are much smaller (more than ten times) than the displacements along z direction. The

estimation of z -displacements (i.e., the ones estimated experimentally using the 1-D ultrasonic speckle correlation tracking approach) is sufficient to image the whole propagation phenomenon. Secondly, tissue displacements occur not only at the surface but everywhere in depth inside the cornea. Thus, local estimation of the shear wave speed will provide an in depth mapping of the elasticity of cornea.

Fig. 7(c) presents the estimation of the shear wave speed deduced from the time of flight algorithm. A homogeneous map is recovered as expected. However, one should notice that the shear wave speed is much smaller ($c = 5.3 \text{ m/s} +/ - 0.1 \text{ m/s}$ for a central frequency of the mechanical excitation) than the local parameter introduced in the simulation ($c_s = 15 \text{ m/s}$). Indeed, as shear wavelength is of the same order of magnitude than the cornea thickness, this is explained by the fact that the shear wave propagation is guided by the cornea. This guided propagation corresponds to a well known case in physics, corresponding to the propagation of a leaky Lamb wave in a plate.

B. Simulation Results: Analysis of Shear Wave Dispersion Due to Leaky Lamb Wave Guided Propagation

The dispersion curves for the wave propagation modeled in the FDTD simulation were estimated. For this purpose, the time profile of the shear wave received at each location along a curvilinear line corresponding to a constant depth inside the cornea are analyzed in the Fourier domain. Indeed, the Fourier transform of each time profile enables to estimate at each frequency the phase changes with the propagation distance. The phase of each spectral component is linearly dependent of distance and a linear fit of this dependence enables the estimation of the shear wave speed at each frequency. The corresponding shear wave speed is plotted for each frequency in Fig. 8. As one can notice the wave propagation is strongly dispersive and the wave phase speed values are in good agreement with the empirical formula proposed in recent works [44].

In the range 500–3000 Hz, this agreement was verified for three different simulations (using three different cornea stiffness corresponding to $c_s = 10, 15,$ and 25 m/s and a fixed cornea thickness). One should notice here that compared to a propagation in free space where the shear wave would propagate at c_s , the cornea plate slows down the mechanical wave (for example, in Fig. 8, $c = 8.25 \text{ m/s}$ at 1500 Hz for a cornea stiffness defined by $c_s = 25 \text{ m/s}$). This permits to track the mechanical wave propagation experimentally without requiring to perform huge ultrasonic frame rates.

C. Experimental Results: Quantitative Imaging of Corneal Elasticity

In the total of six fresh postmortem porcine eyes, the ultrasonic probe was found to be able both to induce a shear wave propagating in depth inside the cornea and to image with an ultrafast frame rate (20 000 Hz) the resulting shear relative displacements. The 1-D cross-correlation of successive ultrasound images provides a set of tissue relative displacements. Fig. 9 represents the 2-D spatial distribution of these tissue relative displacements along z -axis at different time steps after the second radiation force generation (central “push” corresponding to sequence no. 2 described in Fig. 3). Displacements occur in all

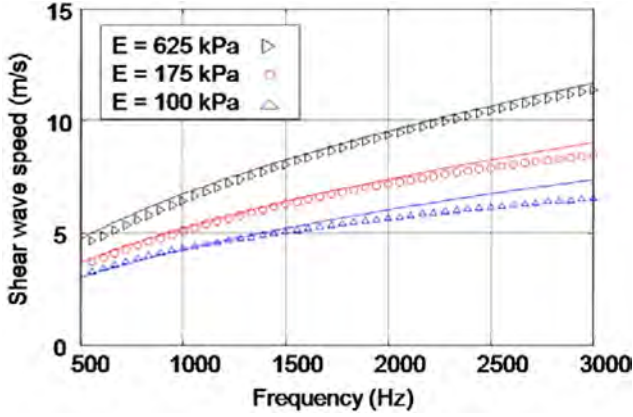


Fig. 8. Shear wave speed dispersion curve obtained from simulated data using three different cornea stiffness ($E = 100, 175$ and 625 kPa corresponding respectively to shear wave speed values $c_s = 10, 15$, and 25 m/s). The solid line corresponds to the analytical formula presented in (2). The cornea stiffness values used in simulations correspond to typical values of cornea stiffness obtained from *ex vivo* experiments.

layers of the cornea and the shear wave propagation from center towards cornea edges is clearly visible. Maximal tissue relative displacements of about 0.6 m/s at a $20\,000$ Hz pulse repetition frequency (corresponding to global displacements of about $100\mu\text{m}$ after time integration) can be reached while preventing to overtake the FDA safety limitations.

Fig. 10 presents an example of the post-processing which enables the recovery of the local shear wave group speed along the dashed line presented in Fig. 9(d).

The value of the shear wave speed at point A outside of the pushing zone is obtained by estimating the time delay τ_A between time profiles at points B and C surrounding point A. The choice of the distance between B and C is optimized based on the data quality (i.e., the signal to noise level of tissue displacements estimates). A high SNR of displacements time profiles enables estimating smaller time delays between signals and consequently reducing the interspace distance between locations used in the time-of-flight algorithm. Typically, in our experiments, this distance corresponds to four times the spatial pitch of the array (4×0.2 mm ≈ 0.8 mm). This time of flight estimation is performed for each location along each curvilinear line inside the cornea resulting in a 2-D mapping of the local shear wave speed in the cornea with a $150\mu\text{m}$ resolution. Fig. 10 shows the resulting 2-D mapping of the cornea obtained using this time of flight algorithm.

D. Experimental Results: Analysis of Shear Wave Dispersion Using Shear Wave Spectroscopy

Shear wave spectroscopy was applied using the experimental data. The time profiles of local z -displacement recorded at each location along a curvilinear line corresponding to a constant depth inside the cornea [dashed line Fig. 9(d)] are displayed in Fig. 11. The three successive “pushes” on the left, center and right side of the cornea and their resulting propagation are clearly visible.

The Fourier transform of each time profile enables to estimate at each frequency the phase changes with the propagation distance. The phase of each spectral component is linearly de-

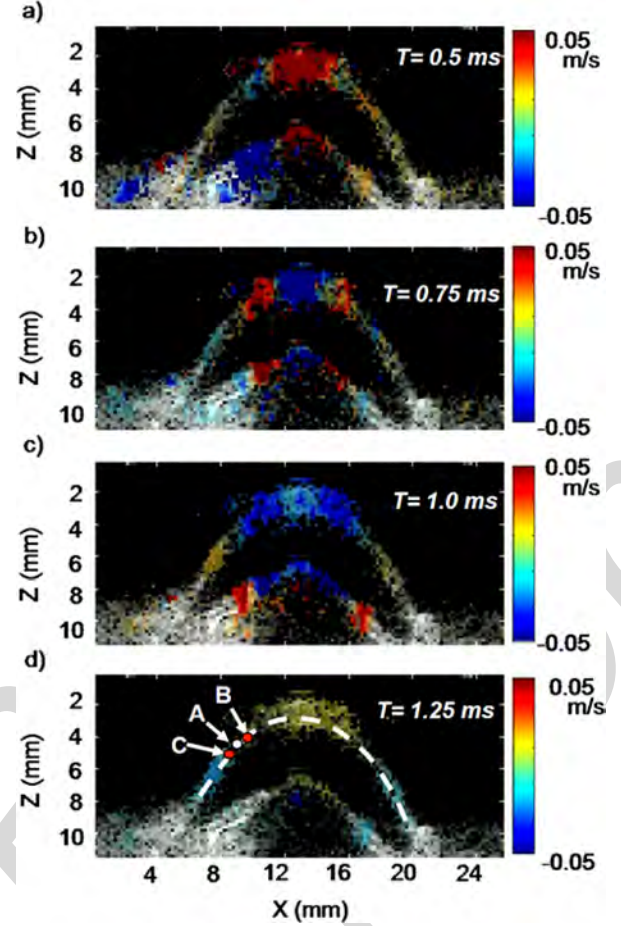


Fig. 9. Images of local corneal tissue relative displacements between successive echographic images (i.e., particle velocity) at different time steps just after the ultrasonic radiation force generated at the center of the cornea. These color relative displacements images depict the shear wave propagation in the cornea and are superimposed on the echographic gray scale image. The resolution of the displacement map is $150\mu\text{m}$.

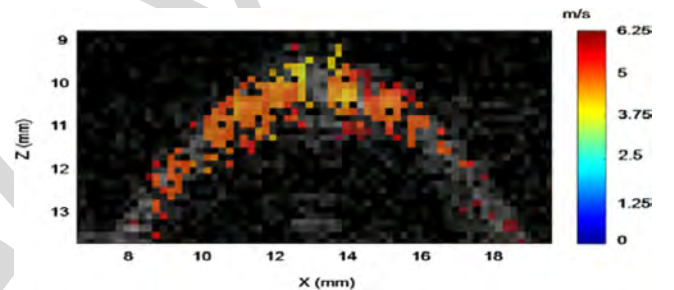


Fig. 10. High-resolution 2-D map of the shear wave speed superimposed on the gray scale ultrasound image of the cornea. From the knowledge of the corneal thickness ($h = 1.5$ mm) and central frequency of the mechanical excitation (1500 Hz), this map can be converted into a quantitative Young’s modulus map using (3). Here, mean wave speed is equal to $5.1\text{ m}\cdot\text{s}^{-1} \pm 0.2\text{ m}\cdot\text{s}^{-1}$ corresponding to a cornea Young’s modulus of $190\text{ kPa} \pm 32\text{ kPa}$.

pendent of distance and a linear fit of this dependence enables the estimation of the shear wave speed at each frequency, see Fig. 12. The three subplots correspond to estimates for the three successive pushing modes.

Finally, from these data, the corresponding shear wave speed dispersion curves deduced from the three successive pushing

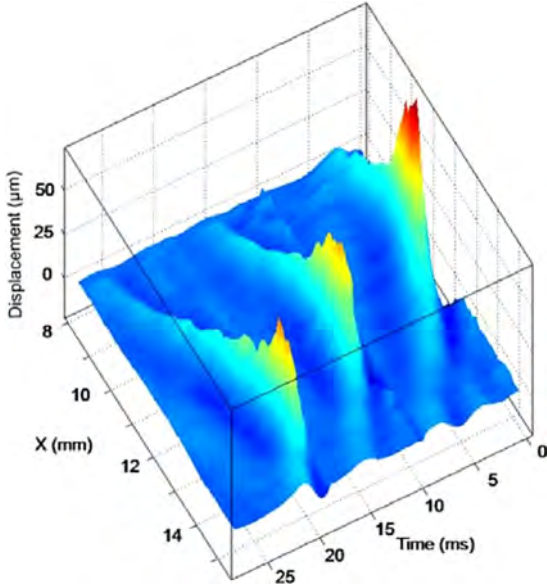


Fig. 11. Time profiles of local z-displacement recorded at each location along a curvilinear line corresponding to a constant depth inside the cornea [dashed line Fig. 9(d)]. One can clearly distinguish the three successive mechanical wave propagations corresponding to the three successive push locations.

modes are plotted in Fig. 13. The assessment of this frequency dependence of the mechanical wave speed is found to be robust as the three curves are in good agreement. The analytical formula corresponding to (2) with a value $c_s = 7.9$ m/s (i.e., $E = 190$ kPa) is also plotted in Fig. 13 and fits the experimental data derived from the shear wave spectroscopy analysis.

The agreement between experiments and the analytical dispersion relation is very good especially in the high frequency range (>1500 Hz). At lower frequency, a discrepancy appears. It is due to two main factors. First, as the wavelength becomes quite large at lower frequency, it is no more negligible compared to the cornea curvature and diffraction due to the spherical shape of the eye can no more be neglected. In terms of Lamb mode propagation, a single A0 mode propagation can no more be considered and contribution of other modes are present. Secondly, at very low frequency the dispersion curve assessment is disturbed by reflections of the wave on the edges of the cornea. A local point can “feel” the reflected Lamb wave before the end of the incident wavefield. This last point emphasizes the interest provided by the acoustic radiation force that permits generating shear waves with a very high frequency range.

E. Elasticity Changes Induced by Photodynamic Riboflavin/UV-A Corneal Cross-Linking

Several fresh porcine eyes were treated using photodynamic Riboflavin/UV-A collagen induced CXL. SSI sequences were performed before and after the UV-A Laser exposure. Fig. 14 shows the time profiles of tissue displacement at each location along a curvilinear line corresponding to a constant depth inside cornea. The mechanical wave speed strongly increases after UV-A exposure clearly exhibiting a strong increase in the cornea stiffness. The shear wave spectroscopy algorithm enables us to recover respective 190 kPa \pm 32 kPa and 890 kPa

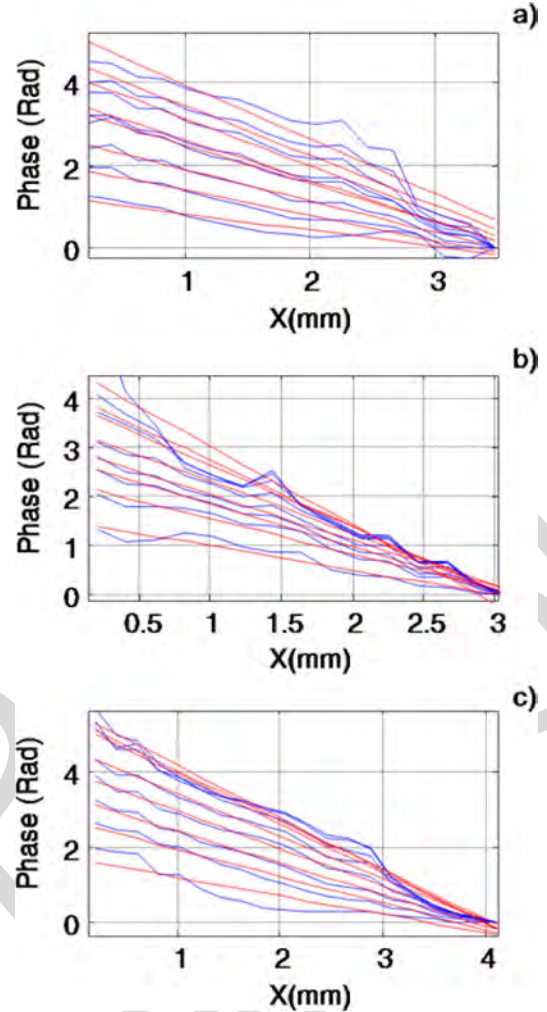


Fig. 12. Phase changes of each frequency component (ranging from 200 Hz to 2900 Hz) of the mechanical wave versus propagation distance for the three “pushing” modes at different push location (a) $x = 5$ mm, (b) $x = 10$ mm, and (c) $x = 15$ mm). The linear fit deduced for each frequency component enables the assessment of the wave speed and consequently the recovery of the shear wave dispersion curve.

± 250 kPa values for cornea Young’s before and after collagen induced crosslinking (corresponding for a 1.2 mm thickness, respectively, to $c = 5.1$ m/s and 8.5 m/s shear wave phase speeds at a 1500 Hz central frequency). This 460% increase ratio is in agreement with recent values provided by Wollensak *et al.* [45] and Kohlhaas *et al.* [46].

Finally, 2-D mapping of cornea stiffness were performed and are presented in Fig. 15. The strong increase in local shear wave speed (and by correlation Young’s modulus) is clearly demonstrated analyzing the slope of the time profiles.

F. High-Resolution Imaging of Corneal Elasticity

Finally, the high-resolution capabilities for corneal stiffness mapping provided by the SSI imaging mode are demonstrated in Fig. 16. This 2-D mapping of shear wave speed corresponds to experimental data acquired on one single case of a porcine eye whose cornea had been probably partially burnt (coagulation) before the animal sacrifice (an opaque scar was observed onto the corneal opening eyelid area). One clearly distinguishes

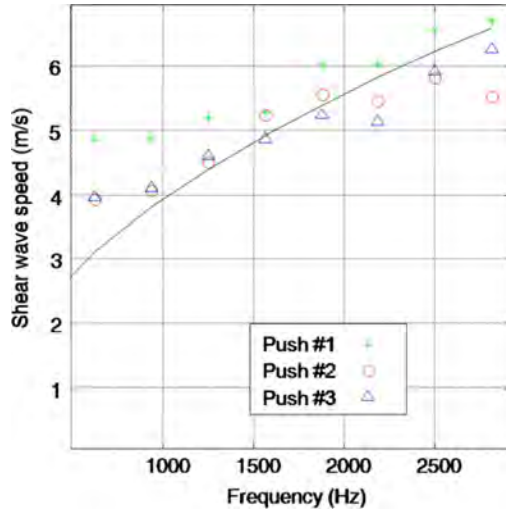


Fig. 13. Shear wave dispersion curves estimated experimentally for the three successive mechanical waves generated by pushing modes no. 1, 2, and 3 into the porcine cornea. The solid line corresponds to (2) with a chosen $c_s = 7.9$ m/s (i.e., cornea Young's Modulus $E \sim 190$ kPa).

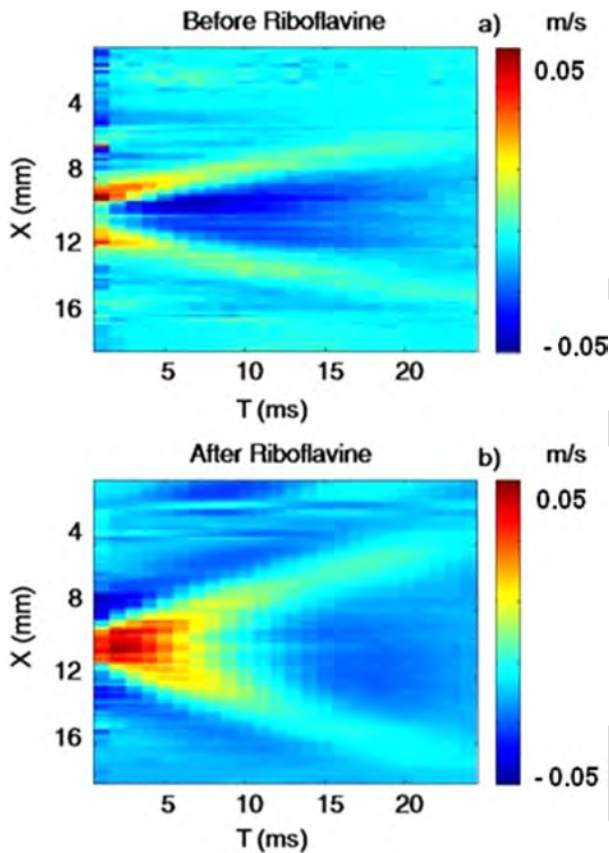


Fig. 14. Time profiles of tissue particle velocity (i.e., relative displacement of tissues between two successive ultrasonic images) at each location along a curvilinear line. This line corresponds to a constant depth inside cornea (a) before and (b) after UV-A exposure. Colors scale is ranging between -0.05 m/s and $+0.05$ m/s.

in Fig. 16 the appearance of a very stiff layer in the cornea ($200\mu\text{m}$ thick). Such layered structure was also confirmed on the movie of the local tissue displacement. The propagation of the mechanical wave is clearly much faster in the upper first

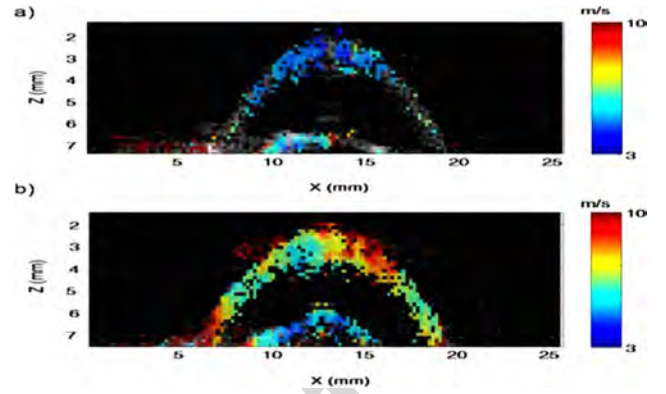


Fig. 15. Influence of CXL on corneal stiffness: 2-D mapping of the local shear wave speed (a) before and (b) after Riboflavine and UV-A exposure.

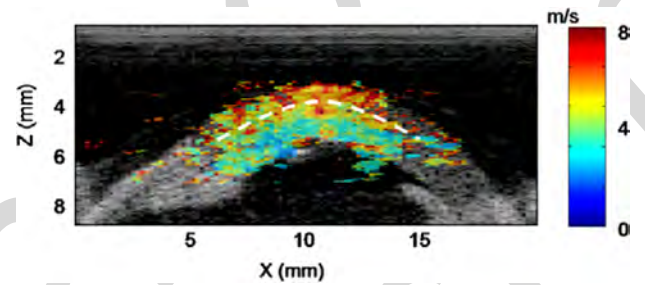


Fig. 16. Two-dimensional mapping of shear wave speed of an excised porcine eye whose cornea had been partially burned. The SSI modality is clearly able to image a very stiff $500\mu\text{m}$ first layer in the cornea.

layer of the cornea than in deeper cornea tissues. The capability of the SSI mode to provide local information in different layers inside the cornea is here shown to be feasible experimentally with a typical $150\mu\text{m}$ resolution.

IV. DISCUSSION

The main purpose of this preliminary clinical study was to evaluate the capability of the SSI mode to provide quantitative elasticity maps of different cornea and to determine the clinical situations where this technique could add potential value to US examinations. Contrary to other investigated applications such as breast cancer diagnosis [2], liver fibrosis staging [16] or muscle properties assessment [17], the transposition to corneal stiffness imaging required to strongly improve spatial resolution of the technique.

For this application, the ultrasonic probe frequency (15 MHz) was strongly increased compared to imaging probes used for deep organs such as breast, liver, or heart (respectively, 8 MHz, 4 MHz, and 2.5 MHz) and leads to two important remarks. First, the resolution of the echographic images is very high ($150\mu\text{m}$) and the ultrasonic focal spot inducing the radiation force in the cornea has a very high lateral resolution (around $100\mu\text{m}$). As the frequency spectrum of the mechanical wave is directly linked to the focal spot size, the mechanical wave induced by the "pushing beam" is characterized by a very high frequency spectrum (typically from 500 Hz to 3000 Hz). This enables the sounding of mechanical properties of cornea with shear waves of small wavelengths, thus enhancing the resolution of the final Young's modulus mapping. Moreover, as the echographic

imaging depth is reduced (20 mm) in comparison with deep seated organs, ultrafast frame rates as high as 20 000 Hz can be reached. It enables a very high temporal resolution for the estimates of the transient tissue displacement time profiles even if the induced shear wave possesses very high frequency components (up to 3000 Hz). Finally, displacements induced by the radiation force are very small (of the order of tens of μm) and a nonlinear biomechanical response of cornea can be rejected on the contrary of other existing approaches such as ocular response analyzer (ORA).

In all investigated porcine eyes, the ultrasonic probe was able both to generate a remote mechanical vibration in the cornea and to track the transient propagation of the resulting shear wave inside cornea.

Porcine eye corneal stiffness was found to be rather homogeneous with a mean 190 kPa value and to strongly increase (460% increase) after riboflavin collagen induced crosslinking. Riboflavin/UVA cross-linking seems to affect the cornea elasticity nonuniformly as seen in Fig. 15. This non uniformity does not correspond to artifacts. Indeed, the areas of higher stiffness visible in Fig. 15 correspond to regions of higher shear wave speed. However, although such a nonuniform spatial distribution of cross-linking stiffening seems to be accepted by clinicians, there is to our knowledge no evidence regarding this point in the literature.

Thanks to the resolution of the echographic image, the resolution obtained in the elasticity image is quite high and permits to estimate local elasticity in different layers of the cornea (see Fig. 16).

Finally, the applicability for clinical investigations can be easily envisioned as the method is insensitive to motion artifacts. Moreover contrary to the only system used today in clinical practice, the O.R.A. system [47], the SSI modality gives access to the real physical parameter (mechanical property parameter), i.e., the Young's modulus, as it is based on the direct visualization and estimation of mechanical wave propagation. By estimating only two applanation pressures times at the single location of the air pulse on the cornea, the ORA cannot resolve the inverse problem of this shear wave propagation and recover direct estimates of physical biomechanical parameters such corneal elasticity or viscosity. Consequently, it provides a cornea hysteresis parameter that cannot be linked easily to stiffness. The same kind of limitation can be encountered for elasticity imaging in deep organs using the ultrasonic radiation force: it is extremely difficult to estimate the Young's modulus only from the knowledge of tissue displacement only at the location of the applied force (see [15, Eq. (22)]. Instead of imaging tissues displacement only at the force location, a 2-D mapping of tissue displacements allows recovering shear wave propagation parameters such as wave speed and consequently Young's modulus. Finally, contrary to transient displacements induced by ORA, tissue motion induced using the SSI modality corresponds to very small micrometric displacements (small perturbations) with typical millimetric wavelengths (transient pulsed perturbation with typical 1500 Hz frequency). For that reason, it should be less influenced than ORA by boundaries conditions such as tissue tension or intra-ocular pressure.

The clinical applicability of the SSI modality for the estimation of cornea elasticity requires ensuring that the acoustic power required for generating the radiation force remains below the FDA limits. This is possible as typical 10 μm local displacements can be generated without overtaking these limitations. Such displacements can be detected using ultrafast ultrasonic sequences that can track tissue displacement as small as 1 μm . Regarding practical *in vivo* applicability, a coupling liquid could easily be inserted in a cup between the eye and the ultrasonic probe. The complete elasticity investigation will not modify at all a conventional ultrasonic procedure in ophthalmology and will provide the biomechanical properties of cornea in addition to the ultrasonic images. Moreover, a detailed signal processing analysis of shear wave propagation enables accessing *in vivo* the complete mechanical behavior of the cornea on a very large bandwidth. Such dynamic mechanical spectroscopy of the cornea was up today only achievable using explanted human corneas [48] in the 0.1–100 Hz range. The SSI modality permits to achieve the shear wave spectroscopy [34] noninvasively and in real time.

For *in vivo* applications, the coupling liquid between the echographic probe and the cornea should probably not influence the cornea stiffness estimates. Indeed, it is well known that hydration by short corneal immersion induces very small changes *in vivo* in corneal thickness and shear compliance at least in the 0.1 mHz to 100 Hz [48]. Although shear wave spectroscopy provided by the SSI modality corresponds to a much higher frequency bandwidth, it seems that these results could be reasonably extrapolated to our mechanical frequency bandwidth. Such assumption will be carefully studied in further *in vivo* works. For *ex vivo* studies where hydration is known to play a role by increasing cornea thickness, it should be carefully studied whether only thickness is affected by hydration or both thickness and Young's modulus are changing. This is a nontrivial problem, as corneal thickness affects the mechanical wave speed. However, the quantitative method proposed in this paper should be able to discriminate the influence of hydration on both parameters.

In terms of resolution, very high-resolution maps were obtained in this study, as the elasticity mapping is only limited by the resolution of the echographic images. Thus, increasing the ultrasonic probe frequency up to 25 MHz could even lead to a 70 μm resolution of the cornea elasticity map provided by the SSI modality.

In this study, shear viscosity of cornea tissue was neglected. Such viscosity definitely also affects the dispersion curves of the mechanical guided wave in the cornea. The discrimination between the distinct influences of both the guided mode propagation and the shear viscous term onto the dispersion of the wave propagation should be studied in further works.

Finally, in this study, corneal tissues were assumed to be isotropic. This assumption is not totally valid. Indeed, the human cornea has the macroscopic structure of a thin shell, originated by the organization of collagen lamellae parallel to the middle surface of the shell. The lamellae, composed of bundles of collagen fibrils, are responsible for an experimentally observed anisotropy of the cornea. Smolek has shown that the mean interlamellar cohesive strength is diminished

in the inferior peripheral portion of the cornea compared to values obtained from the other principal meridians [49]. The mean cohesive strength in the central cornea was shown to be less than that of the superior periphery. However, Smolek concluded that the biomechanical significance of this deficit is probably minor if not irrelevant in the average, intact cornea under physiologically normal tensile loading, but may become significant in corneas with specific forms of degenerative disease or trauma that induces shearing strains between the lamellar sheets of the stroma.

Further work will concentrate on the influence of cornea elastic anisotropy on the shear wave propagation. The ability of the ultrasonic radiation force to polarize the generated shear waves in different orientations could help us to quantify at least an eventual radial anisotropy of cornea elasticity.

V. CONCLUSION

This initial investigation demonstrates the ability of ultrafast and high-resolution echographic systems to provide a real-time and quantitative mapping of corneal elasticity. Quantitative elasticity maps were acquired *ex vivo* on porcine cornea using the SSI technique. Quantitative maps of corneal elasticity were obtained in all fresh porcine eyes. A 190 kPa \pm 32 kPa mean elasticity was obtained for four different specimens. The SSI modality was found able to quantify the influence of photodynamic Riboflavin/UV-A induced CXL on corneal stiffness. A significant Young's modulus increase was obtained with a mean 890 kPa \pm 250 kPa posttreatment Young's modulus (\sim 460% increase). Simulations based on 3-D time domain finite differences simulation were also performed and found to be in good agreement with *in vitro* experiments. The Supersonic Shear Imaging technique can perform real-time, very high-resolution, and quantitative maps of corneal elasticity. This technique can be real time and straightforward adapted for *in vivo* investigations. Further works will study the influence of intra-ocular pressure on corneal elasticity and present first clinical investigations of the SSI modality in ophthalmology.

ACKNOWLEDGMENT

The authors would like to thank Y. Zaitsev for technical assistance.

REFERENCES

- [1] B. S. Garra, I. Cespedes, J. Ophir, S. Pratt, R. Zaubier, C. M. Magnat, and M. F. Pennanen, "Elastography of breast lesions: Initial clinical results, breast imaging," *Radiology*, vol. 202, pp. 79–86, 2002.
- [2] M. Tanter, J. Bercoff, A. Athanasiou, T. Defieux, J. L. Gennisson, G. Montaldo, M. Muller, A. Tardivon, and M. Fink, "Quantitative assessment of breast lesion viscoelasticity: Initial clinical results using supersonic shear imaging," *Ultrasound Med. Biol.*, vol. 34, no. 9, pp. 1373–1386, Sep. 2008.
- [3] L. Sandrin, B. Fourquet, J. M. Hasquenoph, S. Yon, C. Fournier, F. Mal, C. Christidis, M. Ziolo, B. Poulet, F. Kazemi, M. Beauprand, and R. Palau, "Transient elastography: A new non-invasive method for assessment of hepatic fibrosis," *Ultrasound Med. Biol.*, vol. 29, pp. 1705–1713, 2003.
- [4] M. Ziolo, A. Handra-Luca, A. Kettaneh, C. Christidis, F. Mal, F. Kazemi, V. de Lédinghen, P. Marcellin, D. Dhumeaux, J. C. Trinchet, and M. Beauprand, "Noninvasive assessment of liver fibrosis by measurement of stiffness in patients with chronic hepatitis C," *Hepatology*, vol. 41, pp. 48–54, 2005.
- [5] M. Friedrich-Rust, M. F. Ong, E. Herrman, V. Dries, P. Samaras, S. Zeuzem, and C. Sarrazin, "Real-time elastography for noninvasive assessment of liver fibrosis in chronic viral hepatitis," *Am. J. Roentgenol.*, vol. 188, pp. 758–764, 2007.
- [6] C. L. De Korte, G. Pasterkamp, A. F. W. van der Steen, H. A. Woutman, and N. Bom, "Characterization of plaque components with intravascular ultrasound elastography in human femoral and coronary arteries in vitro," *Circulation*, vol. 102, no. 6, pp. 617–623, Aug. 2000.
- [7] C. L. De Korte, A. F. W. van der Steen, E. I. Cespedes, and P. Pasterkamp, "Intravascular ultrasound elastography in human arteries: Initial experience in vitro," *Ultr. Med. Biol.*, vol. 24, no. 3, pp. 401–408, Mar. 1998.
- [8] M. Kowalski, T. Kukulski, F. Jamal, J. D'Hooge, F. Weidemann, F. Rademakers, B. Bijmens, L. Hatle, and G. R. Sutherland, "Can natural strain and strain rate quantify regional myocardial deformation? A study in healthy subjects," *Ultrasound Med. Biol.*, vol. 27, no. 8, pp. 1087–1097, Aug. 2001.
- [9] E. E. Konofagou, J. D'Hooge, and J. Ophir, "Myocardial elastography—A feasibility study in vivo," *Ultrasound Med. Biol.*, vol. 28, no. 4, pp. 475–482, 2002.
- [10] J. Bercoff, M. Pernot, M. Tanter, and M. Fink, "Monitoring thermally-induced lesions with supersonic shear imaging," *Ultrason. Imag.*, vol. 26, no. 2, pp. 71–84, Apr. 2004.
- [11] M. Tanter, J. Bercoff, L. Sandrin, and M. Fink, "Ultrafast compound imaging for 2D motion vector estimation: Application to transient elastography," *IEEE Trans. Ultrason., Ferroelect., Freq. Contr.*, vol. 49, no. 10, pp. 1363–1374, Oct. 2002.
- [12] J. Bercoff, S. Chaffi, M. Tanter, L. Sandrin, S. Catheline, M. Fink, J.-L. Gennisson, and M. Meunier, "In vivo breast tumors detection using transient elastography," *Ultrasound Med. Biol.*, vol. 29, no. 10, pp. 1387–1296, 2003.
- [13] J. Bercoff, M. Tanter, and M. Fink, "Sonic boom in soft materials: The elastic Cerenkov effect," *Appl. Phys. Lett.*, vol. 84, no. 12, pp. 2202–2204, 2004.
- [14] J. Bercoff, M. Tanter, and M. Fink, "Supersonic shear imaging: A new technique for soft tissues elasticity mapping," *IEEE Trans. Ultrason., Ferroelect., Freq. Contr.*, vol. 51, no. 4, pp. 396–409, Apr. 2004.
- [15] A. P. Sarvazyan, O. V. Rudenko, S. D. Swanson, J. B. Fowlkes, and S. Y. Emelianov, "Shear wave elasticity imaging—A new ultrasonic technology of medical diagnostic," *Ultrasound Med. Biol.*, vol. 20, pp. 1419–1436, 1998.
- [16] M. Muller, J.-L. Gennisson, T. Defieux, M. Tanter, and M. Fink, "Quantitative mapping of human liver using supersonic shear imaging: Preliminary in vivo feasibility study," *Ultrasound Med. Biol.*, vol. 35, no. 2, pp. 219–229, 2009.
- [17] T. Defieux, J. L. Gennisson, M. Tanter, and M. Fink, "Assessment of the mechanical properties of the musculoskeletal system using 2-D and 3-D very high frame rate ultrasound," *IEEE Trans. Ultrason., Ferroelect., Freq. Contr.*, vol. 55, no. 10, pp. 2177–2190, Oct. 2008.
- [18] K. W. Hollman, S. Y. Emelianov, J. H. Neiss, G. Joty, G. J. R. Spooner, T. Juhasz, R. M. Kurtz, and M. O'Donnell, "Strain imaging of corneal tissue with an ultrasound elasticity microscope," *Cornea*, vol. 21, no. 1, pp. 68–73, 2002.
- [19] T. Juhasz *et al.*, "Corneal refractive surgery with femtosecond lasers," *IEEE J. Sel. Topics Quant.*, vol. 5, no. 4, pp. 902–910, Jul./Aug. 1999.
- [20] T. Juhasz *et al.*, "Applications of femtosecond lasers in corneal surgery," *Laser Phys.*, vol. 10, pp. 495–500, 2000.
- [21] E. Spoerl, G. Wollensak, and T. Seiler, "Increased resistance of crosslinked cornea against enzymatic digestion," *Curr. Eye Res.*, vol. 29, no. 1, pp. 35–40, Jul. 2004.
- [22] I. F. Comaish and M. A. Lawless, "Progressive post-LASIK keratectasia: Biomechanical instability or chronic disease process?," *J. Cataract Refract. Surg.*, vol. 28, pp. 2206–2213, 2002.
- [23] W. J. Dupps, Jr., "Biomechanical modeling of corneal ectasia," *J. Refract. Surg.*, vol. 21, pp. 186–190, 2005.
- [24] J. S. Friedenwald, "Contribution to the theory and practice of tonometry," *Am. J. Ophthalmol.*, vol. 20, pp. 985–1024, 1937.
- [25] J. Liu and C. J. Roberts, "Influence of corneal biomechanical properties on intraocular pressure measurement: Quantitative analysis," *J. Cataract Refract. Surg.*, vol. 31, pp. 146–155, 2005.
- [26] L. T. Nordan, "Keratoconus: Diagnosis and treatment," *Int. Ophthalmol. Clin.*, vol. 37, no. 1, pp. 51–63, 1997.
- [27] P. S. Binder, "Analysis of ectasia after laser in situ keratomileusis: Risk factors," *J. Cataract Refract. Surg.*, vol. 33, no. 9, pp. 1530–1538, Sep. 2007.

- [28] A. Elsheikh, D. Wang, and D. Pye, "Determination of the modulus of elasticity of the human cornea," *J. Refract. Surg.*, vol. 23, no. 8, pp. 808–818, Oct. 2007.
- [29] J. Ophir, I. Céspedes, H. Ponnekanti, Y. Yasdi, and X. Li, "Elastography: A quantitative method for imaging the elasticity of biological tissues," *Ultrason. Imag.*, vol. 13, pp. 111–134, 1991.
- [30] W. J. Dupps, Jr., M. Netto, S. Herekar, and R. R. Krueger, "Surface wave elastometry of the cornea in porcine and human donor eyes," *J. Refract. Surg.*, vol. 23, no. 1, pp. 66–75, Jan. 2007.
- [31] G. Orsengo and D. Pye, "Determination of the true intraocular pressure and modulus of elasticity of the human cornea in vivo," *Bull. Math. Biol.*, vol. 61, pp. 551–572, 1999.
- [32] J. Bercoff, M. Tanter, M. Muller, and M. Fink, "The role of viscosity in the impulse diffraction field of elastic waves induced by the acoustic radiation force," *IEEE Trans. Ultrason., Ferroelect., Freq. Contr.*, vol. 51, no. 11, pp. 1523–1536, Nov. 2004.
- [33] Information for manufacturers seeking marketing clearance of diagnostic ultrasound system and transducers Food Drug Admin., 1997 [Online]. Available: <http://www.fda.gov/cdrh/ode/ulstran.pdf>
- [34] T. Defieux, G. Montaldo, M. Tanter, and M. Fink, "Shear wave spectroscopy for quantification of human soft tissues visco-elasticity," *IEEE Trans. Med. Imag.*, vol. 28, no. 3, pp. 313–322, Mar. 2009.
- [35] J. Virieux, "P-SV wave propagation in heterogeneous media: Velocity-stress finite-difference method," *Geophys.*, vol. 51, no. 4, pp. 889–901, Apr. 1986.
- [36] J. P. Berenger, "A perfectly matched layer for the absorption of electromagnetic waves," *J. Comp. Phys.*, vol. 114, pp. 185–200, Oct. 1994.
- [37] H. Wang, P. L. Prendiville, P. J. McDonnell, and W. V. Chang, "An ultrasonic technique for the measurement of the elastic moduli of human cornea," *Nature*, vol. 284, pp. 489–491, Apr. 1980.
- [38] G. Wollensak, E. Spoerl, and T. Seiler, "Stress-strain measurements of human and porcine corneas after riboflavin-ultraviolet-A-induced cross-linking," *J. Cataract Refract. Surg.*, vol. 29, no. 9, pp. 1780–1785, Sep. 2003.
- [39] C. Wittig-Silva, M. Whiting, E. Lamoureux, R. G. Lindsay, L. J. Sullivan, and G. R. Snibson, "A randomized controlled trial of corneal collagen cross-linking in progressive keratoconus: Preliminary results," *J. Refract. Surg.*, vol. 24, no. 7, pp. S720–S725, Sep. 2008.
- [40] G. Kymionis and D. Portaliou, "Corneal crosslinking with riboflavin and UVA for the treatment of keratoconus," *J. Cataract Refract. Surg.*, vol. 32, no. 5, pp. 837–845, May 2006.
- [41] H. Lamb, "On waves in an elastic plate," *Proc. R. Soc. Lond. A*, vol. 93, pp. 114–128, 1917.
- [42] P. V. Krauklis and L. A. Molotkov, "Low-frequency Lamb waves in cylindrical and spherical layers in an elastic medium," *J. Math. Sci.*, vol. 3, pp. 82–90, Jan. 1975.
- [43] D. Royer and E. Dieulesaint, *Elastic Waves in Solid*. Berlin, Germany: Springer-Verlag, 1996, vol. 1.
- [44] M. Couade, M. Pernot, Carmen, M. Fink, and M. Tanter, Assessment of transient dynamics of arterial wall elasticity during a single cardiac cycle: Ultrafast imaging of natural pulse and acoustic radiation force induced mechanical waves in the arterial wall.
- [45] G. Wollensak and E. Spoerl, "Collagen crosslinking of human and porcine sclera," *J. Cataract Refract. Surg.*, vol. 30, no. 3, pp. 689–695, Mar. 2004.
- [46] M. Kohlhaas, E. Spoerl, T. Schilde, G. Unger, C. Wittig, and L. E. Pillunat, "Biomechanical evidence of the distribution of cross-links in corneas treated with riboflavin and ultraviolet a light," *J. Cataract Refract. Surg.*, vol. 32, no. 2, pp. 279–283, Feb. 2006.
- [47] S. Shah, M. Laiquzzaman, R. Bhojwani, S. Mantry, and I. Cunliffe, "Assessment of the biomechanical properties of the cornea with the ocular response analyzer in normal and keratoconic eyes," *Invest. Ophthalmol. Vis. Sci.*, vol. 48, no. 7, pp. 3026–3031, Jul. 2007.
- [48] F. Soergel, B. Jean, T. Seiler, T. Bende, S. Mücke, W. Pechhold, and L. Pels, "Dynamic mechanical spectroscopy of the cornea for measurement of its viscoelastic properties in vitro," *Ger. J. Ophthalmol.*, vol. 4, no. 3, pp. 151–156, May 1995.
- [49] M. Smolek, "Interlamellar cohesive strength in the vertical meridian of human eye bank corneas," *Invest. Ophthalmol. Vis. Sci.*, vol. 34, no. 10, Sep. 1993.

High-Resolution Quantitative Imaging of Cornea Elasticity Using Supersonic Shear Imaging

M. Tanter*, D. Touboul, Jean-Luc Gennisson, Jeremy Bercoff, and Mathias Fink

Abstract—The noninvasive estimation of *in vivo* mechanical properties of cornea is envisioned to find several applications in ophthalmology. Such high-resolution measurements of local cornea stiffness could lead to a better anticipation and understanding of corneal pathologies such as Keratoconus. It could also provide a quantitative evaluation of corneal biomechanical response after corneal refractive surgeries and a tool for evaluating the efficacy of new cornea treatments such as cornea transplant using femtosecond laser or therapy based on Riboflavin/UltraViolet-A Corneal Cross Linking (UVA CXL). In the very important issue of glaucoma diagnosis and management, the fine tuning corneal elasticity measurement could also succeed to strongly correlate the applanation tonometry with the “true” intra-ocular pressure (IOP). This initial investigation evaluates the ability of ultrafast and high-resolution ultrasonic systems to provide a real-time and quantitative mapping of corneal viscoelasticity. Quantitative elasticity maps were acquired *ex vivo* on porcine cornea using the supersonic shear imaging (SSI) technique. A conventional 15 MHz linear probe was used to perform conventional ultrasonic imaging of the cornea. A dedicated ultrasonic sequence combines the generation of a remote palpation in the cornea and ultrafast (20 000 frames/s) ultrasonic imaging of the resulting corneal displacements that evolve into a shear wave propagation whose local speed was directly linked to local elasticity. A quantitative high-resolution map (150 μm resolution) of local corneal elasticity can be provided by this dedicated sequence of ultrasonic insonifications. Quantitative maps of corneal elasticity were obtained on *ex vivo* freshly enucleated porcine corneas. In the cornea, a quite homogenous stiffness map was found with a 190 kPa \pm 32 kPa mean elasticity. The influence of photodynamic Riboflavin/UVA induced CXL was measured. A significant Young’s modulus increase was obtained with a mean 890 kPa \pm 250 kPa posttreatment Young’s modulus (460% increase), located in the anterior part of the cornea. Simulations based on 3-D time domain finite differences simulation were also performed and found to be in good agreement with *ex vivo* experiments. The SSI technique can perform real-time, noninvasive, high-resolution, and quantitative maps of the whole corneal elasticity. This technique could be real time and straightforward adapted for a very wide field of *in vivo* investigations.

Index Terms—Biomechanics, cornea, elastography, stiffness, ultrasound.

Manuscript received January 25, 2009; revised April 06, 2009. Asterisk indicates corresponding author.

*M. Tanter is with the Langevin Institute (CNRS UMR 7587), ESPCI, Inserm, Paris 75005, France (e-mail: mickael.tanter@espci.fr).

J.-L. Gennisson and M. Fink are with the Langevin Institute (CNRS UMR 7587), ESPCI, Inserm, Paris 75005, France.

D. Touboul is with the Ophthalmology Department, Centre Hospitalo-Universitaire, Bordeaux 33000, France.

J. Bercoff is with the Supersonic Imagine Company, 13857 Aix en Provence, France.

Color versions of one or more of the figures in this paper are available online at <http://ieeexplore.ieee.org>.

I. INTRODUCTION

IN THE PAST DECADE, ultrasound-based elastography became a major research topic in the medical ultrasound community. Researchers postulated that information about tissue mechanical properties would represent an interesting added value either to conventional B-mode ultrasound imaging or magnetic resonance imaging (MRI) imaging. Ultrasound-based methods assessing viscoelastic properties of tissue are studied for many diagnostic applications such as breast cancer diagnosis [1], [2], liver fibrosis staging [3]–[5], arterial wall [6], [7], and cardiac muscle elasticity imaging [8], [9]. These techniques are also envisioned for the monitoring of thermal ablation using high intensity focused ultrasound [10]. Whereas most proposed ultrasound-based approaches are limited to a qualitative assessment of tissue stiffness, a method based on the use of ultrafast echographic scanners able to reach very high frame rates (higher than a thousand images per second) enables the assessment of the local and quantitative value of tissue Young’s modulus E [11]–[14]. The very high frame rate enables the transient and real time imaging of shear mechanical vibrations induced deep inside organs using the radiation force of an ultrasonic beam [15]. In homogeneous media, the local propagation speed c_s of the resulting shear waves is directly linked with stiffness defined as Young’s modulus E via the theoretical relation $E = 3\rho c_s^2$ where ρ is the tissue density (assumed to be constant in soft tissue, typically 1000 kg/m³). This method, called Supersonic Shear Imaging, was recently applied for breast cancer diagnosis [2] with promising results. Its *in vivo* applicability for the quantitative imaging of liver stiffness [16] and musculoskeletal system [17] was also recently validated.

In ophthalmology, the assessment of viscoelastic properties of cornea could also provide very valuable information for various applications [18]. Indeed, it could provide a powerful tool for evaluating the efficacy of new cornea treatments such as cornea transplant using femtosecond laser [19], [20] or therapy based on Riboflavin/UltraViolet-A corneal cross linking (UVA CXL) [21]. Another potential application could be the quantitative evaluation of the corneal biomechanical response after photo-ablative laser surgeries or cutting relaxant corneal procedures. It could be envisioned for an early clinical detection of corneal ectatic disease [22], [23] or improved accuracy of intraocular pressure (IOP) measurement [24], [25]. Perhaps even more promising, it could also lead to a better management of corneal pathologies such as Keratoconus [26] and to the estimation of risk factors due to abnormal mechanical properties of

Digital Object Identifier 10.1109/TMI.2009.2021471

cornea before refractive surgery (screening of the infra clinical Keratoconus form fruste). Refractive surgery techniques such as Laser-Assisted *in situ* Keratomileusis (LASIK) are currently encountering huge success with considerable growth in terms of annual procedures. A misunderstanding of the corneal biomechanics properties can lead to over-corrections or under-corrections of corneal refractive photo ablative procedures. More important, even if this complication is very rare, the dramatic case of postlaser excimer ectasia (PLE) should be prevented [27]. It is important to mention that in the case of extreme PLE, the use of intracorneal rings or, in worst case, a keratoplasty would be necessary to restore useful vision in these usually young patients.

The precise and quantitative assessment of corneal elasticity (Young's Modulus) is crucial to ensure the safety of LASIK refractive surgery, as the corneal final shape results from the relaxation of the cornea tissue up to a new equilibrium curvature state after cutting a flap of anterior corneal tissue. This new equilibrium state is strongly affected by corneal tissue elasticity. Thus, any technological approach that could provide a reliable and quantitative 3-D mapping of corneal structure Young's modulus would offer new insights in refractive surgery procedures. To date, the assessment of cornea Young's modulus was mainly performed *ex vivo*. *In vivo* applications are usually limited to the estimation of technique-dedicated parameters linked to stiffness but not to stiffness itself [28]. Recently, Hollman *et al.* proposed an ultrasound-based system for strain imaging of corneal tissue [18]. This Ultrasound Elasticity Microscope provided very promising images of strain induced by a compression plate on the corneal surface of *ex vivo* porcine eye. This device corresponds to the application of Static Elastography proposed 20 years ago by Ophir *et al.* [29] to the domain of high-frequency ultrasound. However, the deduction of quantitative estimates of local Young's modulus from the knowledge of the strain field provided in static elastography is a very complex task which is not properly solved to date at least for practical clinical applicability. Surface wave elastometry was also recently proposed in order to assess cornea mechanical properties [30].

A system based on the generation of noncontact transient air-pulse and an dynamic electrooptical system used to record two applanation pressure measurements at the surface of the cornea [31] was recently proposed and named Ocular Response Analyzer (ORA, Reichert). It is still today the only technology available for the *in vivo* corneal biomechanical evaluation. However, despite a very ingenious system, the ORA was not yet proven to characterize with a good predictability the biomechanical normality of the cornea. The estimated parameter called corneal hysteresis (CH) corresponds to the difference of pressure levels at which the applanation of corneal surface is reached during inward and outward corneal displacement. It is linked to the time needed for the corneal displacement at air pulse location to reach a given value during inward and backward motion. Although presented as an estimation of corneal viscous damping, this parameter is linked in a complex way to several geometrical (corneal thickness) and viscoelastic properties (Young's modulus E and shear viscosity η) of cornea and this could explain the limited predictability of the system. Indeed, the generation of an air pulse at the surface of the cornea induces

the generation of a shear mechanical wave that travels in a few milliseconds along the entire corneal wall. Estimating the underlying viscoelastic properties of the propagation medium from these displacements requires a refined imaging and analysis of the shear wave propagation. By estimating only two applanation pressures at a single location on the cornea, the ORA cannot fully resolve the inverse problem of this shear wave propagation and recover direct estimates of physical biomechanical parameters such corneal elasticity or viscosity. Finally, the attainment of applanation requires high cornea displacements (higher than 1 mm), resulting undoubtedly into nonlinear behavior of cornea response to a mechanical stress.

On the contrary, the SSI modality induces only micrometric displacements (much lower than cornea thickness), thus insuring a linear behavior of the cornea tissue. Moreover, instead of estimating only the slope of inward and backward displacement at the transient pushing location, the SSI technique images a complete two-dimensional movie of the displacement field in the corneal layer at an ultrafast frame rate. This set of data is much more complete and contains the required information that enables recovering precisely the local shear wave speed in the cornea.

For corneal stiffness estimation, the relation between Young's modulus and shear wave speed is more complex than the well-known $E = 3\rho c_s^2$ formula. Indeed, contrary to large organs such as breast or liver, where boundary conditions do not affect significantly shear wave propagation, the cornea plate is thin (typically 1 mm) compared to the shear wavelength. Moreover, there is a strong contrast between shear velocities in the Cornea and the surrounding media. Cornea (typical Young's modulus of several hundreds of kPa) is surrounded on one side by the aqueous humor (viscous liquid with nearly 0 kPa Young's modulus) and on the other side by a coupling liquid during the experimental investigation (Young's modulus = 0 kPa). As a consequence, when shear waves propagate along cornea, strong reflections and mode conversions at these interfaces generate partially guided wave propagation. The propagation of elastic waves in infinite and thin elastic plates, known as Lamb waves [41], has been extensively investigated and extended to the case of cylindrical shells [42]. Lamb waves propagate with specific modes that have highly dispersive behaviors but in the very low frequency range, only one symmetric (S0) and one anti-symmetric (A0) modes are found. For thin elastic plates in vacuum, a low-frequency analytical approximation has been established for the phase velocity $c(\omega)$ of the mode A0 [43]

$$c(\omega) = \sqrt{\frac{\omega h c_s}{\sqrt{3}}} \quad (1)$$

where ω is the angular frequency, h the plate thickness, c_s the shear wave speed given by the Young's modulus E and the volumic mass ρ of the plate, via the relation $c_s = \sqrt{E/3\rho}$.

However, when the plate is surrounded by liquids or soft solids instead of vacuum, it becomes more difficult to derive an analytical formula of type (1), due to the fact that the small contrast in longitudinal velocities of the different materials (around 1500 m/s \pm 5%) generates a total leakage of the longitudinal wave at the wall interfaces ("leaky" Lamb wave),

where as the shear part is totally reflected at both interfaces and remains trapped inside cornea. Recently, Pernot *et al.* [44] proposed an empirical analytical formula that approximates with a good accuracy the phase velocity of a leaky Lamb wave propagating in the arterial wall (i.e., in the case of soft tissues surrounded by liquid media). This formula is similar to the classical Lamb wave (1) but corrected by a factor $1/\sqrt{2}$

$$c(\omega) = \sqrt{\frac{\omega h c_s}{2\sqrt{3}}}. \quad (2)$$

Thus, it is possible to deduce the Young's modulus from the knowledge of the shear dispersion curve $c(\omega)$ and local thickness h of the cornea. This frequency dependency of the shear wave speed can be estimated using the SSI modality [34].

To date, to our knowledge, this manuscript proposes a first clinically applicable technique for the *in vivo* imaging of the quantitative Young's modulus of the cornea with a very high resolution. This quantitative elasticity imaging mode is performed using conventional high-frequency ultrasonic probes and can thus be implemented on ultrafast scanners providing both stiffness and ultrasonic images.

II. MATERIAL AND METHODS

A. Experimental Setup

The Supersonic Shear Imaging technique is based on the use of conventional ultrasonic probes. For applying this modality in ophthalmology, a 15 MHz linear array (Vermon, Tours, France) is used. The array is made of 128 elements with a 0.201 mm spatial pitch and a 12 mm elevation focus. Fresh excised postmortem porcine eyes obtained from the slaughterhouse are placed in a positioning cap immersed into a small water tank. In all experiments, the intra-ocular pressure of the *ex vivo* eyes was at atmospheric pressure. The linear array is immersed in water and positioned 5 mm above the cornea surface as described in Fig. 1.

The probe is driven by an ultrasound research prototype (V1 System developed by Supersonic Imagine, Aix en Provence, France) made of 128 programmable transmit channels (70 peak-to-peak transmit voltage, 25 kHz maximal pulse repetition frequency) and 64 multiplexed received channels (10 bits dynamics, 100 dB time gain amplification).

B. Imaging Methods

The *in vivo* SSI mode was described in details in [2]. It consists of a remote palpation induced by the radiation force of a focused ultrasonic beam (typically 100 μ s long burst), the so called "pushing beam" (Fig. 2(a), red arrow). Each "pushing beam" generates a remote vibration that results in the propagation of a transient shear wave (Fig. 2(a), blue arrows) [32]. After generation of this shear wave, an ultrafast echographic imaging sequence is performed in order to acquire successive raw radio-frequencies (RF) data at a very high frame rate. Contrary to conventional ultrasonography where an image is achieved using line by line transmit focused beams (typically 50 frames/s), ultrafast echographic images are achieved by transmitting a single quasi-plane ultrasonic wave in tissues and achieving the beamforming process only in the receive

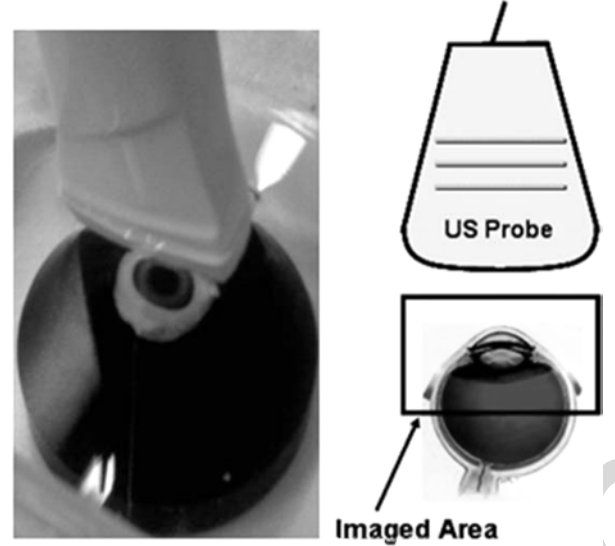


Fig. 1. Experimental setup. A 1-D linear array (128 elements, 15 MHz) is imaging the *ex vivo* freshly enucleated porcine eye. The echographic probe, eye porcine eye, and the eye holder are immersed into pure water.

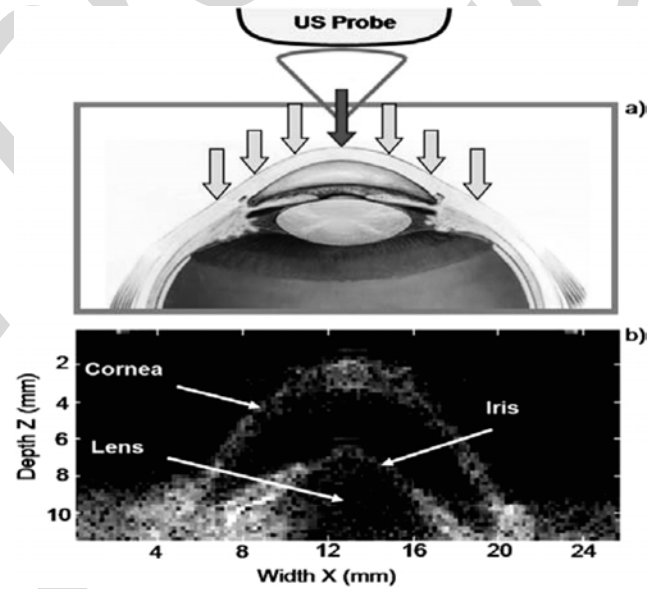


Fig. 2. (a) Echographic probe emits an ultrasonic focused beam that generates a localized radiation force (red arrow) at the surface of the cornea. Resulting shear waves (blue arrows) propagate in the cornea on both side of the pushing location. (b) Conventional B-mode echographic image of an *ex vivo* porcine eye acquired before the generation of the ultrasonic radiation force.

mode. The quasi-plane terminology stands for the fact that the transmitted ultrasonic wavefront is planar in the 2-D imaging plane and slightly diffracting along the probe elevation direction beyond the elevation focal distance. Thus, for ultrafast imaging, the frame rate is only limited by the time of flight of ultrasonic waves. For ophthalmologic applications, the imaging depth does not exceed 20 mm. It corresponds to a typical 27 μ s time of flight that defines a maximal frame rate of 37 000/s. In our experiments, the frame rate was set to 20 000 frames/s.

Before entering into the SSI mode, the device is functioning as a conventional echographic device (transmit/receive beamforming at 50 frames/s). A typical echographic image of *ex*

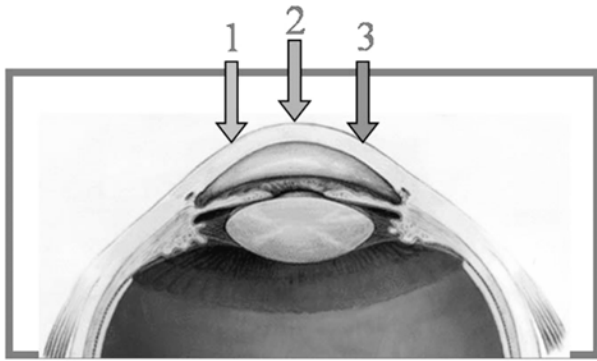


Fig. 3. SSI imaging mode. Three successive pushing beams are transmitted and focused on the left, center and right part of the cornea surface (locations no. 1, 2, 3). After each “push,” the ultrasonic scanner images the resulting transient displacement by entering into an ultrafast frame rate during 3 ms. The total acquisition time for imaging the three generated shear waves is no longer than 12 ms.

in vivo porcine eye is presented in Fig. 2(b). The cornea is clearly visible in the echographic image. The operator is first asked to position the desired locations of three pushing beams using a cursor on the real time echographic images. These pushing beams have to be positioned at the left, center and right parts of the cornea (Fig. 3). Then, a first SSI sequence is performed using the left “pushing” beam and an ultrafast ultrasonic sequence is performed in order to catch the resulting corneal displacements. The total experiment lasts 3 ms (60 frames acquired at a 20 000 Hz frame rate). This first sequence (pushing beam no. 1, Fig. 3) allows elasticity imaging on the right side of the pushing line location. Just at the end of this first sequence, a second SSI sequence (pushing beam no. 2, Fig. 3) is performed with the central “pushing” beam. Finally, a third sequence is performed with a right “pushing” beam (pushing beam no. 3, Fig. 3). The pushing modes no. 1 and 3 enable elasticity imaging in the middle of the imaging plane whereas the pushing mode no. 2 enable elasticity imaging on the edges of the imaged area. The total acquisition time for a complete mapping of cornea elasticity lasts 12 ms (3×4 ms). For practical clinical configurations, this ultra-short acquisition time will prevent the influence of any motion artifacts or natural motion such as arterial pulsatility.

C. Safety Considerations

In order to meet the FDA (Food and Drug Administration) requirements for ophthalmologic applications, the acoustic intensities have been strongly decreased in comparison with other organs such as breast [2], liver [16] or muscle [17]. The acoustic intensity induced during the SSI sequence remained lower than the recommendations provided by the FDA for ultrasonic imaging devices (510 k recommendations). The methodology used for the measurements is described in the paragraph 4.6.1 “acoustic output reporting” of these recommendations [33].

For these *ex vivo* investigations, each “pushing” beam is typically focused between 6 and 12 mm depth. Each focused insonification lasts $30 \mu\text{s}$ for the generation of the “pushing” radiation force. Typically, it corresponds to 1000 sinusoids at 15 MHz. This results in a total of $90 \mu\text{s}$ insonification for the *in vivo* generation of a complete data set for stiffness imaging. The acoustic

TABLE I
ACOUSTIC PARAMETERS USED IN THE SSI MODALITY COMPARISON WITH THE 510 (K) FDA RECOMMENDATIONS FOR ULTRASOUND DIAGNOSTIC IMAGING SYSTEMS

Sequences	Mechanical Index		I_{SPTA} (mW/cm^2)	
	Worst case measurement	510k FDA Limits	Worst case measurement	510k FDA Limits
Shear wave generation	0.21 ¹	0.23	2.2	17
Ultrafast imaging	0.08	0.23	0.13	17
Global SSI sequence	-	-	2.33	17

pressure levels and intensities were measured using a calibrated AH-2020 hydrophone (OndaCorp., Sunnyvale, CA, 0.1 mm resolution, frequency bandwidth ranging from 1 to 25 MHz). Measurements were made in water. For these measurements, the acoustic parameters were estimated at the “worst” focal distance (corresponding to the elevation focus $z = 12$ mm). These parameters correspond respectively to the mechanical index (MI) and the spatial peak time averaged intensity (I_{SPTA}), as defined in the FDA recommendations [33]. All values were not derated in order to take into account the worst case corresponding to a pushing and elevation focus simultaneously located exactly at the external surface of the cornea. The results corresponding to the acquisition of one elasticity image per second (i.e., 3 pushes each lasting $30 \mu\text{s}$ and 3×60 ultrafast images) for this worst pushing case are summarized in Table I.

It can be seen in Table I that the ultrafast imaging mode is characterized by a very low I_{SPTA} value as it does not imply any focusing in the transmit mode. Finally, even in the worst configuration chosen for the acoustic parameter measurements, the SSI mode fulfils the requirements of the 510 (k) FDA recommendations. The total $2.33 \text{ mW}/\text{cm}^2$ I_{SPTA} value for a single elasticity image acquisition per second is much lower than the $17 \text{ mW}/\text{cm}^2$ FDA limit. A maximal frame rate of 7 elasticity frames/s could even be performed while respecting the FDA guidelines.

D. Postprocessing of Raw Data for Quantitative Imaging of the Shear Wave Group Velocity

Raw RF data are transferred via a PCI Xpress bus on a PC board. Signal processing is then divided into the following steps.

- 1) Receive beamforming of the raw RF data acquired in order to produce flat transmit echographic images.
- 2) One dimensional (1-D) speckle tracking using conventional 1-D cross-correlation of successive echographic images for the building of 128 images of tissue relative displacements (along the z -axis, Fig. 1). Relative displacement means tissue displacement between two successive ultrafast echographic images. Consequently, it corresponds to a local tissue particle velocity (in m/s). Out-of-line motion are negligible as tissue displacements along the ultrasonic beam path are typically ten times higher than the ones in transverse directions.

3) Local assessment of the mechanical shear wave speed c_s by means of a time of flight estimation between two points during the shear wave propagation. This time of flight estimation is based on the cross-correlation of local displacement time profiles recorded at two different locations along the s -axis (Fig. 4 dashed white line) corresponding to a curvilinear line that follows the cornea curvature. Lateral distance between the two measurement points along this line corresponds typically to 8 times the inter-element spacing of the linear probe (i.e., $8 \times 0.2 \text{ mm} = 1.6 \text{ mm}$). By estimating a time of flight between two wideband shear displacement signals, this algorithm performs an averaged estimate of the shear wave group velocity over the whole shear wave bandwidth. In a locally homogeneous medium, the Young's modulus E is then directly linked to shear wave speed c_s via the relation $E = 3\rho c_s^2$, where ρ is the density. In the case of cornea, this relationship does not hold anymore as the mechanical wave is constrained and guided in a plate (i.e., the cornea) thinner than the shear wavelength. However, a slightly more complex relationship relating shear wave speed and the Young's modulus can be derived by considering the leaky Lamb wave theory.

Recombination of the shear wave speed image obtained with the pushing mode no. 1, 2, and 3 (Fig. 3). The local wave speed can be converted into the local Young's modulus value as described in the next subsections.

E. Analysis of Shear Wave Dispersion for Quantitative Recovery of Young's Modulus

A more detailed analysis of the local mechanical behavior of the cornea can be performed using a shear wave spectroscopy algorithm as previously described by Deffieux *et al.* [34]. This approach corresponds to the determination of shear wave phase velocity dispersion over a large frequency range. The large bandwidth of the shear wave generated through the ultrasonic radiation force allows this kind of measurement in one single acquisition sequence. Whereas the shear wave spectroscopy analysis can be performed in a typical 100–500 Hz in deep organs like breast or abdominal organs), the bandwidth of the shear wave generated by the ultrasonic beam radiation force is much larger in the cornea application. Fig. 4(a) shows typical waveforms of the shear velocity profile obtained in *ex vivo* porcine eyes at one given depth in the cornea as a function of time [Fig. 4(a)] for an increasing distance from the “pushing location.” Fig. 4(b) shows the corresponding frequency spectrum. It appears that the use of a 15 MHz linear array (generating a remote palpation on an approximate 0.2-mm-diameter sharp beam) enables exploiting a very large 500–3000 Hz bandwidth contrary to deeper organs like breast or liver where the upper limit of the bandwidth is limited to 500 Hz [34], [16]. Such very high shear wave frequencies can only be reached due to the sharpness of the ultrasonic beams generated by very high frequency ultrasonic probes.

The Fourier transform of these signals is then computed. At each frequency, the dependence of the phase versus propagation distance is extracted. The last step consists applying a linear fitting to this phase function in order to retrieve the wave number

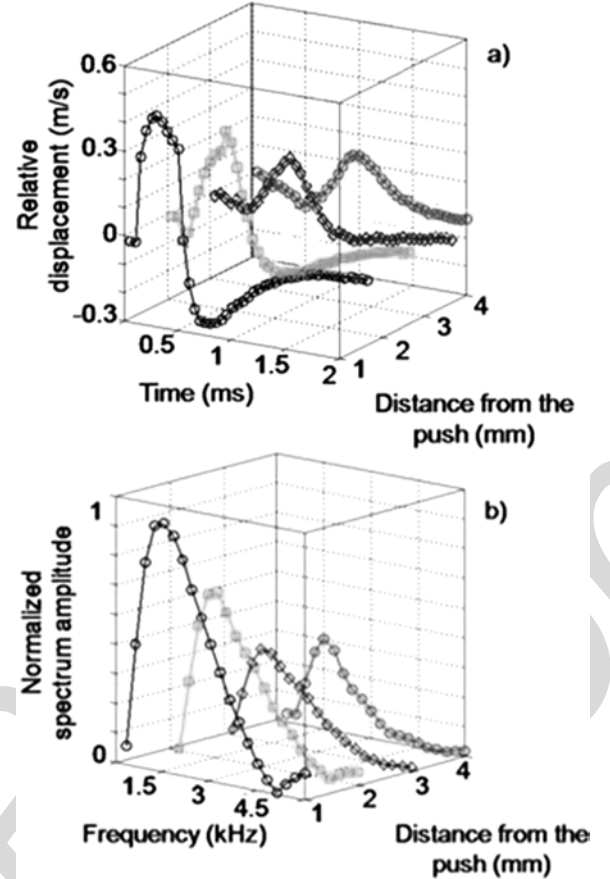


Fig. 4. (a) Typical experimental waveforms of the shear relative displacement profile (displacement from frame to frame at a PRF 20 000 Hz) obtained in *ex vivo* porcine eyes (displacement for different locations at one given depth in the cornea as a function of time for an increasing distance from the “pushing location.”) (b) Corresponding spectra for each shear waves displacement profile presented in Fig. 4(a).

k for each frequency and consequently the phase speed of the shear wave at each frequency. One has thus access to the shear wave dispersion curve.

F. Estimation of Young's Modulus From Leaky Lamb Wave Guided Propagation in the Cornea

Due to the dispersion induced by the guided propagation into the cornea, the conversion of shear wave speed into a quantitative Young's modulus mapping can be deduced by reformulating (2) into the form

$$E = 36 \frac{\rho c(\omega)^4}{h^2 \omega^2}. \quad (3)$$

By using cornea thickness and the central frequency of the mechanical wave spectrum as entry parameter, (3) provides the Young's modulus value from the estimated mechanical wave speed. As an example or a typical $c = 5.1 \text{ m/s}$ propagation and a 1500 Hz central frequency excitation in a 1.2 mm thick cornea, one retrieves $c_s = 7.96 \text{ m/s}$ corresponding to $E = 190 \text{ kPa}$ Young's modulus of the cornea.

G. Simulations

In order to corroborate experimental results, the 3-D displacement field induced by the ultrasonic radiation force in the

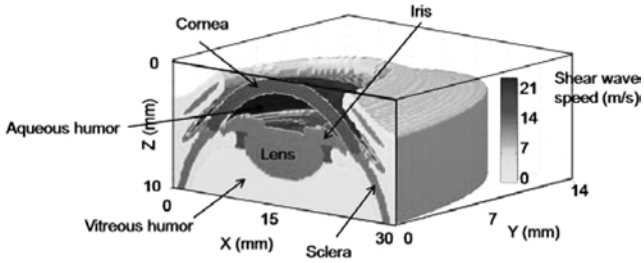


Fig. 5. Three-dimensional spatial distribution of the shear wave speed c_s (corresponding to the local Young's modulus E via $E = 3\rho c_s^2$) used in the time domain finite differences simulations of the cornea mechanical response using Acel, a package of 3-D wave simulation libraries developed at Laboratoire Ondes et Acoustique, Paris, France.

cornea was also fully modeled using a 3-D discretization of the elastodynamic continuity equations. The model is based on a first-order finite-difference time-domain (FDTD) algorithm for elastodynamic equations. The implemented scheme is based on a staggered grid technique initially introduced by Virieux for applications in seismology [35]. Perfectly matched layers [36] were also implemented at the boundaries of the 3-D mesh volume in order to avoid unwanted reflections of the propagating waves. The medium is considered to be elastic, isotropic, and nondissipative. It is discretized into a rectangular volume made of $550 \times 300 \times 550$ points. Each grid voxel is defined by its local density, shear wave speed and bulk wave speed (linked directly to mechanical shear and bulk moduli).

Table II summarizes the physical parameters chosen for the FDTD simulations. The Bulk wave speed was 1500 m/s in all tissues. Aqueous humor was considered as a liquid. Although few and sometimes contradictory values were available in the literature, the chosen parameters were found both to corroborate several reported values and to agree with the typically obtained experimental results [37], [38]. Fig. 5 shows a 3-D view of the shear wave speed values in the 3-D volume. The eye was considered to be immersed in water. Transparent areas of the 3-D volume correspond to a zero-valued Young's modulus (i.e., fluid areas).

H. Photodynamic Riboflavin/UVA Induced Corneal Collagen Cross-Linking (CXL)

Keratoconus is an idiopathic corneal dystrophy characterized by progressive thinning and ectasia which results in a decrease of vision and also the quality of life. As the disease begins in young adults, it affects the most productive years of life. A recent modality of treatment, CXL with the help of UVA, 370 nm, and the photosensitizer Riboflavin phosphate 0.1%, has been described which changes the intrinsic biomechanical properties of the cornea. Resulting in the stiffening of the stroma layer of the cornea, this treatment has shown to slow down or prevent the progression of Keratoconus in numerous studies all over the world [39], [40].

In our study, fresh postmortem porcine eyes were treated using the following procedure: In order to allow the spreading of the Riboflavin into the cornea, the epithelium (first external layer of the cornea) was gently removed with a smooth spatula. Then, corneas were immersed into 0.1% Riboflavin

TABLE II
MECHANICAL PARAMETERS FOR 3-D SIMULATIONS

	Density ($\text{kg}\cdot\text{m}^{-3}$)	Shear Wave Speed ($\text{m}\cdot\text{s}^{-1}$)	Stiffness E (MPa)
Cornea			
Simulation N°1	1000	10	0.3
Simulation N°2	1000	20	1.2
Simulation N°3	1000	25	1.8
Iris	1000	20	1.2
Lens	1000	20	1.2
Sclera	1000	17	0.6
Aqueous humor	1000	0	0
Vitreous humor	1000	0.2	10^{-4}

(Ricola-Sooft-Italy) solution for 15 min (with an handmade system of corneal lens recipe). Finally, UVA irradiation was performed for 30 min by using a UVA diode laser (370 nm, IROC-Germany) with a focusing spot diameter of 8 mm and constant irradiance of $3 \text{ mW}/\text{cm}^2$. One eye drops of isotonic saline solution (BSS) followed by one eye drop of Riboflavin 0.1% was applied on the cornea every five minutes for respectively hydration and renew of the photosensibilizer. Young's modulus imaging sequences were performed just before the CXL and at the end of the CXL with the SSI system and corneal elasticity mapping was performed.

III. RESULTS

A. Simulations

The radiation force induced by the ultrasonic beam focused on the cornea surface was introduced as a transient source term in the elastodynamic equations. In order to mimic the typical experimental configuration, the 3-D spatial distribution of this transient source term corresponds to a $0.2 \times 0.4 \times 2 \text{ mm}^3$ cigar shape volume in which each pixel generates a force along the z -axis. The 0.2 mm dimension corresponds to the lateral resolution of the 1-D linear probe. The 0.4 mm resolution corresponds to the beam width in the probe elevation direction (y -axis). As the ultrasonic "pushing" beam along z -axis is roughly equal to 2 mm, it generates an uniaxial force over the entire depth of the cornea. The black ellipse in Fig. 6(a) corresponds to the trace of this cigar shape on the cornea surface.

The color maps correspond to the spatial distribution of tissue displacements along the z -axis at the cornea surface for different time steps after the force generation. One can notice that the slight asymmetry of the pushing beam does not result in any asymmetry of the shear wave propagation that propagates with a spherical shape. This is easily explained by the fact that the average wavelength of the generated shear wave is much larger than the source dimensions. Moreover, as local microscopic displacements are four orders of magnitudes smaller than

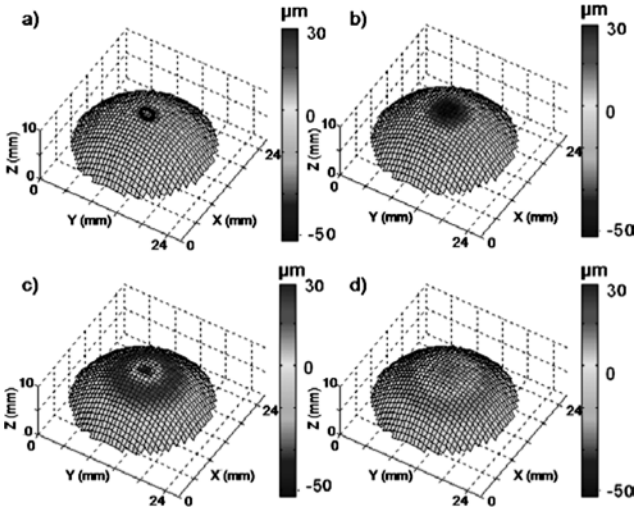


Fig. 6. Spatial distribution of cornea tissue displacements along the z -axis at the cornea surface for different time steps after the force generation: (a) $t = 0.25$ ms, (b) $t = 0.5$ ms, (c) $t = 0.75$ ms, and (d) $t = 1$ ms. The color scale ranges between $-50 \mu\text{m}$ and $+30 \mu\text{m}$. As local displacements are four orders of magnitudes smaller than the global eye dimensions, the eye curvature can be considered as in a steady state.

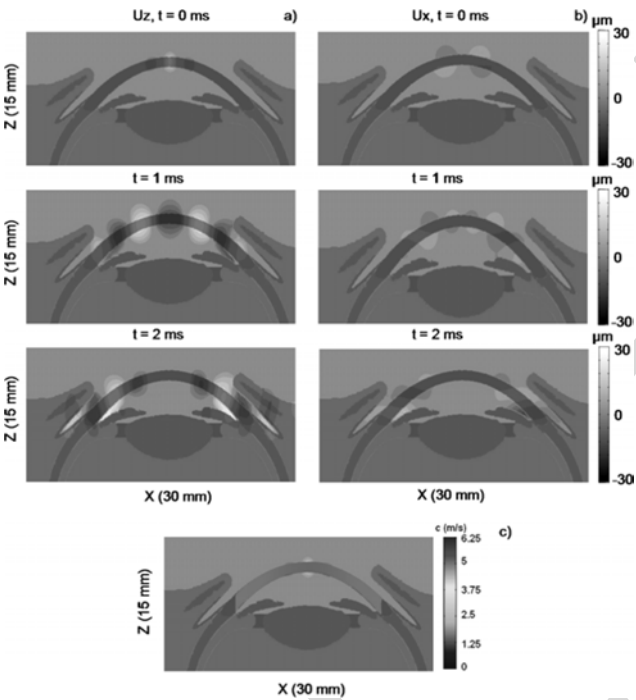


Fig. 7. Spatial distribution of tissue displacements, respectively, (a) along z -axis and (b) along x -axis in a vertical X-Z slice for different time steps after the mechanical force generation. Displacements are ranging from $-30 \mu\text{m}$ to $30 \mu\text{m}$ in both figures. (c) Shear wave speed map estimated by the time of flight algorithm using z -displacements from Fig. 7(a).

the global eye dimensions, the eye curvature can be considered as stationary. Interestingly, Fig. 7(a) and (b) represent for the same simulation the mapping of displacements respectively along z and x axis in a vertical X-Z slice for different time steps after the mechanical force generation. Two points can be noted: first, the displacements along the x -axis are much smaller (more than ten times) than the displacements along z direction. The

estimation of z -displacements (i.e., the ones estimated experimentally using the 1-D ultrasonic speckle correlation tracking approach) is sufficient to image the whole propagation phenomenon. Secondly, tissue displacements occur not only at the surface but everywhere in depth inside the cornea. Thus, local estimation of the shear wave speed will provide an in depth mapping of the elasticity of cornea.

Fig. 7(c) presents the estimation of the shear wave speed deduced from the time of flight algorithm. A homogeneous map is recovered as expected. However, one should notice that the shear wave speed is much smaller ($c = 5.3 \text{ m/s} +/ - 0.1 \text{ m/s}$ for a central frequency of the mechanical excitation) than the local parameter introduced in the simulation ($c_s = 15 \text{ m/s}$). Indeed, as shear wavelength is of the same order of magnitude than the cornea thickness, this is explained by the fact that the shear wave propagation is guided by the cornea. This guided propagation corresponds to a well known case in physics, corresponding to the propagation of a leaky Lamb wave in a plate.

B. Simulation Results: Analysis of Shear Wave Dispersion Due to Leaky Lamb Wave Guided Propagation

The dispersion curves for the wave propagation modeled in the FDTD simulation were estimated. For this purpose, the time profile of the shear wave received at each location along a curvilinear line corresponding to a constant depth inside the cornea are analyzed in the Fourier domain. Indeed, the Fourier transform of each time profile enables to estimate at each frequency the phase changes with the propagation distance. The phase of each spectral component is linearly dependent of distance and a linear fit of this dependence enables the estimation of the shear wave speed at each frequency. The corresponding shear wave speed is plotted for each frequency in Fig. 8. As one can notice the wave propagation is strongly dispersive and the wave phase speed values are in good agreement with the empirical formula proposed in recent works [44].

In the range 500–3000 Hz, this agreement was verified for three different simulations (using three different cornea stiffness corresponding to $c_s = 10, 15,$ and 25 m/s and a fixed cornea thickness). One should notice here that compared to a propagation in free space where the shear wave would propagate at c_s , the cornea plate slows down the mechanical wave (for example, in Fig. 8, $c = 8.25 \text{ m/s}$ at 1500 Hz for a cornea stiffness defined by $c_s = 25 \text{ m/s}$). This permits to track the mechanical wave propagation experimentally without requiring to perform huge ultrasonic frame rates.

C. Experimental Results: Quantitative Imaging of Corneal Elasticity

In the total of six fresh postmortem porcine eyes, the ultrasonic probe was found to be able both to induce a shear wave propagating in depth inside the cornea and to image with an ultrafast frame rate (20 000 Hz) the resulting shear relative displacements. The 1-D cross-correlation of successive ultrasound images provides a set of tissue relative displacements. Fig. 9 represents the 2-D spatial distribution of these tissue relative displacements along z -axis at different time steps after the second radiation force generation (central “push” corresponding to sequence no. 2 described in Fig. 3). Displacements occur in all

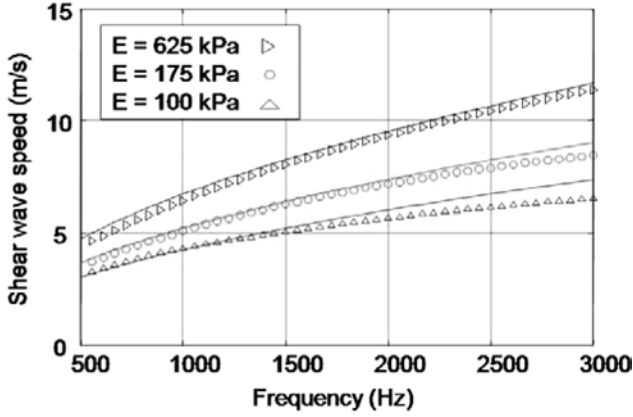


Fig. 8. Shear wave speed dispersion curve obtained from simulated data using three different cornea stiffness ($E = 100, 175$ and 625 kPa corresponding respectively to shear wave speed values $c_s = 10, 15$, and 25 m/s). The solid line corresponds to the analytical formula presented in (2). The cornea stiffness values used in simulations correspond to typical values of cornea stiffness obtained from *ex vivo* experiments.

layers of the cornea and the shear wave propagation from center towards cornea edges is clearly visible. Maximal tissue relative displacements of about 0.6 m/s at a $20\,000$ Hz pulse repetition frequency (corresponding to global displacements of about $100\mu\text{m}$ after time integration) can be reached while preventing to overtake the FDA safety limitations.

Fig. 10 presents an example of the post-processing which enables the recovery of the local shear wave group speed along the dashed line presented in Fig. 9(d).

The value of the shear wave speed at point A outside of the pushing zone is obtained by estimating the time delay τ_A between time profiles at points B and C surrounding point A. The choice of the distance between B and C is optimized based on the data quality (i.e., the signal to noise level of tissue displacements estimates). A high SNR of displacements time profiles enables estimating smaller time delays between signals and consequently reducing the interspace distance between locations used in the time-of-flight algorithm. Typically, in our experiments, this distance corresponds to four times the spatial pitch of the array (4×0.2 mm ≈ 0.8 mm). This time of flight estimation is performed for each location along each curvilinear line inside the cornea resulting in a 2-D mapping of the local shear wave speed in the cornea with a $150\mu\text{m}$ resolution. Fig. 10 shows the resulting 2-D mapping of the cornea obtained using this time of flight algorithm.

D. Experimental Results: Analysis of Shear Wave Dispersion Using Shear Wave Spectroscopy

Shear wave spectroscopy was applied using the experimental data. The time profiles of local z -displacement recorded at each location along a curvilinear line corresponding to a constant depth inside the cornea [dashed line Fig. 9(d)] are displayed in Fig. 11. The three successive “pushes” on the left, center and right side of the cornea and their resulting propagation are clearly visible.

The Fourier transform of each time profile enables to estimate at each frequency the phase changes with the propagation distance. The phase of each spectral component is linearly de-

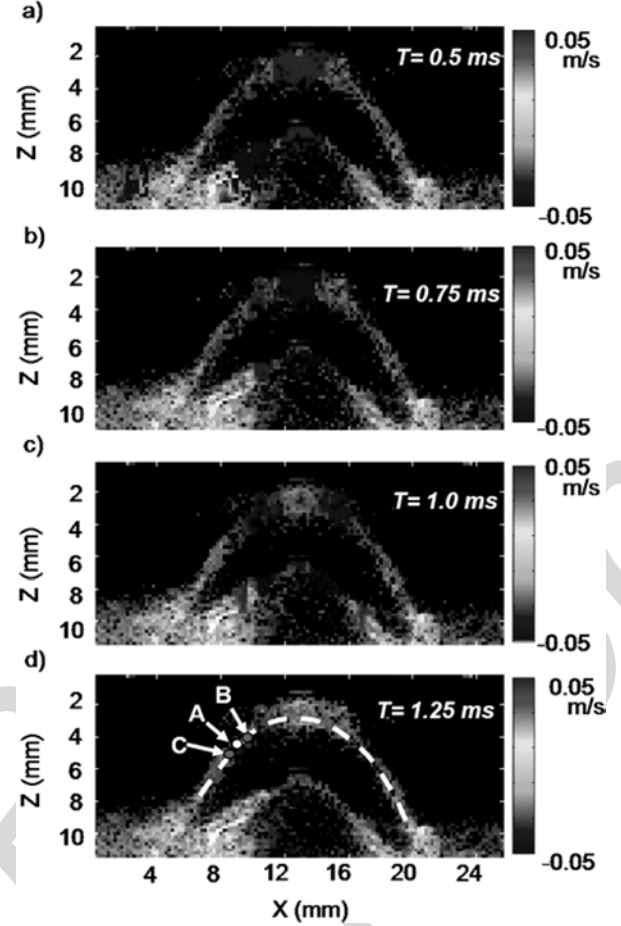


Fig. 9. Images of local corneal tissue relative displacements between successive echographic images (i.e., particle velocity) at different time steps just after the ultrasonic radiation force generated at the center of the cornea. These color relative displacements images depict the shear wave propagation in the cornea and are superimposed on the echographic gray scale image. The resolution of the displacement map is $150\mu\text{m}$.

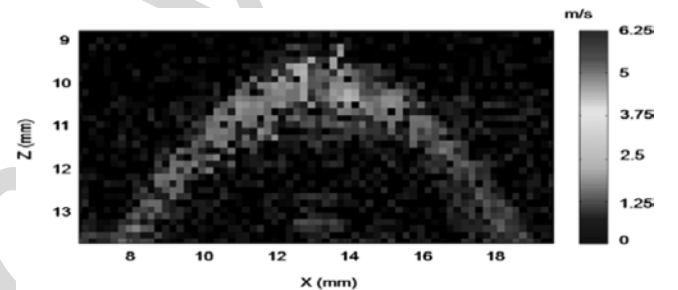


Fig. 10. High-resolution 2-D map of the shear wave speed superimposed on the gray scale ultrasound image of the cornea. From the knowledge of the corneal thickness ($h = 1.5$ mm) and central frequency of the mechanical excitation (1500 Hz), this map can be converted into a quantitative Young’s modulus map using (3). Here, mean wave speed is equal to $5.1\text{ m}\cdot\text{s}^{-1} \pm 0.2\text{ m}\cdot\text{s}^{-1}$ corresponding to a cornea Young’s modulus of $190\text{ kPa} \pm 32\text{ kPa}$.

pendent of distance and a linear fit of this dependence enables the estimation of the shear wave speed at each frequency, see Fig. 12. The three subplots correspond to estimates for the three successive pushing modes.

Finally, from these data, the corresponding shear wave speed dispersion curves deduced from the three successive pushing

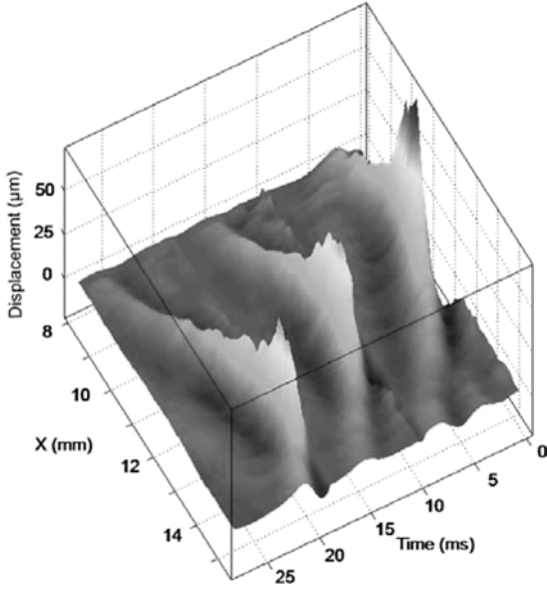


Fig. 11. Time profiles of local z-displacement recorded at each location along a curvilinear line corresponding to a constant depth inside the cornea [dashed line Fig. 9(d)]. One can clearly distinguish the three successive mechanical wave propagations corresponding to the three successive push locations.

modes are plotted in Fig. 13. The assessment of this frequency dependence of the mechanical wave speed is found to be robust as the three curves are in good agreement. The analytical formula corresponding to (2) with a value $c_s = 7.9$ m/s (i.e., $E = 190$ kPa) is also plotted in Fig. 13 and fits the experimental data derived from the shear wave spectroscopy analysis.

The agreement between experiments and the analytical dispersion relation is very good especially in the high frequency range (>1500 Hz). At lower frequency, a discrepancy appears. It is due to two main factors. First, as the wavelength becomes quite large at lower frequency, it is no more negligible compared to the cornea curvature and diffraction due to the spherical shape of the eye can no more be neglected. In terms of Lamb mode propagation, a single A0 mode propagation can no more be considered and contribution of other modes are present. Secondly, at very low frequency the dispersion curve assessment is disturbed by reflections of the wave on the edges of the cornea. A local point can “feel” the reflected Lamb wave before the end of the incident wavefield. This last point emphasizes the interest provided by the acoustic radiation force that permits generating shear waves with a very high frequency range.

E. Elasticity Changes Induced by Photodynamic Riboflavin/UV-A Corneal Cross-Linking

Several fresh porcine eyes were treated using photodynamic Riboflavin/UV-A collagen induced CXL. SSI sequences were performed before and after the UV-A Laser exposure. Fig. 14 shows the time profiles of tissue displacement at each location along a curvilinear line corresponding to a constant depth inside cornea. The mechanical wave speed strongly increases after UV-A exposure clearly exhibiting a strong increase in the cornea stiffness. The shear wave spectroscopy algorithm enables us to recover respective 190 kPa \pm 32 kPa and 890 kPa

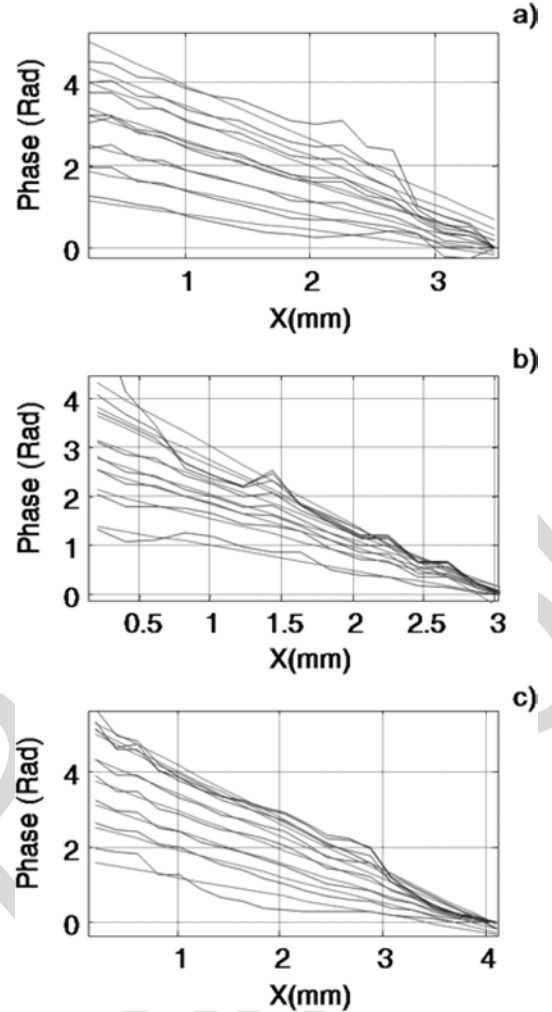


Fig. 12. Phase changes of each frequency component (ranging from 200 Hz to 2900 Hz) of the mechanical wave versus propagation distance for the three “pushing” modes at different push location (a) $x = 5$ mm, (b) $x = 10$ mm, and (c) $x = 15$ mm). The linear fit deduced for each frequency component enables the assessment of the wave speed and consequently the recovery of the shear wave dispersion curve.

± 250 kPa values for cornea Young’s before and after collagen induced crosslinking (corresponding for a 1.2 mm thickness, respectively, to $c = 5.1$ m/s and 8.5 m/s shear wave phase speeds at a 1500 Hz central frequency). This 460% increase ratio is in agreement with recent values provided by Wollensak *et al.* [45] and Kohlhaas *et al.* [46].

Finally, 2-D mapping of cornea stiffness were performed and are presented in Fig. 15. The strong increase in local shear wave speed (and by correlation Young’s modulus) is clearly demonstrated analyzing the slope of the time profiles.

F. High-Resolution Imaging of Corneal Elasticity

Finally, the high-resolution capabilities for corneal stiffness mapping provided by the SSI imaging mode are demonstrated in Fig. 16. This 2-D mapping of shear wave speed corresponds to experimental data acquired on one single case of a porcine eye whose cornea had been probably partially burnt (coagulation) before the animal sacrifice (an opaque scar was observed onto the corneal opening eyelid area). One clearly distinguishes

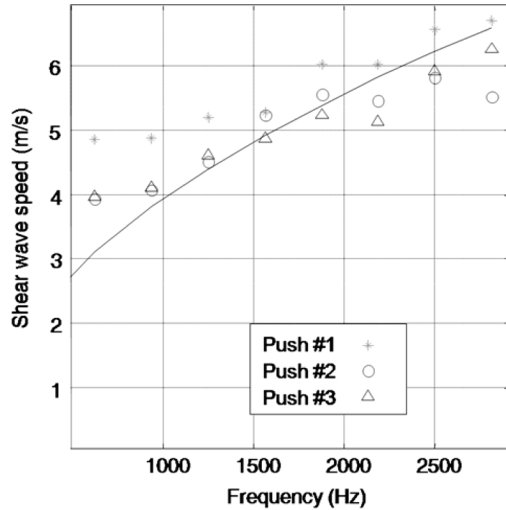


Fig. 13. Shear wave dispersion curves estimated experimentally for the three successive mechanical waves generated by pushing modes no. 1, 2, and 3 into the porcine cornea. The solid line corresponds to (2) with a chosen $c_s = 7.9$ m/s (i.e., cornea Young's Modulus $E \sim 190$ kPa).

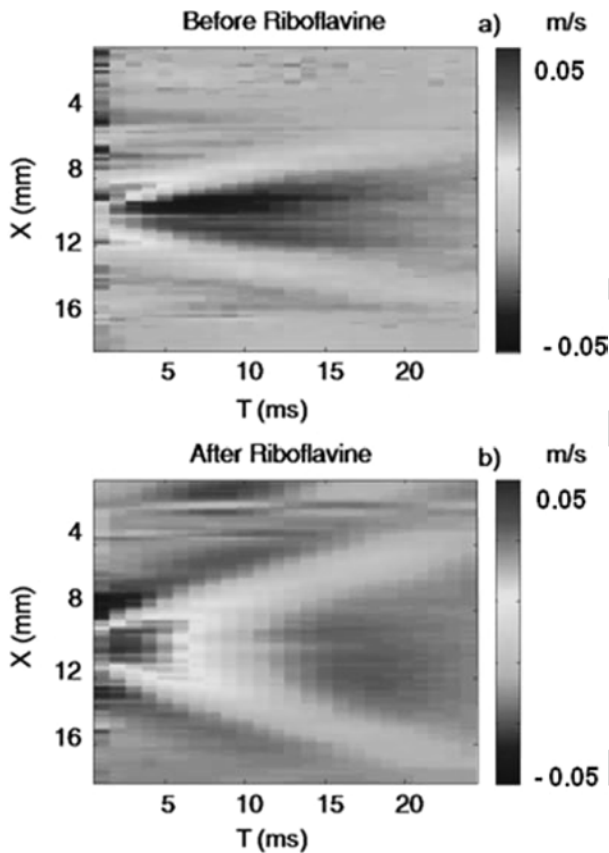


Fig. 14. Time profiles of tissue particle velocity (i.e., relative displacement of tissues between two successive ultrasonic images) at each location along a curvilinear line. This line corresponds to a constant depth inside cornea (a) before and (b) after UV-A exposure. Colors scale is ranging between -0.05 m/s and $+0.05$ m/s.

in Fig. 16 the appearance of a very stiff layer in the cornea ($200\mu\text{m}$ thick). Such layered structure was also confirmed on the movie of the local tissue displacement. The propagation of the mechanical wave is clearly much faster in the upper first

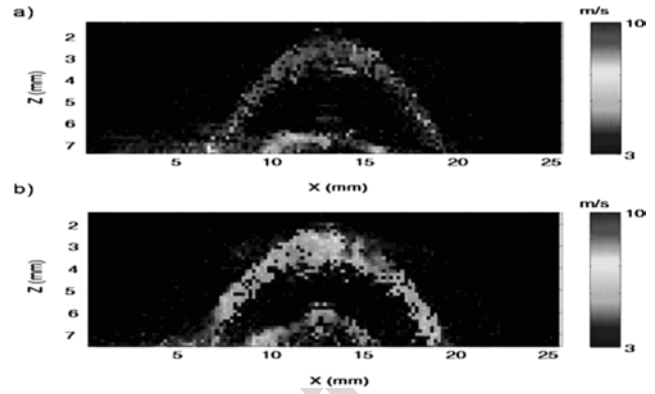


Fig. 15. Influence of CXL on corneal stiffness: 2-D mapping of the local shear wave speed (a) before and (b) after Riboflavine and UV-A exposure.

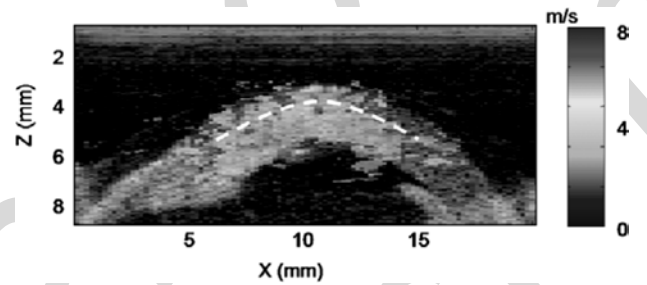


Fig. 16. Two-dimensional mapping of shear wave speed of an excised porcine eye whose cornea had been partially burned. The SSI modality is clearly able to image a very stiff $500\mu\text{m}$ first layer in the cornea.

layer of the cornea than in deeper cornea tissues. The capability of the SSI mode to provide local information in different layers inside the cornea is here shown to be feasible experimentally with a typical $150\mu\text{m}$ resolution.

IV. DISCUSSION

The main purpose of this preliminary clinical study was to evaluate the capability of the SSI mode to provide quantitative elasticity maps of different cornea and to determine the clinical situations where this technique could add potential value to US examinations. Contrary to other investigated applications such as breast cancer diagnosis [2], liver fibrosis staging [16] or muscle properties assessment [17], the transposition to corneal stiffness imaging required to strongly improve spatial resolution of the technique.

For this application, the ultrasonic probe frequency (15 MHz) was strongly increased compared to imaging probes used for deep organs such as breast, liver, or heart (respectively, 8 MHz, 4 MHz, and 2.5 MHz) and leads to two important remarks. First, the resolution of the echographic images is very high ($150\mu\text{m}$) and the ultrasonic focal spot inducing the radiation force in the cornea has a very high lateral resolution (around $100\mu\text{m}$). As the frequency spectrum of the mechanical wave is directly linked to the focal spot size, the mechanical wave induced by the "pushing beam" is characterized by a very high frequency spectrum (typically from 500 Hz to 3000 Hz). This enables the sounding of mechanical properties of cornea with shear waves of small wavelengths, thus enhancing the resolution of the final Young's modulus mapping. Moreover, as the echographic

imaging depth is reduced (20 mm) in comparison with deep seated organs, ultrafast frame rates as high as 20 000 Hz can be reached. It enables a very high temporal resolution for the estimates of the transient tissue displacement time profiles even if the induced shear wave possesses very high frequency components (up to 3000 Hz). Finally, displacements induced by the radiation force are very small (of the order of tens of μm) and a nonlinear biomechanical response of cornea can be rejected on the contrary of other existing approaches such as ocular response analyzer (ORA).

In all investigated porcine eyes, the ultrasonic probe was able both to generate a remote mechanical vibration in the cornea and to track the transient propagation of the resulting shear wave inside cornea.

Porcine eye corneal stiffness was found to be rather homogeneous with a mean 190 kPa value and to strongly increase (460% increase) after riboflavin collagen induced crosslinking. Riboflavin/UVA cross-linking seems to affect the cornea elasticity nonuniformly as seen in Fig. 15. This non uniformity does not correspond to artifacts. Indeed, the areas of higher stiffness visible in Fig. 15 correspond to regions of higher shear wave speed. However, although such a nonuniform spatial distribution of cross-linking stiffening seems to be accepted by clinicians, there is to our knowledge no evidence regarding this point in the literature.

Thanks to the resolution of the echographic image, the resolution obtained in the elasticity image is quite high and permits to estimate local elasticity in different layers of the cornea (see Fig. 16).

Finally, the applicability for clinical investigations can be easily envisioned as the method is insensitive to motion artifacts. Moreover contrary to the only system used today in clinical practice, the O.R.A. system [47], the SSI modality gives access to the real physical parameter (mechanical property parameter), i.e., the Young's modulus, as it is based on the direct visualization and estimation of mechanical wave propagation. By estimating only two applanation pressures times at the single location of the air pulse on the cornea, the ORA cannot resolve the inverse problem of this shear wave propagation and recover direct estimates of physical biomechanical parameters such corneal elasticity or viscosity. Consequently, it provides a cornea hysteresis parameter that cannot be linked easily to stiffness. The same kind of limitation can be encountered for elasticity imaging in deep organs using the ultrasonic radiation force: it is extremely difficult to estimate the Young's modulus only from the knowledge of tissue displacement only at the location of the applied force (see [15, Eq. (22)]. Instead of imaging tissues displacement only at the force location, a 2-D mapping of tissue displacements allows recovering shear wave propagation parameters such as wave speed and consequently Young's modulus. Finally, contrary to transient displacements induced by ORA, tissue motion induced using the SSI modality corresponds to very small micrometric displacements (small perturbations) with typical millimetric wavelengths (transient pulsed perturbation with typical 1500 Hz frequency). For that reason, it should be less influenced than ORA by boundaries conditions such as tissue tension or intra-ocular pressure.

The clinical applicability of the SSI modality for the estimation of cornea elasticity requires ensuring that the acoustic power required for generating the radiation force remains below the FDA limits. This is possible as typical 10 μm local displacements can be generated without overtaking these limitations. Such displacements can be detected using ultrafast ultrasonic sequences that can track tissue displacement as small as 1 μm . Regarding practical *in vivo* applicability, a coupling liquid could easily be inserted in a cup between the eye and the ultrasonic probe. The complete elasticity investigation will not modify at all a conventional ultrasonic procedure in ophthalmology and will provide the biomechanical properties of cornea in addition to the ultrasonic images. Moreover, a detailed signal processing analysis of shear wave propagation enables accessing *in vivo* the complete mechanical behavior of the cornea on a very large bandwidth. Such dynamic mechanical spectroscopy of the cornea was up today only achievable using explanted human corneas [48] in the 0.1–100 Hz range. The SSI modality permits to achieve the shear wave spectroscopy [34] noninvasively and in real time.

For *in vivo* applications, the coupling liquid between the echographic probe and the cornea should probably not influence the cornea stiffness estimates. Indeed, it is well known that hydration by short corneal immersion induces very small changes *in vivo* in corneal thickness and shear compliance at least in the 0.1 mHz to 100 Hz [48]. Although shear wave spectroscopy provided by the SSI modality corresponds to a much higher frequency bandwidth, it seems that these results could be reasonably extrapolated to our mechanical frequency bandwidth. Such assumption will be carefully studied in further *in vivo* works. For *ex vivo* studies where hydration is known to play a role by increasing cornea thickness, it should be carefully studied whether only thickness is affected by hydration or both thickness and Young's modulus are changing. This is a nontrivial problem, as corneal thickness affects the mechanical wave speed. However, the quantitative method proposed in this paper should be able to discriminate the influence of hydration on both parameters.

In terms of resolution, very high-resolution maps were obtained in this study, as the elasticity mapping is only limited by the resolution of the echographic images. Thus, increasing the ultrasonic probe frequency up to 25 MHz could even lead to a 70 μm resolution of the cornea elasticity map provided by the SSI modality.

In this study, shear viscosity of cornea tissue was neglected. Such viscosity definitely also affects the dispersion curves of the mechanical guided wave in the cornea. The discrimination between the distinct influences of both the guided mode propagation and the shear viscous term onto the dispersion of the wave propagation should be studied in further works.

Finally, in this study, corneal tissues were assumed to be isotropic. This assumption is not totally valid. Indeed, the human cornea has the macroscopic structure of a thin shell, originated by the organization of collagen lamellae parallel to the middle surface of the shell. The lamellae, composed of bundles of collagen fibrils, are responsible for an experimentally observed anisotropy of the cornea. Smolek has shown that the mean interlamellar cohesive strength is diminished

in the inferior peripheral portion of the cornea compared to values obtained from the other principal meridians [49]. The mean cohesive strength in the central cornea was shown to be less than that of the superior periphery. However, Smolek concluded that the biomechanical significance of this deficit is probably minor if not irrelevant in the average, intact cornea under physiologically normal tensile loading, but may become significant in corneas with specific forms of degenerative disease or trauma that induces shearing strains between the lamellar sheets of the stroma.

Further work will concentrate on the influence of cornea elastic anisotropy on the shear wave propagation. The ability of the ultrasonic radiation force to polarize the generated shear waves in different orientations could help us to quantify at least an eventual radial anisotropy of cornea elasticity.

V. CONCLUSION

This initial investigation demonstrates the ability of ultrafast and high-resolution echographic systems to provide a real-time and quantitative mapping of corneal elasticity. Quantitative elasticity maps were acquired *ex vivo* on porcine cornea using the SSI technique. Quantitative maps of corneal elasticity were obtained in all fresh porcine eyes. A 190 kPa \pm 32 kPa mean elasticity was obtained for four different specimens. The SSI modality was found able to quantify the influence of photodynamic Riboflavin/UV-A induced CXL on corneal stiffness. A significant Young's modulus increase was obtained with a mean 890 kPa \pm 250 kPa posttreatment Young's modulus (\sim 460% increase). Simulations based on 3-D time domain finite differences simulation were also performed and found to be in good agreement with *in vitro* experiments. The Supersonic Shear Imaging technique can perform real-time, very high-resolution, and quantitative maps of corneal elasticity. This technique can be real time and straightforward adapted for *in vivo* investigations. Further works will study the influence of intra-ocular pressure on corneal elasticity and present first clinical investigations of the SSI modality in ophthalmology.

ACKNOWLEDGMENT

The authors would like to thank Y. Zaitsev for technical assistance.

REFERENCES

- [1] B. S. Garra, I. Cespedes, J. Ophir, S. Pratt, R. Zaubier, C. M. Magnat, and M. F. Pennanen, "Elastography of breast lesions: Initial clinical results, breast imaging," *Radiology*, vol. 202, pp. 79–86, 2002.
- [2] M. Tanter, J. Bercoff, A. Athanasiou, T. Defieux, J. L. Gennisson, G. Montaldo, M. Muller, A. Tardivon, and M. Fink, "Quantitative assessment of breast lesion viscoelasticity: Initial clinical results using supersonic shear imaging," *Ultrasound Med. Biol.*, vol. 34, no. 9, pp. 1373–1386, Sep. 2008.
- [3] L. Sandrin, B. Fourquet, J. M. Hasquenoph, S. Yon, C. Fournier, F. Mal, C. Christidis, M. Ziolo, B. Poulet, F. Kazemi, M. Beauprand, and R. Palau, "Transient elastography: A new non-invasive method for assessment of hepatic fibrosis," *Ultrasound Med. Biol.*, vol. 29, pp. 1705–1713, 2003.
- [4] M. Ziolo, A. Handra-Luca, A. Kettaneh, C. Christidis, F. Mal, F. Kazemi, V. de Lédinghen, P. Marcellin, D. Dhumeaux, J. C. Trinchet, and M. Beauprand, "Noninvasive assessment of liver fibrosis by measurement of stiffness in patients with chronic hepatitis C," *Hepatology*, vol. 41, pp. 48–54, 2005.
- [5] M. Friedrich-Rust, M. F. Ong, E. Herrman, V. Dries, P. Samaras, S. Zeuzem, and C. Sarrazin, "Real-time elastography for noninvasive assessment of liver fibrosis in chronic viral hepatitis," *Am. J. Roentgenol.*, vol. 188, pp. 758–764, 2007.
- [6] C. L. De Korte, G. Pasterkamp, A. F. W. van der Steen, H. A. Woutman, and N. Bom, "Characterization of plaque components with intravascular ultrasound elastography in human femoral and coronary arteries *in vitro*," *Circulation*, vol. 102, no. 6, pp. 617–623, Aug. 2000.
- [7] C. L. De Korte, A. F. W. van der Steen, E. I. Cespedes, and G. Pasterkamp, "Intravascular ultrasound elastography in human arteries: Initial experience *in vitro*," *Ultr. Med. Biol.*, vol. 24, no. 3, pp. 401–408, Mar. 1998.
- [8] M. Kowalski, T. Kukulski, F. Jamal, J. D'Hooge, F. Weidemann, F. Rademakers, B. Bijmens, L. Hatle, and G. R. Sutherland, "Can natural strain and strain rate quantify regional myocardial deformation? A study in healthy subjects," *Ultrasound Med. Biol.*, vol. 27, no. 8, pp. 1087–1097, Aug. 2001.
- [9] E. E. Konofagou, J. D'Hooge, and J. Ophir, "Myocardial elastography—A feasibility study *in vivo*," *Ultrasound Med. Biol.*, vol. 28, no. 4, pp. 475–482, 2002.
- [10] J. Bercoff, M. Pernot, M. Tanter, and M. Fink, "Monitoring thermally-induced lesions with supersonic shear imaging," *Ultrason. Imag.*, vol. 26, no. 2, pp. 71–84, Apr. 2004.
- [11] M. Tanter, J. Bercoff, L. Sandrin, and M. Fink, "Ultrafast compound imaging for 2D motion vector estimation: Application to transient elastography," *IEEE Trans. Ultrason., Ferroelect., Freq. Contr.*, vol. 49, no. 10, pp. 1363–1374, Oct. 2002.
- [12] J. Bercoff, S. Chaffi, M. Tanter, L. Sandrin, S. Catheline, M. Fink, J.-L. Gennisson, and M. Meunier, "In vivo breast tumors detection using transient elastography," *Ultrasound Med. Biol.*, vol. 29, no. 10, pp. 1387–1296, 2003.
- [13] J. Bercoff, M. Tanter, and M. Fink, "Sonic boom in soft materials: The elastic Cerenkov effect," *Appl. Phys. Lett.*, vol. 84, no. 12, pp. 2202–2204, 2004.
- [14] J. Bercoff, M. Tanter, and M. Fink, "Supersonic shear imaging: A new technique for soft tissues elasticity mapping," *IEEE Trans. Ultrason., Ferroelect., Freq. Contr.*, vol. 51, no. 4, pp. 396–409, Apr. 2004.
- [15] A. P. Sarvazyan, O. V. Rudenko, S. D. Swanson, J. B. Fowlkes, and S. Y. Emelianov, "Shear wave elasticity imaging—A new ultrasonic technology of medical diagnostic," *Ultrasound Med. Biol.*, vol. 20, pp. 1419–1436, 1998.
- [16] M. Muller, J.-L. Gennisson, T. Defieux, M. Tanter, and M. Fink, "Quantitative mapping of human liver using supersonic shear imaging: Preliminary *in vivo* feasibility study," *Ultrasound Med. Biol.*, vol. 35, no. 2, pp. 219–229, 2009.
- [17] T. Defieux, J. L. Gennisson, M. Tanter, and M. Fink, "Assessment of the mechanical properties of the musculoskeletal system using 2-D and 3-D very high frame rate ultrasound," *IEEE Trans. Ultrason., Ferroelect., Freq. Contr.*, vol. 55, no. 10, pp. 2177–2190, Oct. 2008.
- [18] K. W. Hollman, S. Y. Emelianov, J. H. Neiss, G. Joty, G. J. R. Spooner, T. Juhasz, R. M. Kurtz, and M. O'Donnell, "Strain imaging of corneal tissue with an ultrasound elasticity microscope," *Cornea*, vol. 21, no. 1, pp. 68–73, 2002.
- [19] T. Juhasz *et al.*, "Corneal refractive surgery with femtosecond lasers," *IEEE J. Sel. Topics Quant.*, vol. 5, no. 4, pp. 902–910, Jul./Aug. 1999.
- [20] T. Juhasz *et al.*, "Applications of femtosecond lasers in corneal surgery," *Laser Phys.*, vol. 10, pp. 495–500, 2000.
- [21] E. Spoerl, G. Wollensak, and T. Seiler, "Increased resistance of crosslinked cornea against enzymatic digestion," *Curr. Eye Res.*, vol. 29, no. 1, pp. 35–40, Jul. 2004.
- [22] I. F. Comaish and M. A. Lawless, "Progressive post-LASIK keratectasia: Biomechanical instability or chronic disease process?," *J. Cataract Refract. Surg.*, vol. 28, pp. 2206–2213, 2002.
- [23] W. J. Dupps, Jr., "Biomechanical modeling of corneal ectasia," *J. Refract. Surg.*, vol. 21, pp. 186–190, 2005.
- [24] J. S. Friedenwald, "Contribution to the theory and practice of tonometry," *Am. J. Ophthalmol.*, vol. 20, pp. 985–1024, 1937.
- [25] J. Liu and C. J. Roberts, "Influence of corneal biomechanical properties on intraocular pressure measurement: Quantitative analysis," *J. Cataract Refract. Surg.*, vol. 31, pp. 146–155, 2005.
- [26] L. T. Nordan, "Keratoconus: Diagnosis and treatment," *Int. Ophthalmol. Clin.*, vol. 37, no. 1, pp. 51–63, 1997.
- [27] P. S. Binder, "Analysis of ectasia after laser *in situ* keratomileusis: Risk factors," *J. Cataract Refract. Surg.*, vol. 33, no. 9, pp. 1530–1538, Sep. 2007.

- [28] A. Elsheikh, D. Wang, and D. Pye, "Determination of the modulus of elasticity of the human cornea," *J. Refract. Surg.*, vol. 23, no. 8, pp. 808–818, Oct. 2007.
- [29] J. Ophir, I. Céspedes, H. Ponnekanti, Y. Yasdi, and X. Li, "Elastography: A quantitative method for imaging the elasticity of biological tissues," *Ultrason. Imag.*, vol. 13, pp. 111–134, 1991.
- [30] W. J. Dupps, Jr., M. Netto, S. Herekar, and R. R. Krueger, "Surface wave elastometry of the cornea in porcine and human donor eyes," *J. Refract. Surg.*, vol. 23, no. 1, pp. 66–75, Jan. 2007.
- [31] G. Orsengo and D. Pye, "Determination of the true intraocular pressure and modulus of elasticity of the human cornea in vivo," *Bull. Math. Biol.*, vol. 61, pp. 551–572, 1999.
- [32] J. Bercoff, M. Tanter, M. Muller, and M. Fink, "The role of viscosity in the impulse diffraction field of elastic waves induced by the acoustic radiation force," *IEEE Trans. Ultrason., Ferroelect., Freq. Contr.*, vol. 51, no. 11, pp. 1523–1536, Nov. 2004.
- [33] Information for manufacturers seeking marketing clearance of diagnostic ultrasound system and transducers Food Drug Admin., 1997 [Online]. Available: <http://www.fda.gov/cdrh/ode/ulstran.pdf>
- [34] T. Defieux, G. Montaldo, M. Tanter, and M. Fink, "Shear wave spectroscopy for quantification of human soft tissues visco-elasticity," *IEEE Trans. Med. Imag.*, vol. 28, no. 3, pp. 313–322, Mar. 2009.
- [35] J. Virieux, "P-SV wave propagation in heterogeneous media: Velocity-stress finite-difference method," *Geophys.*, vol. 51, no. 4, pp. 889–901, Apr. 1986.
- [36] J. P. Berenger, "A perfectly matched layer for the absorption of electromagnetic waves," *J. Comp. Phys.*, vol. 114, pp. 185–200, Oct. 1994.
- [37] H. Wang, P. L. Prendiville, P. J. McDonnell, and W. V. Chang, "An ultrasonic technique for the measurement of the elastic moduli of human cornea," *Nature*, vol. 284, pp. 489–491, Apr. 1980.
- [38] G. Wollensak, E. Spoerl, and T. Seiler, "Stress-strain measurements of human and porcine corneas after riboflavin-ultraviolet-A-induced cross-linking," *J. Cataract Refract. Surg.*, vol. 29, no. 9, pp. 1780–1785, Sep. 2003.
- [39] C. Wittig-Silva, M. Whiting, E. Lamoureux, R. G. Lindsay, L. J. Sullivan, and G. R. Snibson, "A randomized controlled trial of corneal collagen cross-linking in progressive keratoconus: Preliminary results," *J. Refract. Surg.*, vol. 24, no. 7, pp. S720–S725, Sep. 2008.
- [40] G. Kymionis and D. Portaliou, "Corneal crosslinking with riboflavin and UVA for the treatment of keratoconus," *J. Cataract Refract. Surg.*, vol. 32, no. 5, pp. 837–845, May 2006.
- [41] H. Lamb, "On waves in an elastic plate," *Proc. R. Soc. Lond. A*, vol. 93, pp. 114–128, 1917.
- [42] P. V. Krauklis and L. A. Molotkov, "Low-frequency Lamb waves in cylindrical and spherical layers in an elastic medium," *J. Math. Sci.*, vol. 3, pp. 82–90, Jan. 1975.
- [43] D. Royer and E. Dieulesaint, *Elastic Waves in Solid*. Berlin, Germany: Springer-Verlag, 1996, vol. 1.
- [44] M. Couade, M. Pernot, Carmen, M. Fink, and M. Tanter, Assessment of transient dynamics of arterial wall elasticity during a single cardiac cycle: Ultrafast imaging of natural pulse and acoustic radiation force induced mechanical waves in the arterial wall.
- [45] G. Wollensak and E. Spoerl, "Collagen crosslinking of human and porcine sclera," *J. Cataract Refract. Surg.*, vol. 30, no. 3, pp. 689–695, Mar. 2004.
- [46] M. Kohlhaas, E. Spoerl, T. Schilde, G. Unger, C. Wittig, and L. E. Pillunat, "Biomechanical evidence of the distribution of cross-links in corneas treated with riboflavin and ultraviolet a light," *J. Cataract Refract. Surg.*, vol. 32, no. 2, pp. 279–283, Feb. 2006.
- [47] S. Shah, M. Laiqzaman, R. Bhojwani, S. Mantry, and I. Cunliffe, "Assessment of the biomechanical properties of the cornea with the ocular response analyzer in normal and keratoconic eyes," *Invest. Ophthalmol. Vis. Sci.*, vol. 48, no. 7, pp. 3026–3031, Jul. 2007.
- [48] F. Soergel, B. Jean, T. Seiler, T. Bende, S. Mücke, W. Pechhold, and L. Pels, "Dynamic mechanical spectroscopy of the cornea for measurement of its viscoelastic properties in vitro," *Ger. J. Ophthalmol.*, vol. 4, no. 3, pp. 151–156, May 1995.
- [49] M. Smolek, "Interlamellar cohesive strength in the vertical meridian of human eye bank corneas," *Invest. Ophthalmol. Vis. Sci.*, vol. 34, no. 10, Sep. 1993.

Breast Lesions: Quantitative Elastography with Supersonic Shear Imaging—Preliminary Results¹

Alexandra Athanasiou, MD
Anne Tardivon, MD
Mickael Tanter, PhD
Brigitte Sigal-Zafrani, MD
Jeremy Bercoff, PhD
Thomas Deffieux, PhD
Jean-Luc Gennisson, PhD
Mathias Fink, PhD
Sylvia Neuenschwander, MD

Purpose:

To determine the appearance of breast lesions at quantitative ultrasonographic (US) elastography by using supersonic shear imaging (SSI) and to assess the correlation between quantitative values of lesion stiffness and pathologic results, which were used as the reference standard.

Materials and Methods:

This study was approved by the French National Committee for the Protection of Patients Participating in Biomedical Research Programs. All patients provided written informed consent. Conventional US and SSI quantitative elastography were performed in 46 women (mean age, 57.6 years; age range, 38–71 years) with 48 breast lesions (28 benign, 20 malignant; mean size, 14.7 mm); pathologic results were available in all cases. Quantitative lesion elasticity was measured in terms of the Young modulus (in kilopascals). Sensitivity, specificity, and area under the curve were obtained by using a receiver operating characteristic curve analysis to assess diagnostic performance.

Results:

All breast lesions were detected at SSI. Malignant lesions exhibited a mean elasticity value of $146.6 \text{ kPa} \pm 40.05$ (standard deviation), whereas benign ones had an elasticity value of $45.3 \text{ kPa} \pm 41.1$ ($P < .001$). Complicated cysts were differentiated from solid lesions because they had elasticity values of 0 kPa (no signal was retrieved from liquid areas).

Conclusion:

SSI provides quantitative elasticity measurements, thus adding complementary information that potentially could help in breast lesion characterization with B-mode US.

© RSNA, 2010

¹ From the Departments of Radiology (A.A., A.T., S.N.) and Tumor Biology (B.S.), Institut Curie, 26 rue d'Ulm, 752048 Paris Cedex 05, France; Laboratoire Ondes et Acoustique, Centre National de Recherche Scientifique, Unité Mixte de Recherche 7587, Ecole Supérieure de Physique et Chimie Industrielle, Paris, France (M.T., T.D., J.L.G., M.F.); and SuperSonic Imagine, Aix-en-Provence, France (J.B.). Received March 3, 2009; revision requested April 13; final revision received August 14; accepted September 4; final version accepted February 3, 2010. Address correspondence to A.A. (e-mail: alexandra.athanasiou@curie.net).

© RSNA, 2010

Palpation is a standard medical practice relying on qualitative estimation of tissue Young modulus $E = \sigma/\epsilon$, where σ is the external compression (stress) and ϵ is the deformation of the tissue because of this compression (strain). Generally, benign lesions tend to be harder than normal breast tissue but softer than cancers (1). Exceptions can occur, but soft malignant lesions, including medullary, mucinous, papillary, and some necrotic infiltrating ductal carcinomas, are uncommon (2). On the other hand, some benign lesions, such as hyalinized fibroadenomas and fat necrosis, can be hard at palpation. At B-mode ultrasonography (US), there is no correlation between the lesion's echo pattern and the Young modulus; hard and soft lesions may exhibit similar echogenicity. Elastography has emerged as a promising technique for improving lesion differentiation. It can be used to estimate breast tissue elasticity by measuring tissue strain or tissue displacement during sonologist-induced mechanical excitation (3). The principle applied is that strain will be less in harder tissue. Some currently available US systems include a strain imaging software package: strain images, usually color coded, are displayed in real time as the user applies light compression on breast tissue with the transducer. With freehand compression, the influence of probe

movement has certain disadvantages: the elasticity map obtained is highly dependent on the organ's compressibility limits under stress and on the extent of tissue compression applied. The displayed information is about local strain estimated at a given location in tissues, but it depends on surrounding mechanical properties and it is not quantitative. Despite these caveats, the value of this technique in the evaluation of breast lesions already has been reported (4–8).

To overcome this problem, we developed a quantitative elastography technique, supersonic shear imaging (SSI), that combines two concepts. Instead of using mechanical external compression, the system itself remotely induces mechanical vibration by using acoustic radiation force created by a focused ultrasound beam. A very fast (5000 frames per second) US acquisition sequence is used to capture the propagation of shear waves. Both steps are performed by using the same conventional US probe (9–12). The displacement induced at the focus (for example, a breast lesion) generates a shear wave that conveys information linked to the local viscoelastic properties of the tissue, thus enabling a quantitative approach to elasticity values. The shear wave speed v is linked with shear modulus μ by the equation $\mu = \rho v^2$, where ρ is the local density (constant and equal to 1000 $\text{kg} \cdot \text{m}^{-3}$ in soft tissues). In soft tissues, local stiffness is described by the Young modulus E and can be approximated by $E \approx 3\mu$ (13). With imaging in real time, the propagation of the shear wave enables the recovery of local shear wave

speed and, consequently, the mapping of local tissue stiffness. Our purpose was to determine the appearance of breast lesions at quantitative US elastography by using SSI and to assess the correlation between quantitative values of lesion stiffness and pathologic results, which were used as the reference standard.

Materials and Methods

The patent holder for this technique is Laboratoire Ondes et Acoustique, Ecole Supérieure de Physique et Chimie Industrielle (Paris, France), where M.T., T.D., J.L.G., and M.F. are employees. M.T. is a cofounder of and shareholder in, J.B. is a founder of, and M.F. is a shareholder in and scientific adviser to SuperSonic Imagine (Aix-en-Provence, France), which provided the equipment and the technical support for the study (programming of US sequences and data postprocessing). Data were controlled by authors (A.A. and A.T.) who do not have any financial interest.

Patients

This study was approved by the French National Committee for the Protection of Patients Participating in Biomedical Research Programs. All patients provided written informed consent. We performed SSI in 62 consecutive women with mammographically occult lesions seen only at US who were referred to the Curie Institute (Paris,

Advances in Knowledge

- Supersonic shear imaging (SSI) elastography can improve differentiation of solid from atypical B-mode cystic breast lesions (manifesting as hypoechoic lesions) because no signal is retrieved from liquid areas (atypical cyst elasticity value, 0 kPa).
- No external mechanical compression is needed with SSI elastography, which is based on the mechanical excitation that interrogates breast tissue mechanical properties by means of remote palpation induced by the radiation force of ultrasound beams transmitted by a conventional US probe.

Implications for Patient Care

- The addition of the elasticity parameter in the overall Breast Imaging Reporting and Data System classification potentially could improve the specificity of breast US.
- The detection of cystic lesions potentially could reduce the number of fine-needle aspiration biopsies performed for proteinaceous or hemorrhagic cysts that have an atypical B-mode appearance.

Published online before print

10.1148/radiol.10090385

Radiology 2010; 256:297–303

Abbreviations:

BI-RADS = Breast Imaging Reporting and Data System
SSI = supersonic shear imaging

Author contributions:

Guarantors of integrity of entire study, A.A., J.L.G.; study concepts/study design or data acquisition or data analysis/interpretation, all authors; manuscript drafting or manuscript revision for important intellectual content, all authors; manuscript final version approval, all authors; literature research, A.A., M.T., B.S., T.D., J.L.G., M.F., S.N.; clinical studies, A.A., A.T., M.T., B.S., J.B., T.D., J.L.G.; statistical analysis, M.T., J.L.G.; and manuscript editing, A.A., A.T., M.T., B.S., J.B., J.L.G., S.N.

See Materials and Methods for pertinent disclosures.

France) between September 2006 and March 2007 for evaluation and percutaneous procedures. Twelve patients were excluded because of technical hardware problems during SSI acquisition; the prototype power supply encountered a stability problem, and no raw US data were acquired for these patients. Four patients refused to undergo a percutaneous interventional procedure and were excluded because of lack of pathologic result. Final analysis was based on data in 46 patients (mean age, 57.6 years; age range, 38–71 years) who had 48 nonpalpable breast lesions (7–16 mm; mean size, $14.7 \text{ mm} \pm 1.3$ [standard deviation]) detected at US. Six lesions were classified as Breast Imaging Reporting and Data System (BI-RADS) 3; 28 lesions, as BI-RADS 4; and 14 lesions, as BI-RADS 5. Percutaneous procedures for BI-RADS 3 lesions were performed in patients at high risk.

Imaging Workflow

Lesions were depicted at B-mode US by using the hospital US system (Aplio XG, model SSA-790 A; Toshiba Medical Systems Europe, Zoetermeer, the Netherlands) equipped with a 12-MHz probe. Patients originally underwent scanning performed together by A.A. and A.T. (radiologists specialized in breast imaging, with 8 and 15 years of experience, respectively) for clinical indications. Mammograms were available in all cases, but lesions were mammographically occult because of either small size or dense breast parenchyma. Lesion location, size, echo pattern, and BI-RADS classification (14) were noted. The BI-RADS score was recorded by means of consensus by A.A. and A.T.

SSI sequences were performed by using a modified system (ATL HDI 1000; Philips Medical Systems, Best, the Netherlands) with a linear array (L7-4; Philips Medical Systems). The system was reprogrammed to provide, in addition to its standard capabilities, a special SSI acquisition mode by means of button activation. All safety considerations were satisfied according to the U.S. Food and Drug Administration (15). The highest values recorded for our prototype were as follows: mechanical index, 1.4

(<1.9); spatial-peak temporal-average intensity, 603 mW/cm^2 (< 720 mW/cm^2); and thermal index, 0.48 (<6). Spatial-peak temporal-average intensity and thermal index were calculated by assuming a 1-Hz SSI frame rate, which was much lower in practice because two successive acquisitions were launched with a pause of 5 to 10 seconds.

The radiologist (A.A., A.T.) performing the SSI first obtained B-mode images that were saved on the system hard drive (36×44 -mm rectangular window). For each lesion, two SSI sequences were performed; each sequence comprised three successive pushing beams. During the first sequence, the radiologist located the lesion in the center of the screen. The first pushing beam was centered along the central axis of the lesion; the second, on the right side of the lesion; and the third, on the left side of the lesion. Each pushing beam lasted about 3 seconds, and three pushing beams were necessary to produce a full elastography image (12). During the second SSI sequence, the radiologist located the lesion on the left or the right side of the screen to have both the lesion and surrounding parenchyma on the screen; the three pushing beams were used to obtain a full elastography image of both the lesion and the parenchyma.

The total time of the SSI examination was less than 5 minutes. Examination results were transferred to an off-line computer by using an Ethernet cable limited to a 1 Mb/sec transfer rate and were processed with dedicated elastography software. Postprocessing time was 5 seconds for each quantitative elasticity image. The accuracy of SSI values was compared previously with calibrated phantoms in other studies ($\pm 8\%$ error margin) (16). US-guided procedures were then performed during the same session by using the hospital US system.

Elastography Sequence and Data Processing

Each SSI sequence corresponded to the generation of a vibration force by means of successively focusing ultrasound beams at five different depths. Each pushing focused beam consisted

of a 150- μsec burst at 5 MHz. Successive focusing depths were separated by 5 mm, making the pushing line 30 mm long. This supersonic source generated plane shear waves that propagated transversally in tissue in a few tens of milliseconds. These shear waves were imaged by means of a very fast imaging sequence; 60 flat insonications (5-MHz burst of 1 μsec) were performed at a 4000-Hz pulse repetition frequency. Raw radiofrequency data corresponding to back-scattered echoes were recorded and stored. The imaging sequence provided a US video of the tissue during shear wave propagation. On the basis of this video, displacements induced by the shear wave in tissues were calculated by comparing US frames by using classic speckle-tracking algorithms. Shear wave propagation speed then was deduced locally by using a one-dimensional cross-correlation algorithm to estimate the time shift between the two temporal displacement signals separated by 1 mm. Finally, the local Young modulus E was deduced.

Elasticity maps deduced from each of three acquisitions, corresponding to three different pushing lines, were then merged to compute the final elasticity map that covered the entire width of the US image. The result was displayed on a color scale ranging from 0 to 240 kPa; the corresponding shear wave speed thus roughly ranged from 0 to 8 m/sec. Spatial resolution was 1 mm^2 .

Data Analysis

Lesion dimensions were measured by using calipers on recorded B-mode US images obtained with the hospital system and SSI postacquisition images. Two quantitative elasticity values were extracted, the first corresponding to the elasticity value of the lesion and the second to the elasticity value of normal tissue. Two 3×3 -mm boxes were positioned, one box in the lesion area at the location of maximum stiffness and one in normal-appearing tissue (glandular and fatty tissue, which was distinguished by its lobular form, compressibility, and low echogenicity), by A.A. and A.T. together. Cystic lesions were

not used for the estimation of average values because cysts do not have a stiffness value ($E = 0$ kPa). The whole procedure lasted about 5 minutes.

Pathologic Examination

Twenty-eight lesions were benign at percutaneous US-guided biopsy ($n = 16$) or fine-needle aspiration ($n = 12$) (Table); no further surgery was performed except in one lesion that corresponded to a grade I phyllodes tumor. Seven lesions corresponded to cysts (four had a proteinaceous or hemorrhagic component). Twenty lesions were malignant at biopsy, and further surgical excision was performed. Final histologic diagnosis and tumor grade were defined by using the surgical specimen. All diagnoses were made by a pathologist (B.S., with 18 years of experience in breast pathologic examination).

Statistical Analysis

The role of elasticity values in discriminating malignant from benign lesions was studied by using a nonparametric Mann-Whitney test. Receiver operating characteristic curves were used to compare the performance of estimators corresponding to the established BI-RADS variable and to a modified BI-RADS variable taking into account the lesion's mean Young modulus E , named β . Because the elasticity parameter is not envisioned as a stand-alone parameter but rather as an added value to US examination, the combination of the BI-RADS score with the Young modulus variable E was estimated. The distribution of E was rescaled, shifted to the interval $(-1, +1)$, and added linearly to the BI-RADS score. The rescaling process was based on the following equation: $\beta = \text{BI-RADS} + 2E/E_{\max} - 1$, where β stands for the combined parameter BI-RADS + elasticity, which allows the SSI elasticity value to change the BI-RADS score by at most ± 1 unit. To shift elasticity to the interval $[-1, +1]$, we normalized each lesion elasticity value by comparing it to the maximum elasticity found during SSI imaging in the entire study population, defined as E_{\max} . The elasticity value (E) was measured for each lesion and was then normalized by a factor of 2 ($2E/E_{\max}$).

Final Pathologic Diagnosis in 48 Breast Lesions

Pathologic Diagnosis	No. of Lesions
Malignant lesions ($n = 20$)	
Infiltrating ductal carcinoma grade I	3
Infiltrating ductal carcinoma grade II	9*
Infiltrating ductal carcinoma grade III	5
Infiltrating lobular carcinoma grade III	2
Infiltrating mixed ductal and lobular carcinoma	1
Benign lesions ($n = 28$)	
Fibroadenoma	8
Aberrations of normal development and involution	9
Cyst	7
Benign grade I phyllodes tumor	1
Fat necrosis	2
Intramammary lymph node	1

* Includes one lesion with extensive intraductal component.

Then, -1 was added to the normalized score ($2E/E_{\max} - 1$). Any value lower than $E_{\max}/2$ would be given a score of -1 , and any value higher than the mean would be given a score of $+1$. Only values exactly equal to $E_{\max}/2$ would be given a score of 0 . The value calculated was added to the BI-RADS score, thus modifying the BI-RADS score by 0 , -1 , or $+1$.

Areas under the curve were compared by using a Hanley and McNeil test (17). Sensitivity and specificity values and their respective 95% confidence intervals were estimated. $P < .05$ was considered to indicate a statistically significant difference. All data were analyzed by using software (MedCalc version 9.4.2.0; MedCalc Software, Mariakerke, Belgium).

Results

Normal Breast Tissue and Breast Cysts

Quantitative elasticity values in normal breast tissue clearly delineated the different structures. Fatty tissues displayed low values of elasticity (E , approximately 7 kPa), whereas breast parenchyma values ranged from 30 to 50 kPa (Fig 1). All breast cysts had elastography values of 0 (Fig 2).

Solid Lesions

Benign lesions had a mean elasticity value of $45.3 \text{ kPa} \pm 41.1$, whereas

malignant lesions demonstrated mean values of $146.6 \text{ kPa} \pm 40.05$ ($P < .001$) (Figs 3, 4).

Mean values of the new variable β were then compared by using the Mann-Whitney test, and they were also different ($P < .001$). The discriminating power for detection of malignancy of the variable β was significantly higher than that of the BI-RADS score alone, with an area under the receiver operating characteristic curve of 0.985 ± 0.01 (95% confidence interval: 0.884, 0.995) compared with the BI-RADS score area under the receiver operating characteristic curve of 0.917 ± 0.046 (95% confidence interval: 0.764, 0.968; $P < .05$) (Fig 5).

Comparison between receiver operating characteristic curves with a Hanley and McNeil test for BI-RADS and β gave a difference of 0.068 ± 0.033 ($P = .039$). The most important effect of the new variable β was for BI-RADS 4 lesions ($n = 28$). Adding the elasticity score modified the BI-RADS 4 score to BI-RADS 3 for 13 lesions, meaning that we could have avoided performing biopsy in 46% of cases and had a short 6-month follow-up instead. Nine of 28 BI-RADS 4 cases remained at the same score after the elasticity value was added, and six cases were recategorized as BI-RADS 5. No cancers were missed during this modification of BI-RADS score. The specificity of β

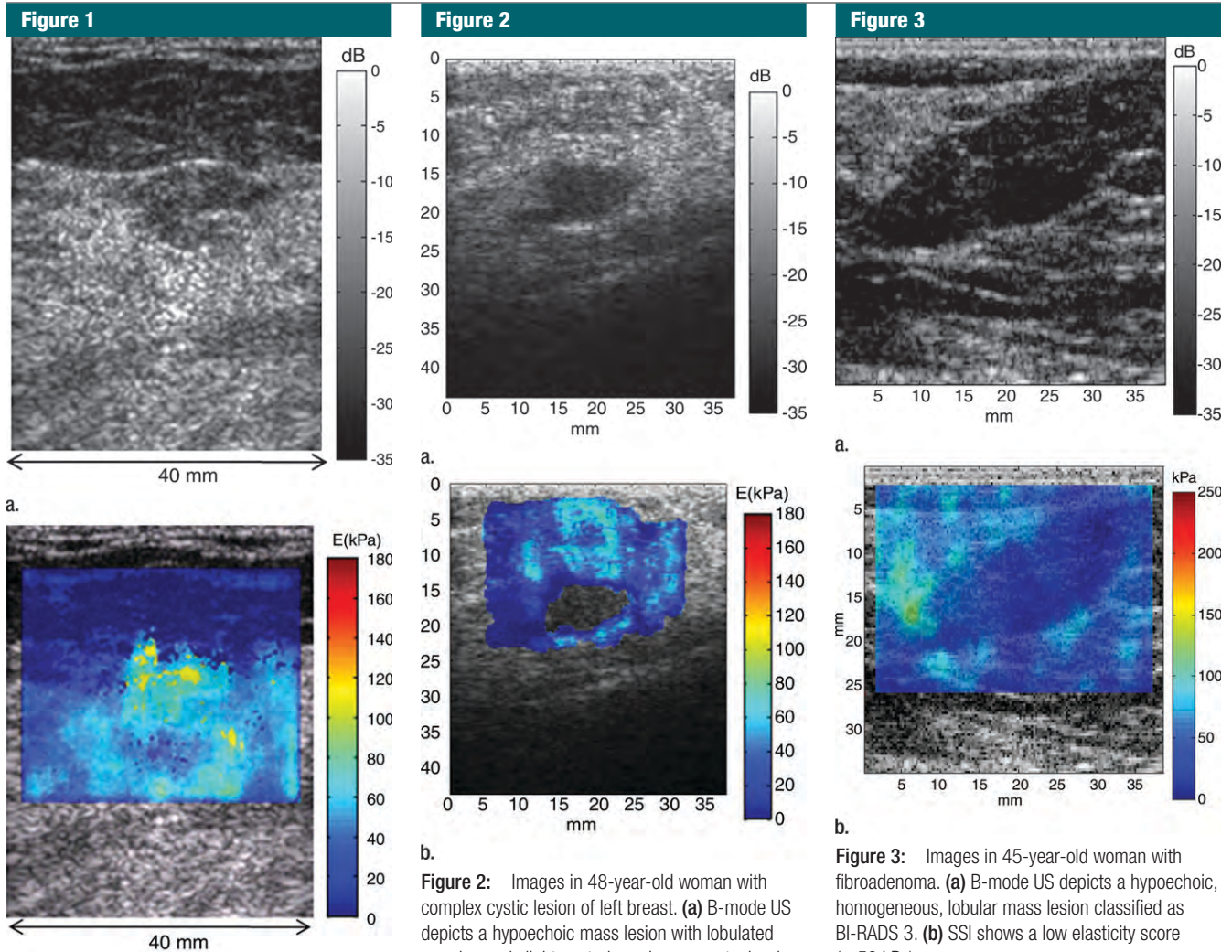


Figure 1: Normal breast tissue in 52-year-old woman. **(a)** B-mode US does not depict any particular lesion. **(b)** Elasticity map obtained by using SSI. The shear wave speed is coded on a color scale ranging from 0 to 8 m/sec, corresponding to a Young modulus ranging between 0 and 192 kPa. The elasticity map exhibits the delineation between soft fatty tissues (E , approximately 7 kPa) and breast parenchyma (E , approximately 30–50 kPa).

was 0.96, and the sensitivity was 0.95, whereas the specificity and sensitivity of the BI-RADS score were 0.63 and 0.96, respectively. No modification was noted in the BI-RADS 3 category. Only one BI-RADS 5 lesion was reduced to BI-RADS 4 according to the variable β , but, in practice, the therapeutic decision remained unchanged because

Figure 2: Images in 48-year-old woman with complex cystic lesion of left breast. **(a)** B-mode US depicts a hypoechoic mass lesion with lobulated margins and slight posterior enhancement, classified as BI-RADS 4. **(b)** SSI shows no elasticity value for this lesion. Fine-needle aspiration was performed with US guidance, and a yellow liquid was evacuated. Final diagnosis was a cyst containing inflammatory cells and debris.

biopsy is also recommended for BI-RADS 4 lesions.

Discussion

Breast lesion detection and characterization at B-mode US is based mainly on specific description criteria defined by the American College of Radiology in the BI-RADS lexicon. For US descriptors, results of a prior study (18) showed that there is substantial agreement for lesion orientation, shape, and boundary ($\kappa = 0.61, 0.66, \text{ and } 0.69$, respectively), but

Figure 3: Images in 45-year-old woman with fibroadenoma. **(a)** B-mode US depicts a hypoechoic, homogeneous, lobular mass lesion classified as BI-RADS 3. **(b)** SSI shows a low elasticity score (<50 kPa).

for lesion margin and posterior acoustic features, the agreement is moderate ($\kappa = 0.40$ for both), and for lesion echo pattern, the agreement is poor ($\kappa = 0.29$). These description criteria often lead to false-positive findings and a number of unnecessary biopsies.

We have evaluated a quantitative elastography technique (ie, SSI) that could complement US examination in an efficient and easy-to-use way. The results of our preliminary work indicate that SSI was useful in demonstrating breast masses and characterizing cystic ones. This potential interesting application of SSI elastography relies on its capacity to reject cystic lesions, regardless of their typical or complicated B-mode US appearance, because of the

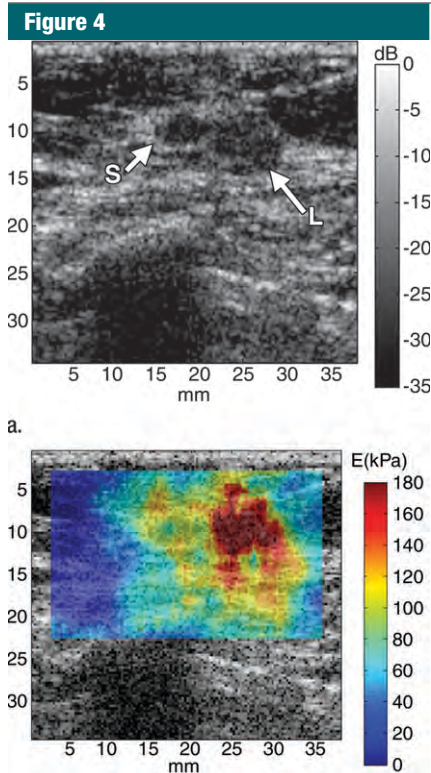


Figure 4: Images in 61-year-old woman already treated for breast cancer and referred because of suspicion of recurrence. **(a)** B-mode US depicts a 15-mm hypoechoic mass lesion (*L*) with irregular margins adjacent to the previous lumpectomy scar (*S*). This suspicious lesion was classified as BI-RADS 4. **(b)** SSI depicts a hard lesion ($E > 200$ kPa) highly suggestive of recurrence. The 90-kPa region on the left of this very stiff lesion corresponds to the scar. SSI depicted the two distinct neighboring zones of different elasticity (very stiff malignant lesion and moderately stiff scar). Biopsy results confirmed infiltrating ductal carcinoma.

absence of any shear wave propagation in liquid areas. During our preliminary study, no solid lesions presented a similar phenomenon of absence of shear wave propagation.

In solid, nonpalpable masses, quantitative elasticity may add potentially valuable information that could help radiologists better differentiate breast lesions. As already shown in the literature (8), less experienced radiologists, in particular, could be helped in their assessment by elasticity imaging. We believe that the SSI technique may have the potential to improve the decision about whether to

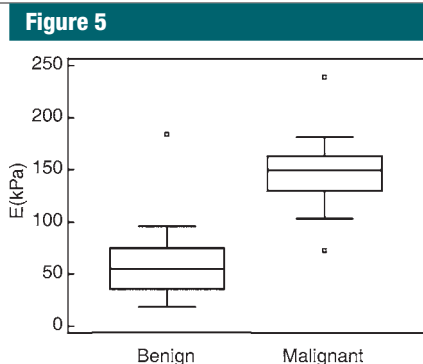


Figure 5: Box-and-whisker plot of Young modulus E estimated by using the SSI modality with respect to malignancy. According to the Mann-Whitney test, E values were significantly different between malignant and benign lesions ($P < .001$). Boxes = values from lower to upper quartiles, central lines = medians; whiskers extend from minimal to maximal values. Dots = outliers.

perform a percutaneous procedure such as biopsy or fine-needle aspiration.

From the user's perspective, one of the major differences of SSI compared with conventional elastography is that the mechanical vibration is induced automatically by the system by using the radiation force of ultrasound beams. The reliability of the imaging technique does not depend on the skills of the sonologist in correctly vibrating or stressing the tissue. The elasticity information is provided by using the same workflow and scanning conditions used for conventional B-mode US.

An interesting consequence is that the user does not need, as in conventional elastography, to subjectively or arbitrarily select one image in a complete image cine loop (7). With the SSI approach, a single set of successive US sequences provides a relevant elasticity image. Acquisition and postprocessing in our preliminary study on a dedicated research platform were limited by the slow transfer rate from electronics to personal computer boards and thus did not permit real-time elastography. However, no technologic issue prevents the SSI mode from providing elasticity images several times per second in the near future. In addition to conventional B-mode imaging, elasticity frame rates of three to four images per second are technologically feasible today.

The SSI approach also overcomes the intrinsic limitation of conventional elastography, which provides only qualitative and relative elasticity measurements. By providing local measurements of the true Young modulus of tissues across a wide stiffness range (from 1 to 240 kPa), SSI could be considered as a quantification tool for breast cancer diagnosis. Our results demonstrate that quantitative elasticity has clinical pertinence. The β variable, taking into account both the BI-RADS categorization and the Young modulus E , can ameliorate the overall diagnostic specificity (0.96 vs 0.63 for BI-RADS alone), whereas sensitivity remains high (0.95 vs 0.96 for BI-RADS alone). Larger clinical trials are necessary to validate these preliminary results.

Quantitative elasticity maps at SSI seem to allow finer assessment of tissue mechanical properties than does qualitative elastography by using external compression. At conventional elastography, the measured strain at one location depends on the surrounding tissues' mechanical properties. For example, a lesion having a softer center surrounded by a hard periphery would be impossible to detect because the whole lesion would move in a block under external stress. The local information provided by the SSI technique could lead to a much finer analysis of the spatial distribution and extension of tissue stiffness.

Our preliminary study had some limitations. All malignant lesions included in the study corresponded to infiltrating carcinomas, so we did not evaluate elasticity mapping in cases of ductal carcinoma in situ. Another limitation concerned the research platform used for SSI; our modified system was limited in terms of acquisition time, and B-mode images were substandard because of the 7.4-MHz array. This system was not capable of performing real-time SSI. Availability of real-time SSI quantitative elastography would be of great interest for evaluating mode robustness, reproducibility, and operator independence.

A major factor that remains to be understood is the effect of static

compression on the method. Human tissues have hardening properties; that is, their elasticity increases if static compression is applied. A study should be performed to quantify the influence of typical static compressions on the diagnostic value of the mode.

Our clinical investigation in 48 lesions showed that quantitative elasticity mapping of breast tissue is feasible in vivo by using the SSI method. Malignant lesions were significantly different from benign solid ones with regard to lesion elasticity quantitative value; because no shear wave propagation occurs in liquid areas, cystic lesions were diagnosed, regardless of their B-mode appearance. SSI could be a valuable complementary method for characterizing indeterminate breast lesions, thus obviating unnecessary biopsies. Large prospective trials are necessary to determine the role of SSI in a clinical setting.

Acknowledgments: The authors are grateful to Anne Badel, PhD, and Lilliane Ollvier, MD, for their essential contribution to this work.

References

1. Sewell CW. Pathology of benign and malignant breast disorders. *Radiol Clin North Am* 1995;33(6):1067-1080.
2. Tavassoli FA, Devilee P. Pathology and genetics: tumours of the breast and female genital organs. Lyon, France: IARC, 2003.
3. Garra BS, Cespedes EI, Ophir J, et al. Elastography of breast lesions: initial clinical results. *Radiology* 1997;202(1):79-86.
4. Hiltawsky KM, Krüger M, Starke C, Heuser L, Ermert H, Jensen A. Freehand ultrasound elastography of breast lesions: clinical results. *Ultrasound Med Biol* 2001;27(11):1461-1469.
5. Thomas A, Kümmel S, Fritzsche F, et al. Real-time sonoelastography performed in addition to B-mode ultrasound and mammography: improved differentiation of breast lesions? *Acad Radiol* 2006;13(12):1496-1504.
6. Itoh A, Ueno E, Tohno E, et al. Breast disease: clinical application of US elastography for diagnosis. *Radiology* 2006;239(2):341-350.
7. Burnside ES, Hall TJ, Sommer AM, et al. Differentiating benign from malignant solid breast masses with US strain imaging. *Radiology* 2007;245(2):401-410.
8. Scaperrotta G, Ferranti C, Costa C, et al. Role of sonoelastography in non-palpable breast lesions. *Eur Radiol* 2008;18(11):2381-2389.
9. Bercoff J, Tanter M, Fink M. Supersonic shear imaging: a new technique for soft tissue elasticity mapping. *IEEE Trans Ultrason Ferroelectr Freq Control* 2004;51(4):396-409.
10. Bercoff J, Tanter M, Muller M, Fink M. The role of viscosity in the impulse diffraction field of elastic waves induced by the acoustic radiation force. *IEEE Trans Ultrason Ferroelectr Freq Control* 2004;51(11):1523-1536.
11. Bercoff J, Chaffai S, Tanter M, et al. In vivo breast tumor detection using transient elastography. *Ultrasound Med Biol* 2003;29(10):1387-1396.
12. Tanter M, Bercoff J, Athanasίου A, et al. Quantitative assessment of breast lesion viscoelasticity: initial clinical results using supersonic shear imaging. *Ultrasound Med Biol* 2008;34(9):1373-1386.
13. Sarvazyan AP. Biophysical bases of elasticity imaging. In: *Acoustical imaging*. Vol 21. New York, NY: Plenum, 1995; 223-240.
14. American College of Radiology. *Ultrasound*. In: *Breast imaging reporting and data system (BI-RADS)*. 4th ed. Reston, Va: American College of Radiology, 2003.
15. U.S. Food and Drug Administration. Information for manufacturers seeking marketing clearance of diagnostic ultrasound system and transducers. <http://www.fda.gov/cdrh/ode/ulstran.pdf>. Published 1997. Accessed October 10, 2009.
16. Bercoff J, Criton A, Bacrie CC, et al. Shear-Wave™ Elastography: a new real time imaging mode for assessing quantitatively soft tissue viscoelasticity. *Proceedings of the 2008 IEEE International Ultrasonics Symposium*, Beijing, China, November 2-5, 2008.
17. Hanley JA, McNeil BJ. A method of comparing the areas under receiver operating characteristic curves derived from the same cases. *Radiology* 1983;148(3):839-843.
18. Lazarus E, Mainiero MB, Schepps B, Koelliker SL, Livingston LS. BI-RADS lexicon for US and mammography: interobserver variability and positive predictive value. *Radiology* 2006;239(2):385-391.